In-Situ Sampling and Spatially Resolved Measuring Approaches for Optical Surface Exposure Dating for Late Quaternary Applications

Tristan Graham Bench

A dissertation

submitted in partial fulfillment of the

requirements for the degree of

Doctor of Philosophy

University of Washington

2024

Reading Committee:

John O. Stone, Chair

James K. Feathers

Terry W. Swanson

Program Authorized to Offer Degree:

Earth and Space Sciences

University of Washington

Abstract

In-Situ Sampling and Spatially Resolved Measuring Approaches for Optical Surface Exposure Dating for Late Quaternary Applications

Tristan Graham Bench

Chair of the Supervisory Committee:

John O. Stone

Department of Earth and Space Sciences

Optically stimulated luminescence (OSL) exposure dating utilizes OSL-at-depth signals to extrapolate an exposure age from rock surfaces. Exposure ages are commonly obtained by fitting the forms of luminescence depth profiles, which depend on parameter estimates of light attenuation and defined rates of luminescence bleaching. Current procedures for obtaining these parameters for a rock surface require matching luminescence depth profiles from compositionally and morphologically matched rock surfaces with known exposure ages, which limits the accuracy and applicability of the technique. Further, traditional measuring procedures for depth profiles involve measuring the OSL of millimeter slices from surface core samples, offering poor resolution datasets and limiting parameter and age fitting accuracies.

With the aim of improving the accuracy and applicability of OSL surface exposure dating, modified sampling and measuring procedures incorporating controlled exposure experiments and spatially resolved OSL laser scanning measures are performed in a trial study on 11-year

exposed quartzite rocks. The first experiment involves trials of controlled exposure sampling approaches, to attempt to reliably determine exposure dating model parameters directly from the rock surface of interest using OSL saturated core samples subjected to controlled light exposures. Measured from wafer derived datasets, natural sunlight controlled exposed parameters were able to produce decadal ages, equivalent in magnitude to that of ages produced from proximal rock sourced parameters. Parameters acquired from simulated light, however, produced centennial to decamillennial ages. Data scatter in the luminescence depth profiles substantially limit parameter and age precision of all techniques, however, warranting more resolute OSL measuring protocols to make more valid conclusions about the use of controlled exposures for rock surface parameterization.

Resultingly, OSL scanning measures were trialed on the Lane Mountain samples to record sub-millimeter resolution OSL depth profiles of the core surface samples, to compare if the parameterizations from these higher resolution datasets would be more precise than parameters acquired from lower resolution wafer derived datasets. Scanning electron microscopy with energy dispersive spectroscopy analyses (SEM-EDS) were used additionally on OSL scanned samples to identify and filter out non-quartz OSL anomalies in scan data, with the aim of generating depth profile data which more closely follows model expectations for quartz-OSL exposure dating, and to see how parameterizations are influenced with this modification to data. The use of spatially resolved OSL depth profiles from scan datasets improved parameter extrapolative precision over wafer derived datasets for individual and combined core datasets, although individual datum error was generally higher than in wafer datasets. The use of non-quartz anomaly filtering on spatially resolved scan data improved data error bounds of anomaly affected regions, and improved the data scatter of spatially resolved depth profiles for both

individual and combined core datasets, but minorly improved or matched parameter precision to nonfiltered OSL scan data. Once core parameterizations were acquired, age calculations using spatially resolved data were performed using proximal rock sampling techniques. For individual age fits from each core sample, filtered and nonfiltered spatially resolved OSL depth profiles produced inconsistent ages between known age surfaces, but the calculated precision was improved when using scan and scan filtered data. Combined core age fits of each rock surface using scan and scan filtered data produced more accurate age results to 11 years than age fits from individual cores, but each fit type produced comparable fit precision. Ages using controlled exposure experiment techniques were unable to be extrapolated from spatially resolved data, given the scan data from the controlled exposed samples were too low in OSL intensity to acquire viable depth profiles for adequate parameter extrapolation.

The promising results in using controlled exposure experiments for parameterization, and the observed precision improvements when using spatially resolved OSL to parameterize rock surfaces, invite the opportunity to apply both sampling and measuring approaches to exposure date quartzite erratic members of the Foothills Erratics Train, which are interpreted to have been deposited during the final retreat stage of the Laurentide and Cordilleran ice sheets and the opening of the ice-free corridor. Inconsistent deposition timelines of the erratics and the opening of the ice-free corridor warrant the application of an alternative surface exposure chronometer more sensitive to millennial timescales, such as luminescence exposure dating, to attempt refining the timeline of Erratics Train deposition. The use of controlled exposure experiments allows for exposure dating trials at the sites, where no known age proximal rocks are available for the erratic surfaces. Further, the use of higher resolution spatially resolved OSL may offer precise age characterizations for decamillennial time.

Lab simulated, unidirectional sunlight exposures were used to extrapolate parameters from the erratic surfaces, given difficulties in facilitating natural sunlight exposures, and depth profiles were measured using spatially resolved OSL laser scanning techniques. Age results for the erratics offered sub-annual to centennial exposure ages, providing no realistic insight on the deposition timelines of the Foothills Erratics Train members. However, the results indicate that the parameterizations of OSL depth profile development in the exposure dating model may be too simple, and that other influences in the experimental setup may affect parameter accuracy and precision. For instance, mineralogical variations in OSL may impact fit precision, which are unaccounted for in the model form, and were not able to be considered for this assessment, as X-ray element maps produced for the cores were not usable for filtering assessments. Second, the higher intensity OSL acquired from the controlled exposure samples indicates that the use of unidirectional, single flux rate solar simulated light, which follows model conditions for light exposure, may oversimplify exposure conditions over decamillennial timescales, producing inaccurate exposure ages. Third, the fit approach for parameterization may also not be effective in obtaining accurate parameters for the rock surface, given inconsistencies observed between physically derived parameters and curve fitted parameters both from Foothills Erratics Train and Lane Mountain samples. Fourth, the presence of weathering rinds may impact the feasibility of controlled exposure rock surface parameterization, and surface altered cores should be incorporated in controlled exposed samples to attempt best emulating rock surface exposure conditions. Finally, erosion rates are likely to impact depth profile evolution in the Foothills Erratics Train study, but are not quantified in the model form, potentially causing the younger than expected exposure ages. With continued physical experiments on depth profile evolution, and application trials to test modified parameterizations, the ability to date millennial-

decamillennial exposed surfaces can be more effectively evaluated. Specific physical experimental studies on depth profile effects from the light source, such as photon flux variations and angle of illumination variations, as well as sample characteristics light surface coverage, weathering rind impacts, and erosion, can offer improved insight on the effective parameterization of depth profile evolution for exposure dating applications.

Still, the use of higher spatially resolved OSL measurements, and the use of controlled exposure parameter sampling, have shown potential in expanding the applicability and precision of the exposure dating technique, and provide more detailed measures of OSL, which can benefit trial experiments aiming to better parameterize depth profiles for exposure dating methods. With these new procedures, continued research on the parameterization of depth profiles for exposure dating can be more effective in execution, and can improve OSL exposure dating to become an established geochronometer.

Table of Contents

1. Introduction

Exposure dating of rock surfaces using luminescence is a technique which offers the ability to determine the duration of time the surface has been exposed to sunlight. The measured chronometer is luminescence, the emission of light induced by the release of electrons trapped in crystal lattice mineral defects. In the case of using optically stimulated luminescence (OSL) for exposure dating, blue-green light wavelengths allow for the detrapping of electrons from quartz and other mineral lattice charge defects, with quartz resultingly emitting ultraviolet light that is measured for dating. The intensity of OSL emitted from quartz corresponds to the amount of time since the mineral was last exposed to light.

The exposure dating technique assumes pre-exposure that all electron traps in quartz are filled within a sample. Electrons become trapped in quartz defects due to exposure to ionizing radiation from naturally occurring radionuclides in and near the sample, as well as from cosmic rays. With long enough exposure, samples will reach a ‘saturated’ state where all viable electron traps in a sample are filled, thus reaching the maximum limit of luminescence that can be emitted from the sample. Then with exposure to daylight, saturated quartz-bearing rock samples will begin to release optically simulated luminescence from the subsurface at a depth dependent rate.

The exposure dating technique warrants the measure of luminescence depth profiles, revealing the extent to which a prior accumulated luminescence signal has been removed by optical bleaching as light has penetrated the rock. Depth profiles are traditionally measured by taking core samples from the rock surface, slicing the core into millimeter depth segments, and measuring the luminescence of each slice in one or several aliquots. The aliquot luminescence is

usually normalized against a test dose luminescence signal, measured after a small radiative dose is applied to an aliquot (Figure 1.1).

The resetting of luminescence on rock surfaces was studied initially in Liritzis et al. 1994 and Liritzis et al. 1997, which observed the possibility of exposure dating calcite building materials using thermoluminescence. Later applications considered the use of IRSL and OSL for exposure dating purposes, proposing novel sampling and measuring protocols for the technique, as well as providing discussion on adequate methods for quantifying exposure ages from luminescence depth profiles (Habermann et al. 2000; Greilich et al. 2005; Vafiadou et al. 2007; Liritzis et al. 2008). Parameters often considered for modeling optical exposure dating in these discussions included rock's luminescence detrapping properties, the ability for light to attenuate into the rock, and the characteristics of sunlight applied to the incident surface.

One of the initial exposure dating models proposed was Polikreti et al.'s (2002) exponential form for thermoluminescence exposure dating:

$$t=(\frac{1}{\lambda_0})e^{kx_{ip}} \qquad (1)$$

where an age t is calculated from a depth profile with the knowledge of three parameters values for the sample, which includes λ_0, a time constant representing the luminescence exponential decay for the sample, k, a light attenuation parameter, and x_{ip}, the depth of the inflection points of the depth profile curve. Obtaining parameters λ_0, x_{ip}, and k for the rock involves fitting depth profiles of known age surfaces to the double exponential model:

$$TL_x=R+Ce^{(\lambda_0 t)e^{-kx}} \qquad (2)$$

Which incorporates recorded thermoluminescence (TL) at depth x, residual thermoluminescence R, and the difference of measured and residual thermoluminescence C.

An exposure dating model for optical dating purposes was later proposed in presentations by Sanderson et al. (2011), which provided more thorough parameterizations concerning polychromatic characterizations of luminescence bleaching rates:

$$\frac{n(x)}{n_0} = e^{-\int \sigma(\lambda)\varphi_0(\lambda)e^{-\alpha x}d\lambda * t}$$

Where σ represents wavelength dependent photoionization cross section values for the rock, α represents sample light attenuation, and φ_0 indicating the incident photon flux on the rock surface. A simpler monochromatic form was also proposed to simply parameterizations:

$$t = \ln\left(\frac{I_0}{I(x)}\right)e^{\alpha x/\sigma\varphi_0}$$

A multi-trap model was also proposed to accommodate expected variations in quartz OSL bleaching components, given as:

$$\frac{n(x)}{\sum n_{0_i}} = \sum_i n_{0,i}e^{-\int \sigma(\lambda)\varphi_0(\lambda)e^{-\alpha x}d\lambda * t}$$

Soon after, a single trap, first order exposure dating model was proposed in Sohbati et al. (2011;2012), defined as:

$$L(x) = L_0 e^{-\overline{\sigma\varphi_0}\, te^{-\mu x}}$$

which characterizes the measured luminescence intensity at depth x (L) relative to a normalized saturated intensity (L_0). The model incorporates parameter estimates of μ (mm^{-1}), the exponential optical attenuation of surface photon fluence rates relative to depth into the surface, and $\overline{\sigma\varphi_0}$

(s^{-1}), representing the integration over the solar spectrum of σ, the effective photo-eviction cross-section for a trapped charge (cm^2), and φ_0, the incident solar photon flux ($cm^{-2}s^{-1}$). Exposure ages (t) are obtained using the equation by fitting known parameters $\overline{\sigma\varphi_0}$ and μ against luminescence depth profiles.

With this proposed first order model, recent exposure dating applications using OSL from quartz or infrared stimulated luminescence (IRSL) from feldspar has presented itself as a legitimate approach in both geological and archaeological applications (Chapot et al., 2012; Sohbati et al., 2012; Lehmann et al., 2018; Luo et al., 2018; Galli et al., 2020; Guralnik and Sohbati, 2019; Liritzis et al., 2019; Souza et al., 2019).

Since the physical parameters and their controlling mineralogical, angular and spectral dependencies are challenging to estimate accurately in rocks, the current approach for parameter extrapolation uses samples of known age and similar lithology found at the site of the rock surface to calibrate for parameters μ and $\overline{\sigma\varphi_0}$ (Figure 1.2; Sohbati et al., 2012; Gliganic et al., 2019; Chapot et al., 2012; Lehmann et al., 2019; Luo et al., 2018). This technique is referred to as the ‘proximal rock’ technique for this thesis.

Figure 1.1

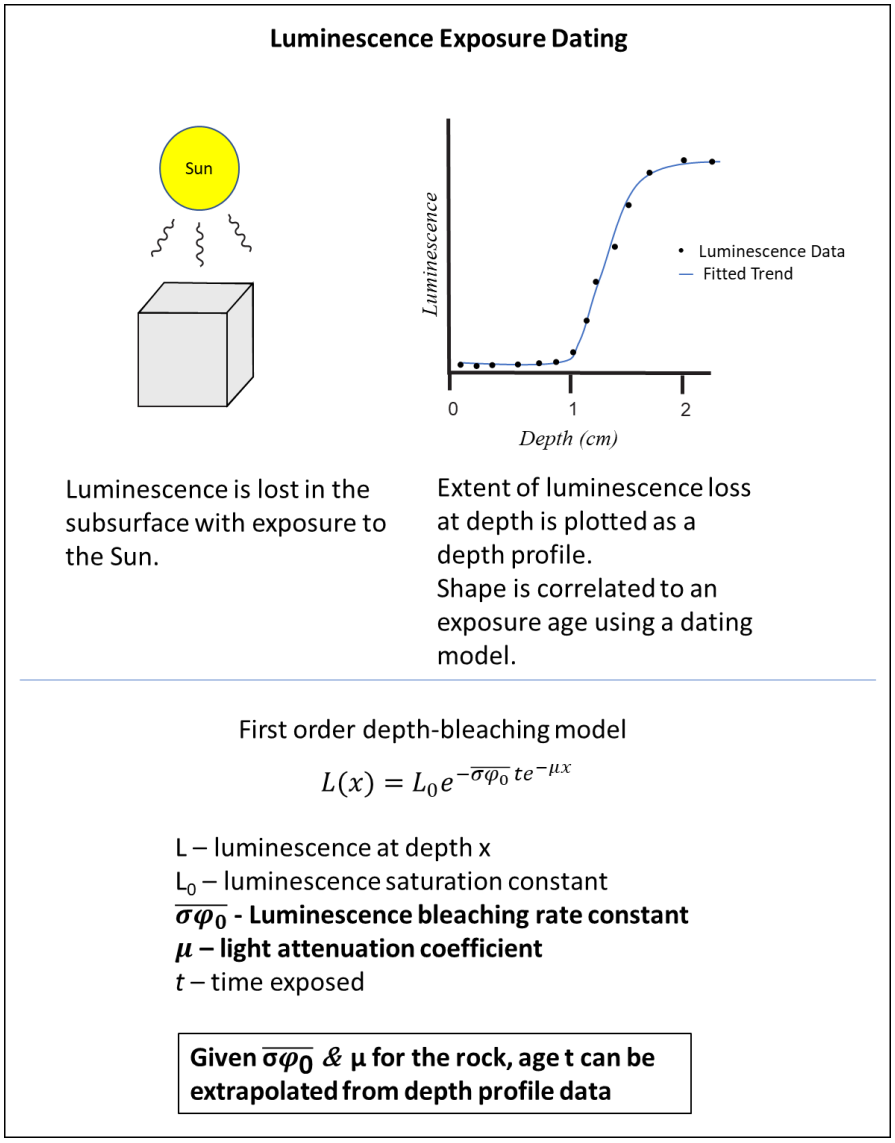

Outline of exposure dating model. Luminescence data at depth x is plotted against the exposure dating model to extrapolate an exposure age. The model utilizes a known luminescence saturation value L_0, representing the maximum value of saturation that can emitted from the material. Parameters for luminescence bleaching $\overline{\sigma\varphi_0}$ and light attenuation μ must also be known for the rock material.

1.1 Limitations in Exposure Dating

The prescribed approaches for extrapolating exposure ages and collecting depth profile data were reasonable when first introducing the dating technique, but when applied in practice, limitations in model accuracy and technique applicability become apparent.

First, with respect to the proximal rock technique for parameter extrapolation, issues can arise in that separate rocks with similar compositions used for calibration can produce inconsistent $\overline{\sigma\varphi_0}$ and μ parameters (Ou et al., 2018; Gliganic et al., 2019). Further, this sampling technique can only be performed where well-dated proximal matches are available, limiting the scope of applications. Any uncertainty in proximal sample exposure ages can additionally reduce parameter extrapolative precision (Chapot et al., 2012). Reformed parameter sampling techniques should be considered to mitigate these issues.

The second limitation is regarding the use of millimeter wafer slices for measuring OSL depth profiles. On measuring the OSL depth profile of quartz dominant rocks such as quartzite, millimeter slice techniques can produce viable datasets, but are often limited in resolution by the number of slices that can be produced from a given core sample, which can be limiting for fitting precision (Bench et al., 2022; Elkadi et al., 2021; Brill et al., 2020; Moayed et al., 2022). What compounds fit precision difficulties further is that slice derived datasets only provide one-dimensional assessments to the observed luminescence for the sample. Luminescence heterogeneities from crystallographic or mineralogical variations in the sample provide complexity to the shape of the depth profile, which are only indirectly indicated in one dimensional, slice derived point data (Ou et al., 2018). For instance, non-quartz minerals like zircon, rutile, potassium feldspar, or micaceous minerals can produce high levels of OSL, but their OSL dosimetry properties are dissimilar than with quartz, making them unwarranted in

common OSL exposure dating applications (Ou et al., 2018; Meyer et al., 2013; Polymeris et al., 2019; Bulur et al., 2014; Sanjurjo-Sanchéz et al., 2013). Other considerations may include weathering rinds or surface coverages in samples also (Ou et al. 2018; Meyer et al. 2018). Such heterogeneities in luminescence have the potential to produce high depth profile scatter, reducing parameter and age fitting certainty (Meyer et al. 2018; Elkadi et al. 2022; Brill et al. 2020). Rock types that are less quartz dominant and host more complicated compositions, such as granite, will be subject to these factors of uncertainty with more complexity and significance.

In response to mitigating fitting issues with wafer slice depth profiles, spatially resolved, higher resolution depth profile data may offer more detailed temporal interpretations of depth profile development, to help improve the precision and accuracy of exposure dating applications.

1.2 Responding to Limitations

Two responses aim to resolve both the limited applicable scope and poor parameter extrapolative accuracy when using proximal rock sampling procedures, as well as improve upon the poor resolution of depth profiles from using millimeter slice luminescence measures. This includes the application of controlled exposure experiments for parameter extrapolations, and the use of OSL scanning instruments for measuring spatially resolved depth profiles. Further, an additional assessment will be undertaken which considers the physical measurements of parameters, to determine if the physical values of light attenuation and photoionization cross section are equivalent to fitted parameter values derived from the exposure dating model.

Two sites of application for these studies will be on Lane Mountain Quarry, Washington, and the Foothills Erratics Train, Canada, elaborated further in this chapter.

1.2.1 Addressing parameter sampling limits with controlled exposure experiments

The ability to eliminate the need for an independent, known age calibration sample, to utilize samples directly instead only from the rock surface to be dated, can potentially address technique sampling limitations where a lack of proximal rock matches exists at a sampling site.

It will be investigated whether one can sample luminescence saturated cores from this rock surface, then exposing the core samples for known periods of time to site equivalent simulated or natural sunlight, to acquire luminescence depth profiles with representative bleaching times (Figure 1.2). This technique allows for the acquisition of parameters μ and $\overline{\sigma\varphi_0}$ from the rock surface without the need of an external age calibrated sample.

In evaluating the effectiveness of controlled experiment procedures for rock surface parameterization, two experimental conditions will be evaluated. The first is to study the feasibility of using a unidirectional photon flux to emulate natural surface exposures in controlled exposure experiment applications. Quartzite samples from Lane Mountain will be exposed to natural sunlight and equivalent solar simulated light to determine the impact of depth profile development between the two light sources.

For the second study, simulated light will be used in examining the Foothills Erratics Train samples to evaluate, in a controlled light environment, the impact of weathering rinds and surface coverage on depth profile development (See 2.3.2). The simulated light exposed cores will also be used to attempt dating decamillennial exposed surfaces from the Foothills Erratics Train.

Figure 1.2

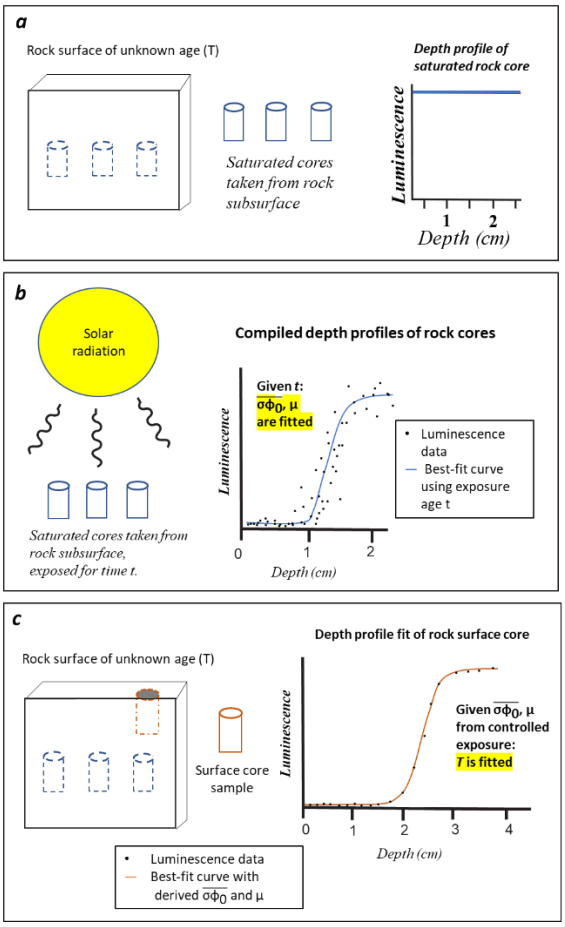

Outline of the controlled exposure experiment technique for rock surface parameterization. (a) Several cores are sampled from the rock of interest in locations where there exhibits a natural saturation of filled traps. Otherwise, to ensure luminescence saturation, core samples can be irradiated with a ^{60}Co or other common irradiation source. (b) Luminescence saturated cores undergo exposure to equivalent solar radiation for a controlled period of time t. Using t, parameters μ and $\overline{\sigma\varphi_0}$ are extrapolated from each core. Luminescence date from the cores should then be fitted to determine the μ and $\overline{\sigma\varphi_0}$ parameters for the rock. (c) A core sampled from the surface of the rock of interest is then used to calculate the rock's surface age T, using the μ and $\overline{\sigma\varphi_0}$ fitted from the controlled exposure experiment.

1.2.2 Addressing depth profile resolution using Two-Dimensional OSL Laser Scanning Analyses

The resolution limits imposed by millimeter slice luminescence measures will attempt to be addressed with the use of spatially resolved OSL laser scanning techniques. Luminescence laser

scanning instruments provide not only sub-millimeter resolution measures of OSL, but also the ability to spatially identify zones of OSL anomalies that may contribute to scattered features of the depth profile form (Figure 1.3, 1.4). Samples from Lane Mountain quarry will be used to evaluate the viability of these OSL measuring techniques.

It will be first assessed whether the use of spatially resolved OSL from laser scanning will offer more resolute depth profile data over millimeter wafer data. It will then be determined if the observed OSL anomalies in scan datasets can be identified with the use of scanning electron microscope electron dispersive x-ray spectroscopy (SEM-EDS) analyses at SUERC, or x-ray microprobe imagery offered at the University of Massachusetts, Amherst (Figure 1.4). If areas of OSL anomalies can have their mineralogy identified through these means, an attempt will be made to remove non-quartz anomalous OSL from the scan datasets to then produce anomaly uninfluenced depth profile points. The fit and age results of these anomaly-free datasets will the results from the nonfiltered depth profile datasets to determine if such filtering techniques will produce depth profiles which better align to the theoretical conditions set by the exposure dating model, which should improve parameter and age certainty.

Figure 1.3

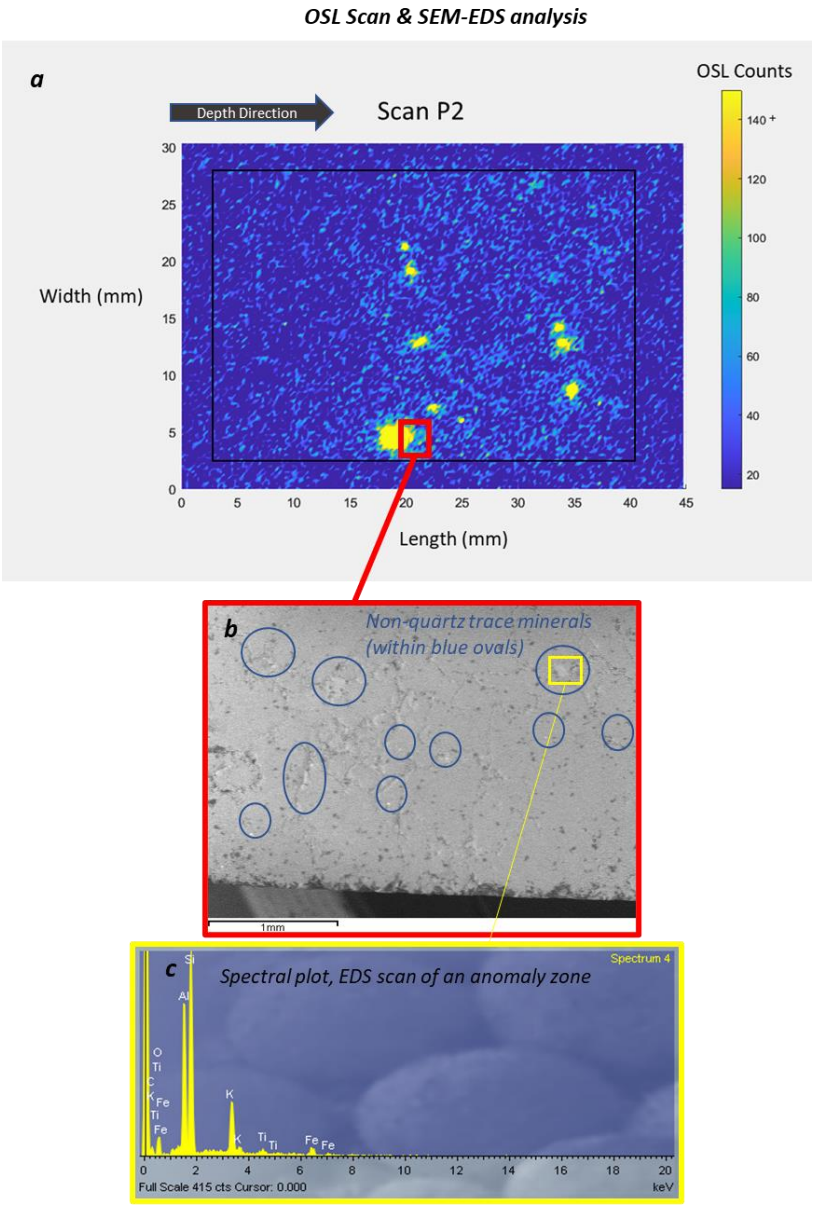

Outline of OSL laser scanning and OSL anomaly mineralogy identification procedure using scanning electron microscopy energy dispersive x-ray spectroscopy. (a) OSL laser scan of sample P2, yellow regions indicating OSL anomalies. (b) SEM-EDS image of subsection of sample P2, extent within red square in subfigure a. Non-quartz minerals are identified within the blue ovals. (c) Energy dispersive spectroscopy (EDS) scan of mineral within yellow square in subfigure b. The high presence of aluminium, potassium, titanium from the measure indicates the mineral is micaceous. It can be interpreted that the OSL anomaly measured in this location could be influenced from this non-quartz mineral.

Figure 1.4

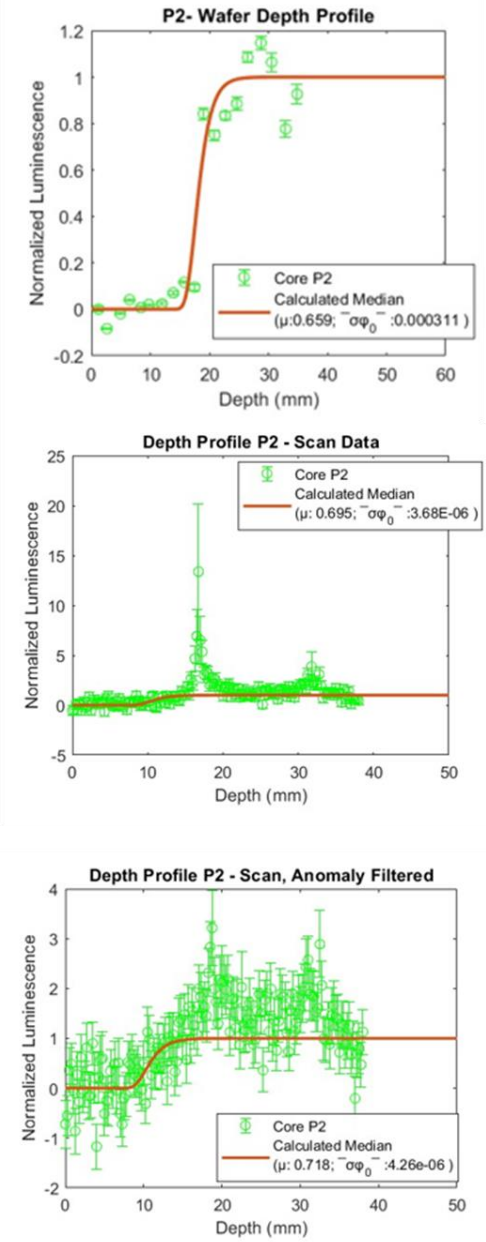

Example of depth profiles derived from wafer (top), laser scan (center), and anomaly filtered laser scan (bottom) OSL data from sample P2. Two details to note are the increase in data of laser scan derived depth profile against the wafer derived dataset, and the reduction of anomalous luminescence data in anomaly filtered depth profiles when compared to non-filtered depth profiles.

1.3 Considering other Parameters, Physical Measurements of Parameters

Results from the controlled exposure and laser scanning applications will provide insight on each technique's ability to estimate depth profile developments of varied timescales. The results can also provide insight on using curve fitting to extrapolate model parameters. For instance, if the improvements produce parameters which consistently produce poorly fitting ages, or if results of light attenuation or luminescence bleaching are physically dubious, such results indicate the use of curve fitting for parameter extrapolation may not be most appropriate for dating applications, regardless if better sampling or measuring procedures are used in application.

Thus, a series of preliminary assessments are additionally planned which aim derive parameter values from physical experiments, to document any observed inconsistencies in parameter values acquired from curve fitting versus from direct physical measurement, and to document the need to re-evaluate single rate parameterizations used in the first order model. This work will mainly focus on performing physical calculations of multispectral light attenuation rates of samples using physical light experiments, to determine the validity of assuming a single rate attenuation value can adequately estimate spectral attenuation behaviors of visible light wavelengths. If distinct wavelengths make up primary components of light attenuation into the rock for luminescence bleaching, the results may warrant the synthesis of an appropriate polychromatic exposure dating model. An attempt will also be performed using linearly modulated OSL (LM-OSL) to estimate photoionization cross section values of a core sample, to directly compare its result to curve fitted estimates, and bring to discussion what may cause inconsistencies in fitted versus physically measured estimates of luminescence bleaching rates. Further, estimates erosion rates, will be used to interpret potential shortcomings of exposure dating applications over longer

timescales, and aim to provide insight on additional parameters needed for more accurate exposure dating procedures.

1.4 Sites of Applied Study

Two sites hosting quartzite rock surfaces will be used to test the new proposed sampling and measuring procedures for exposure dating. What makes quartzite a good choice for testing is its near homogenic composition, which limits the amount of varying trap excitation and light attenuation in the rock core, thereby limiting the variations in the luminescence depth profiles for each given timescale. Any variations observed could then be easily investigated if they come from non- quartz features, such as from the minor concentrations of clay, iron oxide bands and other minerals, or from any other light attenuating surface characteristics. This allows for clearer examinations on any causes for parameter extrapolation inconsistencies. Further, quartz is an effective dosimeter, building up a measurable luminescence signal with increased radiation exposure. Preliminary experiments with this quartzite show that it is sufficiently sensitive to carry out the experiments (Appendix).

The first site of application is Lane Mountain Quarry, an open pit quartzite quarry located in Valley, Washington, USA. The site hosts quartzite from the lower Cambrian member of the Addy Formation which consists of 96–98% coarse-grained quartz, with smaller percentages of clay protolith phyllite consisting of micaceous minerals and iron oxides (Lindsey et al., 1990). This site is used to test the application of controlled exposure experiments in a controlled field setting. The first trial using controlled exposure experiments for rock surface parameterization aims to produce parameters from controlled exposed rocks, which if used to fit the natural exposed rock surface of 11 years, can produce an equivalent age for the site. This site will also be used to directly compare parameter fit precisions and depth profile forms of 11-year exposed

samples from wafer slice derived OSL data, spatially resolved laser scanned OSL datasets, and spatially resolved OSL with non-quartz anomalies filtered from the dataset.

After the Lane Mountain trials, an attempt to date a real geological feature is pertinent to trial the feasibility and potential difficulties of using both OSL laser scanning for depth profile measuring and controlled exposure experiments for parameter extrapolation in less controlled environmental settings.

Thus, the dating application site are three erratic members of the Foothills Erratics Train, a sequence of 10^3-10^4 year exposed quartzite erratics found in southwest Alberta, Canada. These erratics are believed to have been deposited along the margins of the Cordilleran and Laurentide Ice Sheets during their latest glacial retreat (Jackson Jr. et al. 1997). Ongoing controversies concerning the surface exposure dates of these erratics have complicated interpretations of glacial histories and interactions between the Cordilleran and Laurentide ice sheets during the upper Pleistocene, with particular questions of when an ice-free corridor between the Laurentide and Cordilleran ice sheets opened up, which would have allowed for the migration of humans into North America (Froese et al., 2019; Pedersen et al. 2016; Potter et al. 2018; Feathers 2023). As such, the use of OSL exposure dating may provide new insight on Erratic deposition and glacial retreat chronologies.

The decamillennial exposed quartzite surfaces of the Foothills Erratics Train would have been difficult to date using OSL exposure dating, given the lack of presence of known age rocks, and the necessity of acquiring high resolute depth profiles to quantify decamillennial exposure. As such, the site offers a complex setting to evaluate the benefits and limitations of using controlled exposure sampling and laser scanning measuring techniques. Results from the controlled exposure application in this study will provide insight on the experimental conditions and model

parameters needed to accurately estimate decamillennial depth profile development, particularly examining the feasibility of using single rates for photon flux and monochromatic functions for light attenuation and photoionization cross sections to calculate decamillennial exposure. As an addition to evaluating the application of controlled exposures and OSL laser scanning, samples from the Erratics Train will be used to evaluate if weathering rinds or other surface features play an observable role in altering depth profile forms, and how the presence of such features implicates the use of samples with no surface altered features to parameterize naturally exposed rock surfaces for exposure dating. Other considerations for this application will also include erosion and environmental dose rates, and their potential impact in altering depth profile forms over decamillennial time.

Figure 1.5

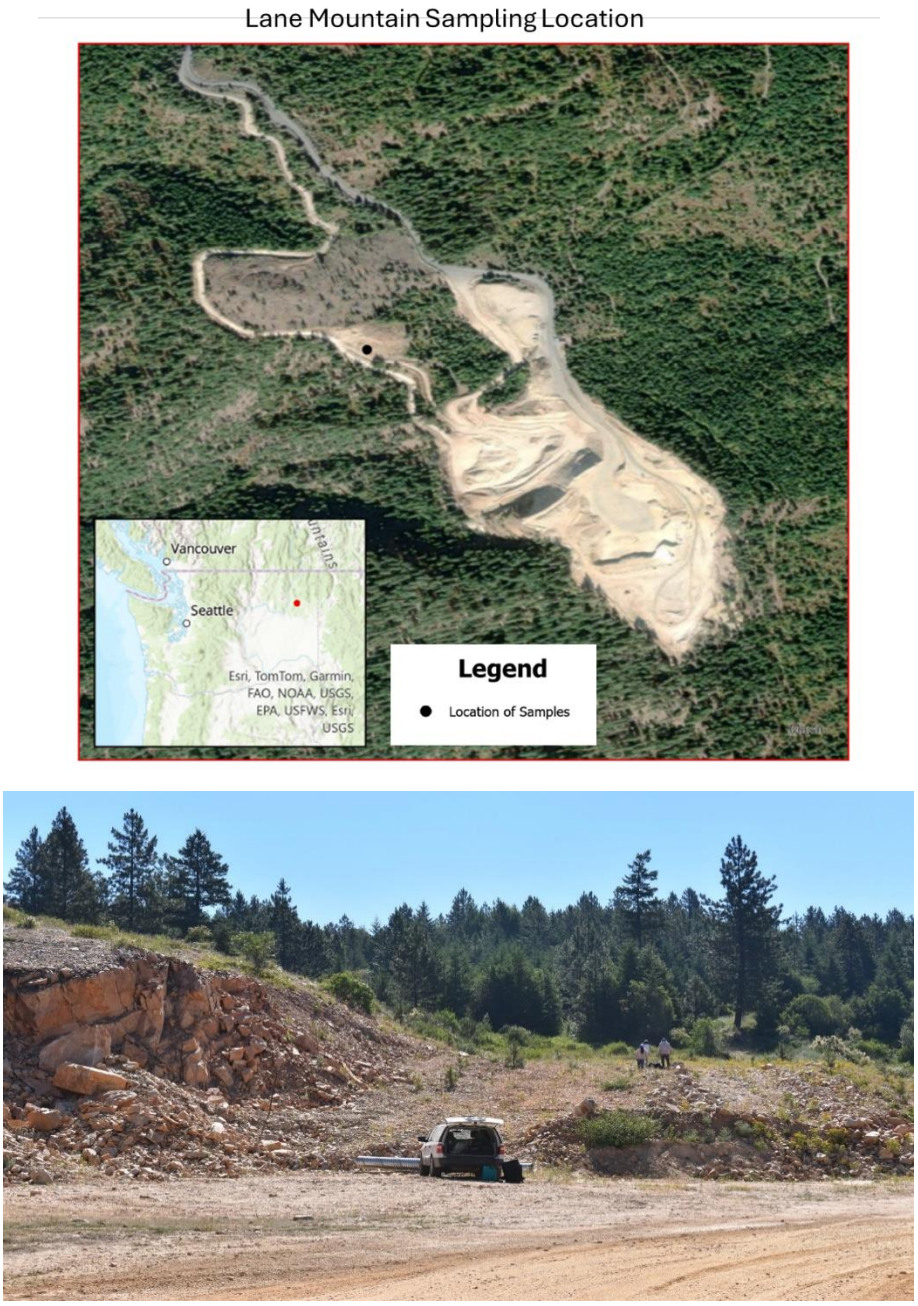

Site of the 'Hard Rock Pit' at Lane Mountain Quarry, located in Valley, Washington. The site hosts 11-year exposed quartzite rock surfaces. Rock surfaces from this quarry will be used to determine the effectiveness of using controlled exposure experiments for parameter extrapolation, and to evaluate the precision of depth profiles acquired from laser scanning instruments and anomaly filtered laser scanning datasets.

Figure 1.6

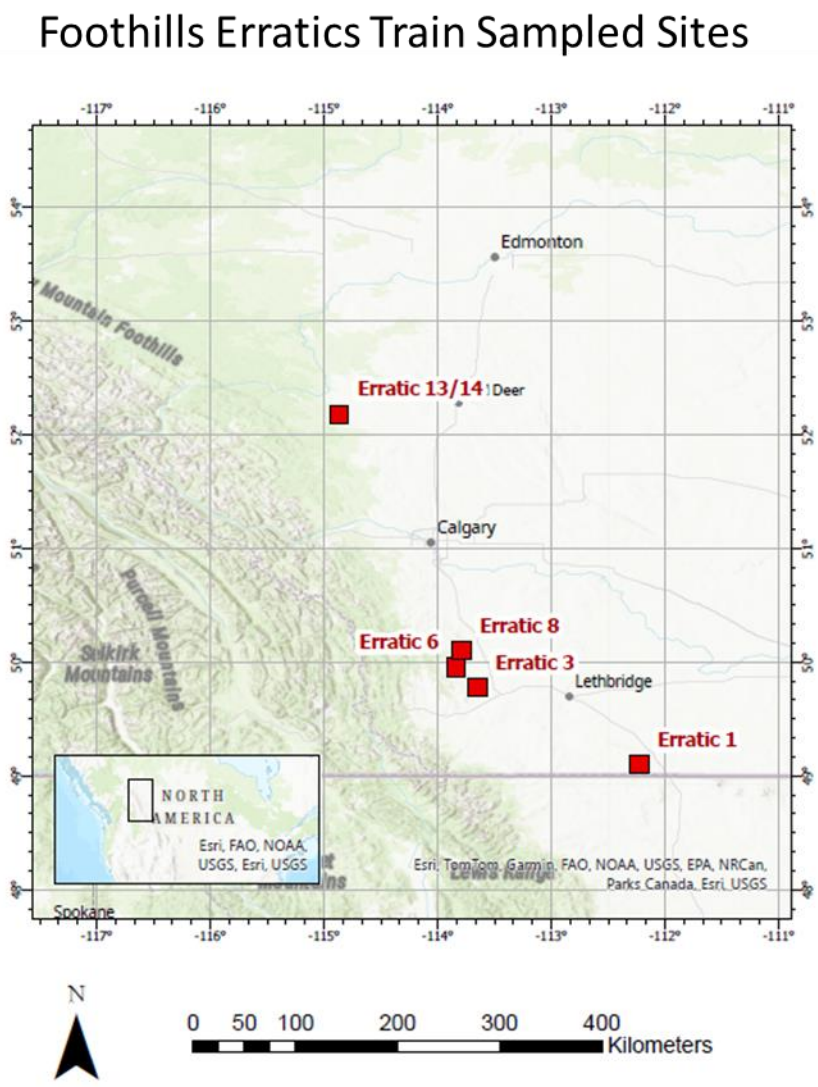

Sample locations of the members of the Foothills Erratics Train taken for exposure dating study. Erratic 3, 6 and 8 were the samples chosen for dating trials.

1.5 Summary

Exposure dating using optically stimulated luminescence is limited by the poor performance of sampling techniques and limited access of sampling sources used for model parameter extrapolations. Further, the poor resolution of depth profiles using slice/wafer measuring

protocols limits extrapolative accuracy and certainty of the parameter values extrapolated for use in exposure dating.

Two responses aim to improve the accuracy and applicability of the dating technique. The first response in using controlled exposure experiments aims to provide the ability to extrapolate exposure dating model parameters without the need of proximal rock surfaces. Further, parameter accuracy may be improved given the source rocks used for extrapolation come from the rock to be dated. The second application response using spatially resolved OSL laser scanning analyses, aim to provide enhanced resolutions of depth profile datasets for exposure dating. Further, the two-dimensional scans offer the chance to examine spatial depth profile trends, and identify mineral characteristics of OSL anomalies with the use of SEM-EDS analyses and X-ray microprobe imagery. Inquiries on the ability to remove non-quartz OSL from depth profile datasets can produce depth profiles which better align to theoretical exposure dating model conditions, and thus hopefully produce more certain age results.

These proposed techniques will be both trialed against traditional proximal sampling and millimeter slice measuring techniques on decade exposed surfaces from Lane Mountain Quarry to determine if controlled exposure experiments and/or the use of spatially resolved OSL measurements will provide the expected improvements in exposure age calculation. Subsequently, controlled exposure experiments and laser scanning measures will also be conducted with samples from the Foothills Erratics Train, to assess the feasibility of using the alternative measuring and sampling techniques in a real application setting. Lastly, a series of inquisitive assessments will be performed on the Foothills Erratics Train samples to document potential accuracy issues with obtaining rock surface parameters from curve fitting for age calculations. Further inquiries include if physical measures of photoionization cross sections and

attenuation coefficients are similar to curve fitted values, and if not, whether the model form needs to be reevaluated. Also, assessments will be conducted to inquire whether erosion rates and environmental radiation dose rates implicate depth profile evolution over long timescales. Success on these investigative fronts hopes to improve the applicable scope and viability of luminescence surface exposure dating for geological and archaeological geochronology studies within late Quaternary timescales.

These assessments are written in three sections. Section 2 will discuss the first trial of controlled exposure experiments, conducted at Lane Mountain Quarry, Washington with the use of wafer derived datasets. Both controlled exposure experiments using natural and simulated sunlight will be performed to extrapolate parameters for dating, in addition to using the proximal rock technique for parameter extrapolation, to evaluate which format of parameter extrapolation performs best for the site.

Section 3 discusses the use of spatially resolved OSL data for measuring OSL depth profiles from samples taken at Lane Mountain Quarry, Washington. Comparisons of depth profile resolution between wafer derived depth profiles and scan derived depth profiles will be made, in addition to the precision of fitted parameters between each dataset. Further, this chapter will evaluate the use of non-quartz mineral filtering of OSL scan datasets to determine the impact to the depth profile form and precision of parameter fits from the altered depth profile. Age results are also provided as supplement to evaluate potential impacts on age calculations using spatially resolved scan OSL data and scan filtered data using the proximal rock technique. Additionally, the section begins to evaluate the curve fitting approach to parameterization, offering a comparison of fitted and physically measured values of light attenuation for Lane Mountain

samples, and evaluating the potential limitations in obtaining accurate rock surface parameters using fit approaches with the first order model against depth profiles.

Section 4 details the application of using OSL scanning measuring and controlled exposure sampling techniques to date the placement of quartzite erratic members of the Foothills Erratics Train, in Alberta, Canada. The study attempts using simulated sunlight controlled exposure experiments to obtain parameters to date three erratics of the Erratics Train without the use of proximal rocks. This application also uses OSL laser scanning techniques to extrapolate depth profiles for dating, and attempts element mapping of samples. The results of the experiment are discussed, with an initial discussion on the impact of data scatter on results, and then with several additional assessments on factors which may impact fit precision of the dating approach. The first discussion determines whether surficial features and weathering rinds alter the parameterization of rock surfaces and impact the use of controlled exposure experiments for dating. The second discussion evaluates the role of using simulated sunlight exposures for controlled exposure experiments, and whether it is viable to use simple, unidirectional light exposures with constant photon flux for controlled exposures, which fit model conditions. A third assessment considers the role of erosion in altering depth profile forms over decamillennial time, and considers how depth profiles would evolve with certain estimates of erosion applied to the rock surface, and how that may implicate ages from such depth profiles without parameterized erosion. Concluding this section, potential steps to improve on the described technique limitations are discussed.

After these three sections, a final section summarizes the results of the Lane Mountain and Foothills Erratics Train studies, and concludes the benefits, promise, and limitations of using controlled exposure experiments and OSL laser scanning techniques for exposure dating, and

promotes the next possible steps in accounting for the discussed limitations of the dating technique.

1.6 References

Aitken, M. J. (1998). Introduction to optical dating: the dating of Quaternary sediments by the use of photon-stimulated luminescence. Clarendon Press.

Applied Photophysics Limited, 1982. 1 kW Solar Simulator (AM2 Radiation) Instruction Manual.

ATG (Department of Atmospheric Sciences, University of Washington) 2021. “Rooftop Observations – ATG Building UW”, Department of Atmospheric Sciences, University of Washington.

Balco, G., Stone, J. O., Lifton, N. A., & Dunai, T. J. (2008). A complete and easily accessible means of calculating surface exposure ages or erosion rates from 10Be and 26Al measurements. Quaternary geochronology, 3(3), 174-195.

Bench, T., & Feathers, J. (2022). Trialing the application of controlled exposure experiments for optical exposure dating on quartzite quarry surfaces in Washington State. Radiation Measurements, 106805.

Brill, D., May, S. M., Mhammdi, N., King, G., Burow, C., Wolf, D., ... & Brückner, H. (2020). OSL rock surface exposure dating as a novel approach for reconstructing transport histories of coastal boulders over decadal to centennial timescales. EGU General Assembly, EGU2020-18537. doi, 10.

Bulur, E. (1996). An alternative technique for optically stimulated luminescence (OSL) experiment. Radiation Measurements, 26(5), 701-709.

Bulur, E., Duller, G. A. T., Solongo, S., Bøtter-Jensen, L., & Murray, A. S. (2002). LM-OSL from single grains of quartz: a preliminary study. Radiation Measurements, 35(1), 79-85.

Bulur, E. N. V. E. R., Kartal, E., & Saraç, B. E. (2014). Time-resolved OSL of natural zircon: A preliminary study. Radiation measurements, 60, 46-52.

Chapot, M. S., Sohbati, R., Murray, A. S., Pederson, J. L., & Rittenour, T. M. (2012). Constraining the age of rock art by dating a rockfall event using sediment and rock-surface luminescence dating techniques. Quaternary Geochronology, 13, 18-25.

Elkadi, J., King, G. E., Lehmann, B., & Herman, F. (2021). Reducing variability in OSL rock surface dating profiles. Quaternary Geochronology, 64, 101169.

Feathers, J. (2023). The Contributions of Luminescence Dating of Sediments to Understanding the First Settlement of the Americas. PaleoAmerica, 9(2), 81-114.

Freiesleben, T. H., Thomsen, K. J., & Jain, M. (2023). Novel Luminescence Kinetic Models for Rock Surface Exposure Dating. Available at SSRN 4131181.

Froese, D., Young, J. M., Norris, S. L., & Margold, M. (2019). Availability and viability of the ice-free corridor and Pacific coast routes for the peopling of the Americas. SAA Archaeol. Rec, 19(3).

Fuhrmann, S., Meyer, M. C., Gliganic, L. A., & Obleitner, F. (2022). Testing the effects of aspect and total insolation on luminescence depth profiles for rock surface exposure dating. Radiation Measurements, 153, 106732.

Gallée, H., Van Yperselb, J. P., Fichefet, T., Marsiat, I., Tricot, C., & Berger, A. (1992). Simulation of the last glacial cycle by a coupled, sectorially averaged climate-ice sheet model: 2. Response to insolation and CO2 variations. Journal of Geophysical Research: Atmospheres, 97(D14), 15713-15740.

Galli, A., Panzeri, L., Rondini, P., Poggiani Keller, R., & Martini, M. (2020). Luminescence Dating of Rock Surface. The Case of Monoliths from the Megalithic Sanctuary of Ossimo-Pat (Valle Camonica, Italy). Applied Sciences, 10(21), 7403.

Gliganic, L. A., Meyer, M. C., Sohbati, R., Jain, M., & Barrett, S. (2019). OSL surface exposure dating of a lithic quarry in Tibet: Laboratory validation and application. Quaternary Geochronology, 49, 199-204.

Gliganic, L. A., Meyer, M. C., May, J. H., Aldenderfer, M. S., & Tropper, P. (2021). Direct dating of lithic surface artifacts using luminescence. Science Advances, 7(23), eabb3424.

Greilich, S., Glasmacher, U. A., & Wagner, G. A. (2005). Optical dating of granitic stone surfaces. Archaeometry, 47(3), 645-665.

Guralnik, B., & Sohbati, R. (2019). Fundamentals of luminescence photo-and thermochronometry. In Advances In Physics And Applications Of Optically And Thermally Stimulated Luminescence (pp. 399-437).

Habermann, J., Schilles, T., Kalchgruber, R., & Wagner, G. A. (2000). Steps towards surface dating using luminescence. Radiation Measurements, 32(5-6), 847-851.

Hauser, N., Feathers, J., Sanderson, D., (2011). Results from a controlled OSL surface illumination experiment. Unpublished manuscript.

Jackson Jr, L. E., Phillips, F. M., Shimamura, K., & Little, E. C. (1997). Cosmogenic 36Cl dating of the Foothills erratics train, Alberta, Canada. Geology, 25(3), 195-198.

Jain, M., Murray, A. S., Bøtter-Jensen, L., & Wintle, A. G. (2005). A single-aliquot regenerative-dose method based on IR (1.49 eV) bleaching of the fast OSL component in quartz. Radiation Measurements, 39(3), 309-318.

Jeong, G. Y., Cheong, C. S., & Choi, J. H. (2007). The effect of weathering on optically stimulated luminescence dating. Quaternary Geochronology, 2(1-4), 117-122.

Jeong, G. Y., & Choi, J. H. (2012). Variations in quartz OSL components with lithology, weathering and transportation. Quaternary Geochronology, 10, 320-326.

Kortekaas, M., & Murray, A. S. (2005). A method for the removal of mica from quartz separates. Ancient TL, 23(2), 43-46.

Kreutzer, S., Friedrich, J., Sanderson, D., Adamiec, G., Chruścińska, A., Fasoli, M., ... & Schmidt, C. (2017). Les sables de fontainebleau: a natural quartz reference sample and its characterisation. Ancient TL, 35(2).

Lehmann, B., Valla, P. G., King, G. E., & Herman, F. (2018). Investigation of OSL surface exposure dating to reconstruct post-LIA glacier fluctuations in the French Alps (Mer de Glace, Mont Blanc massif). Quaternary geochronology, 44, 63-74.

Lehmann, B., Herman, F., Valla, P. G., King, G. E., & Biswas, R. H. (2019). Evaluating post-glacial bedrock erosion and surface exposure duration by coupling in situ optically stimulated luminescence and 10 Be dating. Earth Surface Dynamics, 7(3), 633-662.

Lindsey, K. A., Gaylord, D. R., & Groffman, L. H. (1990). Geology of the Upper Proterozoic to Lower Cambrian Three Sisters Formation, Gypsy Quartzite, and Addy Quartzite, Stevens and Pend Oreille Counties, Northeastern Washington (Vol. 30, p. 37). Washington State Department of Natural Resources, Division of Geology and Earth Resources.

Liritzis, I., Galloway, R., & Theocaris, P. (1994). Thermoluminescence dating of ceramics revisited: optical stimulated luminescence of quartz single aliquot with green light-emitting diodes. Journal of radioanalytical and nuclear chemistry, 188(3), 189-198.

Liritzis, I., Guibert, P., Foti, F., & Schvoerer, M. (1997). The Temple of Apollo (Delphi) strengthens novel thermoluminescence dating method. Geoarchaeology: An International Journal, 12(5), 479-496.

Liritzis, I., Kitis, G., Galloway, R. B., Vafiadou, A., Tsirliganis, N. C., & Polymeris, G. S. (2008). Probing luminescence dating of archaeologically significant carved rock types. Mediterranean Archaeology and Archaeometry, 8(1), 61-61.

Liritzis, I., Bednarik, R. G., Kumar, G., Polymeris, G., Iliopoulos, I., Xanthopoulou, V. Zacharias N, Vafiadou A,, & Bratitsi, M. (2019). Daraki-Chattan rock art constrained OSL chronology and multianalytical techniqes: A first pilot investigation. Journal of Cultural Heritage, 37, 29-43.

Luo, M., Chen, J., Liu, J., Qin, J., Owen, L. A., Han, F., Yang, H., Wang, H., Zhang, B., Yin, J. & Li, Y. (2018). A test of rock surface luminescence dating using glaciofluvial boulders from the Chinese Pamir. Radiation Measurements, 120, 290-297.

Margold, M., Gosse, J. C., Hidy, A. J., Woywitka, R. J., Young, J. M., & Froese, D. (2019). Beryllium-10 dating of the Foothills Erratics Train in Alberta, Canada, indicates detachment of the Laurentide Ice Sheet from the Rocky Mountains at~ 15 ka. Quaternary Research, 92(2), 469-482.

Meyer, M. C., Austin, P., & Tropper, P. (2013). Quantitative evaluation of mineral grains using automated SEM–EDS analysis and its application potential in optically stimulated luminescence dating. Radiation measurements, 58, 1-11.

Meyer, M. C., Gliganic, L. A., Jain, M., Sohbati, R., & Schmidmair, D. (2018). Lithological controls on light penetration into rock surfaces-Implications for OSL and IRSL surface exposure dating. Radiation Measurements, 120, 298-304.

Murray, A. S., & Wintle, A. G. (2000). Luminescence dating of quartz using an improved single-aliquot regenerative-dose protocol. Radiation measurements, 32(1), 57-73.

Ou, X. J., Roberts, H. M., Duller, G. A. T., Gunn, M. D., & Perkins, W. T. (2018). Attenuation of light in different rock types and implications for rock surface luminescence dating. Radiation Measurements, 120, 305-311.

Pedersen, M. W., Ruter, A., Schweger, C., Friebe, H., Staff, R. A., Kjeldsen, K. K., ... & Willerslev, E. (2016). Postglacial viability and colonization in North America's ice-free corridor. Nature, 537(7618), 45-49.

Polikreti, K., Michael, C. T., & Maniatis, Y. (2002). Authenticating marble sculpture with thermoluminescence. Ancient TL, 20(1), 11-18.

Polymeris, G. S., Tsirliganis, N., Loukou, Z., & Kitis, G. (2006). A comparative study of the anomalous fading effects of TL and OSL signals of Durango apatite. physica status solidi (a), 203(3), 578-590.

Potter, B. A., Baichtal, J. F., Beaudoin, A. B., Fehren-Schmitz, L., Haynes, C. V., Holliday, V. T., ... & Surovell, T. A. (2018). Current evidence allows multiple models for the peopling of the Americas. Science Advances, 4(8), eaat5473.

Sanderson, DCW, Smillie M., McCullagh, R., , Feathers, J., Hauser, N. 2011. Surface exposure dating by luminescence : developing and testing models for surface bleaching rates and erosion

rates. 13th International Conference on Luminescence and Electron Spin Resonance Dating, Torun, Poland.

Sanjurjo-Sanchéz, J., Alves, C., & Teixeira, D. (2013). Microscopy studies in support of OSL dating of mortars of historical buildings. Microscopy and Microanalysis, 19(S4), 115-116.
Sellwood, E. L., Kook, M., & Jain, M. (2022). A 2D imaging system for mapping luminescence-depth profiles for rock surface dating. Radiation Measurements, 150, 106697.
Sengupta, M., Y. Xie, A. Lopez, A. Habte, G. Maclaurin, and J. Shelby. 2018. "The National Solar Radiation Data Base (NSRDB)." Renewable and Sustainable Energy Reviews 89 (June): 51-60.

Sohbati, R., Murray, A. S., Jain, M., Buylaert, J. P., & Thomsen, K. J. (2011). Investigating the resetting of OSL signals in rock surfaces. Geochronometria, 38(3), 249-258.

Sohbati, R., Murray, A. S., Chapot, M. S., Jain, M., & Pederson, J. (2012). Optically stimulated luminescence (OSL) as a chronometer for surface exposure dating. Journal of Geophysical Research: Solid Earth, 117(B9).

Souza, P. E., Sohbati, R., Murray, A. S., Kroon, A., Clemmensen, L. B., Hede, M. U., & Nielsen, L. (2019). Luminescence dating of buried cobble surfaces from sandy beach ridges: a case study from Denmark. Boreas, 48(4), 841-855.

UO (University of Oregon) Solar Radiation Monitoring Laboratory, 2013. Cumulative Summary Data Cheney, Washington. University of Oregon.

Vafiadou, A., Murray, A. S., & Liritzis, I. (2007). Optically stimulated luminescence (OSL) dating investigations of rock and underlying soil from three case studies. Journal of Archaeological Science, 34(10), 1659-1669.

Wintle, A. G., & Murray, A. S. (2006). A review of quartz optically stimulated luminescence characteristics and their relevance in single-aliquot regeneration dating protocols. Radiation measurements, 41(4), 369-391.

2. Lane Mountain Part 1- Application of controlled exposure experiments for parameter extrapolation of wafer derived datasets

Abstract

Exposure ages using optically stimulated luminescence (OSL) are commonly obtained by fitting the forms of luminescence depth profiles, which depend on parameter estimates of light attenuation and defined rates of luminescence bleaching. A popular procedure for obtaining these parameters for a rock surface require matching luminescence depth profiles from compositionally and morphologically matched rock surfaces with known exposure ages, which limits the accuracy and applicability of the technique. A modified procedure is presented to improve the accuracy and applicability of luminescence surface exposure dating, that aims to reliably determine light attenuation and luminescence bleaching parameters directly from the rock surface of interest using luminescence saturated samples subjected to controlled light exposures. Both this proposed controlled exposure experiment technique and the proximal rock matching technique were tested on 11 year exposed quartzite quarry surfaces from eastern Washington, USA. Parameters derived from the controlled exposure technique, using natural sunlight equivalent to the sampling site, produced the most accurate ages. Data scatter in the luminescence depth profiles substantially limit age accuracies of all techniques. However, the trials of the controlled exposure experiment techniques show procedural insight and potential in offering comparable depth profiling applications to current extrapolative techniques at sites where either no proximal rock surfaces exist, or proximal samples are deemed problematic.

2.1 Introduction

Recent applications using OSL from quartz or IRSL from feldspar for surface exposure dating has presented itself as a legitimate approach in both geological and archaeological applications (Chapot et al., 2012; Sohbati et al., 2012; Lehmann et al., 2018; Luo et al., 2018; Galli et al., 2019; Guralnik and Sohbati, 2019; Liritzis et al., 2019; Souza et al., 2019).

Since the physical parameters of the first order model and their controlling mineralogical, angular and spectral dependencies are challenging to estimate accurately, the current approach uses control samples of known age and similar lithology found at the site of the rock surface to calibrate for parameters μ and $\overline{\sigma\varphi_0}$ of the first-order Sohbati model (Sohbati et al., 2012; Gliganic et al., 2019; Chapot et al., 2012; Lehmann et al., 2019; Luo et al., 2018). With this approach however, known problems with the technique can arise in that separate rocks with similar compositions used for calibration can produce inconsistent $\overline{\sigma\varphi_0}$ and μ parameters (Ou et al., 2018; Gliganic et al., 2019). Further, this technique can only be performed where well-dated proximal matches are available, limiting the scope of applications. Any uncertainty in proximal sample exposure ages can additionally reduce precision (Chapot et al., 2012).

The ability to eliminate the need for an independent, known age calibration sample, to instead only utilize samples directly from the rock surface to be dated, can directly address technique limitations concerning the lack of proximal rock matches on site. Additionally, the use of in-situ calibrations for parameters μ and $\overline{\sigma\varphi_0}$ could potentially mitigate derived parameter inconsistencies, given they directly represent morphological and compositional characteristics to the dated rock surface. Such improvements with sampling and parameter extrapolations aim to enhance the applicability and accuracy of luminescence exposure dating.

By acquiring luminescence saturated samples from the rock surface to be dated, then exposing them for known periods of time to simulated or natural sunlight, one could acquire luminescence depth profiles with representative bleaching profiles without the need of an external age calibrated sample, allowing for the extrapolation of light attenuation and bleaching parameters representing the material of the rock surface of interest. The general design of a controlled exposure procedure is visualized in Figure 2.1, following artificial sunlight luminescence bleaching procedures and depth profile normalizations presented in Gliganic et al. (2019). Methods incorporating controlled exposures to natural sunlight and solar paths, as well as simulated sunlight, are trialed for this study.

Performing the technique first requires several luminescence saturated cores to be taken from the sample subsurface from a specific depth where it is assumed filled traps are at the maximum natural extent of saturation (Figure 2.1a). If saturation is uncertain, it is possible the cores can undergo trap filling irradiations (i.e.: ^{60}Co, X-ray, etc.) until luminescence saturation is achieved, with the condition that sensitivity characteristics of luminescence after irradiation are understood for the rock. More than one surface core sample hosting the natural luminescence depth profile of the rock surface also needs to be collected.

After sampling, the saturated cores should then be exposed for a known duration of time to a form of light that matches both the average solar irradiance and solar path of the sampling site (Figure 2.1b). Effects from topographic shadowing, and the orientation of the sample with respect to the solar path, should also be considered for recreating an equivalent solar path for controlled exposures, but both influences could be minimized by sampling from locations where the solar path is largely uninterrupted. The duration of light exposure should be long enough to produce a satisfactory depth profile, ideally with at least 1 mm of total luminescence signal

bleached at depth, a visible inflection point of luminescence at depth, and a plateau of luminescence saturation in the deepest portions of the measured core.

Utilizing the applied exposure time to light, the luminescence depth data of each core can be fitted to the exposure age model to extrapolate parameters μ and $\overline{\sigma\varphi_0}$ for the sample, using a non-linear least-squares fitting technique. Parameters should be extrapolated first from each core to display any regional heterogeneities in $\overline{\sigma\varphi_0}$ and μ for the rock. To represent parameters more broadly for the rock surface, all the normalized core profile data can be compiled into one larger cumulative profile for extrapolation, as inspired by studies from Lehmann et al. (2018, 2019). These cumulative fit parameters can be used against luminescence depth profile data of the natural surface, where an exposure age can be calculated for the surface (Figure 2.1c).

Figure 2.1

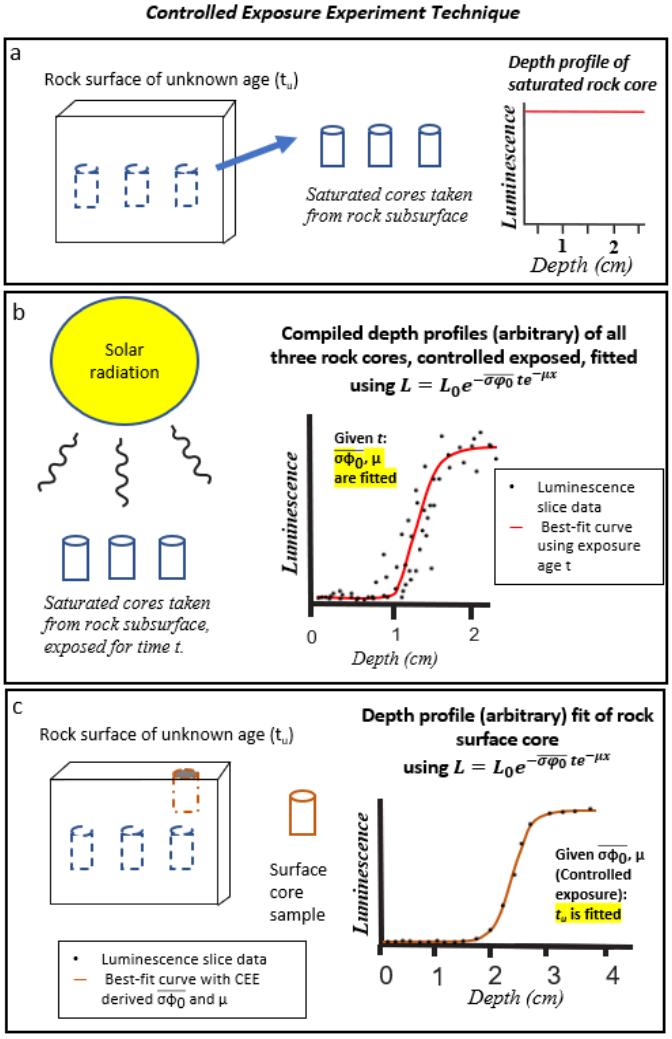

Outline of the controlled exposure experiment technique for extrapolating parameters $\overline{\sigma\varphi_0}$ and μ directly from the rock of interest. (a) At least three cores are sampled from the rock of interest, ideally in locations where there exhibits a natural saturation of filled traps. To ensure complete luminescence saturation, rock core samples can be irradiated to saturation using a preferred radiation source. (b) Luminescence saturated cores undergo exposure to an equivalent solar radiation, considering the solar path, for a controlled period t. The luminescence depth profiles of each core are then measured. Using t, parameters $\overline{\sigma\varphi_0}$ and μ are extrapolated from each core to note heterogeneities in light attenuation and luminescence bleaching. Compiled data from all three cores should be fitted to determine the functional $\overline{\sigma\varphi_0}$ and μ. (c) Cores sampled from the surface of the rock of interest is used to calculate the rock's surface age t_u, using the functional $\overline{\sigma\varphi_0}$ and μ gathered from the controlled exposure experiments.

2.2 Site of Application

To verify the applicability of controlled exposure experiments for parameter extrapolations, a site with an open solar path, hosting a rock type with as homogenous of a composition as possible, and with age verified proximal samples was sought to perform and compare the new technique.

Controlled exposures using simulated sunlight on luminescence saturated quartzite have produced viable depth profiles for extrapolating μ and $\overline{\sigma\varphi_0}$ parameters, even when exposed for timescales as small as 10^4 seconds (Gliganic et al., 2019). Thus, quartzite is used to test an in-field application of utilizing controlled exposures. What additionally makes quartzite a good choice is its near homogenic composition, which limits the amount of varying trap excitation and light attenuation in the rock core, thereby limiting the variations in the luminescence depth profiles for each given timescale. Any variations observed could then be attributable to the quartz, such as minor concentrations of clay, iron oxide bands and micaceous minerals, or any other light attenuating surface characteristics (Lindsey et al., 1990). This allows for clearer examinations on any causes for parameter extrapolation inconsistencies. Further, quartz is an effective dosimeter, building up a measurable luminescence signal with increased radiation exposure. Preliminary experiments with this quartzite show that it is sufficiently sensitive to carry out the experiments (Appendix A1).

The source of quartzite for testing comes from Lane Mountain Quarry, an open pit quartzite quarry located in Valley, Washington, USA, hosting quartzite from the lower Cambrian member of the Addy Formation (Lindsey et al., 1990). The rock consists of 96-98% coarse-grained quartz with smaller percentages of clay protolith phyllite consisting of micaceous minerals and iron oxides. Before sampling on site, to roughly determine the effectiveness of bleaching and time for

the quartzite, random bulk samples of Lane Mountain Quarry quartzite were irradiated to 350 Gy using a ^{60}Co source, and sets of three cores were exposed for 10 and 60 days to natural sunlight from February 24 - April 25th, 2021, on the rooftop of the Atmospheric Sciences and Geophysics Building at the University of Washington, Seattle. Results shown are from 10 day and 60 day exposed cores (Appendix A1), each showing that a substantially bleached profile can be obtained from 1E+6 seconds of sunlight exposure.

The study samples come from the 'Hard Rock Pit', which lies in the southern portion of Lane Mountain Quarry and hosts some of the hardest quartzite in the mine. An attempt to collect material from the bedrock on-site was made by the mining company from June-July 2010, but was since abandoned, providing an estimated exposure age of approximately 11 years for the leftover boulders when arriving at the site on June 30, 2021. This site was chosen at the quarry for this study given these undisturbed conditions of exposure and the site's known resistance to abrasion. Further, the site's solar path is largely uninterrupted onsite, aside for minor partial sky cover south of the samples. Solar data from a Solar Radiation Monitoring Laboratory station in Cheney, Washington, located approximately 100 kilometers south of the quarry but within the Columbia Plateau, provides an estimated daytime annual global solar radiation near 350 W/m^2 for the city, while a broader estimate of 330 W/m^2 is measured at the quarry site from the National Solar Radiation Database (UO; Sengupta et al., 2018; Figure 2.3; Appendix A2). Two approximately .03 m^3 boulders substantially buried in the ground, HRQ and P, were within 10 meters of each other and collected from the pit (Figure 2.2). Both HRQ and P show a range of crystalline and amorphous quartz textures. HRQ shows millimeter thick foliations of iron oxides on the surface, while rock P shows a pronounced orange weathering rind (Figure 2.2; Appendix A3, A4).

In performing the controlled exposure experiment procedure, the surface of HRQ will serve as the surface to be dated. The surface from rock P will serve as the control age sample to mimic the current 'proximal rock' technique for extrapolating μ and $\overline{\sigma\varphi_0}$. Two 25 mm diameter by 60 mm long cores, HRQ1 and HRQ1, were sampled from the surface of HRQ 1 with the aim of collecting the surface's natural exposed luminescence depth profile. Six cores of similar dimension (1NS-3NS, 1SS-3SS) were sampled from the unexposed bottom of HRQ, for use as luminescence saturated samples in controlled exposure experiments. Two surface cores (P1-P2) were sampled from rock P to apply the proximal technique for HRQ. Core sampling locations from HRQ and P can be viewed in Appendix A4.

Given the nature of excavation at Lane Mountain, the sampled boulders could have been overturned for a 1-2 month period, potentially exposing the assumed luminescence saturated base of the boulder. Prior controlled exposure studies from ^{60}Co irradiated Lane Mountain quartzite samples showed that 1-2 months of sunlight exposure produced depth profiles with inflection points from 20-30 millimeters of sample (Appendix A1). As such, the surficial 35 mm of the 6 cores taken from the bottom of each boulder were removed.

Figure 2.2

Site of the ‘Hard Rock Pit’ at Lane Mountain Quarry, Valley, Washington. Site hosts 11-year exposed quartzite rock surfaces. Rock HRQ will be used as the rock surface we wish to determine the age of using controlled exposure and proximal sampling techniques. Rock P will be used as the ‘proximal rock’ for the site study to determine the age of HRQ. The cores gathered from each rock will have their depth profiles measured using millimeter slices to compare resolution and accuracy and certainty of parameter and age extrapolations.

Both natural and simulated sunlight were used to perform light exposures on the saturated cores for known periods of time to configure how influential solar paths are for controlled exposures (Figure 2.1b).

Natural sunlight was used to expose three saturated samples (Cores 1NS, 2NS, 3NS from HRQ 1) for 10^6 daylight seconds from August 1-21 on the roof of the Atmospheric Sciences and Geophysics Building at the University of Washington, Seattle. During this period, the average daylight global irradiance subjected to the samples was approximately 275 W/m^2 as recorded by the radiometer on the roof, nearly representing the average annual daytime global irradiance subjected over Washington (ATG; Sengupta et al., 2018, Appendix A6). The similar latitude of Seattle to Valley, Washington further emulates a similar solar path to the quarry site.

To compare any general effects of luminescence bleaching between natural sunlight, and its associated solar paths, to simulated sunlight, another three cores (Core 1SS, 2SS, 3SS from HRQ 1) were exposed to simulated sunlight for 10^6 seconds using an Applied Photophysics solar simulator with a General Electric 1 kW CID1000/HR/G83 brand metal halide bulb. Cores were positioned in the solar simulator cabin to experience an irradiance of approximately 250 W/m^2, experiencing a spectral output comparable to the Sun (Figure 2.3).

To measure the OSL from each core sample, cores were sliced longitudinally, with one half sliced into millimeter wafters using a Pace Technologies PICO-155P precision saw at the University of Washington Luminescence Dating Laboratory. The 400-micron thickness of the diamond-coated brass blade used for slicing removes roughly the same thickness of sample, and this deficit is incorporated when determining the representative depth of slices. Three aliquots each roughly 40-70 mm^2 were then taken from the center of each hemispherical slice to measure for luminescence using a Riso DA-15 TL/OSL Reader, placing each aliquot in stainless steel

sample cups. A preheat of 240°C for 10 seconds was applied to each sample before measuring the OSL of the natural signal, as well as the signal from a 40 Gy test dose applied using a $^{90}Sr/^{90}Y$ source. Each OSL measure was stimulated using blue LEDs at 3.36 cd (70% power) for 100 seconds at 125°C.

The weighted mean of the three aliquots were calculated to represent the luminescence for the slice depth. Data were then normalized to 1, using 0 to represent the minimum value of the depth profile and 1 representing the weighted mean of the last five weighed slices for the core sample.

Figure 2.3

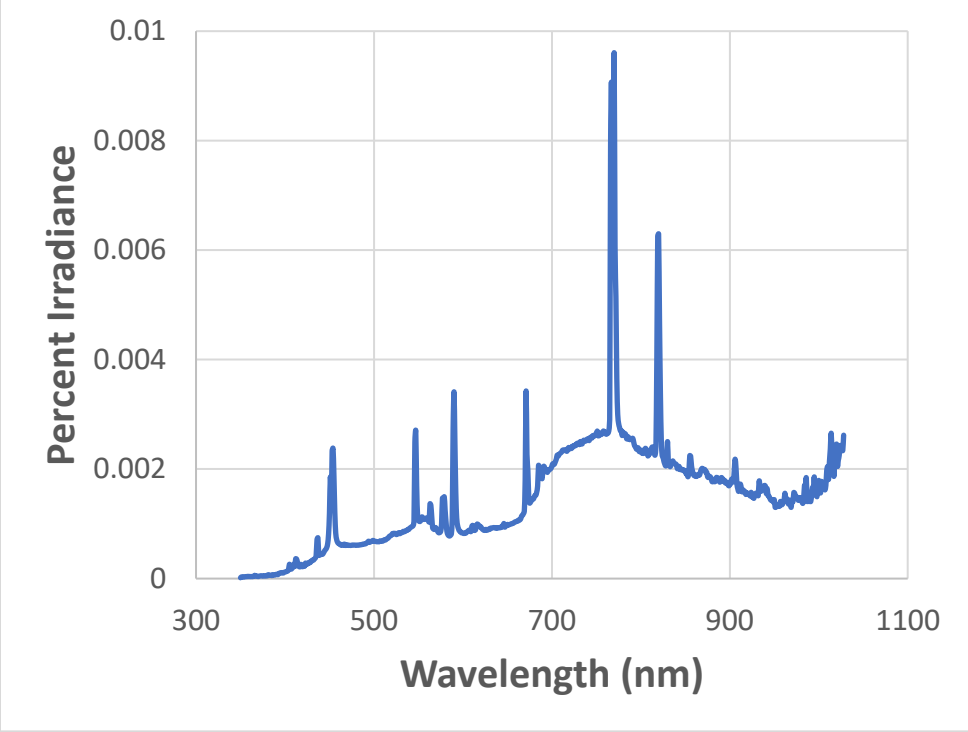

Spectral plot of a 1 kW CID1000/HR/G83 metal halide bulb, taken approximately three meters from the light source of the Applied Photophysics solar simulator.

2.3 Results

A combined least absolute errors – least squares probabilistic fitting technique, as detailed in Lehmann et al. (2018), is used to extrapolate best fit parameters for this study.

To date the age of HRQ, depth profile data from the controlled exposed cores are cumulatively fitted using least absolute errors fitting with their known exposure age to extrapolate fit values for parameter combinations μ and $\overline{\sigma\varphi_0}$ from ten thousand randomized fit simulations (Bench & Feathers 2022). The range of parameters fitted for μ were between 0-1, and for log($\overline{\sigma\varphi_0}$*t) between 0 and 10. Upon determining the median of the distribution of misfit parameter combinations μ and $\overline{\sigma\varphi_0}$, the parameter values for the given misfit metric are applied to cumulative depth profile data of HRQ1 and HRQ2 to extrapolate an exposure age t using a least squares maximum likelihood estimate fitting approach using age ranges from 1 to 10+3 years using NS and P parameters, and 10E+5 years for SS parameters, until a normal distribution of parameter likelihood is calculated from the dataset.

Parameter likelihood plots of μ and $\overline{\sigma\varphi_0}$ for all fits can be accessed in Appendix A7. The six controlled exposed cores from HRQ (1SS, 2SS, 3SS, 1NS, 2NS, 3NS) individually produce a wide range of fit values for both parameters μ and $\overline{\sigma\varphi_0}$ (Table 2.1; Figure 2.4; Appendix A7; Bench & Feathers 2022), influenced by the poor fitting certainty offered from the limited quantity and wide scatter of millimeter slice data. Sources of the scatter may be attributed to traces of micaceous minerals emitting OSL, or variations in hues and non-quartz mineral banding seen in the samples, that can impact the depth profile shape (Figure 2.2; Appendix A3,A4; Kortekaas and Murray 2005; Ou et al.,2018; Gliganic et al., 2019). Cores from rock P (P1, P2) also show wide parameter variations (Table 2.2; Figure 2.5; Appendix A7; Bench & Feathers

2022). 3SS may have been partially shielded from simulated sunlight, giving a shallower than expected bleaching front. As such, it is not incorporated in the cumulative SS fit (1-2SS). Incorporating more saturation plateau data in the normalization could diminish scatter of depth profiles, but requires more certainty in interpreting the start of the saturation plateau.

The wide scatter of luminescence data produces non-normal likelihood fitting distributions, causing uncertainties derived from parameter density distributions to poorly represent the best fit parameters (Table 2.1, 2.2; Appendix A8). Fit-goodness statistics of each core using the best-fit parameters calculated from the technique are provided for reference in Appendix A9.

Table 2.1
HRQ controlled exposure experiment derived parameters. Fits include individual cores exposed to natural sunlight (NS) and simulated sunlight (SS) for 1E+6 seconds. Combined 'cumulative' depth profile data of each experiment (1-3NS, 1-2SS) is fitted as a comprehensive reference to the rock. Certainty is calculated from parameter probabilistic density distributions of each fit. Uncertainties represent infimum and supremum confidence interval values to the median distribution. High depth profile data scatter, cause discrepancies between median distribution uncertainties and best fit parameters. However, best fit cumulative parameters and their corresponding ages in Table 2.3 show potential in utilizing controlled exposure techniques for parameter extrapolations.

Core	μ (mm^{-1})		$\overline{\sigma\varphi_0}$ (s^{-1})	
	Best fit	Median (+1σ sup, -1σ inf)	Best fit	Median (+1σ sup, -1σ inf)
Parameters from Natural Sunlight Exposed Cores of HRQ 1 (NS) (275 W/m^2 average) Parameters from Simulated Sunlight Exposed Cores of HRQ 1 (SS) (250 W/m^2 average)				
1NS	0.568	0.756 (0.176, 0.263)	3.07E-4	2.04E-3 (0.0164, 1.81E-3)
1NS	0.461	0.693 (0.188, 0.283)	2.53E-5	1.62E-4 (6.01E-4, 1.46E-4)
3NS	0.860	1.38 (0.377, 0.566)	8.71E-5	1.71E-3 (1.50E-2, 1.65E-3)
1-3 NS (Cumulative)	0.345	0.555 (0.255, 0.170)	1.18E-5	8.04E-5 (6.18E-4, 6.45E-5)
1SS	2.17	2.22 (0.565, 0.848)	2.04E-2	0.018 (0.519, 0.018)
2SS	0.545	0.594 (0.155, 0.116)	1.53E-5	2.07E-5 (2.73E-5, 8.88E-6)

3SS	0.857	1.35 (0.499, 0.499)	3.01E-5	1.35E-5 (4.60E-5, 1.28E-5)
1SS-2SS (cumulative)	0.647	0.694 (0.163, 0.122)	2.65E-5	2.77Ee-5 (4.1E-5, 1.26E-5)

Table 2.2
HRQ 2 extrapolated parameters, representing the proximal rock used to calculate an age for HRQ 1. Fits of P1 and P2 assume an exposure time of 11 years (3.469e+8 seconds). Combined 'cumulative' depth profile data of each core (P1-2) is fitted as a comprehensive reference to the rock. Uncertainty is calculated from parameter probabilistic density distributions of each fit as similarly described in Table 2.1.

Core	μ (mm^{-1})		$\overline{\sigma\varphi_0}$ (s^{-1})	
	Best fit	Median (+1σ sup, -1σ inf)	Best fit	Median (+1σ sup, -1σ inf)
P1	0.286	0.436 (0.315, 0.180)	2.63E-7	6.44E-6 (6.45E-4, 6.28E-6)
P2	0.391	0.667 (0.222, 0.222)	2.92E-6	8.71E-4 (1.91E-2, 8.66E-4)
P1-2 (cumulative)	0.285	0.438 (0.250, 0.125)	3.20E-7	6.27E-6 (2.86E-4, 5.64E-6)

Figure 2.4

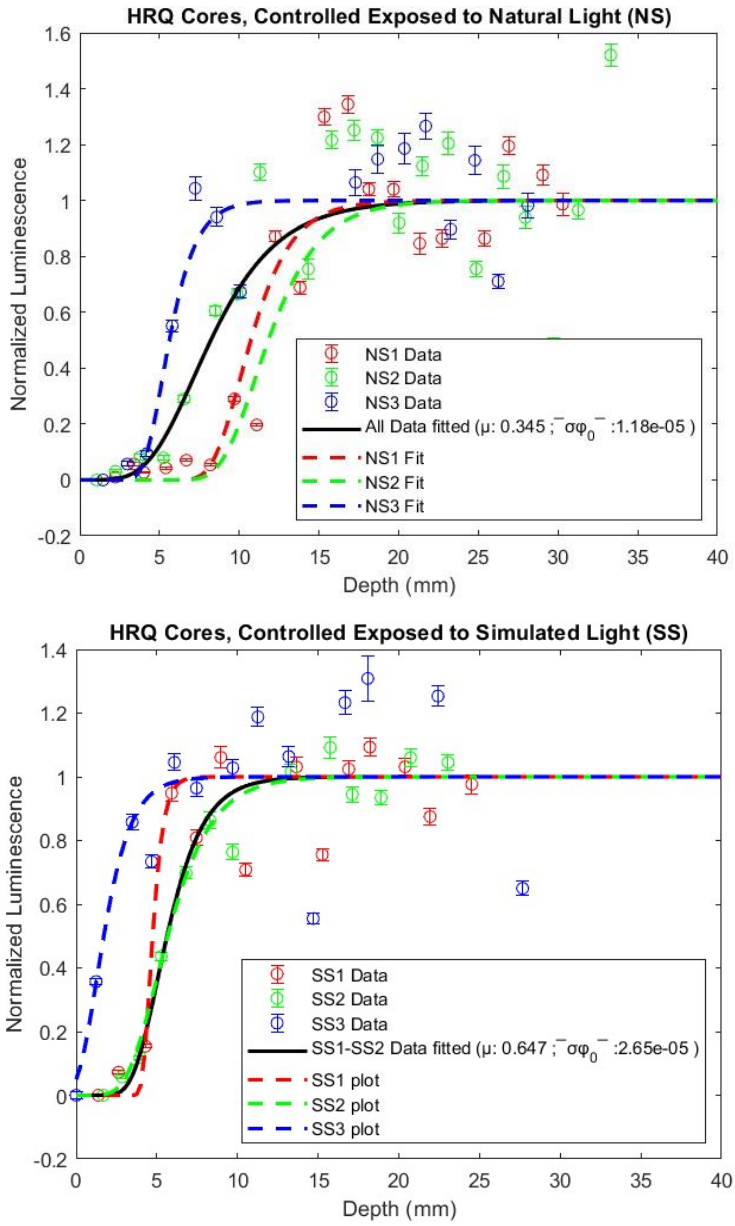

Luminescence depth profiles produced from the controlled exposure experiment approaches to natural sunlight (1NS, 2NS, 3NS) and simulated sunlight (1SS, 2SS, 3SS) from HRQ. Each black solid line represents a cumulative fit using data points from multiple cores. Extrapolated values for parameters μ and $\overline{\sigma\varphi_0}$ for each fit are noted in Table 2.1. Core 3SS may have been partially blocked from simulated sunlight, causing the partially bleached profile. Due to this concern the core data of 3SS was not included in the cumulative fit for the SS cores.

Figure 2.5

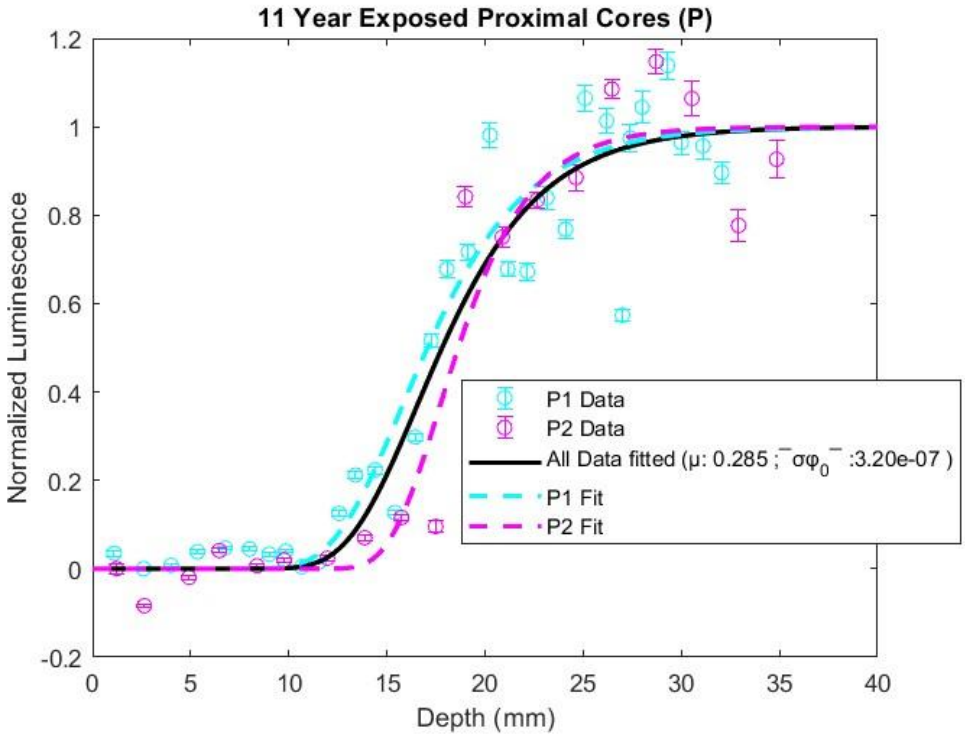

Luminescence depth profiles produced from cores taken from HRQ 2 (P1, P2), for use as proximal cores to date HRQ 1. The black solid line represents a fit using cumulative data points from the cores. Extrapolated values for parameters μ and $\overline{\sigma\varphi_0}$ for each fit are noted in Table 2.2.

Ages from two cores from the surface of HRQ (HRQ1, HRQ2) are produced from the best fit cumulative core fit parameters, using an inversion age calculation incorporating resampling likelihoods as described in Lehmann et al. (2018) (Table 2.3; Figure 2.6). A 'cumulative' representation of data from HRQ, combining both cores' data, is also fitted to represent a more comprehensible depth profile and surface age for the sample. Best fit calculated ages using controlled exposed natural sunlight derived parameters are 15.7, 2.81, and 5.88 years for HRQ1, HRQ2, and the cumulative fit, and were most similar to the true surface age of 11 years for HRQ 1 (Table 2.3). Proximal rock parameters best fitted HRQ1, HRQ2, and the cumulative fit as 118, 27.8, and 52.3 years. Controlled exposed simulated sunlight parameters produced best fit ages of 1.93E+04, 780, and 2947 years for HRQ1, HRQ2 and the cumulative fit. Ages using SS and NS parameters utilized parameters for μ and $\overline{\sigma\varphi_0}$ that do not count periods of darkness in exposure timeline, meaning the fitted ages are equivalent to estimated daytime exposure. As such, for SS and NS fits for each core, the doubled exposure time, a rough estimate of the total exposure time of the rock cores, is provided in Table 2.3 as 'Equivalent Age' for reference. In Figure 2.6, depth profiles using NS and SS parameters are fitted using the uncorrected time; equivalent exposure times roughly incorporating nighttime durations are presented in Appendix A10.

While poor parameter certainty prevents an effective comparison and interpretation of proximal rock and controlled exposed techniques, what is shown with the cumulative best fit parameters provide promise in utilizing controlled exposures for parameter extrapolation. Two relative observations of the best fits are notable, and may be verifiable in other controlled exposure experiments with improved data. One trend seen between cumulative fits from cores P1-2 and 1-3NS, both of which experienced natural sunlight and varied solar incidence angles, is their extrapolated attenuation coefficients μ are lower than what was derived from cores 1-2SS, which

were subjected to simulated sunlight with a single angle of incidence (Table 2.1,2.2). Additionally, cumulative core fits from HRQ (1-2SS, 1-3NS) produced more similar bleaching rate parameters $\overline{\sigma\varphi_0}$ than cumulative fits from P (P1-2). Daylight-only exposure calculations of proximal fits should theoretically increase the bleaching rate by a factor of two, and not change magnitude, indicating either dissimilar trap characteristics or significantly differing influences from trace minerals and hue between HRQ 1 and P could be the cause for this observation (Figure 2.2; Appendix A3).

Table 2.3
Age extrapolation by technique. Ages were calculated using best-fit parameter values for mu and sigphi_o as obtained from the cumulative core fits 1-3NS, 1-2SS and P1-2 (compare Table 2.1, 2.2 and Figs. 2.6 and 2.7). Equivalent age incorporates average nighttime duration for the given daylight exposure duration extrapolated from the controlled exposure cores, which is double the forecasted exposure age. Proximal parameters incorporate nighttime duration already, thus no change is seen between fitted and equivalent ages.

Ages calculated using Cumulative Core Fits (Best Fit Parameters 1-3NS, 1-2SS, P1-2)				
Core	Technique	Best fit (years)	Median (+1 sup, -1 inf)	Equivalent Age
HRQ1	Controlled Exposures, Natural Sunlight	15.7	17.2 (4.61, 3.46)	31.4
	Controlled Exposures, Simulated Sunlight	1.93E+04	2.05E+04 (1.40 E+04, 4.67E+03)	3.87E+04
	Proximal	118	126 (30.7, 30.7)	118
HRQ2	Controlled Exposures, Natural Sunlight	2.81	6.70 (22.4, 0)	5.62
	Controlled Exposures, Simulated Sunlight	780	1.75E+4 (3.48E+4, 1.49E+4)	1560
	Proximal	27.8	77.6 (49.8, 49.8)	27.8
Cumulative Data (HRQ1 and HRQ2)	Controlled Exposures, Natural Sunlight	5.88	10.4 (7.23, 5.42)	11.76
	Controlled Exposures, Simulated Sunlight	2947	1.27E+4 (2.49E+4, 9.96E+4)	5894
	Proximal	52.3	71.2 (49, 32.7)	52.3

Figure 2.6

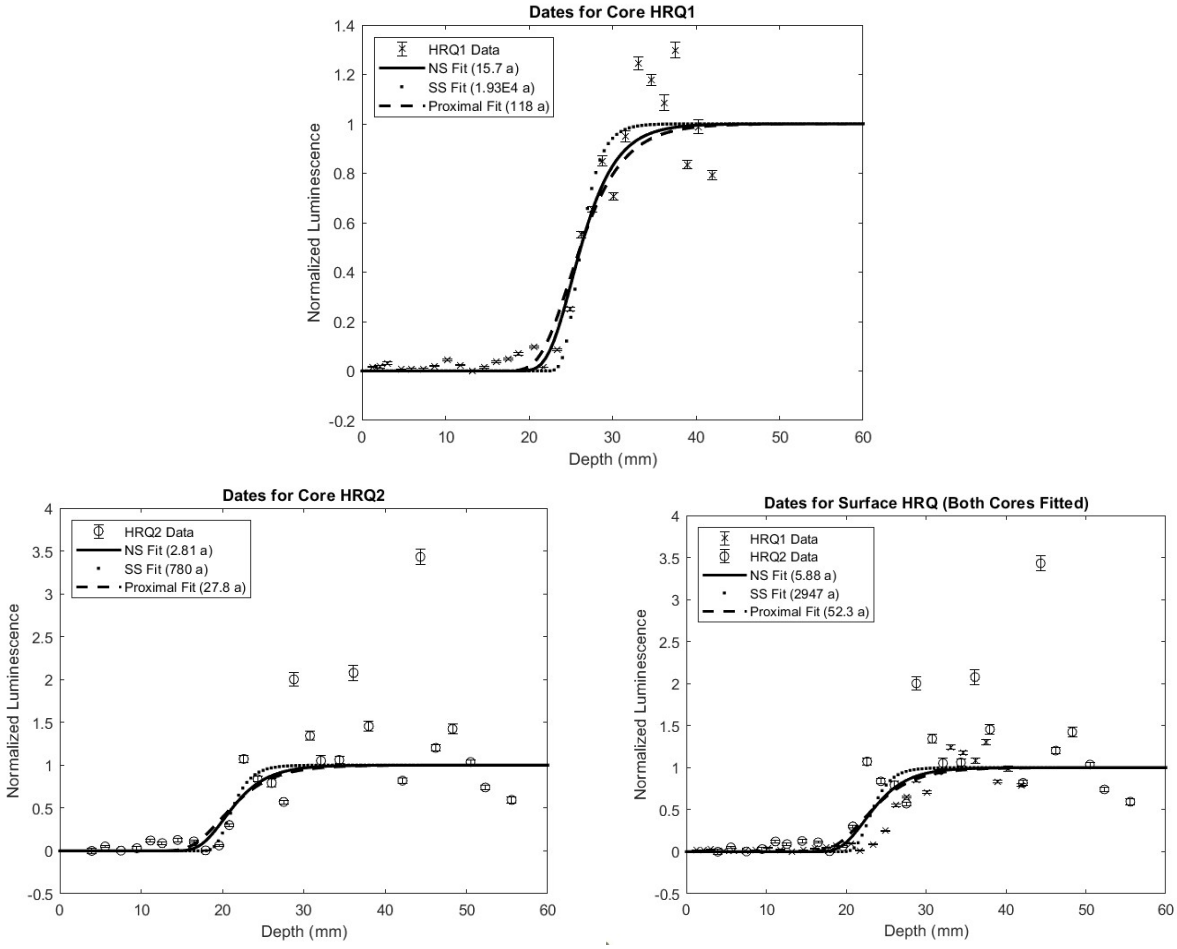

Data from two surface cores of HRQ 1 (HRQ1 and HRQ 2) are fitted to the exposure dating model using cumulative data best fit parameters extrapolated from the three presented techniques: controlled exposure experiments to natural sunlight (1NS – 3NS), controlled exposure experiments to simulated sunlight (1SS – 2SS), and the proximal rock technique (P1 – P2). NS and SS dates apply fitted age, and not equivalent age fits, for this figure. Equivalent age fits can be found in Appendix 10. Parameters of the cumulative fits are used from each technique, the values of which are noted in Tables 2.1-2.2.

2.3 Discussion

Even with large fit uncertainties, the derived ages using best fit parameters indicates the possibility that controlled light exposures applied to luminescence saturated cores from the rock of interest may provide comparable extrapolations of light attenuation and luminescence bleaching to the proximal rock technique. With improved parameter certainties using lower scatter data, stronger conclusions can be made against the observations of this inaugural trial.

Best fit and median parameter fit values experience varying magnitudes of discrepancy for both age and parameter calculations, due to the skew of fit distributions produced from the maximum likelihood estimate fit approach. Most notably, the age fits of HRQ samples using solar simulator parameters produces parameter discrepancies over a magnitude for HRQ2 and the combined HRQ1 and HRQ2 fits. The use of alternative fit approaches, such as least absolute errors, may remove some discrepancy between fit values for age. More resolute depth profile data, or using samples with less measured OSL scatter, may also assist in refining fit precision.

Two observations are worthy of re-examination in future trials. First, the observed differences in the attenuation coefficient μ derived from cumulative fits of simulated sunlight and natural sunlight exposures may verify that the varied solar incidence angles of sunlight, and the resulting wider range of interactions with mineralogy, are influential for shaping the depth profile and its fitting parameters. Second, differences in the cumulative fitted extrapolated bleaching rate constant $\overline{\sigma\varphi_0}$ seen between HRQ and P cores indicates that similar rock samples in identical geologic settings and similar light exposure conditions can produce dissimilar bleaching rate parameter extrapolations, reaffirming that proximal rock sources, which may host significant variations in trap kinetics, can be problematic for use in parameter extrapolations (Gliganic et al., 2019).

The intensity of applied solar radiations performed for controlled exposures are influential in defining extrapolative parameters, as the photon flux subjected to the samples change with the intensity of solar radiation. The resulting similar bleaching rate extrapolations $\overline{\sigma\varphi_0}$ from the cumulative fits of the NS and SS cores may indicate when the intensity of applied solar radiation relatively matches average global irradiance values for the site, controlled exposures to simulated sunlight can produce similar bleaching rate constants of in-situ samples to natural exposed samples of the same rock (Table 2.1). When performing controlled exposures, careful attention should be made to replicate the history of solar radiation of the site. Depending on the site's climatic history and timescale of exposure, accuracy in the derived luminescence bleaching rate constant may be implicated if an average for applied solar radiation is used for controlled exposures (Fuhrmann et al., 2022). While these natural sunlight controlled exposure applications conducted million second timescales of daylight exposure, longer timescales spanning multiple seasons, to better account for solar radiation variabilities, and which incorporate nighttime timescales, can potentially better ensure that solar radiation value averages are achieved for the samples. Such experiments can also determine if, when using parameters from daylight only exposure timelines, it is accurate enough to double fitted ages from daylight exposure as 'equivalent ages'.

Results of the attenuation coefficient parameter reiterate observations from Gliganic et al. (2019) as well as work from Fuhrmann et al. (2022) in that solar paths and their resulting incidence angles may also need to be considered when performing future controlled exposures to accurately derive light attenuation properties. While similar magnitude luminescence bleaching rates $\overline{\sigma\varphi_0}$ were produced between 1-3NS and 1-2SS cumulative fits, attenuation parameters μ were dissimilar, causing significantly different age extrapolations using core data from HRQ1

and HRQ 2 (Table 2.1, 2.3). This trend in parameter μ could also be influenced from hue and mineral heterogeneities between core sampling locations (Figure 2.2, Appendix A3; Kortekaas and Murray 2005; Ou et al.,2018; Gliganic et al., 2019). However, such influences should be less significant between the NS and SS cores, given the cores' surface sampling locations are from the same rock surface of HRQ 1, and appear more similar in hues and trace mineralogy than the P core sampling locations from HRQ 2 (Appendix A3). Thus, differences between simulated and natural sunlight exposure may still be significant in this trial. Given this observation, as well as work from Fuhrmann et al. (2022) indicating solar paths influence depth profile shapes, and that derived parameter μ from the cumulative fit 1-3NS is more comparable to the μ fitted from the cumulative P1-2 fit that also experienced solar path exposure, simulated sunlight controlled exposures are not recommended to extrapolate parameter μ without the incorporation of equivalent solar path angles of the sampling site.

Emulating average solar paths for simulated sunlight controlled exposures presents a difficult issue for the technique. While it is possible yet difficult to develop a simulated controlled exposure setting where solar angles can be emulated, an alternative possibility for accurately defining light attenuation could be to use the light attenuation trends present in the accumulative luminescence depth profile data of in-situ surface samples of the rock of interest, without considering the time of exposure or bleaching rate coefficient for the depth profile. Such an extrapolation could be made in that it is assumed the attenuation coefficient behaves as a constant independent of time and the rate of luminescence bleaching (Sohbati et al., 2011). This behavior is potentially seen in the cumulative fits of cores 1-3NS and P1-2, which were subjected to comparable natural sunlight and associated solar paths at different timescales yet produced similar light attenuation coefficients (Table 2.1, 2.2). Controlled exposure studies on the impact

of solar trajectory and luminescence depth profiles can provide more insight to this problem (Fuhrmann et al., 2022).

What may improve the scatter in future trials, if apparent, is to adjust the preheating protocols of slice samples to account for varied thermal lags (Elkadi et al., 2021). What can improve the acquisition of luminescence data also is by applying the use of luminescence scanning and imaging instruments, which can provide higher resolutions than what millimeter wafers can offer (Sellwood et al., 2022; Kreutzer et al., 2017). Comparing such scanning images with sample mineralogy derived from SEM or XRF imagery could also help identify possible source heterogeneities of luminescence induced by trace mineralogy (Meyer et al., 2013; Gliganic et al., 2021).

Other effects to consider when performing controlled exposures is the effect of weathering on the shape of the depth profile. Luminescence emissions can be impacted by weathering due to surface processes (Jeong et al., 2007). Such considerations may need to be made when sampling cores for controlled exposures.

Future trials should also consider how more heterogeneous rock types and infrared stimulated luminescence respond to controlled exposure experiments. The near homogeny of the Addy quartzite utilized for the controlled exposure trials provides fast and clear depth profiles that other rock materials may not produce as effectively (Meyer et al., 2018; Ou et al., 2018). Improvements in the resolution of depth profiles used in exposure dating studies will also provide more insight on the variations in depth profiles produced in similar rock types. With such improvements and considerations made to the presented trial, it is the hope that in-situ sampling for luminescence exposure dating can become a feasible sampling technique for optical surface exposure dating.

2.4 References

Aitken, M. J. (1998). Introduction to optical dating: the dating of Quaternary sediments by the use of photon-stimulated luminescence. Clarendon Press.

Applied Photophysics Limited, 1982. 1 kW Solar Simulator (AM2 Radiation) Instruction Manual.

ATG (Department of Atmospheric Sciences, University of Washington) 2021. "Rooftop Observations – ATG Building UW", Department of Atmospheric Sciences, University of Washington.

Bench, T., & Feathers, J. (2022). Trialing the application of controlled exposure experiments for optical exposure dating on quartzite quarry surfaces in Washington State. Radiation Measurements, 156, 106805.

Chapot, M. S., Sohbati, R., Murray, A. S., Pederson, J. L., & Rittenour, T. M. (2012). Constraining the age of rock art by dating a rockfall event using sediment and rock-surface luminescence dating techniques. Quaternary Geochronology, 13, 18-25.

Elkadi, J., King, G. E., Lehmann, B., & Herman, F. (2021). Reducing variability in OSL rock surface dating profiles. Quaternary Geochronology, 64, 101169.

Fuhrmann, S., Meyer, M. C., Gliganic, L. A., & Obleitner, F. (2022). Testing the effects of aspect and total insolation on luminescence depth profiles for rock surface exposure dating. Radiation Measurements, 153, 106732.

Galli, A., Panzeri, L., Rondini, P., Poggiani Keller, R., & Martini, M. (2020). Luminescence Dating of Rock Surface. The Case of Monoliths from the Megalithic Sanctuary of Ossimo-Pat (Valle Camonica, Italy). Applied Sciences, 10(21), 7403.

Gliganic, L. A., Meyer, M. C., Sohbati, R., Jain, M., & Barrett, S. (2019). OSL surface exposure dating of a lithic quarry in Tibet: Laboratory validation and application. Quaternary Geochronology, 49, 199-204.

Gliganic, L. A., Meyer, M. C., May, J. H., Aldenderfer, M. S., & Tropper, P. (2021). Direct dating of lithic surface artifacts using luminescence. Science Advances, 7(23), eabb3424.

Guralnik, B., & Sohbati, R. (2019). Fundamentals of luminescence photo-and thermochronometry. In Advances In Physics And Applications Of Optically And Thermally Stimulated Luminescence (pp. 399-437).

Hauser, N., Feathers, J., Sanderson, D., (2011). Results from a controlled OSL surface illumination experiment. Unpublished manuscript.

Jeong, G. Y., Cheong, C. S., & Choi, J. H. (2007). The effect of weathering on optically stimulated luminescence dating. Quaternary Geochronology, 2(1-4), 117-122.

Kortekaas, M., & Murray, A. S. (2005). A method for the removal of mica from quartz separates. Ancient TL, 23(2), 43-46.

Kreutzer, S., Friedrich, J., Sanderson, D., Adamiec, G., Chruścińska, A., Fasoli, M., ... & Schmidt, C. (2017). Les sables de fontainebleau: a natural quartz reference sample and its characterisation. Ancient TL, 35(2).

Lehmann, B., Valla, P. G., King, G. E., & Herman, F. (2018). Investigation of OSL surface exposure dating to reconstruct post-LIA glacier fluctuations in the French Alps (Mer de Glace, Mont Blanc massif). Quaternary geochronology, 44, 63-74.

Lehmann, B., Herman, F., Valla, P. G., King, G. E., & Biswas, R. H. (2019). Evaluating post-glacial bedrock erosion and surface exposure duration by coupling in situ optically stimulated luminescence and 10 Be dating. Earth Surface Dynamics, 7(3), 633-662.

Lindsey, K. A., Gaylord, D. R., & Groffman, L. H. (1990). Geology of the Upper Proterozoic to Lower Cambrian Three Sisters Formation, Gypsy Quartzite, and Addy Quartzite, Stevens and Pend Oreille Counties, Northeastern Washington (Vol. 30, p. 37). Washington State Department of Natural Resources, Division of Geology and Earth Resources.

Liritzis, I., Bednarik, R. G., Kumar, G., Polymeris, G., Iliopoulos, I., Xanthopoulou, V. Zacharias N, Vafiadou A,, & Bratitsi, M. (2019). Daraki-Chattan rock art constrained OSL chronology and multianalytical techniqes: A first pilot investigation. Journal of Cultural Heritage, 37, 29-43.

Luo, M., Chen, J., Liu, J., Qin, J., Owen, L. A., Han, F., Yang, H., Wang, H., Zhang, B., Yin, J. & Li, Y. (2018). A test of rock surface luminescence dating using glaciofluvial boulders from the Chinese Pamir. Radiation Measurements, 120, 290-297.

Meyer, M. C., Austin, P., & Tropper, P. (2013). Quantitative evaluation of mineral grains using automated SEM–EDS analysis and its application potential in optically stimulated luminescence dating. Radiation measurements, 58, 1-11.

Meyer, M. C., Gliganic, L. A., Jain, M., Sohbati, R., & Schmidmair, D. (2018). Lithological controls on light penetration into rock surfaces-Implications for OSL and IRSL surface exposure dating. Radiation Measurements, 120, 298-304.

Ou, X. J., Roberts, H. M., Duller, G. A. T., Gunn, M. D., & Perkins, W. T. (2018). Attenuation of light in different rock types and implications for rock surface luminescence dating. Radiation Measurements, 120, 305-311.

Sellwood, E. L., Kook, M., & Jain, M. (2022). A 2D imaging system for mapping luminescence-depth profiles for rock surface dating. Radiation Measurements, 150, 106697.

Sengupta, M., Y. Xie, A. Lopez, A. Habte, G. Maclaurin, and J. Shelby. 2018. "The National Solar Radiation Data Base (NSRDB)." Renewable and Sustainable Energy Reviews 89 (June): 51-60.

Sohbati, R., Murray, A. S., Jain, M., Buylaert, J. P., & Thomsen, K. J. (2011). Investigating the resetting of OSL signals in rock surfaces. Geochronometria, 38(3), 249-258.

Sohbati, R., Murray, A. S., Chapot, M. S., Jain, M., & Pederson, J. (2012). Optically stimulated luminescence (OSL) as a chronometer for surface exposure dating. Journal of Geophysical Research: Solid Earth, 117(B9).

Souza, P. E., Sohbati, R., Murray, A. S., Kroon, A., Clemmensen, L. B., Hede, M. U., & Nielsen, L. (2019). Luminescence dating of buried cobble surfaces from sandy beach ridges: a case study from Denmark. Boreas, 48(4), 841-855.

UO (University of Oregon) Solar Radiation Monitoring Laboratory, 2013. Cumulative Summary Data Cheney, Washington. University of Oregon.

2.5 Appendix

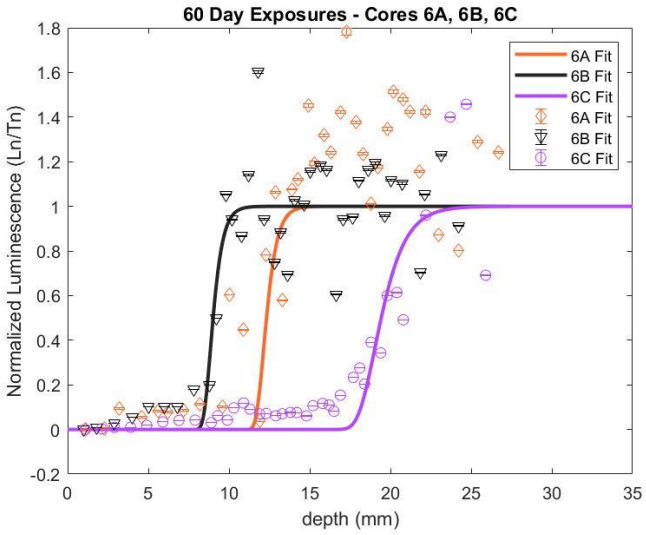

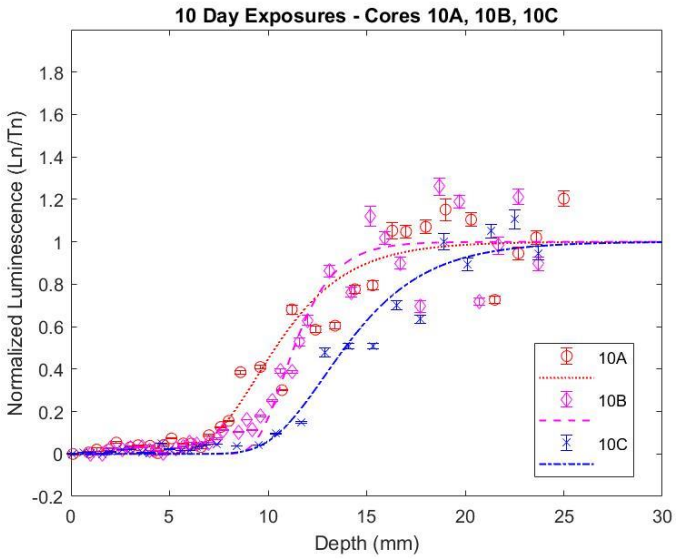

Appendix A1

Results of preliminary controlled exposure experiments of luminescence saturated samples from Lane Mountain Quarry Cores were irradiated to 350 Gy using a 60Co gamma source. Cores were exposed to natural sunlight on the Atmospheric Sciences Building rooftop at the University of Washington From February 24 – April 24, 2021. Shown are the OSL depth profiles of samples exposed to 10 days (~339000 seconds) and 60 days (~2.4 million seconds). The depth profile shapes were used as a relative means to determine luminescence saturation depths for the rock type in order to sample luminescence saturated rock material. Data fits are relative and meant to show the general shape of the depth profiles. Only 1 aliquot was used per slice to gain this rough sense of the depth profiles.

Cheney, WA. Global Data

Cheney, WA. Hourly Average Global Data For 2000 to 2013

Latitude: 47.49 degrees Longitude: 117.59 degrees Altitude: 777 meters

Mon\Hr	4	5	6	7	8	9	10	11	12	13	14	15	16	17	18	19	20	21	Total
Jan	0	0	0	0	5	48	112	167	201	201	171	118	53	6	0	0	0	0	1083
Feb	0	0	0	1	36	121	213	285	324	326	290	232	146	53	3	0	0	0	2030
Mar	0	0	1	32	120	232	337	407	434	421	373	309	222	122	32	1	0	0	3045
Apr	0	1	33	131	255	377	480	536	554	535	485	419	329	219	102	16	0	0	4473
May	0	17	102	226	360	491	591	644	665	637	594	517	414	293	170	62	5	0	5787
Jun	1	32	130	253	384	505	593	651	680	675	621	559	460	345	220	104	18	0	6231
Jul	0	21	122	262	414	556	673	750	793	783	742	658	538	406	253	114	16	0	7100
Aug	0	2	58	186	337	480	596	669	718	707	653	574	456	310	165	43	1	0	5955
Sep	0	0	11	101	238	374	482	554	585	569	514	422	300	168	48	2	0	0	4366
Oct	0	0	0	23	114	219	312	375	402	377	323	241	138	40	2	0	0	0	2565
Nov	0	0	0	1	29	95	158	207	228	214	173	110	41	2	0	0	0	0	1259
Dec	0	0	0	0	5	45	103	148	170	164	133	82	23	0	0	0	0	0	873

Values in Watt hours/meter^2 per hour

Cheney, WA. Daily Average Global Data For 2000 to 2013

Latitude: 47.49 degrees Longitude: 117.59 degrees Altitude: 777 meters

Jan	Feb	Mar	Apr	May	Jun	Jul	Aug	Sep	Oct	Nov	Dec	Yearly	
2000	----	----	----	----	----	----	----	----	----	1.93*	1.47	0.89	----
2001	1.09	2.34	3.25	4.16	6.73	6.00	6.79	6.10	4.70	2.44	1.30	1.08	3.84
2002	1.02	2.18	2.94	4.77	5.60	6.19	6.89	6.12	4.28	3.08	1.51	0.69	3.78
2003	0.79	2.13	2.74	4.12	5.41	7.06	7.58	5.83	4.33	2.68	1.44	0.75	3.75
2004	1.05	1.80	3.60	5.12	5.20	6.50	6.95	5.05	3.70	2.62	1.30	0.79	3.64
2005	1.14	2.71	3.38	4.72	5.50	6.07	7.28	6.40	4.25	2.26	1.15	0.84	3.81
2006	0.91	2.19	2.92	4.34	5.83	6.24	7.30	6.03	4.26	2.67	1.11	0.94	3.73
2007	1.06	1.57	2.92	4.54	6.14	6.15	6.98	5.90	4.46	2.41	1.27	0.86	3.70
2008	1.19	2.22	3.01	4.41	5.88	6.60	7.41	5.75	4.78	2.83	0.98	0.79	3.82
2009	1.24	1.94	3.08	4.75	6.86	7.26	7.30	5.87	4.78	2.53	1.38	1.10	4.02
2010	1.11	1.96	3.51	4.57	5.61	6.07	7.21	6.11	4.25	2.38	1.16	0.97	3.75
2011	1.06	1.90	2.58	3.92	5.13	5.76	6.62	6.20	4.50	2.23	1.41	0.91	3.53
2012	1.24	1.72	2.41	4.34	5.81	5.42	6.84	6.52	5.06	2.71	1.01	0.73	3.65
2013	1.15	1.59	3.17	4.42	5.54	5.85	7.18	5.40	3.36	2.71	1.16	0.89	3.54
Average	1.08	2.02	3.04	4.47	5.79	6.24	7.10	5.94	4.36	2.54	1.26	0.87	3.73
% SD	12	16	11	7	9	8	4	7	10	11	13	14	3

Values in average daily KWhr/meter^2 per Day

* Less than 15 days of data in month.

Univ. of Oregon Solar Radiation Monitoring Lab.

Appendix A2
Solar data - Cheney, WA.

Appendix A3
Thin sections of rocks HRQ and P (below).

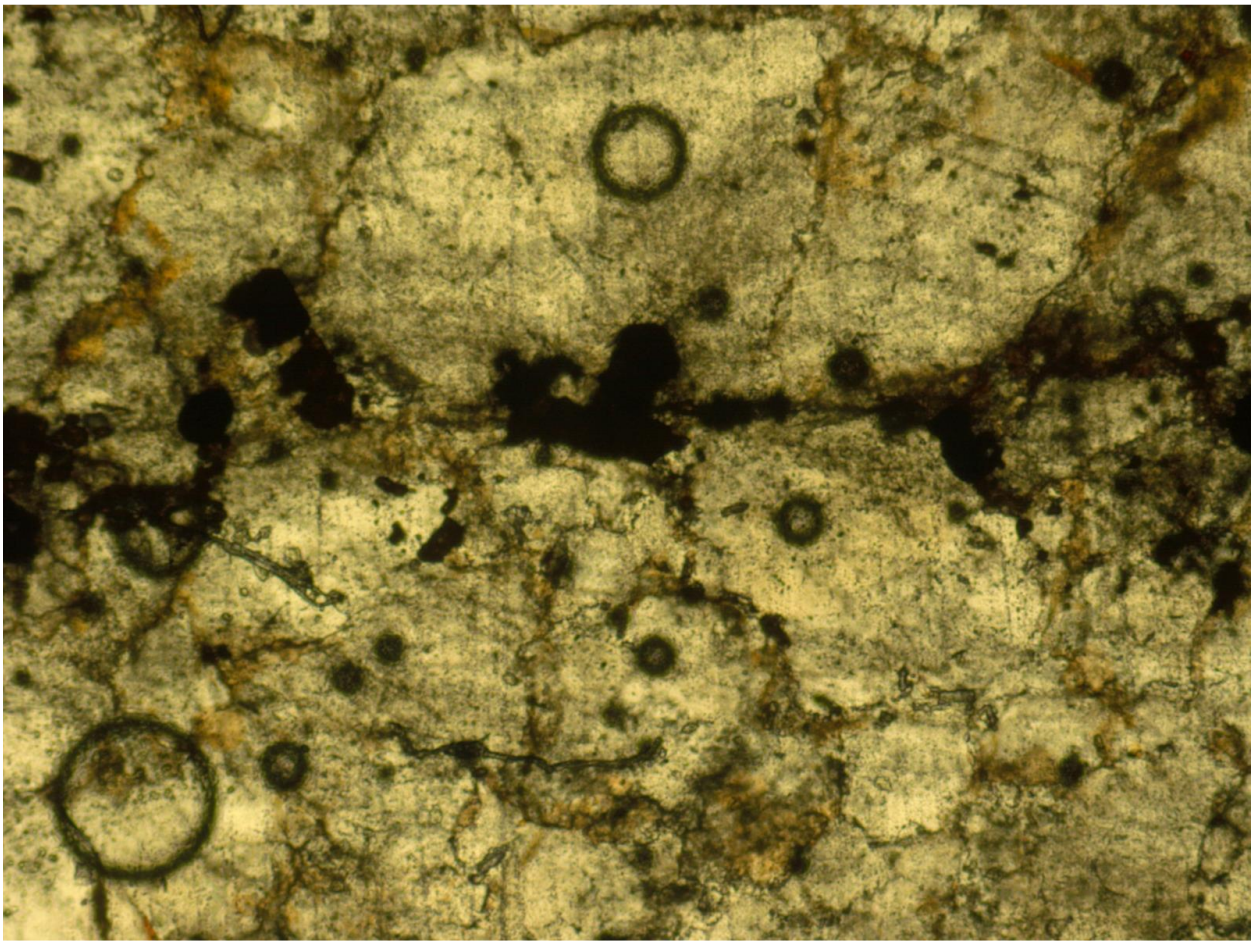

Rock HRQ, thin section ~50 microns thick. Plane polarized light, oriented 0 degrees. Iron oxide band present in center of slice.

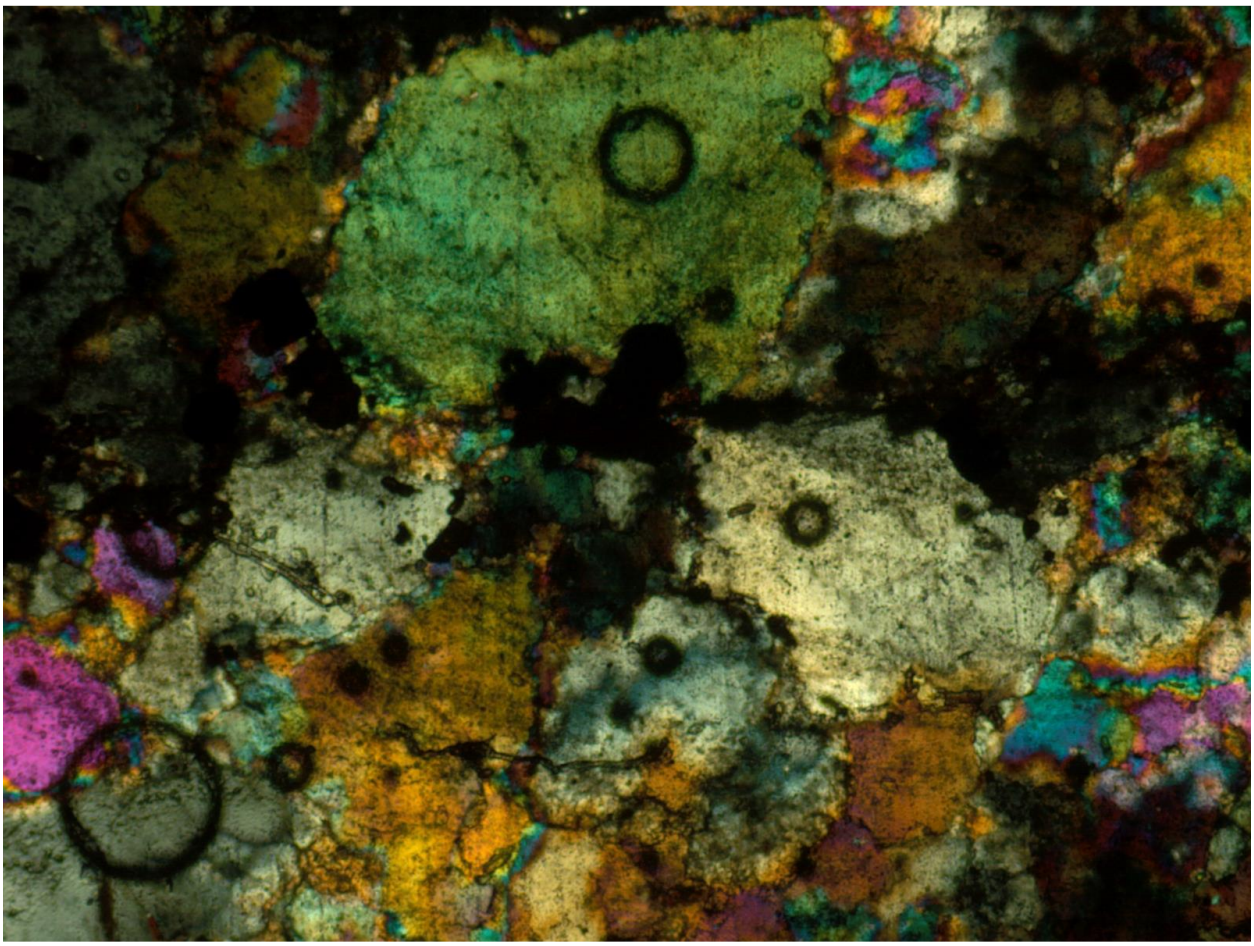

Rock HRQ, thin section ~50 microns thick. Cross polarized light, oriented 0 degrees. Quartz, iron oxides present.

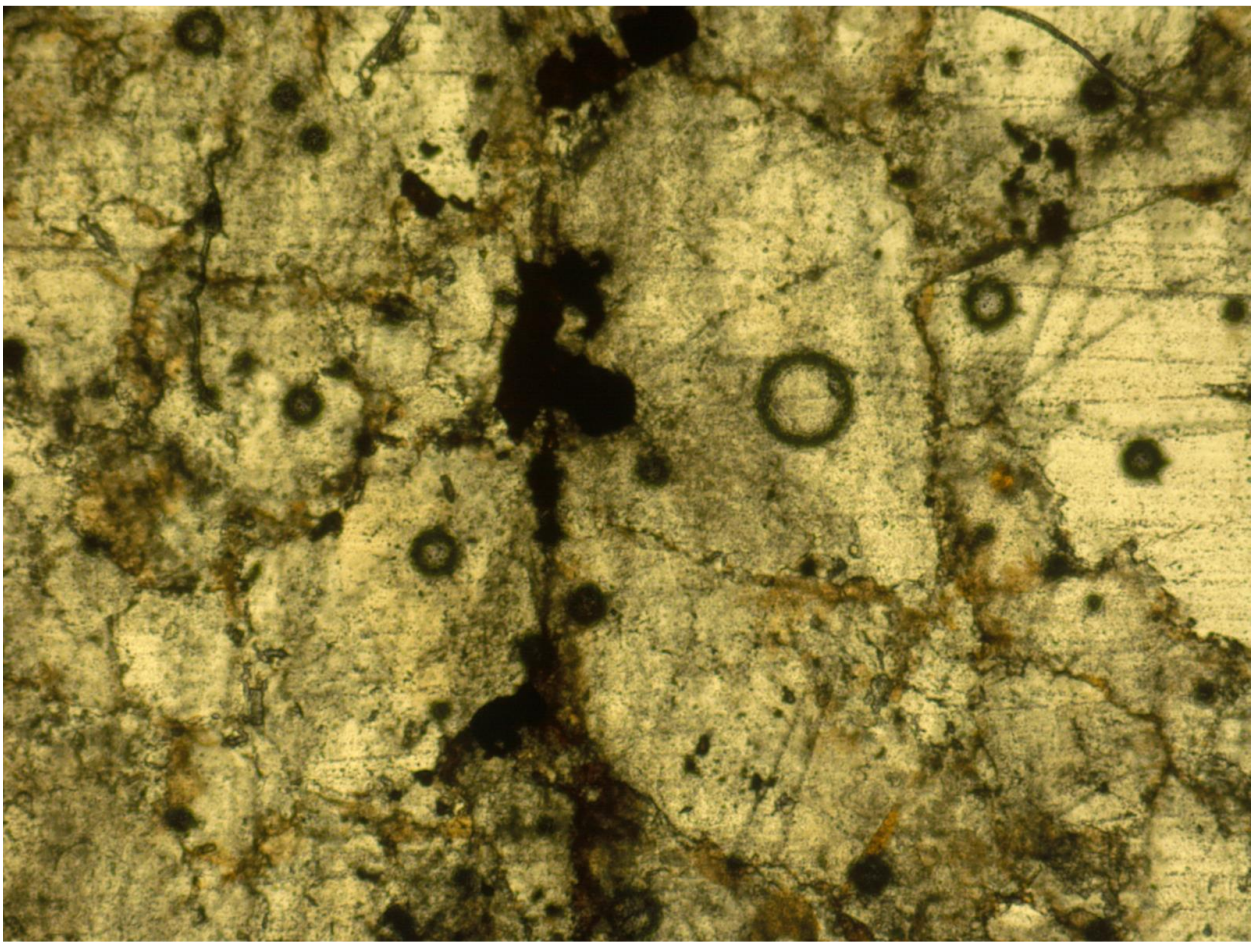

Rock HRQ, thin section ~50 microns thick. Plane polarized light, oriented 90 degrees.

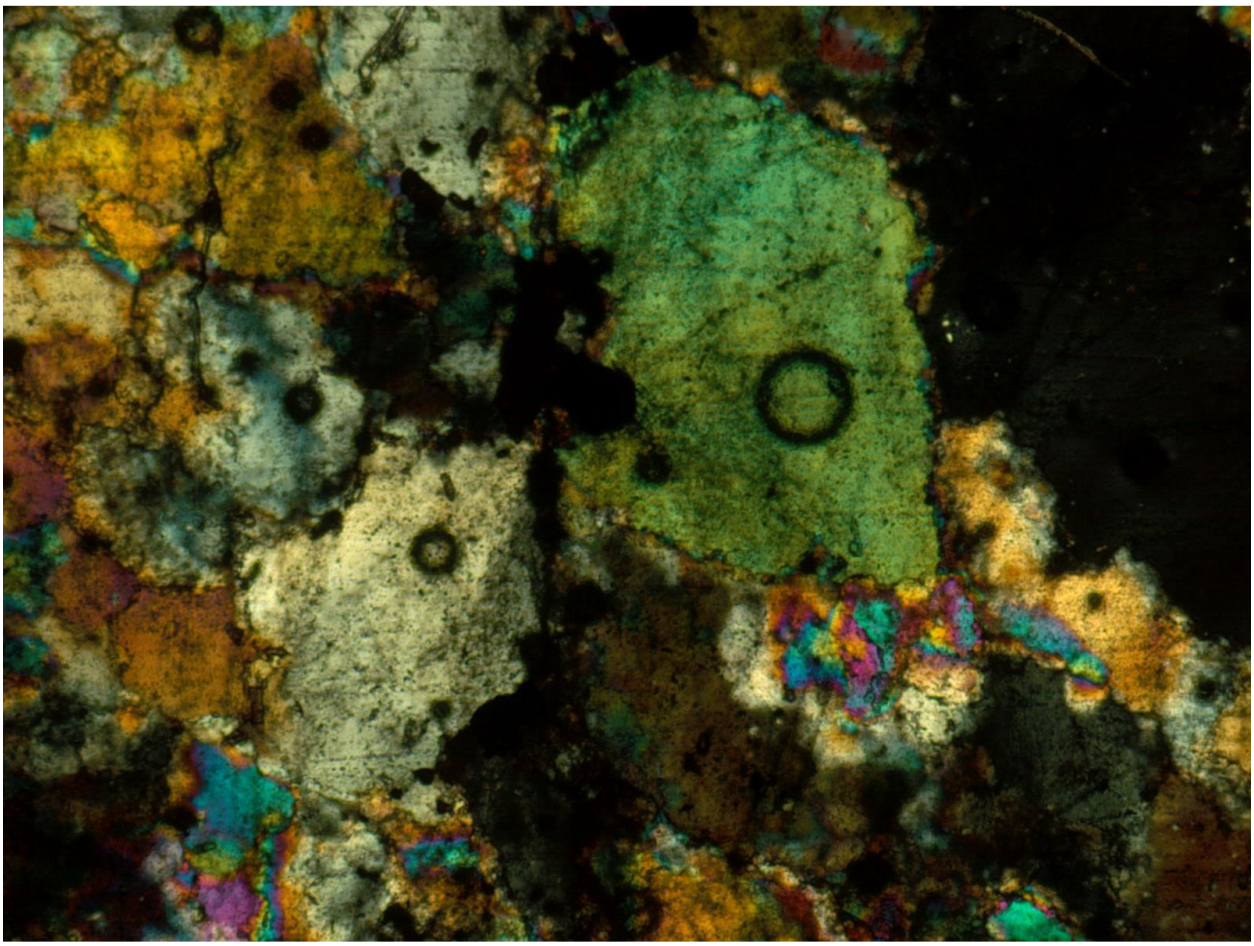

Rock HRQ, thin section ~50 microns thick. Plane polarized light, oriented 90 degrees. Resin giving off iridescence.

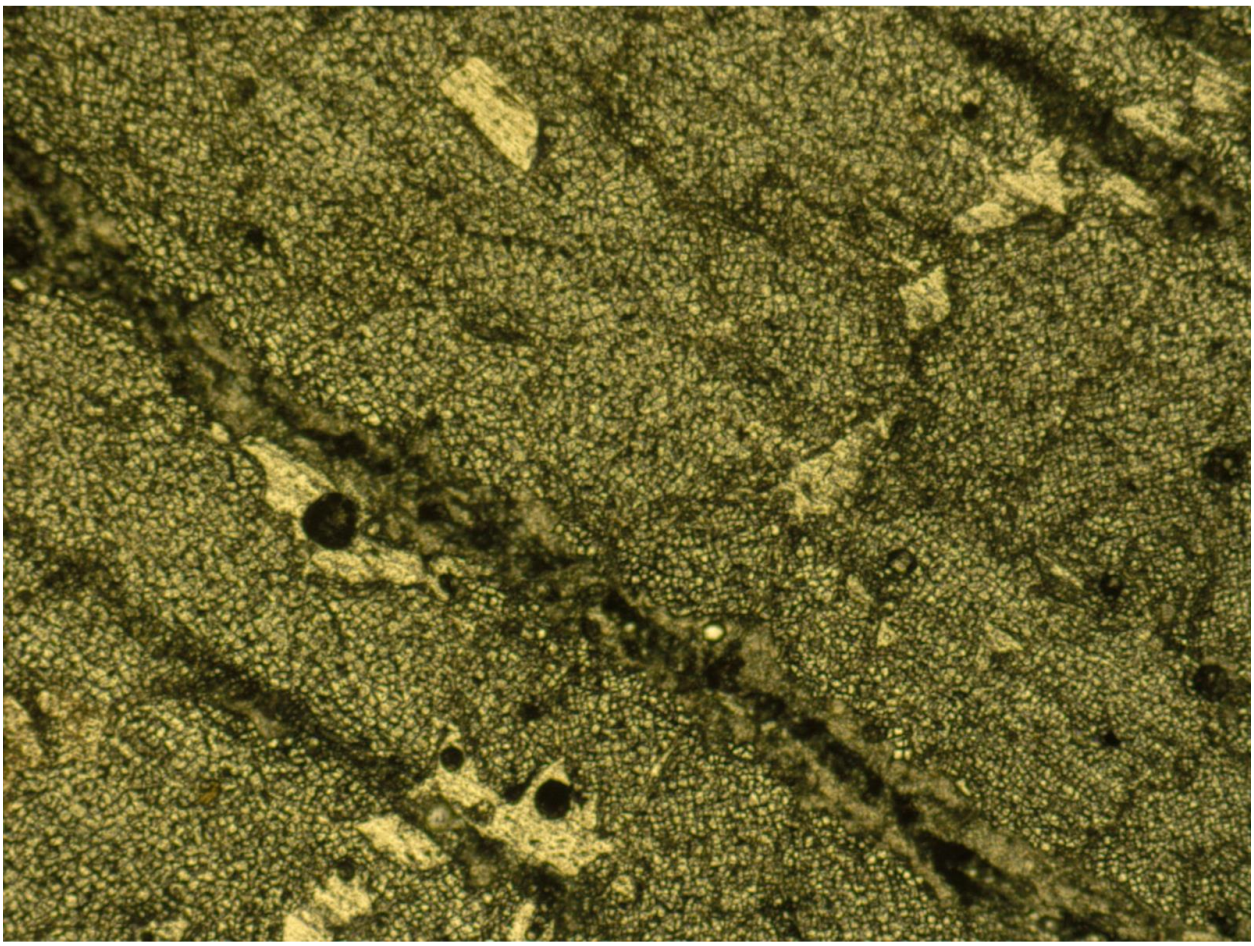

Rock P, ~ 20 microns thick, plane polarized light, oriented 45 degrees. Most of iron oxide band present in thin section was shaved off incidentally.

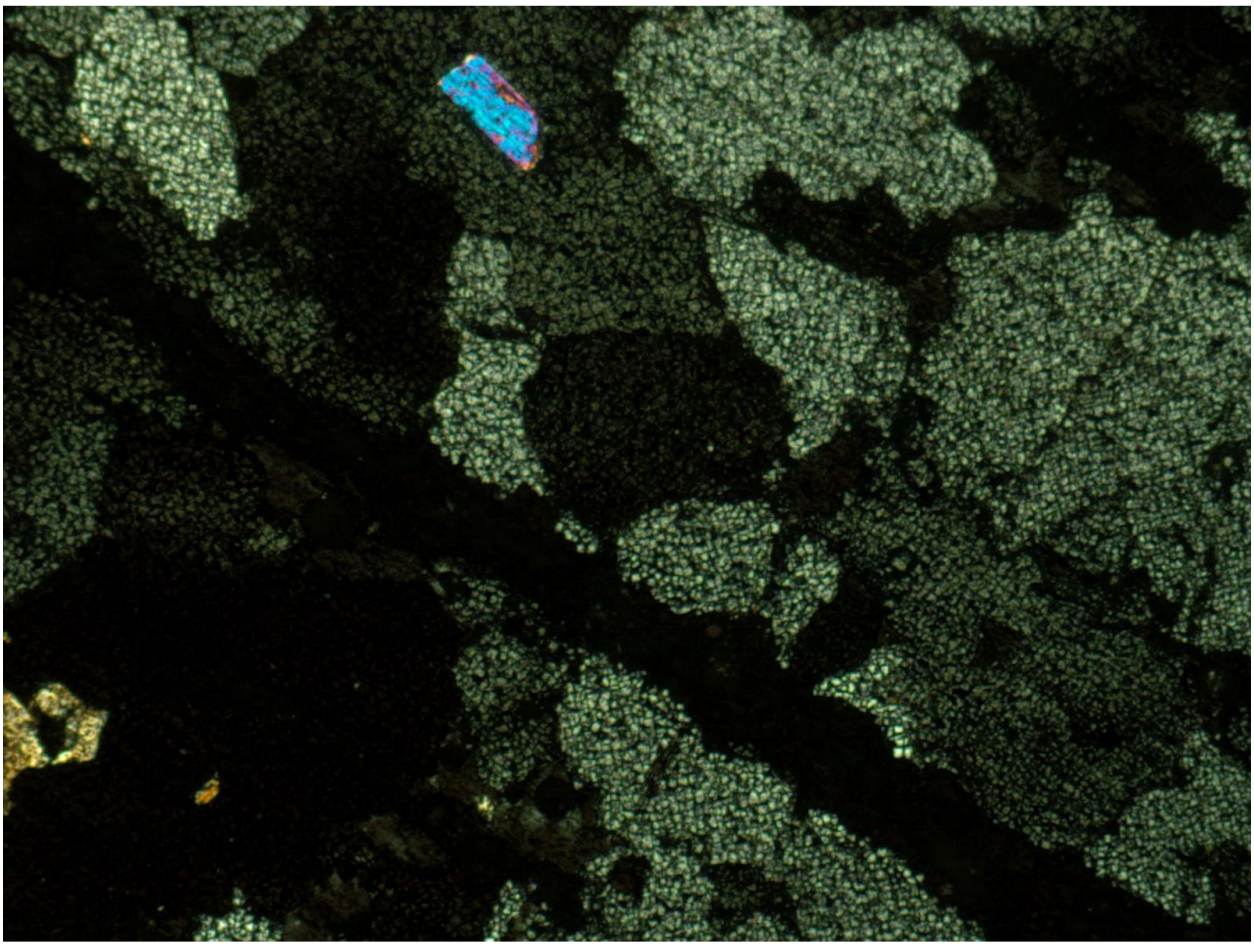

Rock P, ~ 20 microns thick, cross polarized light, oriented 45 degrees. Most of iron oxide band present in thin section was shaved off incidentally. Quartz predominated, trace mica.

Appendix A4
Sampling locations of rocks HRQ and P (below).

11 year natural exposed sample locations from HRQ. HRQ 1-1 is HRQ1. HRQ 1-2 is HRQ2.

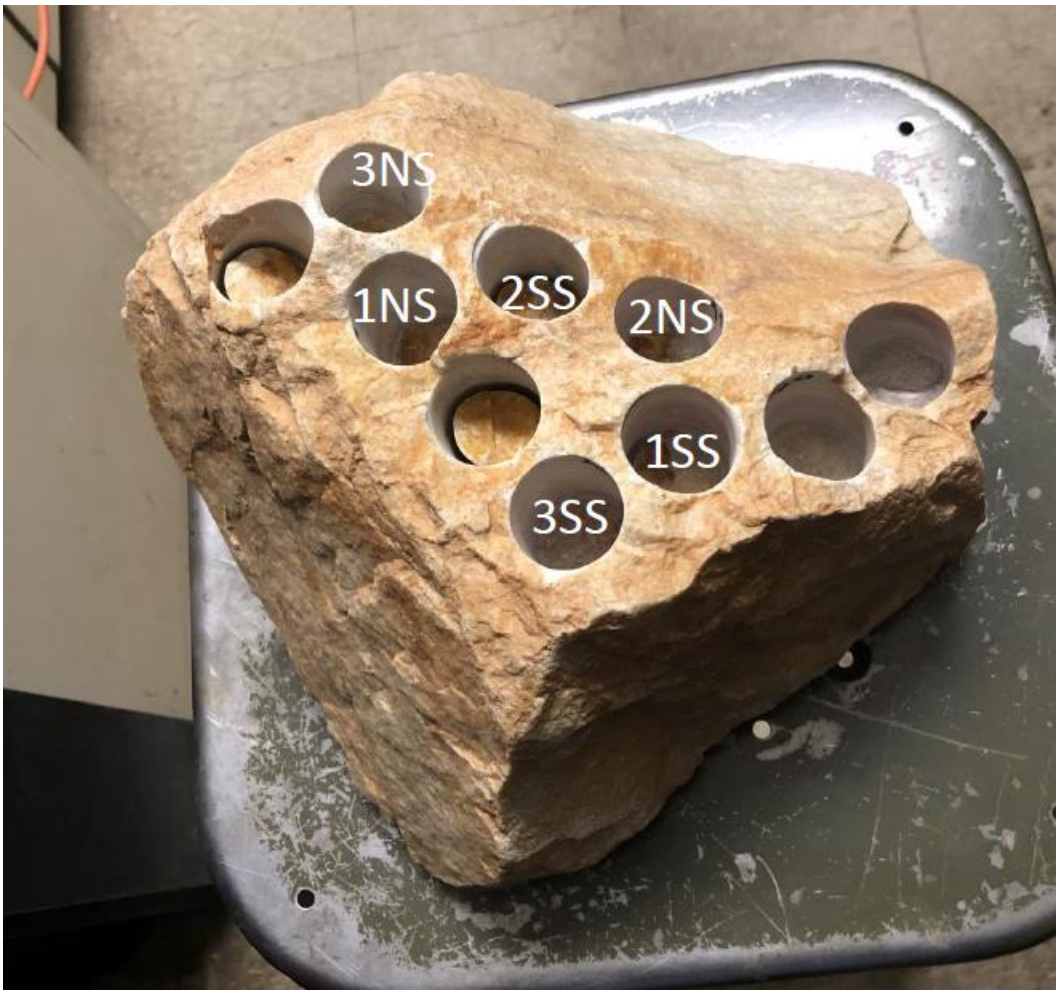

HRQ – saturated samples of HRQ taken from bottom of rock, shielded by light. The exposed sample portions were trimmed to ensure luminescence saturation.

Samples acquired from rock P – rock was cut into two pieces to accommodate the core drilling instrument used acquire some samples.

Appendix A5
Sampling location, Hard Rock Pit, Lane Mountain Quarry, Valley, Washington.

Solar radiaiton data (W/m2) compiled from ATG Rooft	Highlighted regions imply diffuse predomina	Relative fraction of direct/diffuse determined by SOLRAD Seattle Station data														
Global																
		1-Aug	2-Aug	3-Aug	4-Aug	5-Aug	6-Aug	7-Aug	8-Aug	9-Aug	10-Aug	11-Aug				
pst	utc															
8	0	0	0	0	0	0	0	0	0	0	0	0				
9	1	0	0	0	0	0	0	0	0	0	0	0				
10	2	0	0	0	0	0	0	0	0	0	0	0				
11	3	0	0	0	0	0	0	0	0	0	0	0				
12	4	0	0	0	0	0	0	0	0	0	0	0				
13	5	17	39.05	32.16	597.05	29.35556	5.119444	1.283333	5.858333	11.83889	17.93889	45.08333				
14	6	59.8	196.28	166.41	231.2694	150.9028	18.96389	20.65	62.82222	69.13333	166.0833	207.4583				
15	7	121.7	369.19	324.9	401.1056	356.9278	39.80278	50.26667	230.8917	198.6972	378.7889	358.3				
16	8	335.6	436.73	431.09	499.7361	438.0667	65.44444	116.925	319.175	530.1083	522.6111	480.7944				
17	9	373.68	490.15	507.3	586.4972	504.5389	138.0417	132.8083	337.95	518.2222	559.3194	576.1722				
18	10	431.78	585.31	552.87	617.3056	503.5472	152.5361	264.2806	485.4472	556.2139	558.2806	612.6389				
19	11	400	594.03	543.89	622.5528	491.1611	249.225	584.9028	440.5833	592.1028	570	614.6472				
20	12	530.12	586.4	574.34	597.6333	523.0417	460.25	599.4833	502.4083	619.9111	589.1222	603.8667				
21	13	503.54	546.66	548.47	592.6444	518.2111	654.5778	218.9167	610.1972	565.575	572.9417	601.7611				
22	14	420.87	508.73	548.78	550.2806	511.2194	476.2083	483.2889	547.1861	518.1306	587.1611	578.8083				
23	15	328.8	457.16	339.31	464.6917	460.0944	362.0333	339.4444	317.125	398.5111	479.4833	471.7972				
0	16	242.93	343.24	99.7	394.3111	379.5667	389.0833	375.025	204.3972	322.9389	348.7861	357.4472				
1	17	116.73	143.29	33.9	142.0806	81.35833	93.73333	90.21389	138.6	128.3083	137.3556	129.1611				
2	18	37.44	50.18	22.2	28.20278	32.18889	45.11944	17.88611	23.24444	41.18611	18.2	18.125				
3	19	0	8	15.3	5.505556	3.880556	7.336111	0.230556	1.888889	2.322222	1.119444	1.541667				
4	20	0	0	0	0	0	0	0	0	0	0	0				
5	21	0	0	0	0	0	0	0	0	0	0	0				
6	22	0	0	0	0	0	0	0	0	0	0	0				
7	23	0	0	0	0	0	0	0	0	0	0	0				
		12-Aug	13-Aug	14-Aug	15-Aug	16-Aug	17-Aug	18-Aug	19-Aug	20-Aug	21-Aug	22-Aug	23-Aug			
pst	utc															
8	0	0	0	0	0	0	0	0	0	0	0	0	0	0		
9	1	0	0	0	0	0	0	0	0	0	0	0	0	0		
10	2	0	0	0	0	0	0	0	0	0	0	0	0	0		
11	3	0	0	0	0	0	0	0	0	0	0	0	0	0		
12	4	0	0	0	0	0	0	0	0	0	0	0	0	0		
13	5	24.02778	18.09167	17.19722	11.81944	5.336111	5.830556	22.43333	8.138889	5.575	1.519444	1.091667	2.066667	40.21155		
14	6	127.8722	100.3333	123.9028	62.46111	32.96667	39.63056	124.5833	149.1111	35.79167	24.18056	20.58056	16.21944	95.9742		
15	7	273.2167	244.4139	278.2556	151.0972	44.24444	53.46944	182.7889	379.1583	80.09444	45.91667	77.76944	90.52778	205.7184		
16	8	369.0861	396.8611	360.3722	346.5111	116.6417	111.5722	239.3278	434.4417	94.89167	121.2389	148.4	296.8889	313.5876	Est flux	
17	9	448.4917	434.9889	423.5583	505.4056	112.2444	197.5583	523.4139	511.6361	230.5639	264.4333	125.5139	351.2833	384.9466	during	
18	10	505.625	482.8694	479.9167	607.2222	116.7361	100.4333	562.3528	579.325	318.1694	223.9	90.32778	526.3306	431.0182	exposure	
19	11	503.0056	553.9278	500.7278	622.6778	192.4944	162.8306	592.7167	542.2167	163.6194	365.4583	122.6083	609.3833	462.3809	(w/m2):	
20	12	533.9667	501.8306	513.0944	626.2528	356.3083	153.2806	624.15	491.8194	275.5139	444.25	152.075	613.3222	498.8018	276.4812	
21	13	551.85	424.8667	492.5167	591.9278	287.9361	285.5778	583.1806	589.2889	308.0694	463.175	376.1222	599.3	499.4481		
22	14	492.5083	328.9528	439.4472	466.0972	195.1389	396.5194	525.8889	555.1056	178.6667	557.6667	233.4889	561.6611	463.5567		
23	15	447.2556	285.5	347.7194	350.7583	67.71667	357.2528	361.6583	484.5139	192.2028	348.8583	211.0389	454.1972	362.0488		
0	16	330.675	199.9778	234.1389	192.5083	38.67222	296.4028	165.2778	318.7222	200.9889	67.97778	113.525	257.3889	255.3774		
1	17	138.9194	100.3972	112.9583	134.9917	29.79167	128.1417	65.33056	146.0611	46.16667	23.91667	111.1056	155.7333	105.5759		
2	18	27.825	28.65556	28.20556	34.59722	33.47778	31.50556	20.55	18.74444	3.619444	4.511111	26.14444	13.92778	26.33638		
3	19	0.722222	0.813889	0.2	0.413889	0.475	0.897222	0.541667	0.152778	0	0	0.072222	0	2.235386		
4	20	0	0	0	0	0	0	0	0	0	0	0	0	0		
5	21	0	0	0	0	0	0	0	0	0	0	0	0	0		
6	22	0	0	0	0	0	0	0	0	0	0	0	0	0		
7	23	0	0	0	0	0	0	0	0	0	0	0	0	0		

Appendix A6

Solar radiation data referenced to configure solar simulator for near equivalent light exposure conditions.

Appendix A7
Parameter likelihood plots

NS cores

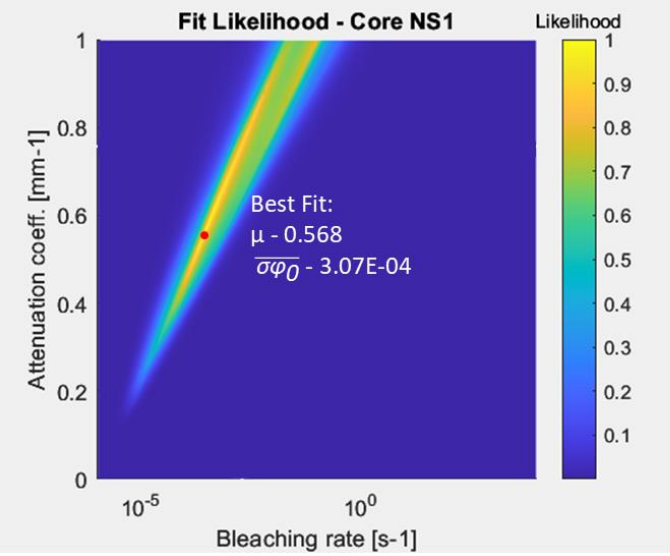

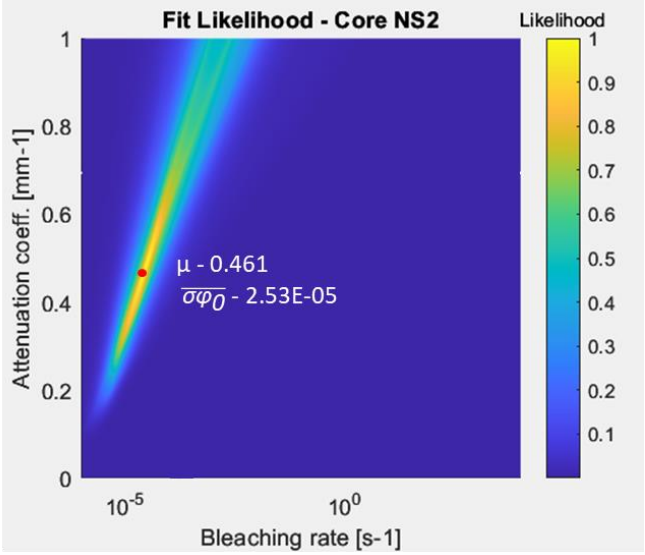

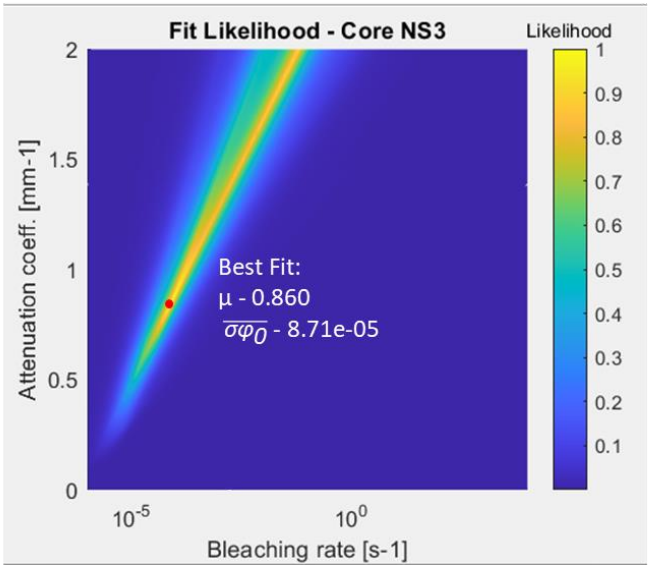

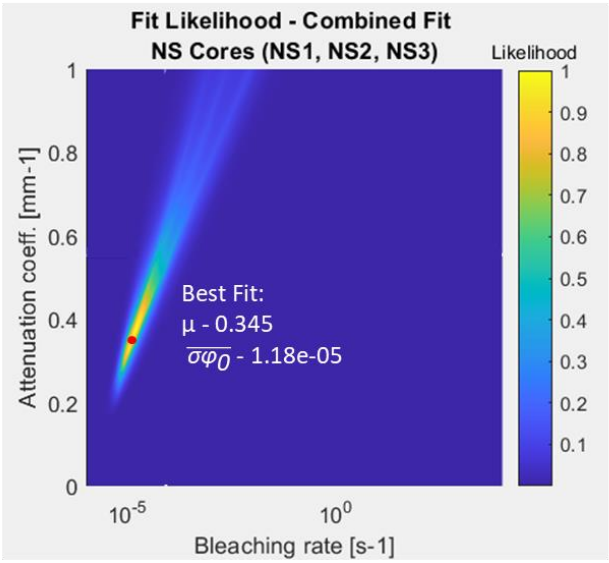

SS cores

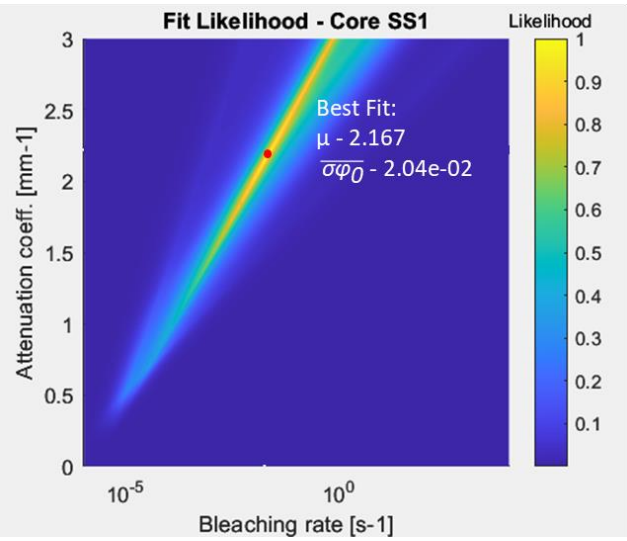
Fit Likelihood - Core SS1
Likelihood
Best Fit:
μ - 2.167
$\overline{\sigma\varphi_0}$ - 2.04e-02
Attenuation coeff. [mm-1]
Bleaching rate [s-1]

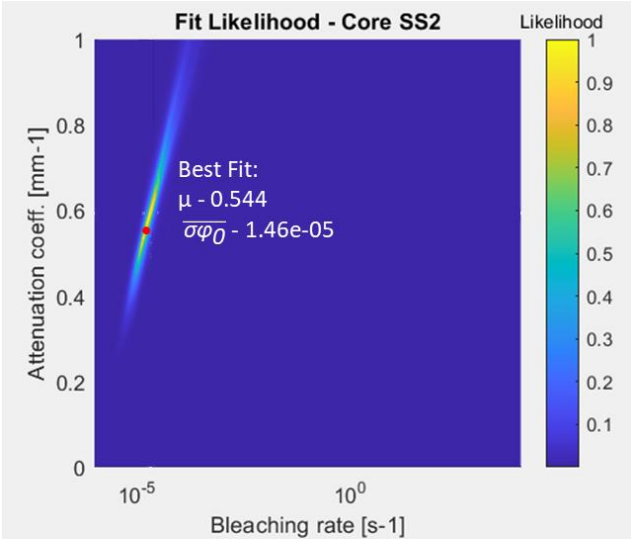
Fit Likelihood - Core SS2
Likelihood
Best Fit:
μ - 0.544
$\overline{\sigma\varphi_0}$ - 1.46e-05
Attenuation coeff. [mm-1]
Bleaching rate [s-1]

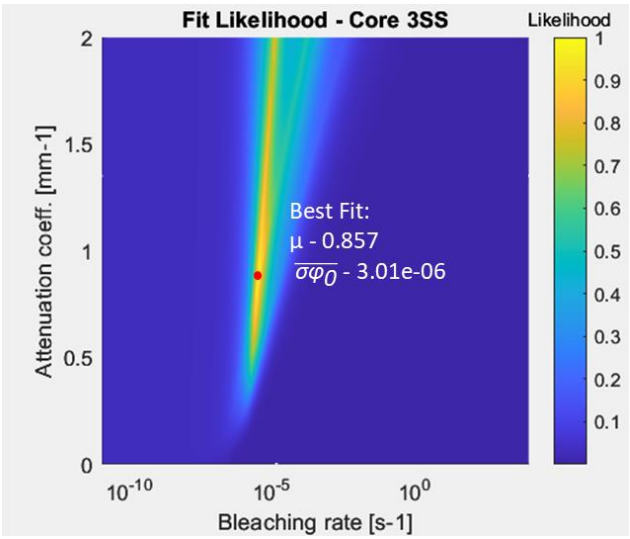
Fit Likelihood - Core 3SS
Likelihood
Best Fit:
μ - 0.857
$\overline{\sigma\varphi_0}$ - 3.01e-06
Attenuation coeff. [mm-1]
Bleaching rate [s-1]

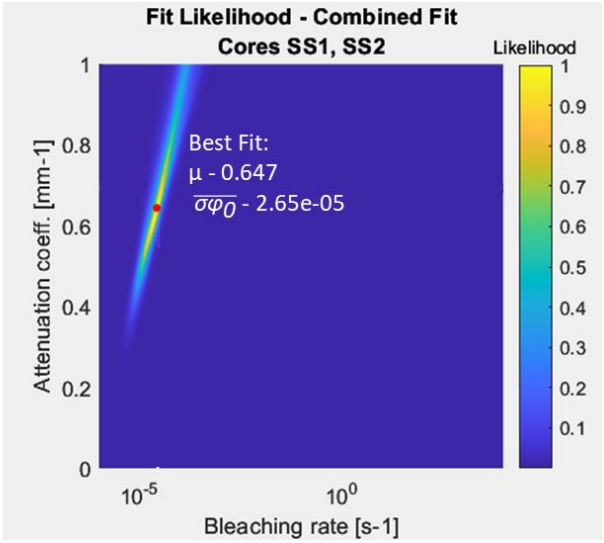
Fit Likelihood - Combined Fit
Cores SS1, SS2
Likelihood
Best Fit:
μ - 0.647
$\overline{\sigma\varphi_0}$ - 2.65e-05
Attenuation coeff. [mm-1]
Bleaching rate [s-1]

P cores

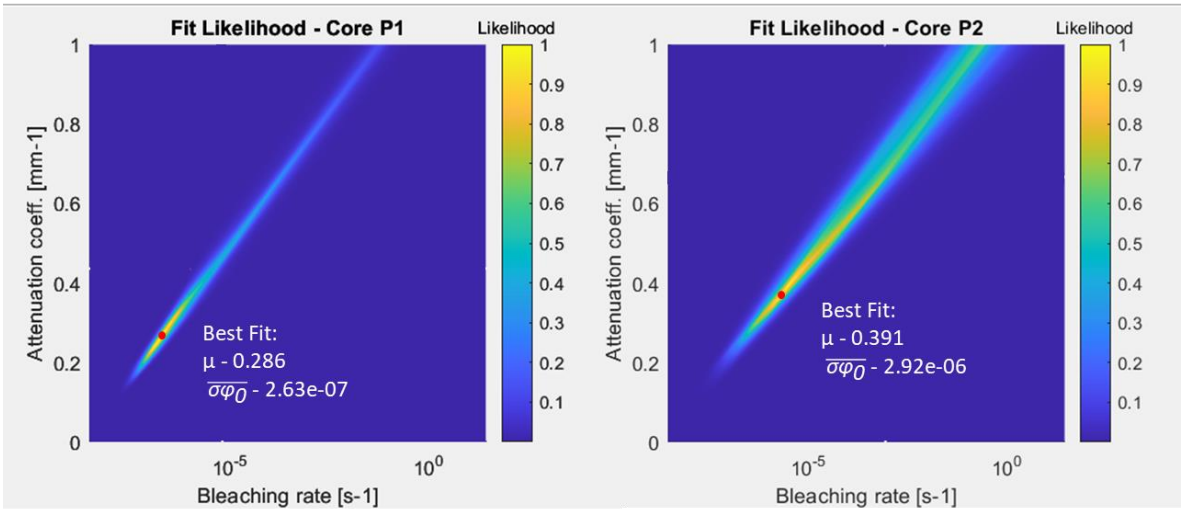
Fit Likelihood - Core P1
Likelihood
Attenuation coeff. [mm-1]
Bleaching rate [s-1]
Best Fit:
μ - 0.286
$\overline{\sigma\varphi_0}$ - 2.63e-07
Fit Likelihood - Core P2
Likelihood
Attenuation coeff. [mm-1]
Bleaching rate [s-1]
Best Fit:
μ - 0.391
$\overline{\sigma\varphi_0}$ - 2.92e-06

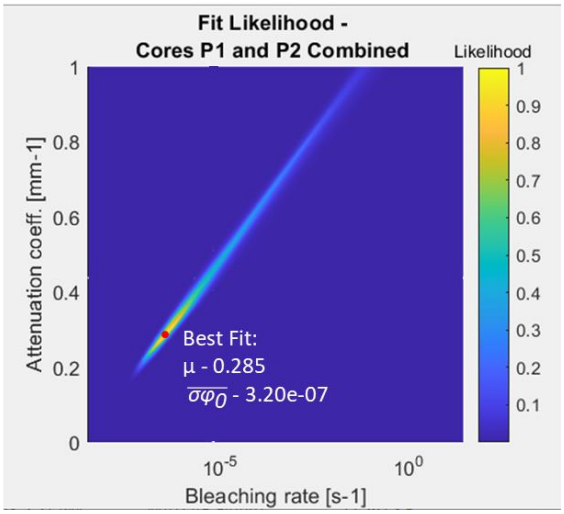
Fit Likelihood -
Cores P1 and P2 Combined
Likelihood
Attenuation coeff. [mm-1]
Bleaching rate [s-1]
Best Fit:
μ - 0.285
$\overline{\sigma\varphi_0}$ - 3.20e-07

Appendix A8

Age fits

least square results:

HRQ1-1 (age range 1-1000 for ns and prox, 1-100000 for ss)

Natural sunlight parameters (NS)

best fit - age = 15.69584437

Result for the inversion

t Median = 17 yr

t 1sigma sup = 4.61 yr

t 1sigma inf = 3.46 yr

t 2sigma sup = 6.92 yr

t 2sigma inf = 6.92 yr

Simulated Sunlight parameters (SS)

best fit - age = 19340.29684

Result for the inversion

t Median = 2.05e+04 yr

t 1sigma sup = 1.4e+04 yr

t 1sigma inf = 4.67e+03 yr

t 2sigma sup = 1.87e+04 yr

t 2sigma inf = 9.33e+03 yr

Proximal rock parameters (P)

best fit - age = 118.0258145

Result for the inversion

t Median = 126 yr

t 1sigma sup = 30.7 yr

t 1sigma inf = 30.7 yr

t 2sigma sup = 40.9 yr

t 2sigma inf = 51.1 yr

HRQ1-1 (age range 1-1000 for ns and prox, 1-100000 for ss)

Natural sunlight parameters (NS)

best fit - age = 2.812639641

Result for the inversion

t Median = 6.7 yr

t 1sigma sup = 22.4 yr

t 1sigma inf = 0 yr

t 2sigma sup = 56 yr

t 2sigma inf = 0 yr

Simulated sunlight parameters (SS)

best fit - age = 780.4075606

Result for the inversion

t Median = 1.75e+04 yr

t 1sigma sup = 3.48e+04 yr

t 1sigma inf = 1.49e+04 yr

t 2sigma sup = 6.47e+04 yr

t 2sigma inf = 1.49e+04 yr

Proximal rock parameters (P)

best fit - age = 27.77685831

Result for the inversion

t Median = 77.6 yr

t 1sigma sup = 49.8 yr

t 1sigma inf = 49.8 yr

t 2sigma sup = 149 yr

t 2sigma inf = 49.8 yr

BOTH HRQ 1 and HRQ 2 fitted

Natural sunlight parameters (NS)

best fit - age = 5.877567774

Result for the inversion

t Median = 10.4 yr

t 1sigma sup = 7.23 yr

t 1sigma inf = 5.42 yr

t 2sigma sup = 9.04 yr

t 2sigma inf = 7.23 yr

Simulated sunlight parameters (SS)

best fit - age = 2947.441058

Result for the inversion

t Median = 1.27e+04 yr

t 1sigma sup = 2.49e+04 yr

t 1sigma inf = 9.96e+03 yr

t 2sigma sup = 4.48e+04 yr

t 2sigma inf = 9.96e+03 yr

Proximal rock parameters (P)

best fit - age = 52.28999918

Result for the inversion

t Median = 71.2 yr

t 1sigma sup = 49 yr

t 1sigma inf = 32.7 yr

t 2sigma sup = 81.6 yr

t 2sigma inf = 49 yr

Appendix A9
Parameter fits for each core

mu – attenuation

SP - sigmaphio

NS1

SP Median = 0.00204 s-1

SP 1sigma sup = 0.0164 s-1

SP 1sigma inf = 0.00181 s-1

SP 2sigma sup = 0.0362 s-1

SP 2sigma inf = 0.00203 s-1

mu Median = 0.756 mm-1

mu 1sigma sup = 0.176 mm-1

mu 1sigma inf = 0.263 mm-1

mu 2sigma sup = 0.22 mm-1

mu 2sigma inf = 0.483 mm-1

NS2

SP Median = 0.000162 s-1

SP 1sigma sup = 0.000601 s-1

SP 1sigma inf = 0.000146 s-1

SP 2sigma sup = 0.0015 s-1

SP 2sigma inf = 0.000158 s-1

mu Median = 0.693 mm-1

mu 1sigma sup = 0.188 mm-1

mu 1sigma inf = 0.283 mm-1

mu 2sigma sup = 0.283 mm-1

mu 2sigma inf = 0.424 mm-1

NS3

SP Median = 0.00171 s-1

SP 1sigma sup = 0.015 s-1

SP 1sigma inf = 0.00165 s-1

SP 2sigma sup = 0.0507 s-1

SP 2sigma inf = 0.0017 s-1

mu Median = 1.38 mm-1

mu 1sigma sup = 0.377 mm-1

mu 1sigma inf = 0.566 mm-1

mu 2sigma sup = 0.566 mm-1

mu 2sigma inf = 0.943 mm-1

NS all

SP Median = 8.04e-05 s-1

SP 1sigma sup = 0.000618 s-1

SP 1sigma inf = 6.45e-05 s-1

SP 2sigma sup = 0.00112 s-1

SP 2sigma inf = 7.5e-05 s-1

mu Median = 0.555 mm-1

mu 1sigma sup = 0.255 mm-1

mu 1sigma inf = 0.17 mm-1

mu 2sigma sup = 0.339 mm-1

mu 2sigma inf = 0.297 mm-1

SS 1

Result for the calibration

SP Median = 0.0181 s-1

SP 1sigma sup = 0.519 s-1

SP 1sigma inf = 0.0175 s-1

SP 2sigma sup = 1.65 s-1

SP 2sigma inf = 0.018 s-1

mu Median = 2.22 mm-1

mu 1sigma sup = 0.565 mm-1

mu 1sigma inf = 0.848 mm-1

mu 2sigma sup = 0.707 mm-1

mu 2sigma inf = 1.55 mm-1

SS2

Result for the calibration

SP Median = 2.07e-05 s-1

SP 1sigma sup = 2.73e-05 s-1

SP 1sigma inf = 8.88e-06 s-1

SP 2sigma sup = 6.35e-05 s-1

SP 2sigma inf = 1.39e-05 s-1

mu Median = 0.594 mm-1

mu 1sigma sup = 0.155 mm-1

mu 1sigma inf = 0.116 mm-1

mu 2sigma sup = 0.271 mm-1

mu 2sigma inf = 0.232 mm-1

SS3

Result for the calibration

SP Median = 1.35e-05 s-1

SP 1sigma sup = 4.6e-05 s-1

SP 1sigma inf = 1.28e-05 s-1

SP 2sigma sup = 0.000249 s-1

SP 2sigma inf = 1.35e-05 s-1

mu Median = 1.35 mm-1

mu 1sigma sup = 0.499 mm-1

mu 1sigma inf = 0.499 mm-1

mu 2sigma sup = 0.599 mm-1

mu 2sigma inf = 1.1 mm-1

SS 1 and SS2 combined

SP Median = 2.77e-05 s-1

SP 1sigma sup = 4.1e-05 s-1

SP 1sigma inf = 1.26e-05 s-1

SP 2sigma sup = 9.81e-05 s-1

SP 2sigma inf = 2.16e-05 s-1

mu Median = 0.694 mm-1

mu 1sigma sup = 0.163 mm-1

mu 1sigma inf = 0.122 mm-1

mu 2sigma sup = 0.244 mm-1

mu 2sigma inf = 0.285 mm-1

P1

Result for the calibration

SP Median = 6.44e-06 s-1

SP 1sigma sup = 0.000645 s-1

SP 1sigma inf = 6.28e-06 s-1

SP 2sigma sup = 0.0104 s-1

SP 2sigma inf = 6.38e-06 s-1

mu Median = 0.436 mm-1

mu 1sigma sup = 0.315 mm-1

mu 1sigma inf = 0.18 mm-1

mu 2sigma sup = 0.451 mm-1

mu 2sigma inf = 0.225 mm-1

P2

Result for the calibration

SP Median = 0.000871 s-1

SP 1sigma sup = 0.0191 s-1

SP 1sigma inf = 0.000866 s-1

SP 2sigma sup = 0.16 s-1

SP 2sigma inf = 0.000871 s-1

mu Median = 0.667 mm-1

mu 1sigma sup = 0.222 mm-1

mu 1sigma inf = 0.222 mm-1

mu 2sigma sup = 0.266 mm-1

mu 2sigma inf = 0.4 mm-1

P1 and P2 combined fit

Result for the calibration

SP Median = 6.27e-06 s-1

SP 1sigma sup = 0.000286 s-1

SP 1sigma inf = 5.64e-06 s-1

SP 2sigma sup = 0.00293 s-1

SP 2sigma inf = 6.13e-06 s-1

mu Median = 0.438 mm-1

mu 1sigma sup = 0.25 mm-1

mu 1sigma inf = 0.125 mm-1

mu 2sigma sup = 0.375 mm-1

mu 2sigma inf = 0.208 mm-1

Appendix A10
Age fits of cumulative cores using equivalent exposure ages (twice the time of fitted age).

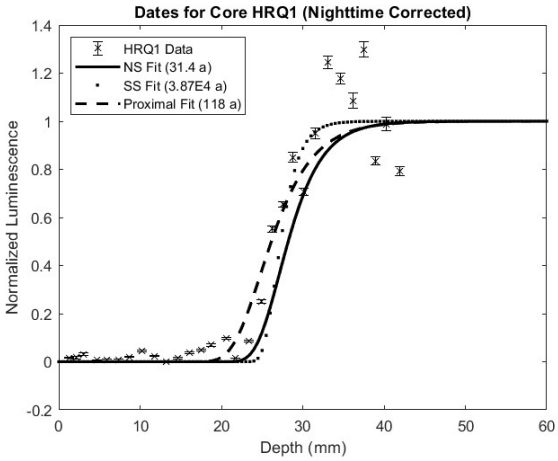

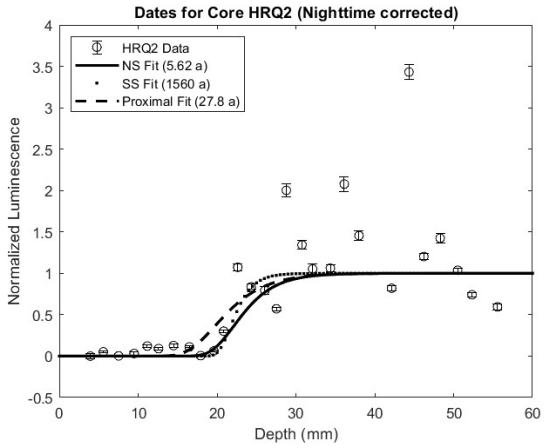

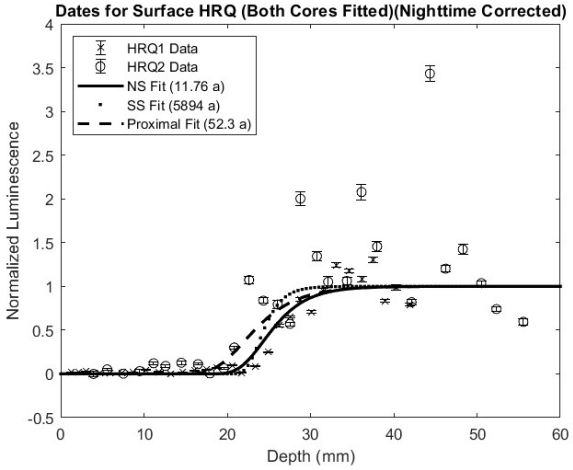

3. Lane Mountain Part 2 – Investigating Spatially Resolved OSL Laser Scanning and Energy Dispersive X-ray Spectroscopy Applications for Exposure Dating Applications

Abstract

Optically Stimulated Luminescence (OSL) depth profiles can be used to extrapolate rock surface exposure ages by understanding a sample's light attenuation and OSL bleaching behaviors. However, the current measuring procedure for producing depth profiles, by measuring the luminescence of millimeter slices from surface core samples, offers limited resolution data, limiting parameter extrapolative precision. The use of OSL laser scanning measuring protocols on transverse core slices has potential for improving the data resolution of OSL depth profiles from core samples. An 11-year exposed rock surface was parameterized for light attenuation and luminescence bleaching rates using depth profile data from four surface cores collected via wafer and scan measuring techniques, to show the potential of OSL laser scanning to improve depth profile dataset resolutions and parameter extrapolative accuracy. Additionally, non-quartz OSL anomalies were filtered from scan datasets to determine if non-quartz mineral filtering can further improve the resolution and parameterization of depth profile datasets. OSL scanning measures improved the resolution of depth profiles over wafer derived depth profiles for the measured samples, and in comparing uncertainties of parameters, broadly improved parameter precision using maximum likelihood estimate fitting protocols. Non-test dose corrected spatially resolved data error bounds were generally larger than from wafer derived data. When compared to unfiltered spatially resolved depth profile data, OSL anomaly filtered scanned depth profiles improved error bounds of anomaly affected data, and improved parameter extrapolative precision with roughly a similar effect as using non-filtered scan data. The uncertainty in parameterization

was impacted by scatter prevalent from scan datasets, which is caused by low OSL sensitivity from samples, the potential recording of remnant OSL, the lack of regenerative dose normalization applied to the scan dataset, as well as other scanning instrument measuring limitations.

3.1 Introduction

In luminescence exposure dating applications, luminescence depth profiles are commonly measured from rock surfaces by taking core samples from the rock surface, slicing the core into millimeter-thick depth segments, and measuring the luminescence of each slice in one or several aliquots (Sohbati et al. 2012).

The measuring approach can produce viable datasets for certain dating applications, but limitations become apparent. For instance, data scatter has been documented in several applications using wafer derived datasets, resulting in depth profiles that poorly fit the traditional model form and therefore inaccurate exposure ages, high uncertainty, or both (Bench & Feathers 2022; Elkadi et al. 2021; Brill et. al 2020; Moayed et al. 2022). The cause of scatter in depth profiles may include luminescence count heterogeneities from crystallographic or mineralogical variations in the slices, which traditionally are not separated from the measured aliquots. When dating quartzites or quartz rich rocks, non-quartz minerals like zircon, rutile, potassium feldspar, or micaceous minerals can produce high levels of OSL, but their OSL dosimetry properties are dissimilar and less reliable than those of quartz (Ou et al. 2018; Meyer et al. 2013; Polymeris et al. 2019; Bulur et al. 2014; Sanjurjo-Sanchéz et al. 2013). The presence of such minerals can provide complexity to the shape of the depth profile, and can only be partially indicated in one dimensional slice derived point data (Ou et al., 2018).

In response to the limitations imposed on depth profile measurements from prior studies using millimeter wafer slices, this study will explore the potential of using OSL laser scanning approaches to improve the data resolution of luminescence depth profiles with spatially resolved OSL imagery. It is the aim that the use of higher resolution depth profile data will improve the precision of fitted parameterizations for the first-order exposure dating model over wafer derived datasets. The assessment will be conducted by comparing OSL measures and parameter fits from wafer derived and luminescence laser scan derived luminescence depth profiles from 11-year exposed rock surfaces.

In recognizing previous works, some of the first spatially resolved luminescence studies were utilized for characterizing luminescence heterogeneities in samples, with initial applications using color imaging and CCD cameras (Hashimoto et al. 1989, Duller et al. 1997). Laser scanning OSL techniques have also been presented for spatially resolved measures, but like with CCD imaging, signal to noise ratios and data scatter issues limited use in dating applications (Bailiff & Mikhailik, 2003). More recent applications introduce the use of electron multiplying CCD (EM-CCD) cameras for producing enhanced sub-millimeter imaging resolutions of TL, OSL and IRSL datasets, which improved the data resolution compared to prior imaging techniques, yet instrumentation resolution is still limited in its ability for practical applied study using OSL, IRSL, and TL (Clark-Balzan & Schwenninger, 2012; Duller et al. 2015). Recent applications using EM-CCD imagery for IRPL exposure dating applications show promise in reducing data scatter, producing higher resolution images which improve upon the dataset resolutions that traditional wafering sampling techniques can offer (Sellwood et al. 2019; Sellwood et al. 2022a,b).

While laser scanning applications face resolution limitations in spatially resolved luminescence mapping, its use may still provide enhanced data resolutions over what millimeter wafer derived datasets can offer for depth profile measurement. Even if resolution issues are persistent like in prior spatially resolved measuring experiments, the assessments can still provide the ability to identify areas of OSL heterogeneities, which may be useful for containing depth profile curve shapes for dating (Clark-Balzan & Schwenninger, 2012). Specifically, one can determine mineralogically the source of such OSL, with particular attention on whether the OSL anomaly sources are from non-quartz mineralogy. Sample mineralogy is important for determining the viability of OSL as an effective dosimeter for a rock sample, and identifying mineralogy where its OSL will be less reliable as a dosimeter may help interpret causes of scatter found in depth profile data.

Thus, as a second aim with the collected spatially resolved data, an attempt will be made to filter non-quartz OSL anomalies from depth profile datasets to attempt determining if such a procedure can refine the shape and improve data error and parameter extrapolative precision of the spatially resolved depth profile. The mineral identification of the OSL scanned samples will be attempted with the use of scanning electron microscope energy dispersive x-ray spectroscopy. With the compositions of OSL anomalous data identified from SEM-EDS measures, the anomalies identified as non-quartz can be filtered from the spatially resolved data to produce a depth profile that purely express quartz OSL emission.

Finally, this assessment aims to note differences in depth profile forms and extrapolated parameters between similar sourced rock surfaces using the spatially resolved datasets. It is a common assumption for exposure dating applications that rocks of similar composition and proximity to each other have similar optical bleaching and light attenuation properties, but this

may not be true (Sohbati et al. 2012, Chapot et al. 2012, Lehmann et al. 2019; Luo et al. 2018; Gliganic et al. 2019; Brill et al. 2020). The use of spatially resolved datasets may provide enhanced visual insight on the spatial variations of the depth profiles taken from the same site, to examine if compositional or textural differences seen in samples show an obvious impact to the depth profile form. Such observations collected from scanning techniques can offer insight on the accuracy of using proximal sourced rocks with known exposure ages for model parameter extrapolation.

3.2 Application Site

Spatially resolved OSL and OSL from wafer slices will be measured from quartzite samples from an 11-year exposed portion of Lane Mountain Quarry, an open pit quartzite quarry located in Washington State. The quartzite comes from the lower Cambrian member of the Addy Formation, made up of 96–98% coarse-grained quartz with smaller percentages of clay protolith phyllite consisting of micaceous minerals and iron oxides (Lindsey et al., 1990).

Quartzite was chosen in this study for its near homogenic quartz composition, which limits the amount of varying trap excitation and light attenuation in the rock core, and should hopefully limit the variations in the luminescence depth profiles between core samples. Any variations in OSL from non-quartz trace mineralogy can be easily identifiable in spatially resolved data, allowing for clear interpretations on the impact of non-quartz mineralogy in spatially resolved data. Further, quartz is an effective dosimeter, building up a measurable luminescence signal with increased radiation exposure.

Two rock surfaces were sampled from the site, denoted as ‘HRQ’ and ‘P’ (Figure 3.1). Two cores were sampled from rock P, cores P2 and P3, while two were sampled from rock HRQ, which are HRQ1 and HRQ2 (Figure 3.2). Core locations from the samples are presented in the

appendix (A0). The cores were originally sampled for a controlled exposure experiment comparative study, Bench & Feathers (2022).

Figure 3.1

Site of the 'Hard Rock Pit' at Lane Mountain Quarry, Valley, Washington. Site hosts 11-year exposed quartzite rock surfaces, HRQ and P. Two cores, HRQ 1 and HRQ 2, are sampled from rock HRQ, while two cores, P2 and P3 are sampled from rock P for this study. The cores gathered from each rock will have their depth profiles measured using both millimeter wafer slices and OSL spatially resolved scans to compare the precision of parameter extrapolations between datasets. Sampling holes of the processed rock samples are found in the Appendix.

Figure 3.2

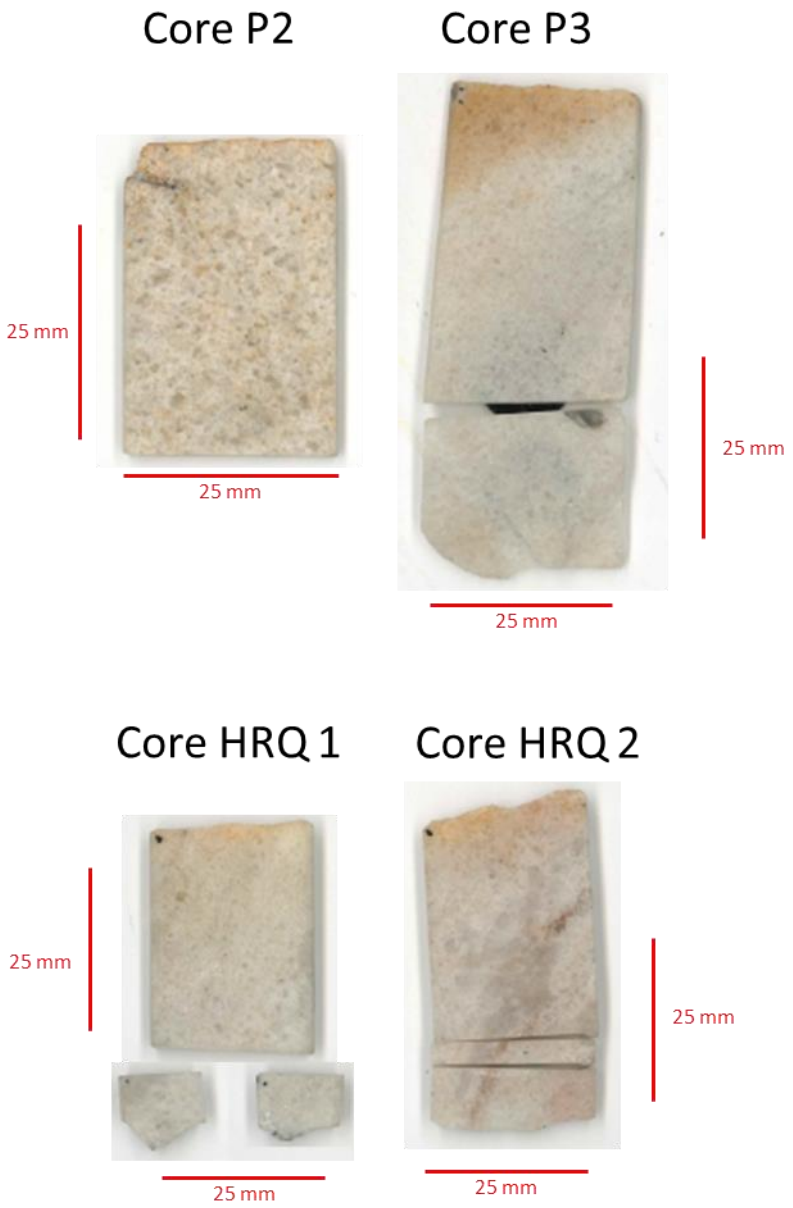

Core samples P2, P3, HRQ 1 and HRQ 2. The black area of Core P3 is adhesive tape used to hold the two core pieces together. Thicknesses of each sample are 2.56 mm for P2, 2.18 mm for P3, 2.31 mm for HRQ 1, and 2.91 mm for HRQ 2.

In comparing parameter values from each core, using wafer and laser scan datasets, it is expected that scan derived datasets will offer higher resolution depth profiles and more precise parameter fits than what wafer derived datasets can produce. In examining the mineralogy of the anomalous

OSL identified in the spatially resolved scan data, it can be determined whether OSL anomalies are quartz or non-quartz in composition. With this information, spatially resolved OSL data can be anomaly filtered to remove non-quartz minerals from scan datasets, to attempt improving the scatter, error bounds, and parameter precision of depth profile data. Finally, comparisons of the parameterizations of the cores can denote variations in light attenuation and luminescence bleaching properties seen among similar sourced samples, which offers further insight on the use of proximal rocks for model parameterizations for exposure dating applications.

3.3 Measuring Procedures

Sample preparation:

Cores were collected in the field in subdued light with a diamond tipped corer. Those cores used for measurement in this study were bisected longitudinally, with one half sliced into millimeter wafers, and the other half cut into one longitudinal slice roughly 2 mm in thickness (Figure 3.2). The cutting was performed using a Pace Technologies PICO–155 P precision saw at the University of Washington Luminescence Dating Laboratory. The 400-μm thickness of the diamond-coated brass blade used for slicing removes roughly the same thickness of sample, and this deficit is incorporated when determining the representative depth of millimeter slices.

Wafer Measures:

For the millimeter slices, three aliquots each roughly 40–70 mm^2 were taken from the center of each hemispherical for luminescence measurement on a Risø DA-15 TL/OSL Reader, placing each aliquot in stainless steel sample cups (Gliganic et al. 2019; Bray et al. 2002). A preheat of 240°C for 10 s was applied to each sample before measuring the OSL of the natural signal, as well as before the signal from a 40 Gy test dose applied using a $^{90}Sr/^{90}Y$ source. Each OSL

measure was stimulated using a 470 nm blue LED at 3.36 cd (70% power) for 100 s at 125°C. The weighted mean and error of the three aliquots were calculated to represent the OSL for the slice depth. Data were then normalized using 0 to represent the minimum value of the depth profile and 1 representing the mean of the last five weighed slices, which are OSL saturated.

Scanning Measures:

Luminescence scans were performed on laser scanning equipment at the Luminescence Research Lab at the Scottish Universities Environmental Research Center (SUERC), funded by the UK Food Standards Agency (Sanderson et al. 2001; Bench et al. 2023) (Figure 3.3). The configuration of the scanner utilizes an Acculase brand 520 nm, 10 mW laser with a 20-micron diameter beam. The laser is placed in a fixed position for stimulating OSL from a sample placed on a moving X-Y stage. Above the X-Y stage is a photomultiplier which measured the emitted OSL after every laser stimulation through a 9 mm UG-5 and 2 mm UG-11 light filters. The scanning procedure was set to record OSL in 0.1 second increments from 1 second of laser stimulation for each X-Y step, following 1 second of 0.1 second incremented background photon measures. Beam scattering within the sample subsurface has the potential to cause OSL to stimulate beyond the 20-um beam diameter, thus 250-micron resolution steps were used to limit the effect of measuring sample area which could have been stimulated from prior laser steps. This step resolution produces 250-micron OSL maps of each sample, with 16 datapoints per square millimeter of sample (Figure 3.4).

Figure 3.3

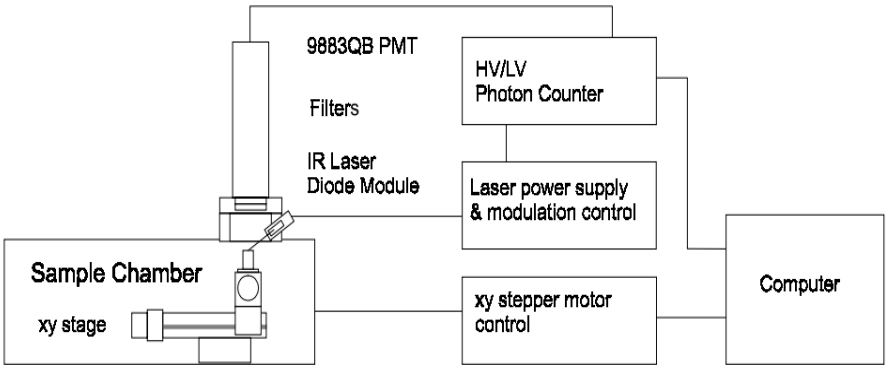

Schematic of OSL laser scanning instrument, originally presented in Sanderson et al. (2001). A fixed laser module allows for the OSL stimulation of a sample placed on a moving X-Y stage, to where the X-Y stepper motor control sequence and laser power supply is configured for the desired scanning application. A photomultiplier rests above the X-Y moving stage to where stimulated OSL is measured for each commanded X-Y step. 250 micron steps were used with an Acculase brand 520 nm, 10 mW laser for this study to reduce interference of the laser toward unscanned regions. Filters used for the study include a 9 mm UG-5 light filter and a 2 mm UG-11 light filter.

Before scanning, each sample was preheated in a furnace for 30 minutes at 135°C. After the spatially resolved scans are produced, the scan data is then converted onto spreadsheets. OSL values from each pixel are corrected for background by subtracting the lowest 0.1 s increment multiplied by 10 from the 1 second background measure. Minimum background values were chosen for pixels to best amplify the weak OSL trends seen in the samples by reducing potential overlap in recorded OSL from prior scans.

A depth profile of 250-micron increments is then produced from the scan data by taking the average and standard error of pixels from each 250 micron depth. Each depth profile data point incorporates roughly over 150 pixels along the width of the transverse core slice for the given depth. The resulting depth profile data are then normalized using 0 to represent the mean OSL of the first 3 millimeters of the depth profile and 1 representing the mean of the last 5 millimeters for the core sample.

Scanning Electron Microscope Energy Dispersive X-ray Backscatter Spectroscopy (SEM-EDS):

The composition of OSL anomalies in scan datasets can be identified with the use of scanning electron microscope energy dispersive x-ray spectroscopy (SEM-EDS) (Figure 3.5). Anomalies are identified from scan data as an area of at least two pixels (0.125 mm^2) with counts roughly two times above average OSL count datasets (generally over 120 counts) at similar sample depth extent, (yellow-colored zones in Figure 3.4, 3.5a). Anomaly zones are imaged using a Hitachi S3400-N scanning electron microscope with an Oxford Instruments X-Act silicon drift detector with INCA SEM-EDS image analysis software. The mineralogy of the measured anomaly is interpreted based on the spectral distribution of elements measured by the instrument (Figure 3.5c). Appendix A1 offers images and EDS measures of all anomaly zones identified in the OSL scans.

Once an anomaly has been identified as non-quartz, it can be removed from the scan dataset manually in the spreadsheet to produce anomaly filtered depth profile points. Appendix A1 documents the OSL anomalies identified for each sample.

Fitting Protocol:

Least absolute error regressions are used on both wafer and scan derived OSL depth profile data to extrapolate parameter values from each core, using Lehmann et al.'s (2019) parameter fitting approach. The use of least absolute errors, although promoting higher uncertainties, allows for more robust fitting to the shape of the depth profile, with less influence of outlier data that is common in depth profiles.

Figure 3.4

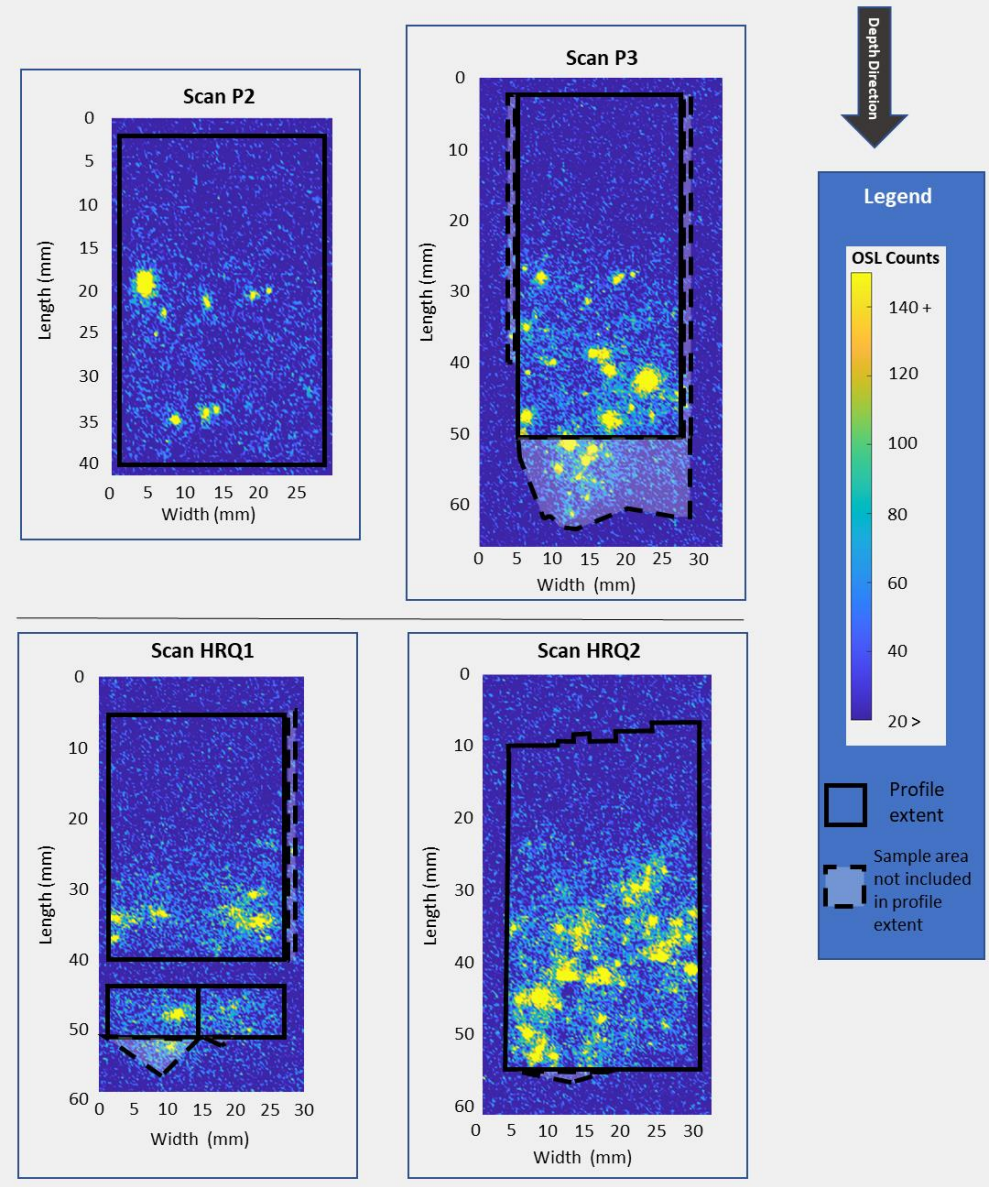

OSL scans from core samples HRQ1, HRQ2, P2 and P3. Areas within black rectangles are transverse slice dimensions used in depth profile plots. Grey areas represent scanned material which is not incorporated in depth profile data due to dimensional complexity. OSL counts greater than 140 counts, roughly at least double the value of OSL seen in most of the core, are presented as yellow anomalous regions in the scan images. The sparsity of OSL anomalies to the OSL scan extent indicates specific mineral presences of high trap density or mineralogy uncharacteristic to most of the quartz in the sample. Identified anomalies via SEM-EDS are presented in the Appendix.

Figure 3.5

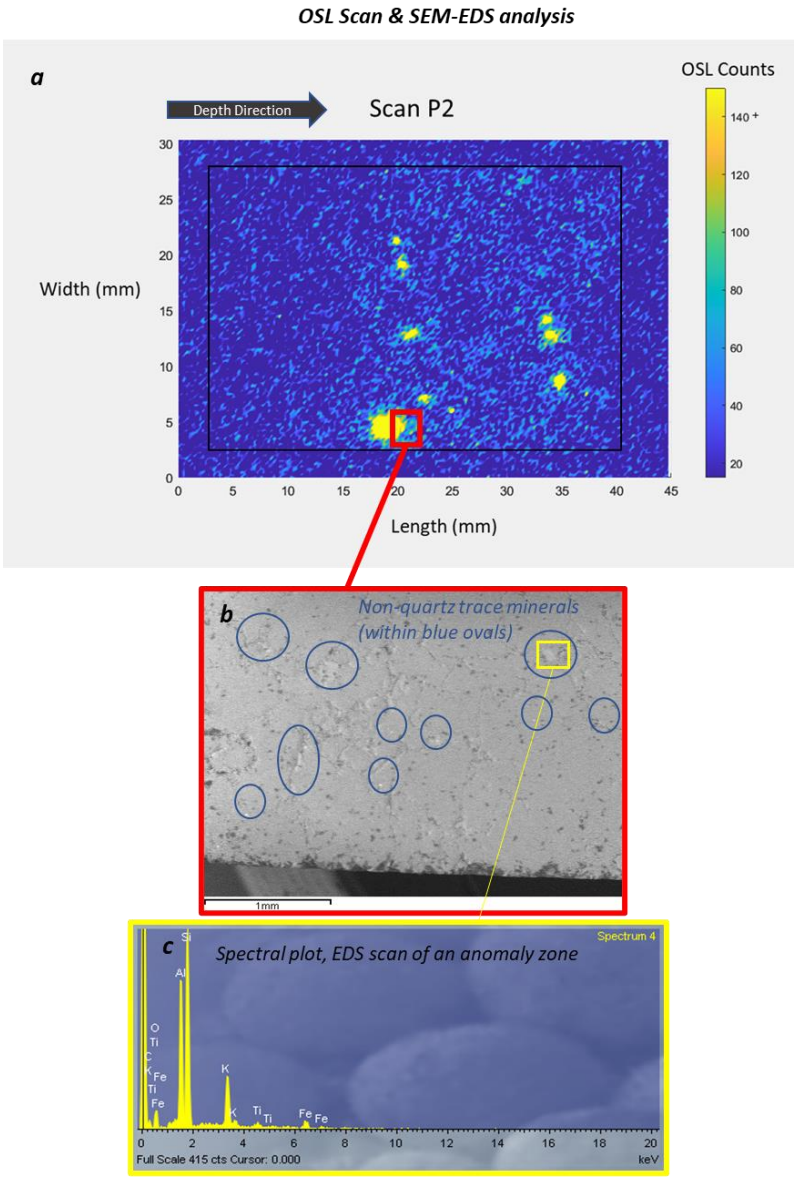

Presentation of OSL anomaly identification process from OSL scan datasets. (a) Scan assessment of core sample P2, yellow regions indicating OSL anomalies. (b) SEM image of location of Core P2, area extent highlighted in red in subfigure a. Non-quartz trace minerals are identified with blue ovals. (c) Energy dispersive spectroscopy (EDS) scan of the mineral, location highlighted in yellow in subfigure b. Peaks indicate element specified keV emissions, as proportion of full scale counts shown in lower right of plot. Higher presence of aluminum, potassium, titanium from the measure indicates the mineral is non-quartz. Thus, it can be interpreted that part of the OSL anomaly present in this location could be influenced from a non-quartz mineral and could be excluded from the depth profile measure.

The approach calculates $\overline{\sigma\varphi_0}$ and μ from core depth profile data, applying known age of 11 years (3.469e+8 seconds), using least absolute residuals misfits from 10^6 randomized fit simulations. The range of parameters fitted for μ were between 0-1, and for log($\overline{\sigma\varphi_0}$*t) between 0 and 10. A maximum likelihood estimate is calculated from the misfit of each parameter combination, which is then randomly resampled to produce a probability density function of parameter likelihoods for the tested parameters. The resultant distribution is then used to produce median parameter and absolute uncertainty values for the fitted cores.

Through these means, parameters $\overline{\sigma\varphi_0}$ and μ are retrieved for each core. Parameters were also acquired from combined datasets of HRQ and P surfaces, where data from HRQ1 and HRQ2, and P2 and P3 were treated as a single depth profile. The justification for fitting two depth profiles as one is to produce parameters which attempt to represent the potential variations in OSL depth profiles seen in rock surfaces. Further, the precision of parameterizations between single and combined datasets will also be evaluated in this assessment.

3.3.1 Proximal Age Calculations - Supplement

In acquiring parameters from individual and combined core datasets, age calculations were also performed on the HRQ and P surfaces using least absolute error regressions, to investigate how age calculations differ between wafer, scan, and anomaly filtered scan datasets. The use of least absolute error regressions for age calculations is used in this study, rather than least squares fits like in the prior chapter using wafer data, as depth profile data resolutions are improved enough to provide fit values using the model form, and that least absolute errors offer more robust fitting results than what least squares fits can offer.

While the primary motivation of this chapter is to document potential improvements in parameterization and data resolution with spatially resolved OSL and mineral identification, supplemental rough age fits of the Lane Mountain site using known age cores provides worthwhile insight on what the benefits of age extrapolation could be when using such improvements in data collection and non-quartz filtering.

Like with calculating $\overline{\sigma\varphi_0}$ and μ, parameter ranges for age t were fitted to the samples to produce 10^6 misfit values, to where a probability density function of parameter likelihoods is produced to acquire fitted median and uncertainty values. For individual cores, ages were calculated using parameters $\overline{\sigma\varphi_0}$ and μ from the other core surfaces. Age ranges from 0-10^3 years were initially applied to each erratic to determine the estimated best fit age and uncertainty ranges, then the erratic data were subsequently refitted to smaller age ranges to produce the most precise statistics for the age distributions.

The combined parameter values of $\overline{\sigma\varphi_0}$ and μ from fitting P2 & P3 combined, as well as HRQ1 and HRQ 2 combined, were also used to calculate ages for individual cores of the opposing surfaces. This entails producing ages for P2, P3 and the combined dataset of P2 and P3 using the parameters acquired from fitting HRQ1 and HRQ2 combined, as well as fitting ages to HRQ1, HRQ2 and HRQ 1 and HRQ 2 combined using the parameters from fitting P2 and P3 datasets combined. The purpose of this assessment is to determine the effectiveness of using $\overline{\sigma\varphi_0}$ and μ parameters from combined datasets for accurate age calculations, and whether such parameterizations improve age calculations over parameters retrieved from single cores.

3.4 Results

3.4.1 Individual Core Parameterizations

Figure 3.4 shows the two-dimensional OSL scan images of the four cores measured in this study. Figures 3.6, and 3.7 present the depth profiles produced from wafer and scanned datasets, and the fitted median parameters. Figure 3.8 presents the depth profiles produced from scan datasets with non-quartz OSL anomalies filtered from the spatially resolved data. Parameter fits and absolute uncertainties for each core are also summarized in Table 3.1. Likelihood plots of parameter combinations with 1σ bounds are presented for each core dataset in figures 3.9 (wafer data), 3.10 (scan data), and 3.11 (scan-filtered data).

OSL scans document several anomalous zones in both P and HRQ cores, impacting shapes of depth profiles to varying effect. The most significant impact can be seen in Core P2, where at roughly the 20–23 millimeters depth the presence of several OSL anomalies produces a deviation in the depth profile shape for the core (Figure 3.5, 3.6).

The EDS measures of all identified anomalies are given in the appendix, and can be interactively viewed (Appendix A1). A total of 10 anomalies of millimeter to sub millimeter area were identified from core P2, while 23 anomalies were identified for core P3, 14 for HRQ 1, and 19 for HRQ 2. All OSL anomaly zones contained at least trace EDS spectra resemblant of non-quartz mineralogy, with all but 6 anomalies identified as feldspars, micaceous mineral, rutile (Ti bearing), corundum (Al bearing), and zircon (See Appendix A1 for index of EDS identified mineralogy; Cabaleiro et al. 2013; Chen et al. 2020; Guo et al. 2020; Li et al. 2022). The remaining 6 produce EDS spectra indicative of either brass sawblade contaminant (Cu, Fe, Zn) or rare earth elements. Anomalies which were potentially caused by brass contaminant were also filtered from the depth profile datasets, given the potential for brass coating to reflect excessive

laser light into the photomultiplier. Estimated parameters using scanned data with anomalies removed are also given in Table 3.1.

Wafer derived depth profiles estimated parameter μ as 0.582 mm^{-1} (+1σ .174, -1σ .174) for HRQ 1 and 0.676 mm^{-1} (+1σ 0.199, -1σ 0.249) for HRQ 2 (Figure 3.9). These values are over twice as high, and with uncertainties a magnitude larger, when compared to the parameters derived from scan data for HRQ 1 and HRQ 2; parameter μ was calculated as 0.304 (+1σ 0.224, -1σ 0.05) for HRQ 1, and 0.283 (-1σ 0.039, +1σ 0.079) for HRQ 2 (Figure 3.10). Scan-filtered datasets produce μ values and uncertainties like that of scan derived datasets, with a value 0.243 mm^{-1} (-1σ 0.0326, +1σ 0.0652) for HRQ 1, and HRQ 2 producing a value of 0.295 mm^{-1} (-1σ 0.032, +1σ 0.096) (Figure 3.11).

Parameter $\overline{\sigma\varphi_0}$ derived from the HRQ cores also differ, with wafer derived datasets of HRQ 1 producing a $\overline{\sigma\varphi_0}$ value of 0.0052 s^{-1} (-1σ 0.0051, +1σ 0.817), and HRQ 2 producing a value of 0.0016 s^{-1} (-1σ 1.60E-03, +1σ 0.503) (Figure 3.9). Scan derived datasets, on the other hand, provide $\overline{\sigma\varphi_0}$ parameter values of 1.79e-06 s^{-1} (-1σ 1.57E-06, +1σ 1.14E-4) for HRQ 1, and 1.65E-07 s^{-1} (-1σ 8.13E-08, +1σ 4.78E-07) for

Table 3.1
Median parameter values of samples HRQ1, HRQ2, P2, and P3 using scan and scan-anomalies removed depth profile datasets, assuming an exposure age of 11 years. Median parameters and associated absolute uncertainty estimated using maximum likelihood estimate protocol as published in Lehmann et al. (2019).

Sample		Median (Best fit; -1σ infimum, +1σ supremum)
HRQ1	Wafer	$\mu = 0.582\ mm^{-1}$ (0.468; 0.174, 0.174) $\overline{\sigma\varphi_0} = 0.0052\ s^{-1}$ (3.80E-4; 0.0051, 0.817)
	Scan	$\mu = 0.304\ mm^{-1}$ (0.244; 0.0499, 0.224) $\overline{\sigma\varphi_0} = 1.79e\text{-}06\ s^{-1}$ (3.02E-07; 1.57E-06, 1.14E-4)
	Scan-filtered	$\mu = 0.243\ mm^{-1}$ (0.214; 0.0326, 0.0652) $\overline{\sigma\varphi_0} = 3.88e\text{-}07\ s^{-1}$ (1.57E-07; 2.95E-07, 1.23E-06)
HRQ2	Wafer	$\mu = 0.676\ mm^{-1}$ (0.662; 0.249, 0.199) $\overline{\sigma\varphi_0} = 0.0016\ s^{-1}$ (3.30E-03; 1.60E-03, 0.503)
	Scan	$\mu = 0.283\ mm^{-1}$ (0.268; 0.039, 0.079) $\overline{\sigma\varphi_0} = 1.65E\text{-}07\ s^{-1}$ (1.51E-07; 8.13E-08, 4.78E-07)
	Scan-filtered	$\mu = 0.295\ mm^{-1}$ (0.278; .0321, 0.096) $\overline{\sigma\varphi_0} = 3.55E\text{-}07\ s^{-1}$ (1.75E-07; 2.33E-07, 6.83E-07)
P2	Wafer	$\mu = 0.659\ mm^{-1}$ (0.394; 0.226, 0.226) $\overline{\sigma\varphi_0} = 3.11E\text{-}04\ s^{-1}$ (3.11E-06; 3.06E-04, 0.0206)
	Scan	$\mu = 0.695\ mm^{-1}$ (0.581; 0.234, 0.234) $\overline{\sigma\varphi_0} = 3.68E\text{-}06\ s^{-1}$ (8.57E-07;3.6E-6, 5.97E-05)
	Scan-filtered	$\mu = 0.718\ mm^{-1}$ (0.620; 0.173, 0.217) $\overline{\sigma\varphi_0} = 4.62E\text{-}06 s^{-1}$ (1.75E-07; 4.28E-06, 5.88-E05)
P3	Wafer	$\mu = 0.496\ mm^{-1}$ (0.172; 0.24, 0.335) $\overline{\sigma\varphi_0} = 2.21E\text{-}05\ s^{-1}$ (5.59E-08; 2.18E-05, 0.0189)
	Scan	$\mu = 0.13\ mm^{-1}$ (0.122; 0.0122, 0.0367) $\overline{\sigma\varphi_0} = 9.3E\text{-}08\ s^{-1}$ (6.80E-08; 1.55E-07, 4.47E-08)
	Scan-filtered	$\mu = 0.14\ mm^{-1}$ (0.138; 0.015, 0.015) $\overline{\sigma\varphi_0} = 7.64E\text{-}08\ s^{-1}$ (7.27E-08; 2.45E-08, 3.61E-08)

Figure 3.6

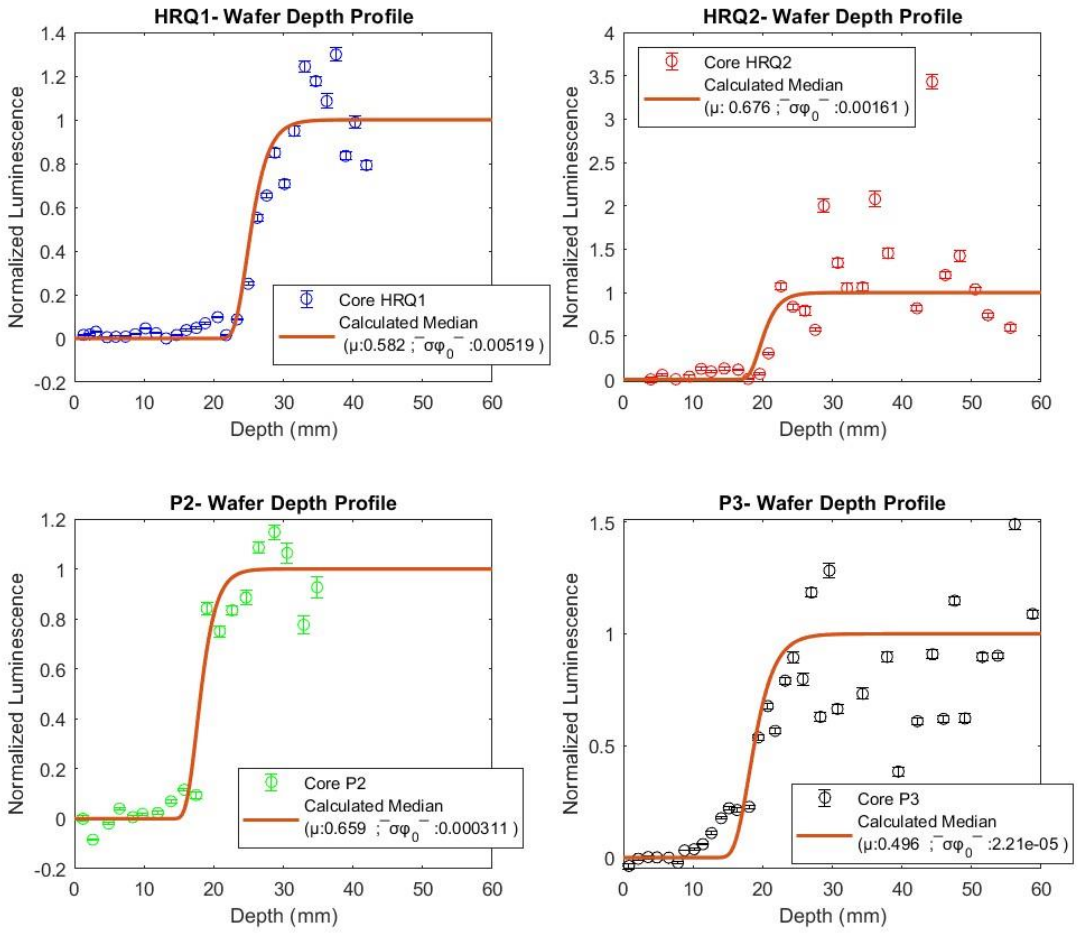

Individual depth profiles of cores HRQ 1, HRQ 2, P2 and P3, produced from wafer derived datasets. Median parameter fit values are presented in each plot. Cores are fitted to the exposure dating model using known exposure age of 11 years (3.469e+8 seconds) to produce the fitted median parameters, using Lehmann et al.'s (2019) maximum likelihood estimate approach.

Figure 3.7

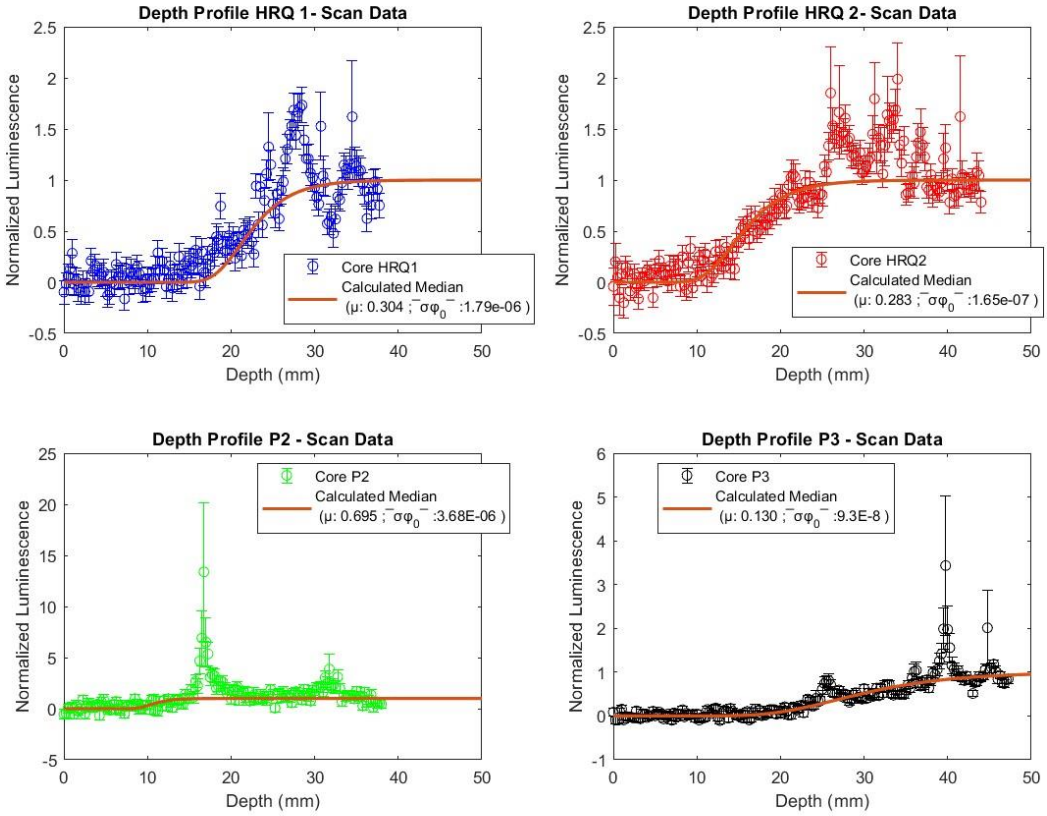

Individual depth profiles of cores HRQ 1, HRQ 2, P2 and P3, produced from scan derived datasets. Each depth profile datum is produced from the average count across a 250 micron depth extent of the core sample scan. Median parameter fit values are presented in each plot. Each core is fit to the exposure dating model using known exposure age of 11 years (3.469e+8 seconds) to produce the fitted median parameters, using Lehmann et al.'s (2019) maximum likelihood estimate approach.

Figure 3.8

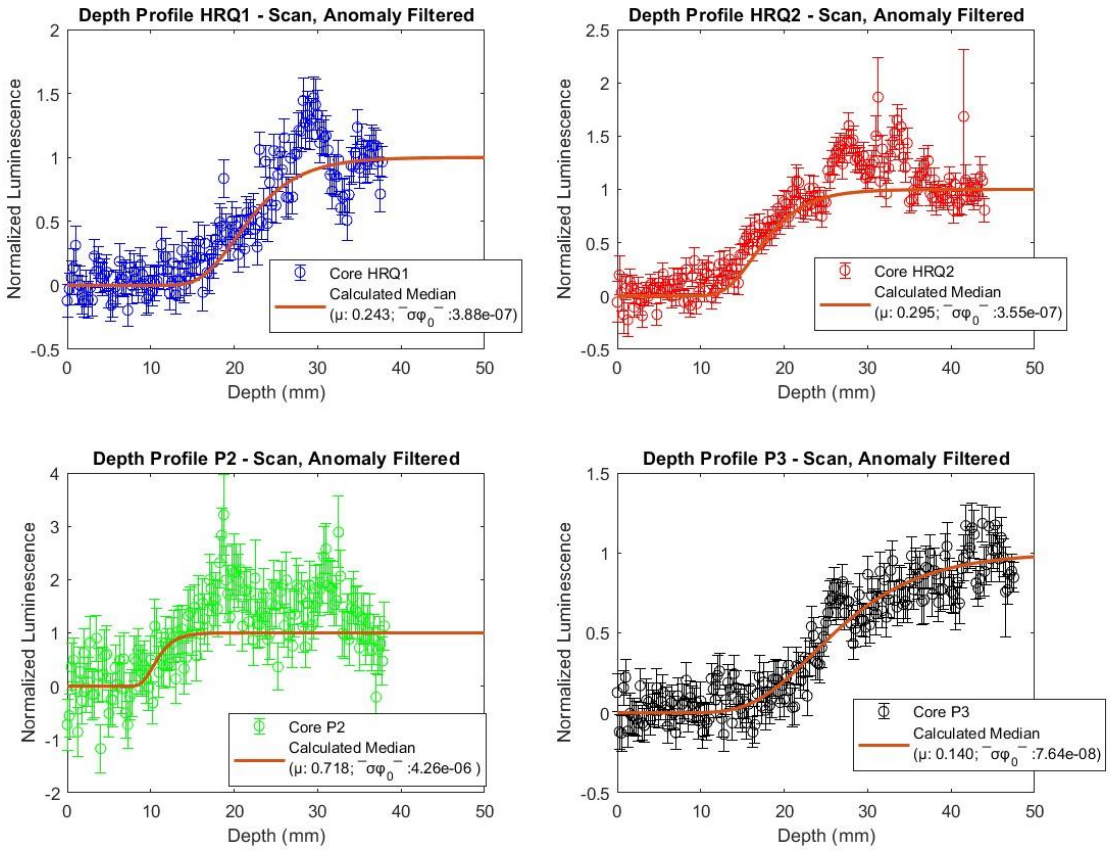

Individual depth profiles of cores HRQ 1, HRQ 2, P2 and P3, produced from scan derived datasets that had OSL anomaly zoned filtered from the datasets. OSL anomalies are filtered based on their non-quartz compositions. Each depth profile datum is produced from the average count across a 250-micron depth extent of the core sample scan. Median parameter fit values are presented in each plot. Each core is fit to the exposure dating model using known exposure age of 11 years (3.469e+8 seconds) to produce the fitted median parameters, using Lehmann et al.'s (2019) maximum likelihood estimate approach.

HRQ 2 (Figure 3.10). Anomaly filtered scan datasets produce similar magnitude parameters for $\overline{\sigma\varphi_0}$ as the unfiltered scan data, and also with tightened uncertainties, with HRQ 1 producing a value of 3.88e-07 s^{-1} (-1σ 2.95E-07, +1σ 1.23E-06) and HRQ 2 producing a value of 3.55E-07 s^{-1} (-1σ 2.33E-07, +1σ 6.83E-07) (Figure 3.11).

For samples P2 and P3, individual differences in the depth profile shapes and point scatter result in dissimilar parameterizations. For instance, parameter μ for P2 is calculated at 0.659 mm^{-1} (+1σ 0.226, -1σ 0.226) using wafer derived data, as opposed to P3's wafer derived μ value of 0.496 mm^{-1} (-1σ 0.24, +1σ 0.335) (Figure 3.9). This dissimilarity in μ between the cores is further expressed in scan datasets, where for P2, the parameter for μ is fitted as 0.695 mm^{-1} (+1σ 0.234, -1σ 0.234), while P3 scan data produces a value of 0.13 mm^{-1} (-1σ 0.0122, +1σ 0.0367) (Figure 3.10). Scan filtered datasets still produced similar μ parameters to the unfiltered scan datasets, with P2 producing a μ parameter value of 0.718 mm^{-1} (-1σ 0.173, +1σ 0.217), and P3 producing a value of 0.14 mm^{-1} (+1σ 0.015, -1σ 0.015) (Figure 3.11). While parameter values for μ are lower with the use of scan or scan filtered datasets, the uncertainty constraints improve in core P3. For core P2 however, uncertainty constraints are still of similar magnitude when using wafer or scan-derived datasets. Only when anomaly filtered scan datasets are used for parameterization, the uncertainty constraints for μ improve for this core.

Dissimilarities in parameter $\overline{\sigma\varphi_0}$ are also apparent from the sampled P cores. Core P2 produces a value for $\overline{\sigma\varphi_0}$ of 3.11E-04 s^{-1} (-1σ 3.06E-04, +1σ 0.0206) with wafer derived data, while core P3 wafer data fits a value of 2.21E-05 s^{-1} (-1σ 2.18E-05, +1σ 0.0189) (Figure 3.9). Again, Like with HRQ cores, it is shown that with the use of scan derived datasets that $\overline{\sigma\varphi_0}$ lowers in value by several magnitudes; core P2 produces a $\overline{\sigma\varphi_0}$ of 3.68E-06 s^{-1} (-1σ 3.6E-6, +1σ 5.97E-05), and P3

produces a value of 9.3E-08 s^{-1} (-1σ 1.55E-07, +1σ 4.47E-08) (Figure 3.10). Scan-filtered datasets offer similar trends against wafer derived depth profile data, with P2 offering a $\overline{\sigma\varphi_0}$ value of 4.62E-06s^{-1} (-1σ 4.28E-06, +1σ 5.88E-05), and P3 a value of 7.64E-08 s^{-1} (-1σ 2.45E-08, +1σ 3.61E-08) (Figure 3.11). Again, parameter absolute uncertainty constraints are improved by several magnitudes with the use of spatially resolved data for Core P3. Specifically, the fits for P3 shows improvement in parameter constraints with the use of scan derived depth profile data, however with the use of anomaly filtered data, parameter constraints are comparable to what was produced using unfiltered scan data.

3.4.2 Combined Parameter Fits

Appendix A7 shows likelihood plots for combined core fits of HRQ1 and HRQ2, as well as P2 and P3, for wafer, scan, and scan-anomalies removed datasets. The parameters for these fits are also summarized in Table 3.3.

HRQ combined fits using wafer data show higher parameter values for both attenuation (0.64 mm^{-1} median, -1σ 0.239, +1σ 0.191) and bleaching rate (6.71E-03 s^{-1} median; 6.68E-03 -1σ, 1.75 +1σ) over scan derived attenuation (0.293 mm^{-1} median; 0.037 -1σ, 0.074 +1σ) and bleaching rate (3.28E-07 s^{-1} median; 1.59E-07 -1σ, 9.02E-07 +1σ). Anomalies removed scan derived parameters of the combined core fits produce slightly lower values for attenuation (Median μ= 0.271 mm^{-1}; .0.037 -1σ, 0.056 +1σ)

Figure 3.9

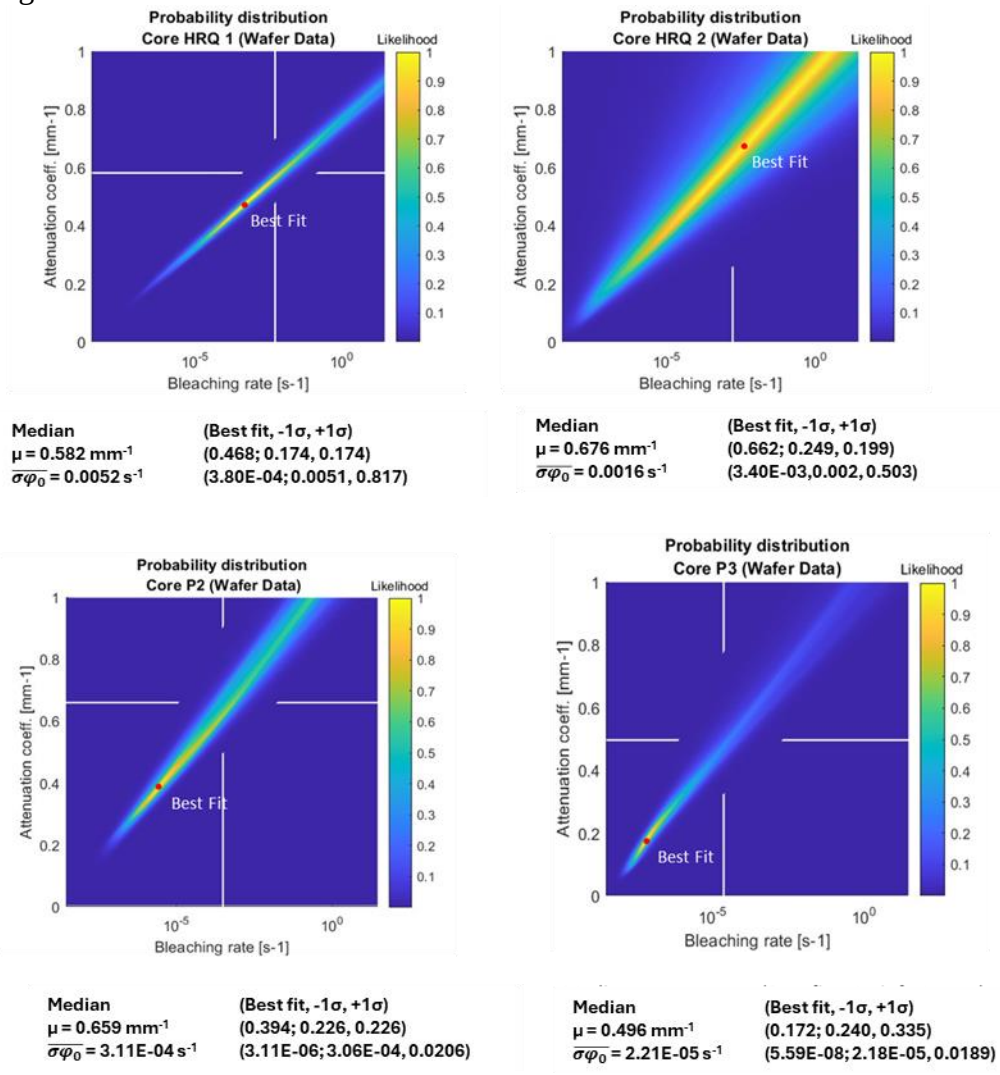

Likelihood plots of tested parameter values $\overline{\sigma\varphi_0}$ and μ from wafer derived depth profile data from cores HRQ 1, HRQ 2, P2 and P3, using MATLAB script from Lehmann et al. (2019). OSL data from each core is fit to the exposure dating model using an exposure age of 11 years to produce misfit values for tested combinations of parameters $\overline{\sigma\varphi_0}$ and μ. The misfit values from each parameter combination are normalized to show the viable range of parameter values for each dataset. The value with the highest likelihood is documented 'Best Fit', shown as a red dot with parameter values listed below the plot. Median parameters and uncertainties are calculated from extrapolating likelihood estimates of parameter fits into probability density functions. Ranges of resampled parameter misfits are presented by the edges of the white lines shown in the likelihood plots. Note the distinct separation between best fit and median parameter values seen in all cores, indicating data scatter is influential in reducing the precision of parameter fits.

Figure 3.10

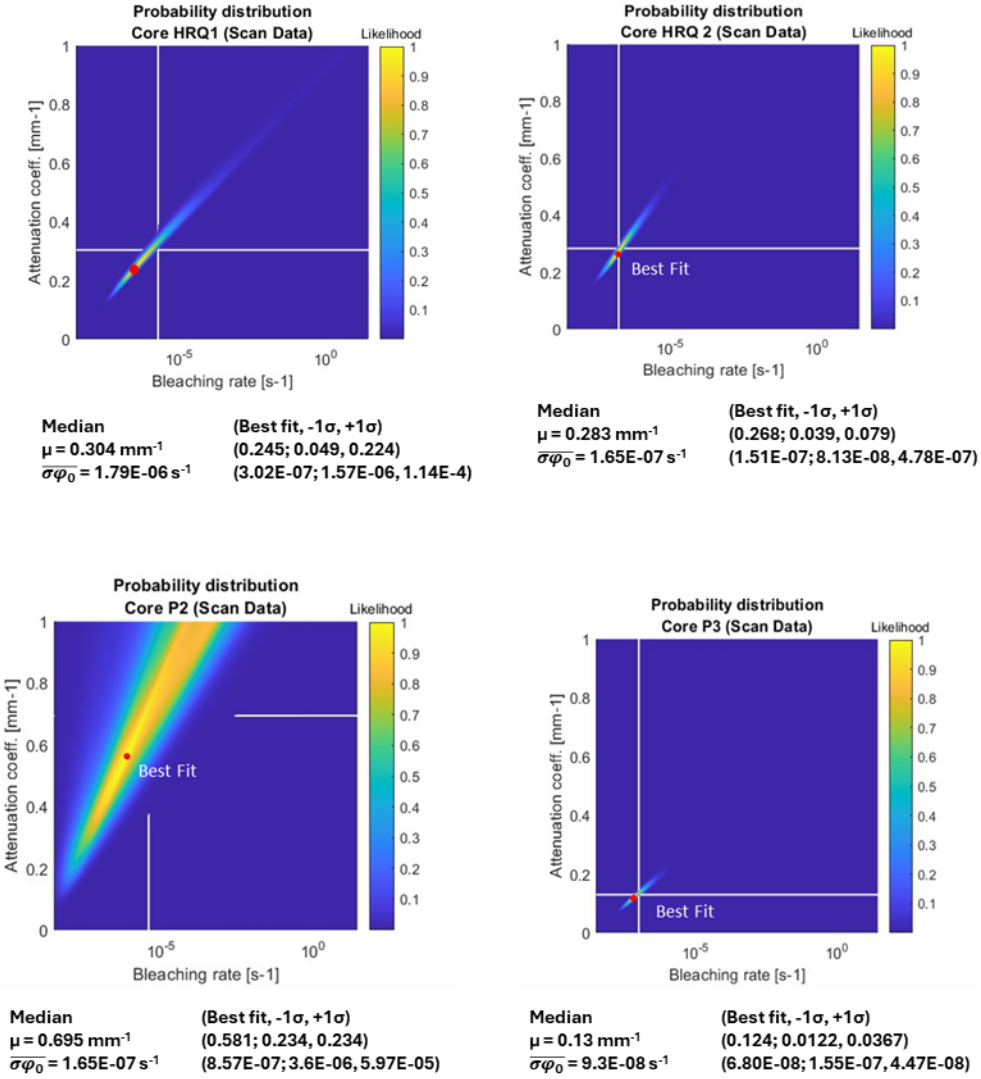

Likelihood plots of tested parameter values $\overline{\sigma\varphi_0}$ and μ from spatially resolved scan derived depth profile data from cores HRQ 1, HRQ 2, P2 and P3, using MATLAB script from Lehmann et al. (2019). OSL data from each core is fit to the exposure dating model using an exposure age of 11 years to produce misfit values for tested combinations of parameters $\overline{\sigma\varphi_0}$ and μ. The misfit values from each parameter combination are normalized to show the viable range of parameter values for each dataset. The value with the highest likelihood is documented 'Best Fit', shown as a red dot with parameter values listed below the plot. Median parameters and uncertainties are calculated from extrapolating likelihood estimates of parameter fits into probability density functions. Ranges of resampled parameter misfits are presented by the edges of the white lines shown in the likelihood plots. Using scan data for fitting, there is less separation between best fit and median parameter values for the maximum likelihood estimate parameter fitting technique.

Figure 3.11

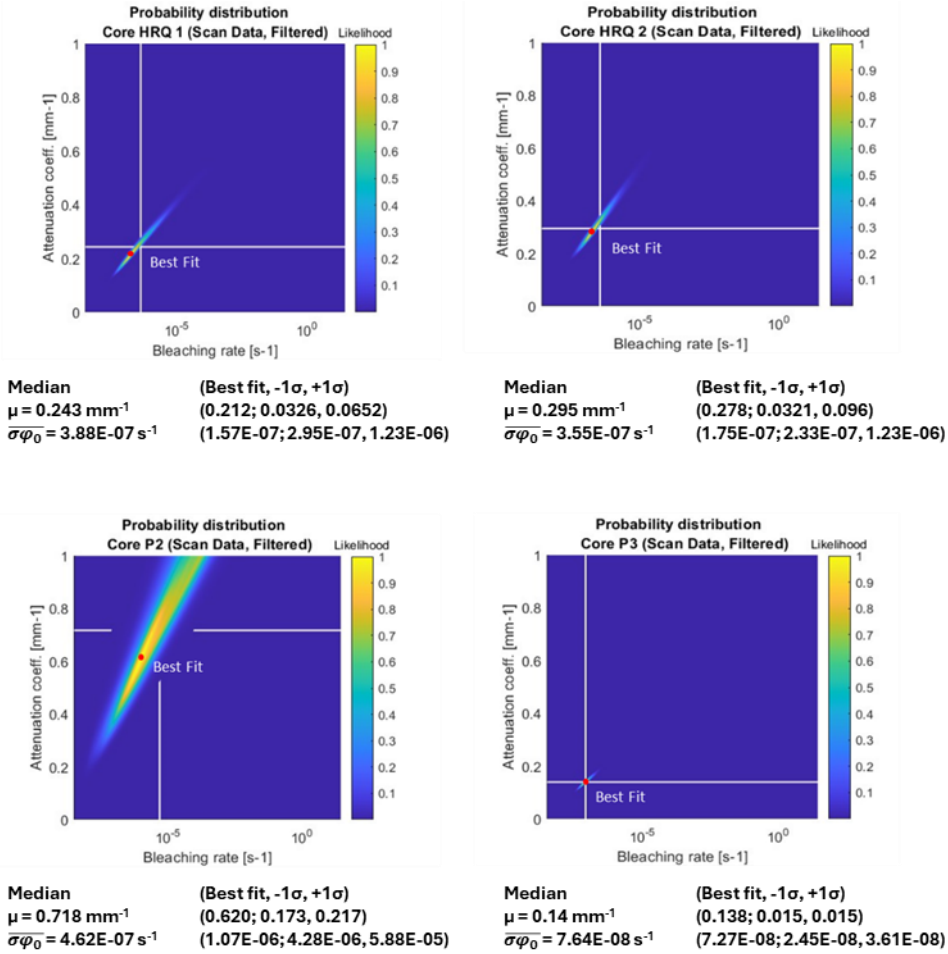

Likelihood plots of tested parameter values $\overline{\sigma\varphi_0}$ and μ from spatially resolved scan-filtered derived depth profile data from cores HRQ 1, HRQ 2, P2 and P3, using MATLAB script from Lehmann et al. (2019). OSL data from each core is fit to the exposure dating model using an exposure age of 11 years to produce misfit values for tested combinations of parameters $\overline{\sigma\varphi_0}$ and μ. The misfit values from each parameter combination are normalized to show the viable range of parameter values for each dataset. The value with the highest likelihood is documented 'Best Fit', shown as a red dot with parameter values listed below the plot. Median parameters and uncertainties are calculated from extrapolating likelihood estimates of parameter fits into probability density functions. Ranges of resampled parameter misfits are presented by the edges of the white lines shown in the likelihood plots. Interestingly, anomaly filtered scan datasets produce constrained median parameter fits that closely align to best fit parameter values of the core, of comparable precision to what is observed in unfiltered scan parameter fits in Figure 10. The influence of anomalous OSL in the cores may be minimal for the depth profile fitting technique given all cores have less than 25 identified anomalies each in their spatially resolved scan.

and bleaching rate (Median $\overline{\sigma\varphi_0}$ = 2.13E-07 s^{-1}; 5.95E-08 -1σ, 5.76E-07 +1σ) against unfiltered scan data, with comparable precision.

Wafer parameterizations for P2 and P3 combined produce a μ median of 0.463 mm^{-1} (0.183 -1σ, 0.275 +1σ) and a $\overline{\sigma\varphi_0}$ median of 2.61E-05 s^{-1} (2.57E-05 -1σ, 5.31E-03 +1σ). This μ parameter is comparable to the scan derived μ of 0.491 mm^{-1} (0.337 -1σ, 0.337 +1σ), but the $\overline{\sigma\varphi_0}$ is lower by several magnitudes from the scan derived dataset (6.27E-06 s^{-1} median; 6.20E-06 -1σ, 0.0054 +1σ). Anomaly filtered datasets produce a smaller value of 0.118 mm^{-1} (0.046 -1σ, 0.28 +1σ) for μ, and a smaller $\overline{\sigma\varphi_0}$ value of 3.11E-08 s^{-1} (0 -1σ, 3.33 E-06 +1σ).

For each fit type, scan and scan-filtered datasets improve the fit precision of parameter μ generally, by roughly a magnitude. For parameter $\overline{\sigma\varphi_0}$, its precision from HRQ1 and HRQ2 combined fits are improved using scan and scan-filtered data to where bounds are within a magnitude of the fitted value. For cores P2 and P3 combined however, the precision of the fitted values is comparable in magnitude for the fitted median for both scan and scan-filtered datasets. This is likely from the discrepancies in depth profile forms between P2 and P3 cores, causing a wider range of fit uncertainty to be produced (Appendix A12, A14, A16). Still, these parameter precision results are generally comparable to the improvements in precision to what was observed with individual core data, indicating the use of spatially resolved data can improve the precision of parameterization.

3.4.3 Age Calculations for Individual Cores, and Ages from Combined Core Data - Supplement

For investigative supplement, age calculations of individual cores, using μ and $\overline{\sigma\varphi_0}$ parameters derived from individual cores, are presented in Appendix figures A8 – A10, and are summarized in Table 3.2. Fit products which were not able to produce an age fit distribution with one solution

are designated as ‘NaN’. Age discrepancies of individual cores spanning sub-annual to centennial age are apparent for all cases and data types, indicating significant variations in depth profile shapes between P and HRQ surfaces impact the ability to calculate consistent ages between cores. This observation is expected, given the varied parameterization of individual cores from P and HRQ surfaces, which are comparable to results from Gliganic et al. (2019) that documented variations of depth profile parameterizations of similar sourced surfaces, at similar magnitudes of parameter variation. Still, with the use of scan and scan-filtered data, uncertainty values of fitted parameters are generally improved, with most age fit uncertainty values a magnitude lower than the fitted median. Wafer data age uncertainty, in contrast, generally matches the magnitude of the calculated median age. However, if ages from scan or scan-filtered data are calculated as centennial in magnitude, uncertainty values generally range centennial scale, matching the magnitude of the median age.

Responding to the inconsistent results of individual fits, parameters from combined data fitting of P and HRQ surfaces were used to calculate the ages of individual cores, as well as combined datasets of HRQ and P surfaces. Results are summarized in Table 3.4, and the plots of ages are presented in Appendix figures A11-A16. Generally, age calculation discrepancies are also recorded between data types, with wafer data producing the wide set of median ages, with an age of 0.874 years produced for surface P when fitting with the HRQ 1 and HRQ 2 combined parameter fit, and an age of 177 years for HRQ when using P2 and P3 parameter fits.

Table 3.2
Individual age calculations of cores, using individual parameters.

Scan (median (best fit, -1σ, +1σ))				
Parameters used	HRQ 1 Age	HRQ 2 Age	P2 Age	P3 Age
HRQ 1	x	1.77 (1.59, 0.103, 0.205)	0.460 (0.218, 0.333, 0.242)	99.5 (111.4, 46.1, 46.1)
HRQ 2	45.5 (40.41, 9.49, 12.6)	x	3.22 (1.88, 1.25, 1.88)	518 (653, 229, 229)
P2	NaN	605 (361, 181, 544)	x	NaN
P3	3.77 (3.87, .189, .252)	1.88 (1.89, .302, .168)	0.83 (.739, .18, .42)	x
Scan, Anomalies Removed (median, (best fit, -1σ, +1σ))				
Parameters used	HRQ 1 Age	HRQ 2 Age	P2 Age	P3 Age
HRQ 1	x	2.7 (2.88, .213, .355)	.557 (.557, .218, .091)	26 (25.22, 3.12, 2.08)
HRQ 2	26.8 (27.01, 5.52, 5.52)	x	1.21 (1.2, .249, .125)	96 (88.38, 13.8, 18.4)
P2	NaN	505 (404, 171, 257)	x	No fit
P3	4.91 (10.94, .129, .775)	2.68 (2.41, .305, .109)	.903 (.877, .063, .532)	X
Wafer (median (best fit, -1σ, +1σ))				
Parameters used	HRQ 1 Age	HRQ 2 Age	P2 Age	P3 Age
HRQ 1	x	174 (1.24; 149, 398)	0.308 (0.346; 0.172, 0.43)	0.835 (0.335; 0.482 3.38)
HRQ 2	645 (592; 187, 237)	x	7.55 (6.58; 2.51, 12.5)	24.8 (6.83; 0, 145)
P2	2.96 E+3 (1.97E+3; 971, 2.43E+3)	425 (112; 300, 350)	x	124 (22.30; 98.8, 148)
P3	501 (465; 142, 189)	325 (53; 249, 399)	15.6 (12.9; 4.79 9.59)	x

Table 3.3
Fits for combined parameters.

Scan (median, best fit, -1σ, +1σ)	
HRQ 1 & HRQ 2	$\mu = 0.293\ mm^{-1}$ (0.252; 0.037, 0.074) $\overline{\sigma\varphi_0} = 3.28E\text{-}07\ s^{-1}$ (1.60E-07; 1.59E-07, 9.02E-07)
P2 & P3	$\mu = 0.491\ mm^{-1}$ (0.105; .0.337, 0.337) $\overline{\sigma\varphi_0} = 6.27E\text{-}06\ s^{-1}$ (1.98E-08; 6.20E-06, 0.0054)
Scan, anomalies removed	
HRQ 1 & HRQ 2	$\mu = 0.271\ mm^{-1}$ (0.265; .0.037, 0.056) $\overline{\sigma\varphi_0} = 2.13E\text{-}07\ s^{-1}$ (1.98-07; 5.95E-08, 5.76E-07)
P2 & P3	$\mu = 0.118\ mm^{-1}$ (0.114; .0.046, 0.028) $\overline{\sigma\varphi_0} = 3.11E\text{-}08\ s^{-1}$ (1.82 E-08; 0, 3.33 E-06)
Wafer	
HRQ 1 & HRQ 2	$\mu = 0.64$ (0.486; 0.239, 0.191) $\overline{\sigma\varphi_0} = 6.71E\text{-}03$ (5.87E-04; 6.68E-03, 1.75)
P2 & P3	$\mu = 0.463$ (0.306; 0.183, 0.275) $\overline{\sigma\varphi_0} = 2.61E\text{-}05$ (6.54E-07; 2.57E-05, 5.31E-03)

The use of scan data for age calculation produces a wide range of ages still. When fitting HRQ core data with P parameters, an age of 24.3 years is produced. When fitting P core data with HRQ parameters, ages of 29 years for P2 and P3 are produced.

Scan-filtered data produced the most accurate ages against 11 years, with the most consistent ages between fits. When fitting HRQ core data with P parameters, an age of 5.54 years for HRQ1 and HRQ2 are produced. When fitting P data to HRQ parameters, an age of 11.3 years for P2 and P3 data are produced. Uncertainty of the age fits are not generally improved much over age calculations from other data types from combined curve fitting.

Individual age calculations of cores using combined parameter values are also presented in Table 3.4, and are plotted alongside cumulative data age fits in Appendices A11-A16. Wafer and scan age results span annual to centennial ages, while scan and scan-filtered ages of the cores are within annual to decadal ages. Each individual core fit has age uncertainties of similar magnitude

to the median age for most wafer and scan data results, however, scan-filtered age uncertainties are generally a magnitude lower than the median age.

Summarizing the age results from combined parameter fits, age calculations of individual cores produce large varieties in ages which provide limited insight on which data type is better suited for use in exposure dating. P2 and P3 cores show no obvious improvement in age accuracy when using scan or scan filtered data instead of wafer data. Further, the precision of age fits are not improved with the use of scan or scan filtered data when fitting individual cores. For the case of HRQ 1, age calculations decrease from centennial age using wafer and scan data to 8.51 years using scan-filtered data, closer to the 11 year exposure estimate. The scan-filtered data also improved fit precision, offering ranges one magnitude lower than the calculated age, which for scan and wafer data provided uncertainties matching the median age magnitude. HRQ2 calculations produce a centennial age with wafer data, but offer ages of 11.2 and 4.14 years using scan and scan filtered data. The use of filtered scan data provides uncertainties a magnitude lower than the median age value, an improvement over other datasets, which provide similar magnitude uncertainties to the calculated median age. Still the discrepancies in trends seen between the individual P and HRQ cores prevent further conclusions on the benefit of combined parameterizations for individual core fits.

When fitting combined datasets P2 and P3, as well as HRQ 1 and HRQ 2, there is an improvement in age accuracy when using scan data rather than wafer data. The use of scan filtered data produces accurate age calculations for the surfaces when using this fitting approach, producing 11.3 years for surface P and 5.54 years for surface HRQ. Still, precision remains similar in magnitude to fitted medians for all data types.

Table 3.4
Age calculations using combined parameter fits.

Core fitted for age	Wafer Age Fit Median (best fit, -1σ, +1σ):	Scan Age Fit Median (best fit, -1σ, +1σ)	Scan-filtered Age Fit Median (best fit, -1σ, +1σ):	Parameters used
P3	4.99 (0.81, 0, 0)	364 (441, 187, 187)	87.3 (86.3, 8.87, 13.3)	HRQ1 and HRQ2
P2	1.39 (0.86, .984 .492)	1.88 (1.12; 1.42, 3.94)	1.52 (1.49, 0.602 0.772)	
HRQ1	180 (145.7; 46.9, 93.9)	129 (92.2, 46, 46)	8.51 (8.54; 0.643, .107)	P2 and P3
HRQ2	22.58 (175; 150, 400)	11.2 (8.5, 3.42, 2.74)	4.14 (4.52; 0.218, 0.514)	
P2 and P3	0.874 (0.797, 0.284, 1.7)	29 (9.99, 10.4, 31.1)	11.3 (5.62, 6.92, 20.8)	HRQ1 and HRQ2
HRQ1 and HRQ2	177 (136.4; 99, 198)	24.3 (20.15, 6.67, 10)	5.54 (5.72; .42, 0.7)	P2 and P3

3.5 Discussion

3.5.1 Scatter in Spatially Resolved Data

The spatially resolved images of the cores allow for direct spatial assessments of the intensity of OSL, which was not previously possible with the use of one-dimensional wafer derived datasets using standard measuring protocols on the wafers (Figure 3.3). For instance, it can be viewed that core P2 generally shows lower OSL sensitivity compared to sample P3. What can also be assessed from spatially resolved OSL scans are areas of high OSL emissions which impact the shape of depth profiles. For instance, the unfiltered scan derived depth profile of core P2 produces a high value anomalous peak in OSL intensity within the 20-30 mm depth extent; this excessive intensity of OSL can also be observed in the spatially resolved image of core P2 at similar depth dimensions (Figures 3.3,3.7).

Further, the presence of anomalous OSL in spatially resolved data provides insight to the source of error and scatter in depth profile data. Core HRQ 2 hosts many anomalous OSL zones in its saturation plateau (depths > 25 mm), producing high error bounds and scattered OSL values for datapoints in the region. When the non-quartz anomalous zones are filtered from the depth profile data of HRQ 2, the values and error bounds of affected datapoints in spatially resolved data are reduced (Figures 3.7, 3.8). Such results from anomaly filtering are also reflected in cores P2 (more obviously), and less obviously in P3 and HRQ 1 (Figures 3.7, 3.8).

With or without anomaly filtering, datum error is generally high in depth profile datasets produced from spatially resolved data, with error bounds commonly reaching ranges greater than 10-15% of the datum value (Figure 3.6, 3.7). Wafer derived datasets on the other hand generally have error bounds of less than 5-10% of the datum value (Figure 3.6). While OSL anomaly

filtering can reduce error bounds for the affected datapoints, most error bounds for the depth profile data are still greater than 10% of the datum value (Figure 3.7, 3.8).

Several causes can influence the high data scatter and error observed in the scan derived datasets. One cause of this high error is likely due to the natural count variability of quartz OSL grains, which is also commonly observed in single grain quartz OSL studies (Bøtter-Jensen et al., 2000). Such variability in OSL can be potentially mitigated with thorough preheating protocols for a given sample thickness, which for this study was attempted using 30 minute preheats at 135° (Elkadi et al. 2021). What also can contribute to high datum error is the high level of background count fluctuations recorded by the photomultiplier used in the scanning instrument, in some cases nearly matching or exceeding the measured OSL from the scanned pixel region. Other instrument characteristics that could diminish OSL signals included the thicker filters (11 mm) used to mitigate background counts, than that used in the wafer applications (7.5 mm). Scatter is also a function of the sample signal as well. Low OSL counts, even at saturation depths, were emitted from the samples in this experiment. Metamorphic rocks tend to have weak fast component OSL counts (Jeong and Choi 2012); using a rock type with higher OSL sensitivity may mitigate such resolution issues.

Data scatter may also be influenced by the recording of remnant OSL from prior scan steps after laser stimulation. To mitigate the influence of background scatter and to amplify low OSL trends, the minimum recorded background value from each pixel scan assessment was used as representative of the background. This provided distinguishable OSL from samples with low sensitivity, although potentially inflating the OSL value. The standard deviation values for pixel background counts fall generally near 10 percent of the mean. Ideally, more representative background metrics should be used for scanning, such as background count averages, which for

samples with higher OSL sensitivity can be used without diminishing OSL depth trends. In retrospect, longer wait times between laser scan steps to allow the photomultiplier to drop to lower background count levels after a scan may have been beneficial. Such a technique has been shown in other scan studies to mitigate background scatter (Sellwood et al. 2022a). Further, filter combinations in the photomultiplier tube, or a more sensitive photomultiplier could have been better optimized to improve the OSL/background ratio. Sample thickness may also contribute to the observed data scatter, as laser scatter into the subsurface may emit more OSL than from thinner samples, however the limitations of the scanning instrument used were unable to detect major differences in scan resolution with sample thickness (Appendix A18).

The use of dose normalization of spatially resolved data may mitigate scatter observed in the spatially resolved data. To limit data scatter and sensitivity variations in wafer derived datasets of unequal area, test dose normalization procedures are performed on wafer aliquots (Gliganic et al. 2019). This style of normalization was not feasible for the laser scanning study, where test dose irradiations for the transverse slices were not ready at the time of the laser scanning procedure. Similar spatially resolved studies for exposure dating have presented the difficulty of obtaining regenerative irradiation doses for centimeter scale transverse slices (Sellwood et al. 2022b). In the case where samples of varying sensitivities are compared, the use of test dose correction could be used to compare observed luminescence dosimetry characteristics more effectively. For instance, the major shape discrepancies between Cores P2 and P3 may be more easily compared by reducing the dependence of sample characteristics on OSL sensitivity via test dose normalization.

As an alternative to applying a regenerative test dose, only one depth profile datum is produced from each 250-micron depth extent of the spatially resolved datasets by taking the average OSL

counts across the 250-micron depth extents to produce each datum. Such a normalization protocol still produces scatter of depth profile data, which limits the fitting accuracy and comparisons of scatter from test dose corrected wafer data. However, insights are still possible in evaluating the expected improvement in parameterizations of depth profiles with the use of spatially resolved data against wafer derived datasets. For instance, when variations in sensitivity are not extreme, similar depth profile forms can still be observed from similar sourced samples, as seen in the depth profiles of scanned cores HRQ 1 and HRQ 2 (Figure 3.7, 3.8).

Future assessments should attempt acquiring the means for test dose irradiations in spatially resolved luminescence exposure dating applications to affirm that such improvements in parameterizations are the result of the use of higher resolution data and are not strongly influenced by sensitivity variations in samples (Sellwood et al. 2022a). For more insight, test doses are performed on two samples of the Foothills Erratics Train in Section 4.

In addition to the presented laser scanning applications, other scanning equipment such as electron multiplying charge-coupled device (EM-CCD) imagers can still be utilized for exposure dating applications, assuming instrumentation is best optimized for accurate sample measuring (Sellwood et al. 2019, Sellwood et al. 2022a,b). Like with laser scanning instruments, waiting for the EM-CCD imager to record lower background levels before scanning again may assist in reducing the impact of background count scatter in scan data (Sellwood et al. 2022a).

3.5.2 Effects of Depth Profile Parameterizations on Individual Cores, Combined Data Fitted Cores

The quantity of data used in each depth profile point from scan derived datasets (100-150+ pixels per datapoint) greatly exceeds that of wafer derived datasets (<10 aliquots), which offers better fit resolutions, even when test dose normalization is not incorporated in the data. When

examining the parameter results of cores individually, the use of laser scanned depth profile datasets, ether filtered or unfiltered, generally produces parameter values with lower standard deviation bounds compared to the values produced from wafer datasets. This reduction in uncertainty bounds is expressed visually in Figures 3.9-3.11, as likelihood zones diminish in area when using spatially resolved depth profile data. The likelihood distributions also tend to centralize near the best fitting parameter combination for the core depth profile with the use of spatially resolved datasets, resulting in median parameter values and uncertainty bounds which better reflect the best fitting profile shape for the core. Similar to Sellwood et al.'s (2022b) scanning observations, the scan data fits result in lower attenuation coefficients, producing more gradual slopes for luminescence depth profiles and lower absolute uncertainties than what wafer derived datasets can provide. When parameterizing rock surfaces with combined core datasets, the resultant fits produced parameter values which followed similar fitting trends of individual cores, to where precision was refined with the use of spatially resolved data. However, both scan and scan filtered data produced similar precision ranges for both fit combinations.

With individual core fits, the use of OSL anomaly filtering to constrain depth profile shapes of spatially resolved scan data did improve the error bounds and lower the values of affected data over the unfiltered spatially resolved versions. However, the filtered depth profiles seemed to produce only slightly improved or near equivalent parameter precisions to that of unfiltered scan data of the same core (Table 3.1, Figures 3.10, 3.11). This is possibly due to the near homogenous composition of the quartzite, enabling the limited anomalous OSL data to have a minimal impact on the overall misfit calculation for the fitted parameters. The number of OSL anomalies was minimal in most spatially resolved datasets, with 10-30 anomalies generally identified for each core, and each anomaly usually only covers sub-millimeters of area (Figures

3.2, 3.5; Appendix A1). With more heterogeneous luminescence data, the use of luminescence anomaly filtering with spatially resolved data may provide more insight on its effectiveness in better constraining depth profile forms for exposure dating.

However, an exception to this trend is observed in core P2. Specifically, the uncertainty of parameter $\overline{\sigma\varphi_0}$ from scan filtered depth profile of core P2 (5.97E-05 infimum, 2.83-E05 supremum) is lower than what the fits from wafer and scan data can provide (3.6E-6 infimum, 1.6 supremum). The reason for this improvement is likely the effect of the low OSL sensitivity of the sample, which causes anomalous OSL measures to skew and scatter the shape of the depth profile and offer a wide range of high parameter likelihoods (Figures 3.5, 3.7, 3.10). After having the anomalous OSL filtered from the core scan data, the shape of the depth profile improves to better accommodate the physical assumptions used in the model, and thus calculated fit certainty for parameter μ improves for the sample (Figure 3.4, 3.8, 3.11).

While the use of spatially resolved data produces different profile shapes and fitted parameter values of the individual cores to that of wafer derived results, it does little to reduce the parameterized ranges of the cores. While there is a significant range in median parameterizations for μ (0.676-0.496 mm^{-1}) and $\overline{\sigma\varphi_0}$ (0.0052 – 2.21E-05 s^{-1}) when fitting wafer derived datasets, the use of unfiltered scan derived datasets still casts a wide range for the parameter $\overline{\sigma\varphi_0}$ (1.79e-06 – 9.3E-08 s^{-1}), and still a wide range for parameter μ (0.695-0.13 mm^{-1}). Filtered scan datasets offer similar ranges for fitted parameter $\overline{\sigma\varphi_0}$ among cores (4.62E-06 – 7.64E-08 s^{-1}), as well as similar ranges for parameter μ (0.718-0.14 mm^{-1}). It should be noted that for core P2, the OSL sensitivity of this sample is low, causing anomalous OSL to dominate the shape of the depth profile. Resultingly, both wafer and scan data for P2 provide near equivalent parameters for μ (0.659 mm^{-1} from wafer data, 0.695 mm^{-1} from scan data). The range of μ between HRQ 1, HRQ

2, and P3 (0.283-0.13 mm^{-1}) did tighten with use of scan data, however. Anomaly filtered data also produces similar parameter ranges to that of scan derived data (μ range of 0.295-0.14 mm^{-1} between HRQ 1, HRQ, 2, and P3; μ value of 0.718 mm^{-1} from P2; 3.68E-6 – 7.64E-08 s^{-1} for parameter $\overline{\sigma\varphi_0}$ between all cores). Such ranges from the spatially resolved datasets echo the results of dissimilar parameterizations of similar sourced luminescence depth profiles presented in Gliganic et al. (2019), indicating that the low resolution of wafer derived datasets may not have subjugated the assessment's inconsistencies in depth profile shapes from similar rock sources.

Combined core fits, which attempt to summarize parameter values between cores, produce μ and $\overline{\sigma\varphi_0}$ values generally within the parameter ranges supplied by the individual core fits. Specifically, the parameter ranges from scan (0.294 – 0.491 μ; 6.27e-06 – 3.28e-07 $\overline{\sigma\varphi_0}$) and scan-filtered data (0.118 - 0.271 μ; 2.13e-07 – 3.11 e-08 $\overline{\sigma\varphi_0}$) are more constrained than ranges from individual core fits, but for wafer data, parameter ranges are equivalent between individual and combined core fits (0.463 - 0.64 μ; 6.71E-03 – 2.61e-05 $\overline{\sigma\varphi_0}$). As such, the values from these combined fits are still representative to the expected parameterization values of the tested rock surfaces, and this fitting approach may be useful in other applications which aims to summarize rock surface parameters for dating applications.

While the lack of test dose normalization of the depth profiles limits interpretations that can be made on the accuracy of depth profile parameterizations for dating in this experiment, laser scan data still offers practical two-dimensional considerations of OSL and sample composition. Such observations assist in determining the reliability of the depth profile form, independent of model parameter fitting. The benefits of this measuring protocol are shown to be effective in quartzite

material, but this OSL measuring technique could also isolate quartz OSL signals from more heterogeneous samples. Granites or sandstones, which are commonly measured by IRSL due to their high feldspar content, could be measured for spatially resolved OSL and used for exposure dating if the quartz components of the spatially resolved data can be isolated. The anomaly filtering technique would avoid requiring mineral separation processes to obtain quartz OSL free from non-quartz sources, which are commonly done for traditional single grain luminescence dating techniques to improve ages (Duller et al. 2003). While SEM-EDS measures on individual anomaly zones were performed for this application, other compositional detection techniques may be useful such as thin section X-ray mapping or EDS imagery (Baker et al. 2012; Han et al. 2022). Such techniques for mineral mapping may be more practical when documenting mineralogically heterogeneous samples.

3.5.3 Implications for Exposure Dating Applications

Given the acquisition of physical parameters for exposure dating is challenging to estimate accurately, it is common in dating applications to use rock samples of known age and similar lithology on the surface one wishes to date to calibrate for parameters μ and $\overline{\sigma\varphi_0}$ for the rock (Sohbati et al.,2012; Gliganic et al., 2019; Chapot et al., 2012; Lehmann et al., 2019; Luo et al., 2018). However, wafer derived datasets of separate rocks with similar compositions used for calibration have been shown to produce inconsistent $\overline{\sigma\varphi_0}$ and μ parameters (Ou et al., 2018; Gliganic et al., 2019).

For this quarry site, the parameterization of cores from surfaces P and HRQ are compared using wafer and spatially resolved data to assess whether spatially resolved data could determine more clearly if these two rocks could be viable proximal rocks for each other in the event sample parameterization is needed for dating. In evaluating the parameterizations of individual core

depth profiles from P and HRQ, it is still found that inconsistencies in the extrapolated parameters are apparent between individual cores, regardless of the type of data used for depth profiling (Table 3.1; Figure 3.9-3.11).

The use of the spatially resolved datasets reiterates previous conclusions about observed variations in parametrization of similar sourced rock surfaces that were observed from wafer derived datasets. Still, the causes for the variations in depth profiles are likely very complex. Of course, variations in OSL sensitivity can play a factor in the shape of the depth profile and the resultant parameterizations for the core. Further, the rocks used in the study have visible differences in hue, mineralogy, and optical properties of the samples, which may uniquely impact light attenuation and luminescence bleaching rate properties for the sample. For example, the more orange surface hue and the more massive crystal compositions of sample P2 may produce variations in depth profile characteristics different to what is seen from core P3, which comes from a more color varied and finer grained sample taken from the same surface (Figures 3.1, 3.2, 3.4). The spatially resolved depth profiles in this assessment of reiterates that by using proximal rocks for parameter extrapolation, it will always be the reality that samples will hose compositional heterogeneities which uniquely impact the shapes of depth profiles, and thus produce inequivalent parameters for the first order exposure dating model.

Prior attempts to quantify or account for compositional heterogeneities in the samples for age calibration have been conducted with the use of wafer derived datasets in other studies. Excess surface core samples have been collected in past exposure dating assessments to better represent the natural compositional and textural heterogeneities of studied rock surfaces (Sohbati et al. 2018; Freiesleben et al. 2023). However, results generally indicate this sampling technique benefits age calculations if the age calibration samples are close to the expected age of the dated

rock surface. The use of higher resolution spatially resolved data may provide further insight on using such techniques for surface age calibration.

In response to such prior attempts, an alternative sampling protocol was attempted for this Lane Mountain application to potentially minimize the heterogenic influence of rock samples sourced from independent locations within the site. Rather than utilize proximal rocks for age calibration, it was proposed to instead utilize lab controlled exposed rock samples directly from the rock surface of interest, which may offer light attenuation and luminescence bleaching properties more similar to the rock material from the rock surface of interest (Bench & Feathers 2022; Ou et al., 2018; Gliganic et al., 2019; Freiesleben et al., 2023). However, the scans did not produce viable depth profile forms due to resolution issues from recording low OSL counts. As such, the scan datasets and examples of calculated parameters and ages are placed in the appendix to show insight on performing this style of assessment (Appendix A18).

Regardless of sampling technique, while samples for parameter calibration are commonly from the same lithology source and from similar source locations, there are still unaccounted for environmental or compositional characteristics which impact depth profile forms that are not quantified effectively in the exposure dating model. Variations in solar incidence angles, weathering rinds, and non-first order light attenuation and luminescence bleaching kinetics for the rock sample warrant further investigation (Bench & Feathers 2022; Fuhrmann et al. 2022; Gliganic et al. 2019; Freiesleben et al. 2023). Thus, rather than attempting to improve age accuracies with higher resolution data, what may also be needed to improve parameterization for exposure dating is a more specific dating model which more accurately incorporates rue light attenuating behaviors and luminescence bleaching characteristics for the rock.

The use of spatially resolved data for examining potential other parameters for dating can offer these insights with greater resolutions and spatial insight than what wafer derived datasets can provide. For instance, the shape of the bleaching front can be more clearly observed with higher resolution spatially resolved scan data, providing the opportunity for detailed examinations of solar path angles to the sample surface like prior studies have attempted performing (Fuhrmann et al. 2018).

3.5.3.1 Physical Parameterization of light attenuation

However, perhaps rather than deriving parameters from fitting the first order model, direct physical measurements of light attenuation and luminescence bleaching rates may also provide insight into the correct kinetics model for dating. Direct derivations of light attenuation are possible with experiments using the Beer Lambert Law (Ou et al. 2018). Further, spectral dependent photoionization cross sections can be directly estimated with LM-OSL protocols (Singarayer & Bailey 2003). Incident photon flux, another feature of the bleaching rate constant, can be estimated also with a record of solar radiation measurements near the site. Portions of sampled cores can be utilized to perform these experiments, while still obtaining OSL depth profile data from a transverse slice of the core, thus requiring no additional core samples for measurement.

A brief study was performed evaluating measured attenuation coefficient values of the Lane Mountain samples. The Beer-Lambert Law of Attenuation was used to derive light attenuation metrics for reach sample:

$$I = I_o e^{-\mu x}$$

Where I_0 is incident light intensity, I is the light intensity after transmission through the sample, x is the sample thickness, and μ is the attenuation coefficient for the sample.

The equation can be adjusted to solve for the attenuation coefficient, with the knowledge of the fraction of measured light intensity and thickness of the sample:

$$\mu=-\ln(\frac{I}{I_o})/x$$

The configuration of the light attenuation experiment is presented in Appendix A17a, with the setup of the experiments inspired from prior works from Smillie et al. (2011), Sanderson et al. (2011), and Ou et al. (2018). A gooseneck microscope illuminator was used as a light source, where an Ocean Optics USB 200 spectrometer was used to measure initial and post-incidence light intensity at a range of 347-980 nm or 347 – 1010 nm. Two one-millimeter diameter holes were used to concentrate light toward the sample and spectrometer.

The procedure for the measure of light intensity begins with an initial background light recording, following by a light recording with the light source turned on and unimpeded by a sample. An integration time of 5 ms is used for recording light intensity from the light source 50 times, given the light source intensity is very high for the spectrometer. Background counts are also recorded at 5 ms integration times. The background measure is recorded at an integration time of 700 ms. After these measures, a sample is then placed between the light filter holes, where the resulting change in light intensity is recorded at an integration time of 700 ms fifty times.

The integration times of the photon count spectrum is made equivalent between background, light, and attenuated values. Then, two attenuation calculations are produced, with the first being

a ‘summed attenuation’ average which measures the fraction of light intensity based on the total sum of photon counts measured. The second measure the average light attenuation coefficient measured from each individual spectra component that was measured by the spectrometer.

Table 3.5 presents results of the physical attenuation measurements of the Lane Mountain samples. Graphs of spectral attenuation for each sample in Appendix A17. Results found that physically measured attenuation values were a magnitude higher generally than what was produced from fitted parameter values. The measured values are similar to quartz rich sample attenuation values measured in Ou et al. (2018).

With these results, it can be indicated that the attenuation coefficient utilized in the exposure dating model may be characterizing other properties of luminescence depth profile development, or it is misattributed to the model form, which causes inconsistency between fitted and measured values. Continued work in analyzing attenuation, and other parameters for exposure dating such as angles of illumination or photon flux variations, can help better characterize light attenuation in depth profile evolution. Hese evaluation then can also evaluate the practical use of curve fitting for parameter extrapolation in exposure dating, and explain inconsistencies in fitted and physical parameter values using the dating procedure.

Table 3.5
Light attenuation experiment, Lane Mountain samples

Lane Mountain			
Sample Portion	Beer-Lambert attenuation calculation (mm^{-1})	Average attenuation across visible light spectrum (mm^{-1})	Fitted Attenuation (mm^{-1})
HRQ 1 Bottom Half	2.97	2.47 ± 0.62	Wafer fit: 0.582; Scan fit: 0.304; Scan fit, anomalies removed: 0.243
HRQ 1 Top Half	3.33	2.83 ± 0.67	
HRQ 2 Bottom Half	1.42	0.97 ± 0.49	Wafer fit: 0.676; Scan fit: 0.283; Scan fit, anomalies removed: 0.295
HRQ 2 Top Half	1.89	1.32 ± 0.66	
P2 Bottom Half	2.47	1.71 ± 0.87	Wafer fit: 0.659; Scan fit: 0.695; Scan fit, anomalies removed: 0.718
P2 Top Half	2.52	1.90 ±0.72	
P3 Bottom Half	2.16	1.44 ± 0.82	Wafer fit: 0.496; Scan fit: 0.13; Scan fit, anomalies removed: 0.14
P3 Top Half	2.32	1.76 ± 0.63	

3.5.3.2 Proximal Age Calculations from Lane Mountain

From examining every individual age calculation for each individual core, it is evident, much like on comparing parameter fits of μ and $\overline{\sigma\varphi_0}$, that individual cores from similar rock sources and exposure environments can host unique depth profile forms that do not adequately compare to each other, yet technically offer the same exposure age histories (Table 3.2). The variety of the age did not improve using higher resolution datasets, reaffirming concerns that proximal rock parameterization faces limitations in consistent parameterization that will impact age extrapolative accuracy.

A response to these inconsistencies is to produce parameterizations which come from combining multiple core data into one depth profile as a representative surface, and fitting this depth profile

for age or other parameter calculations. In trial, however, parameters for μ and $\overline{\sigma\varphi_0}$ acquired from fitting the combination of P or HRQ data together, when applied to individual cores, still produced large varieties in ages, regardless of data type. P2 and P3 cores show no obvious improvement in age accuracy or precision when using combined parameters, regardless of data type. For the case of core HRQ 1 though, age calculations using combined parameters decrease from centennial age, using wafer and scan data, to 8.51 years, using scan-filtered data. Scan-filtered data improved fit precision also, offering ranges one magnitude lower than the calculated age, which for scan and wafer data provided uncertainties matching the median age magnitude. For core HRQ2, calculations produce a centennial age with wafer data, but offer ages of 11.2 and 4.14 years using scan and scan filtered data. The use of filtered scan data generally provides uncertainties a magnitude lower than the median age value for this core, an improvement over other datasets, which provide similar magnitude uncertainties to the calculated median age. Still, in evaluating the individual cores, the discrepancies in trends seen between the individual P and HRQ cores prevent further conclusions on the benefit of combined parameterizations for individual core fits.

Another response is fitting only combined core data, both for parameterization and age calculations. When fitting combined datasets P2 and P3 as one depth profile, as well as HRQ 1 and HRQ 2, there is an improvement in age accuracy when using scan data rather than wafer data. The use of scan filtered data produces the most accurate age calculations for the surfaces when using this fitting approach, producing 11.3 years for surface P and 5.54 years for surface HRQ. Still, precision remains similar in magnitude to fitted medians for all data types in using this fitting approach.

The results from this study of age fitting indicates that if using proximal rocks for parameterizing rock surfaces, that combining datasets from the same rock surface, in addition to using higher resolution, anomaly filtered OSL data, could allow for more accurate age calculations when using the first order model for exposure age calculations. The generalized parameters acquired from the combined data fits in this study also appeared to mitigate the age ranges acquired from individual cores, and in fitting ages to combined datasets, produced results that were within years of the 11-year true exposure age of the rock surfaces. Still, these trends in age fitting are limited to only four cores from surfaces, and the physical processes contributing to the variability of the depth profiles are not well quantified. Even with more ideal parameterizations, there are still varied ages across what should be environmentally identical samples.

Future applications using proximal rock parameterizations will likely record inconsistencies in age fitting, even in using spatially resolved data. The facilitation of other applications on other rock surfaces and exposure environments may offer more insight into the difficulties in acquiring more precise and accurate exposure dates.

3.6 Conclusion

OSL depth profiles measured using laser scanning offers two-dimensional, submillimeter depth profile data that improves the resolution of depth profiles over wafer derived datasets, and grants the ability to identify and filter non-quartz OSL from samples to refine depth profile shape accuracy. The use of spatially resolved data for parameter fitting was attempted on four core samples of quartzite sampled from two 11-year exposed surfaces, and the results were compared with parameter fits from wafer derived depth profiles of the same core samples. The uncertainties of parameters produced from the application study (Table 3.1, 3.3) show that using filtered and unfiltered scan data broadly improves precision of calculated parameters using

maximum likelihood estimate fitting approaches either when parameterized individually or through combined core data fits, when compared against wafer derived depth profiles of the same cores. Further, spatially resolved datasets provide enhanced information on the sensitivity variations of cores, and assist in determining the impact of anomalous OSL counts to the shape and fit of the depth profile. Wafer derived datasets still provided lower error bounds than non-test dose corrected scan datasets. When compared to unfiltered spatially resolved depth profile data, the use of OSL non-quartz anomaly filtering did improve error bounds of affected depth profile data, however had only slightly improved or matched the precision of parameterization of the core depth profiles given the limited number of non-quartz OSL heterogeneities present. Applications of luminescence anomaly filtering of more heterogeneous samples may provide more insight on its use to improve the precision of exposure dating parameterizations.

Novel age calculations using proximal rock techniques were also performed, producing inconsistencies in ages between known age surfaces of rocks P and HRQ, but with improved calculated precision when using scan and scan filtered data. Combined core age fits using scan and scan filtered data produced more accurate age results than from individual core fits generally, but with comparable precision to that of individual core fits. Still, variations in ages are produced, and inconsistencies in age fitting, even in using spatially resolved data, are likely to be produced when using proximal rock surfaces for exposure dating parameterization.

For other applications, the sensitivity of the laser scanning instrumentation can be improved to acquire OSL data which is less susceptible to background count fluctuations. Further, the use of test dose normalization should be investigated in its benefit to potentially improve depth profile parameterized precision and accuracy. Other trials conducted on rock samples with stronger OSL sensitivity, and from different environments, could improve the resolution of data, and may offer

more insight for acquiring more precise and accurate exposure dates. Further, the use of physical parameterization experiments can attempt validating the viability of the fit approaches of parameter values in future studies, and potentially offer insight on new parameterized approaches for depth profile evolution, or the limitations of the current first order parameter approach and reasons for fit and age results. For instance, physical measurements of light attenuation from the Lane Mountain samples were generally a magnitude higher than fitted values, and implicate interpretations of the parameter fit values, precisions, and age results.

Still, the application at Lane Mountain shows benefit in using OSL scans and non-quartz mineral filtering to interpret the form of depth profile shapes and improve parameter extrapolative precision, offering potential new insights for alternative proposed models for exposure dating, influences on the shape of the depth profile, and insights for performing experimental sampling protocols to obtain luminescence dating parameters more accurately.

3.7 Summarizing the Trials at Lane Mountain, Incentive to Conduct Future Work

The studies at Lane Mountain provide a summary of the benefits and limits of using controlled exposure experiments and laser scanning techniques for rock surface exposure dating using luminescence. These results guided the subsequent chapter, which applies controlled exposure experiments and laser scanning measuring techniques to interpret glacial retreat chronology. A summary of the Lane Mountain results is provided to assist in explaining the general approach of study conducted in Section 4, and why a geological application was considered for additional study:

The first trial on Lane Mountain Quarry investigated the viability of using controlled exposure experiments for rock surface parameterization, where rather than relying on known age rock surfaces for rock surface parameterization, the technique can sample cores from the rock of

interest and subject them to controlled light exposures, to where the created depth profiles can be parameterized for light attenuation and a luminescence bleaching rate using the known age. The study, initially conducted with wafer data, showed potential in utilizing controlled exposure experiments for rock surface parameterization, as exposure ages produced for the site using natural sunlight controlled exposed parameters were within years of the true exposure age of 11 years. However, the resolution issues imposed by the wafer derived datasets limited the precision of the results, preventing confident interpretations of the sampling technique.

This result led to the second investigation at Lane Mountain, to determine if using spatially resolved OSL laser scanning techniques can measure more resolute OSL depth profiles for parameter extrapolation, and if such depth profiles can improve parameter extrapolative precision. Spatially resolved OSL scans were able to improve the precision of parameterizations of the tested cores over wafer derived depth profiles of the same core. Further, the extra assessment of identifying and filtering OSL from non-quartz mineralogy present in the samples produced depth profiles which had lower data error bounds and slightly improved parameter fit precision over wafer derived data fits. Controlled exposed cores were going to be measuring using spatially resolved laser scanning also, however the OSL from the samples were too weak to produce viable depth profiles. As supplement to this study, rough age calculations were performed using the separate, known age surfaces HRQ and P to evaluate the improvements that spatially resolved data can bring for age fit precision. However, as documented in prior applications using separate, known age surfaces for parameter extrapolation, the wide variability of parameterizations of individual cores prevented consistent ages from being produced from individual core samples. In response, combined data parameterizations were attempted to see if this approach mitigates parameter variabilities, with improvements in calculating more precise

and accurate ages for the rock surfaces, yet parameterization precision of μ and $\overline{\sigma\varphi_0}$ remained similar when compared to the individual core parameterizations of μ and $\overline{\sigma\varphi_0}$.

The promising results from controlled exposure experiments using wafer data, coupled with the results of using spatially resolved OSL for exposure dating, warrant further investigations to determine if the use of controlled exposure experiments, using more resolute luminescence measuring protocols such as with spatially resolved laser scanning, can produce precise parameterizations for less environmentally controlled exposure dating applications. It is also still worth investigating the use of simulated light exposures for exposure dating study, with more OSL sensitive samples, to make stronger observations of the limits of using constant light flux and unidirectional light for simulated light exposure in controlled exposure dating applications.

In response, a geological dating application was considered to evaluate the benefits and limitations of performing controlled exposure experiments and spatially resolved luminescence for exposure dating in a geological application, as well as assess the feasibility of dating rock surfaces hosting millennial-decamillennial timescales using luminescence. The ability to date rock surfaces within this timescale using luminescence is worthwhile investigating, as the chronometer is more sensitive to later Quaternary timescales ($>10^2 – 10^4$ years) than what other geochemical surface exposure dating techniques may offer. Further, such an application will test the feasibility of luminescence dating a rock surface where no known-age calibrated surfaces are available in certain sample settings.

3.8 References

Bailiff, I. K., & Mikhailik, V. B. (2003). Spatially-resolved measurement of optically stimulated luminescence and time-resolved luminescence. Radiation Measurements, 37(2), 151-159.

Baker, D. R., Mancini, L., Polacci, M., Higgins, M. D., Gualda, G. A. R., Hill, R. J., & Rivers, M. L. (2012). An introduction to the application of X-ray microtomography to the three-dimensional study of igneous rocks. Lithos, 148, 262-276.

Bench, T., & Feathers, J. (2022). Trialing the application of controlled exposure experiments for optical exposure dating on quartzite quarry surfaces in Washington State. Radiation Measurements, 156, 106805.

Bench, T., Sanderson, D., Feathers, J., & Warfield, E. (2023). Investigating the use of two-dimensional OSL laser scanning instruments and energy-dispersive x-ray spectroscopy for OSL exposure dating. Radiation Measurements, 167, 106999.

Bøtter-Jensen, L., Bulur, E., Duller, G. A. T., & Murray, A. S. (2000). Advances in luminescence instrument systems. Radiation Measurements, 32(5-6), 523-528.

Bray, H. E., Bailey, R. M., & Stokes, S. (2002). Quantification of cross-irradiation and cross-illumination using a Risø TL/OSL DA-15 reader. Radiation Measurements, 35(3), 275-280.

Brill, D., May, S. M., Mhammdi, N., King, G., Burow, C., Wolf, D., ... & Brückner, H. (2020). OSL rock surface exposure dating as a novel approach for reconstructing transport histories of coastal boulders over decadal to centennial timescales. EGU General Assembly, EGU2020-18537. doi, 10.

Bulur, E. N. V. E. R., Kartal, E., & Saraç, B. E. (2014). Time-resolved OSL of natural zircon: A preliminary study. Radiation measurements, 60, 46-52.

Cabaleiro, D. & Pastoriza Gallego, Maria & Gracia-Fernández, Carlos & Piñeiro, Manuel & Lugo, Luis. (2013). Rheological and volumetric properties of TiO2-ethylene glycol nanofluids. Nanoscale research letters. 8. 286. 10.1186/1556-276X-8-286.

Chapot, M. S., Sohbati, R., Murray, A. S., Pederson, J. L., & Rittenour, T. M. (2012). Constraining the age of rock art by dating a rockfall event using sediment and rock-surface luminescence dating techniques. Quaternary Geochronology, 13, 18-25.

Chen, Xiaoyan & Leng, Jinhua & Zhang, Dongsheng & He, Bobing. (2020). Study of modified potassium feldspar as a novel β-nucleating agent to the crystal morphology and properties of polypropylene. SN Applied Sciences. 2. 10.1007/s42452-020-2485-x.

Clark-Balzan, L. & Schwenninger, J. L. First steps toward spatially resolved OSL dating with electron multiplying charge-coupled devices (EMCCDs): System design and image analysis. Radiat. Meas. 47, 797–802 (2012).

Duller, G. A. T., BØtter-Jensen, L. & Markey, B. G. A luminescence imaging system based on a CCD camera. Radiat. Meas. 27, 91–99 (1997).

Duller, G. A. T. (2003). Distinguishing quartz and feldspar in single grain luminescence measurements. Radiation measurements, 37(2), 161-165.

Duller, G. A. T., Kook, M., Stirling, R. J., Roberts, H. M. & Murray, A. S. Spatially-resolved thermoluminescence from snail opercula using an EMCCD. Radiat. Meas. 81, 157–162 (2015).

Elkadi, J., King, G. E., Lehmann, B., & Herman, F. (2021). Reducing variability in OSL rock surface dating profiles. Quaternary Geochronology, 64, 101169.

Freiesleben, T. H., Thomsen, K. J., & Jain, M. (2023). Novel luminescence kinetic models for rock surface exposure dating. Radiation Measurements, 160, 106877.

Fuhrmann, S., Meyer, M. C., Gliganic, L. A., & Obleitner, F. (2022). Testing the effects of aspect and total insolation on luminescence depth profiles for rock surface exposure dating. Radiation Measurements, 153, 106732.

Gliganic, L. A., Meyer, M. C., Sohbati, R., Jain, M., & Barrett, S. (2019). OSL surface exposure dating of a lithic quarry in Tibet: Laboratory validation and application. Quaternary Geochronology, 49, 199-204.

Guo, Jianming & Ye, Mingquan & Han, Aijun & Liao, Jun & Chen, Chenlu. (2020). Studies on the preparation and characterization of composite La-doped γ-Ce2S3-coated mica cool pigments. Applied Physics A. 126. 10.1007/s00339-020-03641-z.

Han, S., Löhr, S. C., Abbott, A. N., Baldermann, A., Farkaš, J., McMahon, W., ... & Owen, M. (2022). Earth system science applications of next-generation SEM-EDS automated mineral mapping. Frontiers in Earth Science, 10, 2244.

Hashimoto, T., Yokosaka, K., Habuki, H. & Hayashi, Y. Provenance search of dune sands using thermoluminescence colour images (TLCIs) from quartz grains. Int. J. Radiat. Appl. Instrumentation. Part 16, 3–10 (1989).

Jeong, G. Y., & Choi, J. H. (2012). Variations in quartz OSL components with lithology, weathering and transportation. Quaternary Geochronology, 10, 320-326.

Lehmann, B., Valla, P. G., King, G. E., and Herman, F. (2018). Investigation of OSL surface exposure dating to reconstruct post-LIA glacier fluctuations in the French Alps (Mer de Glace, Mont Blanc massif). Quaternary Geochronology, 44:63–74

Lehmann, B., Herman, F., Valla, P. G., King, G. E., & Biswas, R. H. (2019). Evaluating post-glacial bedrock erosion and surface exposure duration by coupling in situ optically stimulated luminescence and 10 Be dating. Earth Surface Dynamics, 7(3), 633-662.

Li, Shaofei & Chen, Ding & Gu, Huazhi & Huang, Ao & Fu, Lvping. (2022). Investigation on Application Prospect of Refractories for Hydrogen Metallurgy: The Enlightenment from the Reaction between Commercial Brown Corundum and Hydrogen. Materials (Basel, Switzerland). 15. 10.3390/ma15197022.

Lindsey, K. A., Gaylord, D. R., & Groffman, L. H. (1990). Geology of the Upper Proterozoic to Lower Cambrian Three Sisters Formation, Gypsy Quartzite, and Addy Quartzite, Stevens and Pend Oreille Counties, Northeastern Washington (Vol. 30, p. 37). Washington State Department of Natural Resources, Division of Geology and Earth Resources.

Luo, M., Chen, J., Liu, J., Qin, J., Owen, L. A., Han, F., ... & Li, Y. (2018). A test of rock surface luminescence dating using glaciofluvial boulders from the Chinese Pamir. Radiation Measurements, 120, 290-297.

Meyer, M. C., Austin, P., & Tropper, P. (2013). Quantitative evaluation of mineral grains using automated SEM–EDS analysis and its application potential in optically stimulated luminescence dating. Radiation measurements, 58, 1-11.

Moayed, N. K., Sohbati, R., Murray, A. S., Rades, E. F., Fattahi, M., & Ruiz López, J. F. (2022). Rock surface luminescence dating of prehistoric rock art from central Iberia. Archaeometry.

Ou, X. J., Roberts, H. M., Duller, G. A. T., Gunn, M. D., & Perkins, W. T. (2018). Attenuation of light in different rock types and implications for rock surface luminescence dating. Radiation Measurements, 120, 305-311.

Polymeris, G. S., Tsirliganis, N., Loukou, Z., & Kitis, G. (2006). A comparative study of the anomalous fading effects of TL and OSL signals of Durango apatite. physica status solidi (a), 203(3), 578-590.

Sanderson, D.C.W., Carmichael, L., Murphy, S., Whitely, V., Scott, E. and Cresswell, A. (2001) Investigation of Statistical and Imaging Methods for Luminescence Detection of Irradiated Ingredients. Project Report. Food Standards Agency, London, UK. http://eprints.gla.ac.uk/58359/ Deposited on: 31 January 2012

Sanderson, D., Smillie, M. McCullagh R., Feathers, J., Hauser, N. (2011). Dating exposed rock surfaces by luminescence: developing and testing models for surface bleaching rates. 2011 International Meeting on Luminescence and Electron Spin Resonance Dating.

Sanjurjo-Sanchéz, J., Alves, C., & Teixeira, D. (2013). Microscopy studies in support of OSL dating of mortars of historical buildings. Microscopy and Microanalysis, 19(S4), 115-116.

Sellwood, E. L., Guralnik, B., Kook, M., Prasad, A. K., Sohbati, R., Hippe, K., ... & Jain, M. (2019). Optical bleaching front in bedrock revealed by spatially-resolved infrared photoluminescence. Scientific reports, 9(1), 1-12.

Sellwood, E. L., Kook, M., & Jain, M. (2022a). A 2D imaging system for mapping luminescence-depth profiles for rock surface dating. Radiation Measurements, 150, 106697.

Sellwood, E. L., Kook, M., & Jain, M. (2022b). Investigating the potential of rock surface burial dating using IRPL and IRSL imaging. Radiation Measurements, 155, 106783.

Smillie, M. 2011. 5th Year Report: Progress Towards Surface Exposure Dating. Scottish Universities Environmental Research Centre. Glasgow, United Kingdon. Unpublished.

Singarayer, J. S., & Bailey, R. M. (2003). Further investigations of the quartz optically stimulated luminescence components using linear modulation. Radiation Measurements, 37(4-5), 451-458.

Sohbati, R., Murray, A. S., Chapot, M. S., Jain, M., & Pederson, J. (2012). Optically stimulated luminescence (OSL) as a chronometer for surface exposure dating. Journal of Geophysical Research: Solid Earth, 117(B9).

3.9 Appendix

A0 – Sampling Holes

HRQ 1-1 – sample HRQ1

HRQ1-2 – sample HRQ2

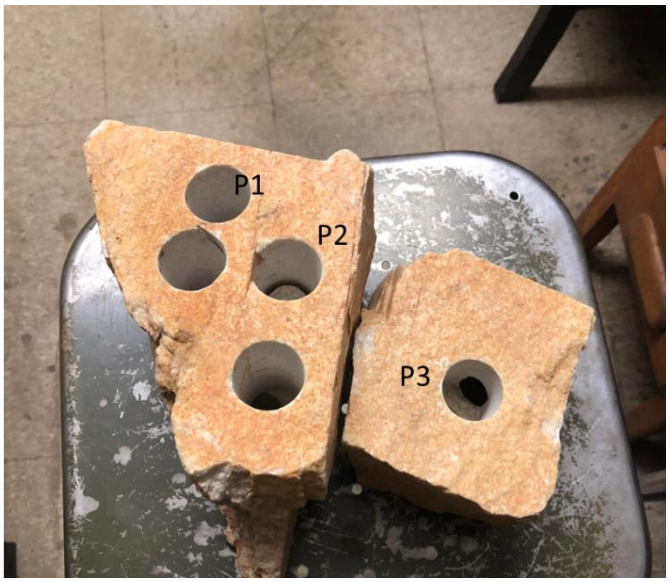
P1
P2
P3

A1 – Anomaly Identification Summary

The goal of this SEM-EDS study was to identify the composition of OSL anomalies in quartzite OSL scans to see if there were non-quartz minerals present. The purpose of this assessment is to identify causes for OSL depth profile scatter from non-quartz minerals disproportionately affecting OSL scan depth profile data.

Anomalies were identified from OSL scan data, which then the dimensions of each anomaly were measured using EDS. The associated anomaly, if determined hosted characteristic spectra of non-quartz mineralogy from the EDS measurement, was recorded as an anomaly and filtered from the scan dataset.

All but 6 anomalies hosted significant element contents chemically resemblant of feldspars, micas, zircon mineral, and corundum/aluminum oxides, which can impact OSL signals in rock samples.

The 6 anomalies which do not contain mineral resemblant compositions include sawblade contaminants, iron oxides, or rare earth elements:

- Core P3's top half: anomaly 2 (Fe bearing) and anomaly 4 (Sn/Cu bearing).
- Core P3's Bottom half: Anomaly 6 (C/Br dominant), Anomaly 10 (Fe bearing), and anomaly 12 (Al present, but also presence of brass staining from sawblade)
- HRQ 2 top portion, Anomaly 6 (Cu dominant).

All assessments and data collections were performed by Tristan Bench. The organization of this data in the appendix was conducted by Tristan Bench and with the assistance of Emily Warfied.

Assistance in organization from undergraduate Emily Warfield was appreciated!

P2

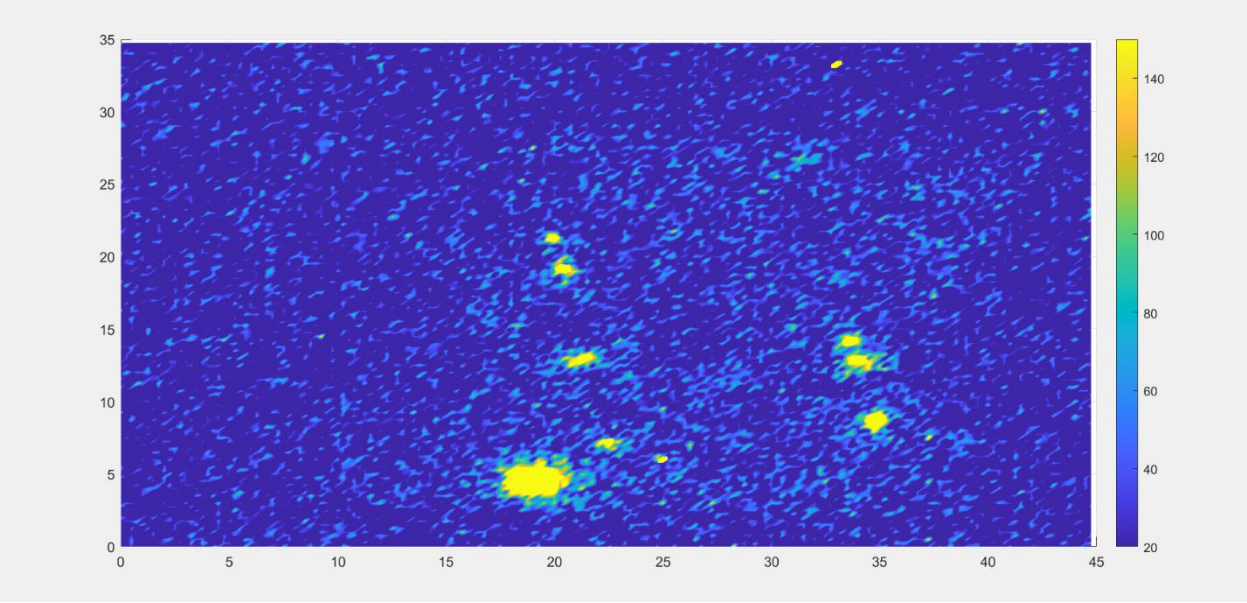
35
30
25
20
15
10
5
0
0
5
10
15
20
25
30
35
40
45
140
120
100
80
60
40
20

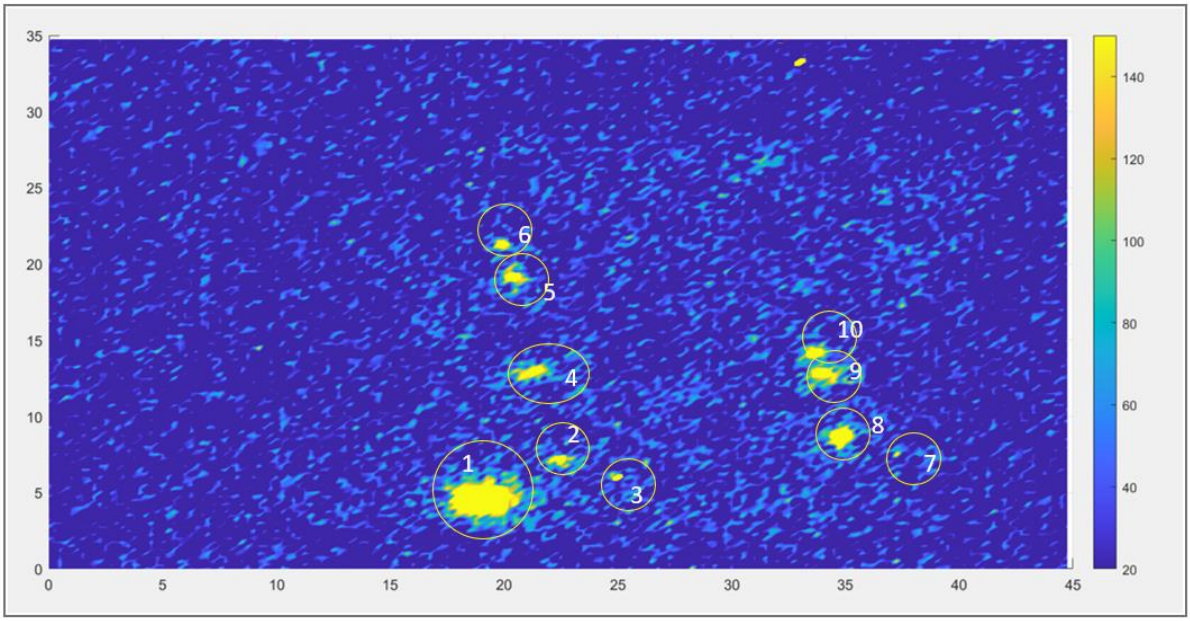
35
30
25
20
15
10
5
0
0
5
10
15
20
25
30
35
40
45
140
120
100
80
60
40
20
1
2
3
4
5
6
7
8
9
10

Anomaly 1:

Site of interest 1

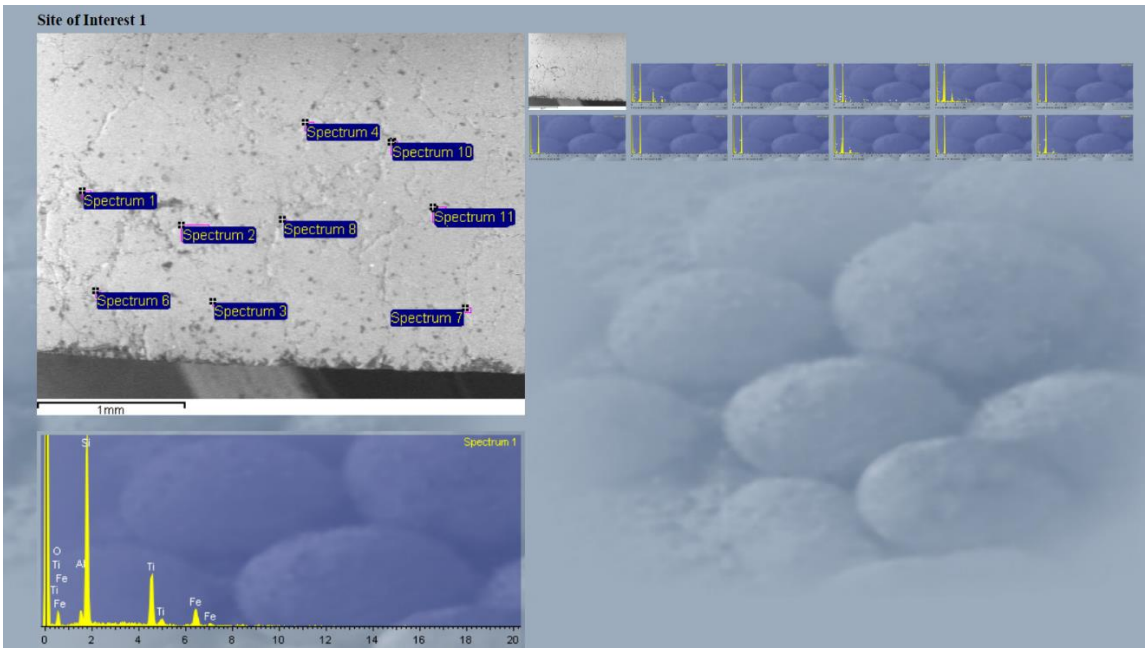

Site of interest 2

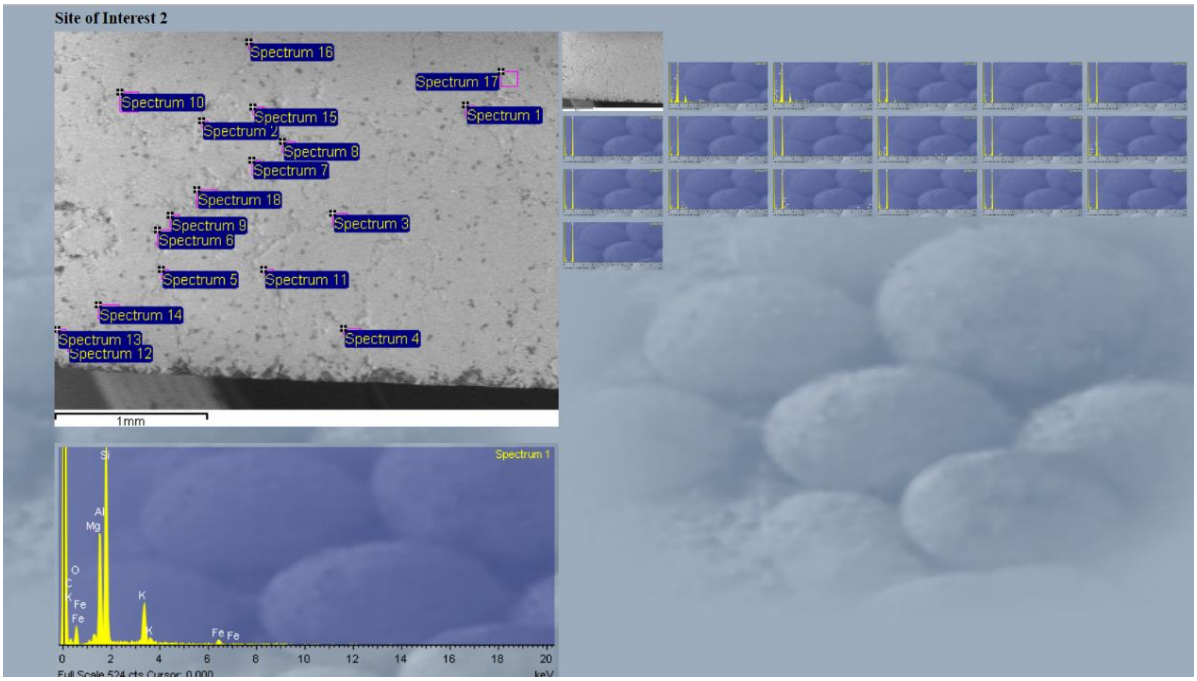

Notes

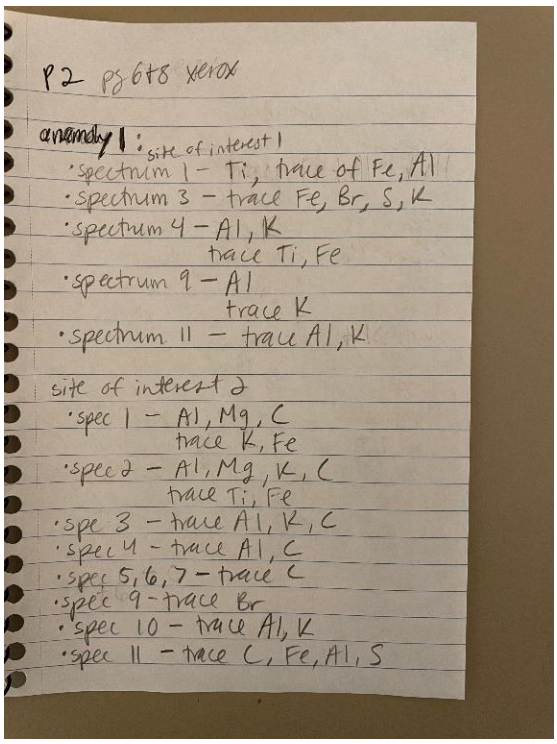

P2 pg 68 xerox

anamoly 1: site of interest 1
- spectrum 1 – Ti, trace of Fe, Al
- spectrum 3 – trace Fe, Br, S, K
- spectrum 4 – Al, K
  trace Ti, Fe
- spectrum 9 – Al
  trace K
- spectrum 11 – trace Al, K

site of interest 2
- spec 1 – Al, Mg, C
  trace K, Fe
- spec 2 – Al, Mg, K, C
  trace Ti, Fe
- spe 3 – trace Al, K, C
- spec 4 – trace Al, C
- spec 5, 6, 7 – trace C
- spec 9 – trace Br
- spec 10 – trace Al, K
- spec 11 – trace C, Fe, Al, S

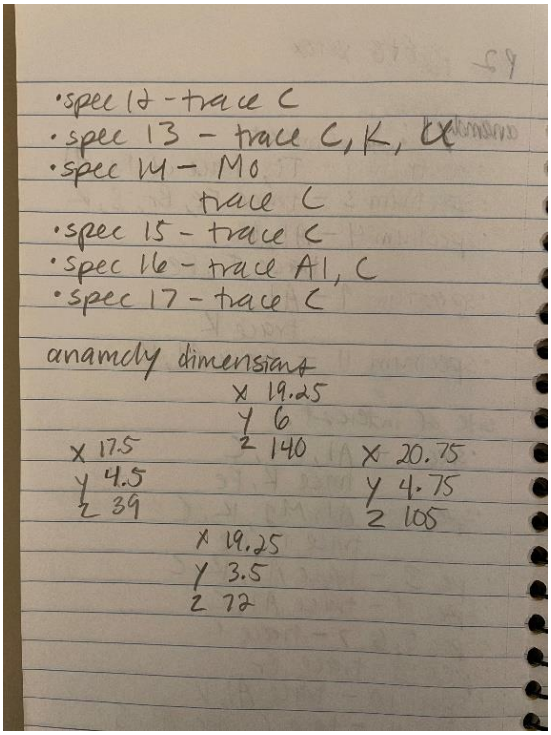

- spec 12 – trace C
- spec 13 – trace C, K, [illegible]
- spec 14 – Mo
  trace C
- spec 15 – trace C
- spec 16 – trace Al, C
- spec 17 – trace C

anamoly dimensions
X 19.25
Y 6
Z 140

X 17.5
Y 4.5
Z 39

X 20.75
Y 4.75
Z 105

X 19.25
Y 3.5
Z 72

Anomaly 2:

Site of interest 3

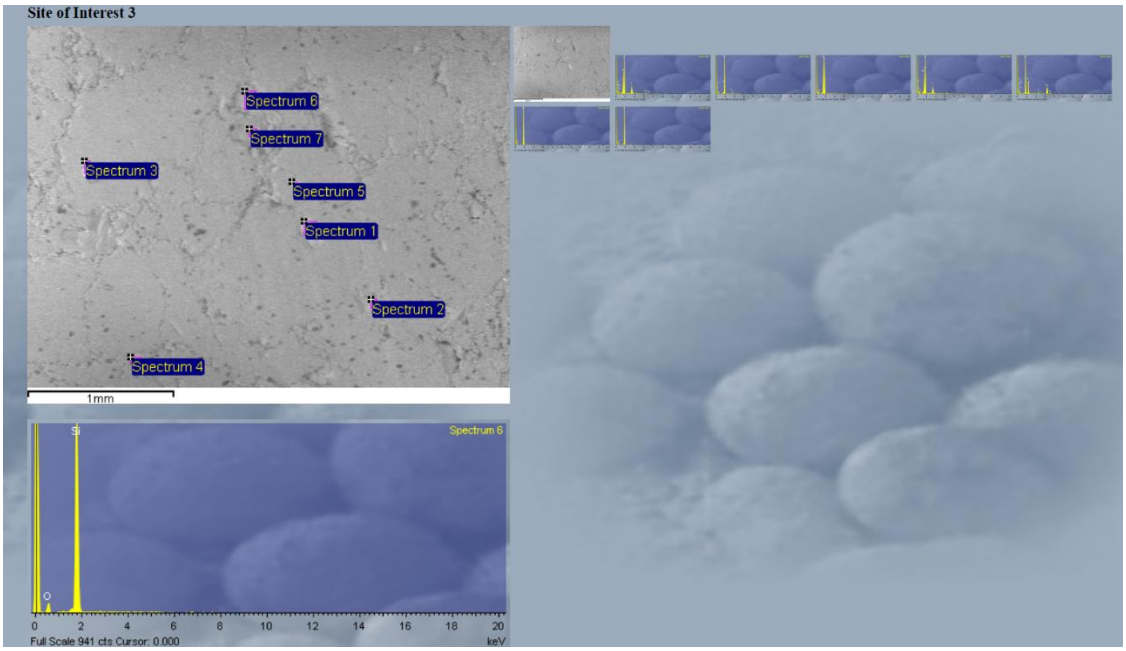

Notes

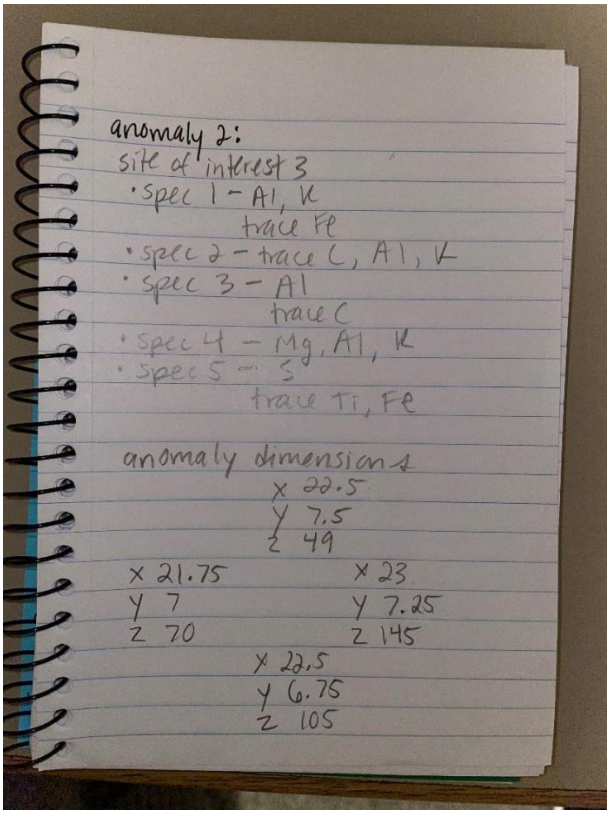
anomaly 2:
site of interest 3
• spec 1 - Al, K
trace Fe
• spec 2 - trace C, Al, K
• spec 3 - Al
trace C
• spec 4 - Mg, Al, K
• spec 5 - S
trace Ti, Fe
anomaly dimensions
x 22.5
y 7.5
z 49
x 21.75
y 7
z 70
x 23
y 7.25
z 145
x 22.5
y 6.75
z 105

Anomaly 3:

Site of interest 4

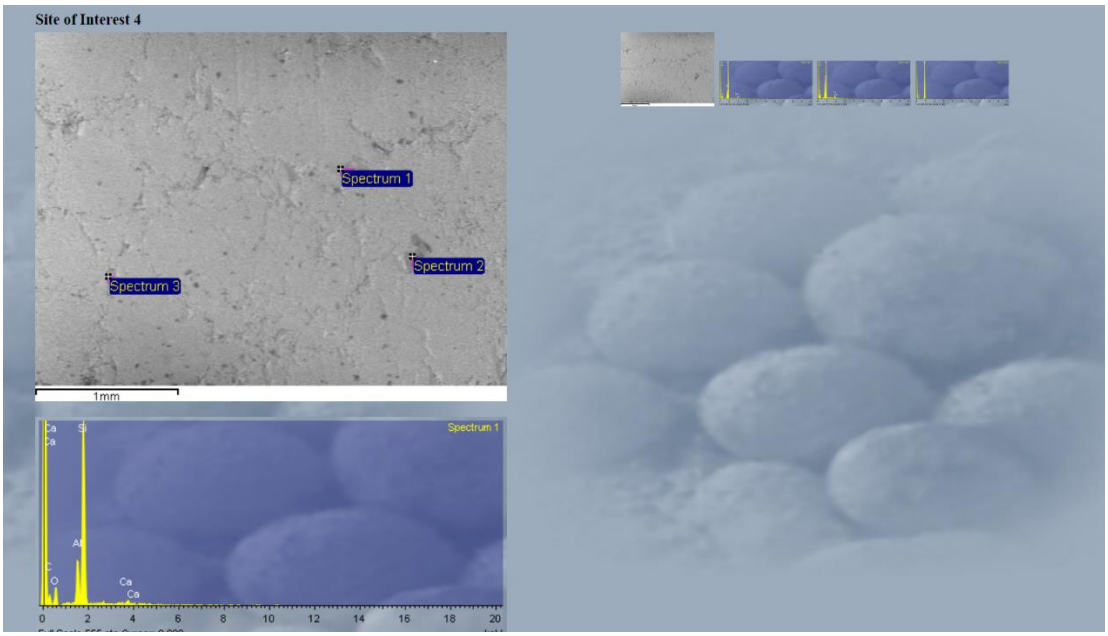

Notes

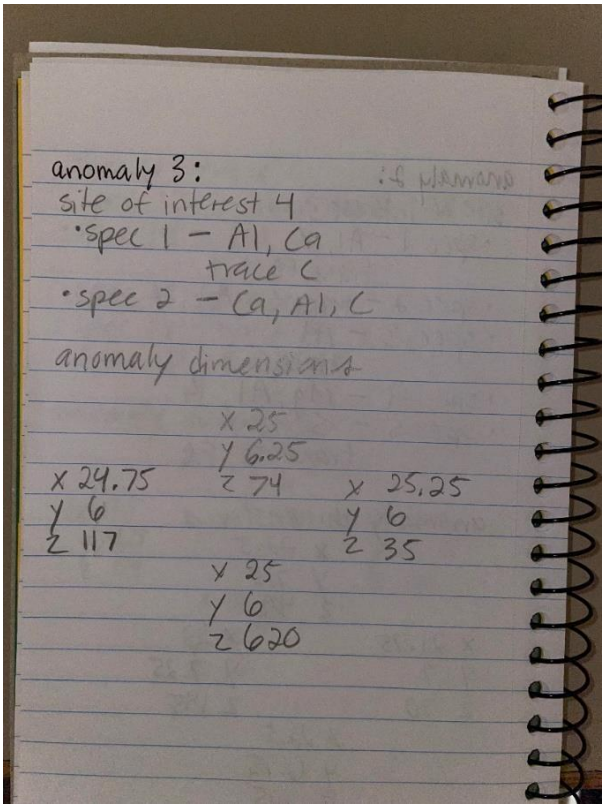
anomaly 3:
site of interest 4
•spec 1 – Al, Ca
trace C
•spec 2 – Ca, Al, C
anomaly dimensions
x 25
y 6.25
z 74
x 24.75
y 6
z 117
x 25.25
y 6
z 35
x 25
y 6
z 620

Anomaly 4:

Site of interest 5

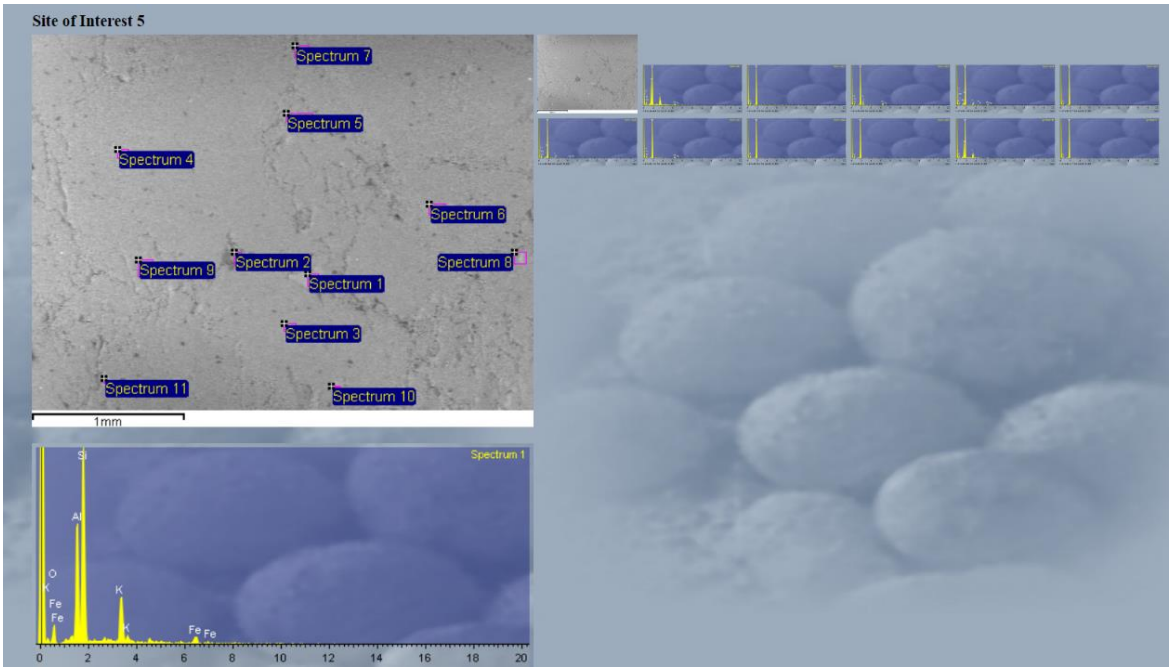

Notes

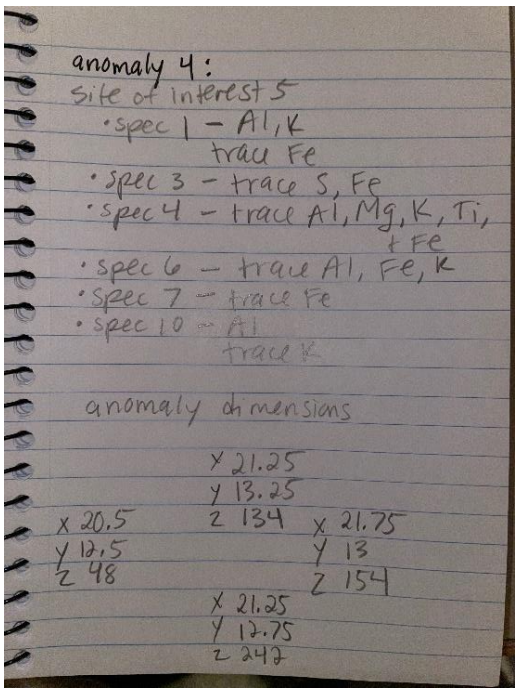
anomaly 4:
site of interest 5
• spec 1 – Al, K
trace Fe
• spec 3 – trace S, Fe
• spec 4 – trace Al, Mg, K, Ti,
+ Fe
• spec 6 – trace Al, Fe, K
• spec 7 – trace Fe
• spec 10 – Al
trace K
anomaly dimensions
x 21.25
y 13.25
z 134
x 20.5
y 12.5
z 48
x 21.75
y 13
z 154
x 21.25
y 12.75
z 242

Anomaly 5:

Site of interest 6

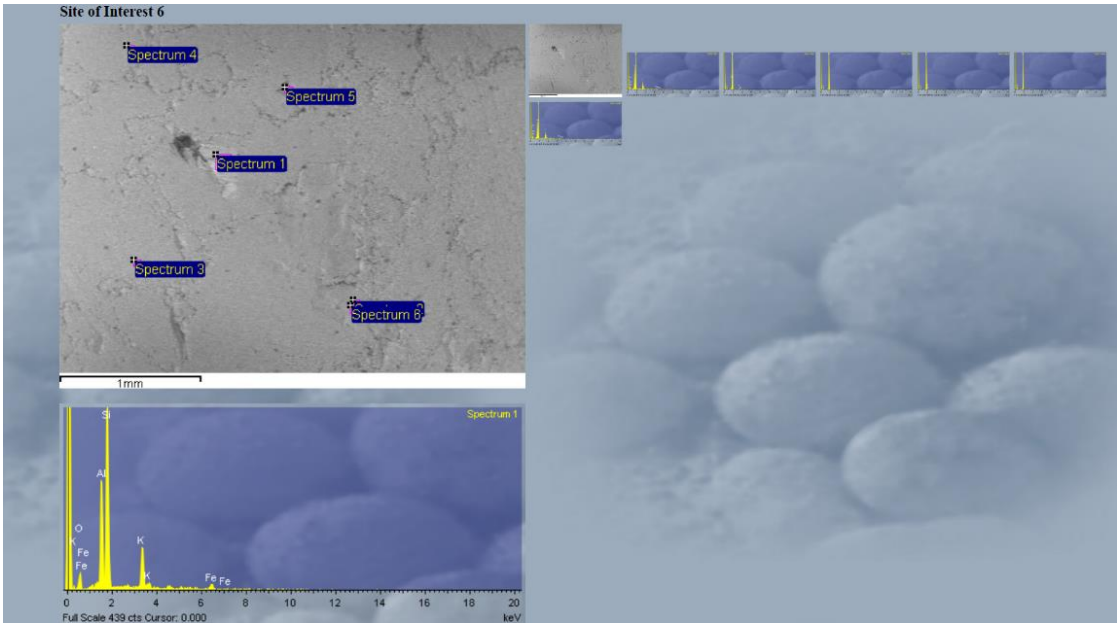

Notes

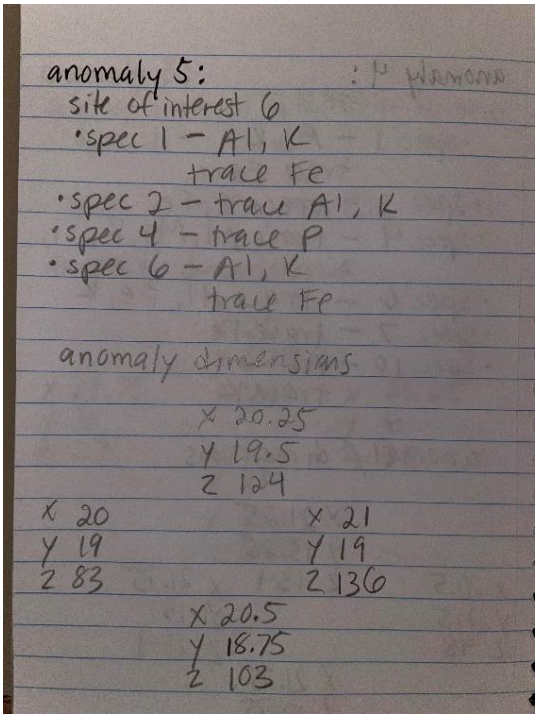
anomaly 5:
site of interest 6
•spec 1 – Al, K
trace Fe
•spec 2 – trace Al, K
•spec 4 – trace P
•spec 6 – Al, K
trace Fe
anomaly dimensions
X 20.25
Y 19.5
Z 124
X 20
Y 19
Z 83
X 21
Y 19
Z 136
X 20.5
Y 18.75
Z 103

Anomaly 6:

Site of interest 8

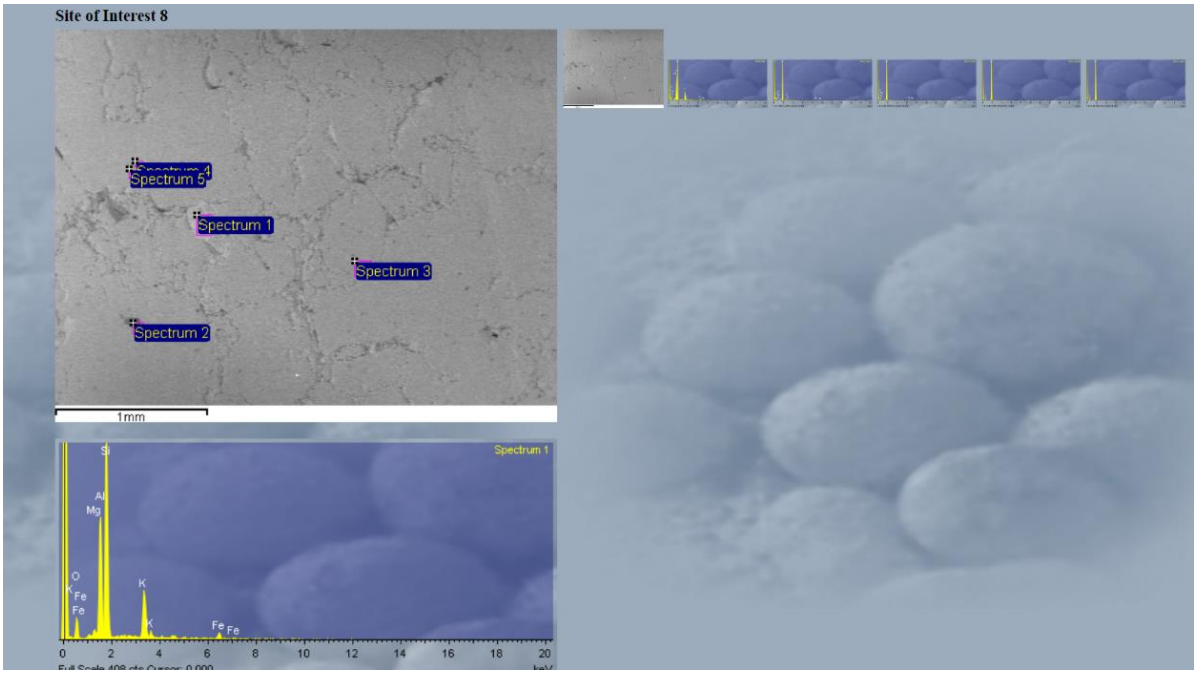

Notes

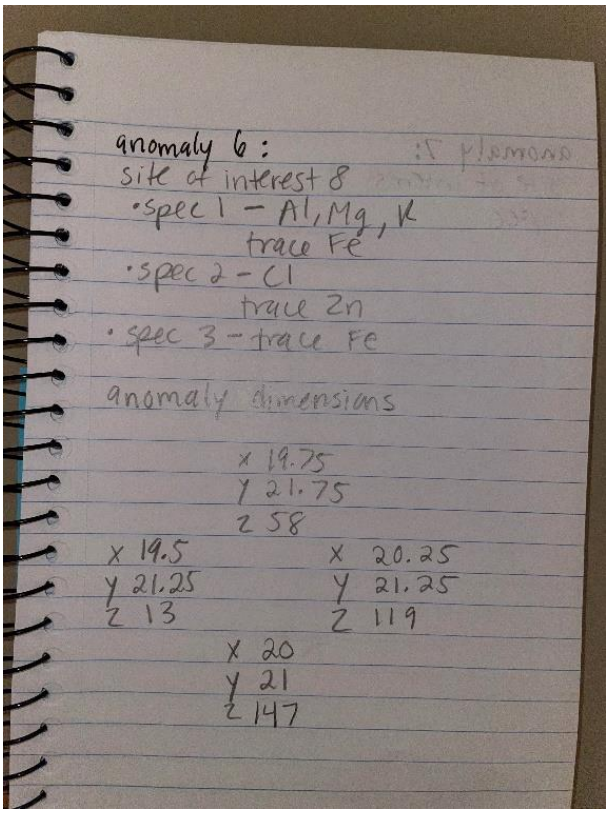
anomaly 6:
site of interest 8
•spec 1 - Al, Mg, K
trace Fe
•spec 2 - Cl
trace Zn
•spec 3 - trace Fe
anomaly dimensions
x 19.75
y 21.75
z 58
x 19.5
y 21.25
z 13
x 20.25
y 21.25
z 119
x 20
y 21
z 147

Anomaly 7:

Site of interest 9

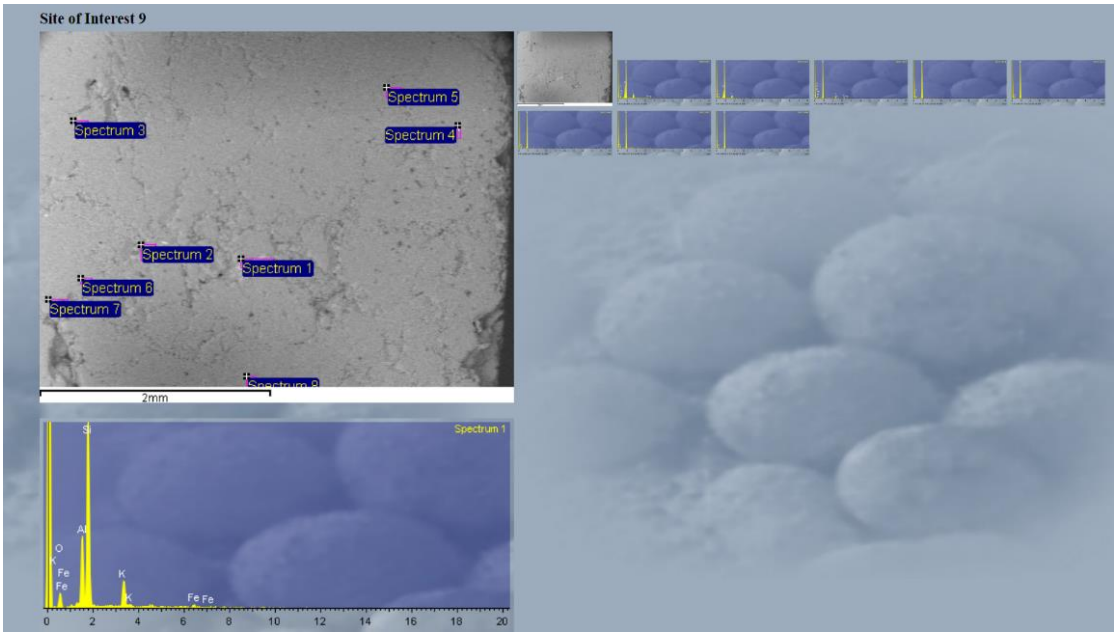

Notes

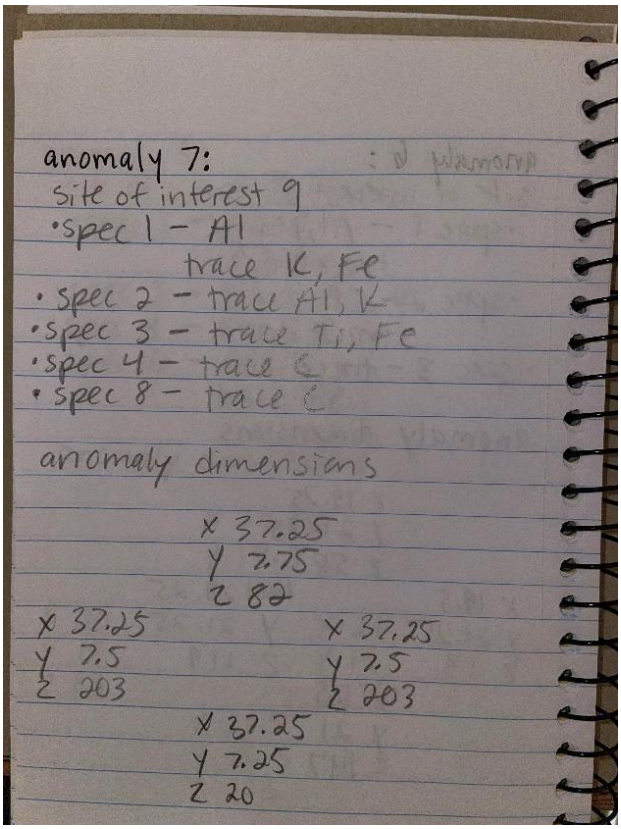
anomaly 7:
site of interest 9
•spec 1 – Al
trace K, Fe
• spec 2 – trace Al, K
•spec 3 – trace Ti, Fe
•spec 4 – trace C
• spec 8 – trace C
anomaly dimensions
X 37.25
Y 7.75
Z 82
X 37.25
Y 7.5
Z 203
X 37.25
Y 7.5
Z 203
X 37.25
Y 7.25
Z 20

Anomaly 8:

Site of interest 10

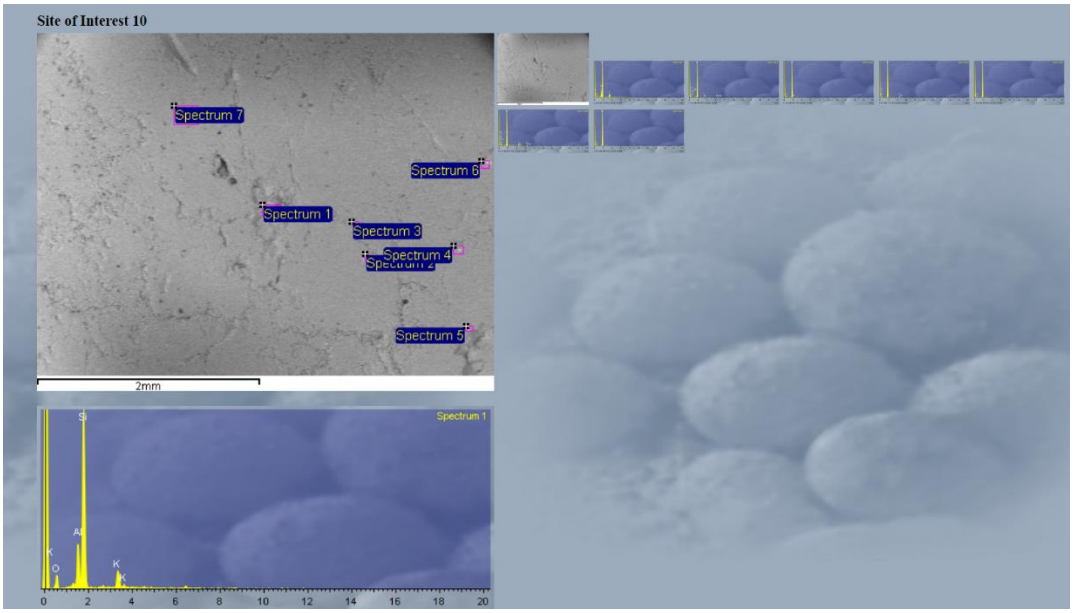

Notes

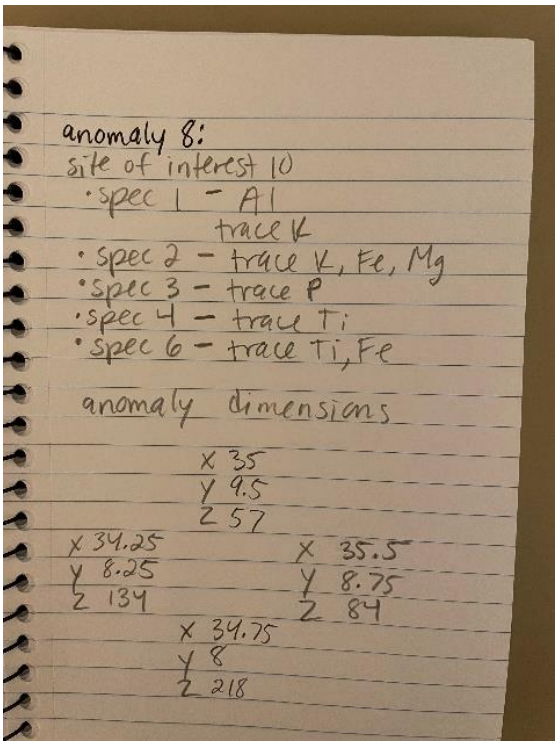
anomaly 8:
site of interest 10
• spec 1 - Al
trace K
• spec 2 - trace K, Fe, Mg
• spec 3 - trace P
• spec 4 - trace Ti
• spec 6 - trace Ti, Fe
anomaly dimensions
X 35
Y 9.5
Z 57
X 34.25
Y 8.25
Z 134
X 35.5
Y 8.75
Z 84
X 34.75
Y 8
Z 218

Anomaly 9:

Site of interest 11

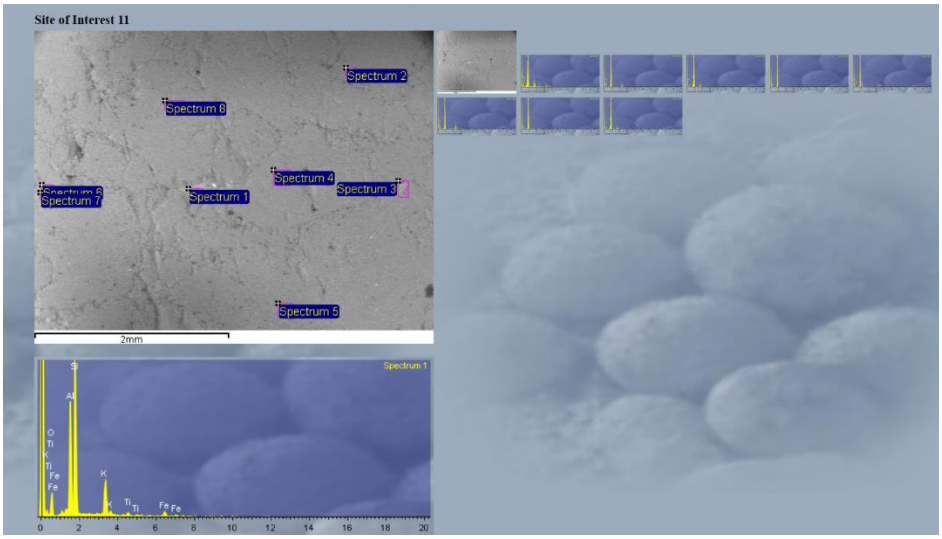

Notes

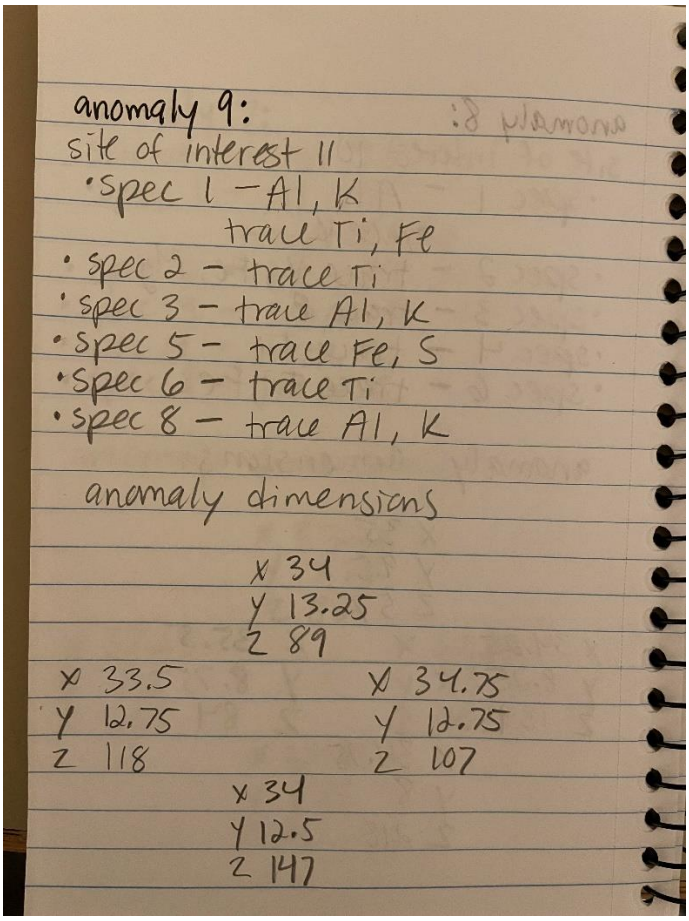
anomaly 9:
:8 plasma
site of interest 11
• spec 1 – Al, K
trace Ti, Fe
• spec 2 – trace Ti
• spec 3 – trace Al, K
• spec 5 – trace Fe, S
• spec 6 – trace Ti
• spec 8 – trace Al, K
anomaly dimensions
x 34
y 13.25
z 89
x 33.5
y 12.75
z 118
x 34.75
y 12.75
z 107
x 34
y 12.5
z 147

Anomaly 10:

Site of interest 12

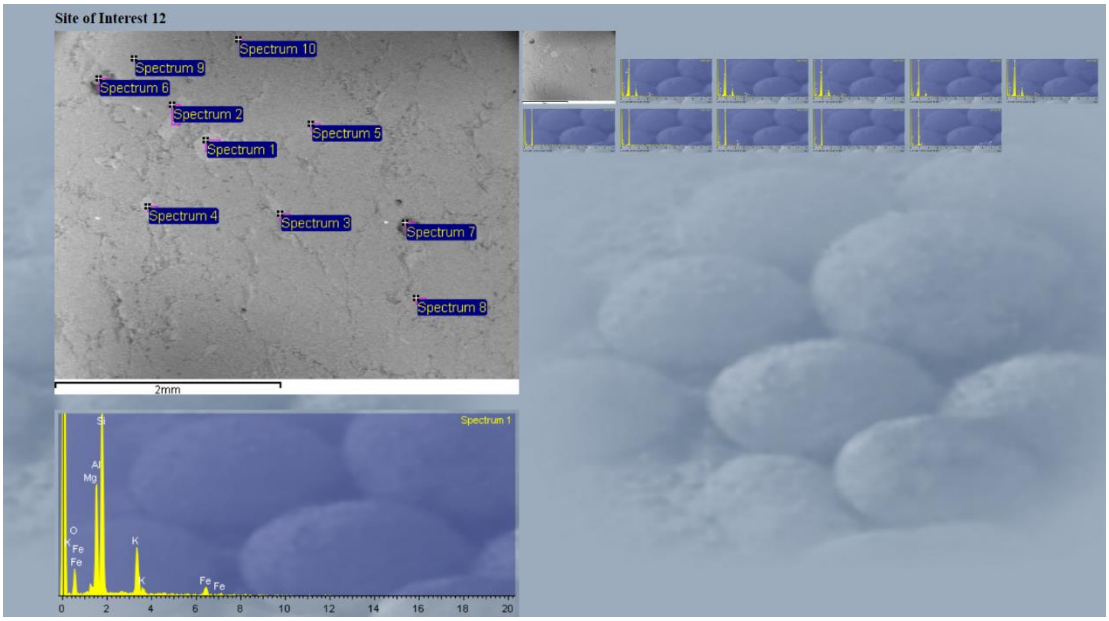

Notes

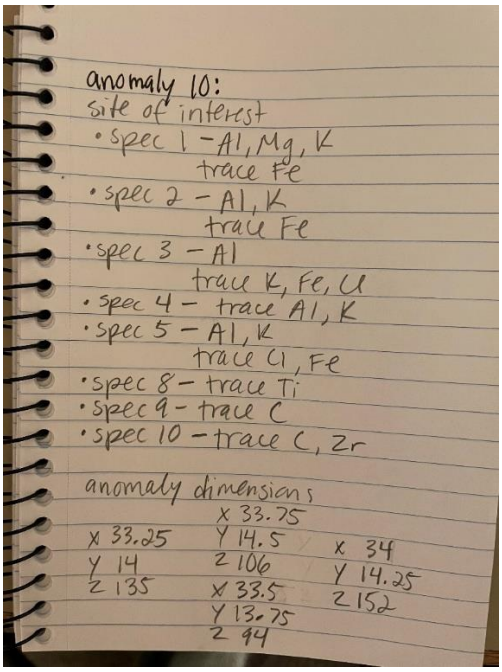
anomaly 10:
site of interest
• spec 1 - Al, Mg, K
trace Fe
• spec 2 - Al, K
trace Fe
• spec 3 - Al
trace K, Fe, Cl
• spec 4 - trace Al, K
• spec 5 - Al, K
trace Cl, Fe
• spec 8 - trace Ti
• spec 9 - trace C
• spec 10 - trace C, Zr
anomaly dimensions
x 33.25
Y 14
Z 135
x 33.75
Y 14.5
Z 106
x 33.5
Y 13.75
Z 94
x 34
Y 14.25
Z 152

P3

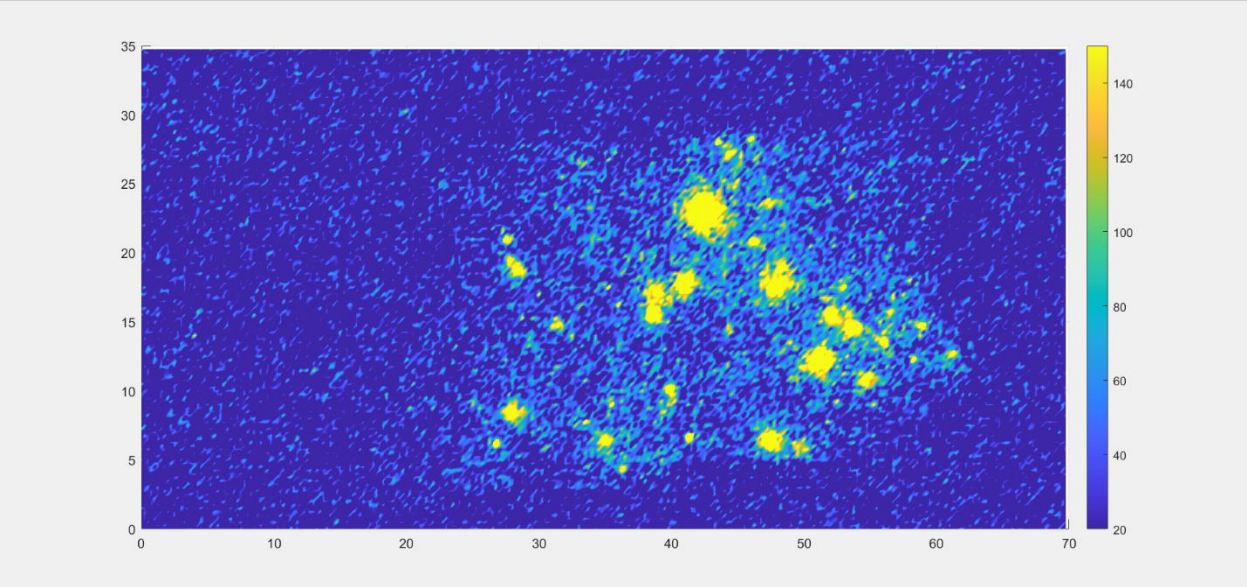
35
30
25
20
15
10
5
0
0
10
20
30
40
50
60
70
140
120
100
80
60
40
20

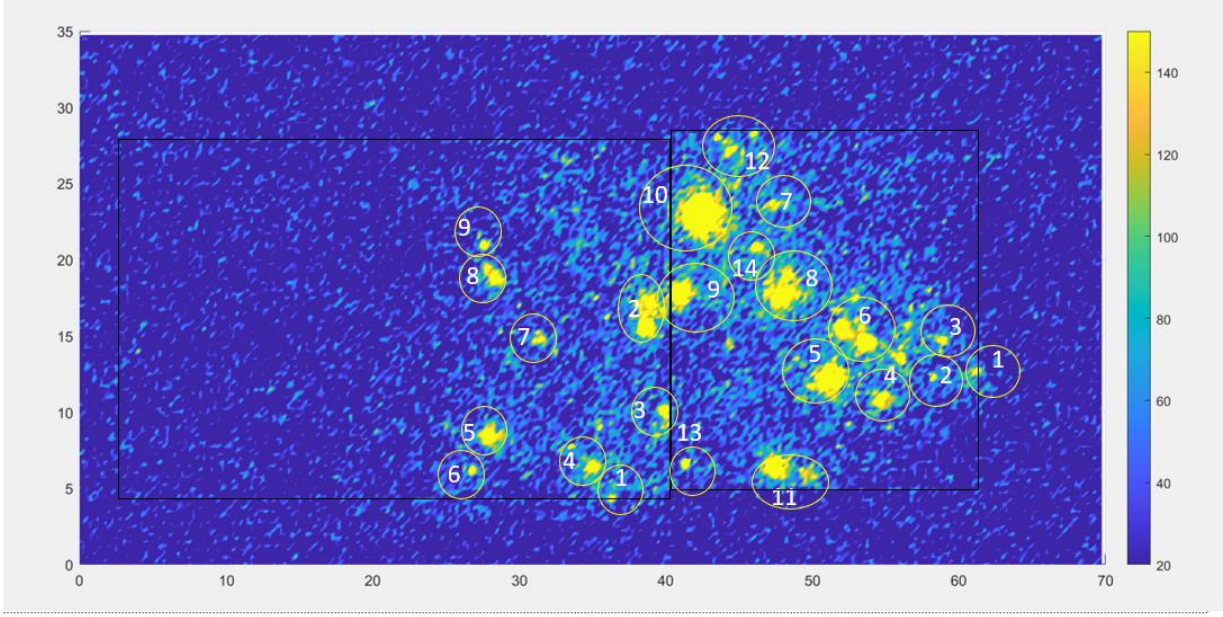
35
30
25
20
15
10
5
0
0
10
20
30
40
50
60
70
140
120
100
80
60
40
20
12
10
7
9
8
14
9
8
2
6
3
7
5
4
2
1
3
13
5
4
6
1
11

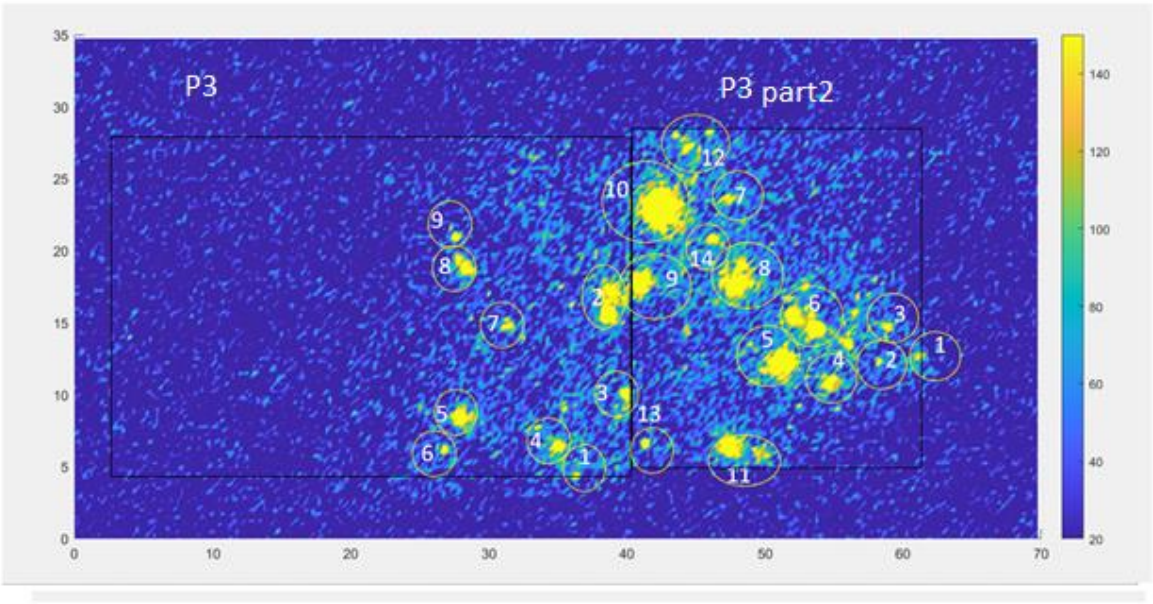
P3
P3 part2
0
5
10
15
20
25
30
35
0
10
20
30
40
50
60
70
20
40
60
80
100
120
140

Anomaly 1:

Site of interest 1

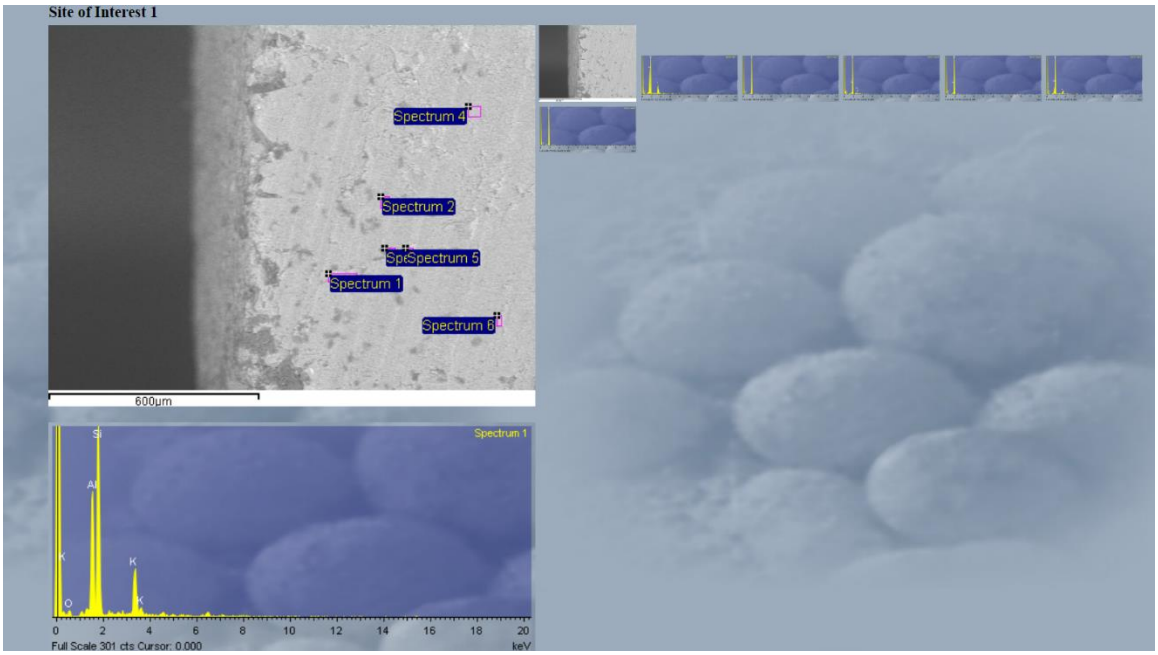

Site of interest 2

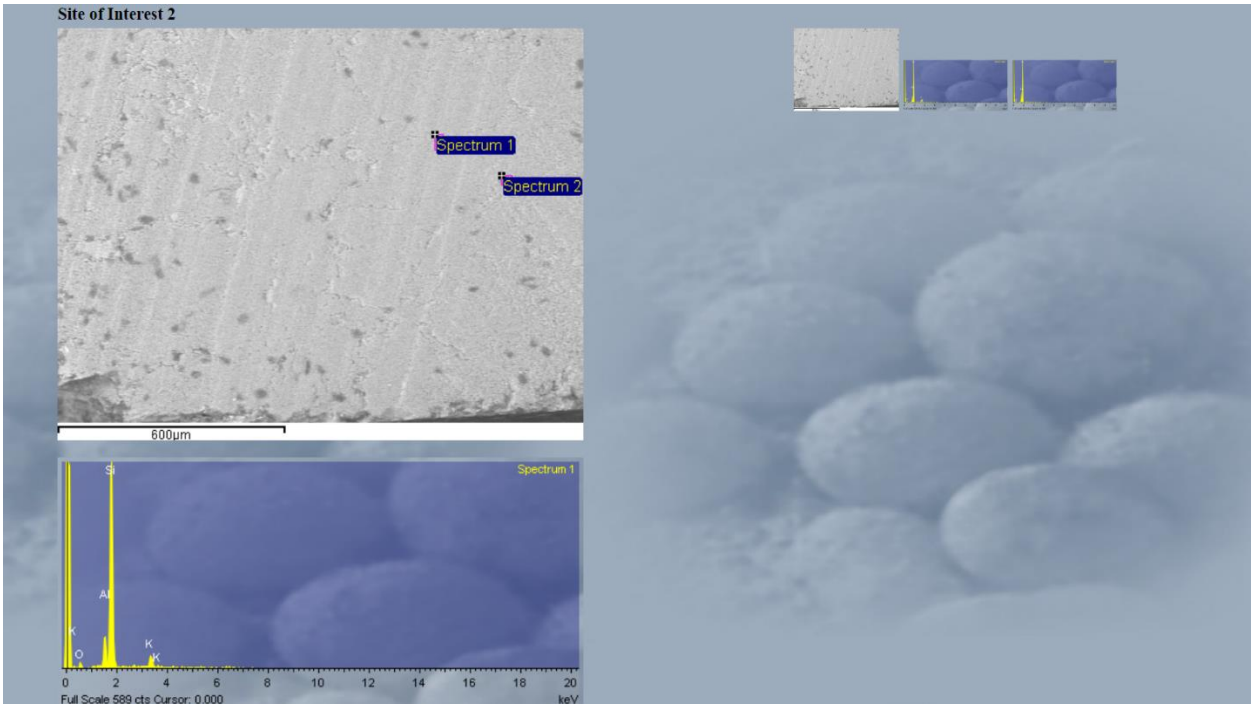

Notes

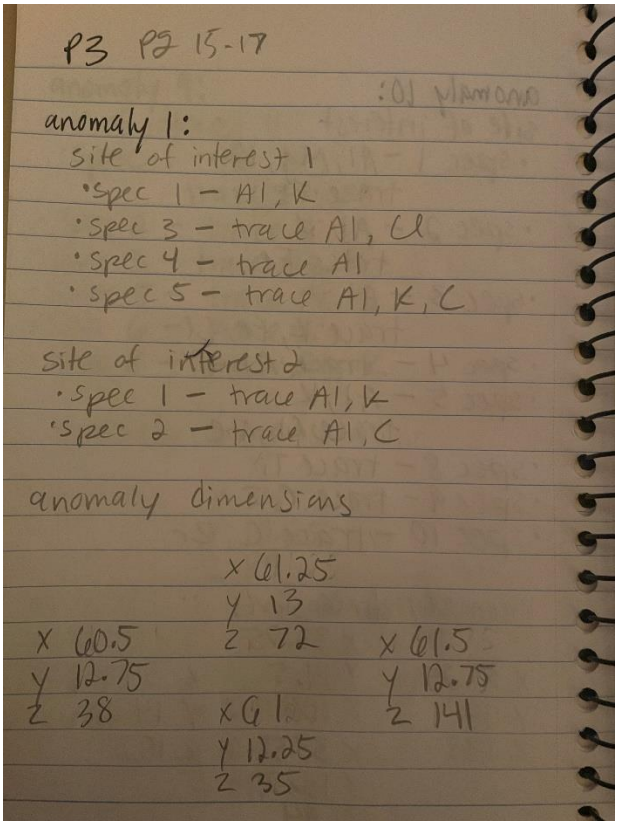
P3 P2 15-17
:01 diamond
anomaly 1:
site of interest 1
•spec 1 – Al, K
•spec 3 – trace Al, Cl
•spec 4 – trace Al
•spec 5 – trace Al, K, C
site of interest 2
•spec 1 – trace Al, K
•spec 2 – trace Al, C
anomaly dimensions
x 61.25
y 13
z 72
x 60.5
y 12.75
z 38
x 61.5
y 12.75
z 141
x 61
y 12.25
z 35

Anomaly 2:

Site of interest 3

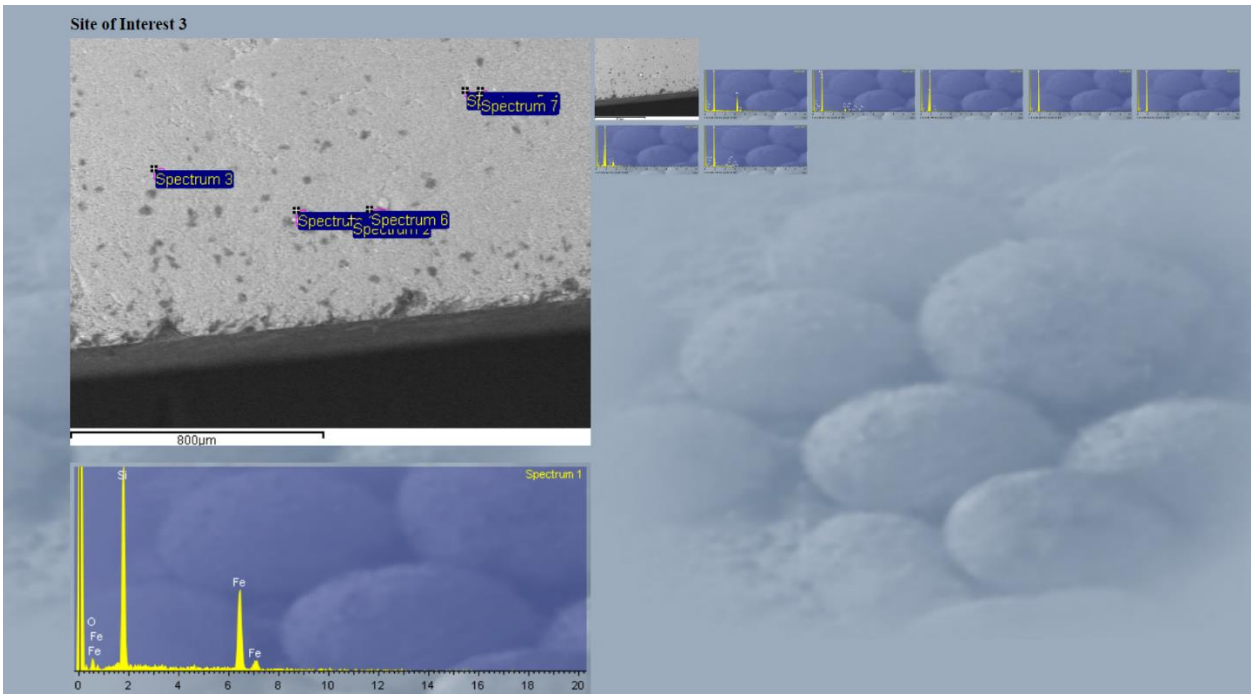

Notes

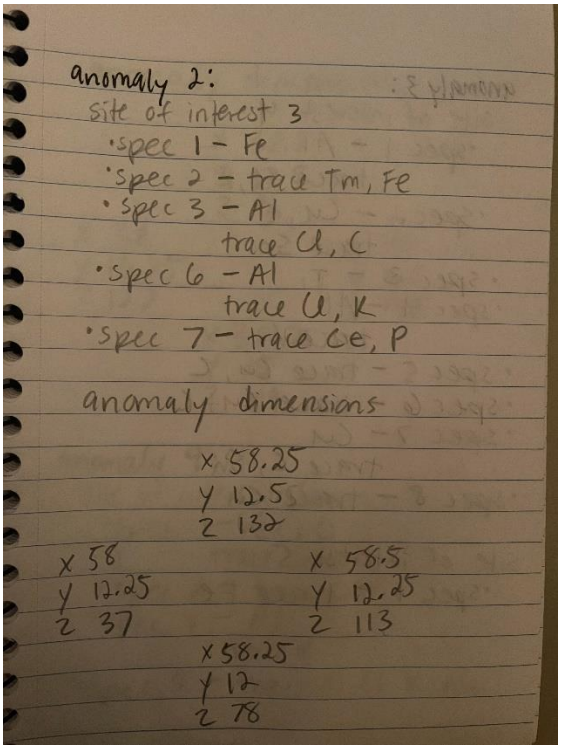
anomaly 2:
site of interest 3
•spec 1 - Fe
•spec 2 - trace Tm, Fe
•spec 3 - Al
trace Cl, C
•spec 6 - Al
trace Cl, K
•spec 7 - trace Ce, P
anomaly dimensions
x 58.25
y 12.5
z 132
x 58
y 12.25
z 37
x 58.5
y 12.25
z 113
x 58.25
y 12
z 78

Anomaly 3:

Site of interest 4

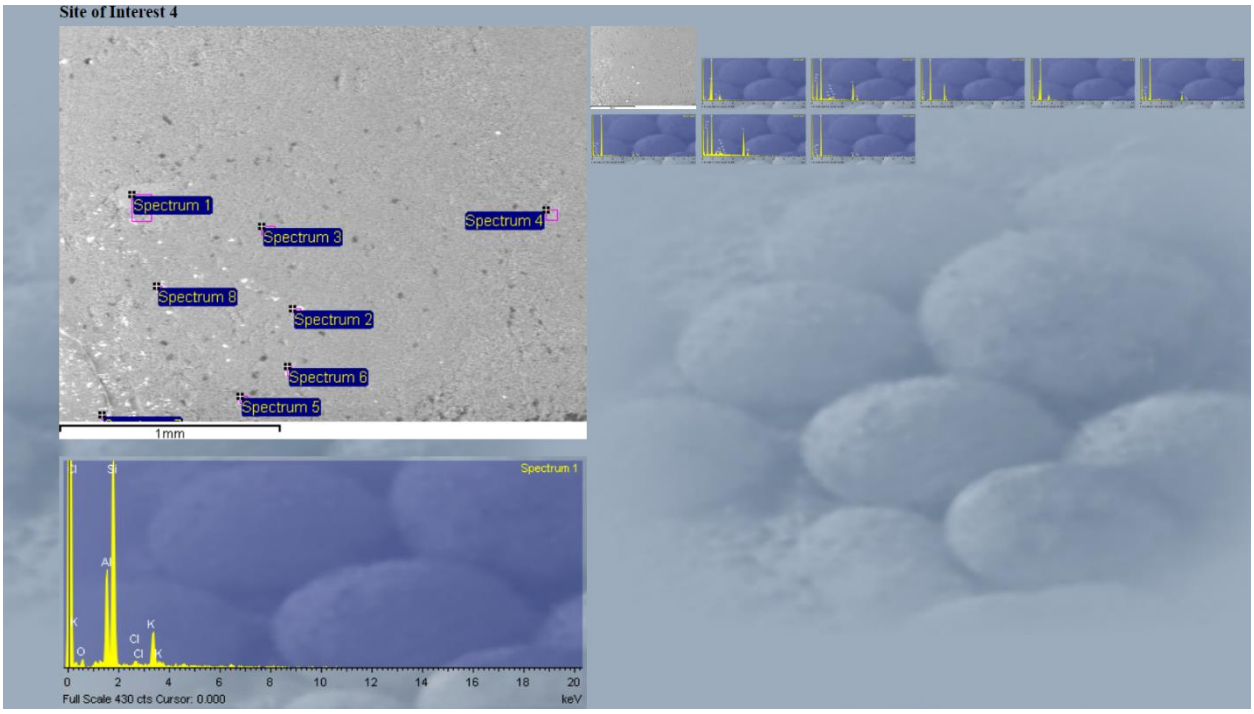

Site of interest 5

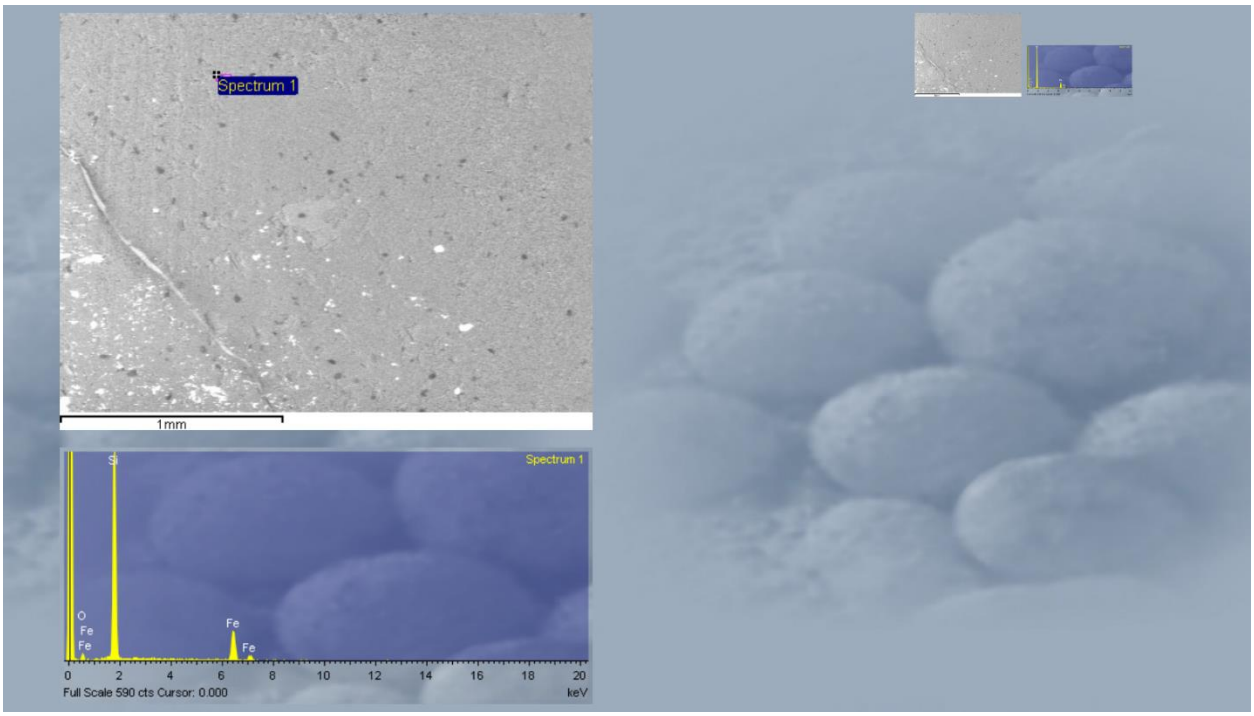

Notes

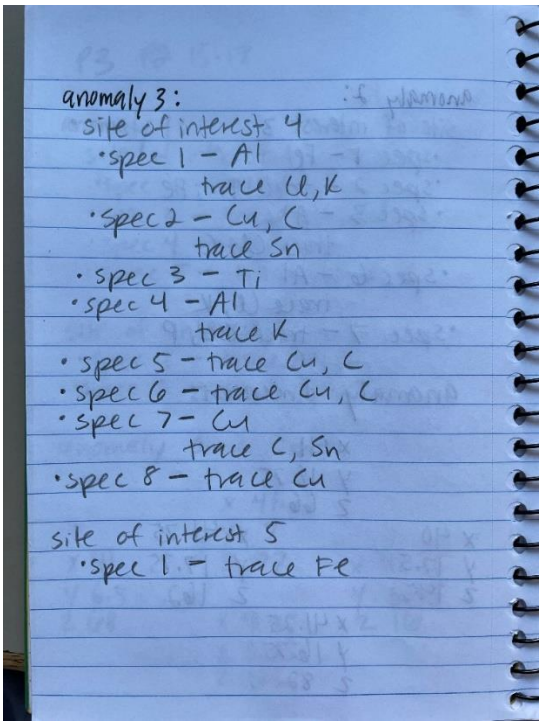

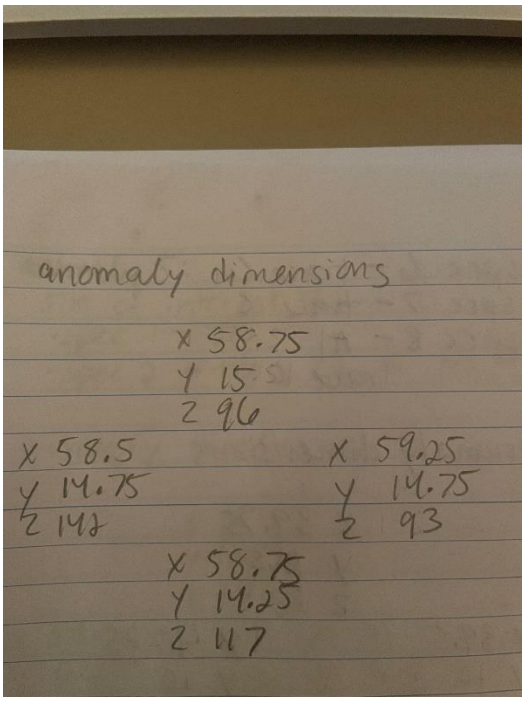

Anomaly 4:

Site of interest 6

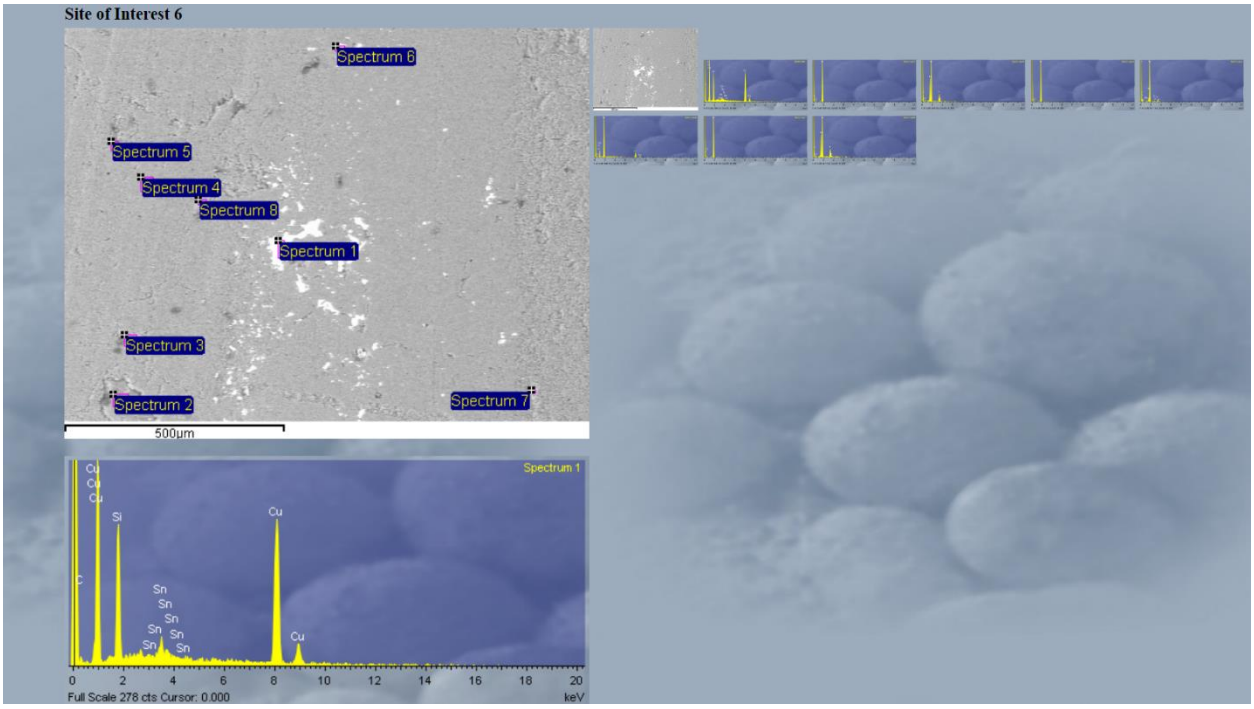

Notes

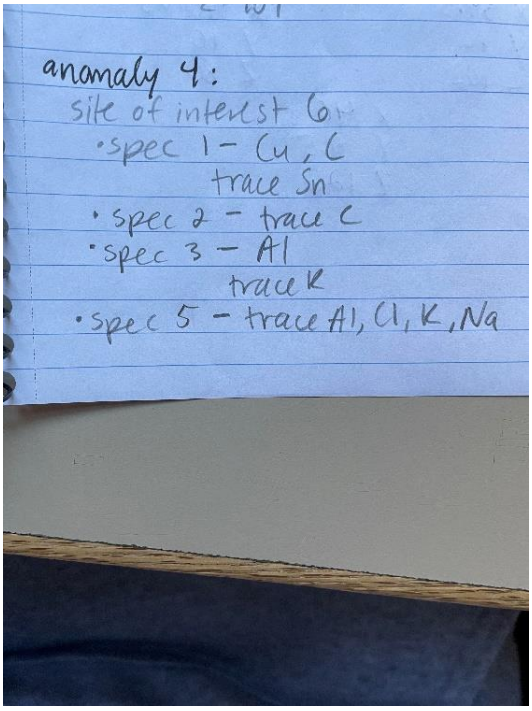
anomaly 4:
site of interest 6
•spec 1 – Cu, C
trace Sn
• spec 2 – trace C
•spec 3 – Al
trace K
•spec 5 – trace Al, Cl, K, Na

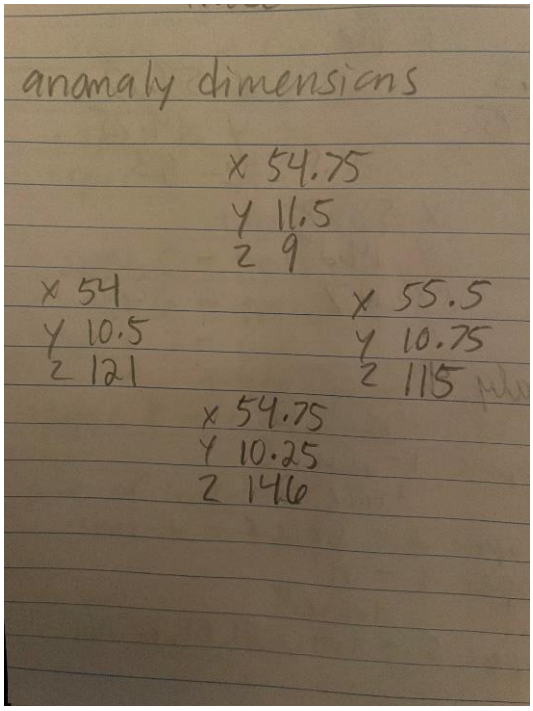
anomaly dimensions
x 54.75
y 11.5
z 9
x 54
y 10.5
z 121
x 55.5
y 10.75
z 115
x 54.75
y 10.25
z 146

Anomaly 5:

Site of interest 7

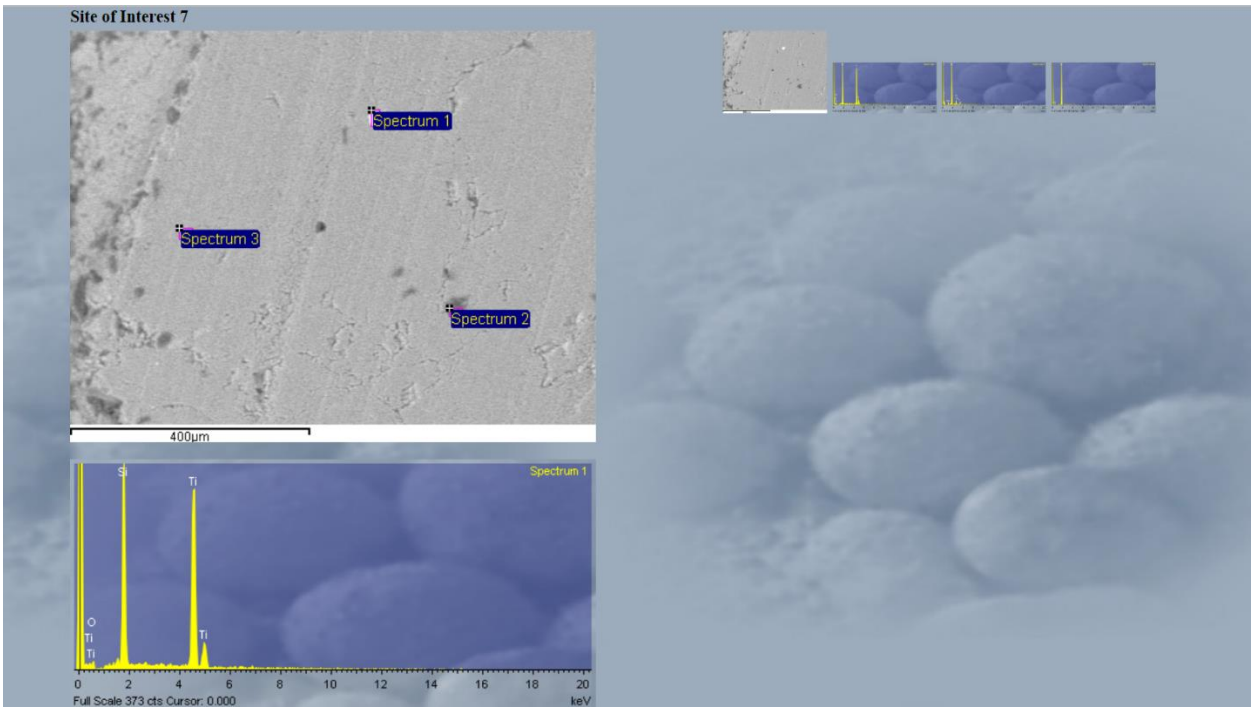

Notes

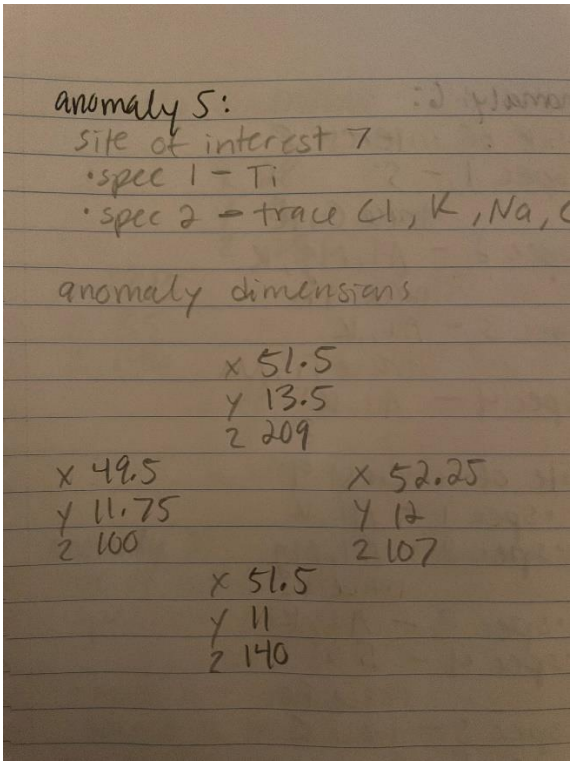
anomaly 5:
site of interest 7
•spec 1 - Ti
•spec 2 - trace Cl, K, Na,
anomaly dimensions
x 51.5
y 13.5
z 209
x 49.5
y 11.75
z 100
x 52.25
y 12
z 107
x 51.5
y 11
z 140

Anomaly 6:

Site of interest 8

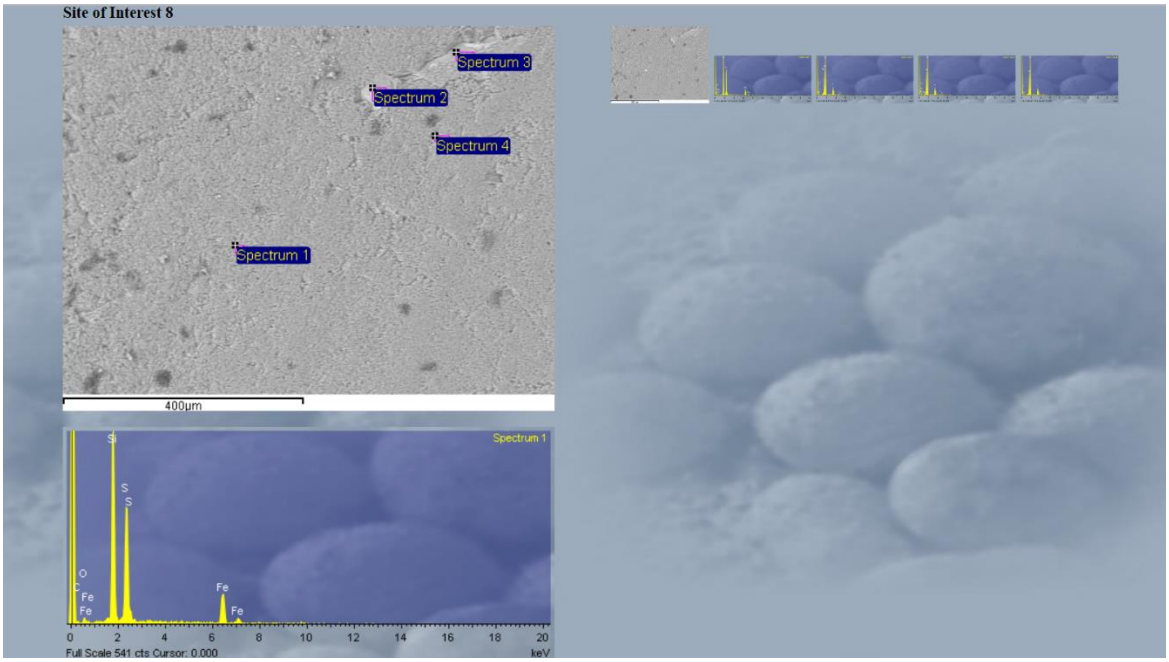

Site of interest 9

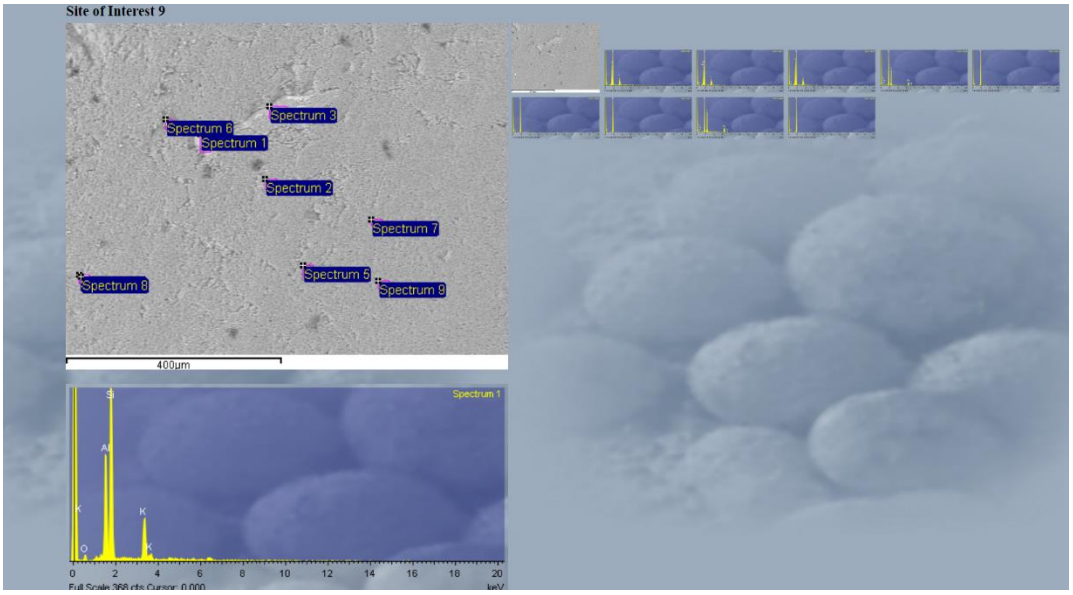

Notes

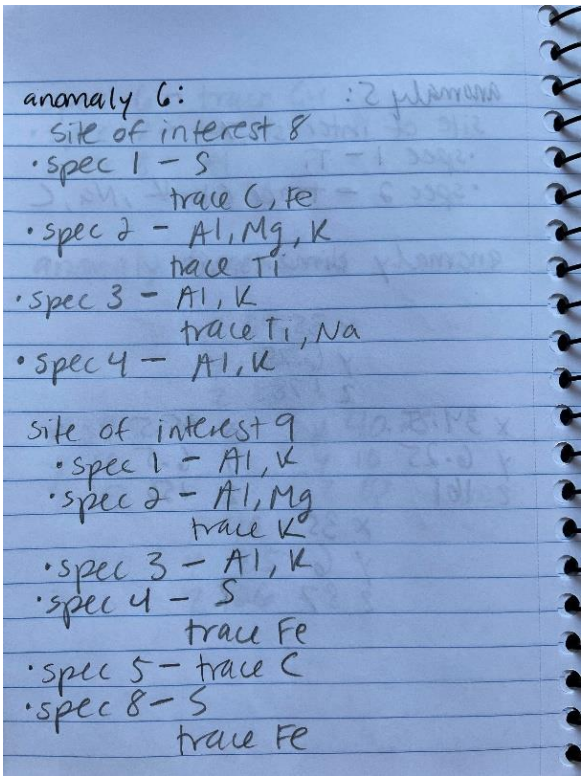
anomaly 6:
site of interest 8
• spec 1 – S
trace C, Fe
• spec 2 – Al, Mg, K
trace Ti
• spec 3 – Al, K
trace Ti, Na
• spec 4 – Al, K
site of interest 9
• spec 1 – Al, K
• spec 2 – Al, Mg
trace K
• spec 3 – Al, K
• spec 4 – S
trace Fe
• spec 5 – trace C
• spec 8 – S
trace Fe

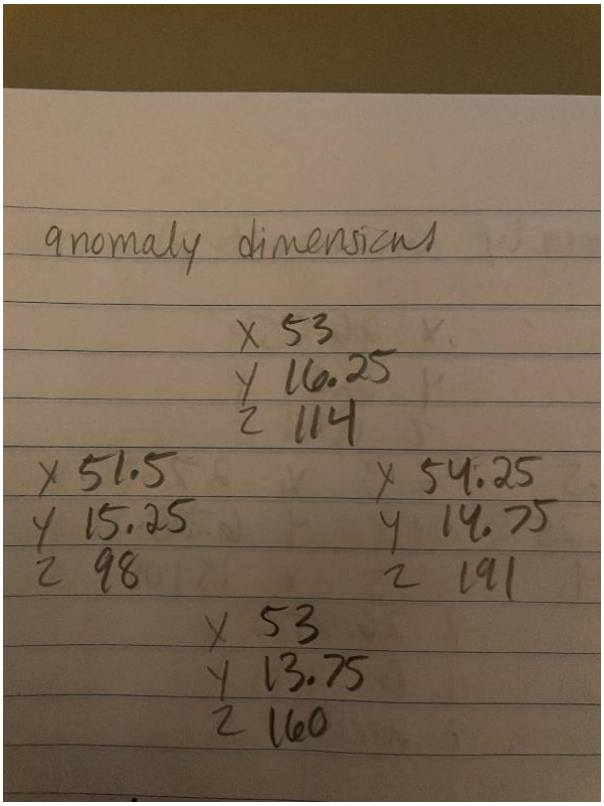
anomaly dimensions
X 53
Y 16.25
Z 114
X 51.5
Y 15.25
Z 98
X 54.25
Y 14.75
Z 191
X 53
Y 13.75
Z 160

Anomaly 7:

Site of interest 11

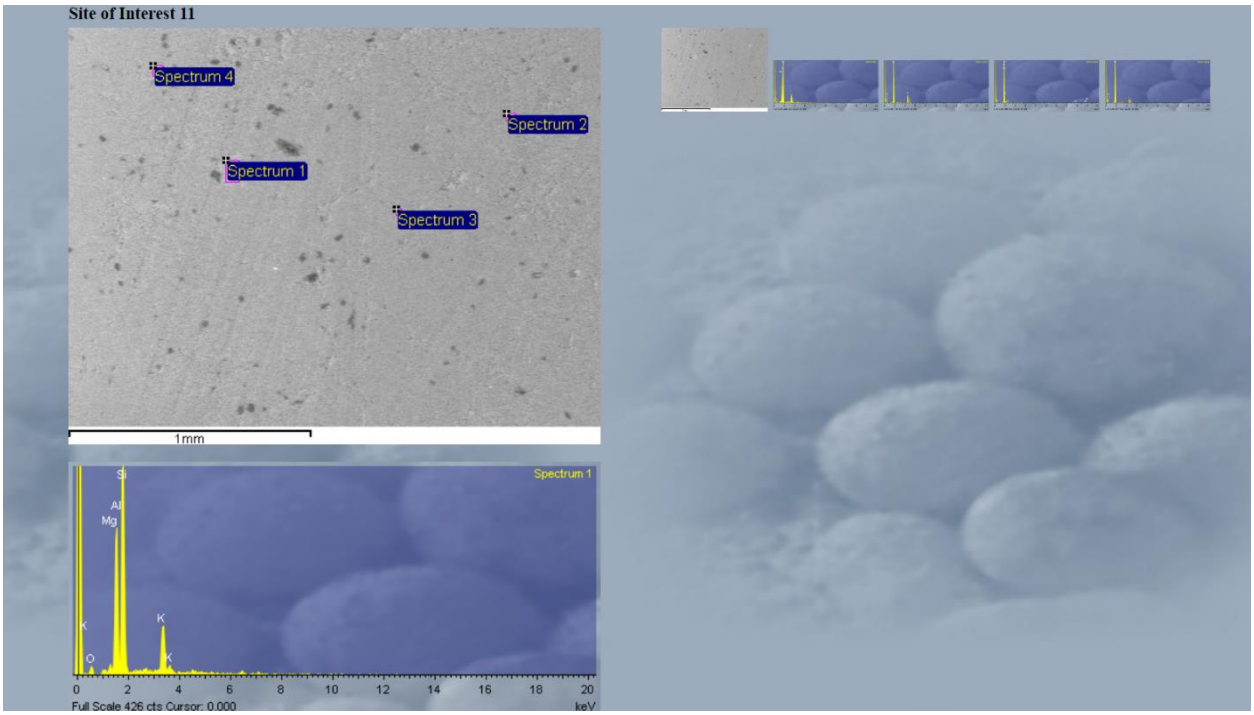

Notes

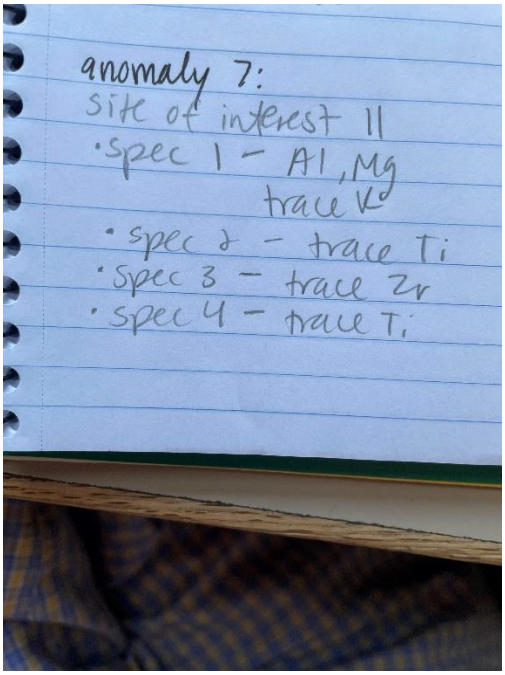
anomaly 7:
site of interest 11
·spec 1 – Al, Mg
trace K
·spec 2 – trace Ti
·spec 3 – trace Zr
·spec 4 – trace Ti

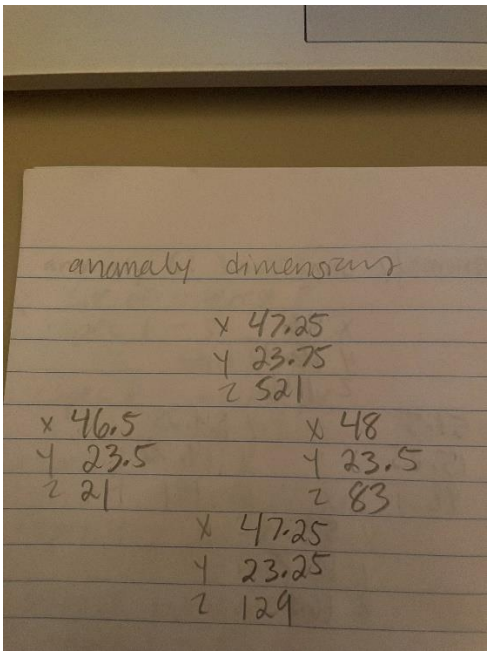
anomaly dimensions
x 47.25
y 23.75
z 521
x 46.5
y 23.5
z 21
x 48
y 23.5
z 83
x 47.25
y 23.25
z 129

Anomaly 8:

Site of interest 12

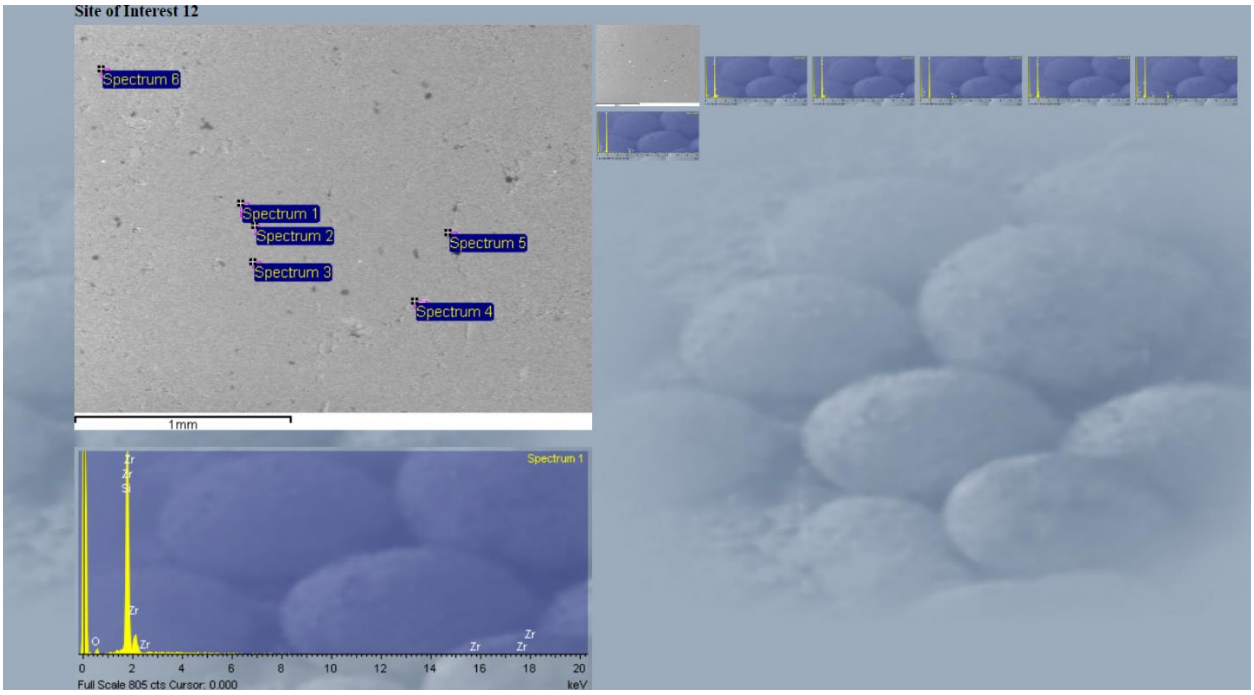

Notes

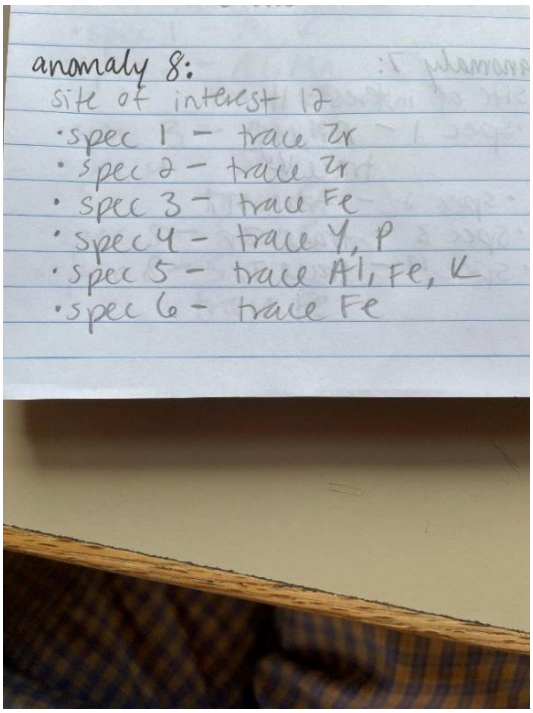
anomaly 8:
site of interest 12
·spec 1 – trace Zr
·spec 2 – trace Zr
·spec 3 – trace Fe
·spec 4 – trace Y, P
·spec 5 – trace Al, Fe, K
·spec 6 – trace Fe

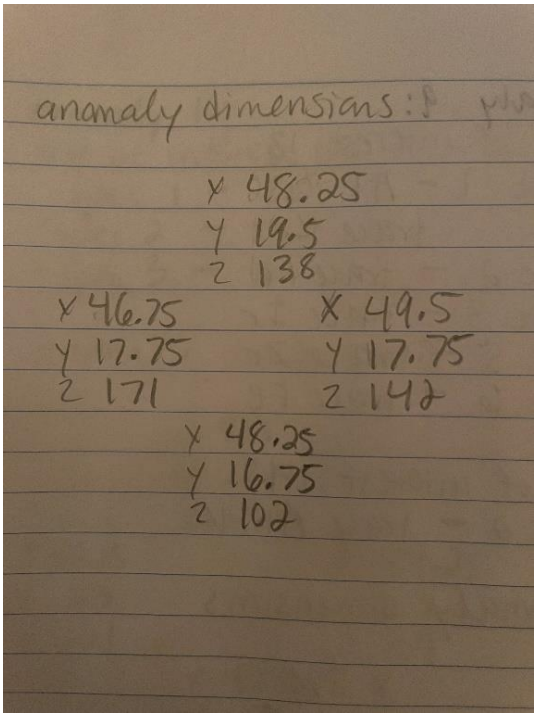
anomaly dimensions:
X 48.25
Y 19.5
Z 138
X 46.75
Y 17.75
Z 171
X 49.5
Y 17.75
Z 142
X 48.25
Y 16.75
Z 102

Anomaly 9:

Site of interest 13

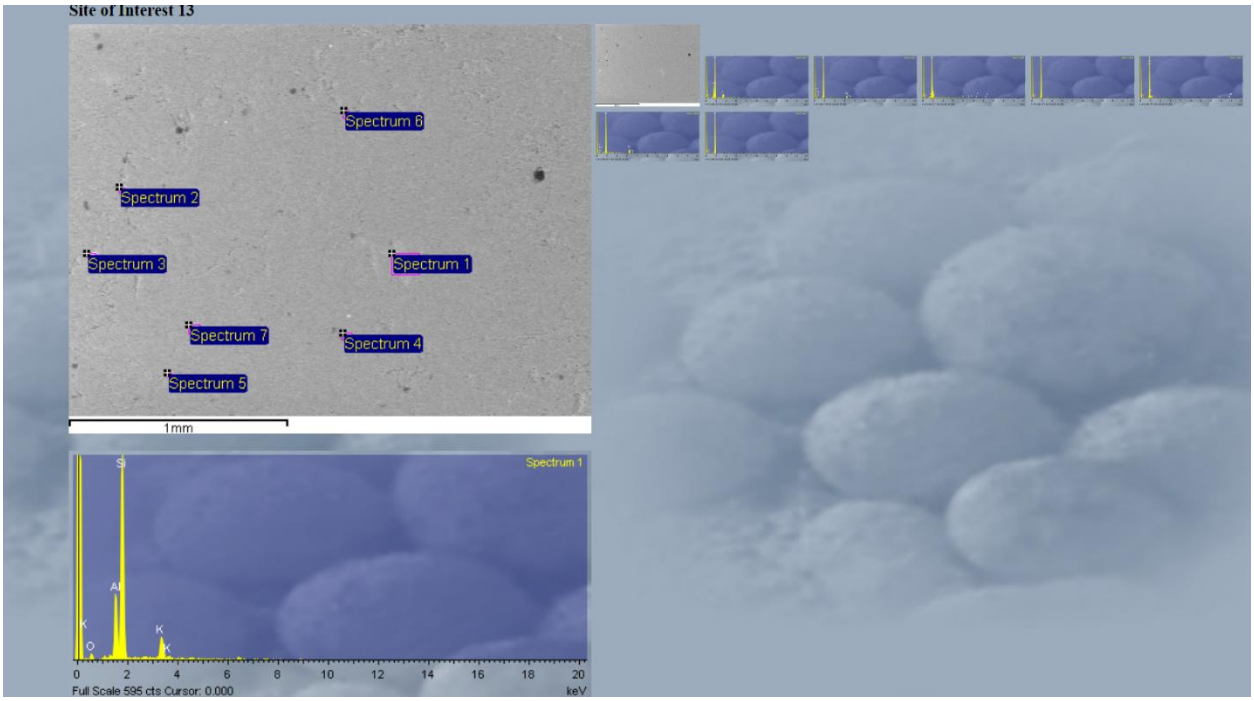

Site of interest 14

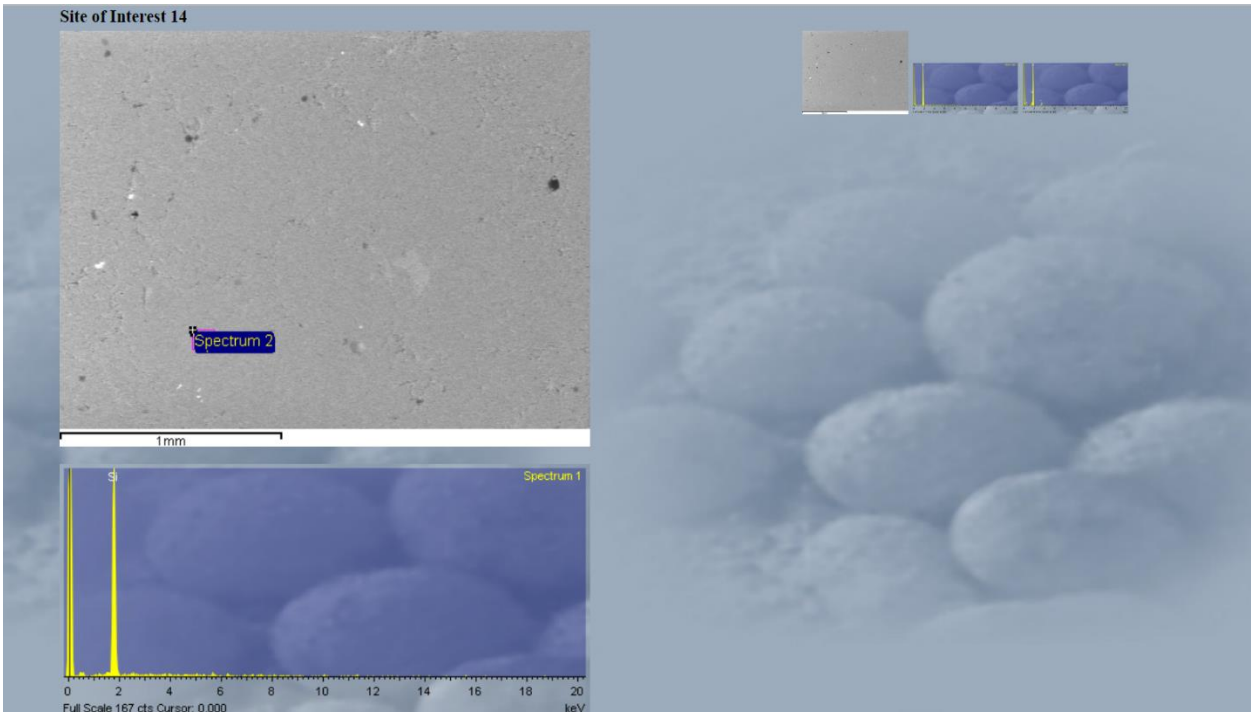

Notes

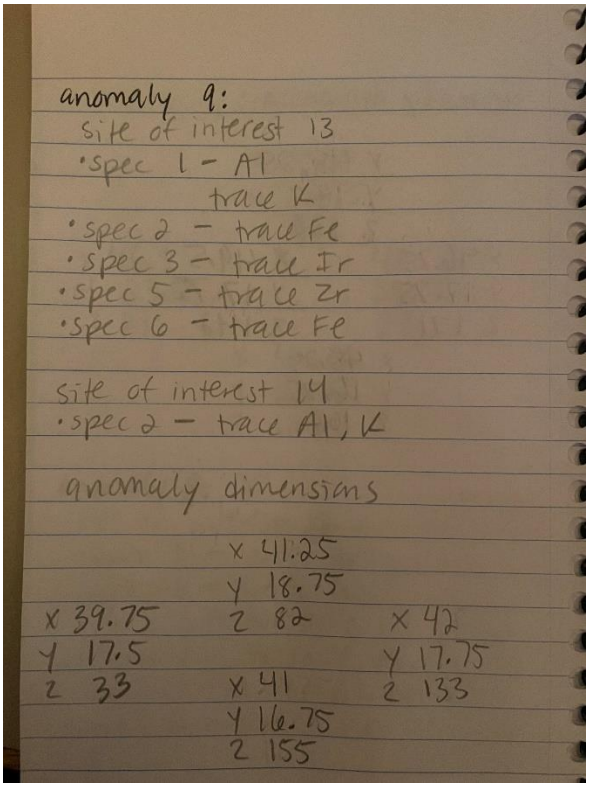
anomaly 9:
site of interest 13
•spec 1 - Al
trace K
•spec 2 - trace Fe
•spec 3 - trace Ir
•spec 5 - trace Zr
•spec 6 - trace Fe
site of interest 14
•spec 2 - trace Al, K
anomaly dimensions
x 41.25
y 18.75
z 82
x 39.75
y 17.5
z 33
x 42
y 17.75
z 133
x 41
y 16.75
z 155

Anomaly 10:

Site of interest 15

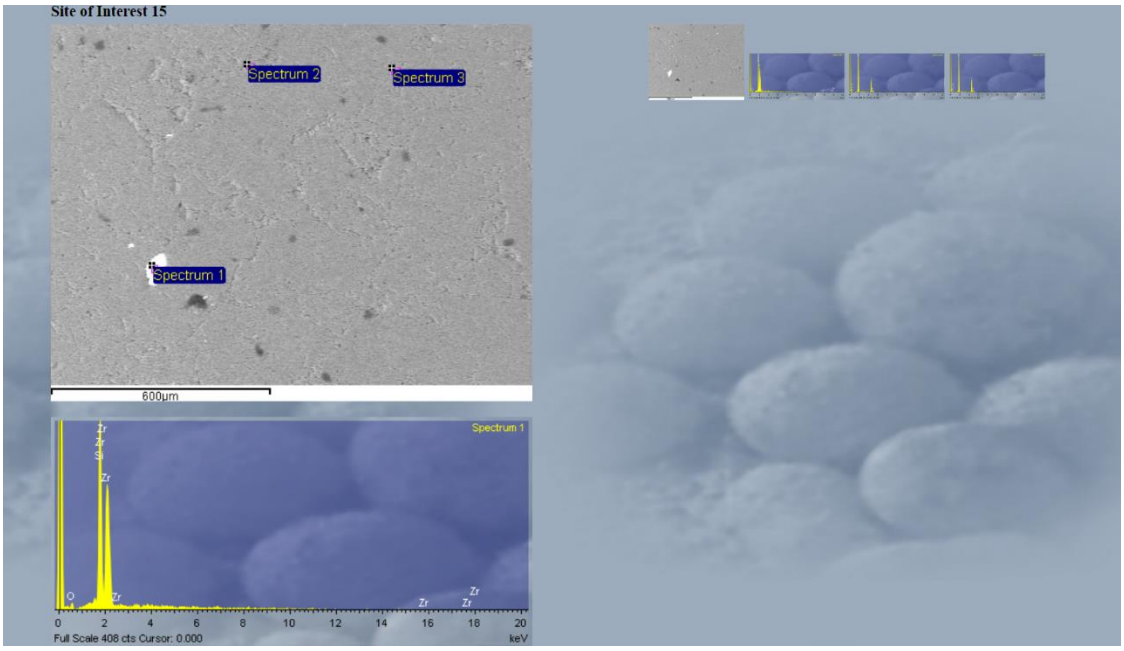

Notes

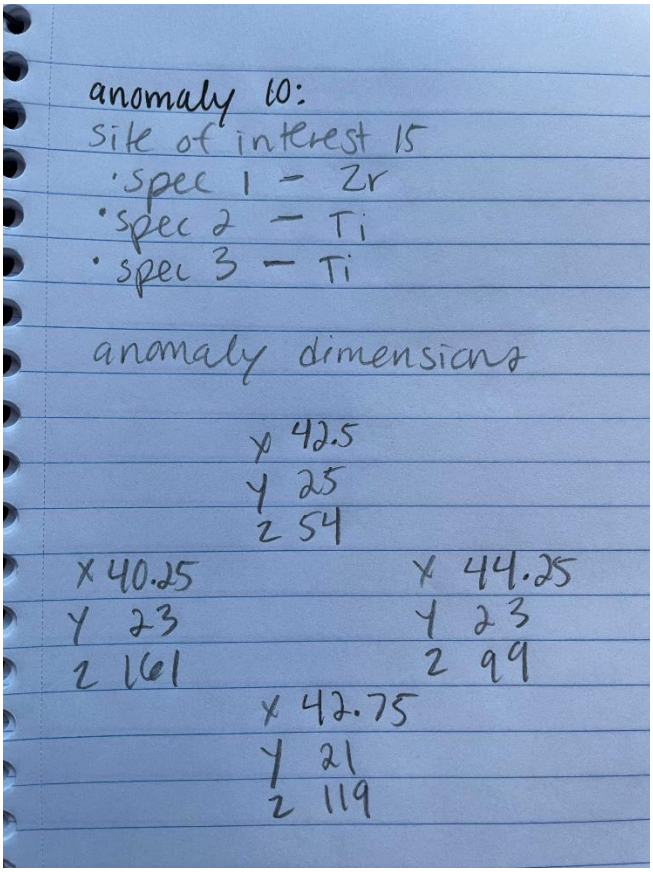
anomaly 10:
site of interest 15
·spec 1 – Zr
·spec 2 – Ti
·spec 3 – Ti
anomaly dimensions
x 42.5
y 25
z 54
x 40.25
y 23
z 161
x 44.25
y 23
z 99
x 42.75
y 21
z 119

Anomaly 11:

Site of interest 16

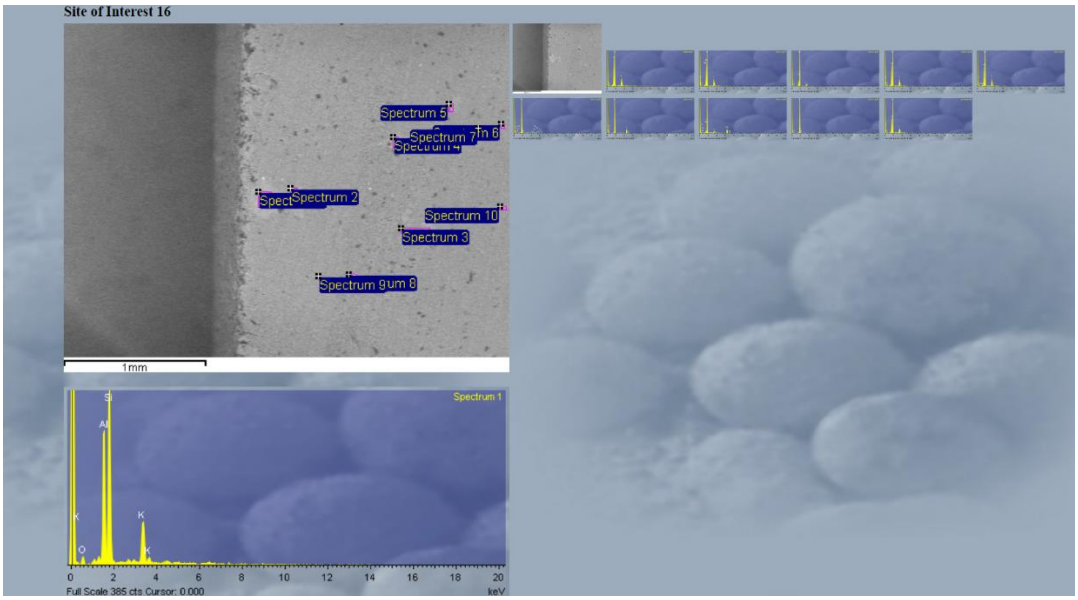

Notes

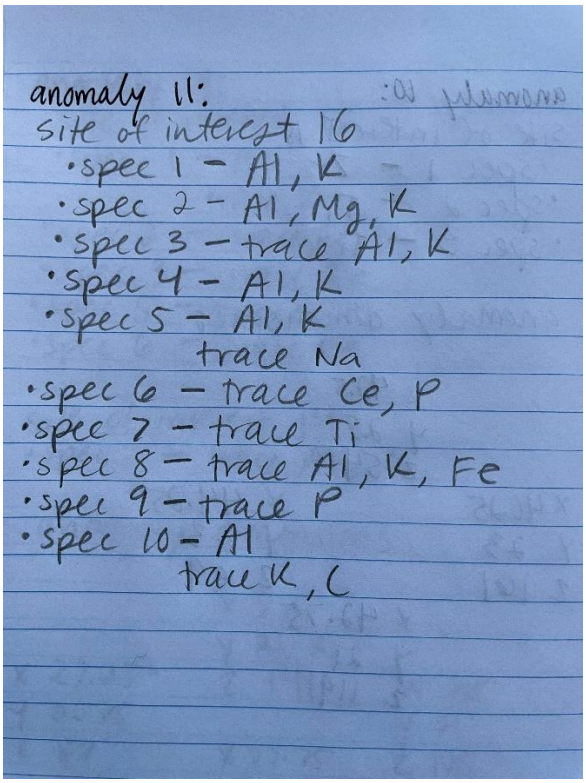

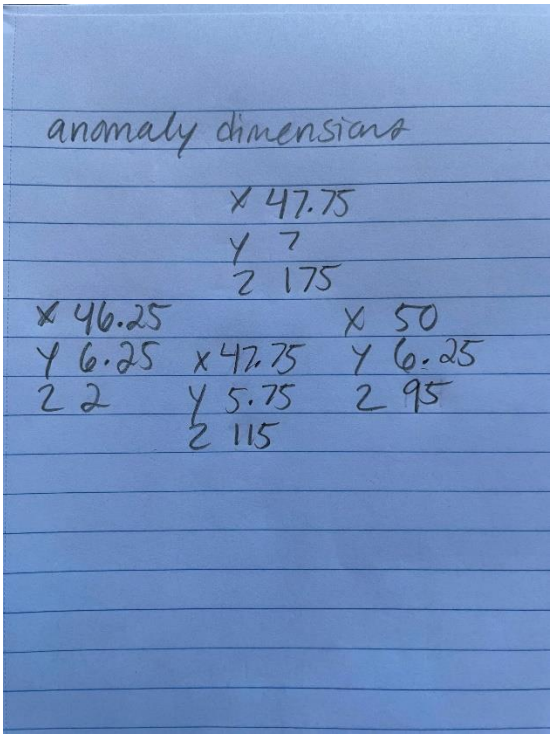

Anomaly 12:

Site of interest 20

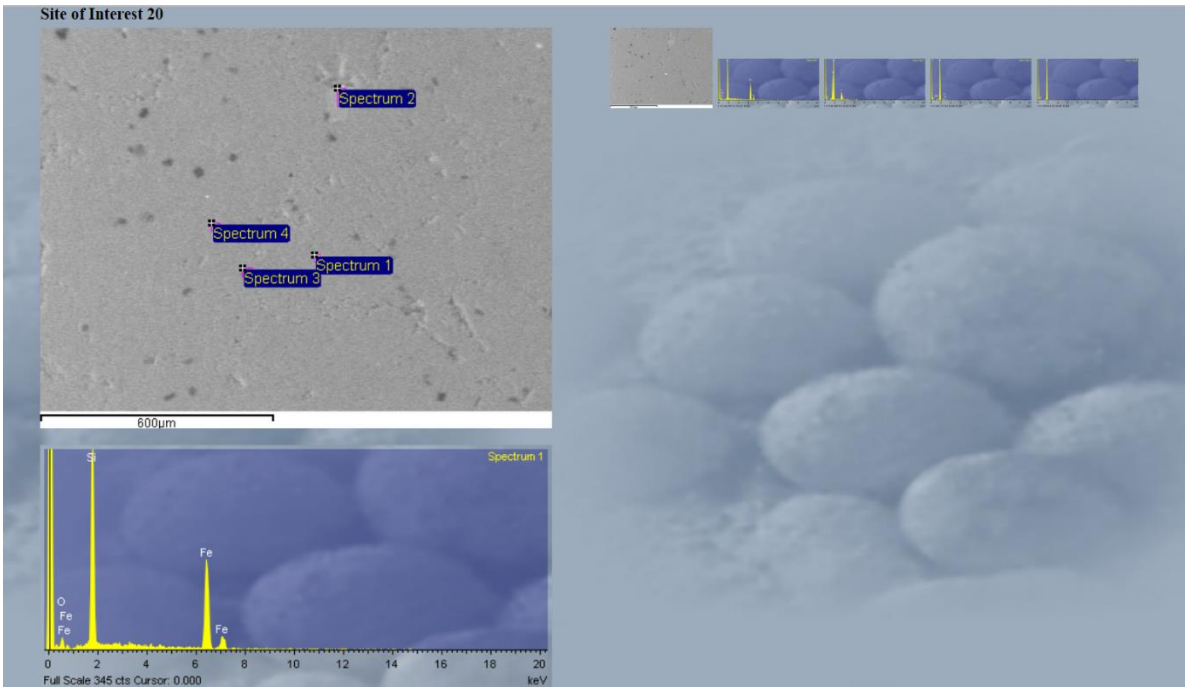

Notes

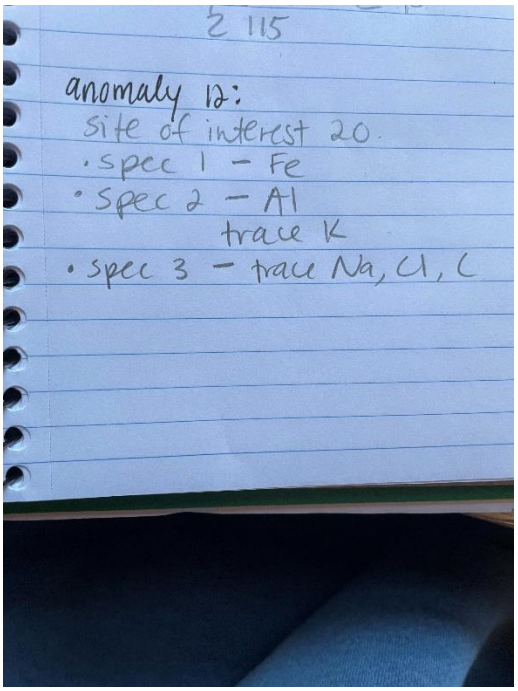

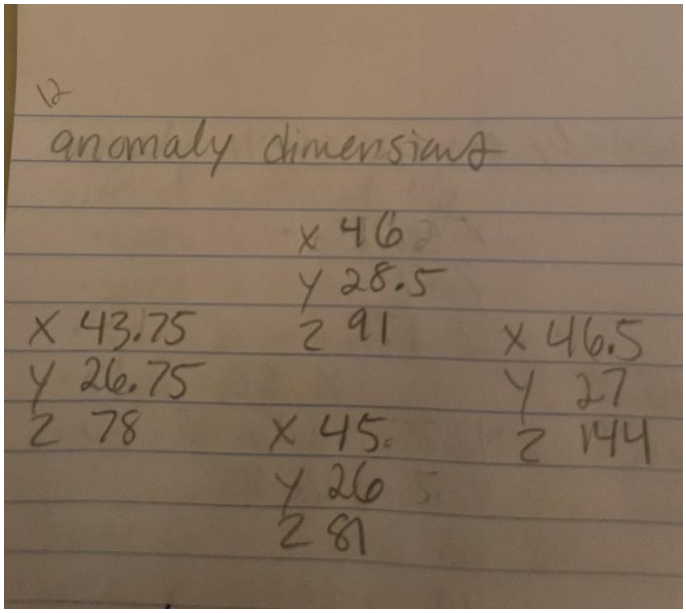

Anomaly 13:

Site of interest 21

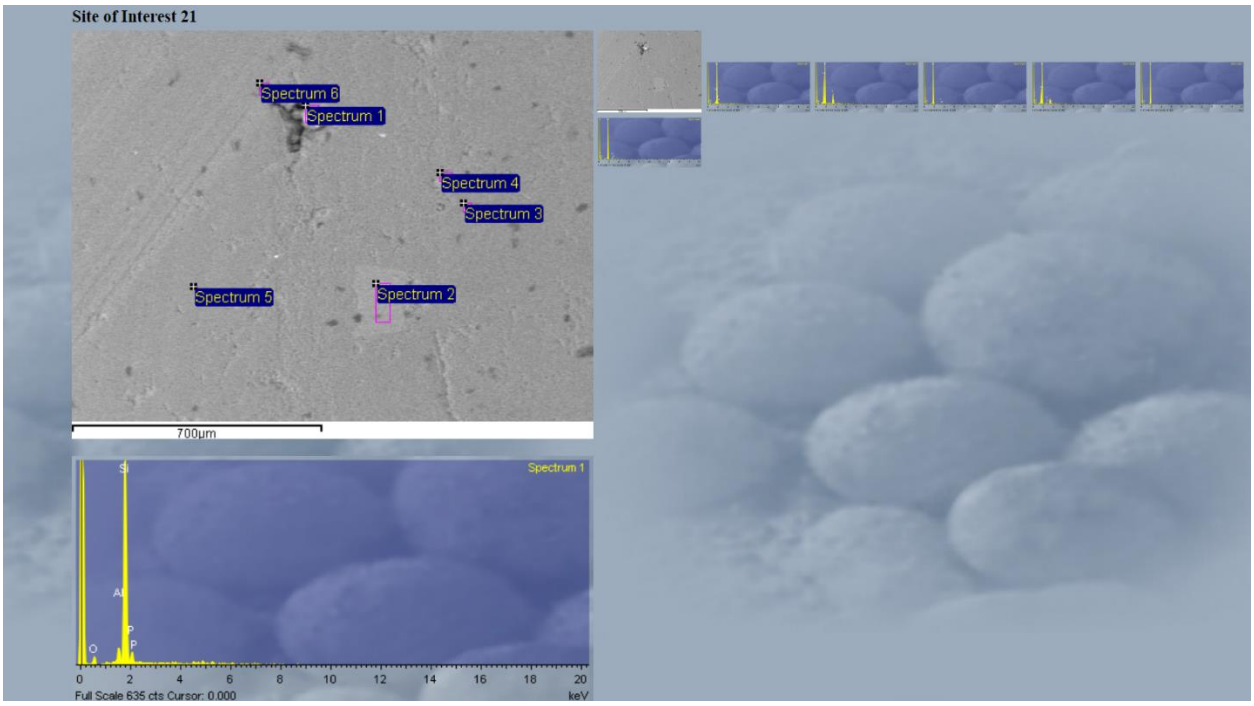

Notes

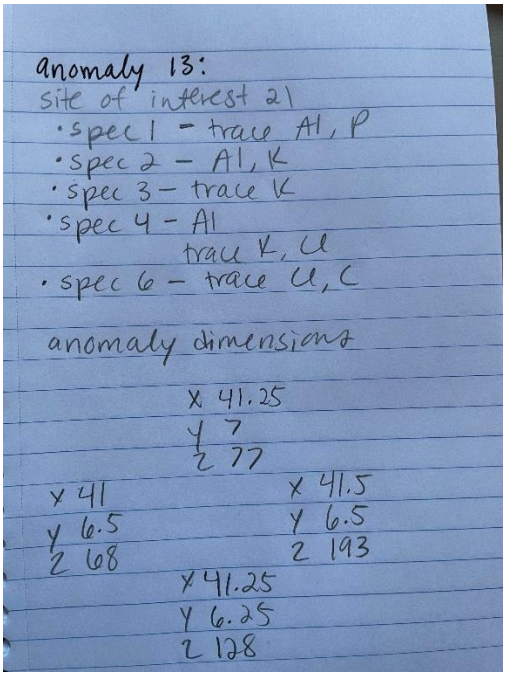
anomaly 13:
site of interest 21
• spec 1 - trace Al, P
• spec 2 - Al, K
• spec 3 - trace K
• spec 4 - Al
trace K, Cl
• spec 6 - trace Cl, C
anomaly dimensions
x 41.25
y 7
2 77
x 41
y 6.5
2 68
x 41.5
y 6.5
2 193
x 41.25
y 6.25
2 128

Anomaly 14:

Site of interest 22

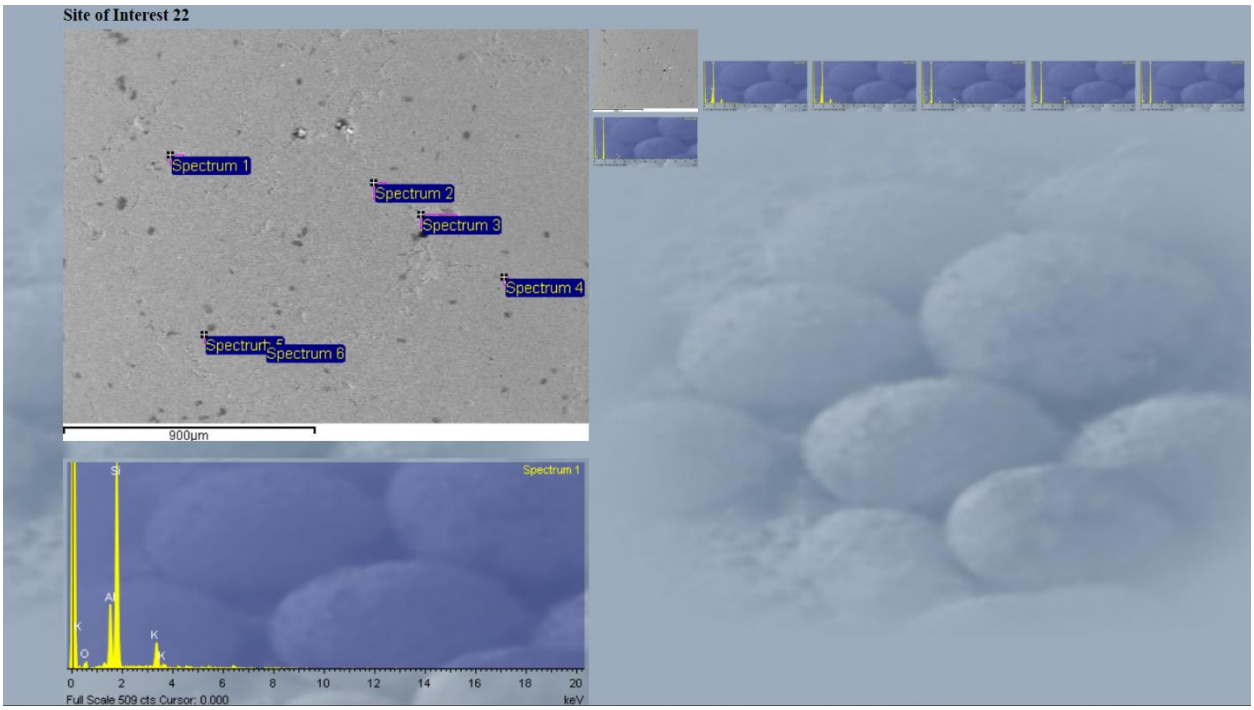

Notes

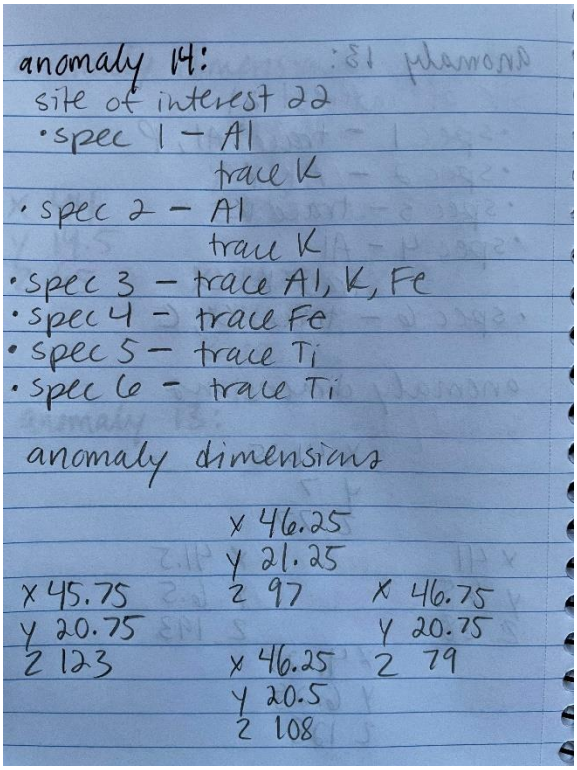
anomaly 14:
site of interest 22
• spec 1 – Al
trace K
• spec 2 – Al
trace K
• spec 3 – trace Al, K, Fe
• spec 4 – trace Fe
• spec 5 – trace Ti
• spec 6 – trace Ti
anomaly dimensions
x 46.25
y 21.25
z 97
x 45.75
y 20.75
z 123
x 46.75
y 20.75
z 79
x 46.25
y 20.5
z 108

Bottom half P3 (P3Part2)

Anomaly 1:

Site of interest 1

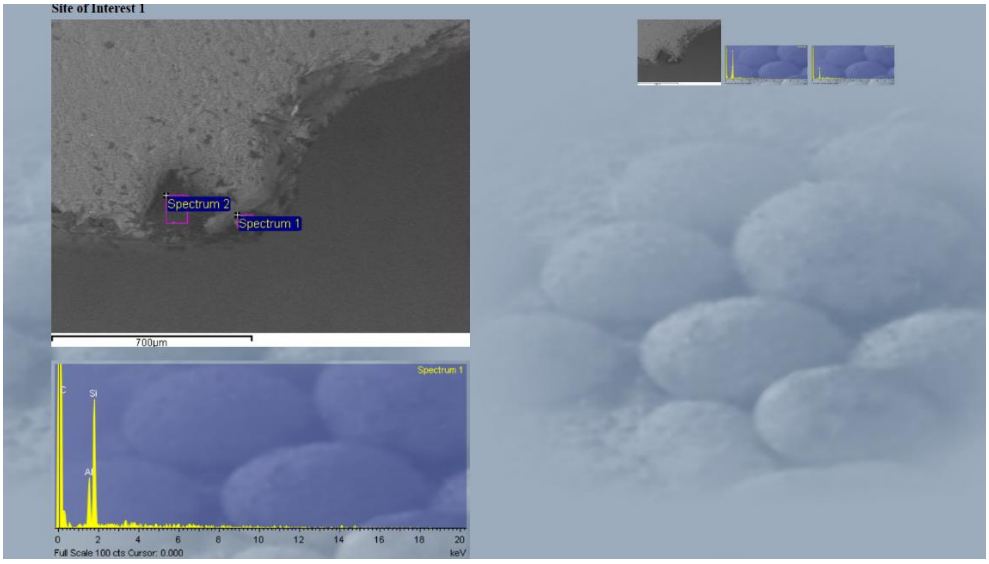

Site of interest 2

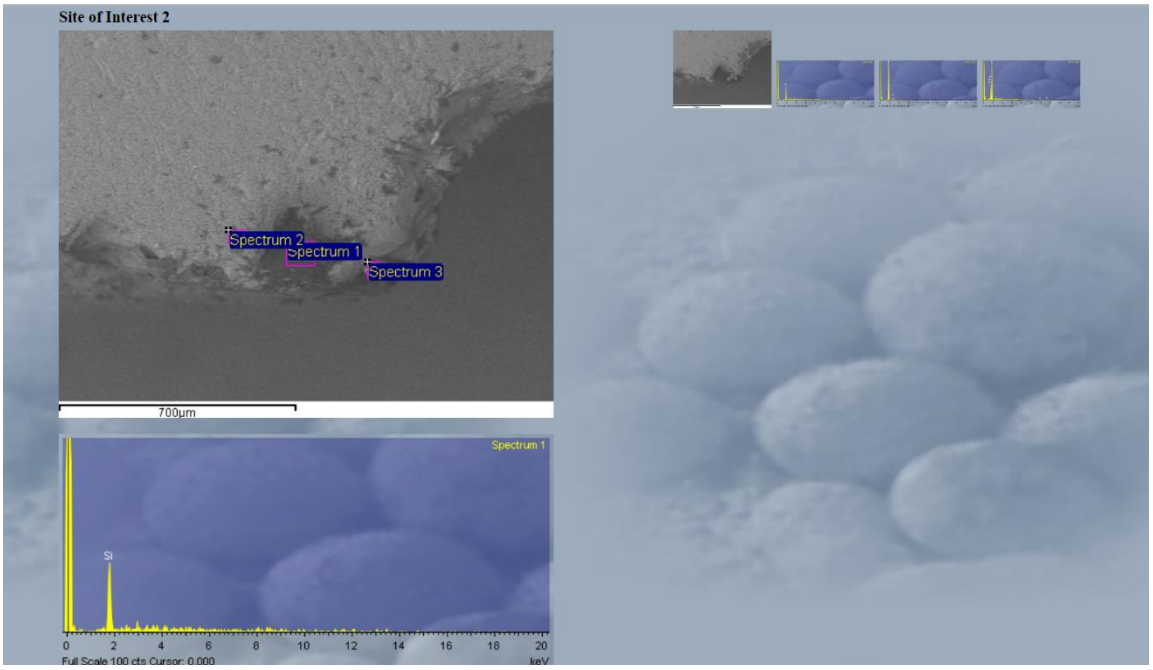

Notes

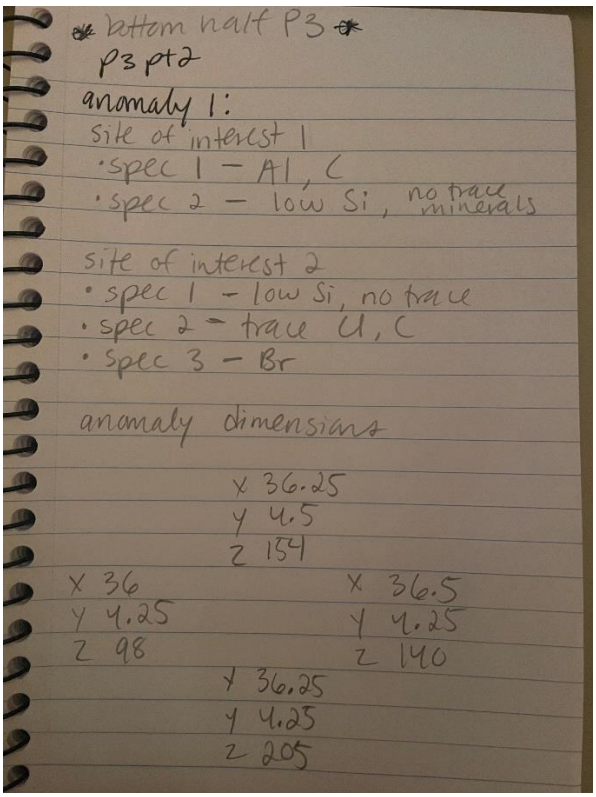
bottom half P3
P3 pt2
anomaly 1:
site of interest 1
• spec 1 – Al, C
• spec 2 – low Si, no trace minerals
site of interest 2
• spec 1 – low Si, no trace
• spec 2 – trace Cl, C
• spec 3 – Br
anomaly dimensions
x 36.25
y 4.5
z 154
x 36
y 4.25
z 98
x 36.5
y 4.25
z 140
x 36.25
y 4.25
z 205

Anomaly 2:

Site of interest 4

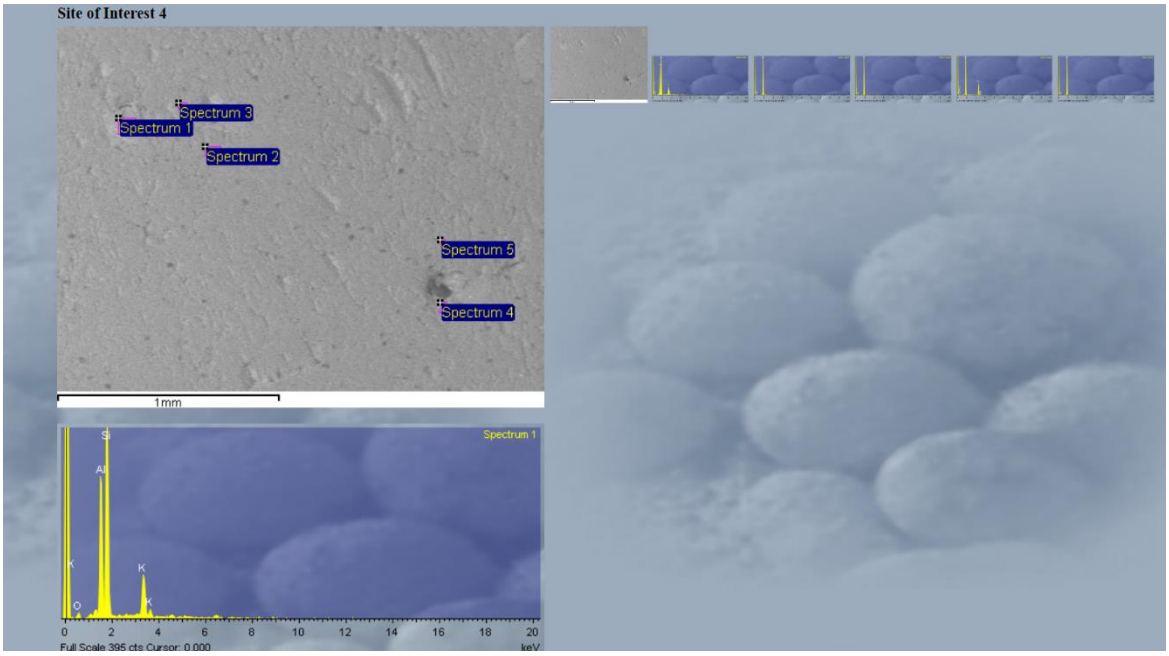

Notes

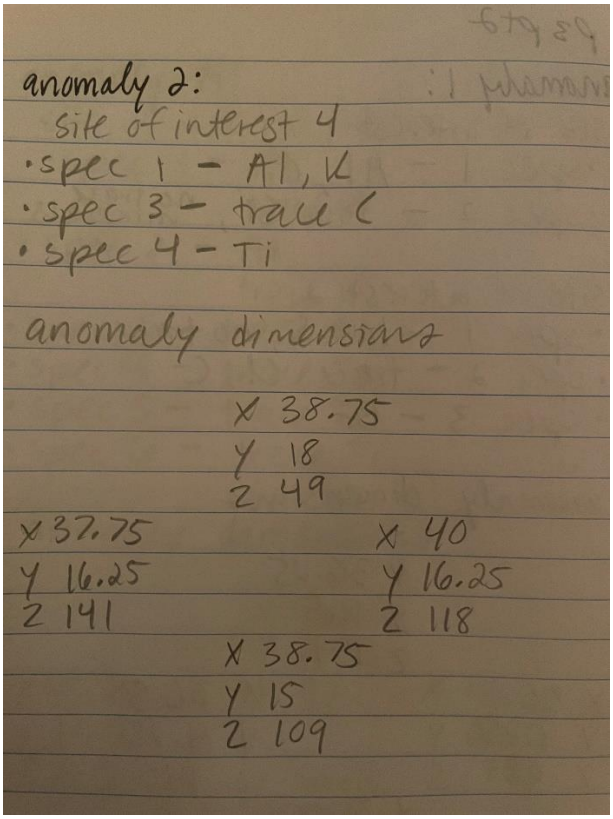
anomaly 2:
site of interest 4
• spec 1 - Al, K
• spec 3 - trace C
• spec 4 - Ti
anomaly dimensions
X 38.75
Y 18
Z 49
X 37.75
Y 16.25
Z 141
X 40
Y 16.25
Z 118
X 38.75
Y 15
Z 109

Anomaly 3:

Site of interest 7

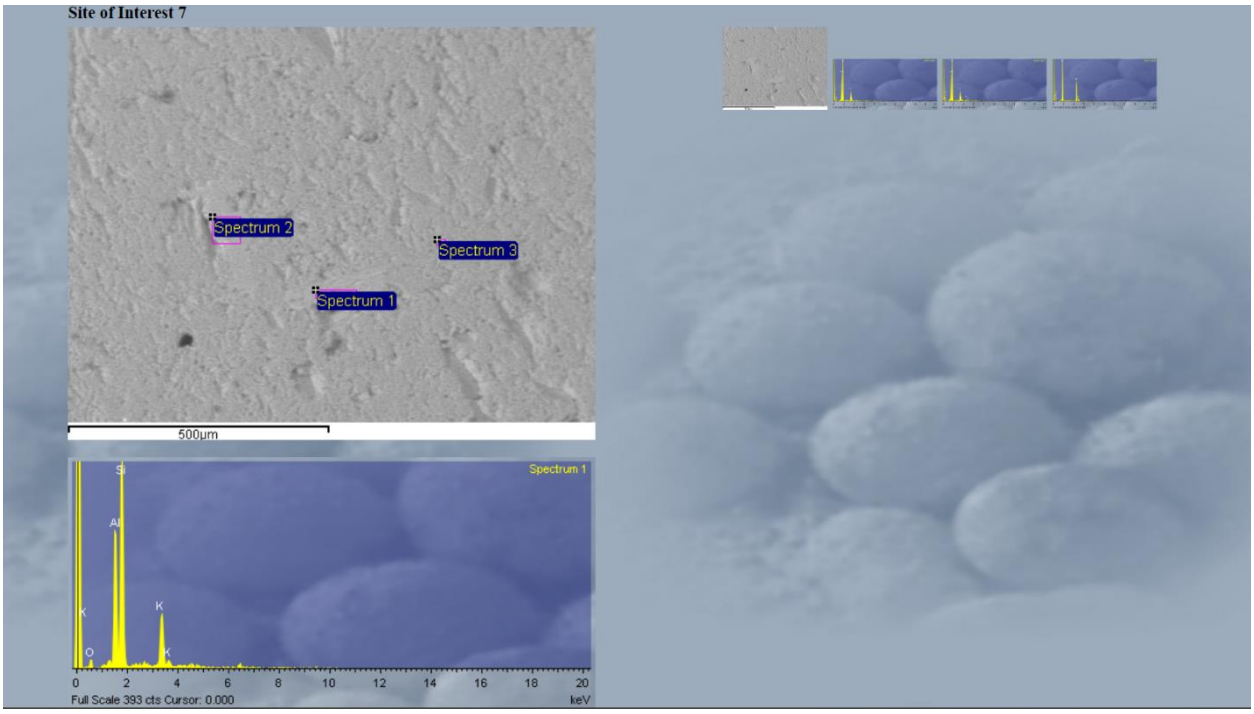

Notes

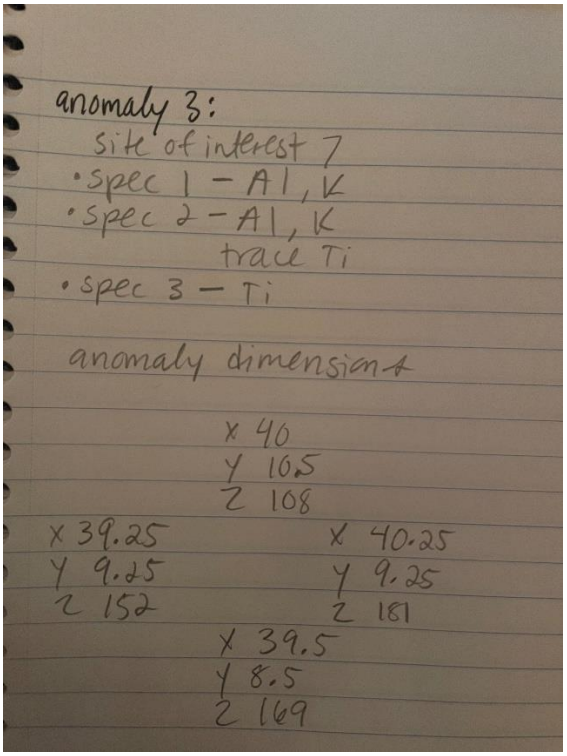
anomaly 3:
site of interest 7
• spec 1 – Al, K
• spec 2 – Al, K
trace Ti
• spec 3 – Ti
anomaly dimensions
x 40
y 10.5
z 108
x 39.25
y 9.25
z 152
x 40.25
y 9.25
z 181
x 39.5
y 8.5
z 169

Anomaly 4:

Site of interest 8

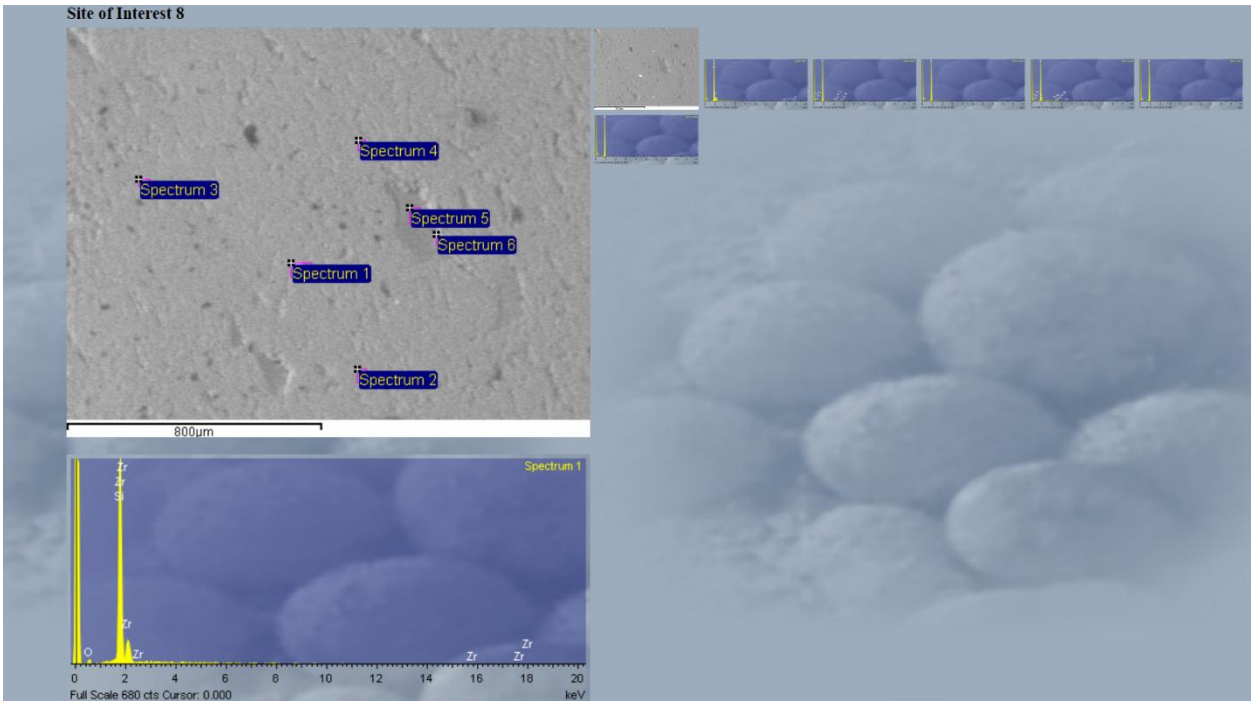

Notes

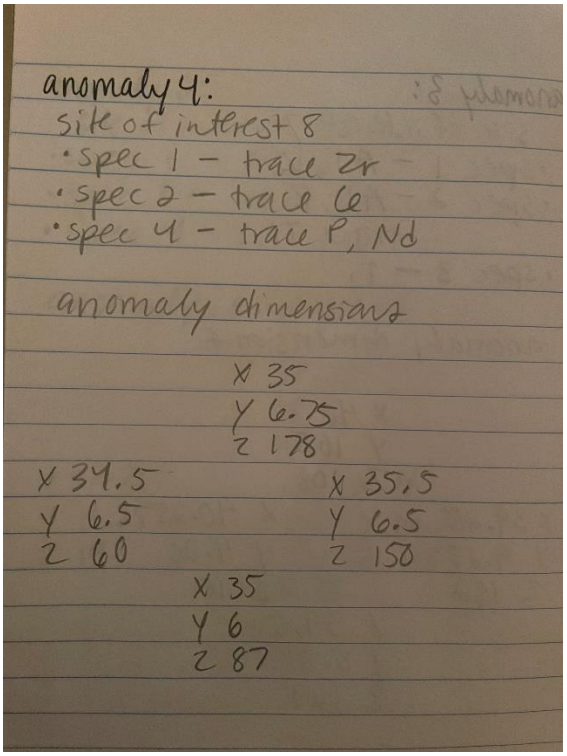
anomaly 4:
site of interest 8
• spec 1 – trace Zr
• spec 2 – trace Ce
• spec 4 – trace P, Nd
anomaly dimensions
X 35
Y 6.75
Z 178
X 34.5
Y 6.5
Z 60
X 35.5
Y 6.5
Z 150
X 35
Y 6
Z 87

Anomaly 5:

Site of interest 9

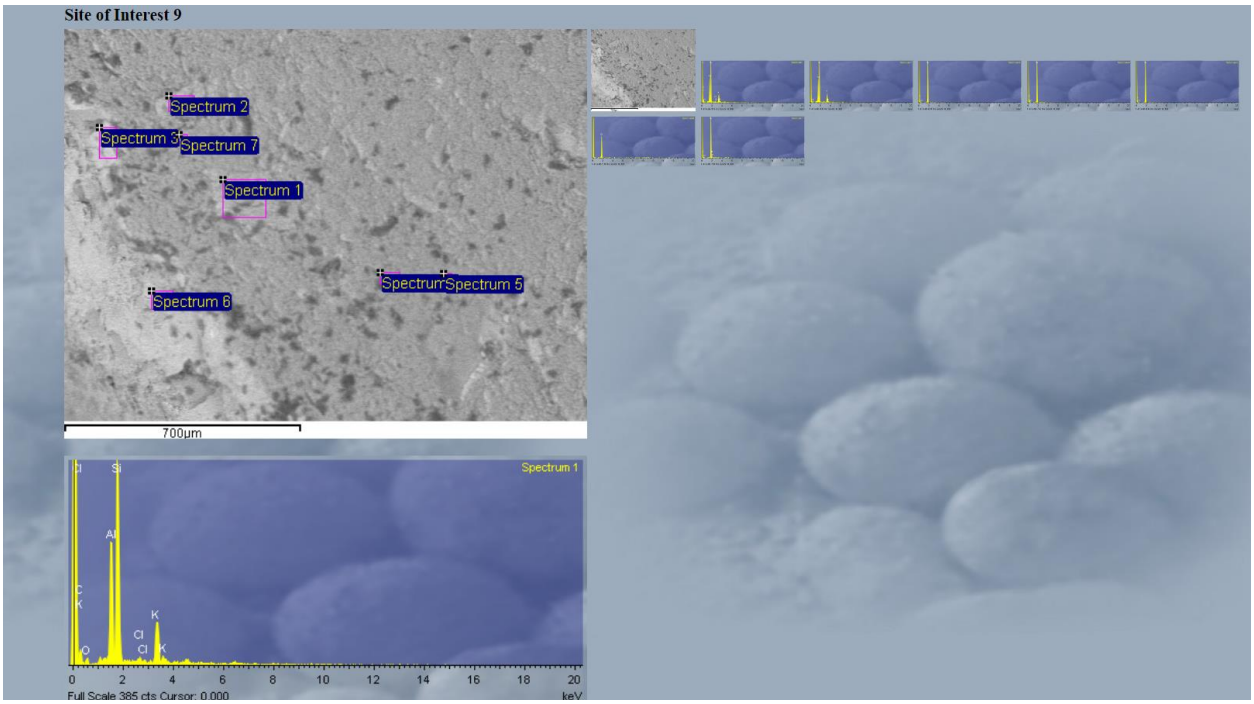

Notes

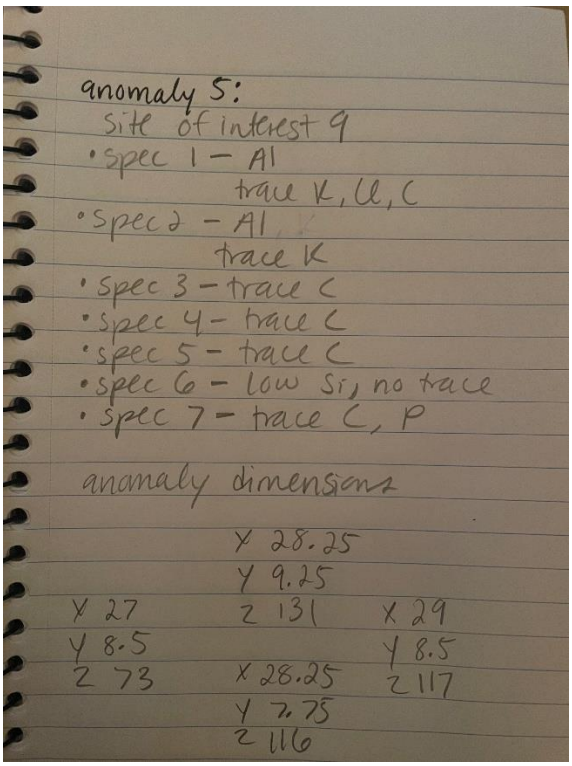
anomaly 5:
site of interest 9
• spec 1 – Al
trace K, Cl, C
• spec 2 – Al
trace K
• spec 3 – trace C
• spec 4 – trace C
• spec 5 – trace C
• spec 6 – low Si, no trace
• spec 7 – trace C, P
anomaly dimensions
X 28.25
Y 9.25
Z 131
X 27
Y 8.5
Z 73
X 29
Y 8.5
Z 117
X 28.25
Y 7.75
Z 116

Anomaly 6:

Site of interest 10

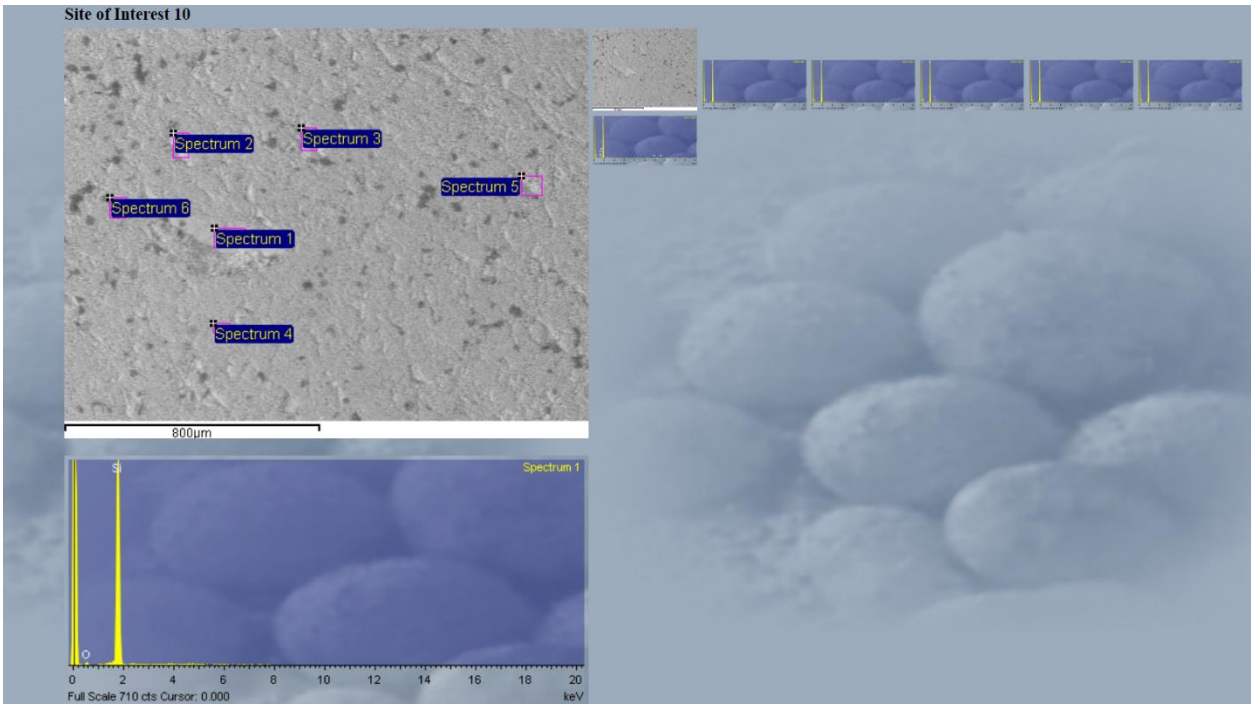

Notes

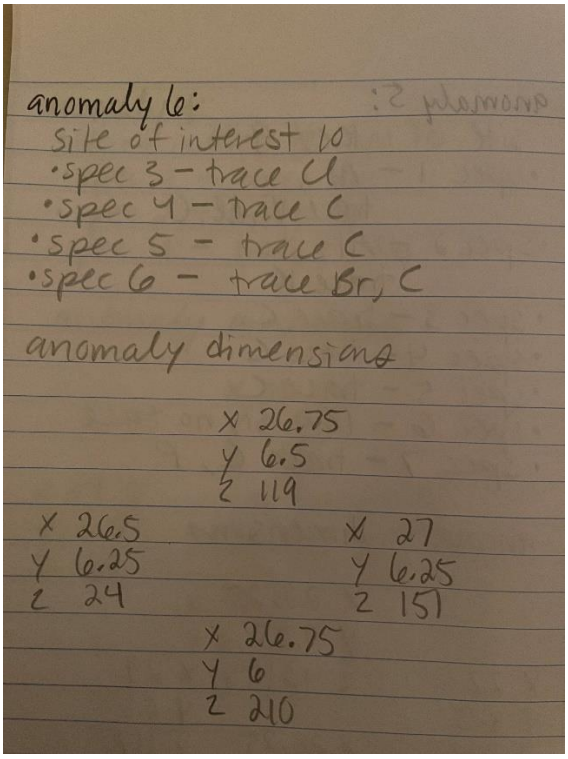
anomaly 6:
site of interest 10
•spec 3 - trace Cl
•spec 4 - trace C
•spec 5 - trace C
•spec 6 - trace Br, C
anomaly dimensions
X 26.75
Y 6.5
Z 119
X 26.5
Y 6.25
Z 24
X 27
Y 6.25
Z 151
X 26.75
Y 6
Z 210

Anomaly 7:

Site of interest 11

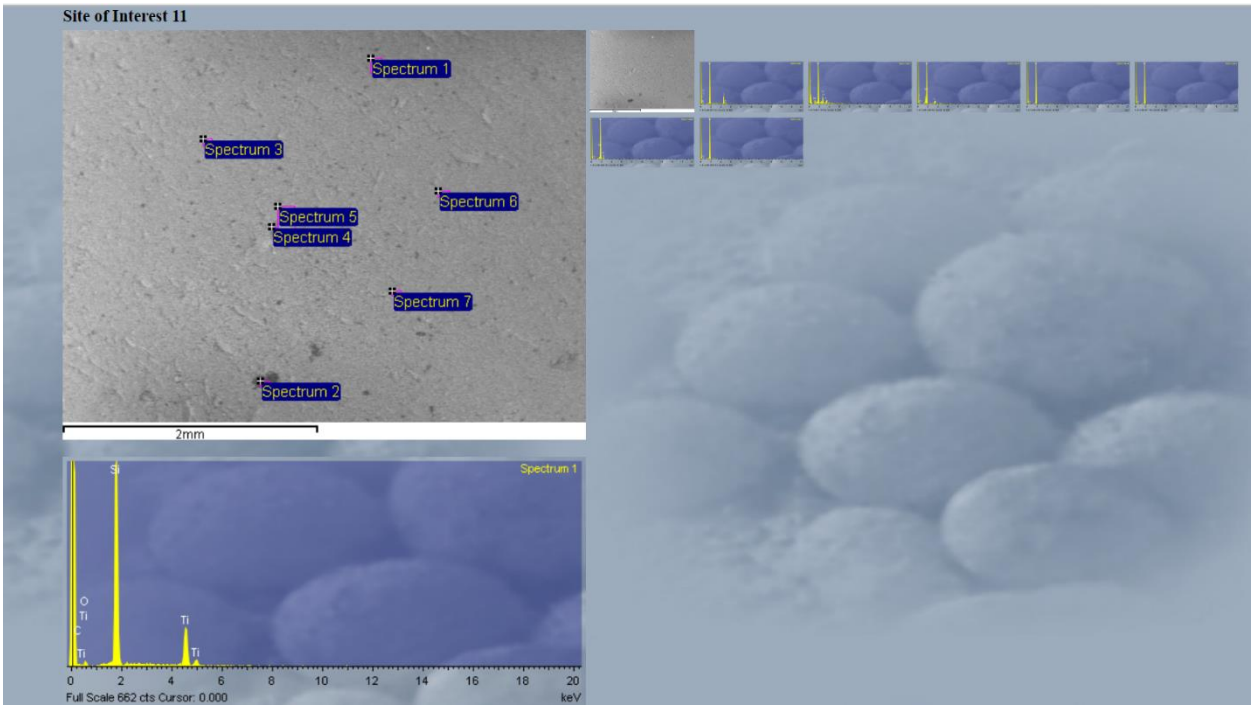

Site of interest 12

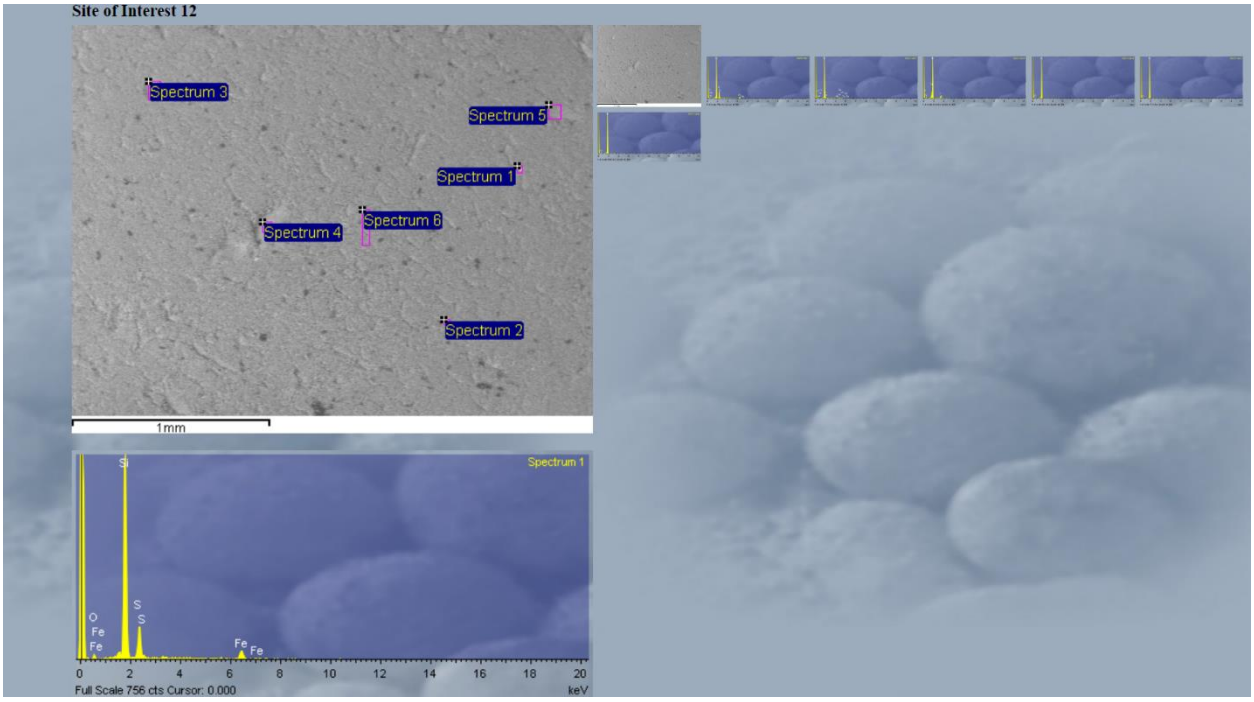

Notes

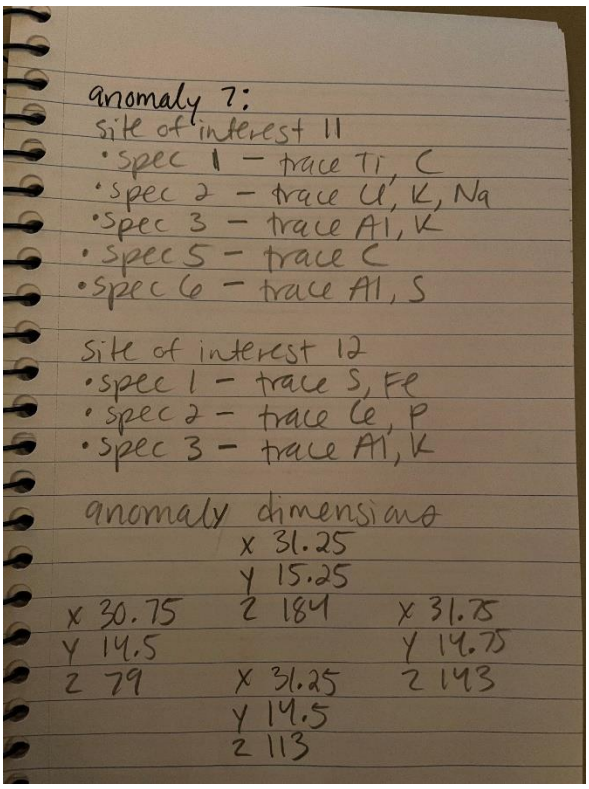
anomaly 7:
site of interest 11
• spec 1 – trace Ti, C
• spec 2 – trace Ca, K, Na
• spec 3 – trace Al, K
• spec 5 – trace C
• spec 6 – trace Al, S
site of interest 12
• spec 1 – trace S, Fe
• spec 2 – trace Ce, P
• spec 3 – trace Al, K
anomaly dimensions
x 31.25
y 15.25
z 184
x 30.75
y 14.5
z 79
x 31.25
y 14.75
z 143
x 31.25
y 14.5
z 113

Anomaly 8:

Site of interest 13

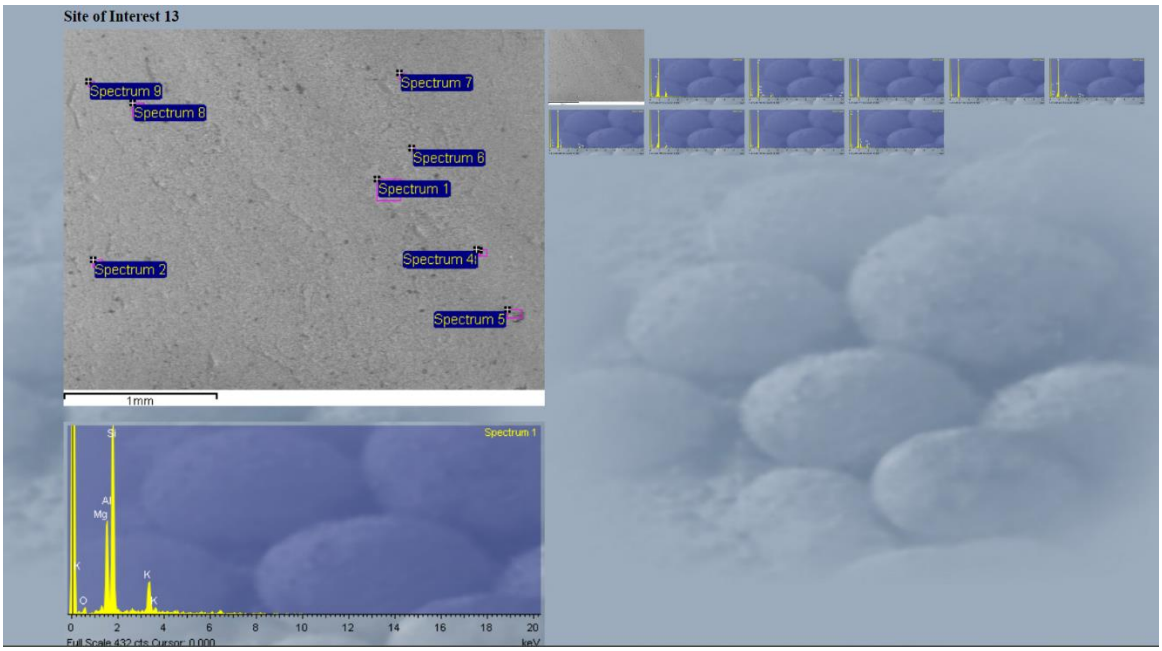

Notes

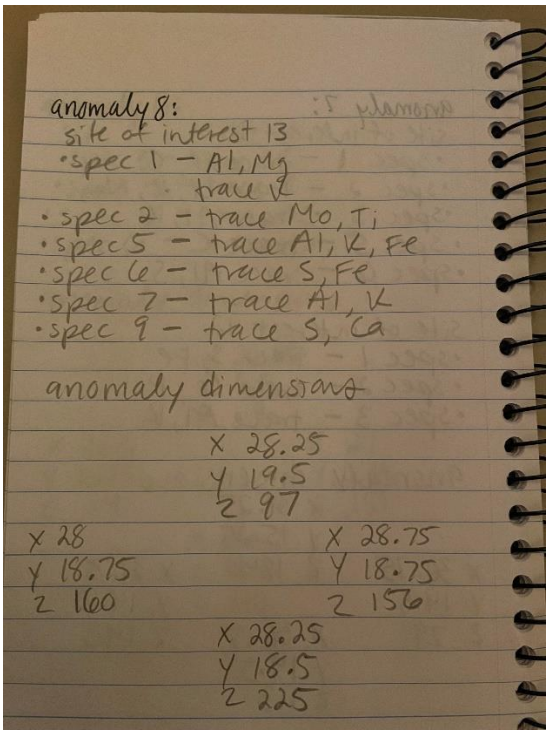

Anomaly 9:

Site of interest 14

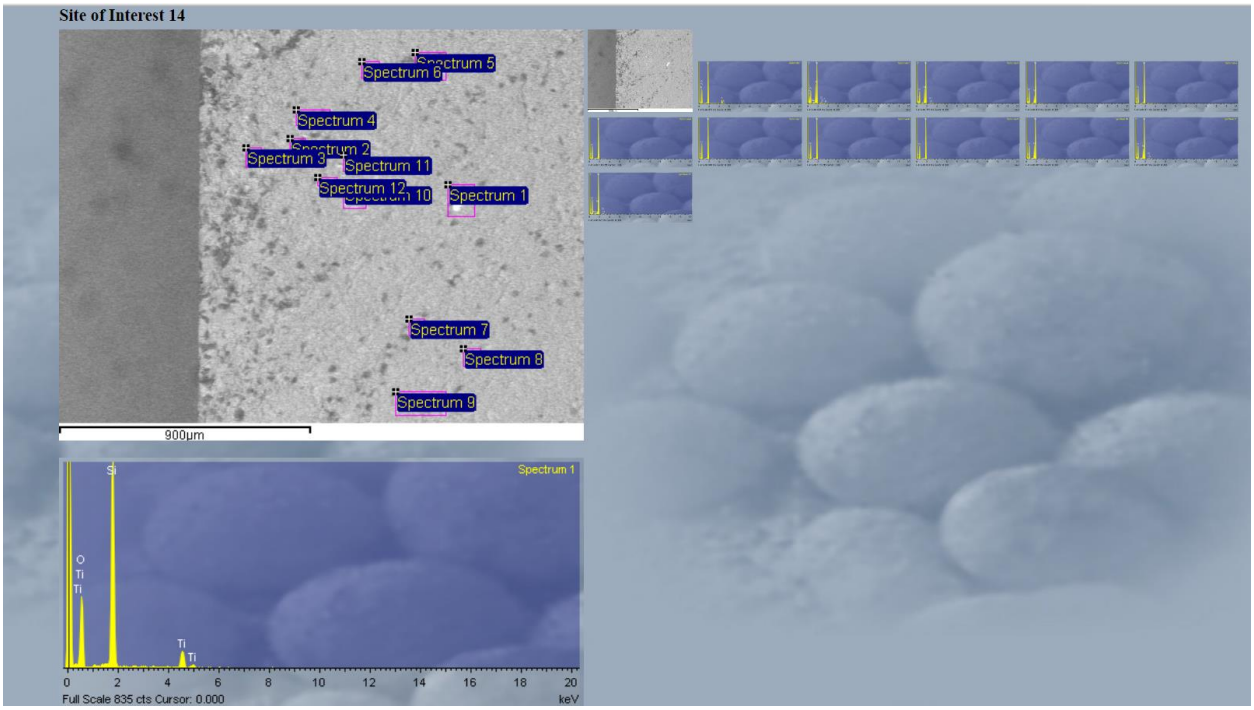

Notes

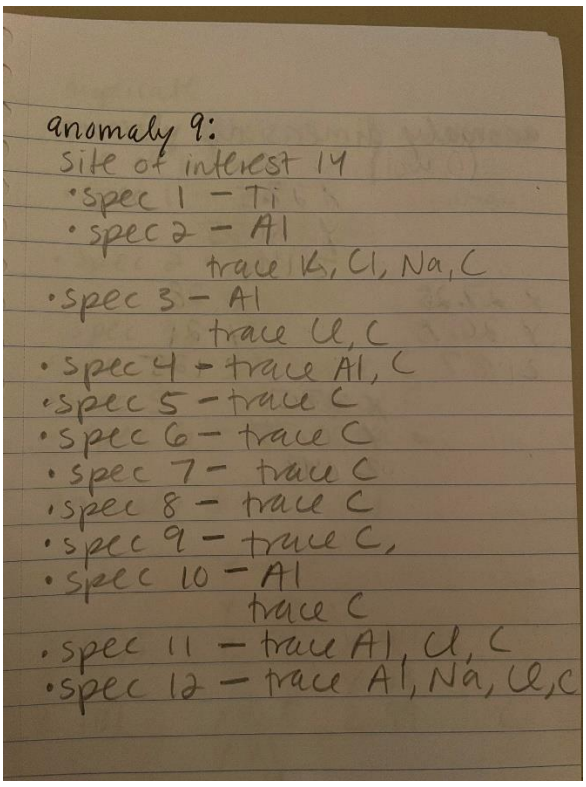
anomaly 9:
site of interest 14
- spec 1 – Ti
- spec 2 – Al
  trace K, Cl, Na, C
- spec 3 – Al
  trace Cl, C
- spec 4 – trace Al, C
- spec 5 – trace C
- spec 6 – trace C
- spec 7 – trace C
- spec 8 – trace C
- spec 9 – trace C,
- spec 10 – Al
  trace C
- spec 11 – trace Al, Cl, C
- spec 12 – trace Al, Na, Cl, C

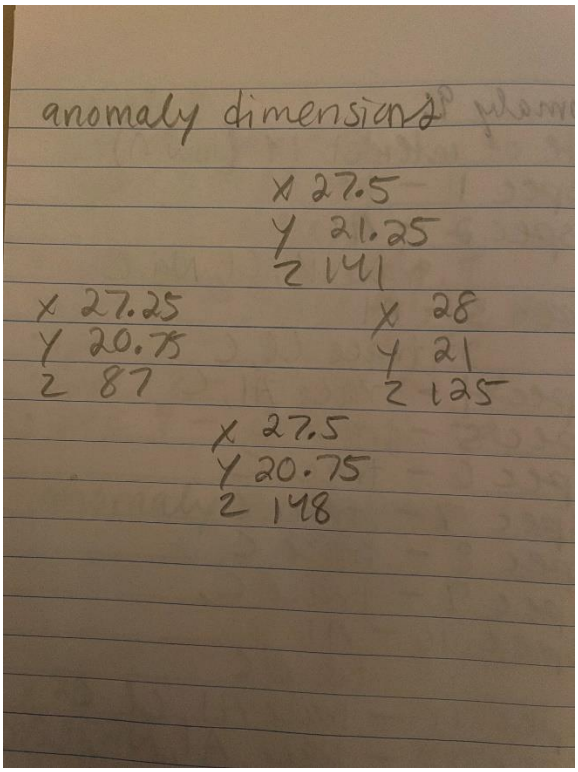
anomaly dimensions
X 27.5
Y 21.25
Z 141
X 27.25
Y 20.75
Z 87
X 28
Y 21
Z 125
X 27.5
Y 20.75
Z 148

Anomaly 10 (duplicate):

Site of interest 17

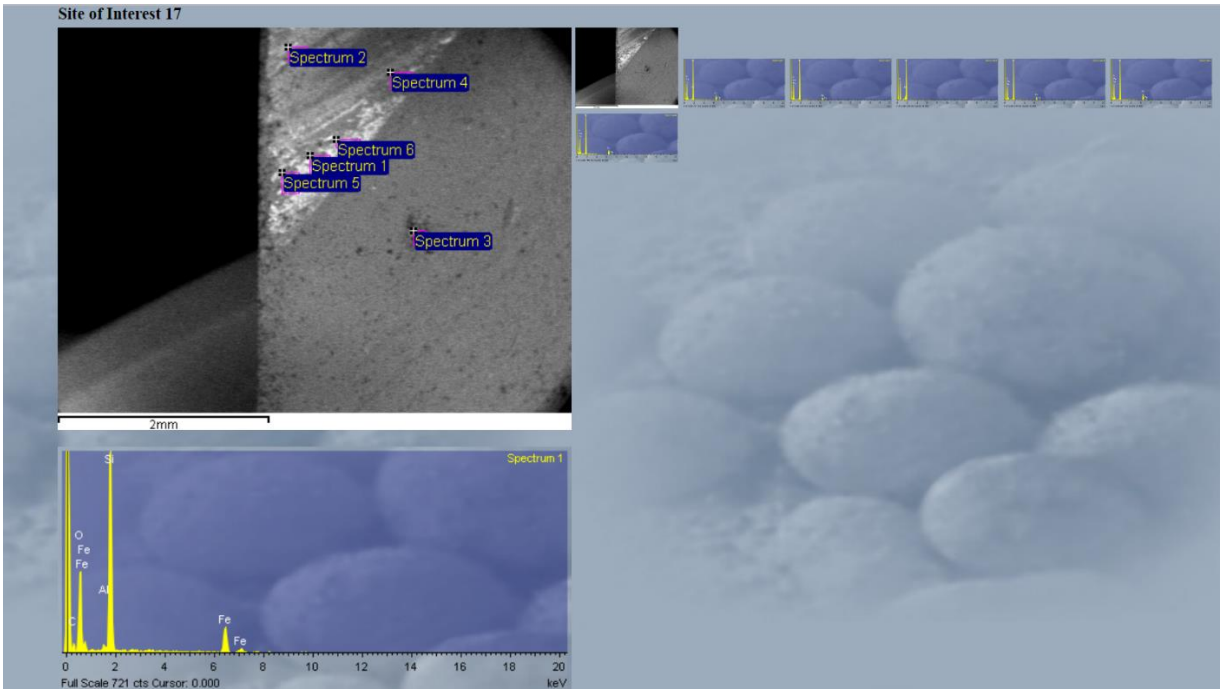

Notes

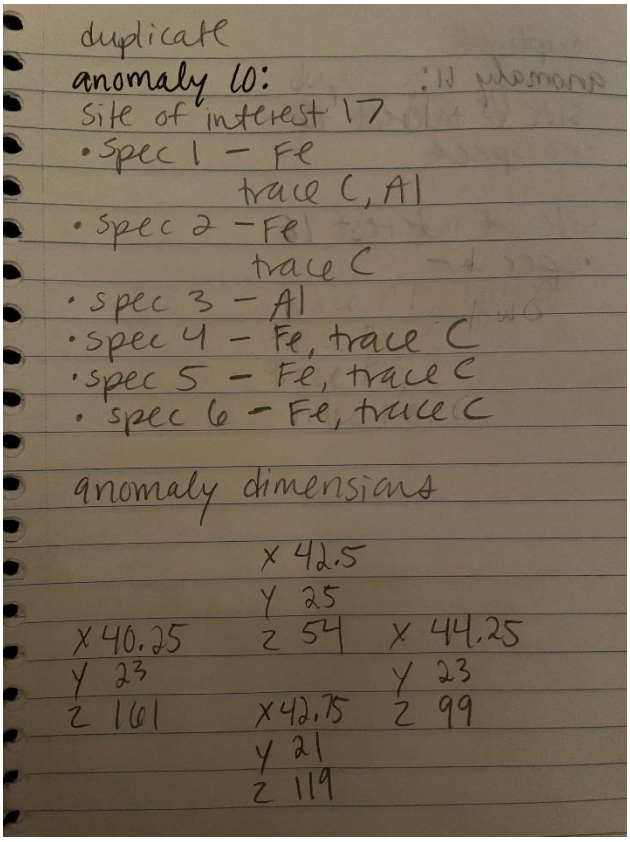
duplicate
anomaly 10:
site of interest 17
• spec 1 – Fe
trace C, Al
• spec 2 – Fe
trace C
• spec 3 – Al
• spec 4 – Fe, trace C
• spec 5 – Fe, trace C
• spec 6 – Fe, trace C
anomaly dimensions
x 42.5
y 25
z 54
x 40.25
y 23
z 161
x 44.25
y 23
z 99
x 42.75
y 21
z 119

Anomaly 11 (duplicate):

Site of interest 15

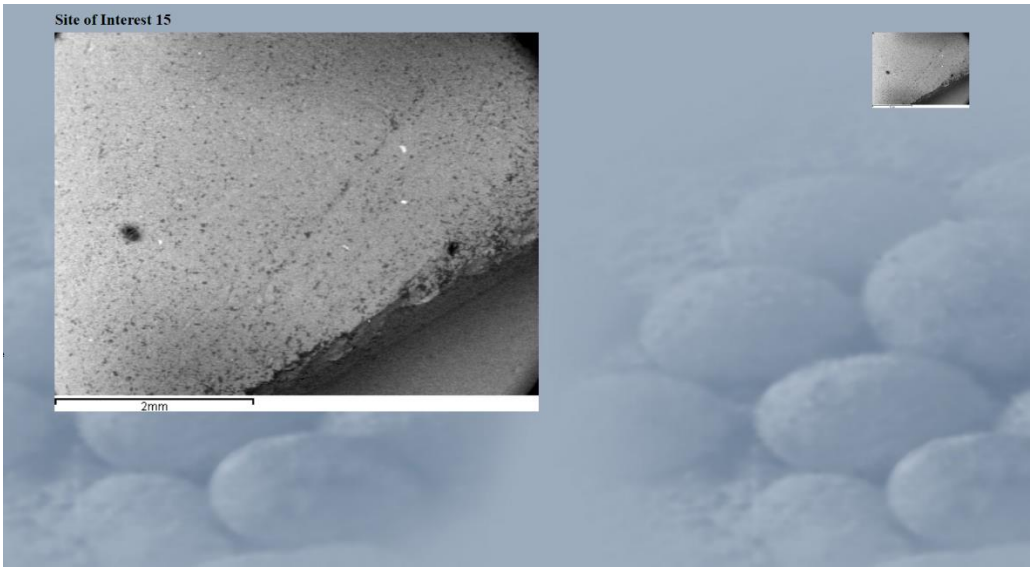

Site of interest 16

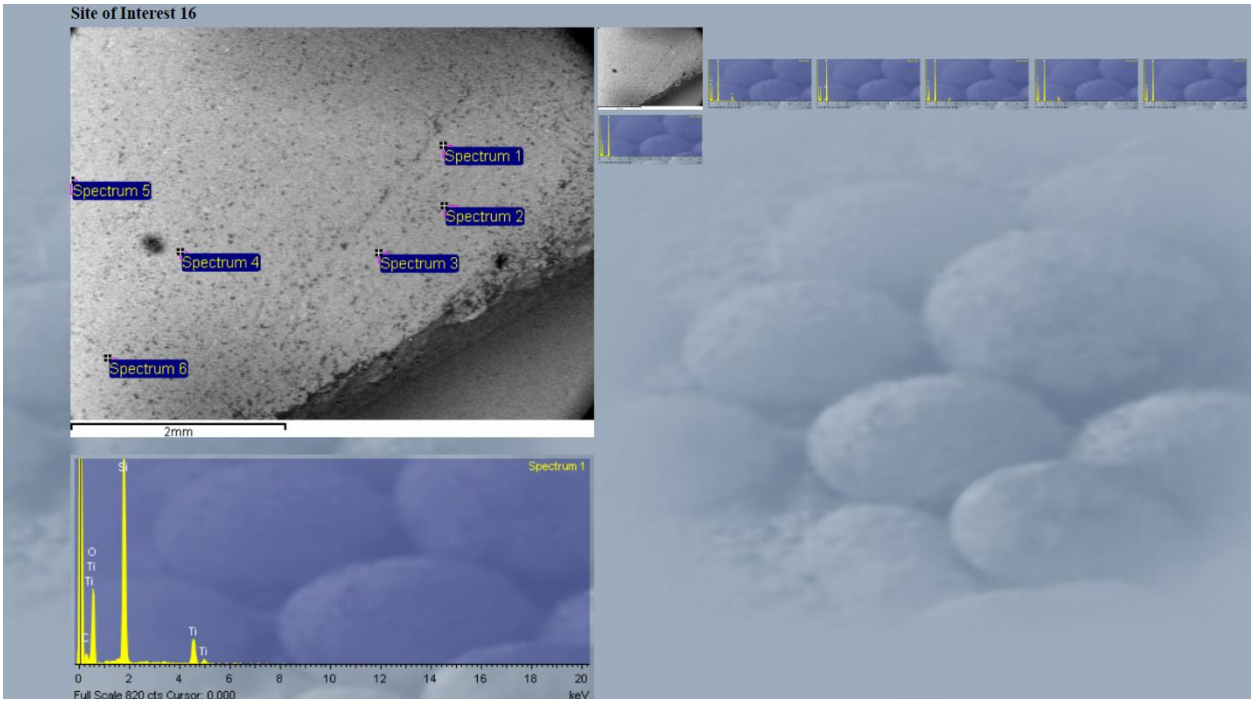

Notes

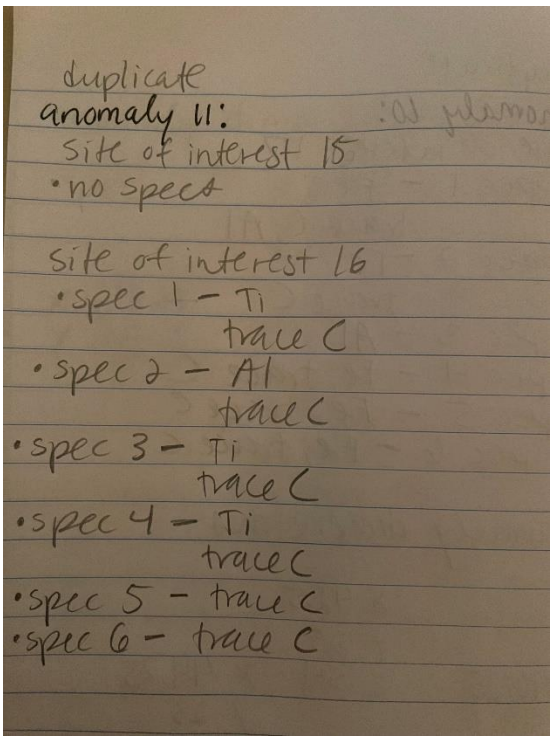
duplicate
anomaly 11:
site of interest 15
• no specs
site of interest 16
• spec 1 – Ti
trace C
• spec 2 – Al
trace C
• spec 3 – Ti
trace C
• spec 4 – Ti
trace C
• spec 5 – trace C
• spec 6 – trace C

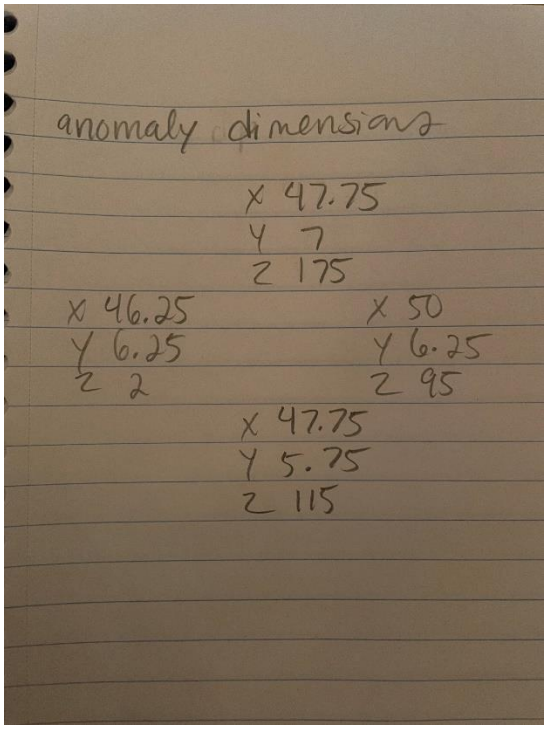
anomaly dimensions
X 47.75
Y 7
Z 175
X 46.25
Y 6.25
Z 2
X 50
Y 6.25
Z 95
X 47.75
Y 5.75
Z 115

Anomaly 12 (duplicate):

Site of interest 18

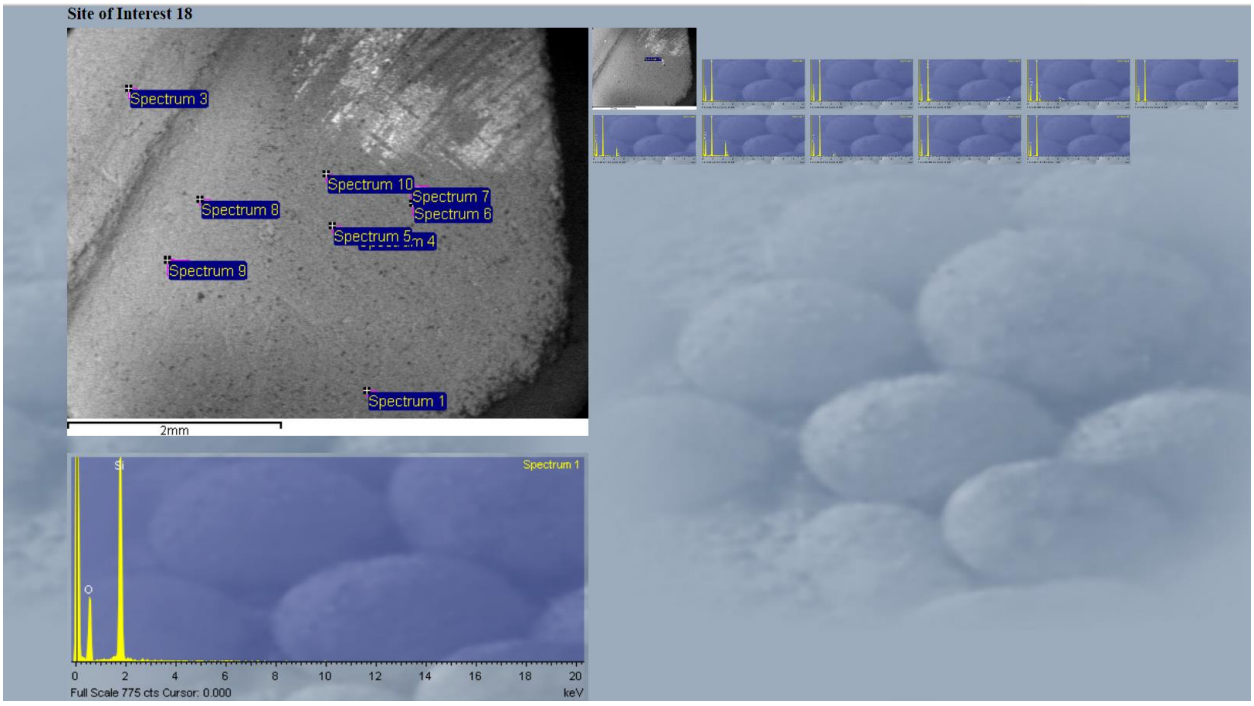

Notes

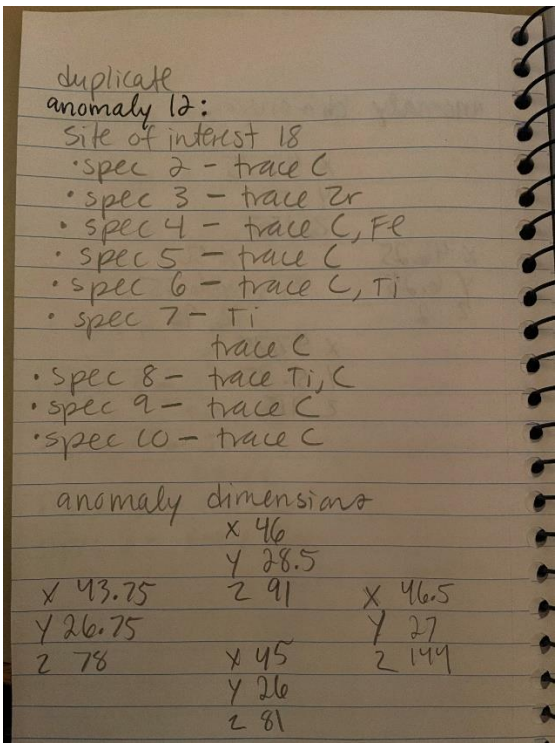
duplicate
anomaly 12:
site of interest 18
• spec 2 - trace C
• spec 3 - trace Zr
• spec 4 - trace C, Fe
• spec 5 - trace C
• spec 6 - trace C, Ti
• spec 7 - Ti
trace C
• spec 8 - trace Ti, C
• spec 9 - trace C
• spec 10 - trace C
anomaly dimensions
X 46
Y 28.5
Z 91
X 43.75
Y 26.75
Z 78
X 46.5
Y 27
Z 144
X 45
Y 26
Z 81

HRQ1-1

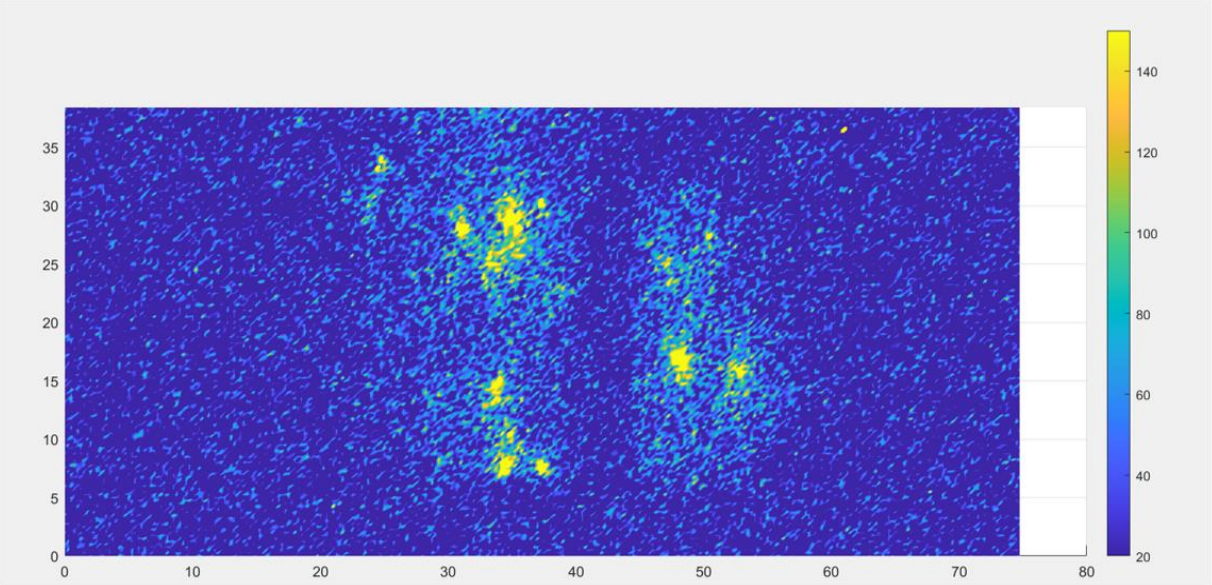
0
5
10
15
20
25
30
35
0
10
20
30
40
50
60
70
80
20
40
60
80
100
120
140

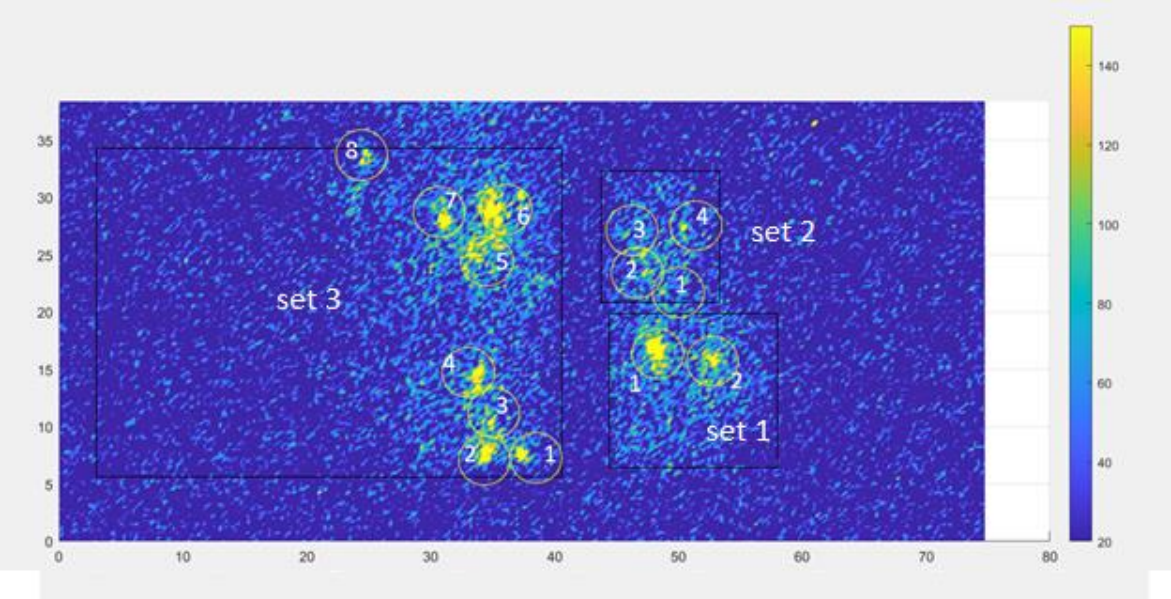
set 3
set 2
set 1
8
7
6
5
4
3
2
1
4
3
2
1
1
2
0
5
10
15
20
25
30
35
0
10
20
30
40
50
60
70
80
20
40
60
80
100
120
140

Set 1

Anomaly 1:

Site of interest 2

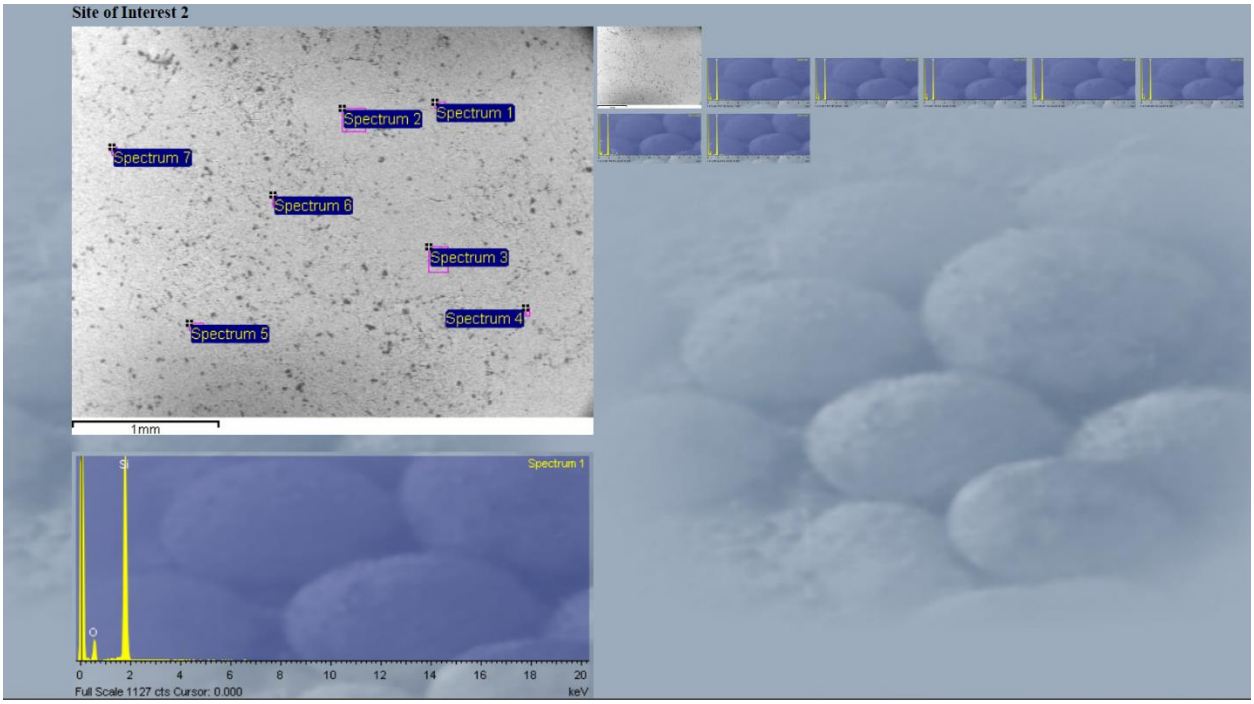

Notes

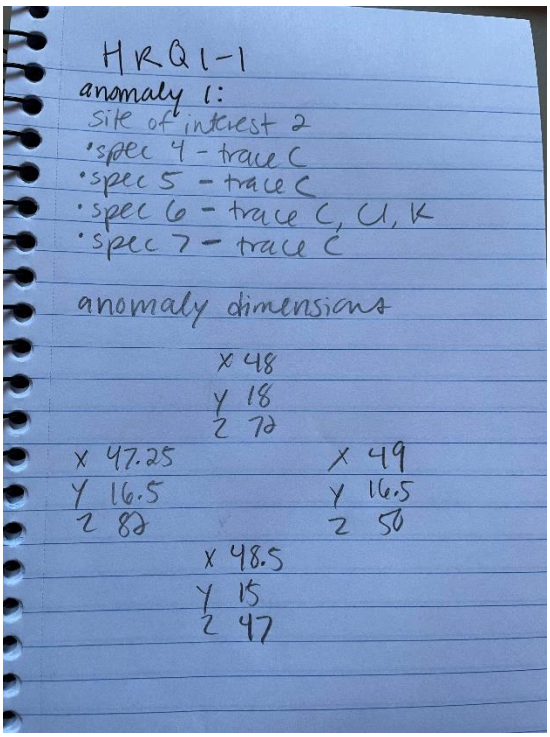
HRQ1-1
anomaly 1:
site of interest 2
•spec 4 - trace C
•spec 5 - trace C
•spec 6 - trace C, Cl, K
•spec 7 - trace C
anomaly dimensions
x 48
y 18
2 72
x 47.25
y 16.5
2 82
x 49
y 16.5
2 50
x 48.5
y 15
2 47

Anomaly 2:

Site of interest 3

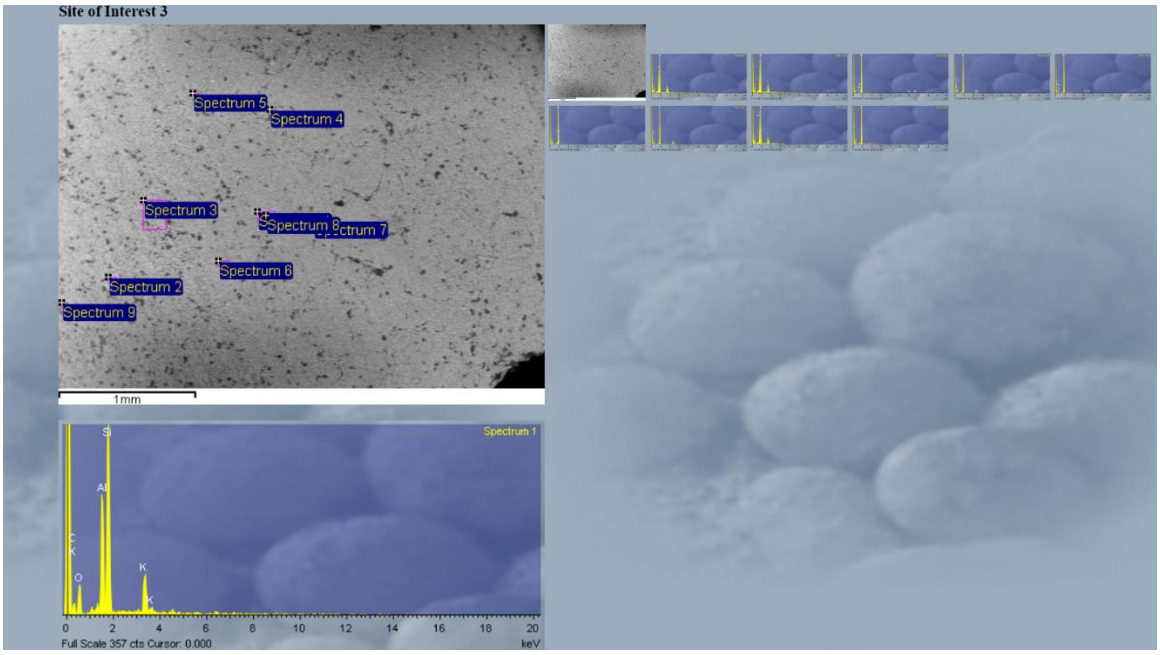

Site of interest 4

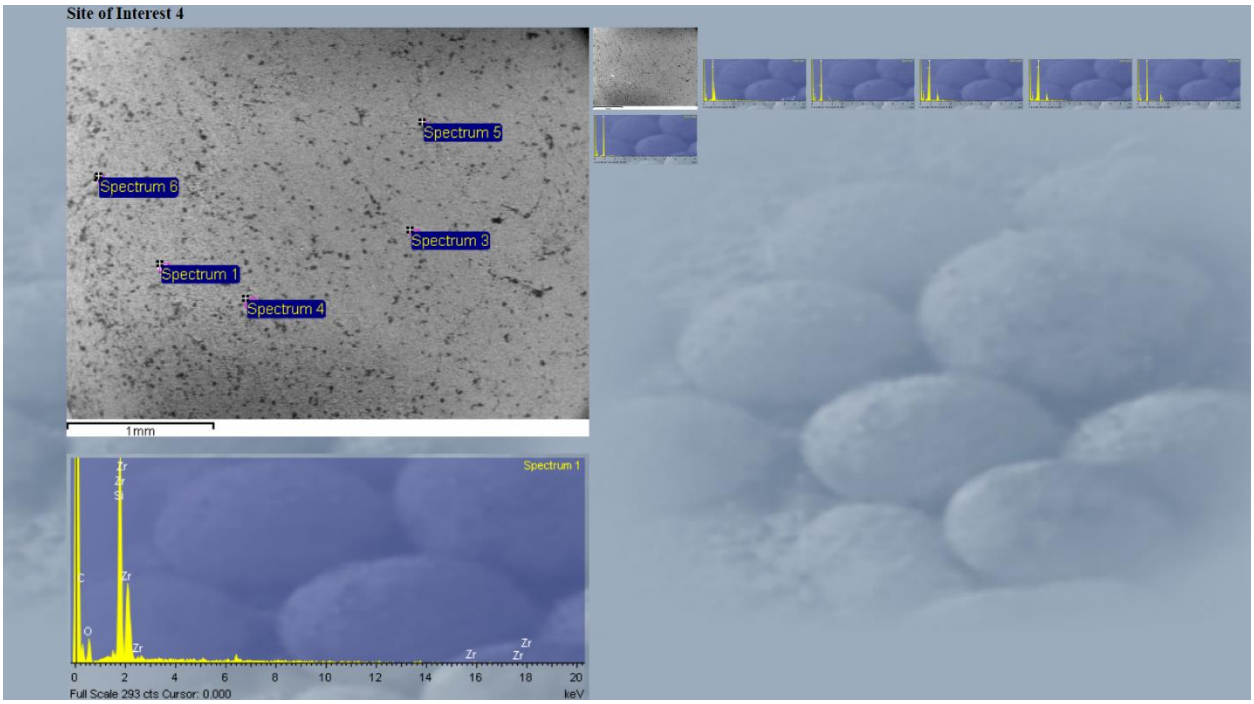

Notes

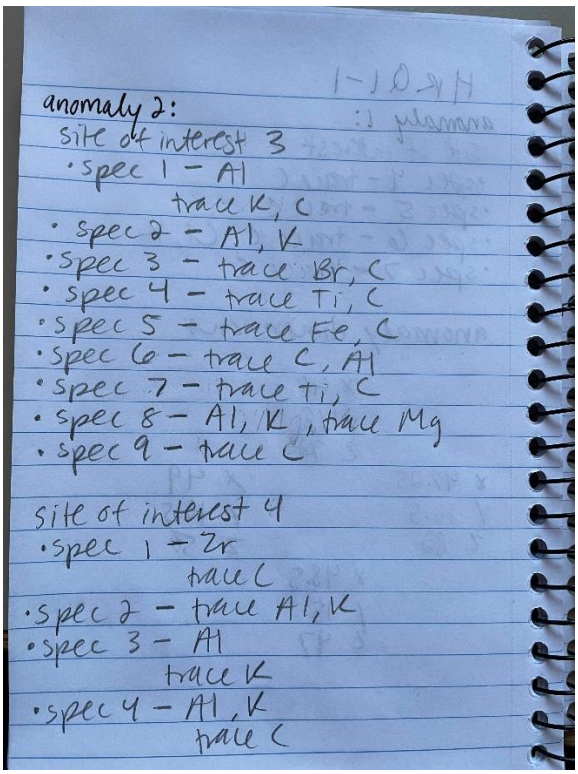
anomaly 2:
site of interest 3
• spec 1 – Al
trace K, C
• spec 2 – Al, K
• spec 3 – trace Br, C
• spec 4 – trace Ti, C
• spec 5 – trace Fe, C
• spec 6 – trace C, Al
• spec 7 – trace Ti, C
• spec 8 – Al, K, trace Mg
• spec 9 – trace C

site of interest 4
• spec 1 – Zr
trace C
• spec 2 – trace Al, K
• spec 3 – Al
trace K
• spec 4 – Al, K
trace C

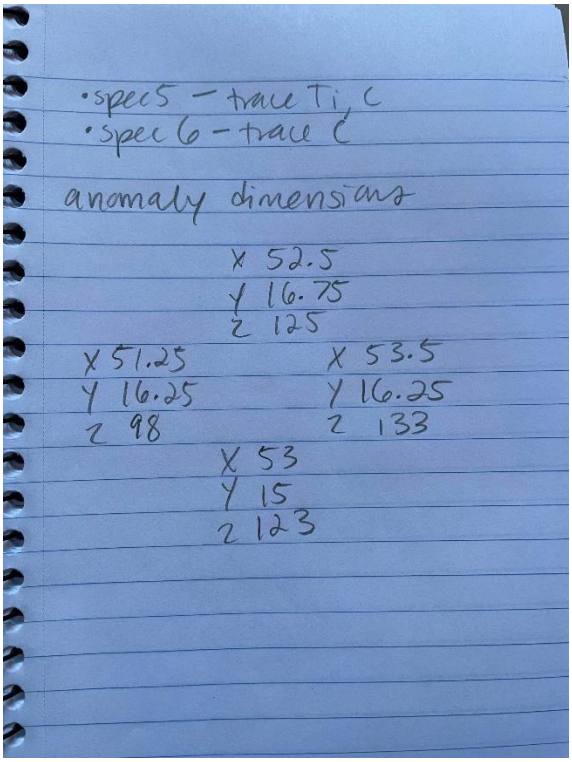
• spec 5 – trace Ti, C
• spec 6 – trace C

anomaly dimensions

X 52.5
Y 16.75
Z 125

X 51.25
Y 16.25
Z 98

X 53.5
Y 16.25
Z 133

X 53
Y 15
Z 123

Set 2

Anomaly 1:

Site of interest 5

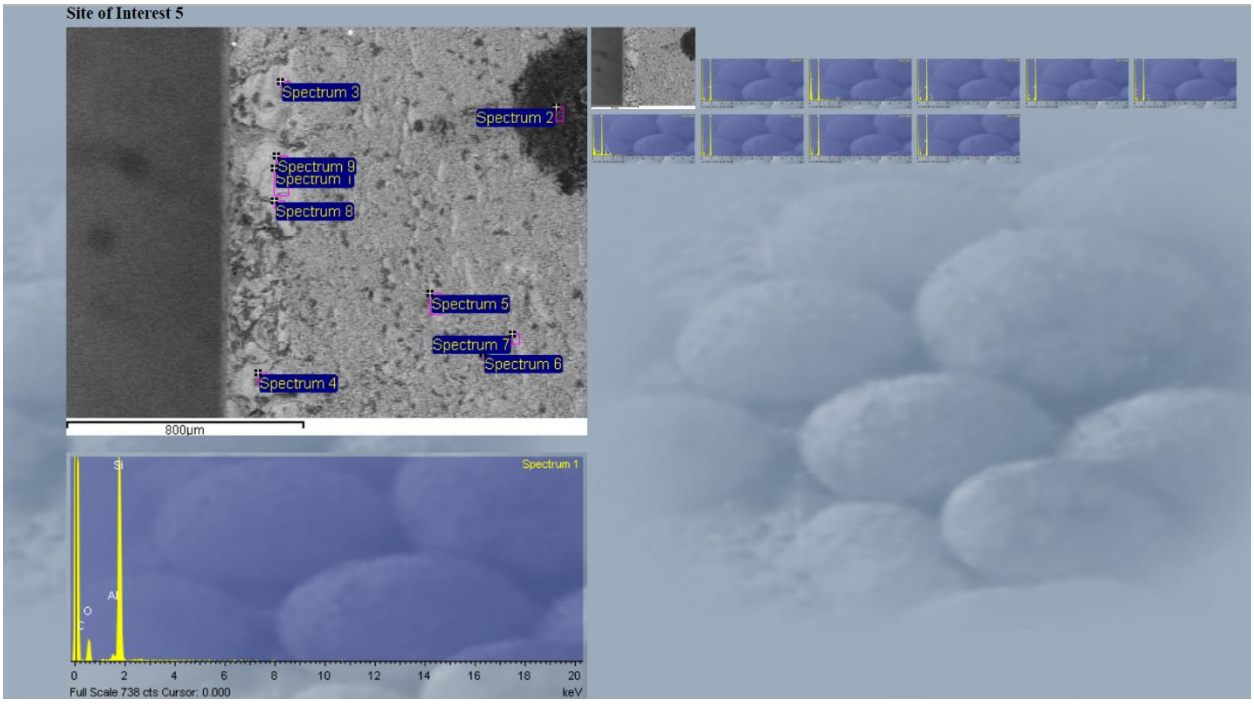

Site of interest 6

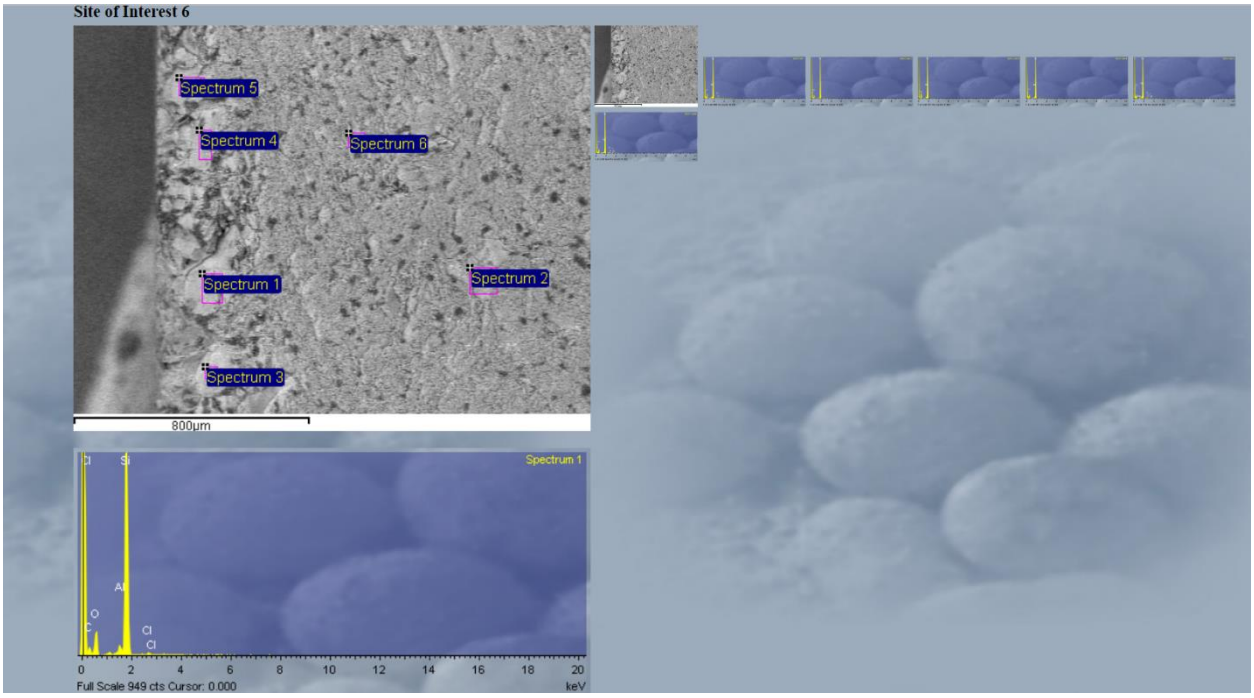

Notes

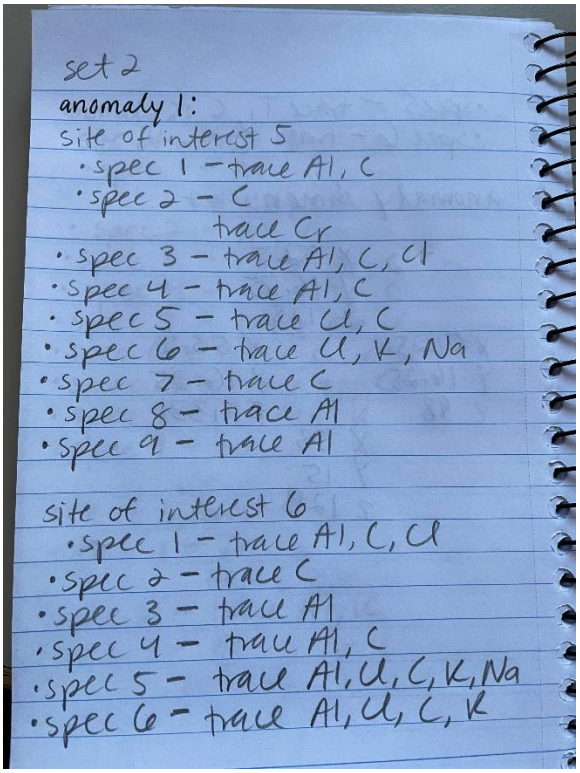

set 2
anomaly 1:
site of interest 5
- spec 1 – trace Al, C
- spec 2 – C
  trace Cr
- spec 3 – trace Al, C, Cl
- spec 4 – trace Al, C
- spec 5 – trace Cl, C
- spec 6 – trace Cl, K, Na
- spec 7 – trace C
- spec 8 – trace Al
- spec 9 – trace Al

site of interest 6
- spec 1 – trace Al, C, Cl
- spec 2 – trace C
- spec 3 – trace Al
- spec 4 – trace Al, C
- spec 5 – trace Al, Cl, C, K, Na
- spec 6 – trace Al, Cl, C, K

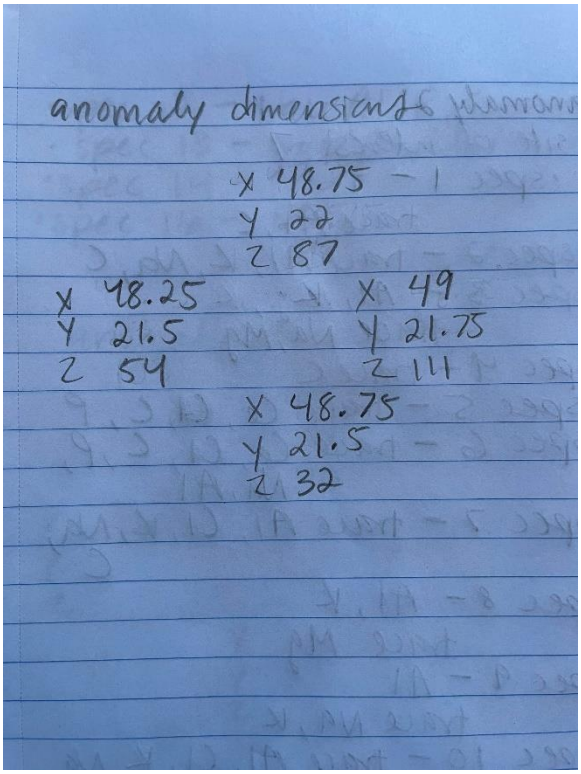

anomaly dimensions (in mm)

X 48.75 – 1
Y 22
Z 87

X 48.25
Y 21.5
Z 54

X 49
Y 21.75
Z 111

X 48.75
Y 21.5
Z 32

Anomaly 2:

Site of interest 7

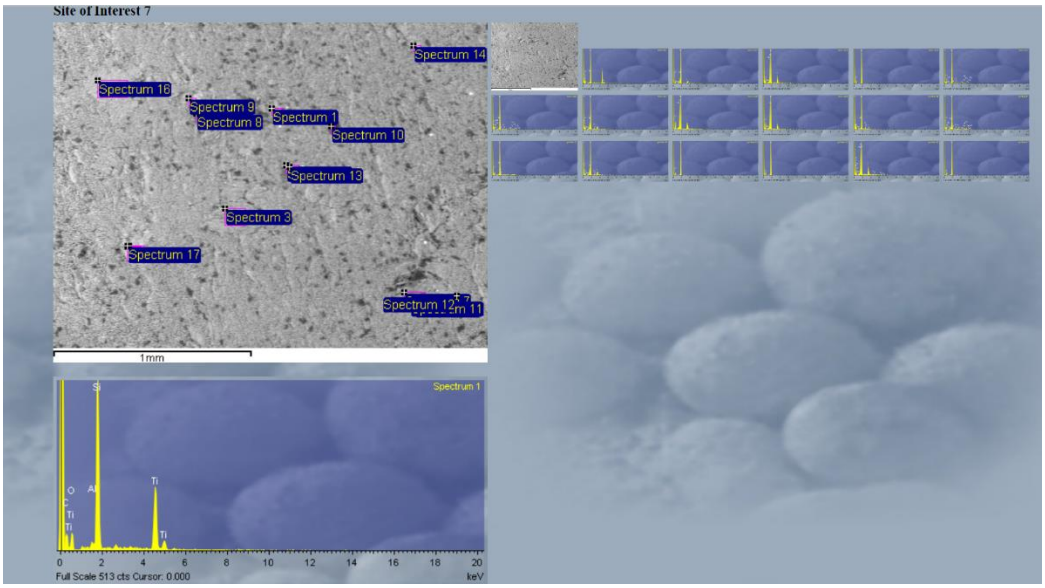

Notes

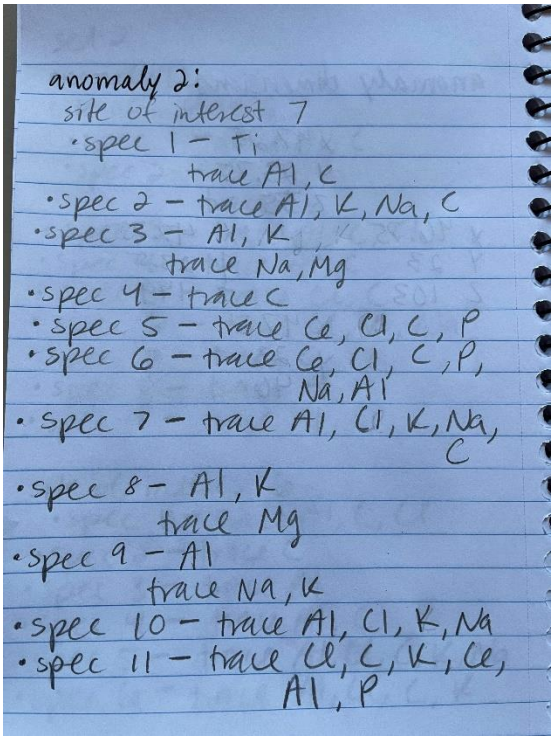
anomaly 2:
site of interest 7
•spec 1 – Ti
trace Al, C
•spec 2 – trace Al, K, Na, C
•spec 3 – Al, K
trace Na, Mg
•spec 4 – trace C
•spec 5 – trace Ce, Cl, C, P
•spec 6 – trace Ce, Cl, C, P,
Na, Al
•spec 7 – trace Al, Cl, K, Na,
C
•spec 8 – Al, K
trace Mg
•spec 9 – Al
trace Na, K
•spec 10 – trace Al, Cl, K, Na
•spec 11 – trace Cl, C, K, Ce,
Al, P

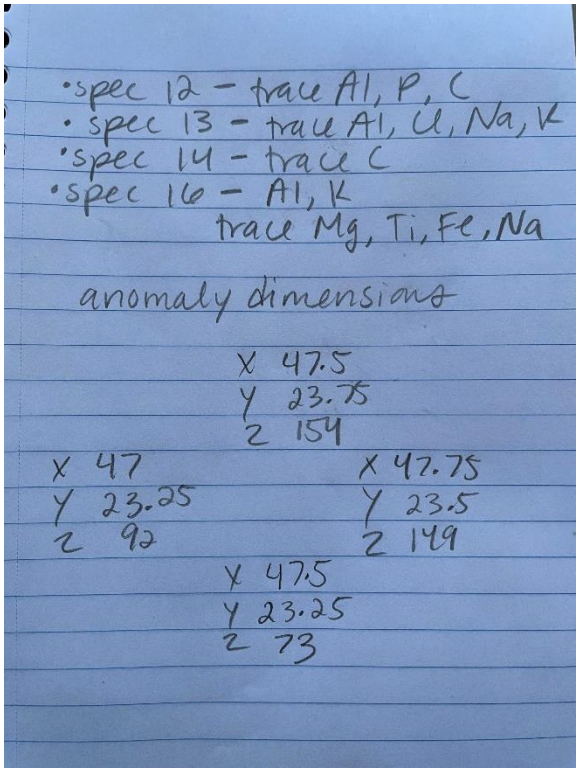
•spec 12 – trace Al, P, C
•spec 13 – trace Al, Cl, Na, K
•spec 14 – trace C
•spec 16 – Al, K
trace Mg, Ti, Fe, Na
anomaly dimensions
X 47.5
Y 23.75
Z 154
X 47
Y 23.25
Z 92
X 47.75
Y 23.5
Z 149
X 47.5
Y 23.25
Z 73

Anomaly 3:

Site of interest 9

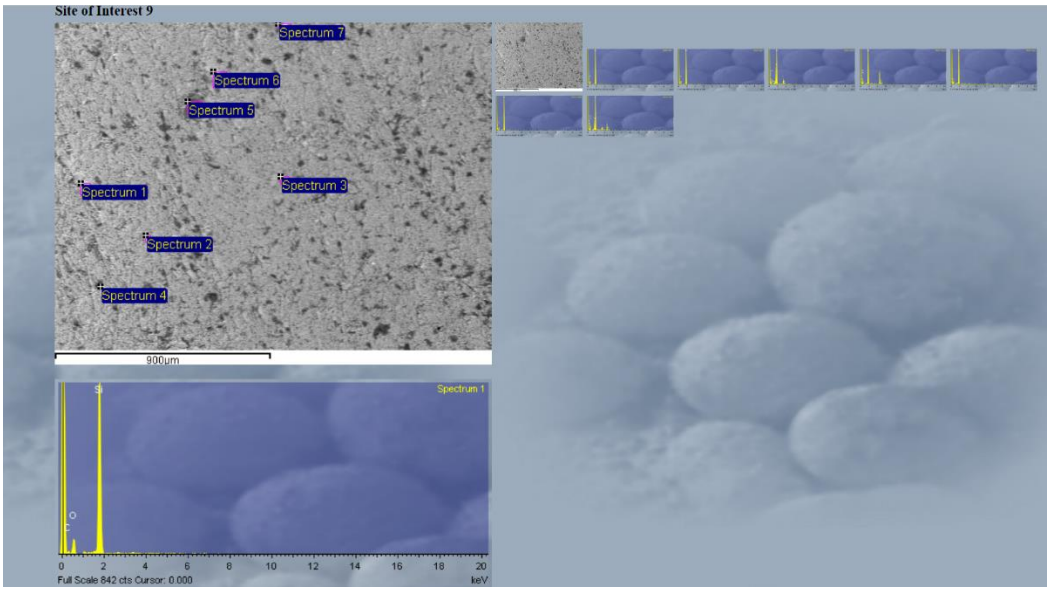

Notes

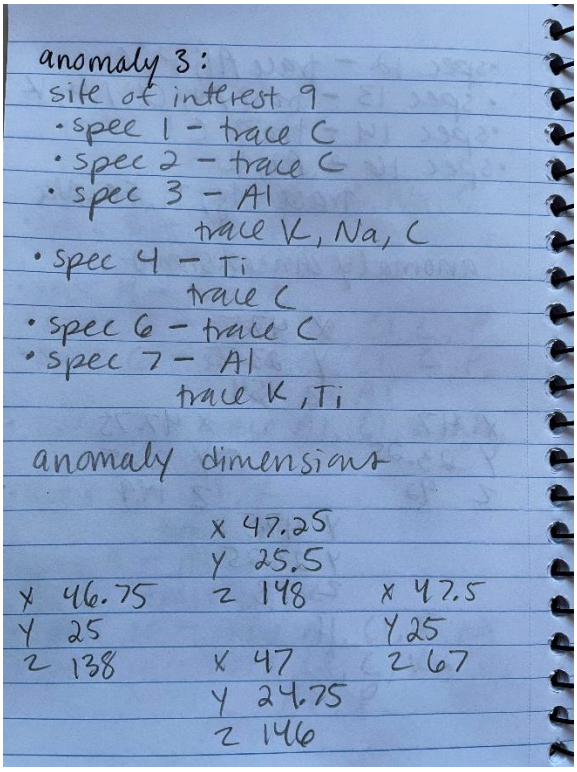
anomaly 3:
site of interest 9
• spec 1 - trace C
• spec 2 - trace C
• spec 3 - Al
trace K, Na, C
• spec 4 - Ti
trace C
• spec 6 - trace C
• spec 7 - Al
trace K, Ti
anomaly dimensions
x 47.25
y 25.5
z 148
x 46.75
y 25
z 138
x 47.5
y 25
z 67
x 47
y 24.75
z 146

Anomaly 4

Site of interest 10

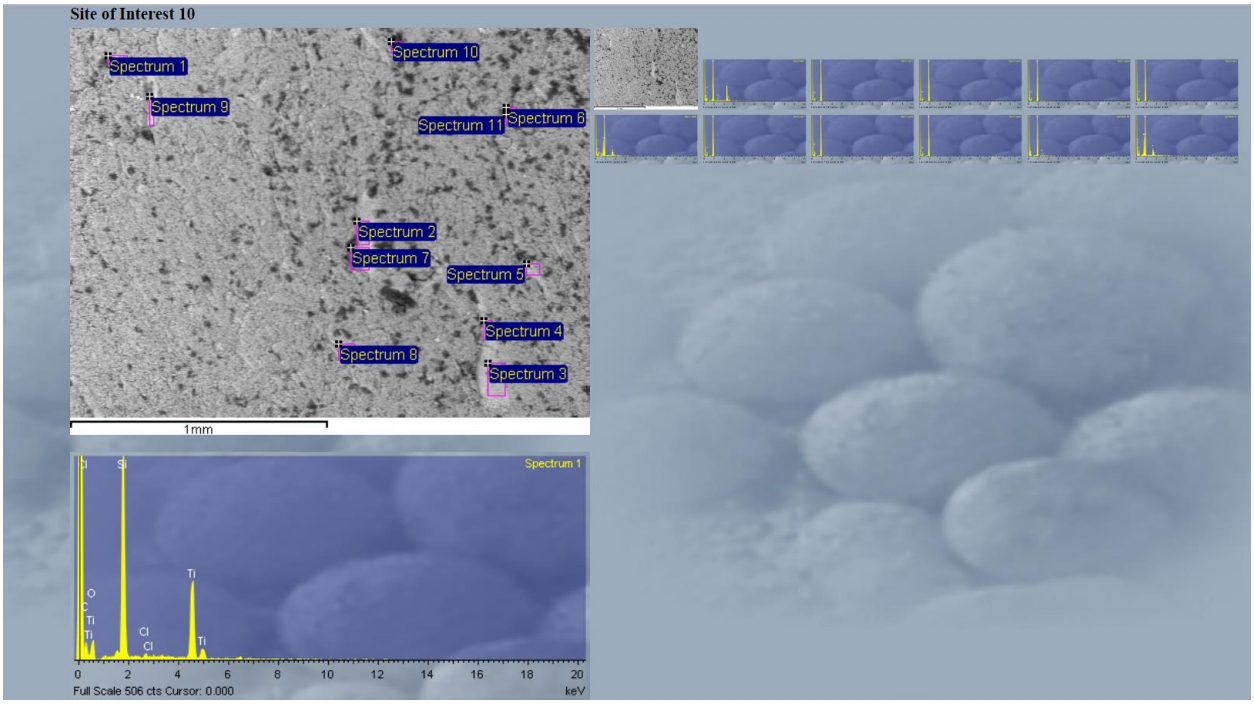

Site of interest 11

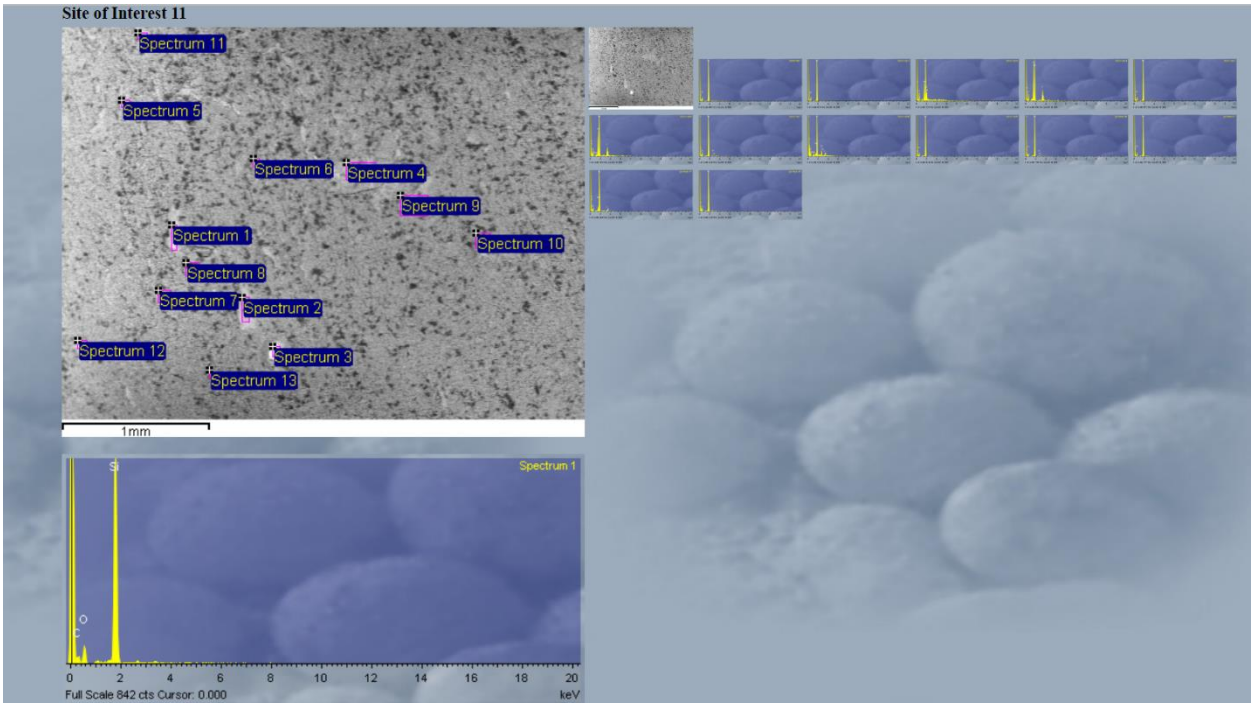

Notes

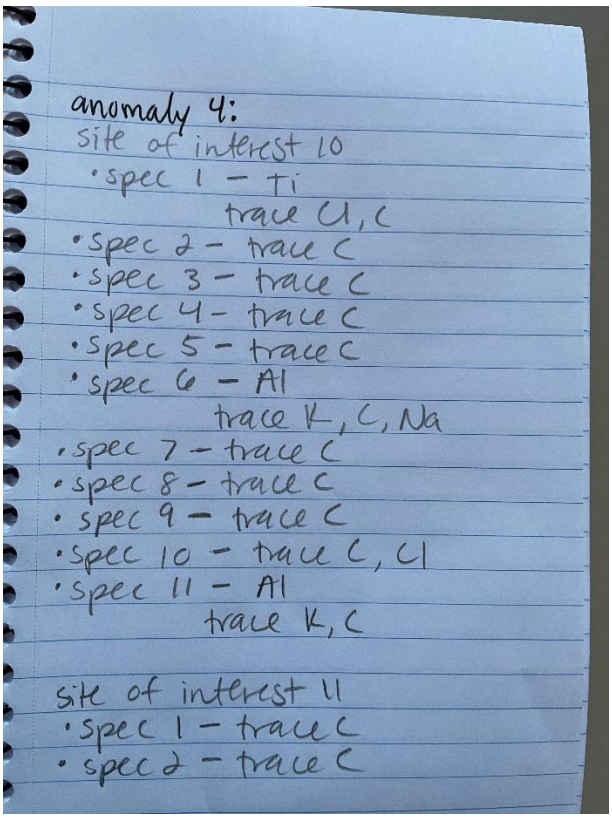

anomaly 4:
site of interest 10
- spec 1 – Ti
  trace Cl, C
- spec 2 – trace C
- spec 3 – trace C
- spec 4 – trace C
- spec 5 – trace C
- spec 6 – Al
  trace K, C, Na
- spec 7 – trace C
- spec 8 – trace C
- spec 9 – trace C
- spec 10 – trace C, Cl
- spec 11 – Al
  trace K, C

site of interest 11
- spec 1 – trace C
- spec 2 – trace C

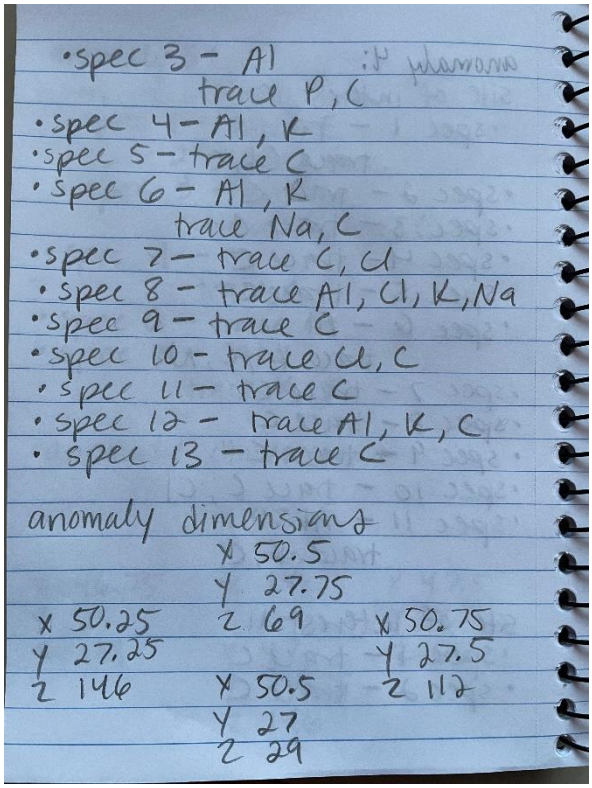

- spec 3 – Al
  trace P, C
- spec 4 – Al, K
- spec 5 – trace C
- spec 6 – Al, K
  trace Na, C
- spec 7 – trace C, Cl
- spec 8 – trace Al, Cl, K, Na
- spec 9 – trace C
- spec 10 – trace Cl, C
- spec 11 – trace C
- spec 12 – trace Al, K, C
- spec 13 – trace C

anomaly dimensions

X 50.5
Y 27.75
Z 69

X 50.25
Y 27.25
Z 146

X 50.75
Y 27.5
Z 112

X 50.5
Y 27
Z 29

Set 3

Anomaly 1:

Site of interest 12

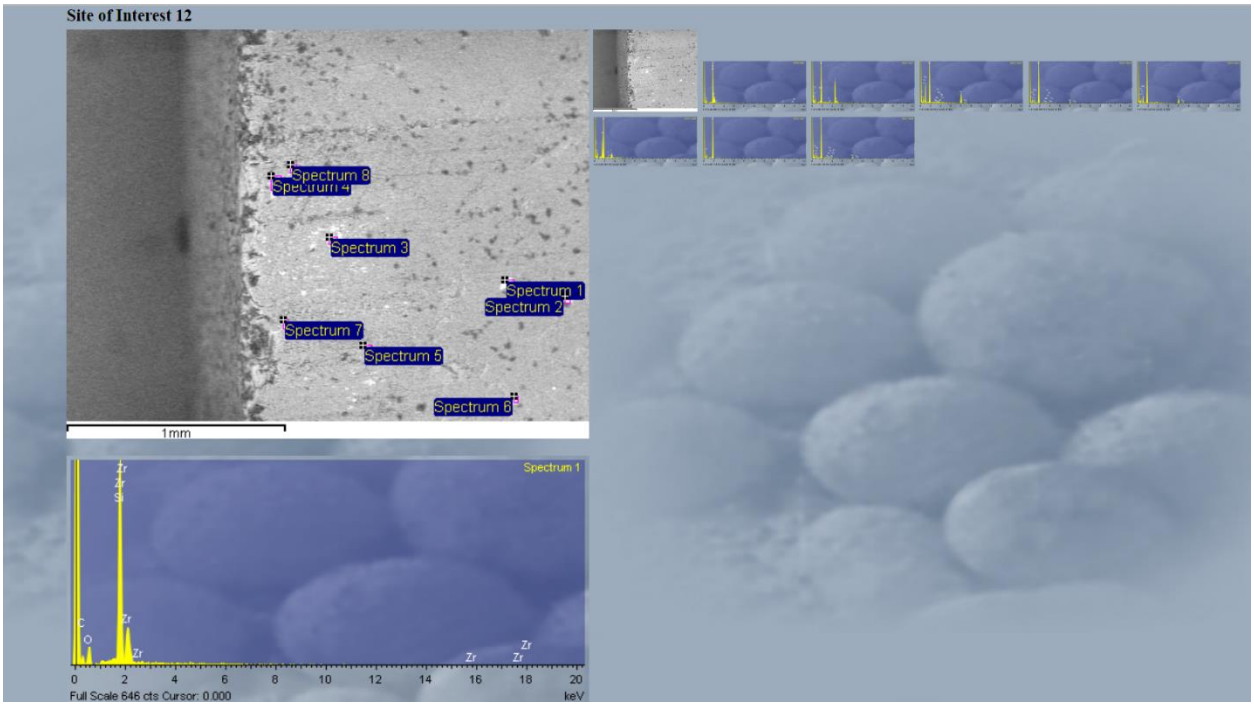

Notes

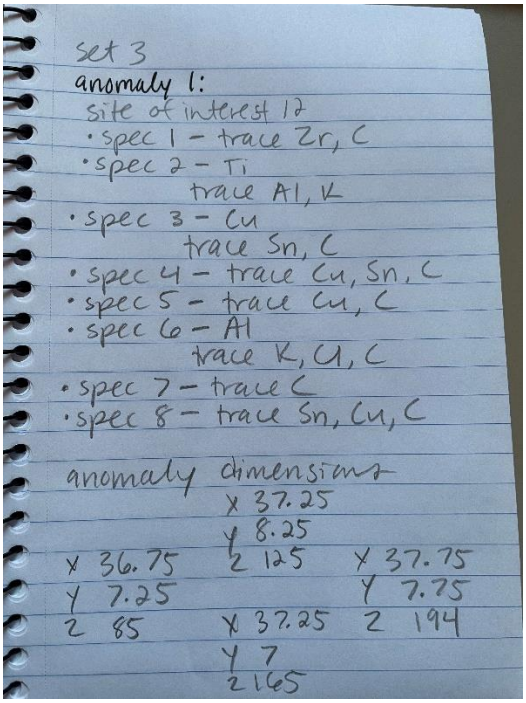
set 3
anomaly 1:
site of interest 12
• spec 1 – trace Zr, C
• spec 2 – Ti
trace Al, K
• spec 3 – Cu
trace Sn, C
• spec 4 – trace Cu, Sn, C
• spec 5 – trace Cu, C
• spec 6 – Al
trace K, Cl, C
• spec 7 – trace C
• spec 8 – trace Sn, Cu, C
anomaly dimensions
X 37.25
Y 8.25
Z 125
X 36.75
Y 7.25
Z 85
X 37.75
Y 7.75
Z 194
X 37.25
Y 7
Z 165

Anomaly 2:

Site of interest 13

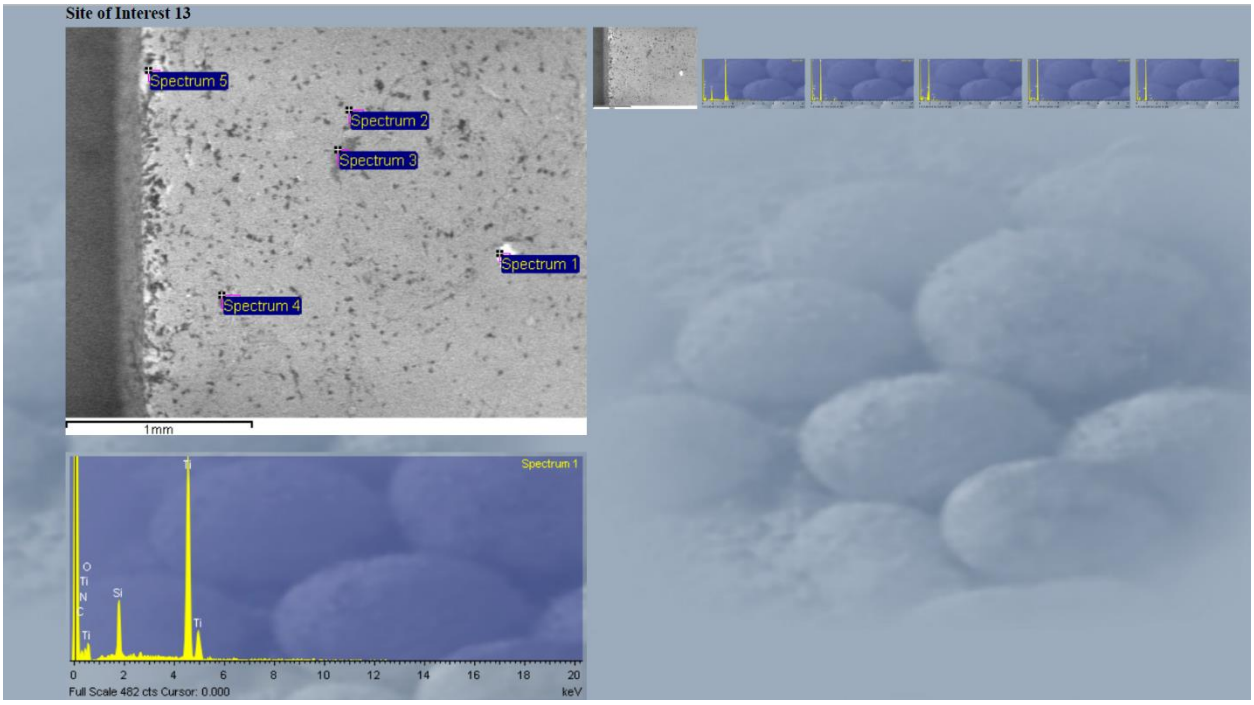

Notes

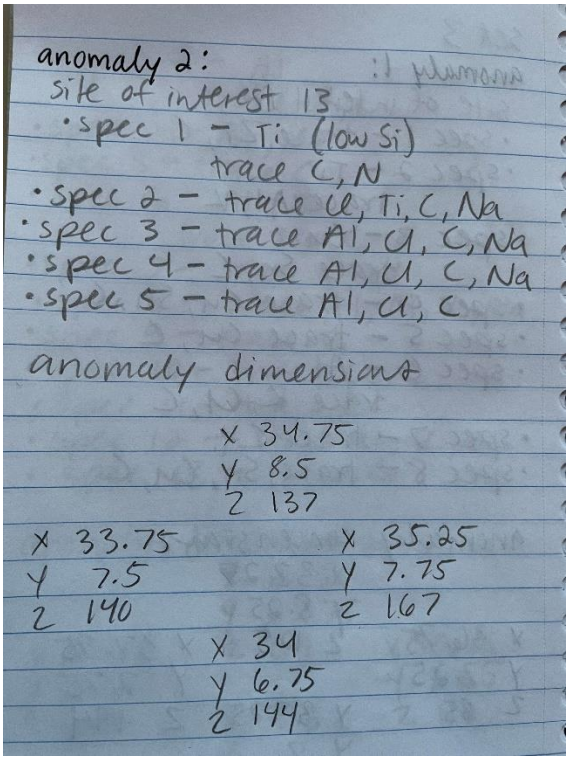

anomaly 2:
site of interest 13
- spec 1 – Ti (low Si)
  trace C, N
- spec 2 – trace Cl, Ti, C, Na
- spec 3 – trace Al, Cl, C, Na
- spec 4 – trace Al, Cl, C, Na
- spec 5 – trace Al, Cl, C

anomaly dimensions

X 34.75
Y 8.5
Z 137

X 33.75
Y 7.5
Z 140

X 35.25
Y 7.75
Z 167

X 34
Y 6.75
Z 144

Anomaly 3:

Site of interest 14

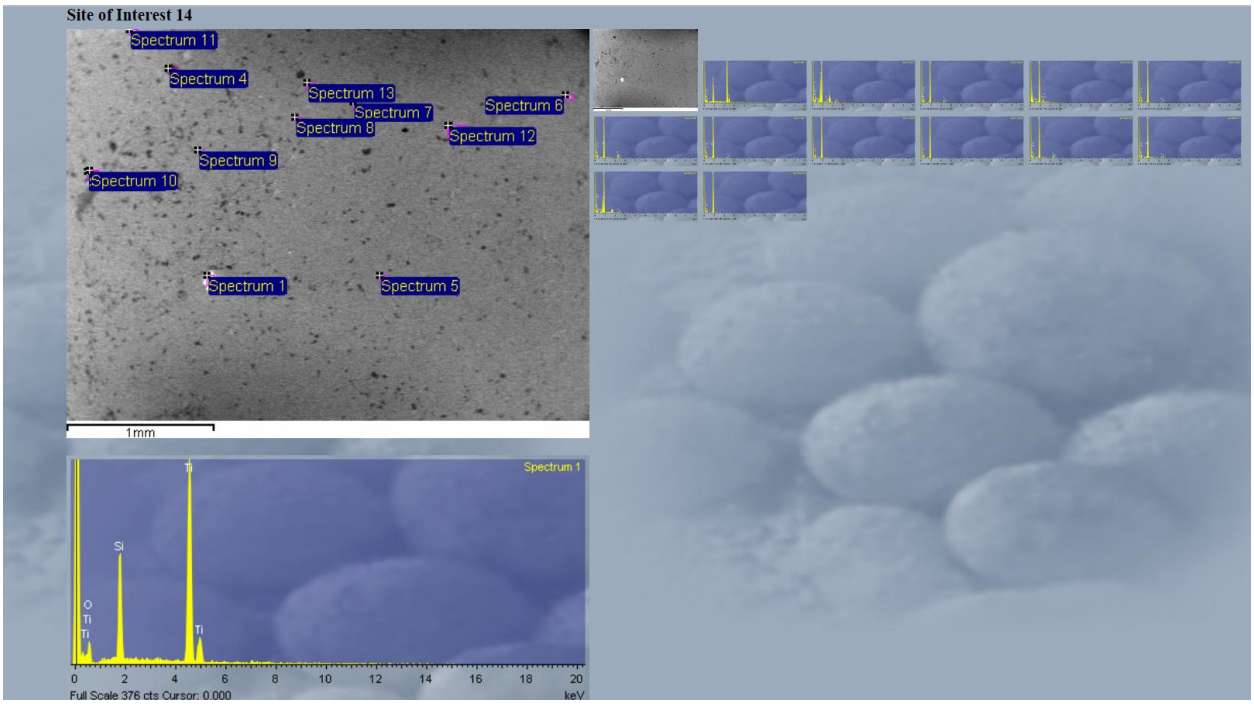

Notes

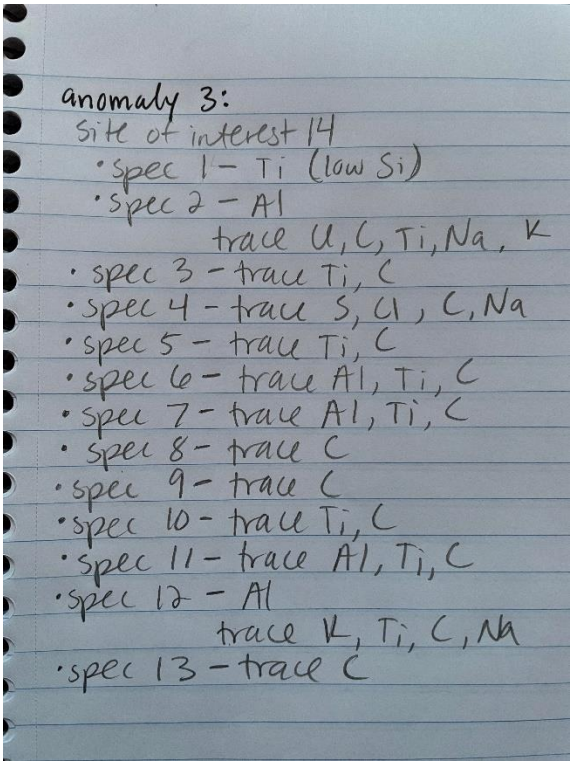
anomaly 3:
site of interest 14
• spec 1 – Ti (low Si)
• spec 2 – Al
trace U, C, Ti, Na, K
• spec 3 – trace Ti, C
• spec 4 – trace S, Cl, C, Na
• spec 5 – trace Ti, C
• spec 6 – trace Al, Ti, C
• spec 7 – trace Al, Ti, C
• spec 8 – trace C
• spec 9 – trace C
• spec 10 – trace Ti, C
• spec 11 – trace Al, Ti, C
• spec 12 – Al
trace K, Ti, C, Na
• spec 13 – trace C

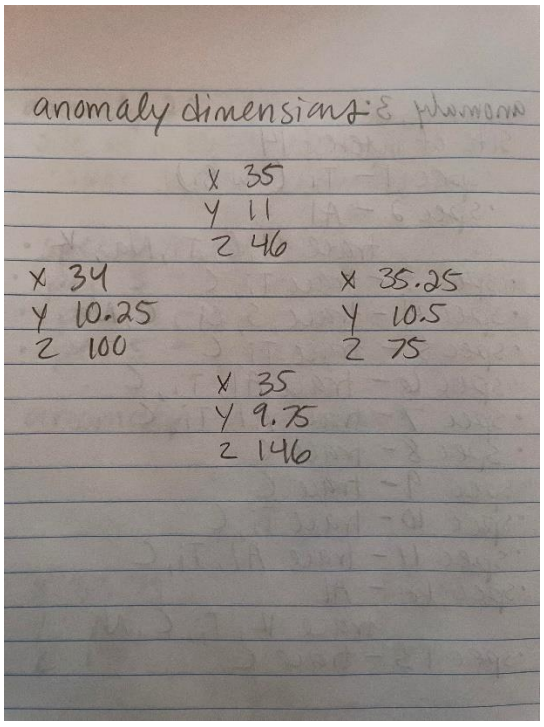
anomaly dimensions & plummb
X 35
Y 11
Z 46
X 34
Y 10.25
Z 100
X 35.25
Y 10.5
Z 75
X 35
Y 9.75
Z 146

Anomaly 4

Site of interest 15

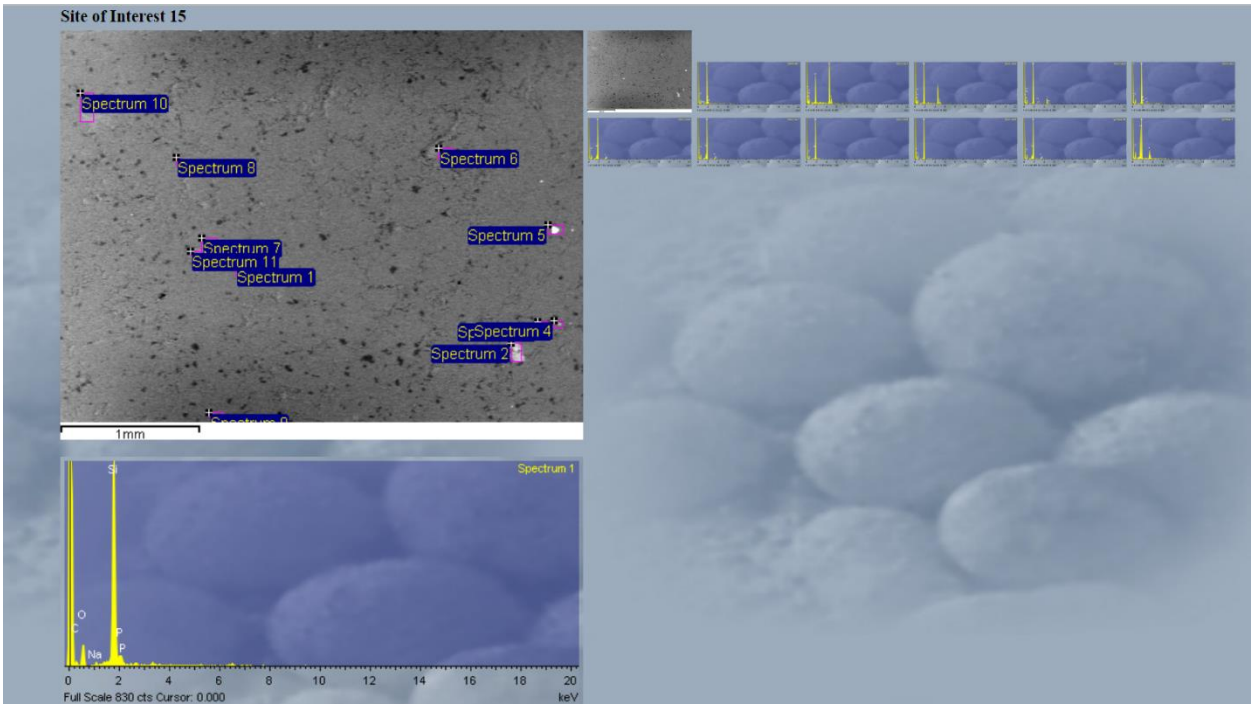

Notes

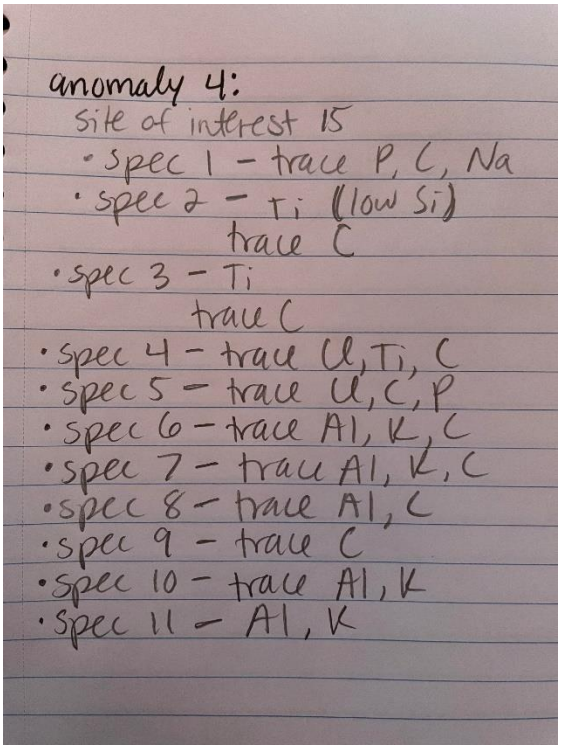
anomaly 4:
site of interest 15
• spec 1 – trace P, C, Na
• spec 2 – Ti (low Si)
trace C
• spec 3 – Ti
trace C
• spec 4 – trace U, Ti, C
• spec 5 – trace U, C, P
• spec 6 – trace Al, K, C
• spec 7 – trace Al, K, C
• spec 8 – trace Al, C
• spec 9 – trace C
• spec 10 – trace Al, K
• spec 11 – Al, K

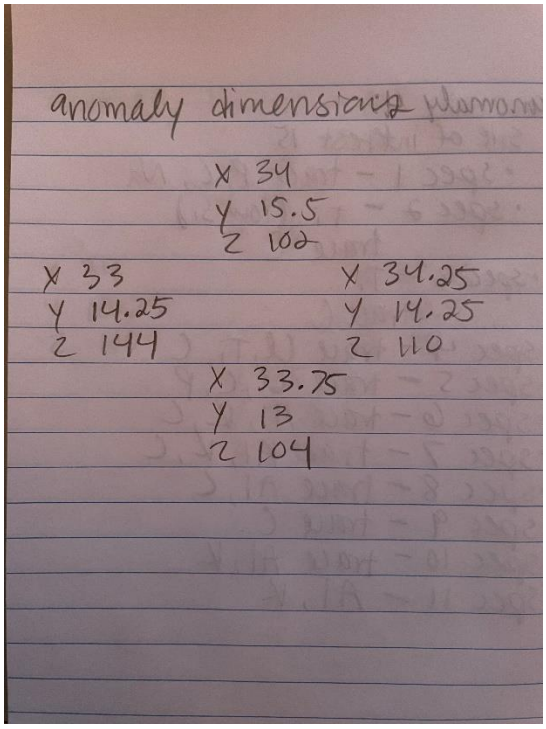
anomaly dimensions
X 34
Y 15.5
Z 102
X 33
Y 14.25
Z 144
X 34.25
Y 14.25
Z 110
X 33.75
Y 13
Z 104

Anomaly 5:

Site of interest 16

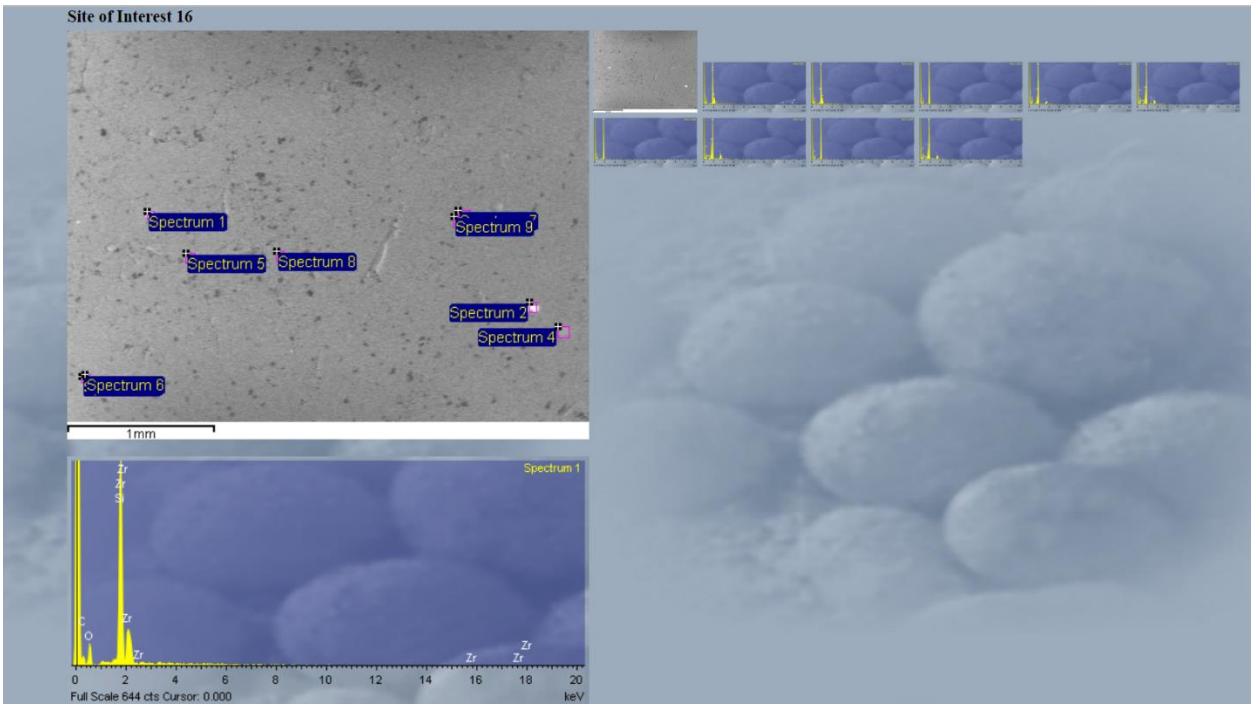

Notes

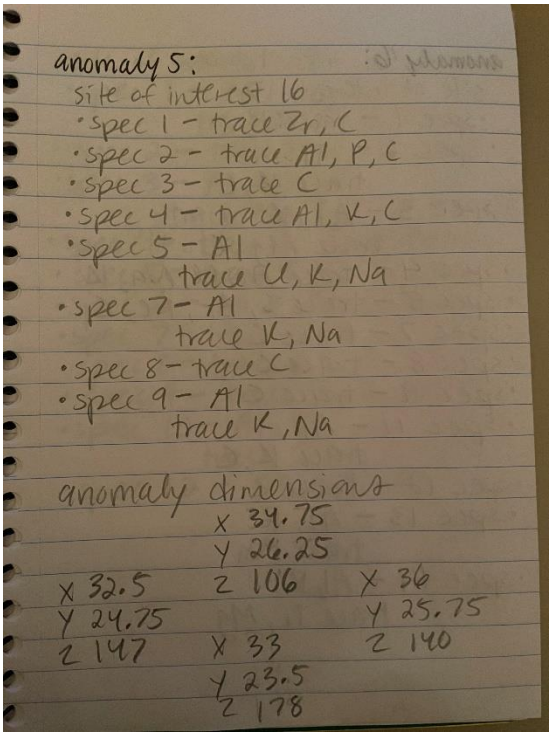
anomaly 5:
site of interest 16
• spec 1 - trace Zr, C
• spec 2 - trace Al, P, C
• spec 3 - trace C
• spec 4 - trace Al, K, C
• spec 5 - Al
trace U, K, Na
• spec 7 - Al
trace K, Na
• spec 8 - trace C
• spec 9 - Al
trace K, Na
anomaly dimensions
X 34.75
Y 26.25
X 32.5
Y 24.75
Z 147
Z 106
X 33
Y 23.5
Z 178
X 36
Y 25.75
Z 140

Anomaly 6:

Site of interest 17

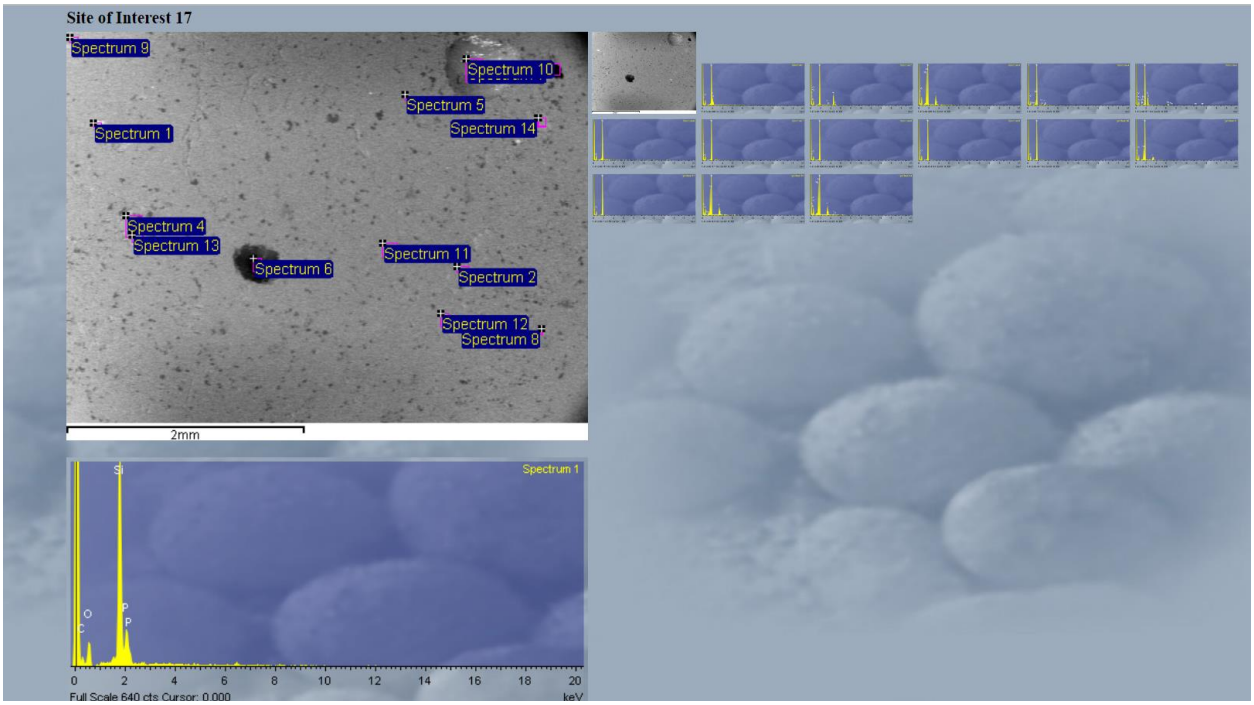

Site of interest 19

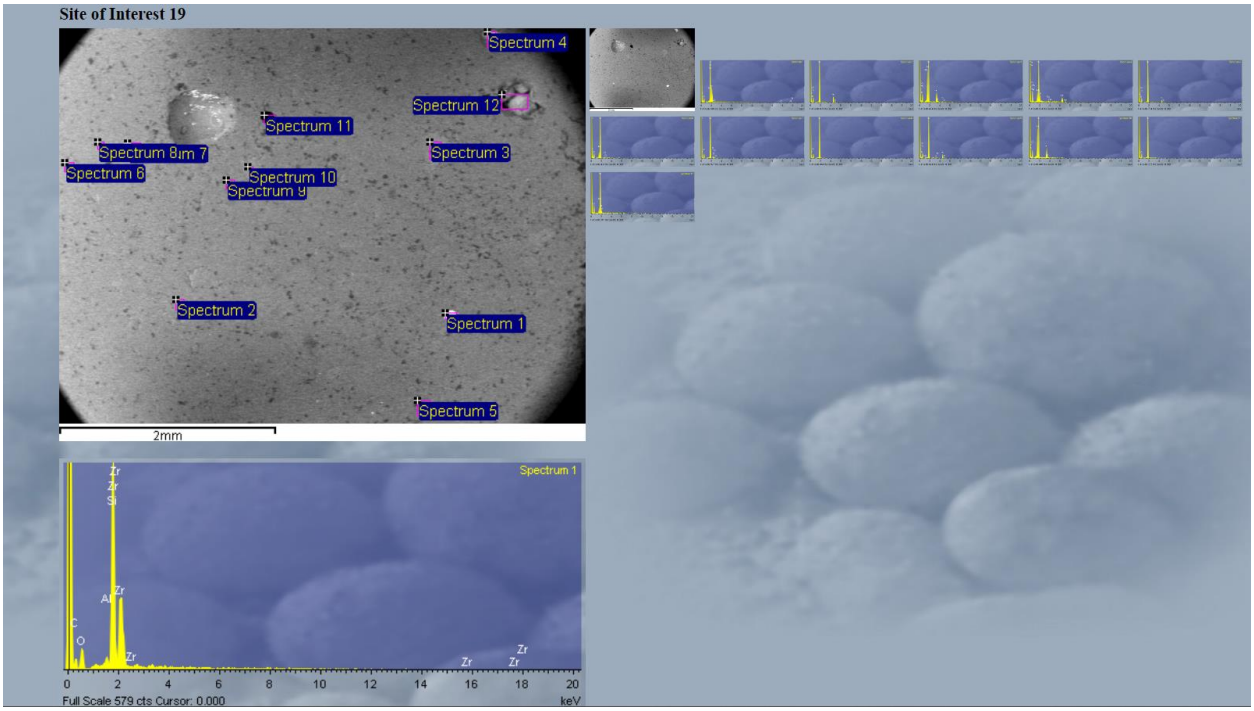

Notes

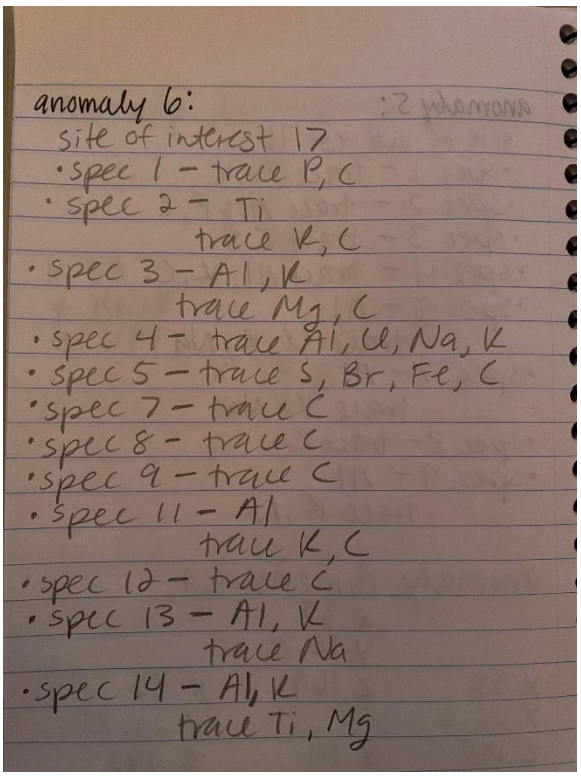
anomaly 6:
site of interest 17
- spec 1 – trace P, C
- spec 2 – Ti
  trace K, C
- spec 3 – Al, K
  trace Mg, C
- spec 4 – trace Al, Cl, Na, K
- spec 5 – trace S, Br, Fe, C
- spec 7 – trace C
- spec 8 – trace C
- spec 9 – trace C
- spec 11 – Al
  trace K, C
- spec 12 – trace C
- spec 13 – Al, K
  trace Na
- spec 14 – Al, K
  trace Ti, Mg

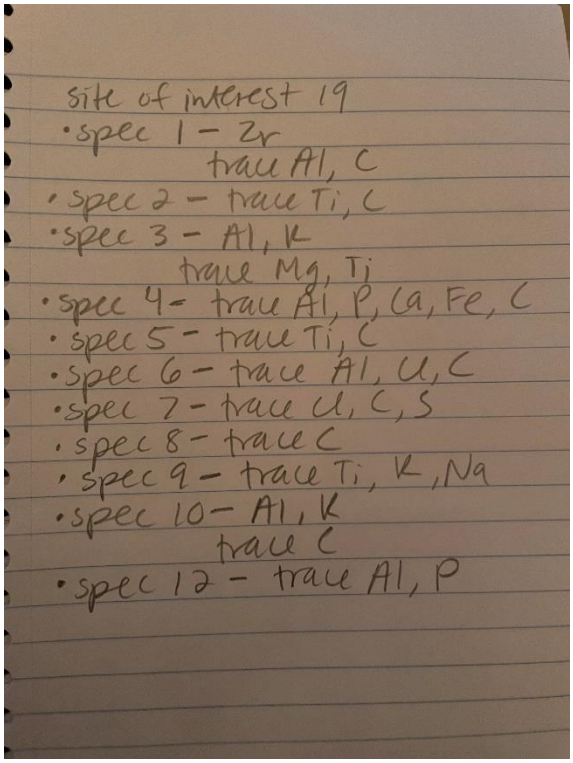
site of interest 19
- spec 1 – Zr
  trace Al, C
- spec 2 – trace Ti, C
- spec 3 – Al, K
  trace Mg, Ti
- spec 4 – trace Al, P, Ca, Fe, C
- spec 5 – trace Ti, C
- spec 6 – trace Al, Cl, C
- spec 7 – trace Cl, C, S
- spec 8 – trace C
- spec 9 – trace Ti, K, Na
- spec 10 – Al, K
  trace C
- spec 12 – trace Al, P

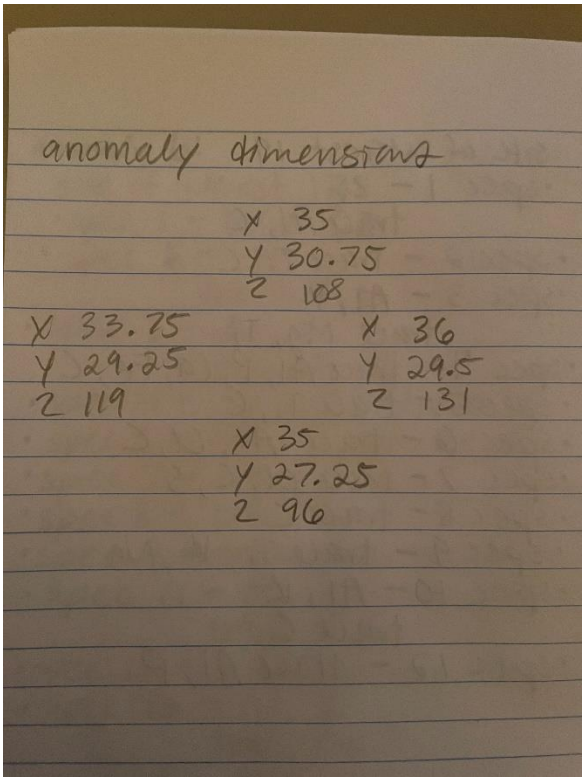
anomaly dimensions

X 35
Y 30.75
Z 108

X 33.75
Y 29.25
Z 119

X 36
Y 29.5
Z 131

X 35
Y 27.25
Z 96

Anomaly 7:

Site of interest 18

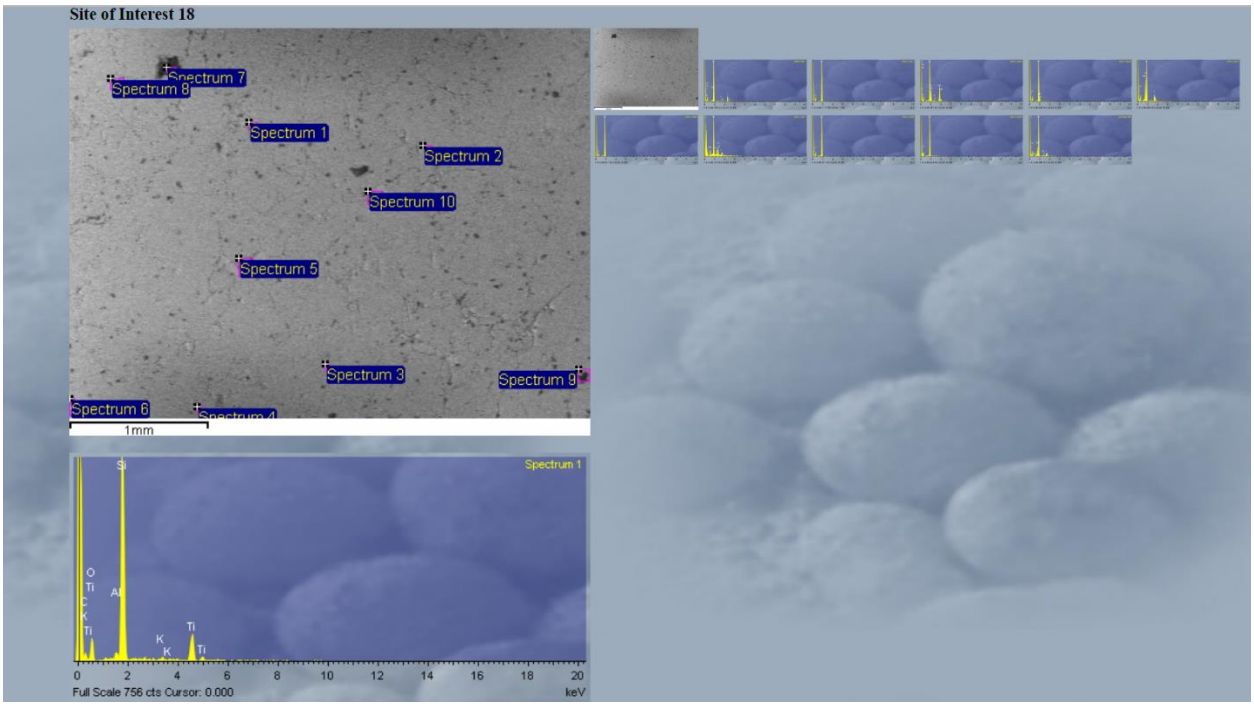

Notes

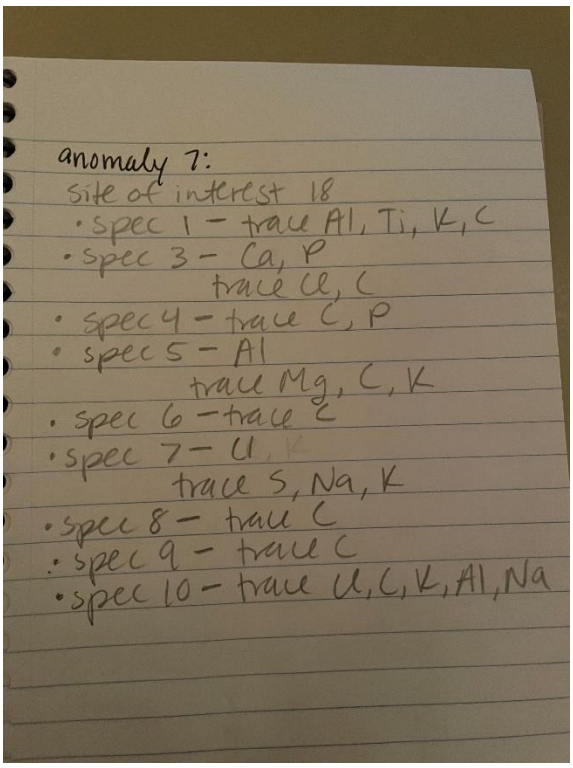
anomaly 7:
site of interest 18
• spec 1 – trace Al, Ti, K, C
• spec 3 – Ca, P
trace Cl, C
• spec 4 – trace C, P
• spec 5 – Al
trace Mg, C, K
• spec 6 – trace C
• spec 7 – Cl
trace S, Na, K
• spec 8 – trace C
• spec 9 – trace C
• spec 10 – trace Cl, C, K, Al, Na

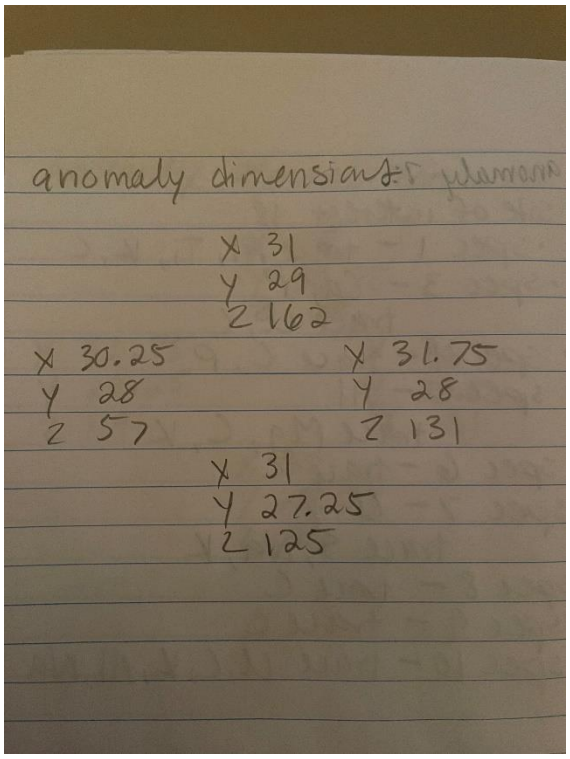
anomaly dimensions: plume
X 31
Y 29
Z 162
X 30.25
Y 28
Z 57
X 31.75
Y 28
Z 131
X 31
Y 27.25
Z 125

Anomaly 8:

Site of interest 20

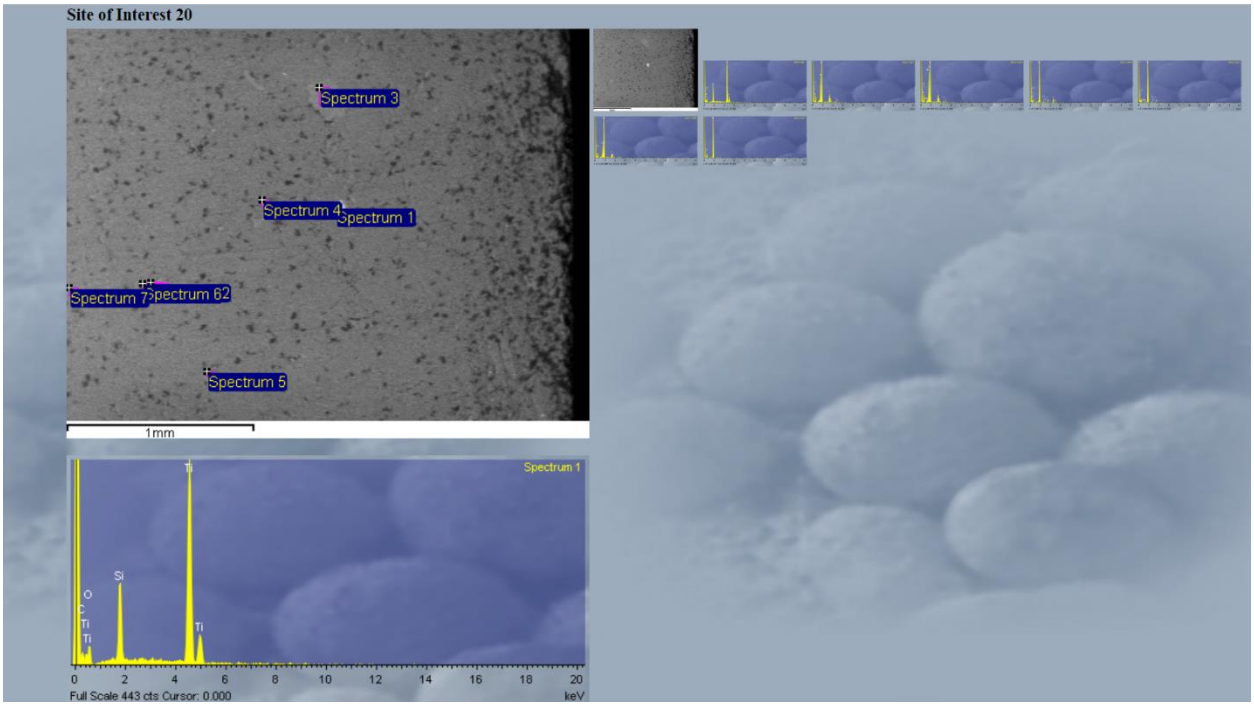

Notes

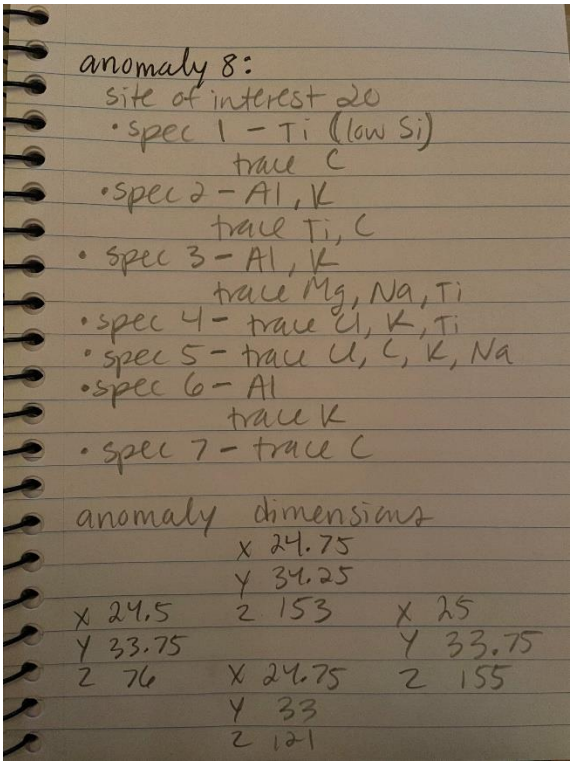
anomaly 8:
site of interest 20
• spec 1 – Ti (low Si)
trace C
• spec 2 – Al, K
trace Ti, C
• spec 3 – Al, K
trace Mg, Na, Ti
• spec 4 – trace Cl, K, Ti
• spec 5 – trace Cl, C, K, Na
• spec 6 – Al
trace K
• spec 7 – trace C
anomaly dimensions
X 24.75
Y 34.25
Z 153
X 24.5
Y 33.75
Z 76
X 25
Y 33.75
Z 155
X 24.75
Y 33
Z 121

HRQ1-2

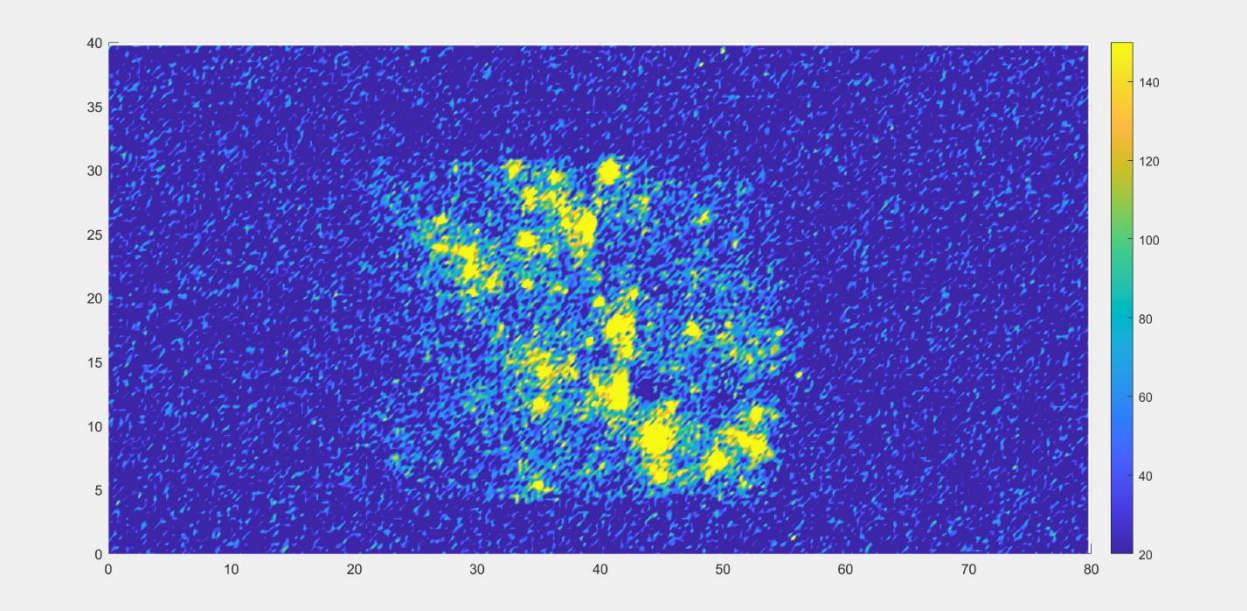

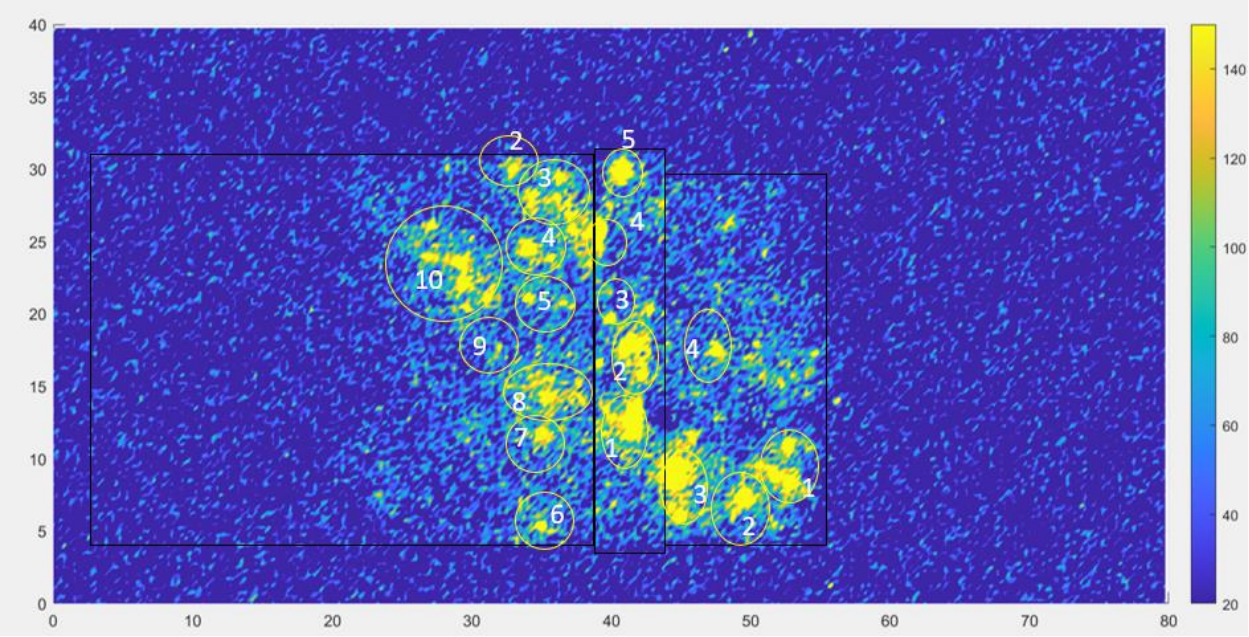

Bottom piece

Anomaly 1:

Site of interest 4

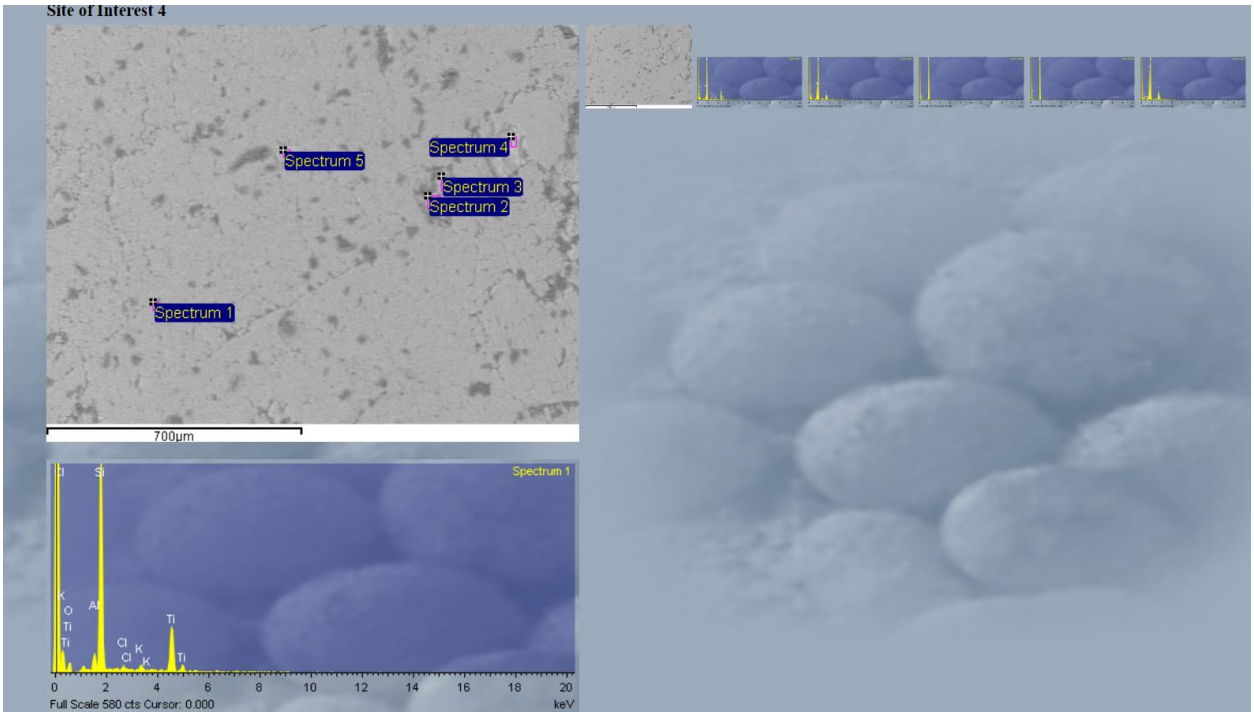

Notes

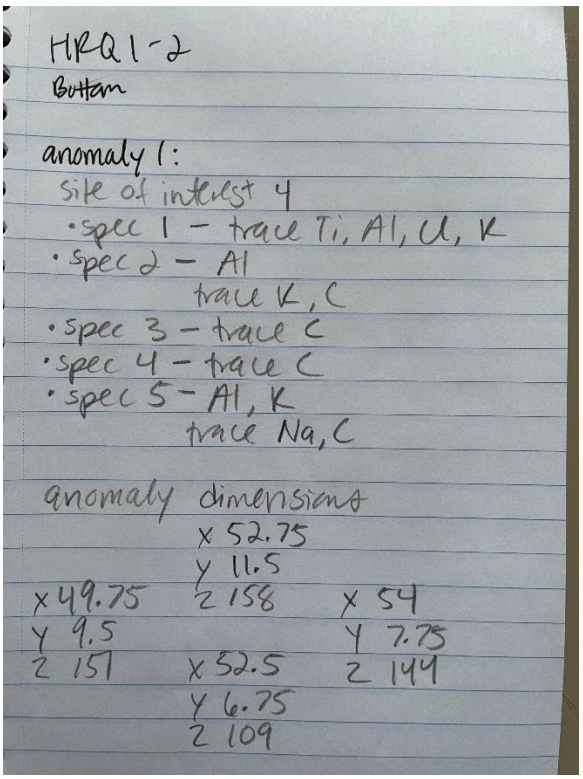
HRQ1-2
Bottom
anomaly 1:
site of interest 4
• spec 1 – trace Ti, Al, Cl, K
• spec 2 – Al
trace K, C
• spec 3 – trace C
• spec 4 – trace C
• spec 5 – Al, K
trace Na, C
anomaly dimensions
x 52.75
y 11.5
z 158
x 49.75
y 9.5
z 151
x 54
y 7.75
z 144
x 52.5
y 6.75
z 109

Anomaly 2:

Site of interest 5

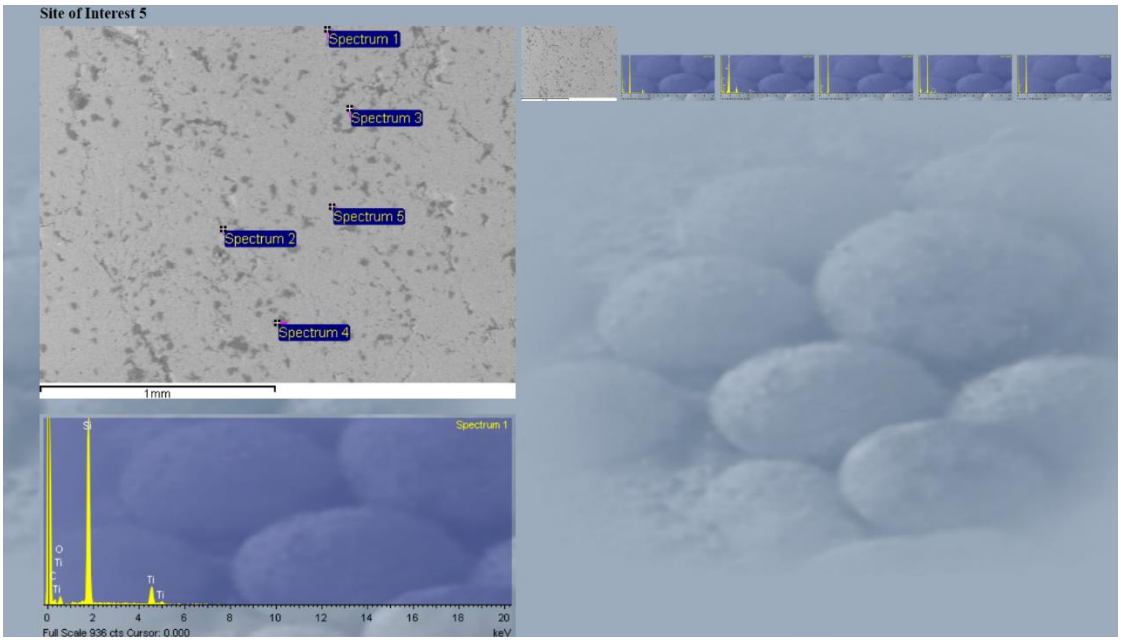

Notes

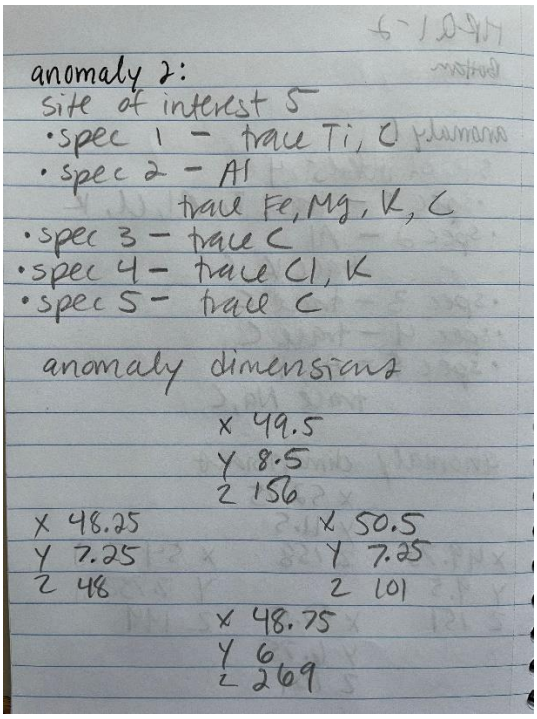
anomaly 2:
site of interest 5
- spec 1 – trace Ti, O
- spec 2 – Al
  trace Fe, Mg, K, C
- spec 3 – trace C
- spec 4 – trace Cl, K
- spec 5 – trace C

anomaly dimensions

X 49.5
Y 8.5
Z 156

X 48.25
Y 7.25
Z 48

X 50.5
Y 7.25
Z 101

X 48.75
Y 6
Z 269

Anomaly 3:

Site of interest 6

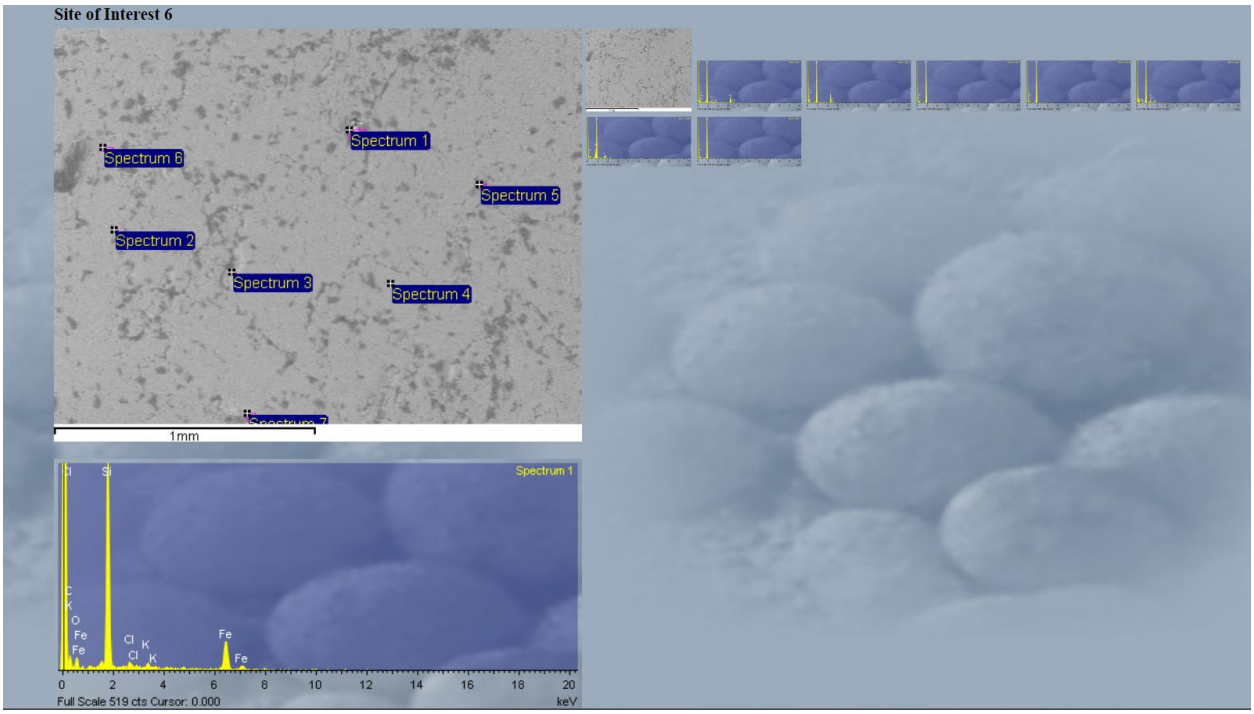

Notes

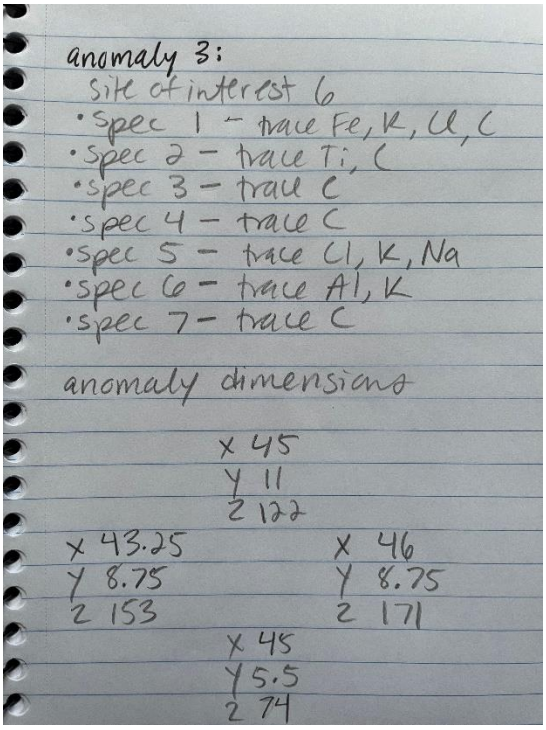
anomaly 3:
site of interest 6
• spec 1 – trace Fe, K, Cl, C
• spec 2 – trace Ti, C
• spec 3 – trace C
• spec 4 – trace C
• spec 5 – trace Cl, K, Na
• spec 6 – trace Al, K
• spec 7 – trace C
anomaly dimensions
x 45
y 11
z 122
x 43.25
y 8.75
z 153
x 46
y 8.75
z 171
x 45
y 5.5
z 74

Anomaly 4:

Site of interest 7

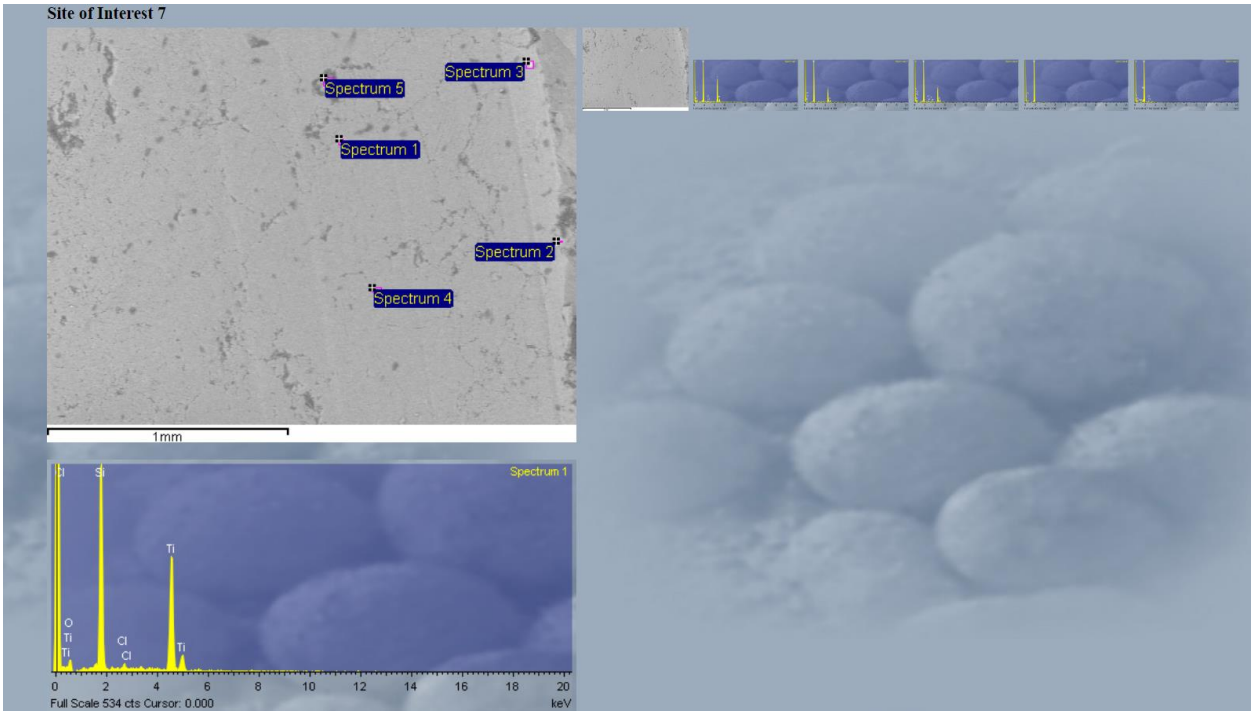

Notes

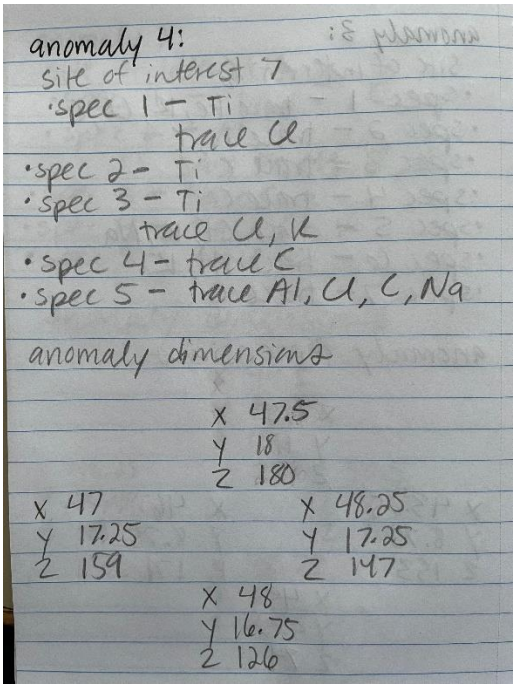
anomaly 4:
site of interest 7
·spec 1 – Ti
trace Cl
·spec 2 – Ti
·spec 3 – Ti
trace Cl, K
·spec 4 – trace C
·spec 5 – trace Al, Cl, C, Na
anomaly dimensions
X 47.5
Y 18
Z 180
X 47
Y 17.25
Z 159
X 48.25
Y 17.25
Z 147
X 48
Y 16.75
Z 126

Middle piece

Anomaly 1:

Site of interest 1

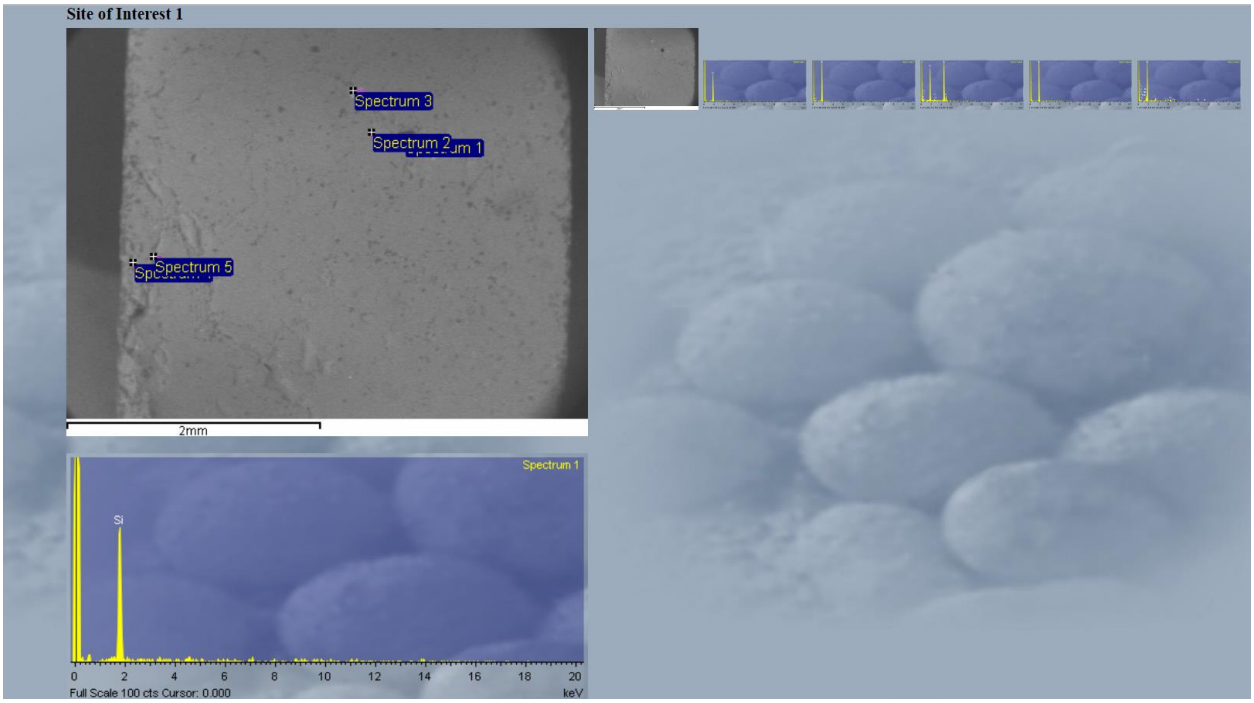

Notes

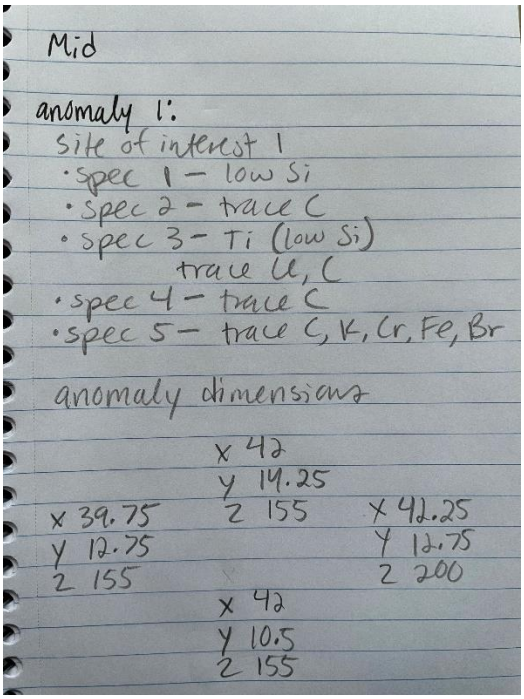
Mid
anomaly 1:
site of interest 1
• spec 1 – low Si
• spec 2 – trace C
• spec 3 – Ti (low Si)
trace Cl, C
• spec 4 – trace C
• spec 5 – trace C, K, Cr, Fe, Br
anomaly dimensions
x 42
y 14.25
z 155
x 39.75
y 12.75
z 155
x 42.25
y 12.75
z 200
x 42
y 10.5
z 155

Anomaly 2:

Site of interest 2

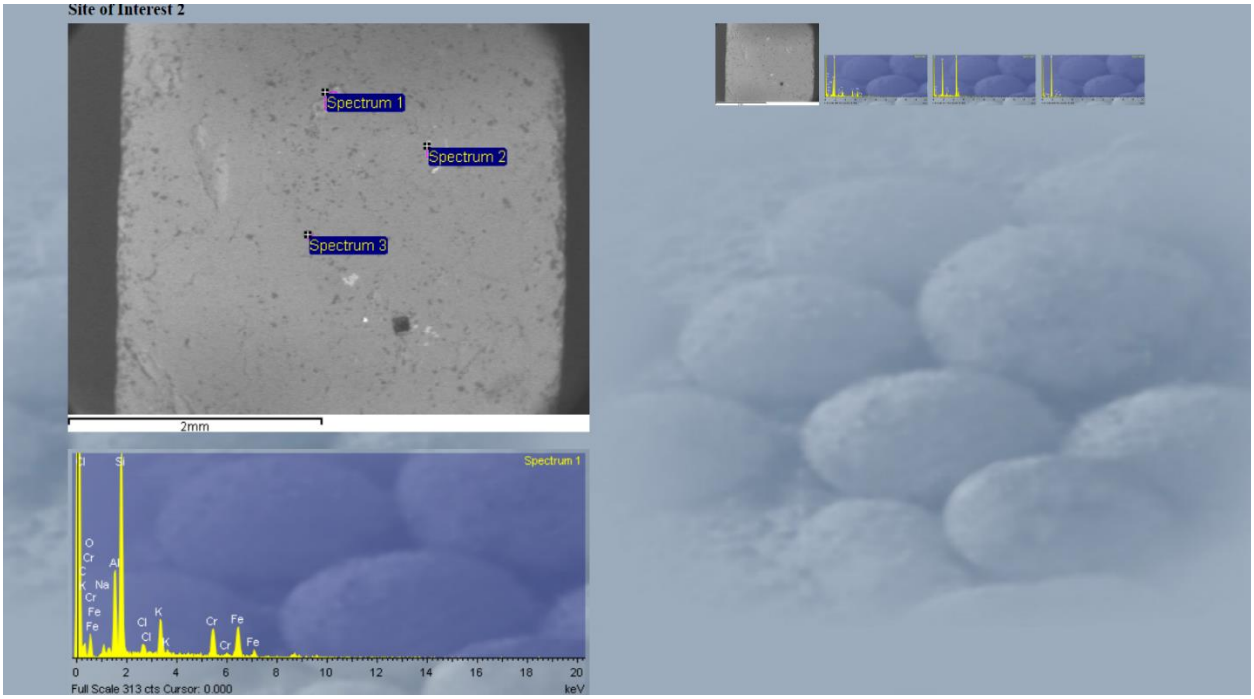

Notes

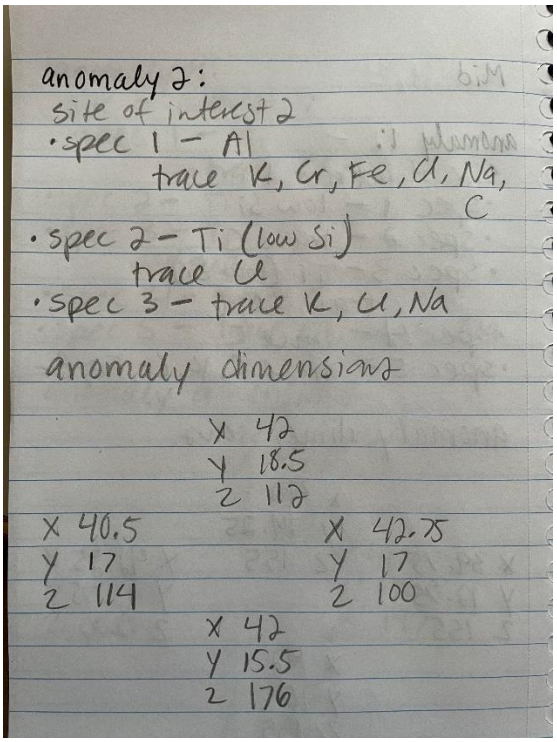
anomaly 2:
site of interest 2
• spec 1 – Al
trace K, Cr, Fe, Cl, Na, C
• spec 2 – Ti (low Si)
trace Cl
• spec 3 – trace K, Cl, Na
anomaly dimensions
X 42
Y 18.5
Z 117
X 40.5
Y 17
Z 114
X 42.75
Y 17
Z 100
X 42
Y 15.5
Z 176

Anomaly 3:

Site of interest 3

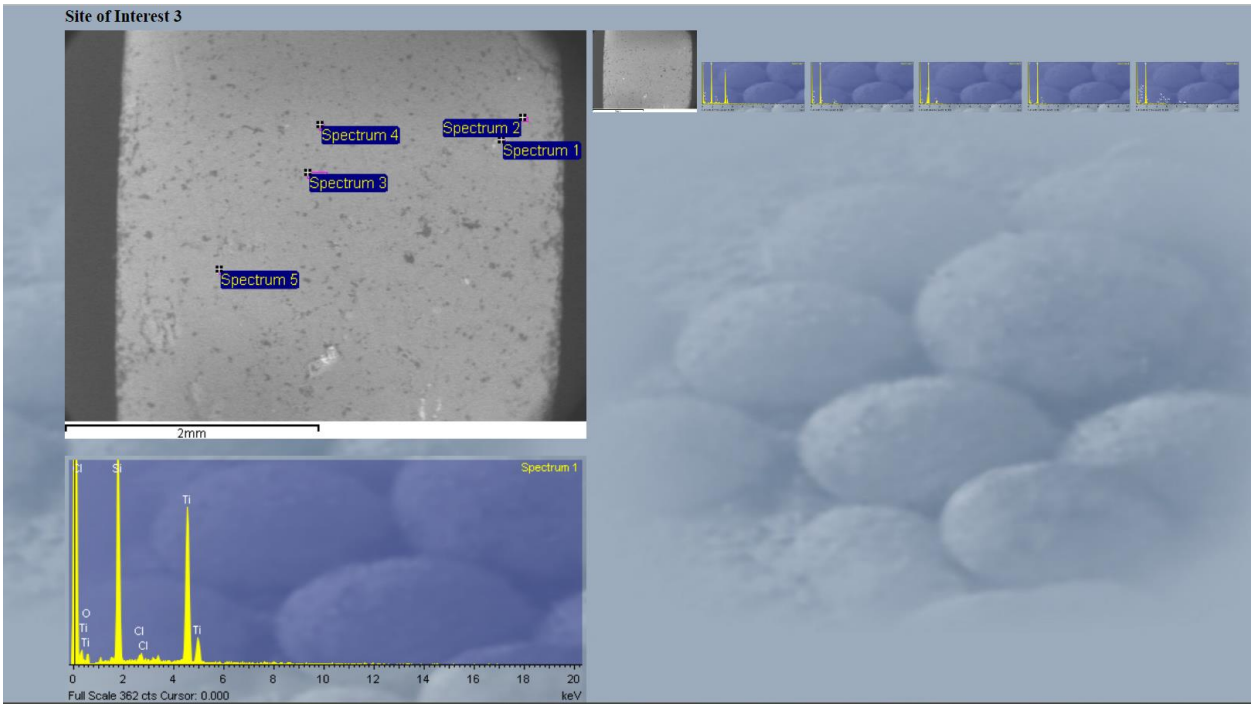

Notes

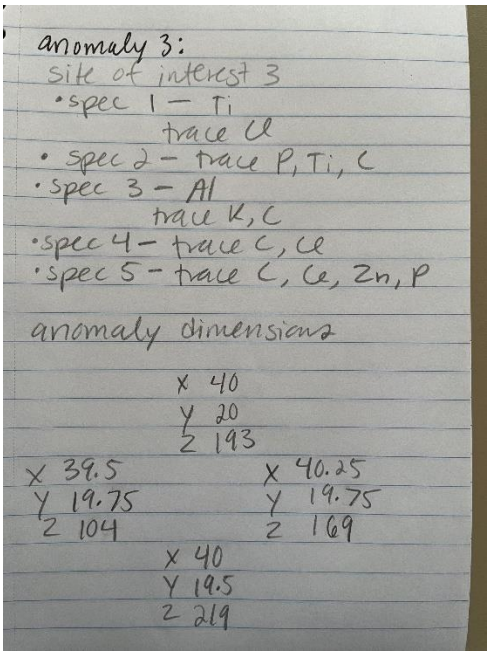

Anomaly 4:

Site of interest 4

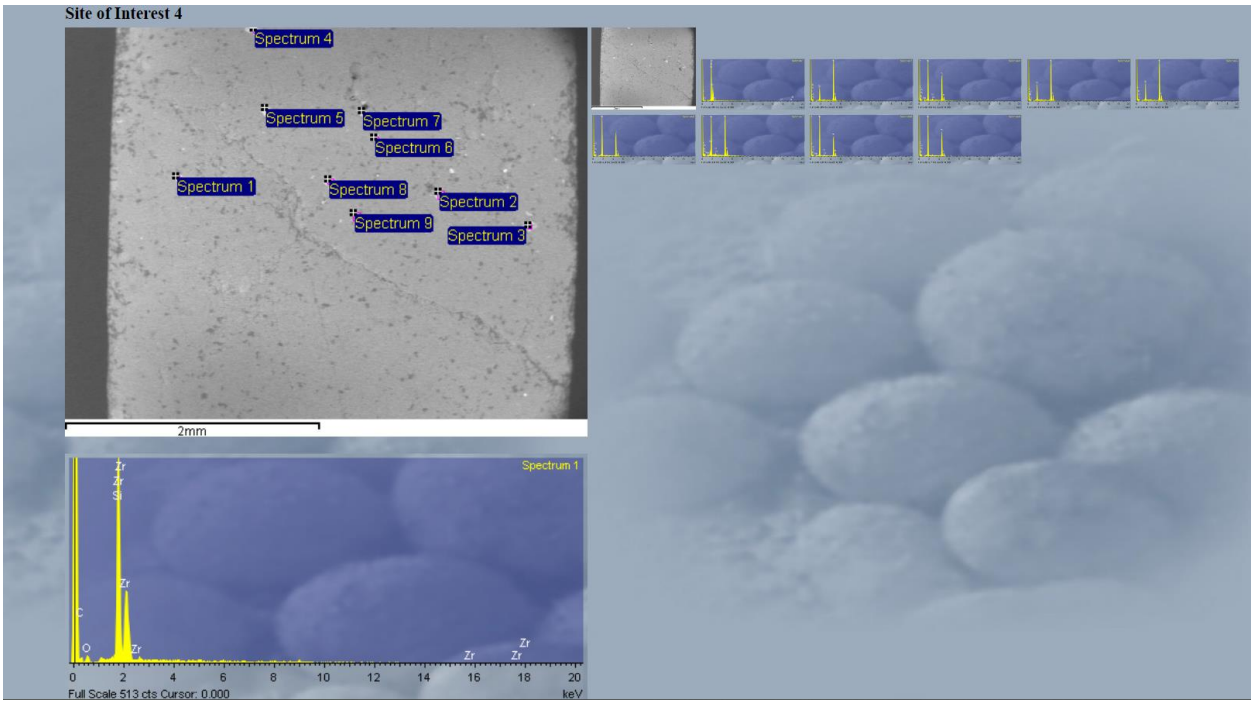

Site of interest 5

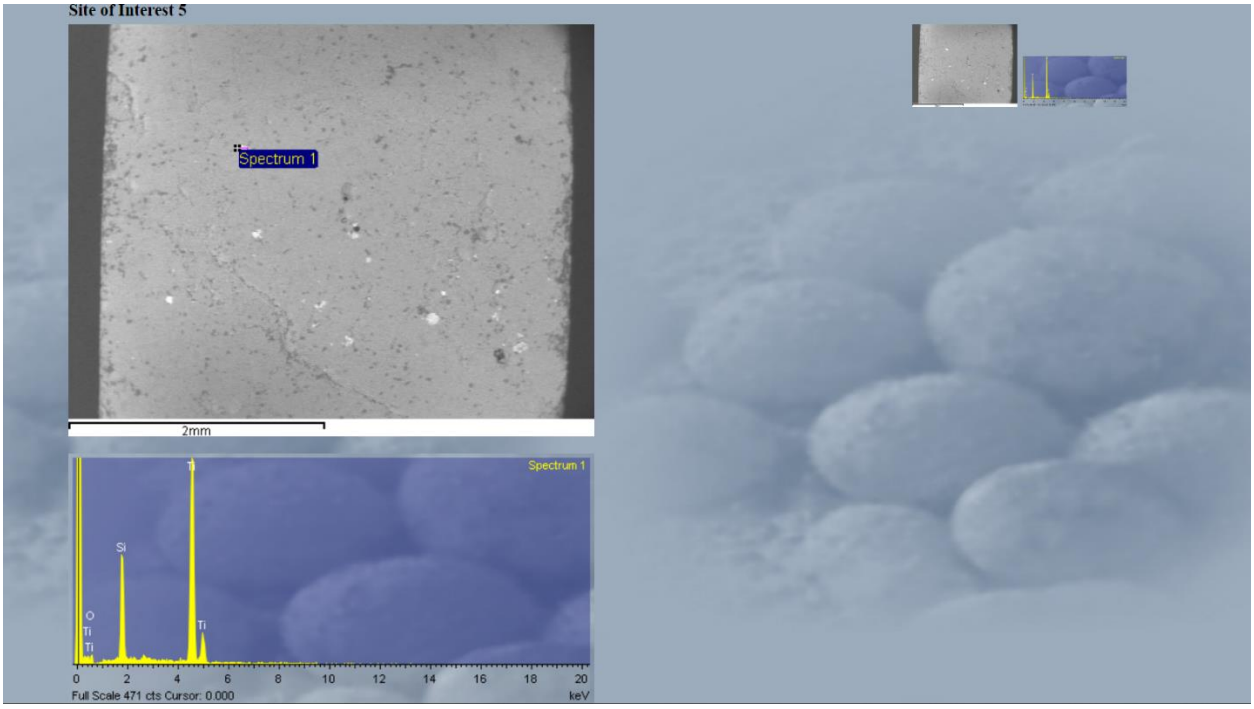

Notes

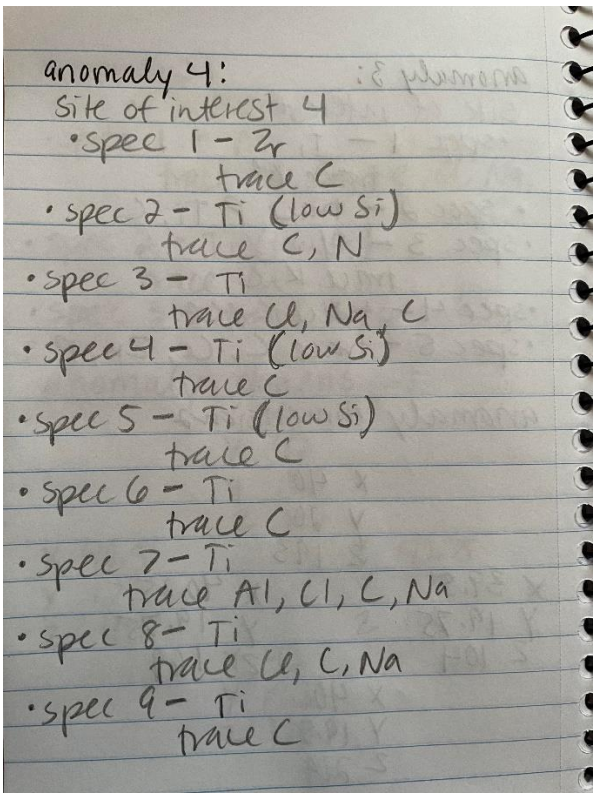
anomaly 4:
site of interest 4
- spec 1 - Zr
  trace C
- spec 2 - Ti (low Si)
  trace C, N
- spec 3 - Ti
  trace Cl, Na, C
- spec 4 - Ti (low Si)
  trace C
- spec 5 - Ti (low Si)
  trace C
- spec 6 - Ti
  trace C
- spec 7 - Ti
  trace Al, Cl, C, Na
- spec 8 - Ti
  trace Cl, C, Na
- spec 9 - Ti
  trace C

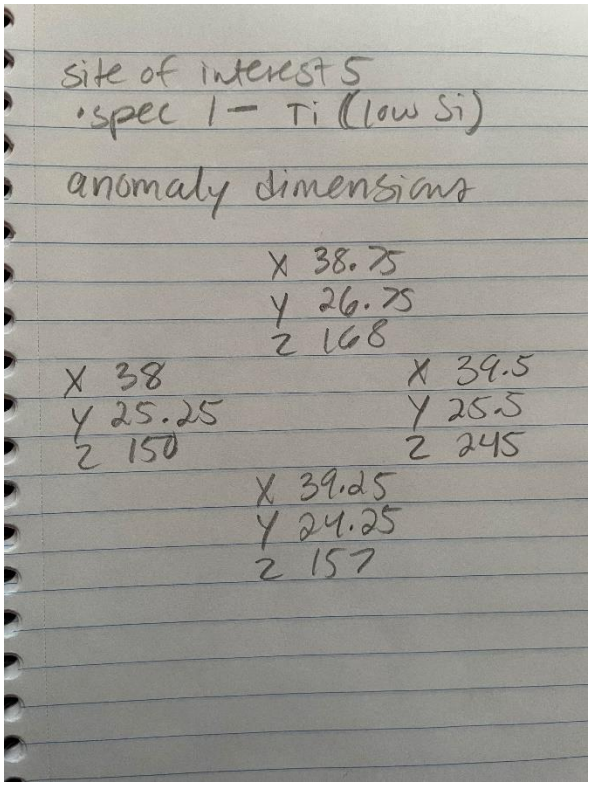
site of interest 5
- spec 1 - Ti (low Si)

anomaly dimensions

X 38.75
Y 26.75
Z 168

X 38
Y 25.25
Z 150

X 39.5
Y 25.5
Z 245

X 39.25
Y 24.25
Z 157

Anomaly 5:

Site of interest 6

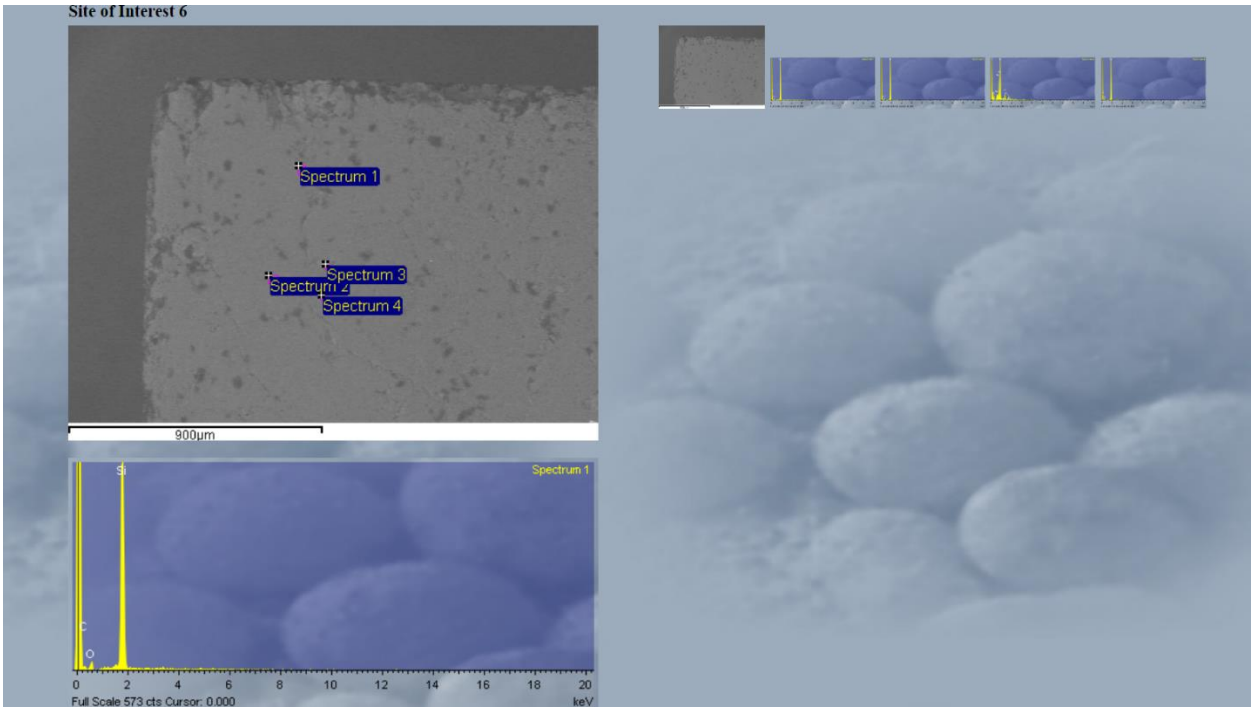

Notes

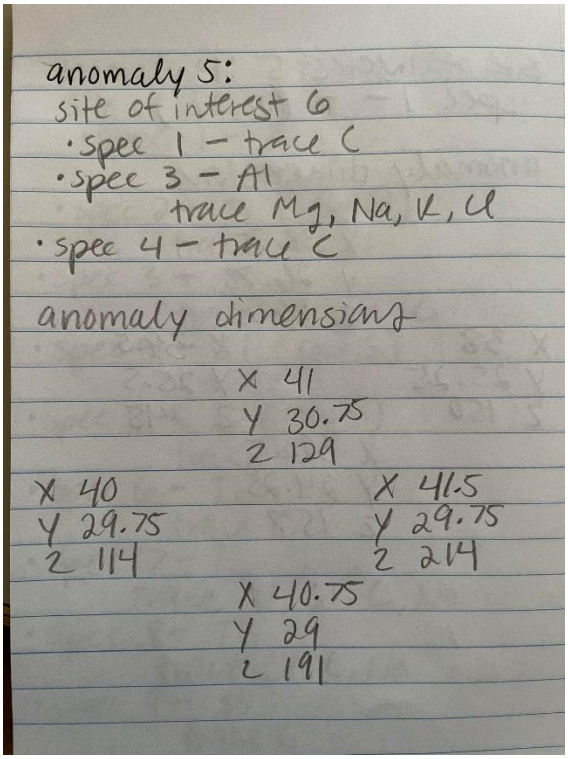
anomaly 5:
site of interest 6
• spec 1 – trace C
• spec 3 – Al
trace Mg, Na, K, Cl
• spec 4 – trace C
anomaly dimensions
X 41
Y 30.75
Z 129
X 40
Y 29.75
Z 114
X 41.5
Y 29.75
Z 214
X 40.75
Y 29
Z 191

Front piece

Anomaly 2:

Site of interest 2

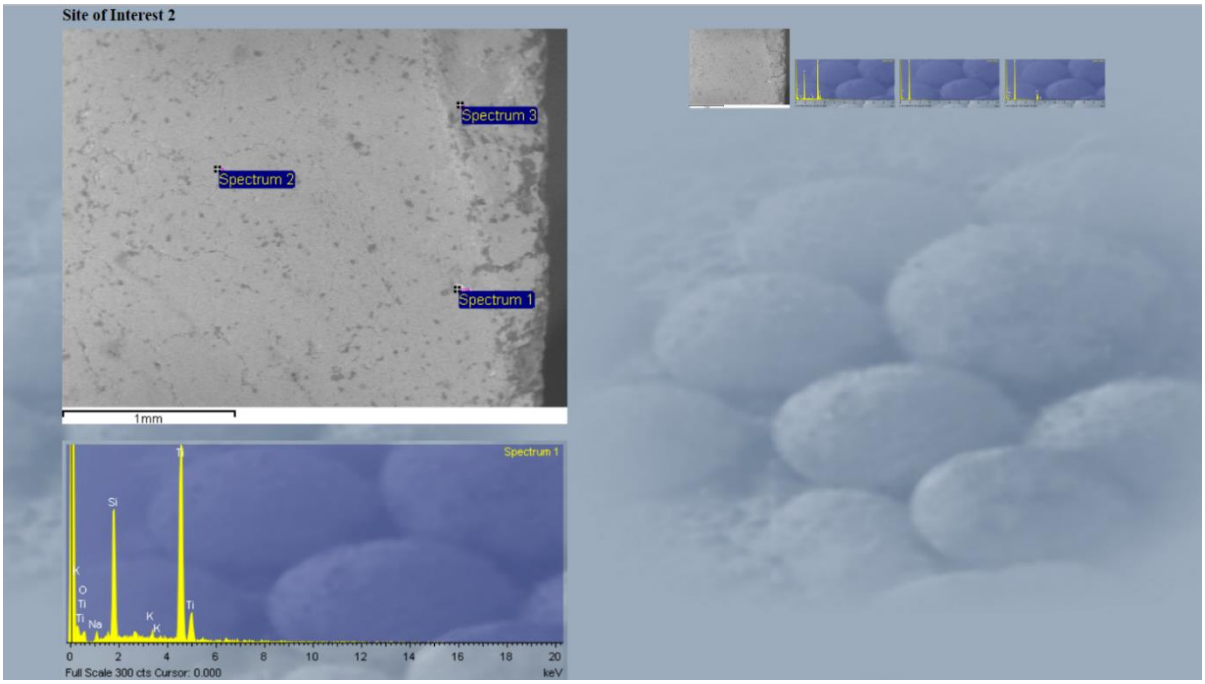

Notes

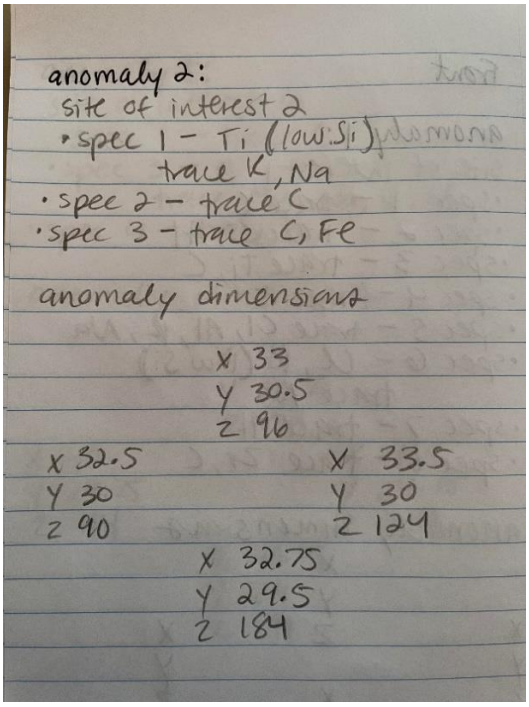
anomaly 2:
site of interest 2
• spec 1 - Ti (low Si)
trace K, Na
• spec 2 - trace C
• spec 3 - trace C, Fe
anomaly dimensions
X 33
Y 30.5
Z 96
X 32.5
Y 30
Z 90
X 33.5
Y 30
Z 124
X 32.75
Y 29.5
Z 184

Anomaly 3:

Site of interest 3

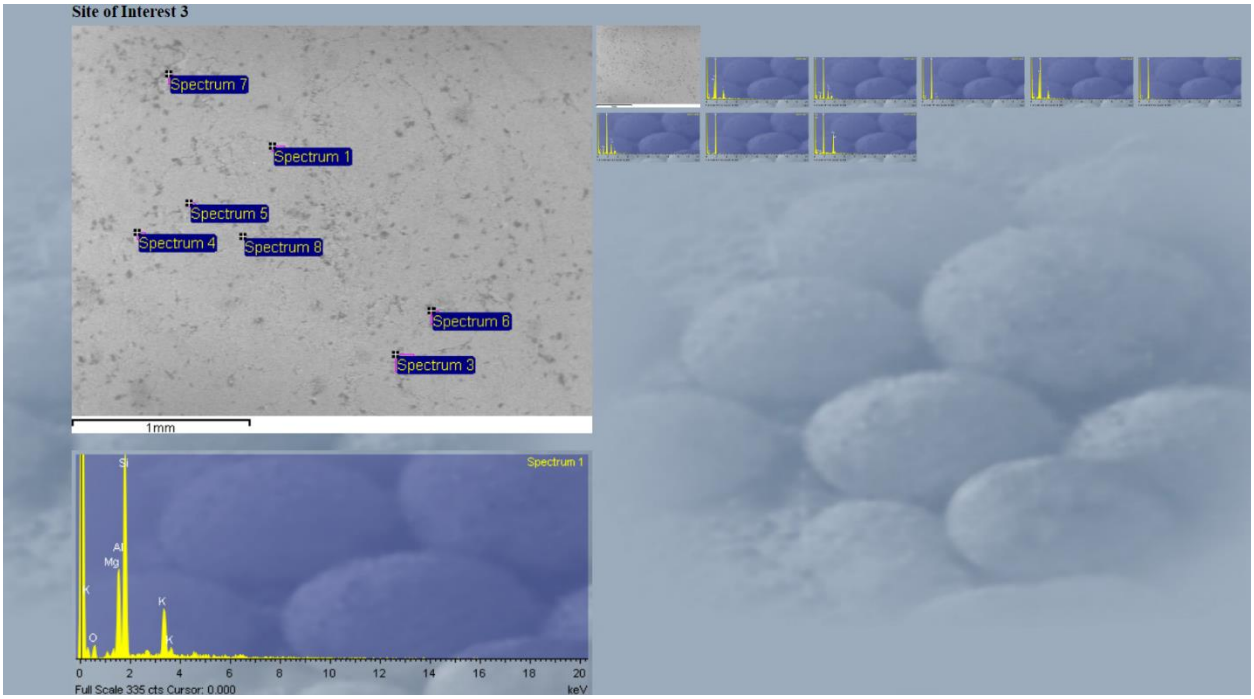

Notes

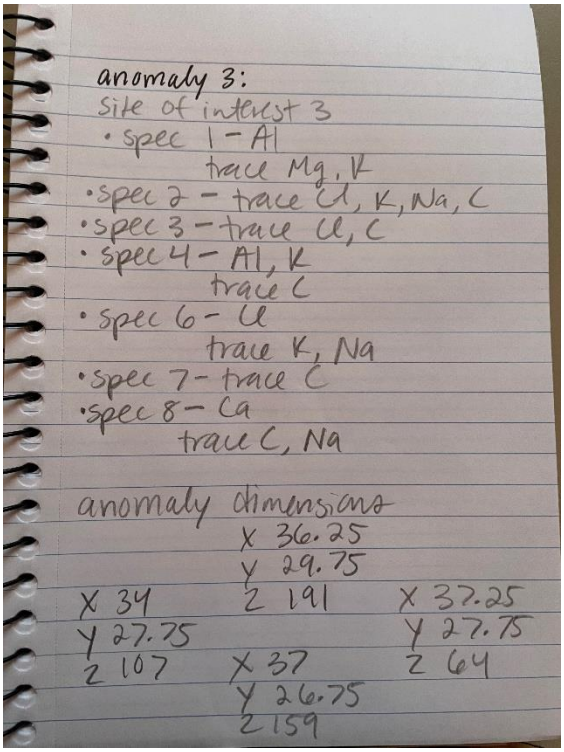
anomaly 3:
site of interest 3
• spec 1 - Al
trace Mg, K
• spec 2 - trace Cl, K, Na, C
• spec 3 - trace Cl, C
• spec 4 - Al, K
trace C
• spec 6 - Cl
trace K, Na
• spec 7 - trace C
• spec 8 - Ca
trace C, Na
anomaly dimensions
X 36.25
Y 29.75
Z 191
X 34
Y 27.75
Z 107
X 37.25
Y 27.75
Z 64
X 37
Y 26.75
Z 159

Anomaly 4:

Site of interest 4

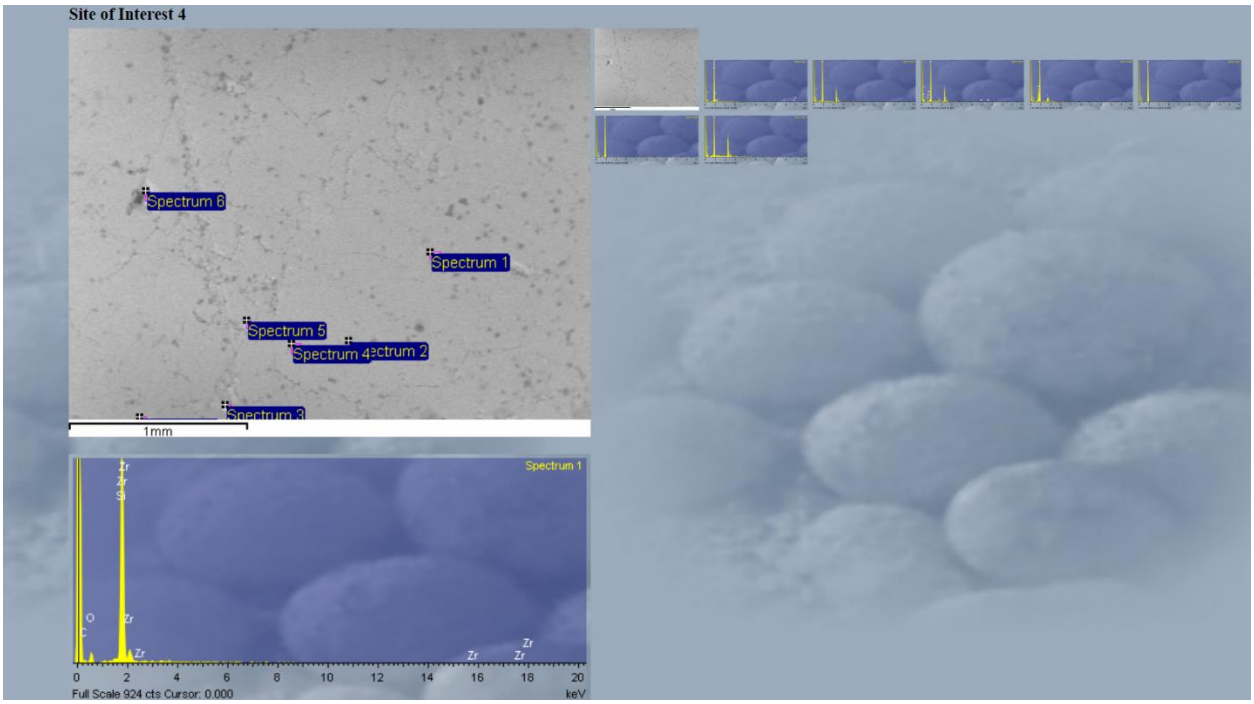

Site of interest 5

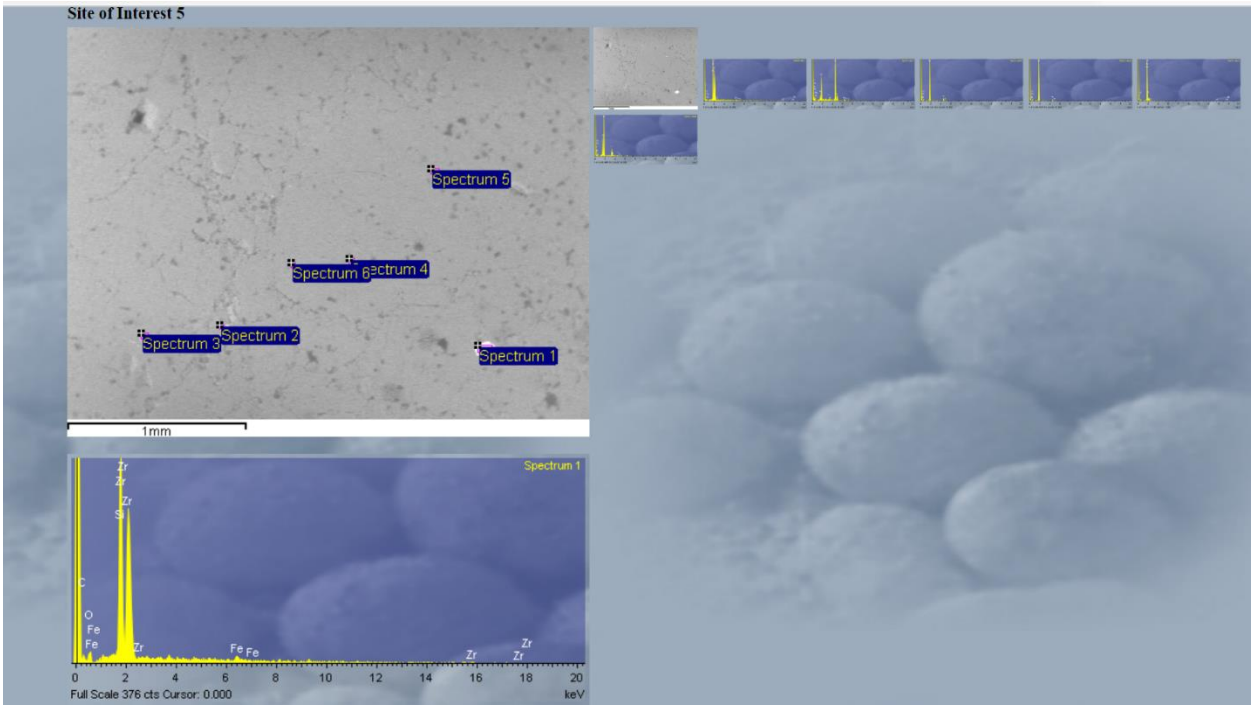

Notes

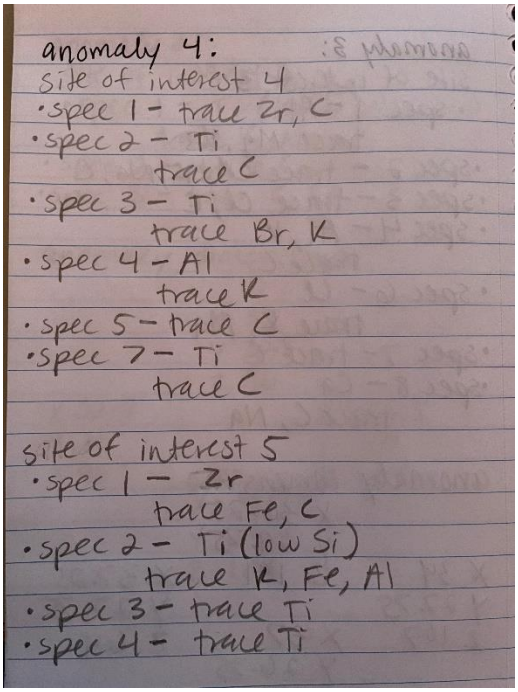

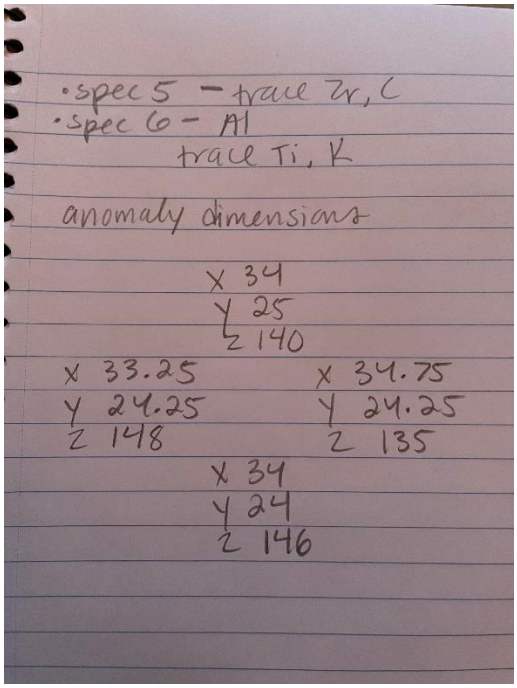

Anomaly 5:

Site of interest 6

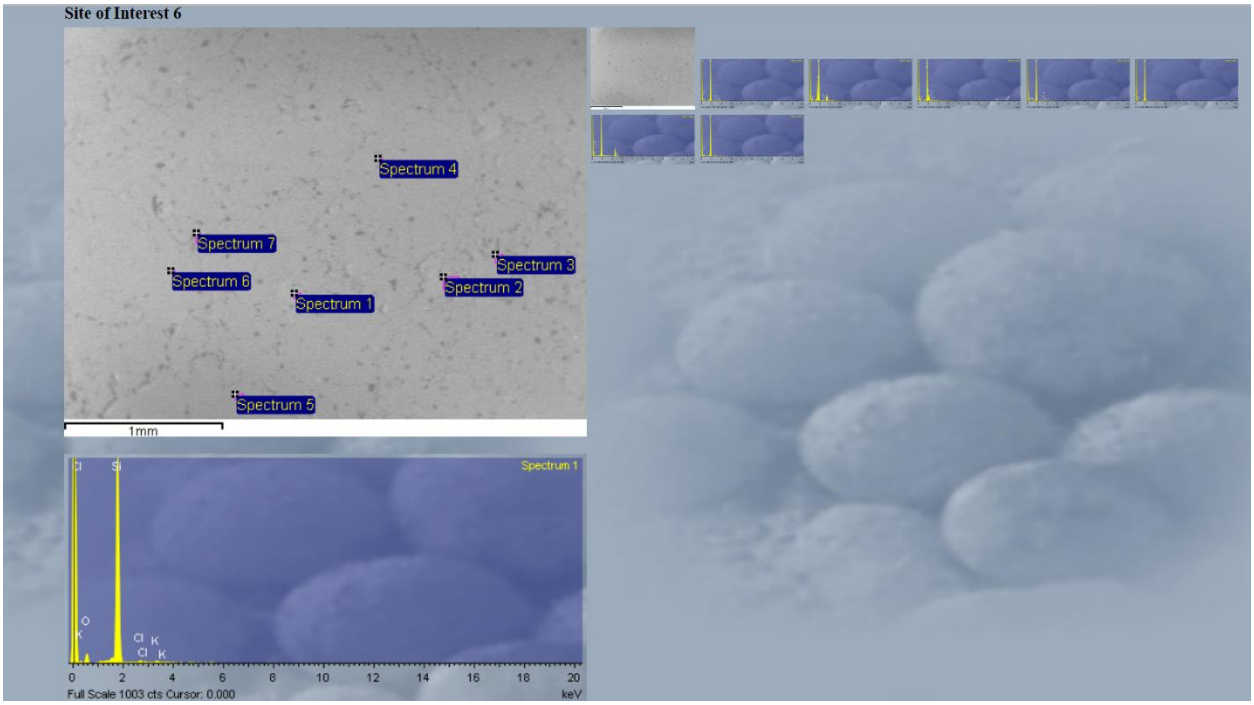

Notes

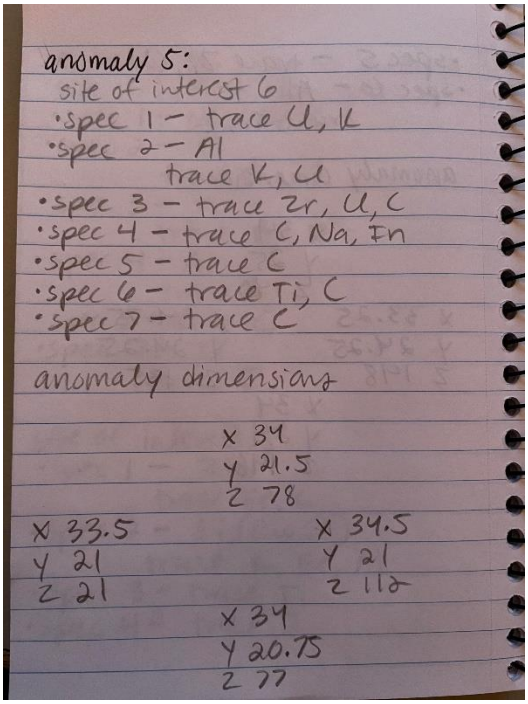
anomaly 5:
site of interest 6
•spec 1 – trace U, K
•spec 2 – Al
trace K, U
•spec 3 – trace Zr, U, C
•spec 4 – trace C, Na, Fn
•spec 5 – trace C
•spec 6 – trace Ti, C
•spec 7 – trace C
anomaly dimensions
X 34
Y 21.5
Z 78
X 33.5
Y 21
Z 21
X 34.5
Y 21
Z 112
X 34
Y 20.75
Z 77

Anomaly 6:

Site of interest 7

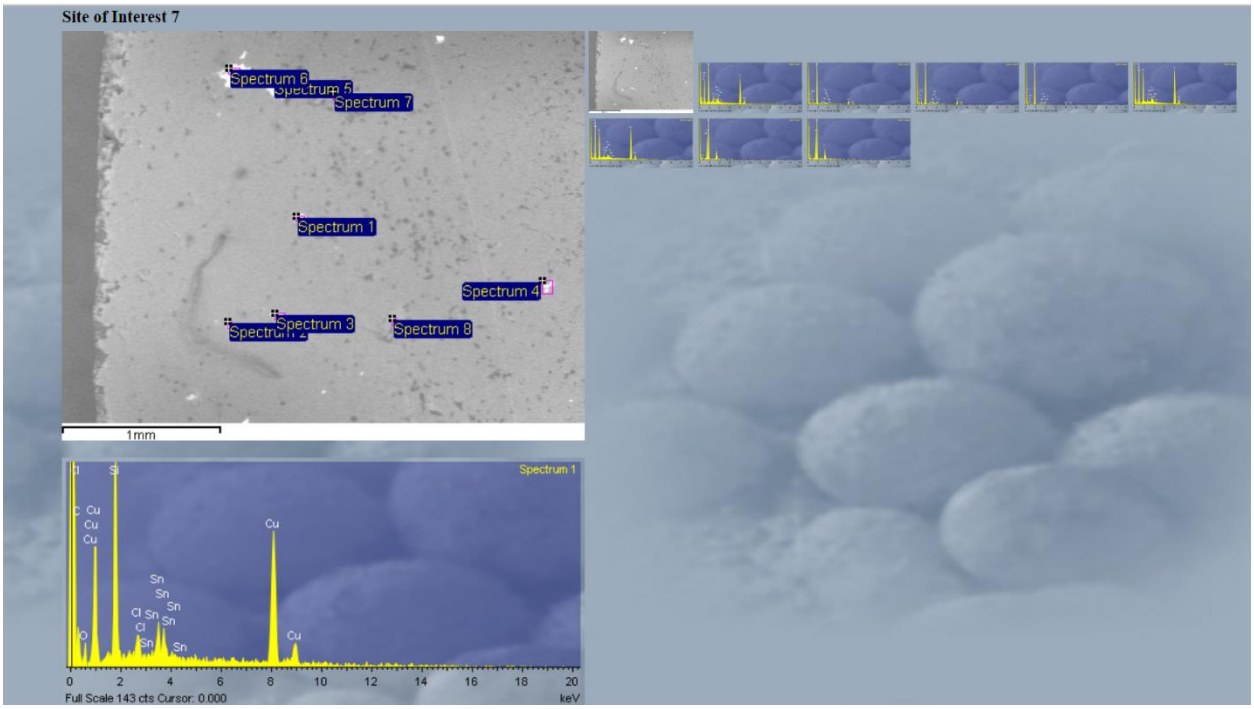

Notes

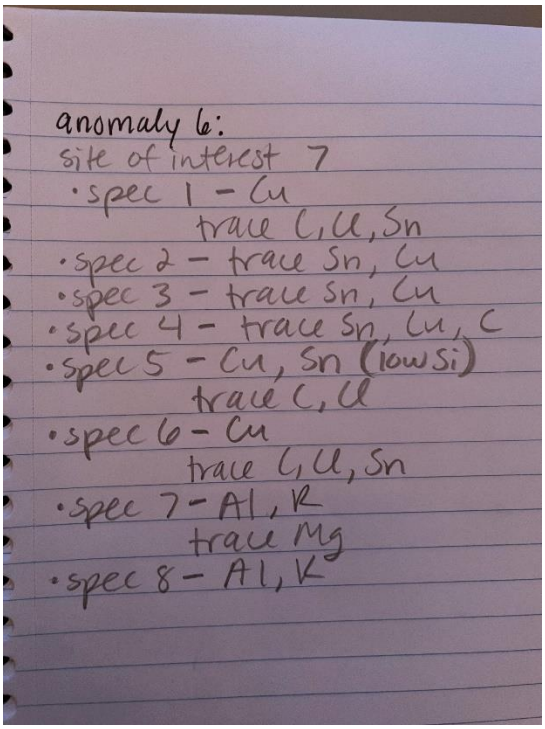
anomaly 6:
site of interest 7
• spec 1 - Cu
trace C, Cl, Sn
• spec 2 - trace Sn, Cu
• spec 3 - trace Sn, Cu
• spec 4 - trace Sn, Cu, C
• spec 5 - Cu, Sn (low Si)
trace C, Cl
• spec 6 - Cu
trace C, Cl, Sn
• spec 7 - Al, K
trace Mg
• spec 8 - Al, K

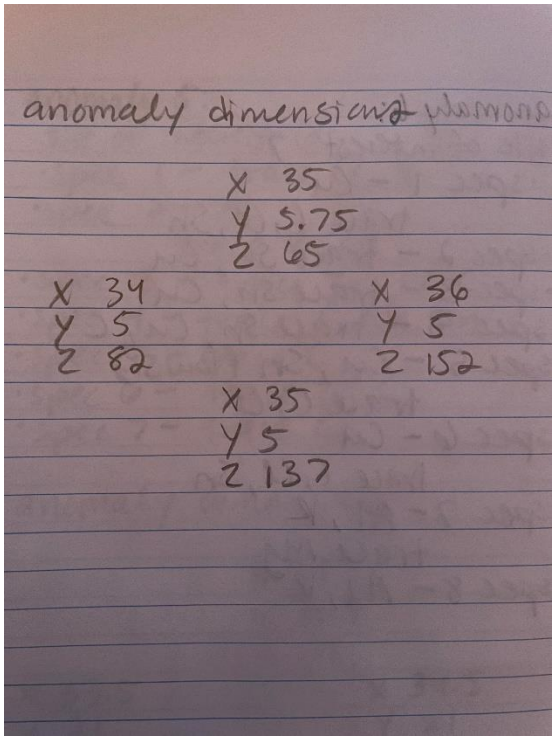
anomaly dimensional
X 35
Y 5.75
Z 65
X 34
Y 5
Z 82
X 36
Y 5
Z 152
X 35
Y 5
Z 137

Anomaly 7:

Site of interest 8

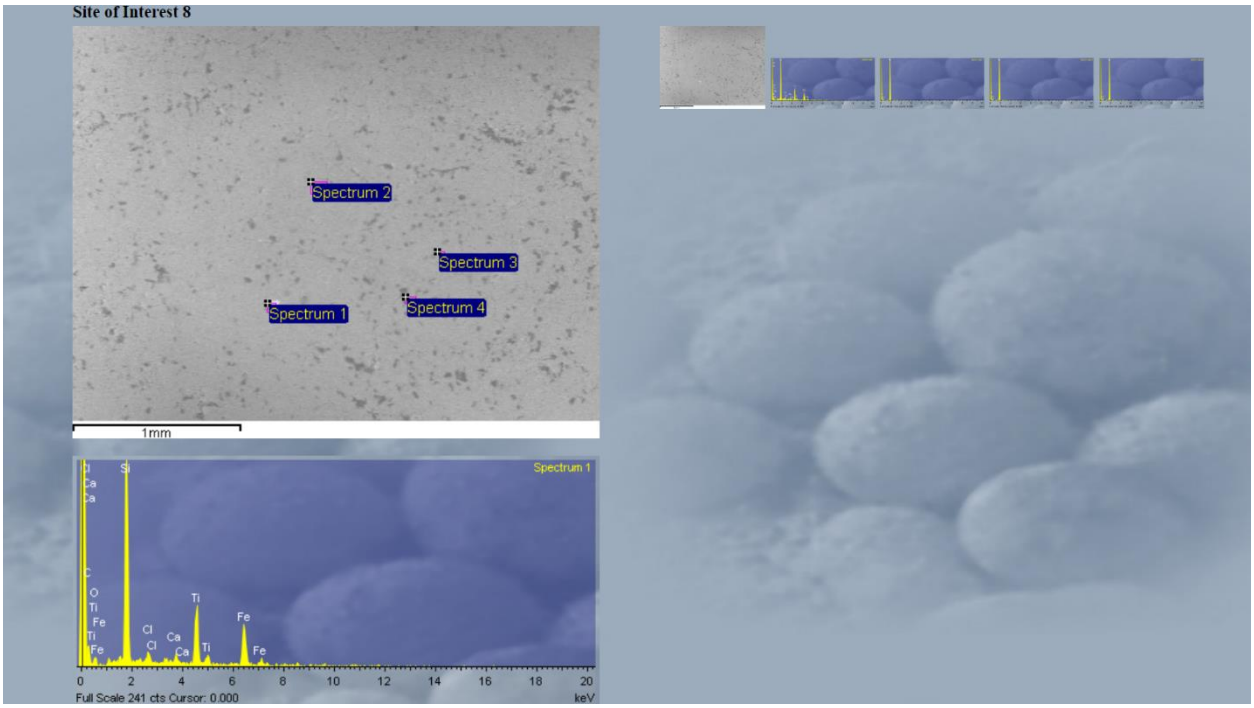

Notes

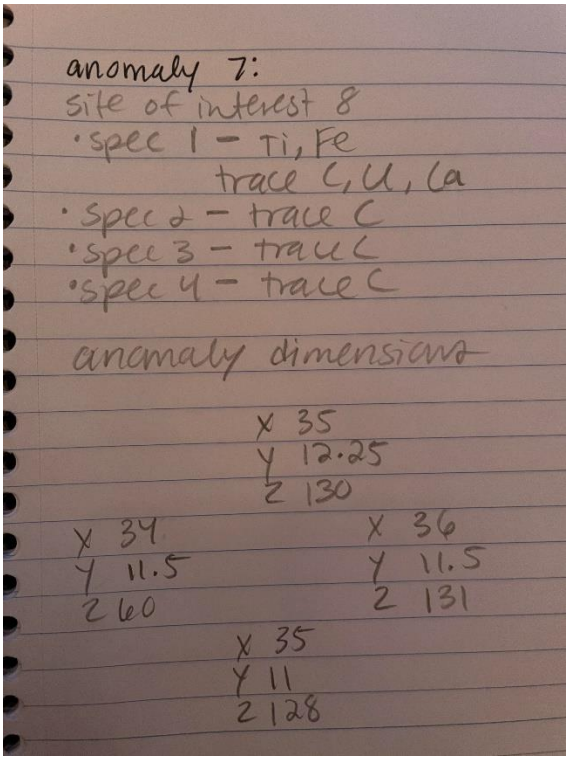
anomaly 7:
site of interest 8
• spec 1 – Ti, Fe
trace C, U, Ca
• spec 2 – trace C
• spec 3 – trace C
• spec 4 – trace C
anomaly dimensions
X 35
Y 12.25
Z 130
X 34
Y 11.5
Z 60
X 36
Y 11.5
Z 131
X 35
Y 11
Z 128

Anomaly 8:

Site of interest 9

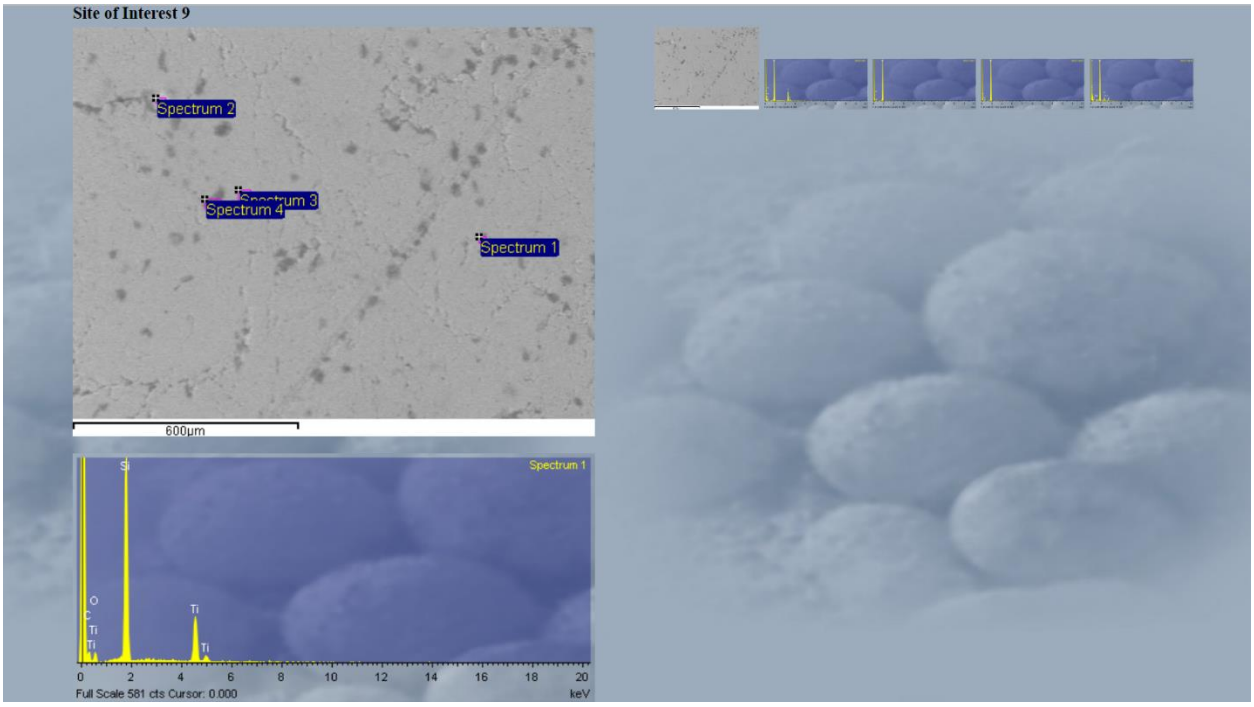

Notes

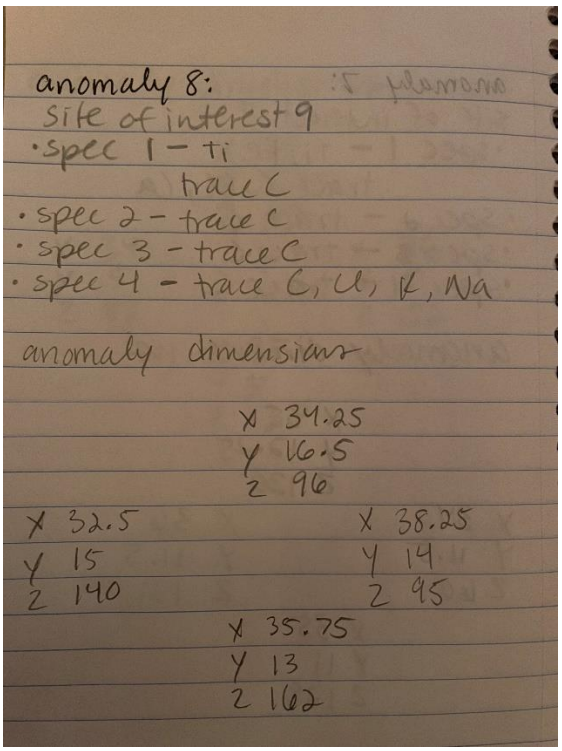
anomaly 8:
site of interest 9
• spec 1 - Ti
trace C
• spec 2 - trace C
• spec 3 - trace C
• spec 4 - trace C, Cl, K, Na
anomaly dimensions
X 34.25
Y 16.5
Z 96
X 32.5
Y 15
Z 140
X 38.25
Y 14
Z 95
X 35.75
Y 13
Z 162

Anomaly 9:

Site of interest 10

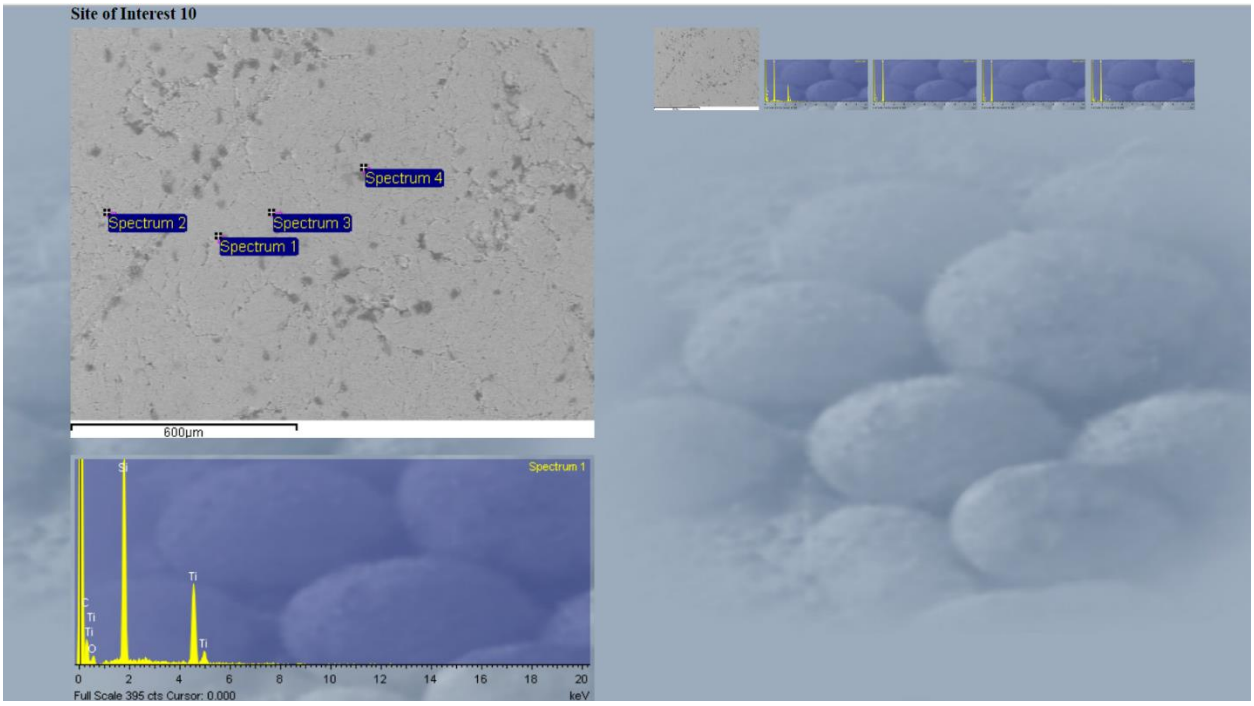

Notes

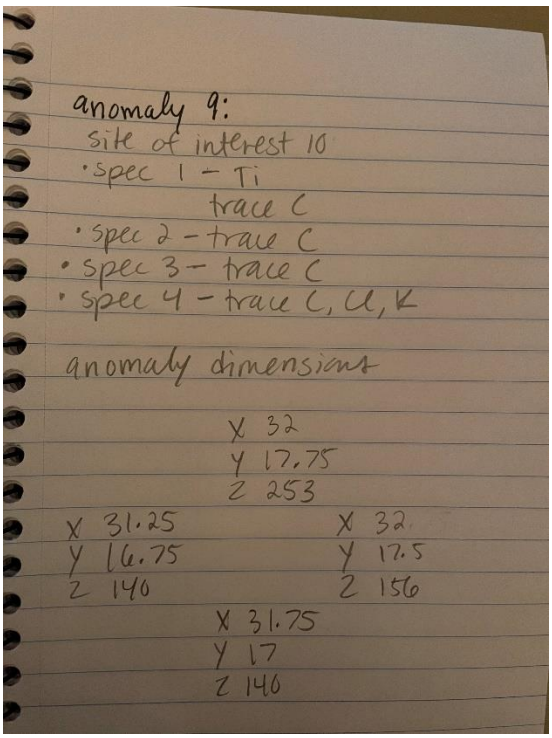
anomaly 9:
site of interest 10
• spec 1 – Ti
trace C
• spec 2 – trace C
• spec 3 – trace C
• spec 4 – trace C, Cl, K
anomaly dimensions
X 32
Y 17.75
Z 253
X 31.25
Y 16.75
Z 140
X 32
Y 17.5
Z 156
X 31.75
Y 17
Z 140

Anomaly 10:

Site of interest 11

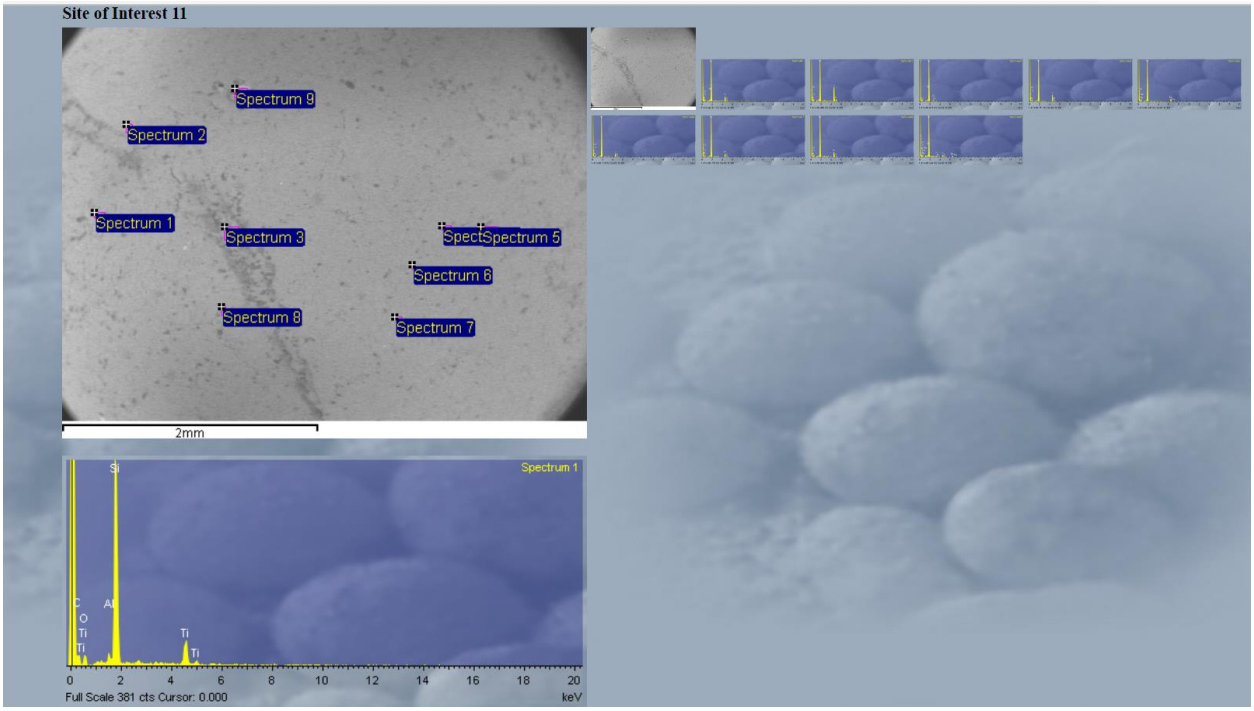

Notes

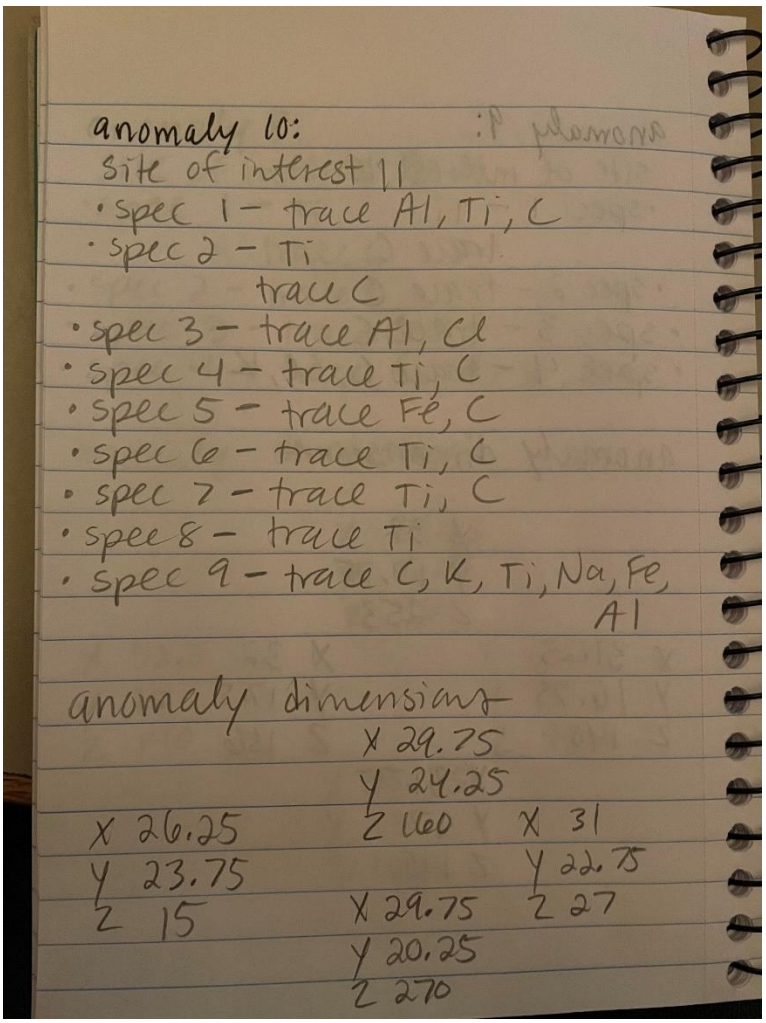
anomaly 10: :P plasma
site of interest 11
• spec 1 – trace Al, Ti, C
• spec 2 – Ti
trace C
• spec 3 – trace Al, Cl
• spec 4 – trace Ti, C
• spec 5 – trace Fe, C
• spec 6 – trace Ti, C
• spec 7 – trace Ti, C
• spec 8 – trace Ti
• spec 9 – trace C, K, Ti, Na, Fe, Al
anomaly dimensions
X 29.75
Y 24.25
Z 160
X 26.25
Y 23.75
Z 15
X 31
Y 22.75
Z 27
X 29.75
Y 20.25
Z 270

Non-quartzite minerals in EDS spectral images

(Thanks to Emily Warfield for assistance in finding some of the sources)

Zirconium

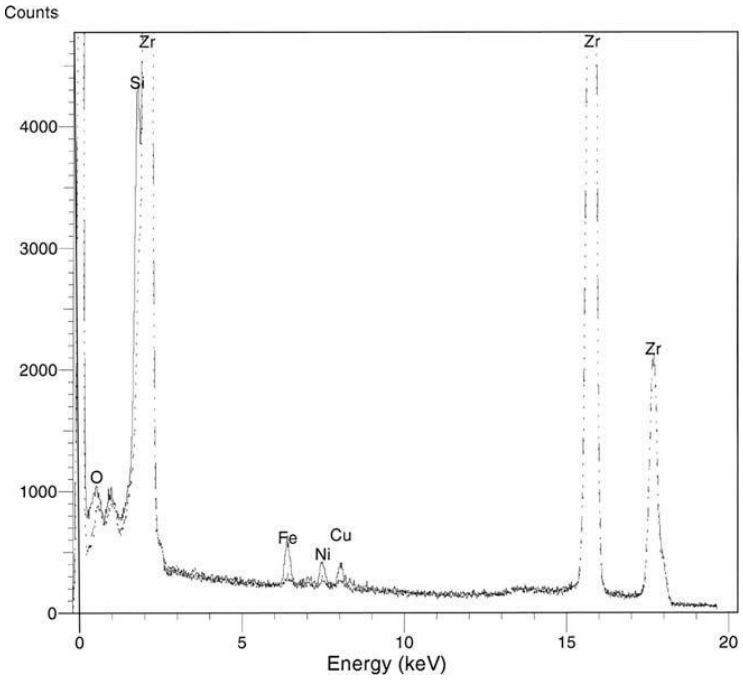

(Woo and Griffiths, 2009)

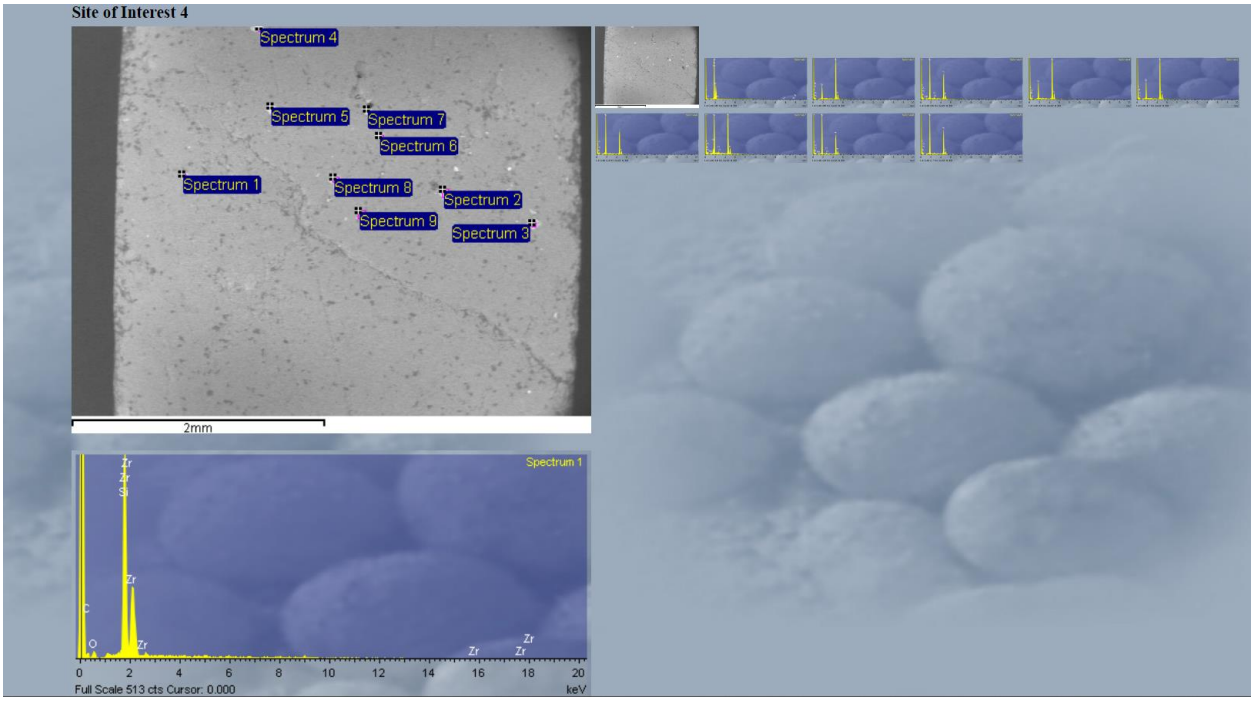

Anomaly 4, Site of interest 4, mid piece HRQ1-2

Rutile

a) b)

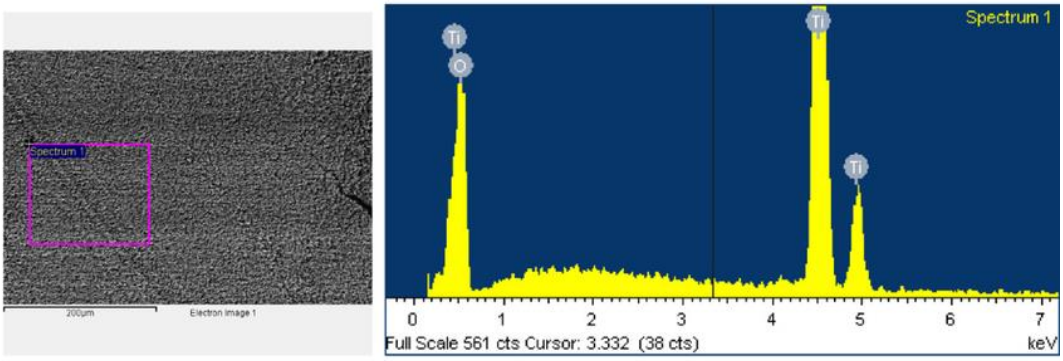

c) d)

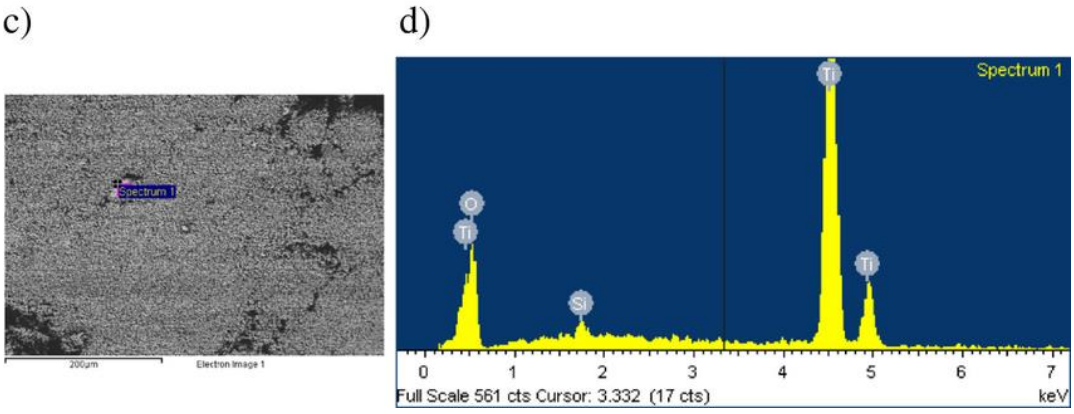

(Caba et al., 2013)

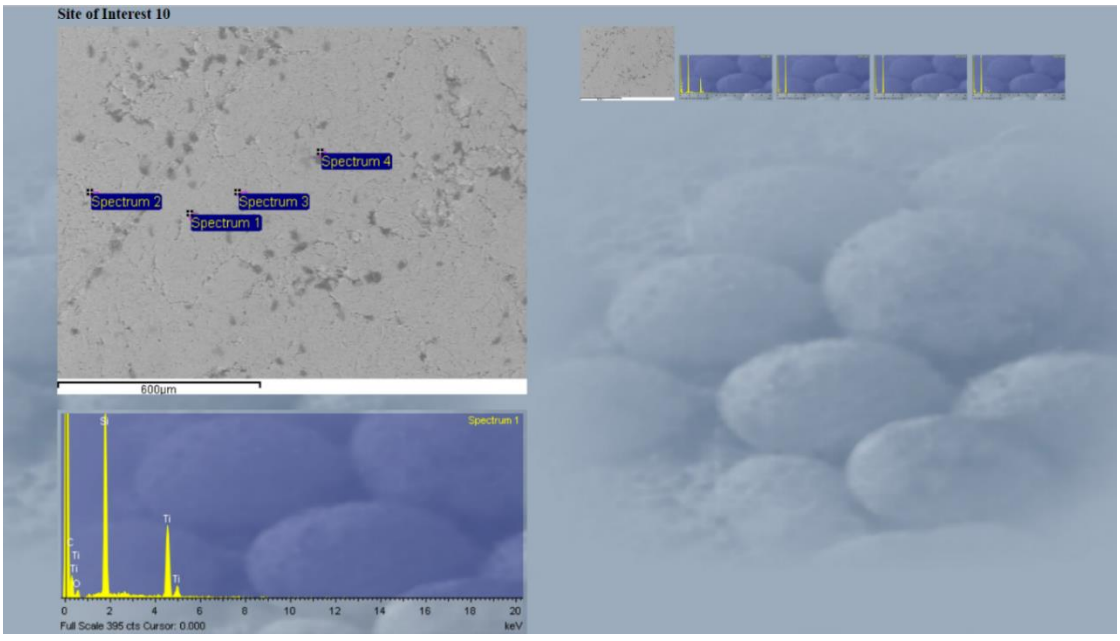

Anomaly 9, Site of interest 10, front piece HRQ1-2

Feldspar

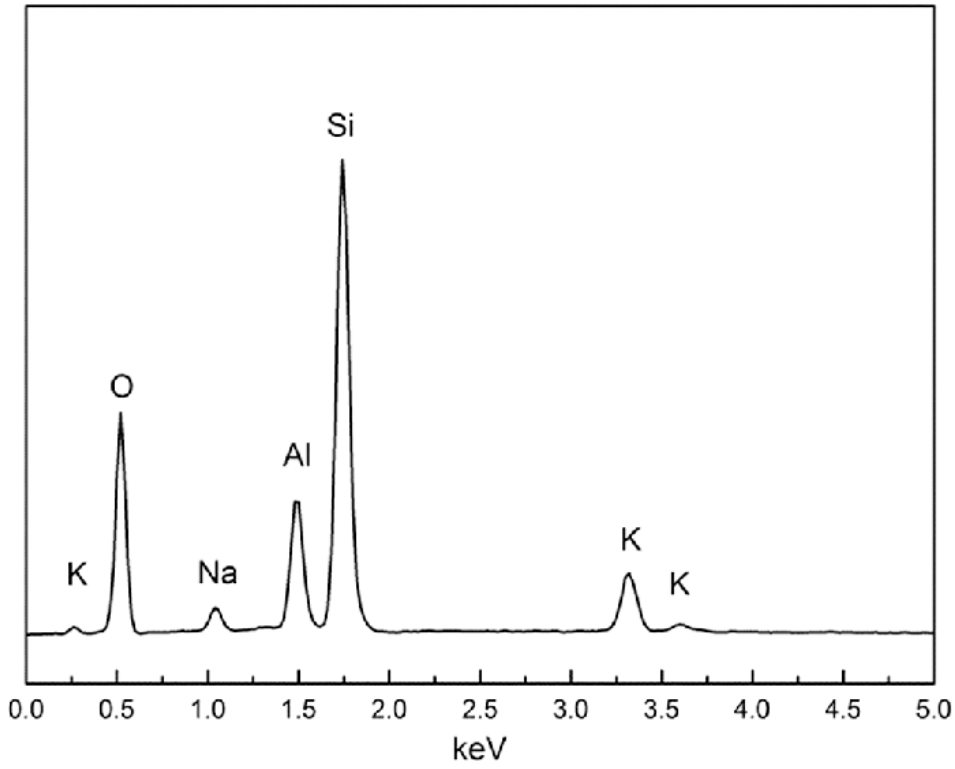

(Chen et al., 2020)

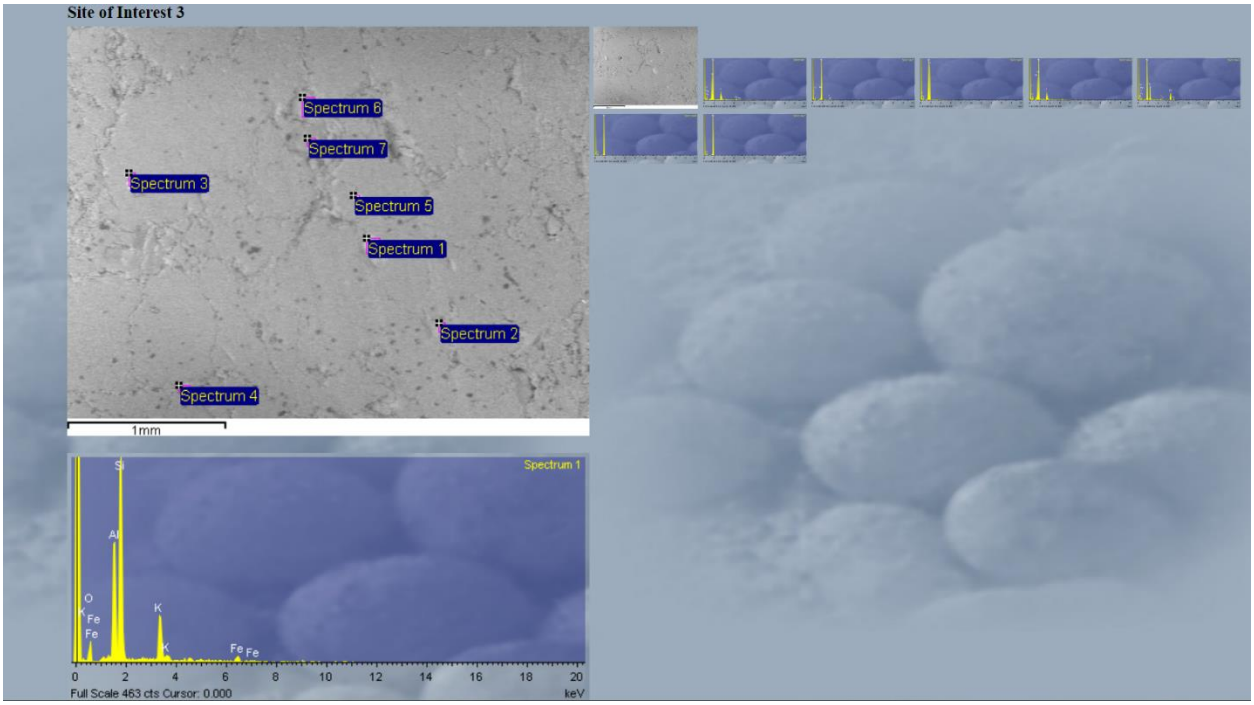

Anomaly 2, Site of interest 3, P2

Mica

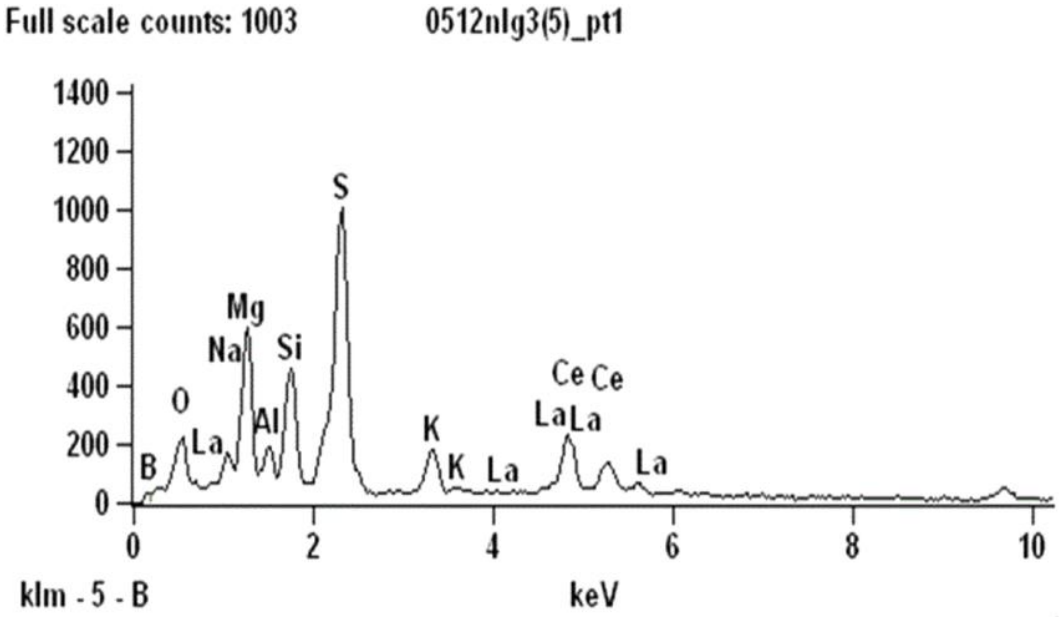

(Guo et al., 2020)

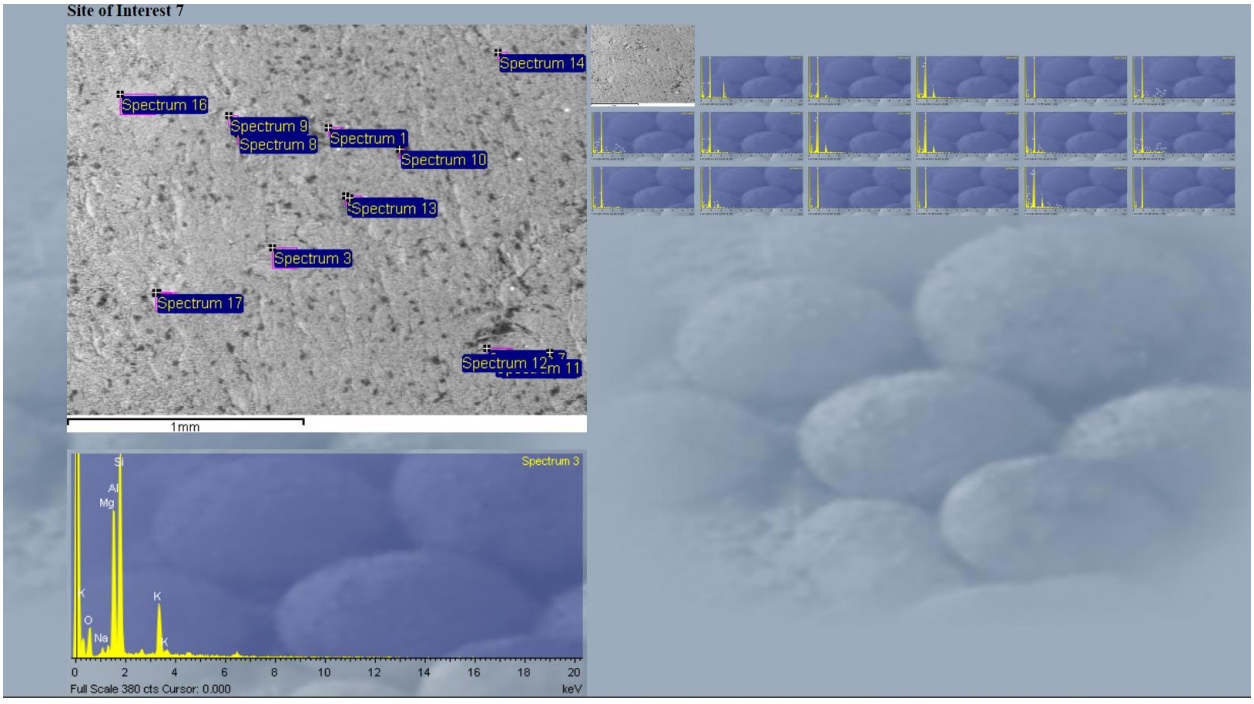

Anomaly 2, Site of interest 7, HRQ1-1 Set 2

Corundum

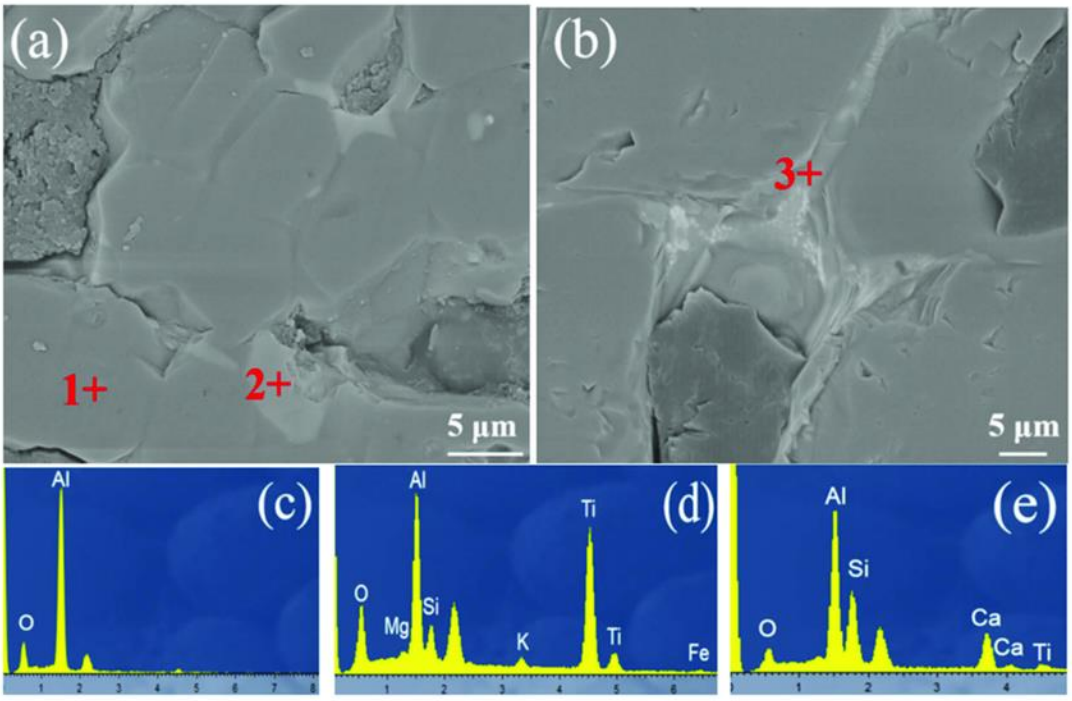

(Li et al., 2022)

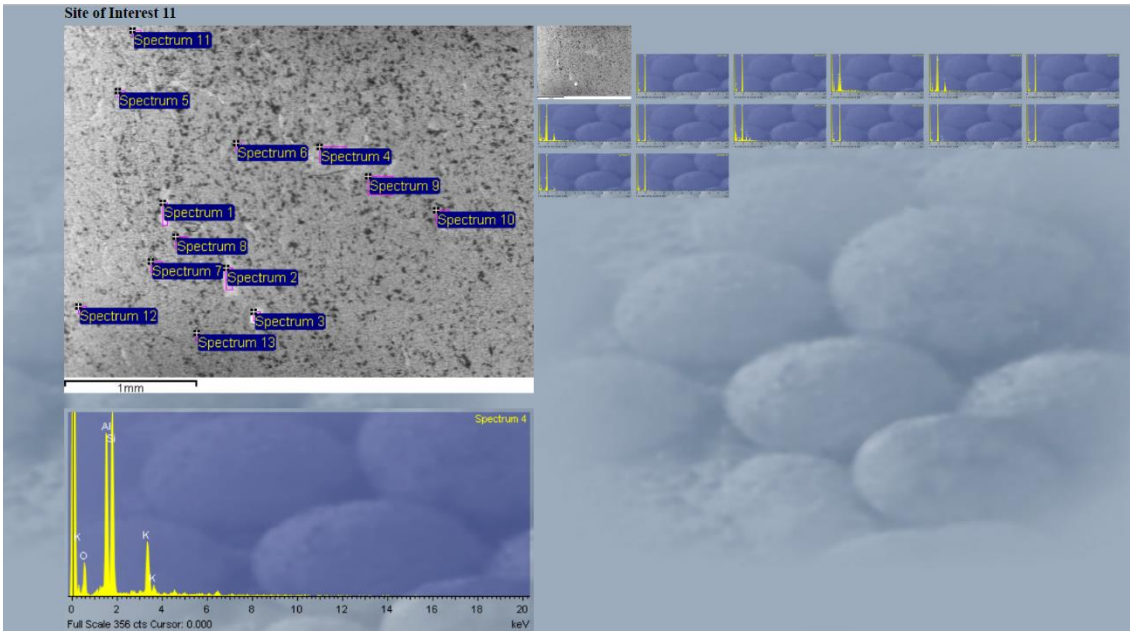

Anomaly 4, Site of interest 11, HRQ 1-1 Set 2

Summary report, from Emily Warfield and Tristan Bench:

These EDS spectral images were found to show the presence of non-quartzite minerals. These non-quartzite minerals mainly include zirconium, rutile, feldspar, mica, and corundum. The similarities between the EDS scans and referenced spectral plots exemplify the presence of

these other minerals in our scans. As a result of their presence, non-quartz minerals impact the shape of OSL depth profiles, since they add OSL signal that is incongruous to quartz OSL contributions in the core sample scans. These non-quartz minerals should thus be considered a factor in the effect of luminescence depth profile forms.

Citation

Bench, T., & Feathers, J. (2022). Trialing the application of controlled exposure experiments for optical exposure dating on quartzite quarry surfaces in Washington State. Radiation Measurements, 106805.

Cabaleiro, D. & Pastoriza Gallego, Maria & Gracia-Fernández, Carlos & Piñeiro, Manuel & Lugo, Luis. (2013). Rheological and volumetric properties of TiO2-ethylene glycol nanofluids. Nanoscale research letters. 8. 286. 10.1186/1556-276X-8-286.

Chen, Xiaoyan & Leng, Jinhua & Zhang, Dongsheng & He, Bobing. (2020). Study of modified potassium feldspar as a novel β-nucleating agent to the crystal morphology and properties of polypropylene. SN Applied Sciences. 2. 10.1007/s42452-020-2485-x.

Guo, Jianming & Ye, Mingquan & Han, Aijun & Liao, Jun & Chen, Chenlu. (2020). Studies on the preparation and characterization of composite La-doped γ-Ce2S3-coated mica cool pigments. Applied Physics A. 126. 10.1007/s00339-020-03641-z.

Li, Shaofei & Chen, Ding & Gu, Huazhi & Huang, Ao & Fu, Lvping. (2022). Investigation on Application Prospect of Refractories for Hydrogen Metallurgy: The Enlightenment from the Reaction between Commercial Brown Corundum and Hydrogen. Materials (Basel, Switzerland). 15. 10.3390/ma15197022.

Sohbati, R., Murray, A. S., Chapot, M. S., Jain, M., & Pederson, J. (2012). Optically stimulated luminescence (OSL) as a chronometer for surface exposure dating. Journal of Geophysical Research: Solid Earth, 117(B9).

Woo, O. & Griffiths, Malcolm. (2009). The role of Fe on the solubility of Nb in α-Zr. Journal of Nuclear Materials - J NUCL MATER. 384. 77-80. 10.1016/j.jnucmat.2008.10.004.

A2 – Controlled Exposure Experiment OSL Scans

Controlled exposure experiment scan datasets (below). (a) Laser scans of natural sunlight exposed cores (NS1, NS2, NS3) provided limited sensitivity in OSL, making it difficult to visually distinguish depth profile forms. Core NS2 was switched in orientation to where the top portion faced to the right of the scan extent, which limits the precision of recording the OSL from surface edges of the sample. The low sensitivity of core NS2 in tandem prevents the ability to accurately determine the true dimensional extent of the sample scan. As such, the sample is not depth profile plotted for this study. (b) OSL scans of simulated sunlight exposed cores (SS1, SS2, SS3) are also low in OSL sensitivity, making it difficult to plot depth profile forms from these samples. (c) Anomalies of NS cores NS1 and NS3 are identified in this study – For NS1, only the anomalies within the area which produced the depth profile are noted in the figure.

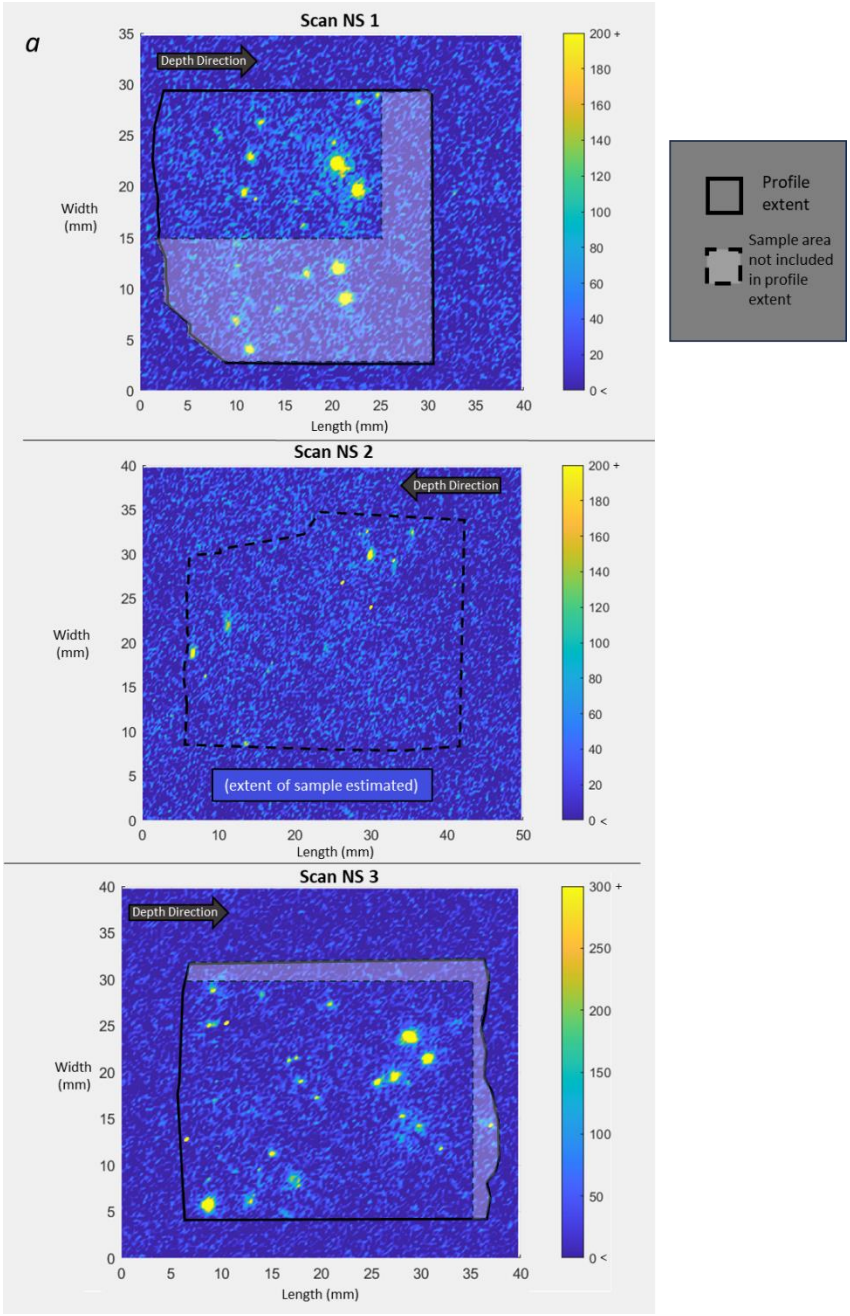
a
Scan NS 1
Depth Direction
Width (mm)
Length (mm)
Scan NS 2
Depth Direction
(extent of sample estimated)
Width (mm)
Length (mm)
Scan NS 3
Depth Direction
Width (mm)
Length (mm)
Profile extent
Sample area not included in profile extent

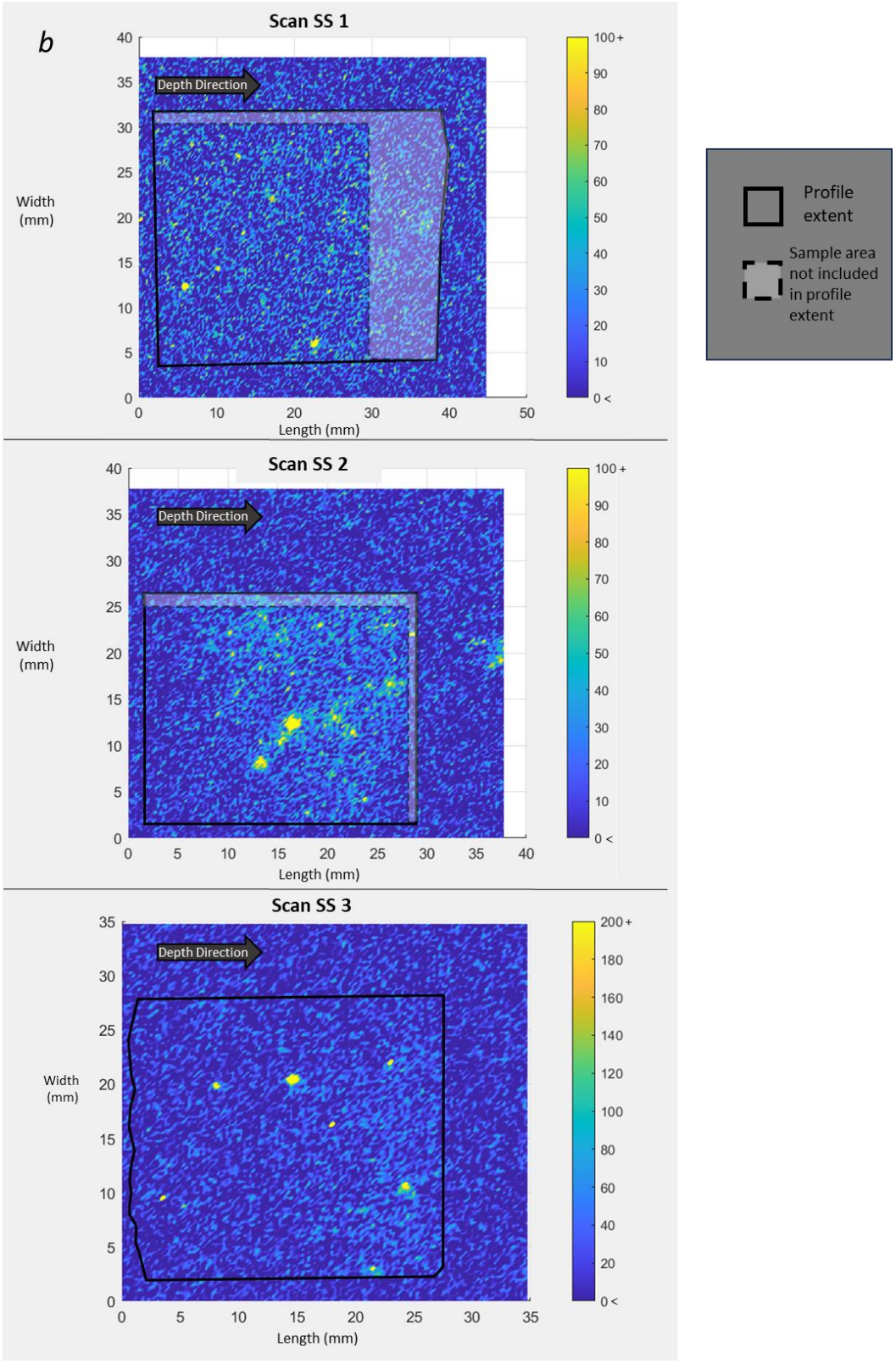
b
Scan SS 1
Depth Direction
Width (mm)
Length (mm)
Scan SS 2
Depth Direction
Width (mm)
Length (mm)
Scan SS 3
Depth Direction
Width (mm)
Length (mm)
Profile extent
Sample area not included in profile extent

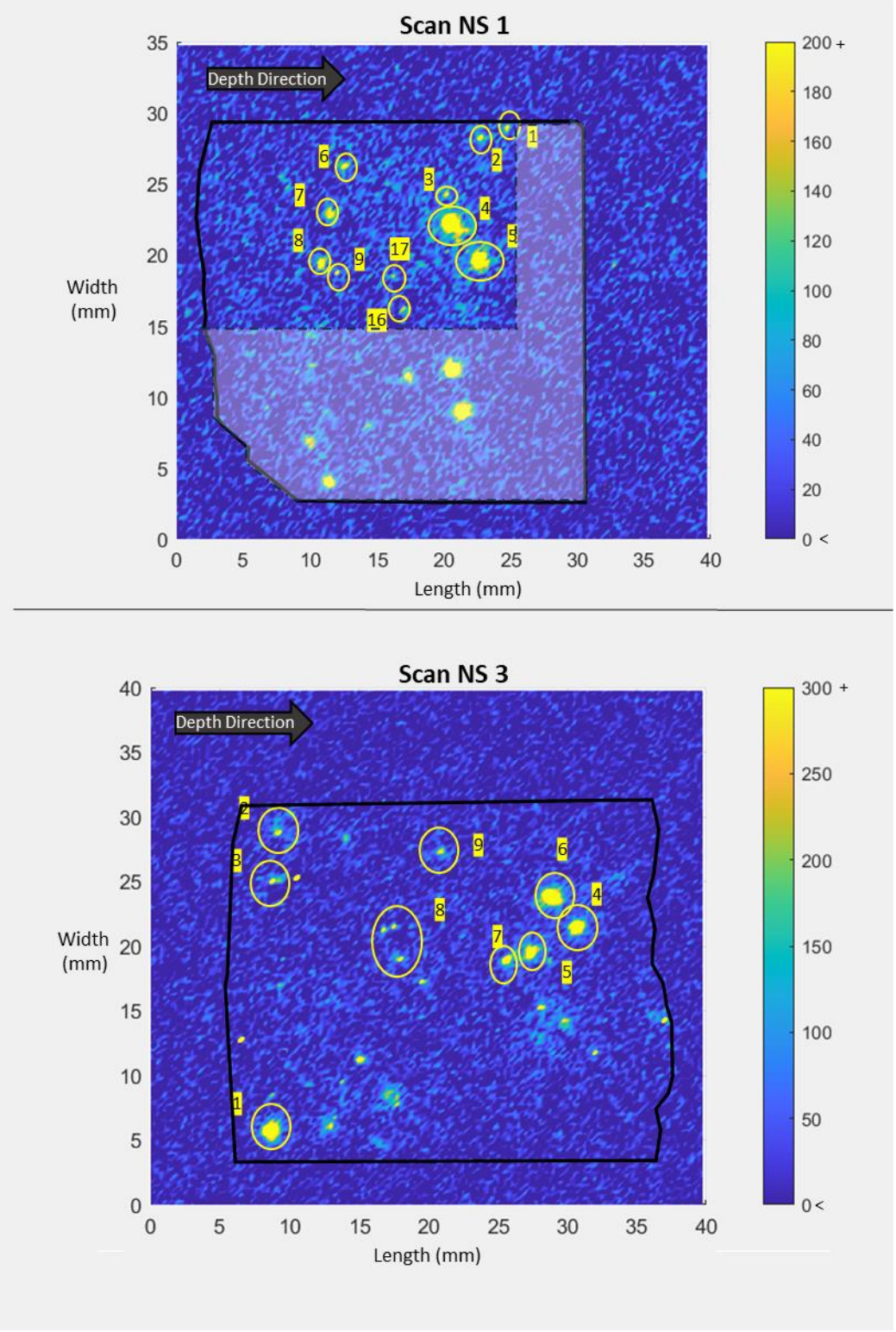

Anomalies observed via SEM-EDS

A3 – Anomaly Identification Summary of NS1, N3 Cores
Anomaly Identification of NS Cores

Shown are core anomaly zones and associated regions where non-quartz mineralogy is presented. Examples of choice spectra are provided for each anomaly zone to provide evidence of non-quartz mineralogy presented in zone. Anomaly identifications for these cores are investigative, and may lack precision, however provide insight on the nature of identifying trace mineralogy in OSL anomaly zones.

Instructions of figures: Each anomaly is identified by number in the main scan images. Then, individual spectra are identified and categorized with numbers in each anomaly area, with the SEM image of the anomaly region. From there, individual spectra presented for the anomaly, with the spectra number found in the upper right of the spectral image.

Core NS3

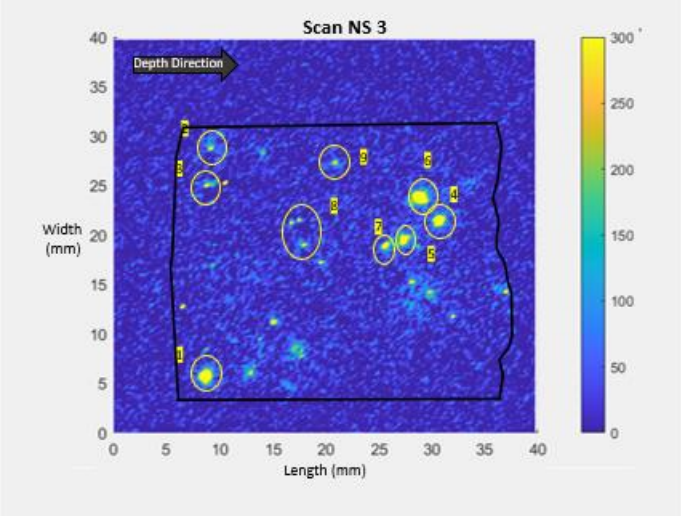

Anomaly 1

Brass varnish – not supposed to give off OSL, but may reflect laser into photomultiplier and give off enhanced signal. Or, may be surficial and covering non-quartz mineralogy. Given foreign substances, anomaly zone here is removed from scan profile.

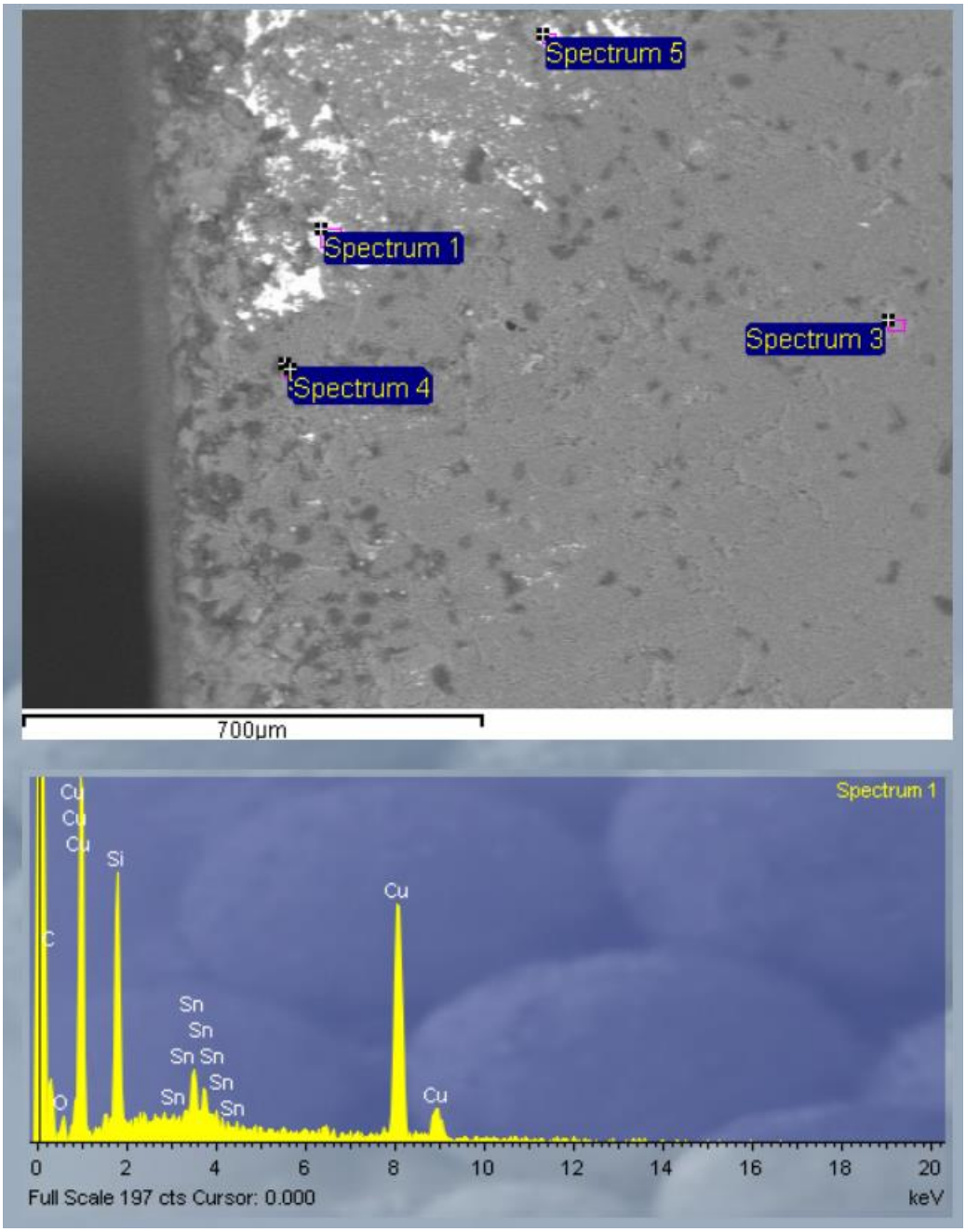

Anomaly 2

Collection of micas present in spectrum 1, 2

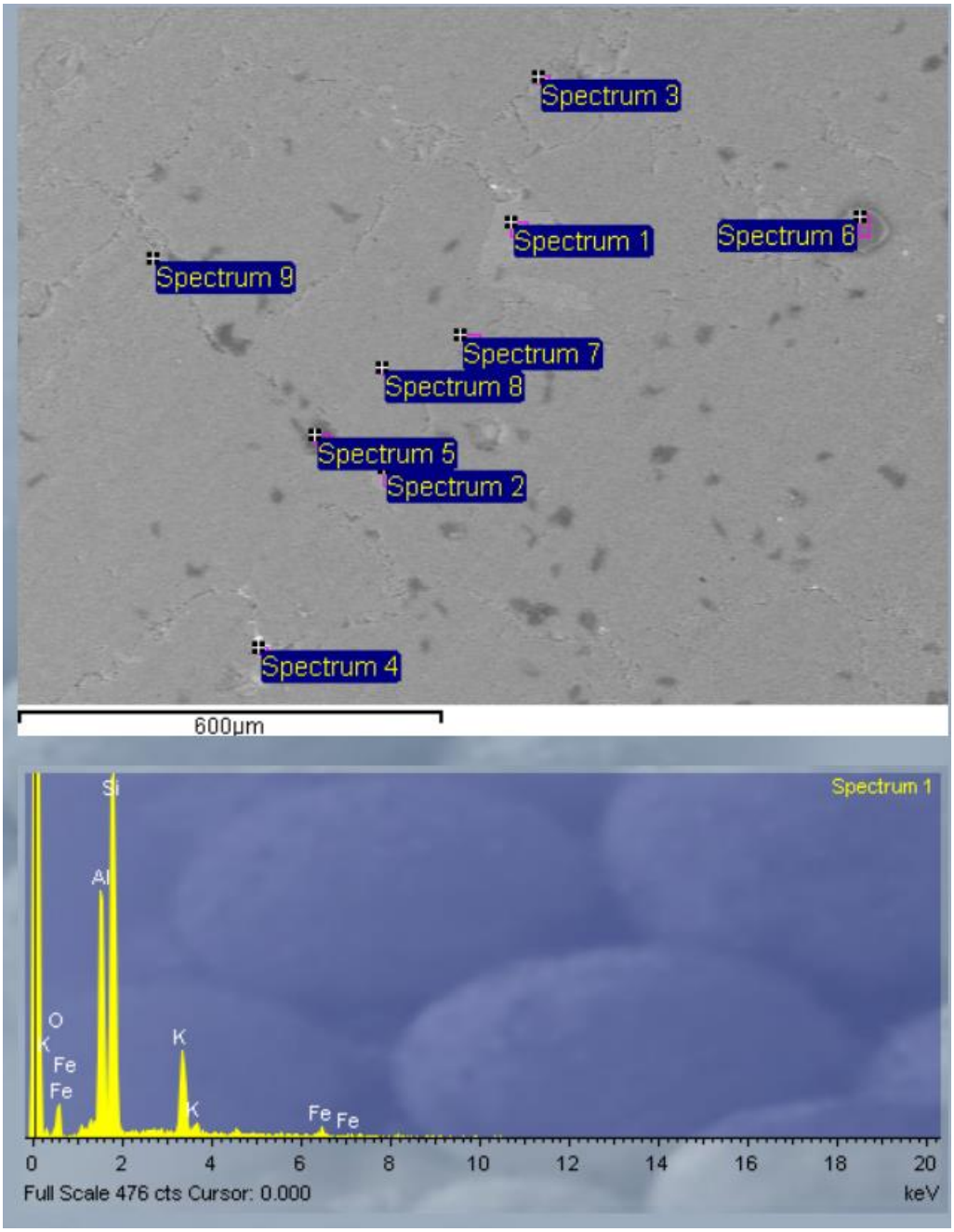

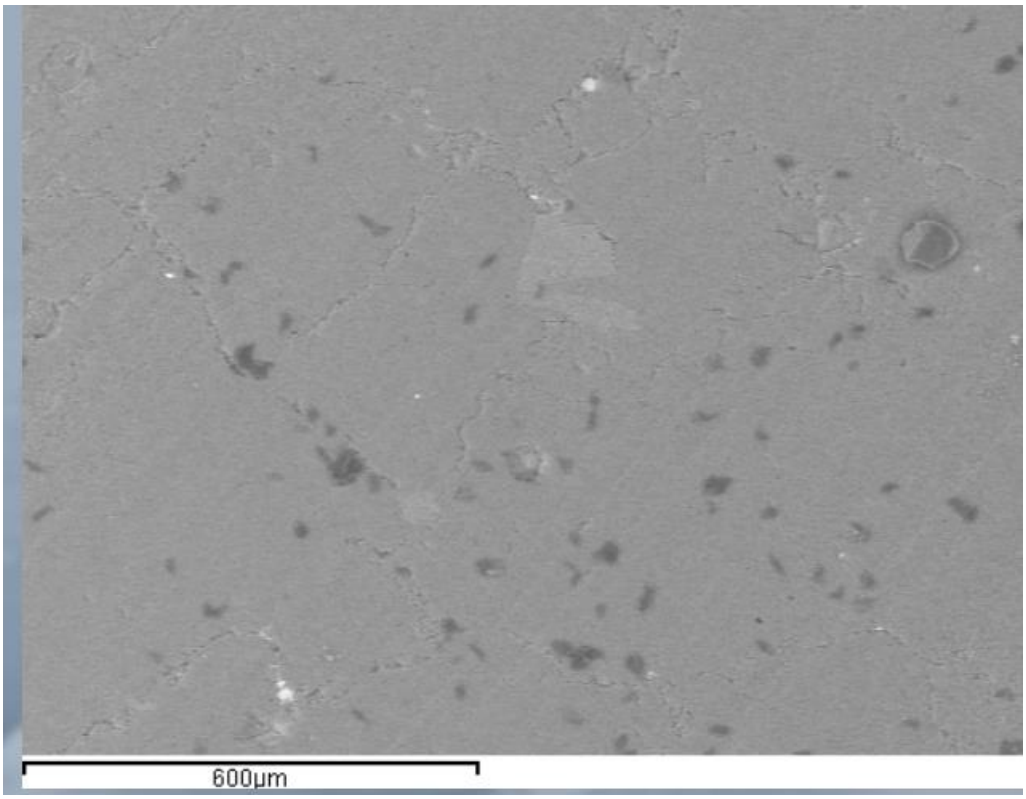
600µm

Anomaly 3

Divot in core sample, iron oxides present within divot (spectrum 1-3), rutile on outside of fracture also (spectrum 5). Spectrum 7, 10 host REE's.

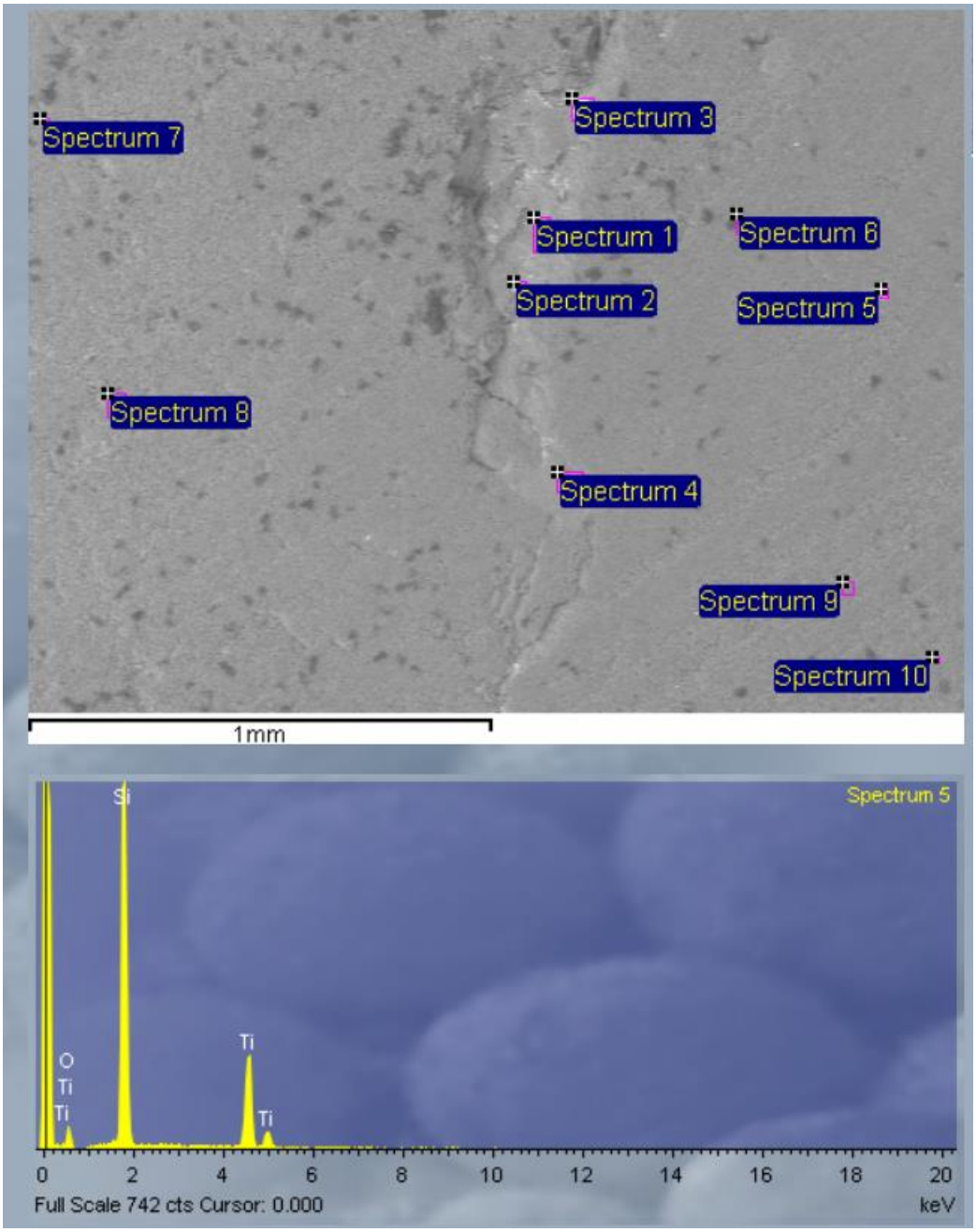

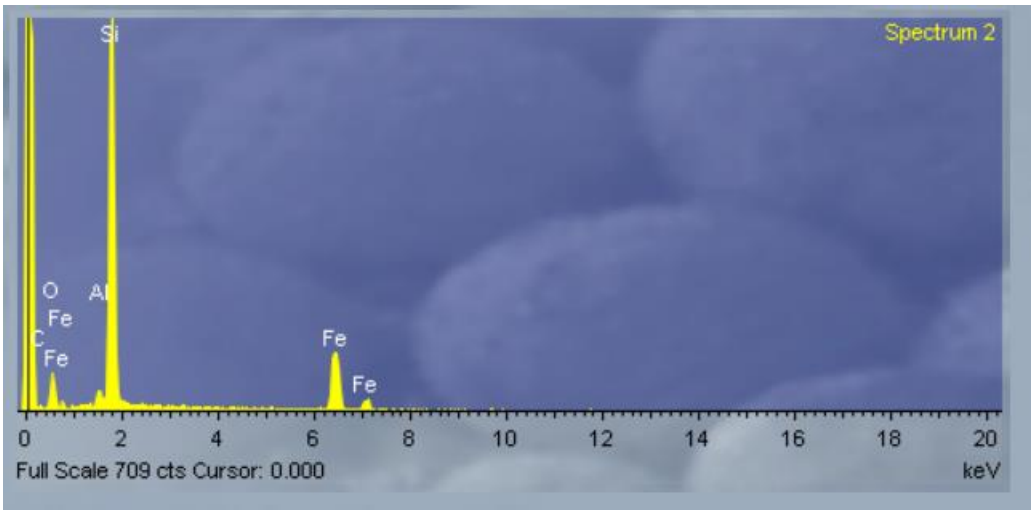
Spectrum 2
Si
O
Al
Fe
C
Fe
Fe
Fe
0
2
4
6
8
10
12
14
16
18
20
Full Scale 709 cts Cursor: 0.000
keV

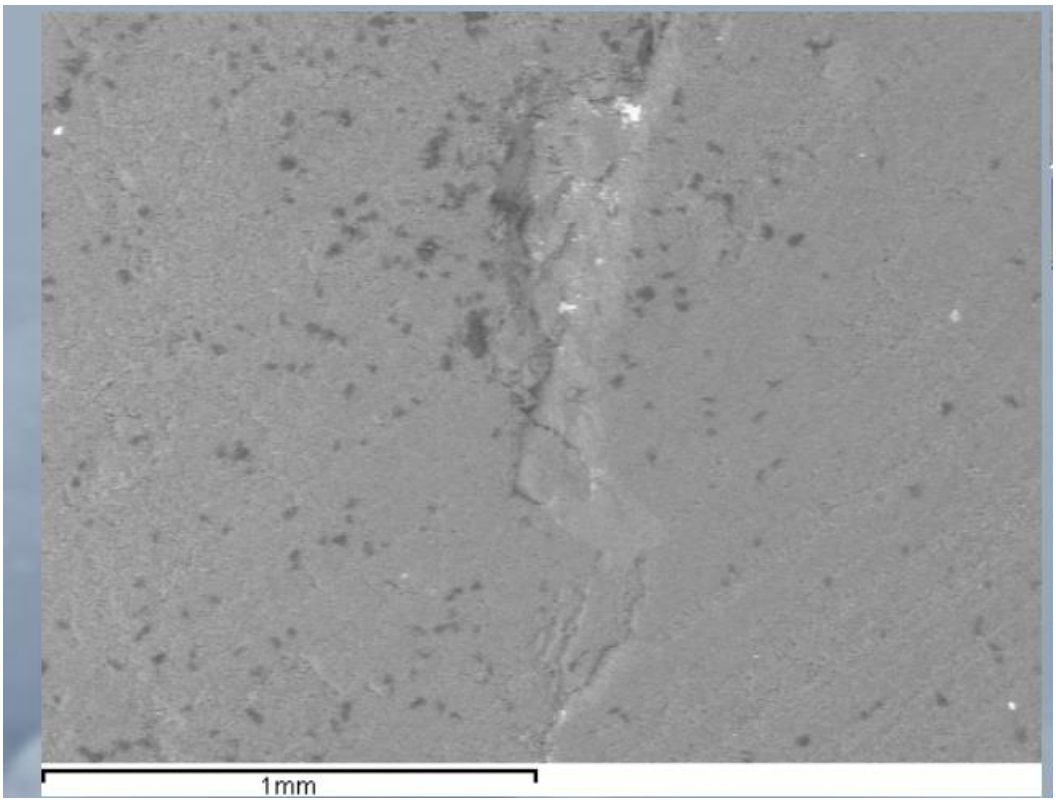
1mm

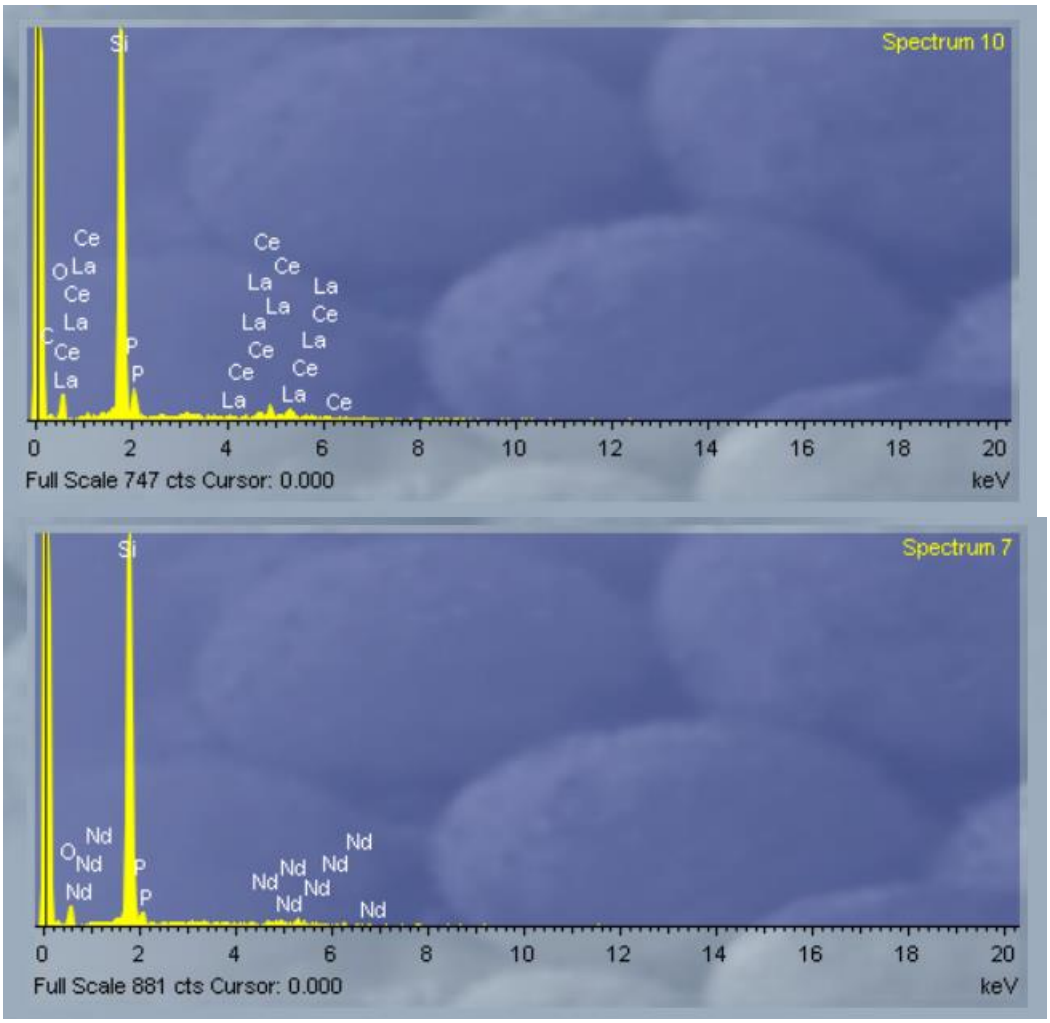
Spectrum 10
Si
Ce
La
O
P
0 2 4 6 8 10 12 14 16 18 20
Full Scale 747 cts Cursor: 0.000
keV
Spectrum 7
Si
Nd
O
P
0 2 4 6 8 10 12 14 16 18 20
Full Scale 881 cts Cursor: 0.000
keV

Anomaly 4

K-Al minerals, rutile common in this anomaly zone

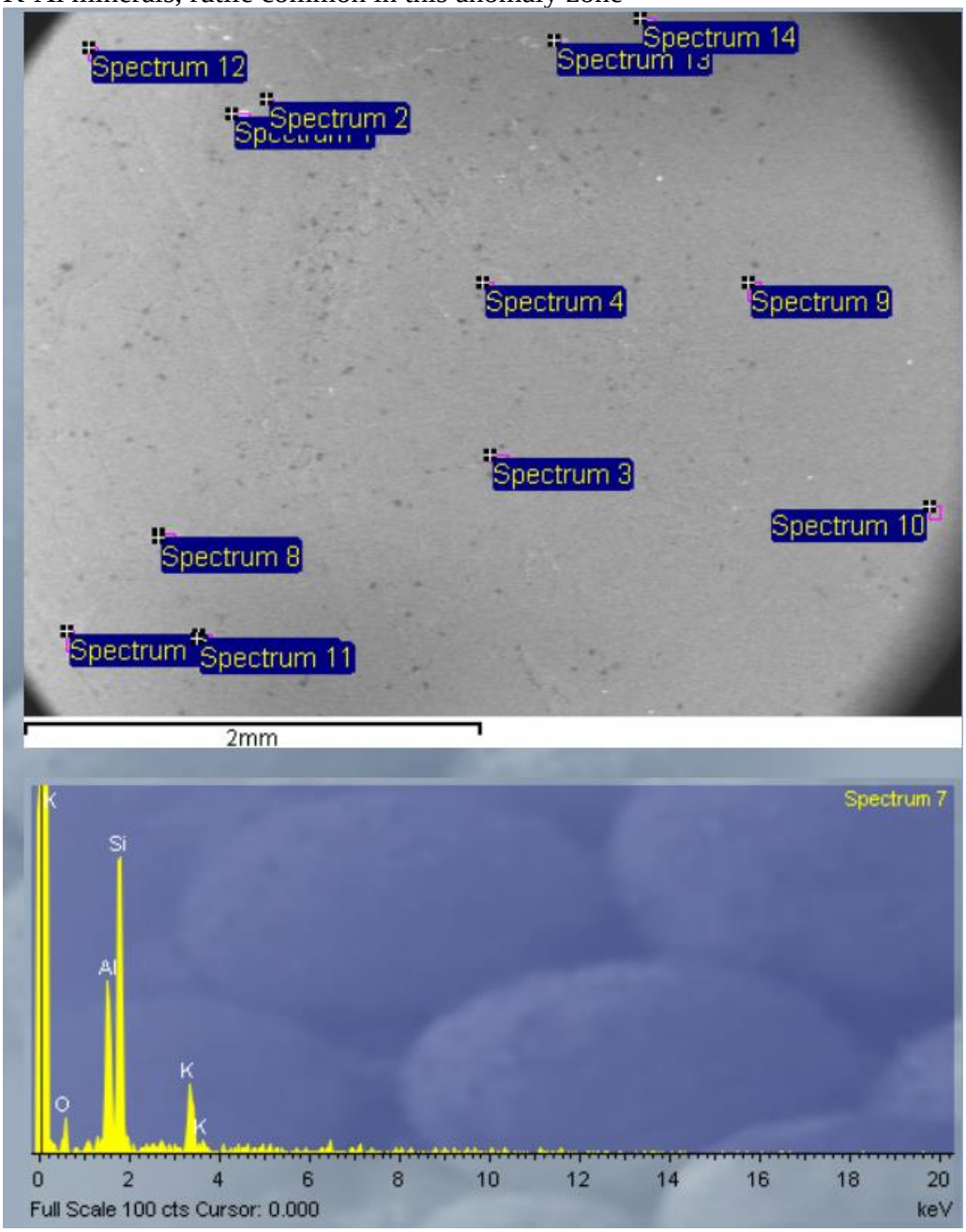

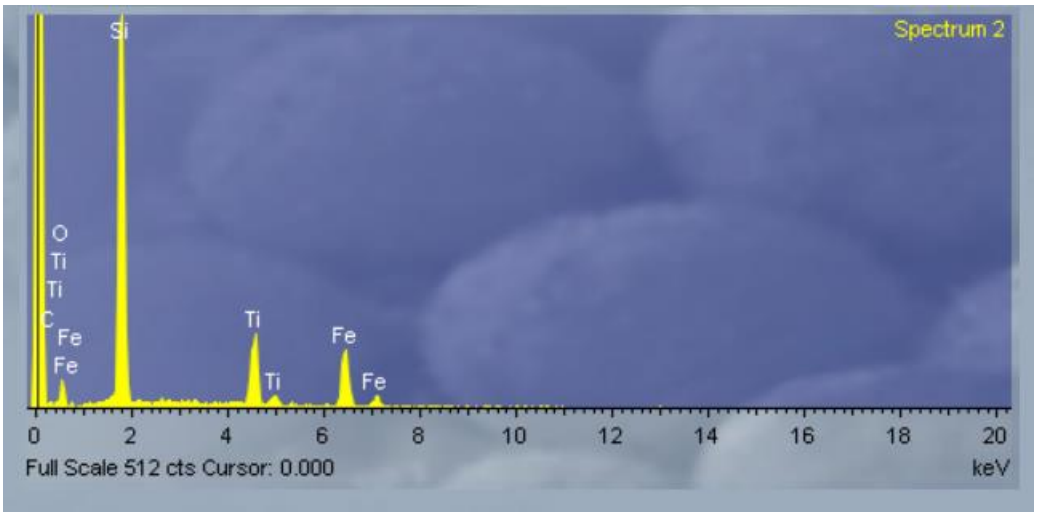
Spectrum 2
Si
O
Ti
Ti
C
Fe
Fe
Ti
Ti
Fe
Fe
0 2 4 6 8 10 12 14 16 18 20
Full Scale 512 cts Cursor: 0.000
keV

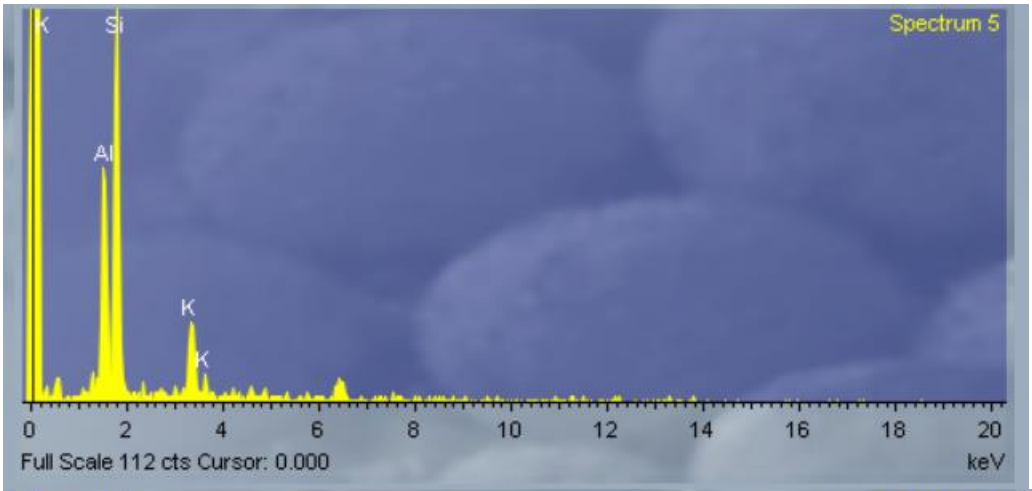
Spectrum 5
K
Si
Al
K
K
0 2 4 6 8 10 12 14 16 18 20
Full Scale 112 cts Cursor: 0.000
keV

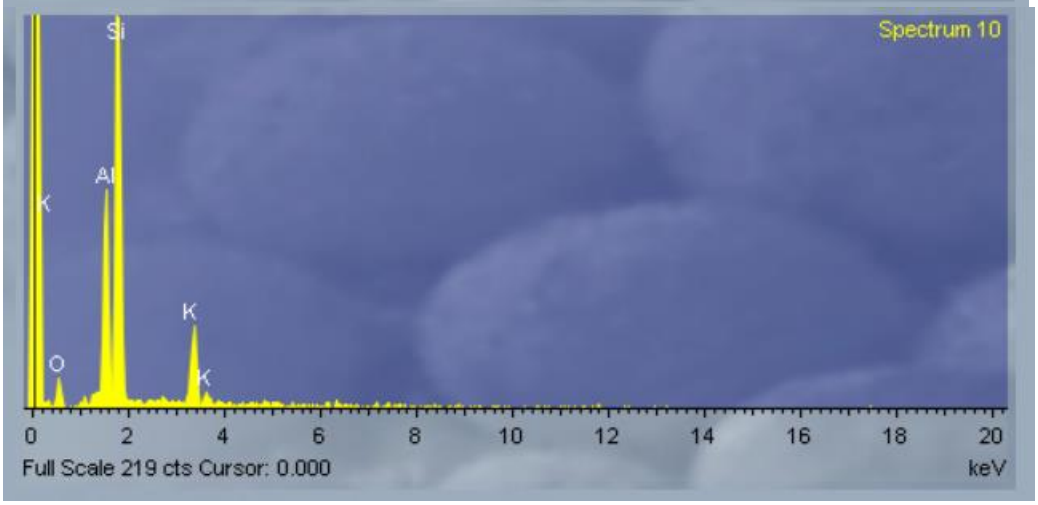
Spectrum 10
Si
Al
K
K
O
K
0 2 4 6 8 10 12 14 16 18 20
Full Scale 219 cts Cursor: 0.000
keV

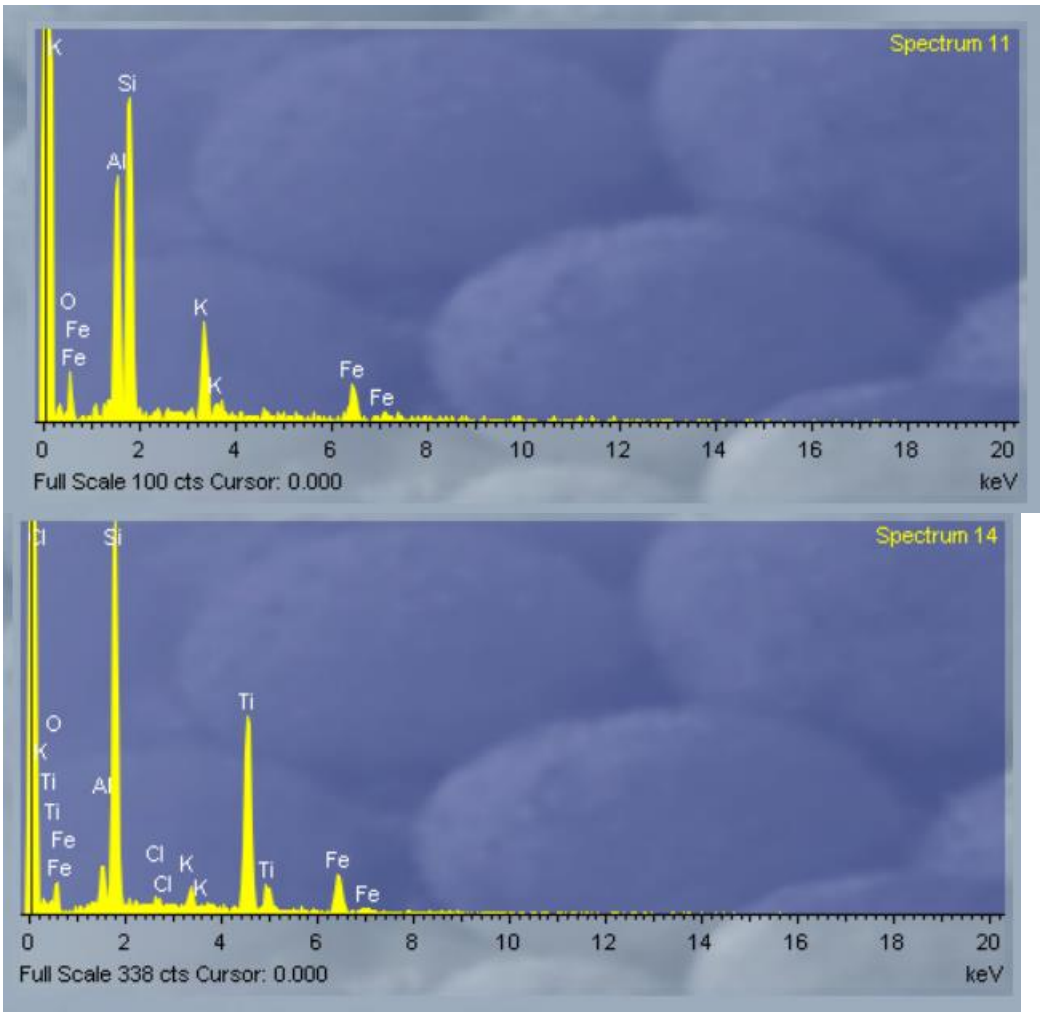
Spectrum 11
K
Si
Al
O
Fe
Fe
K
K
Fe
Fe
0 2 4 6 8 10 12 14 16 18 20
Full Scale 100 cts Cursor: 0.000
keV
Spectrum 14
Cl
Si
Ti
O
K
Ti
Ti
Al
Fe
Fe
Cl
Cl
K
K
Ti
Fe
Fe
0 2 4 6 8 10 12 14 16 18 20
Full Scale 338 cts Cursor: 0.000
keV

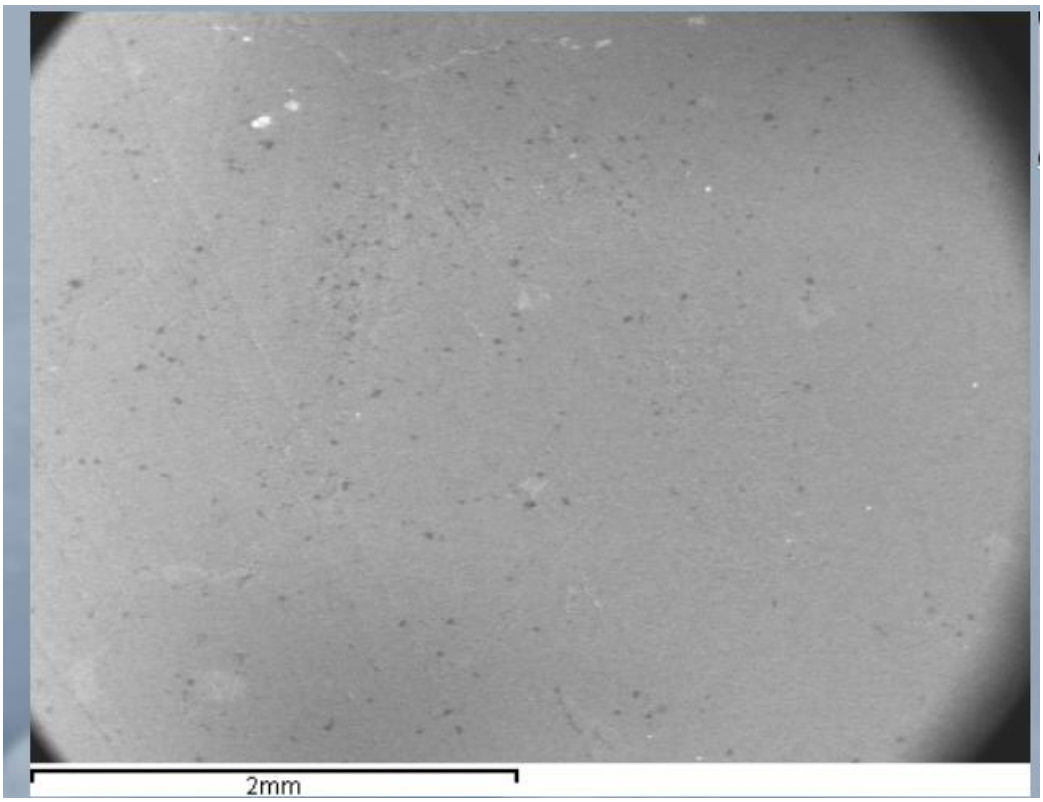
2mm

Anomaly 5

Mg, Al and K, Al element combinations present in trace minerals here

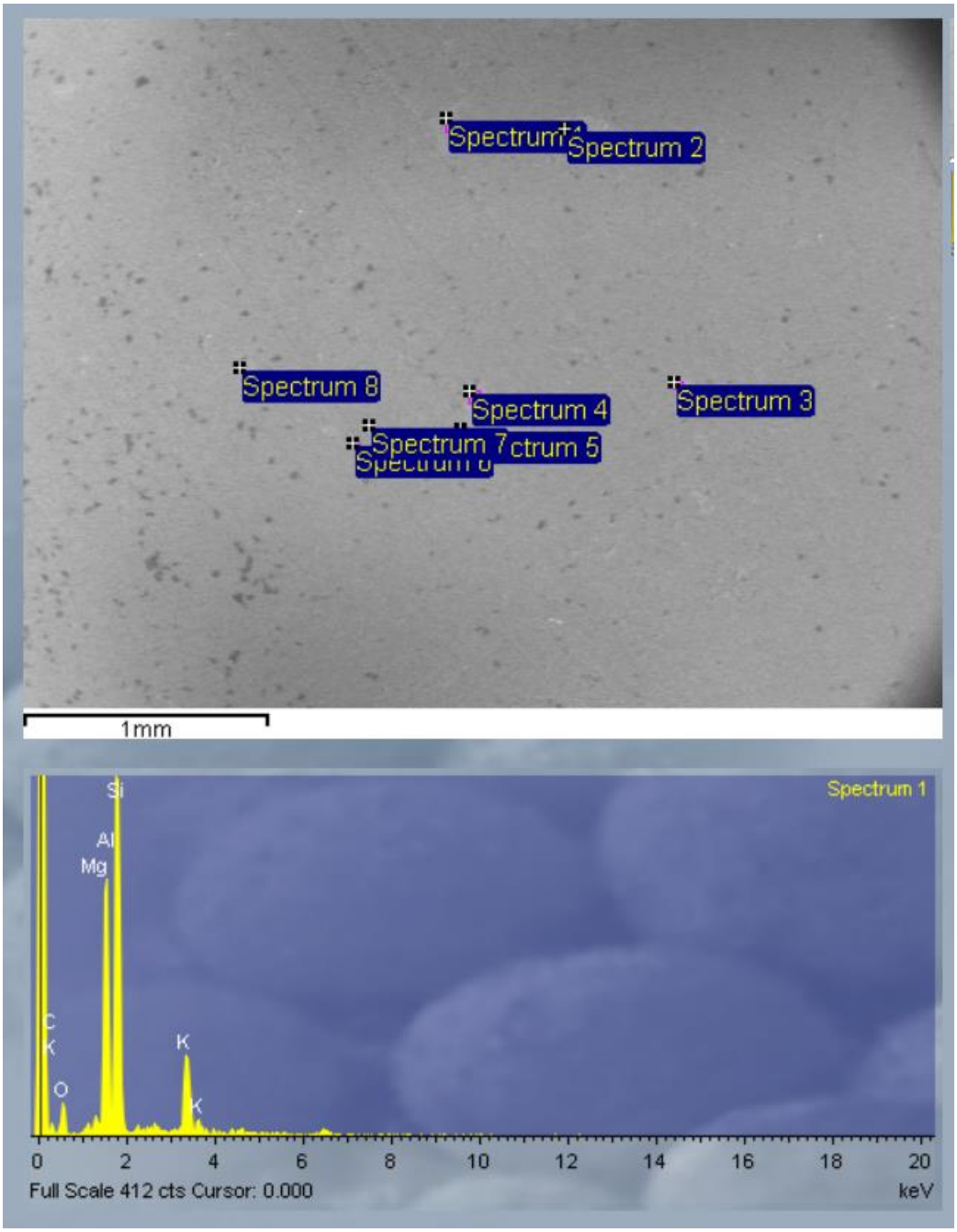

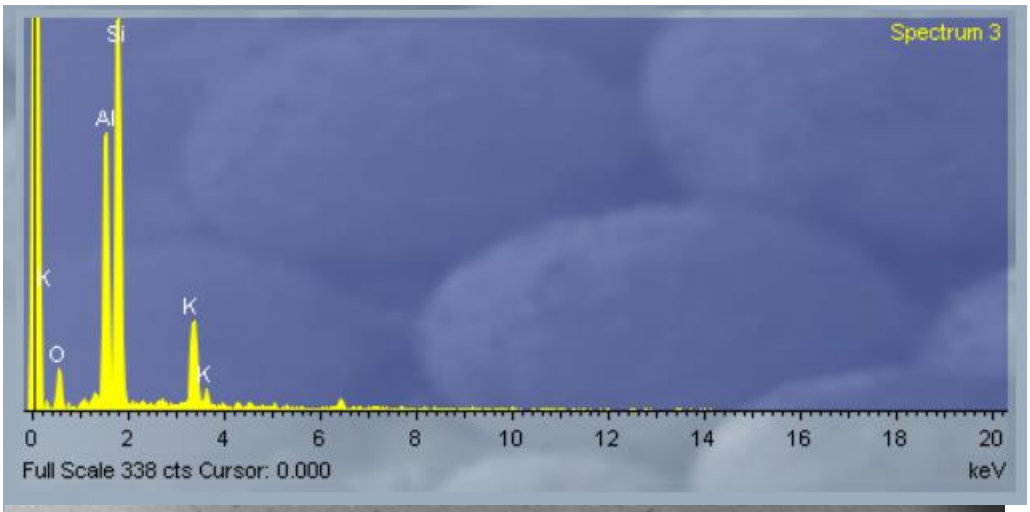
Spectrum 3
Si
Al
K
O
K
K
0
2
4
6
8
10
12
14
16
18
20
Full Scale 338 cts Cursor: 0.000
keV

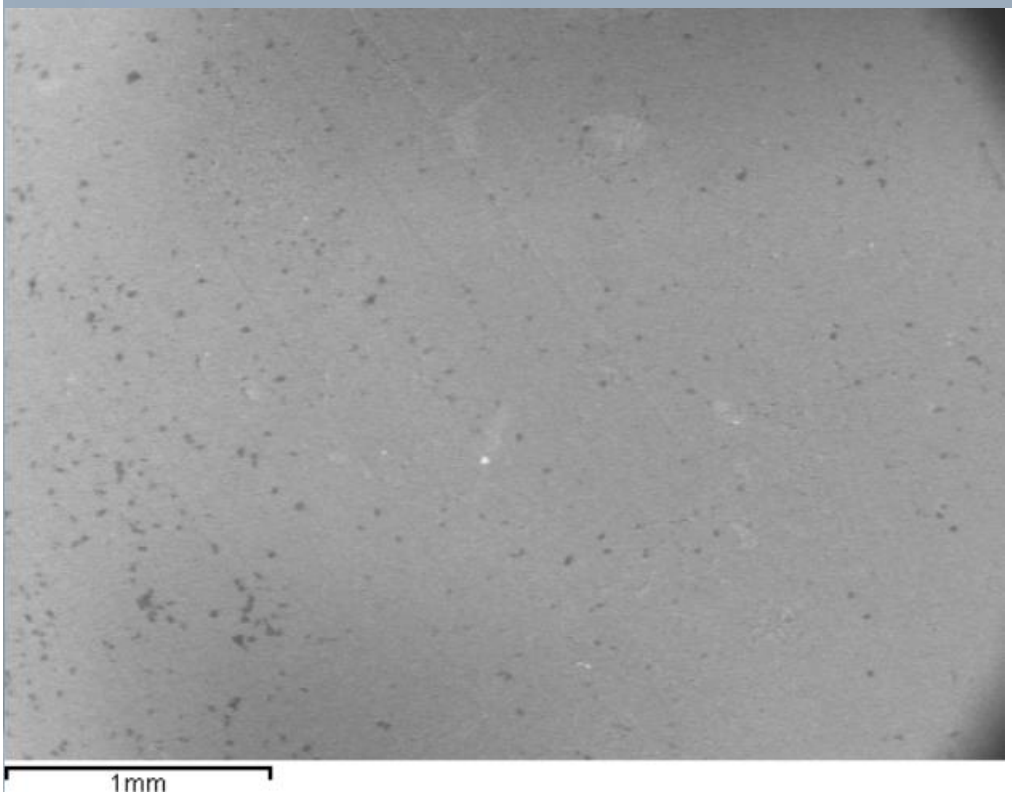
1mm

Anomaly 6

K, Al minerals, Ti minerals present in region

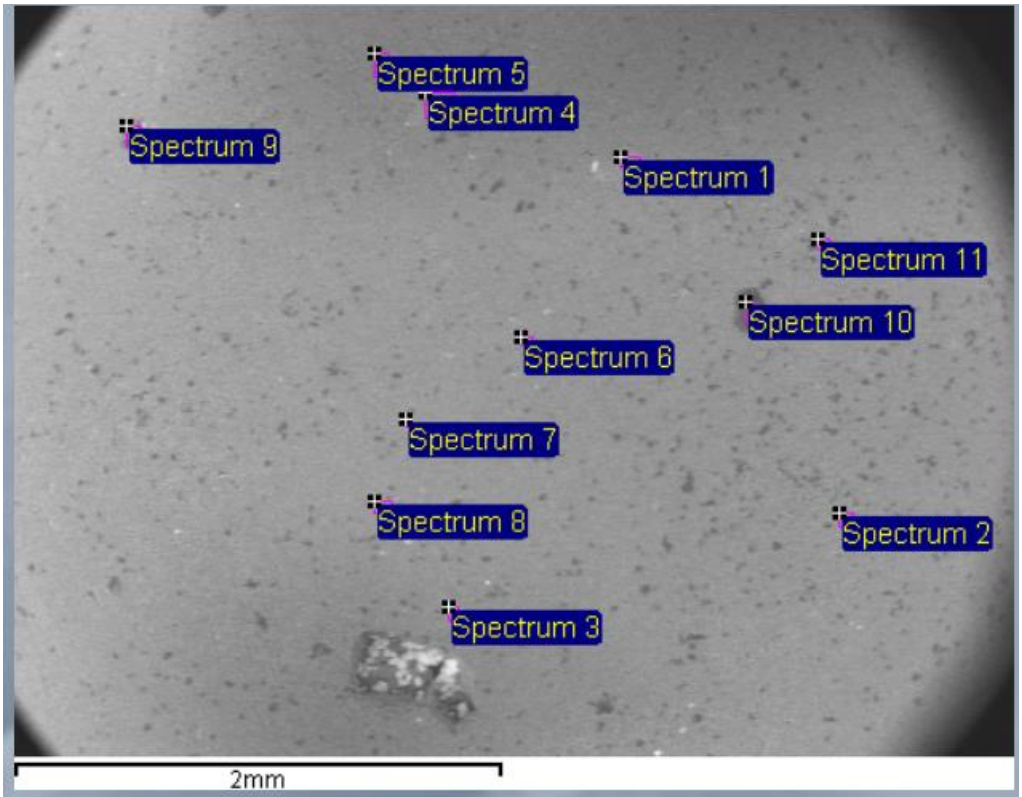

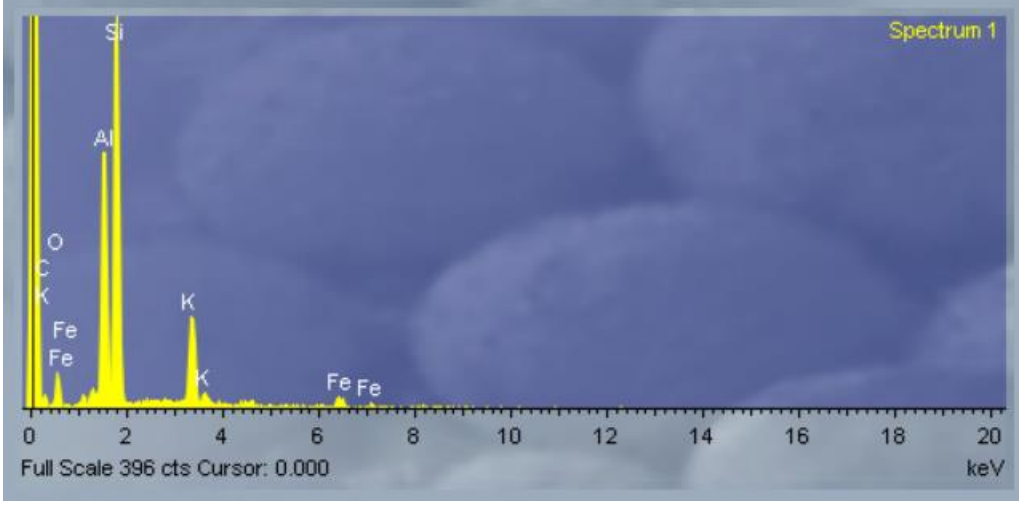

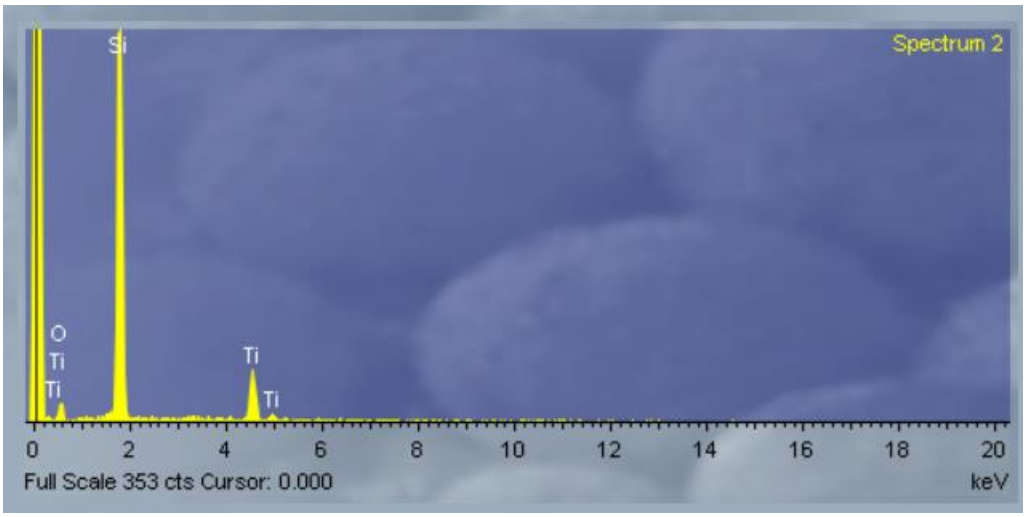
Spectrum 2
Si
O
Ti
Ti
Ti
Ti
0 2 4 6 8 10 12 14 16 18 20
Full Scale 353 cts Cursor: 0.000
keV

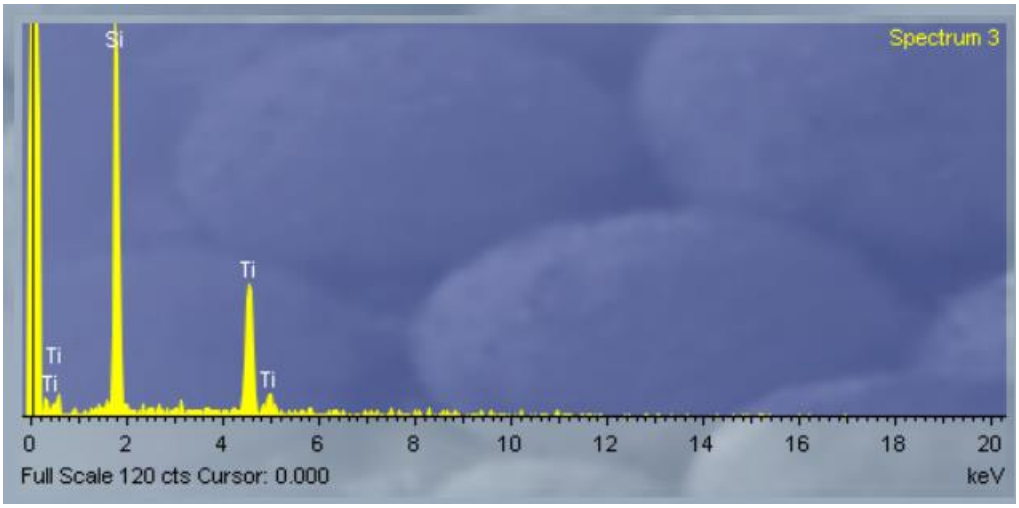
Spectrum 3
Si
Ti
Ti
Ti
Ti
0 2 4 6 8 10 12 14 16 18 20
Full Scale 120 cts Cursor: 0.000
keV

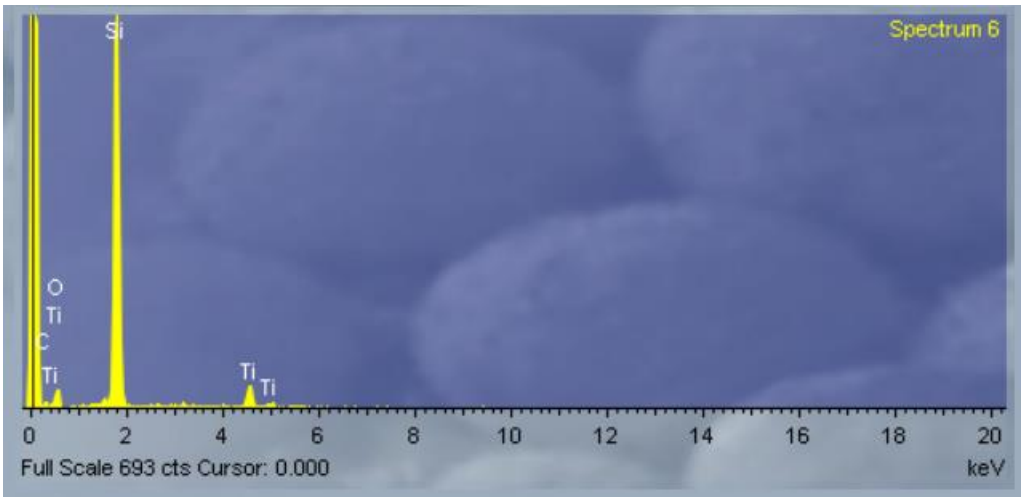
Spectrum 6
Si
O
Ti
C
Ti
Ti
Ti
0 2 4 6 8 10 12 14 16 18 20
Full Scale 693 cts Cursor: 0.000
keV

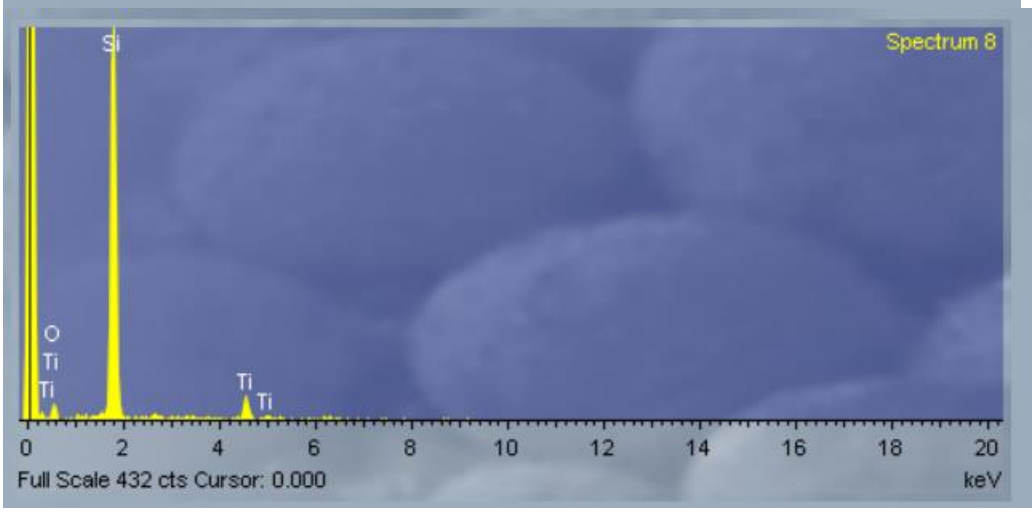
Spectrum 8
Si
O
Ti
Ti
Ti
Ti
0 2 4 6 8 10 12 14 16 18 20
Full Scale 432 cts Cursor: 0.000
keV

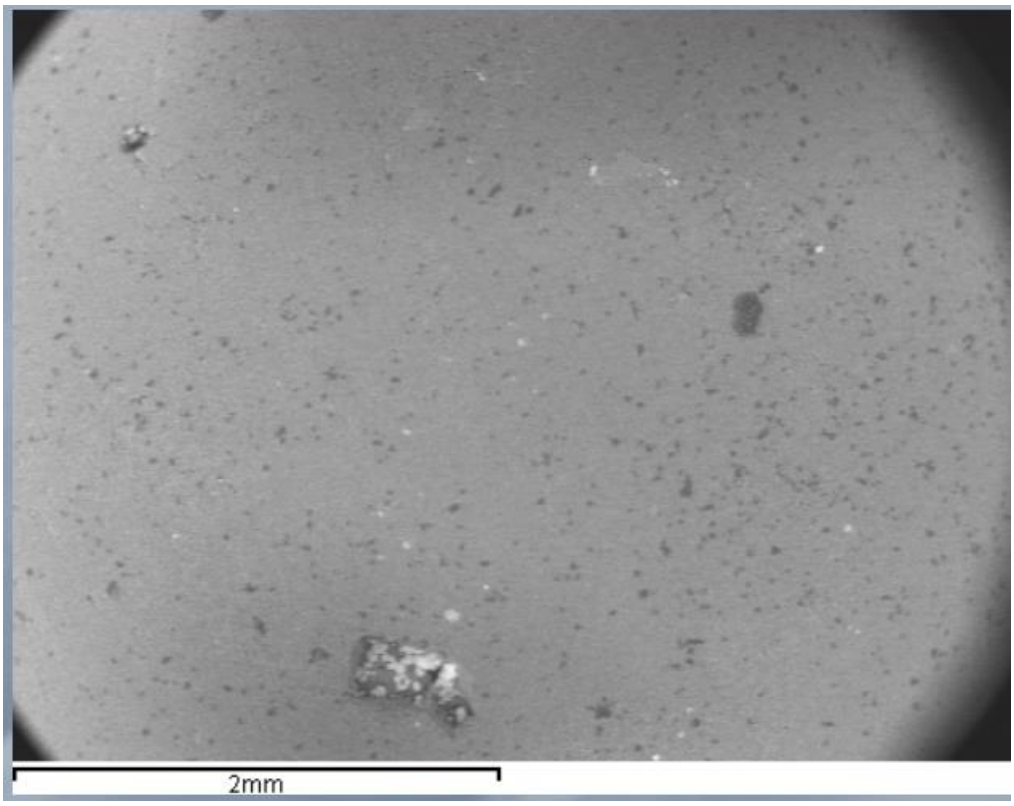
2mm

Anomaly 7

K, Al, Ti, Zr minerals present in region.

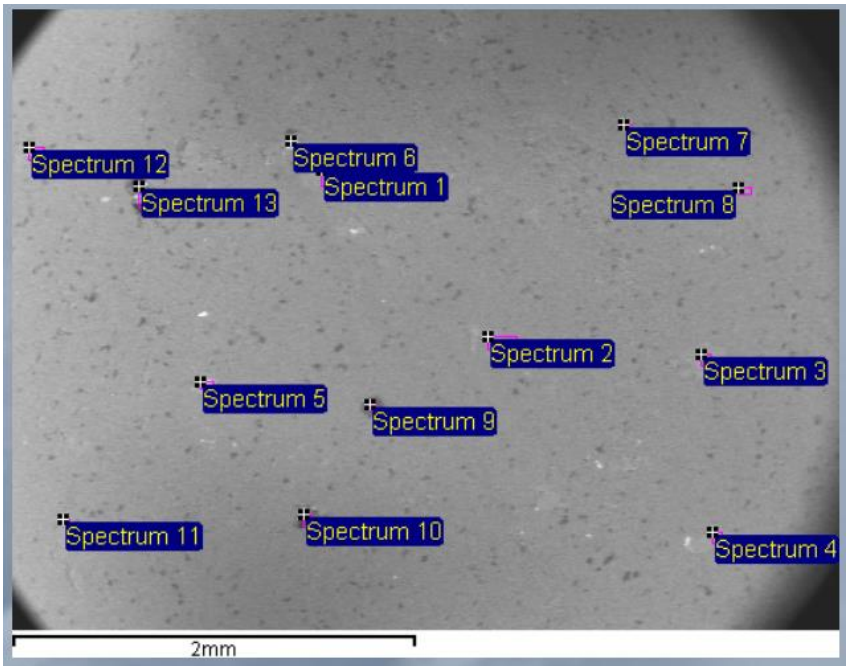

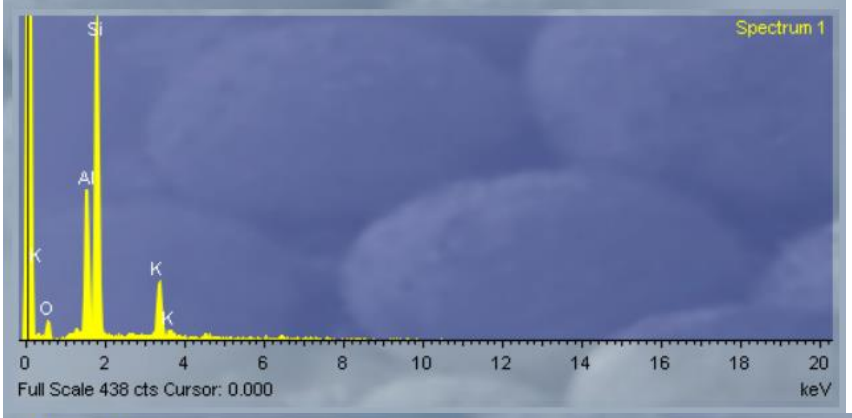

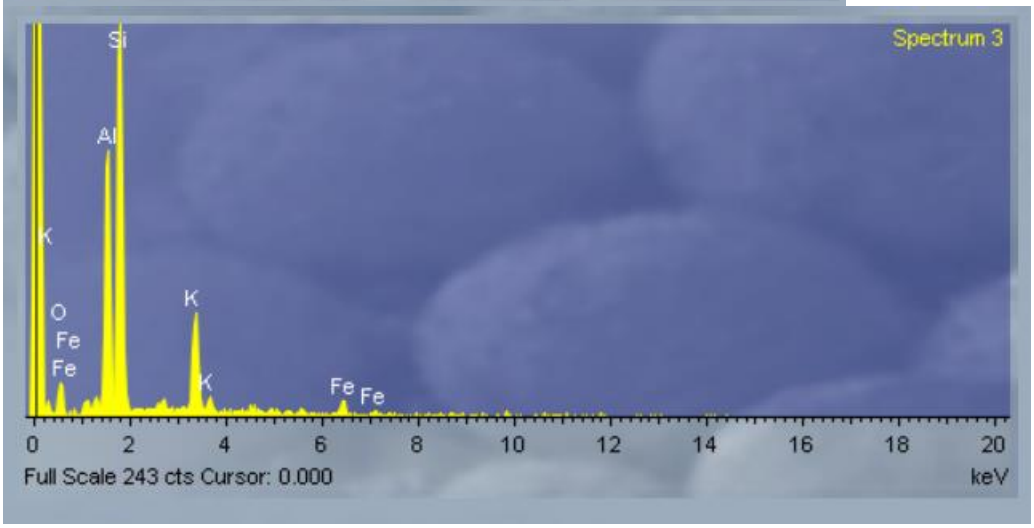

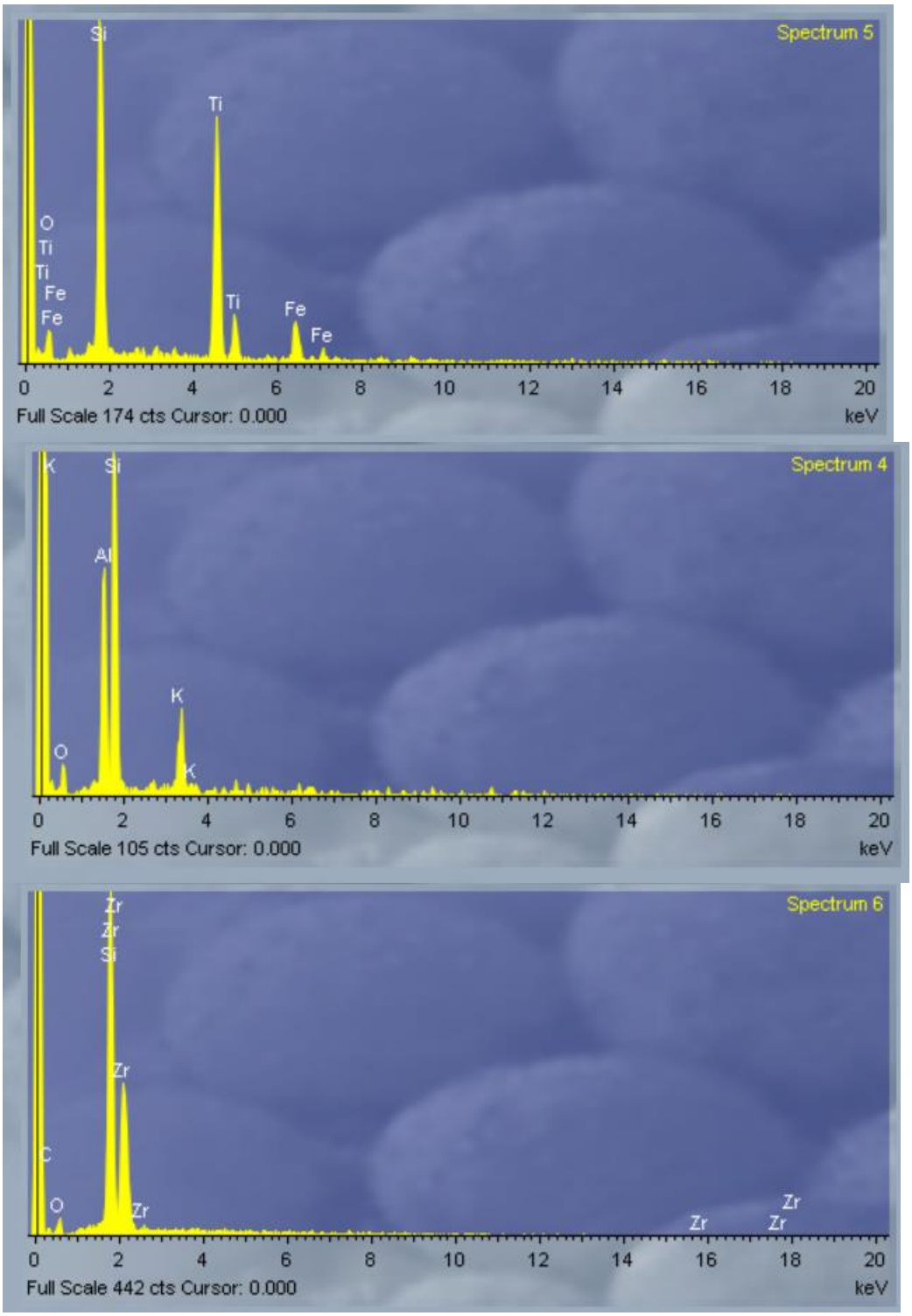
Spectrum 5
Si
Ti
O
Ti
Ti
Fe
Fe
Ti
Fe
Fe
0 2 4 6 8 10 12 14 16 18 20
Full Scale 174 cts Cursor: 0.000
keV
Spectrum 4
K
Si
Al
K
O
K
0 2 4 6 8 10 12 14 16 18 20
Full Scale 105 cts Cursor: 0.000
keV
Spectrum 6
Zr
Zr
Si
Zr
C
O
Zr
Zr
Zr
Zr
0 2 4 6 8 10 12 14 16 18 20
Full Scale 442 cts Cursor: 0.000
keV

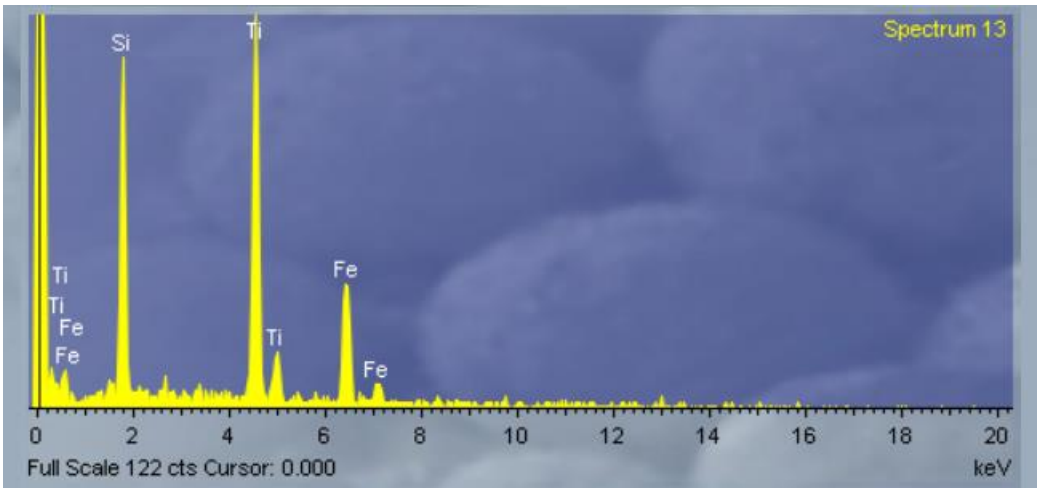
Spectrum 13
Si
Ti
Ti
Ti
Fe
Fe
Ti
Fe
Fe
0
2
4
6
8
10
12
14
16
18
20
Full Scale 122 cts Cursor: 0.000
keV

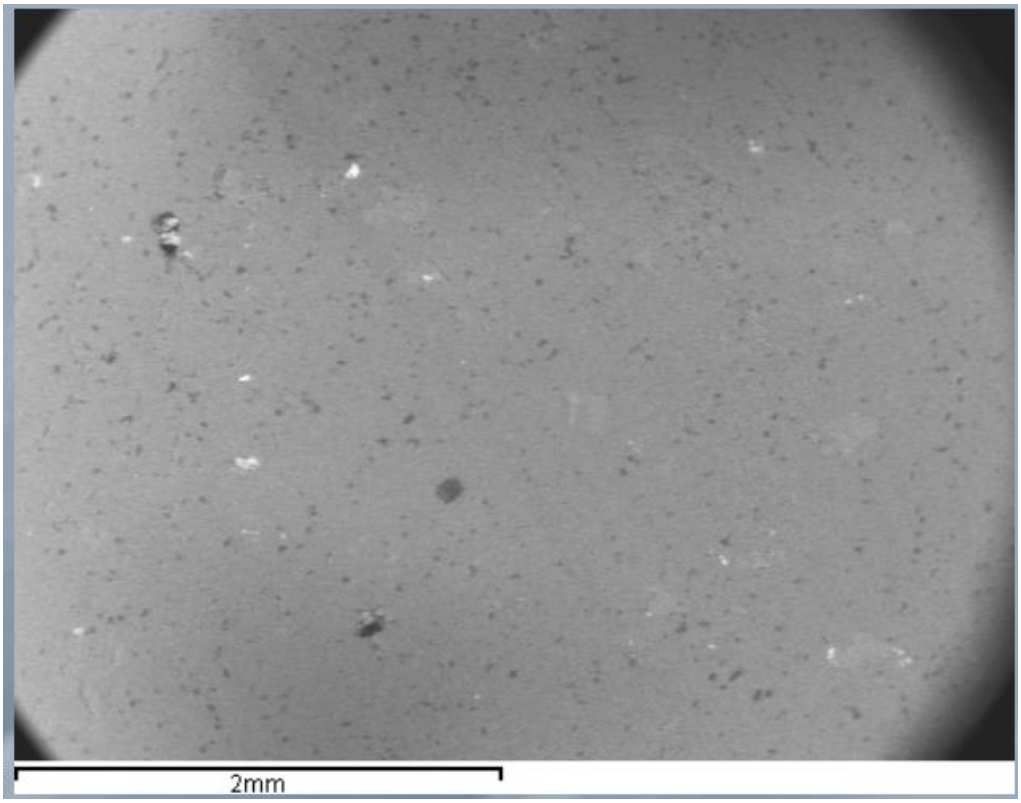
2mm

Anomaly 8

Ti, Zr bearing minerals present in region

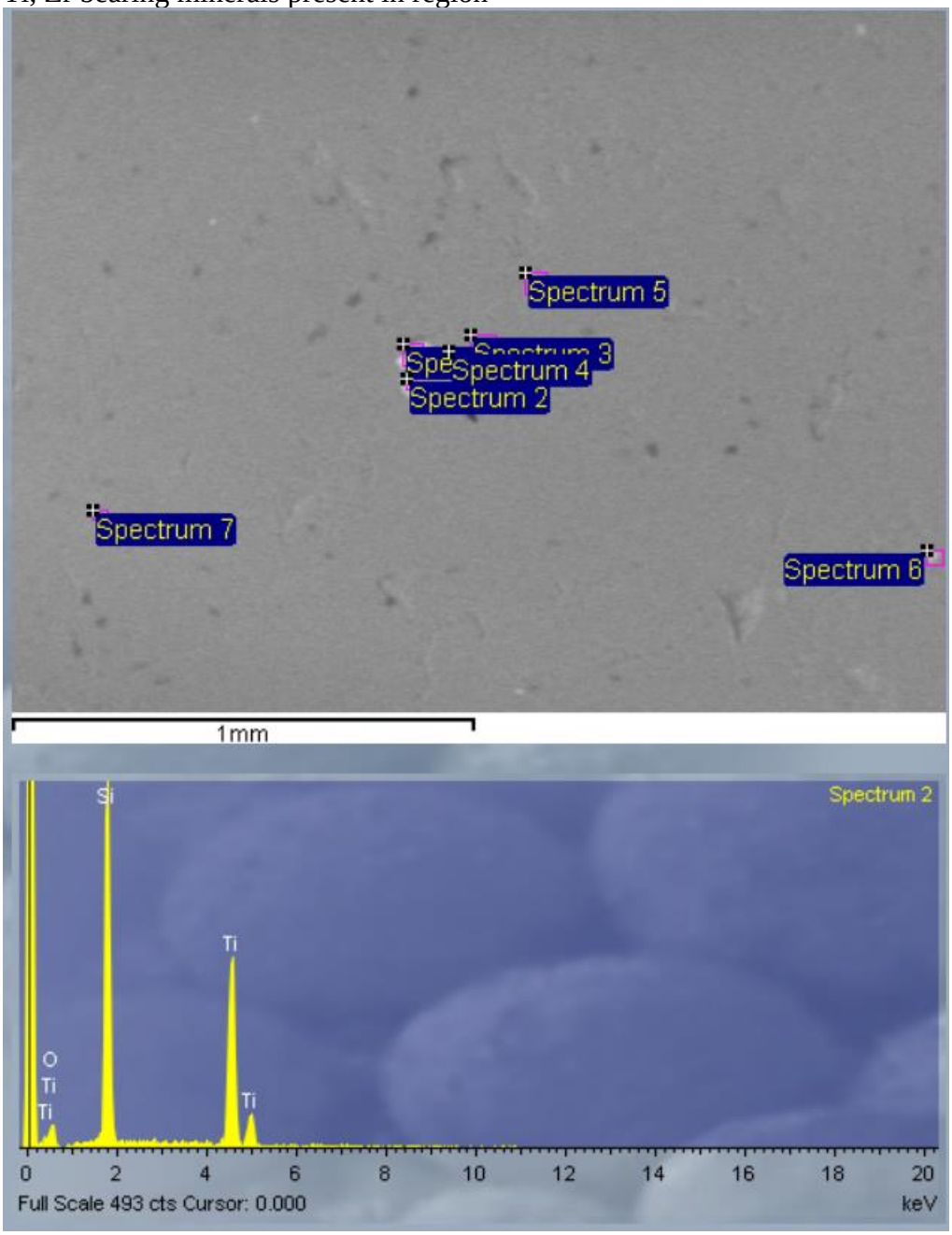

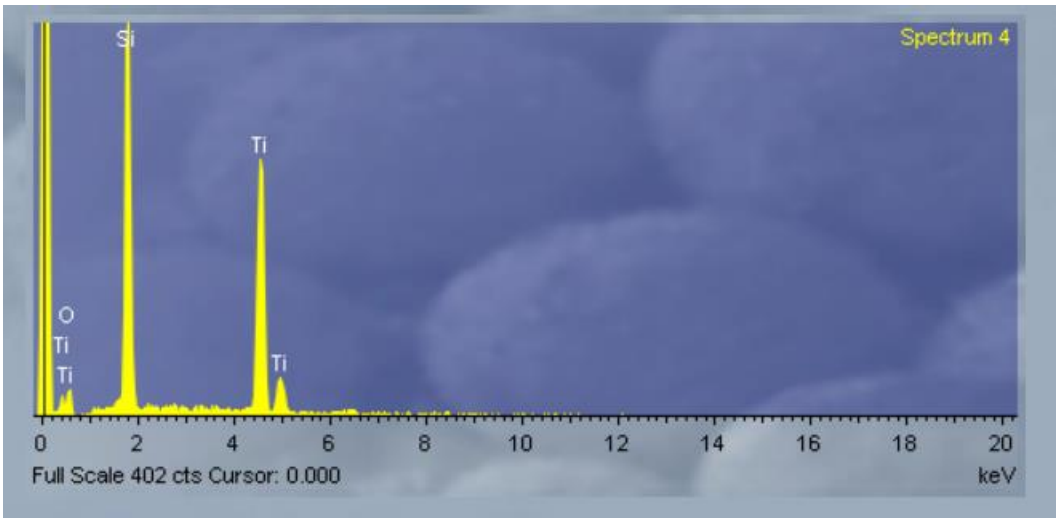
Spectrum 4
Si
Ti
O
Ti
Ti
Ti
0
2
4
6
8
10
12
14
16
18
20
Full Scale 402 cts Cursor: 0.000
keV

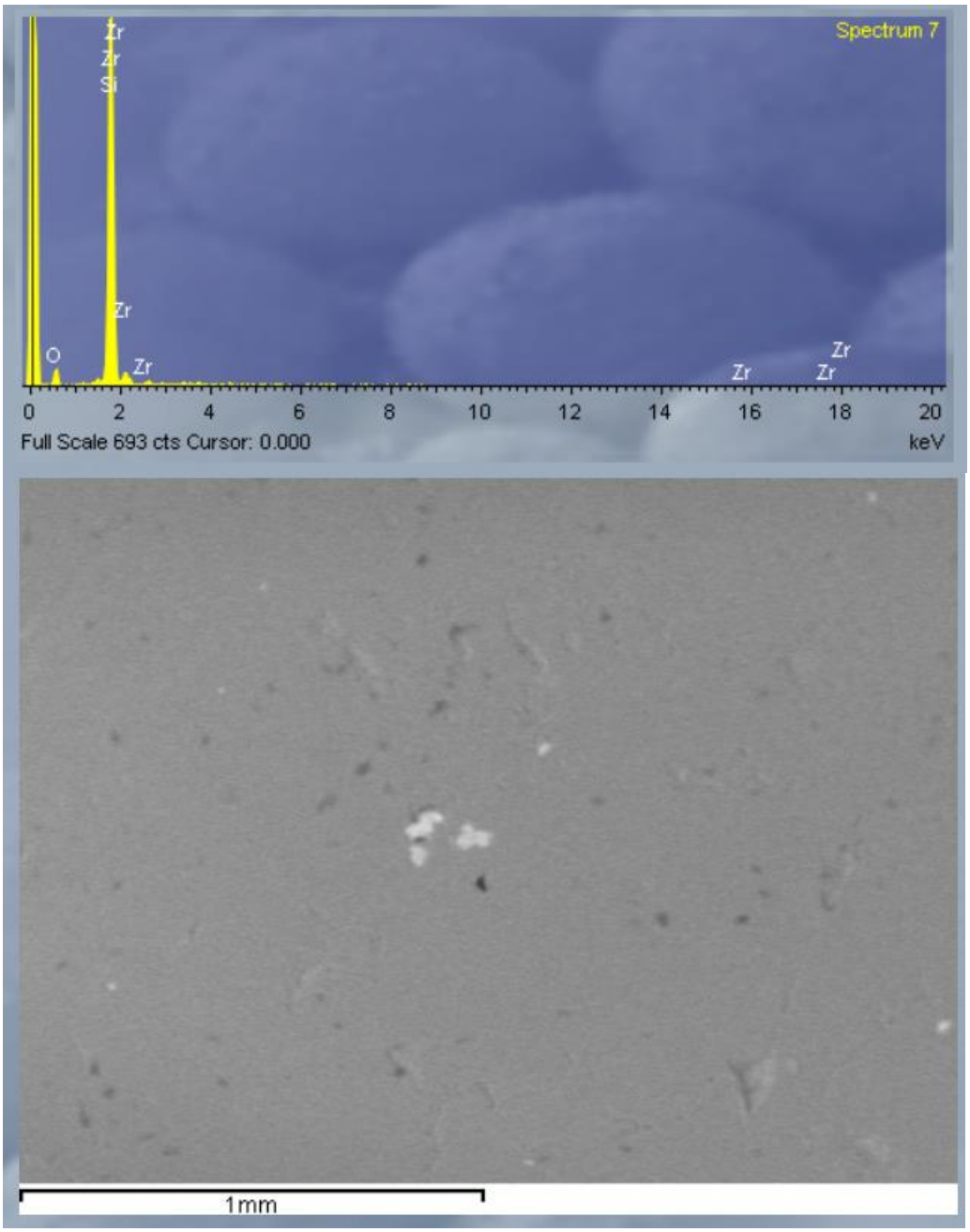
Spectrum 7
Zr
Zr
Si
Zr
O
Zr
Zr
Zr
Zr
0
2
4
6
8
10
12
14
16
18
20
Full Scale 693 cts Cursor: 0.000
keV
1 mm

Anomaly 9

Minor presence of K, Al

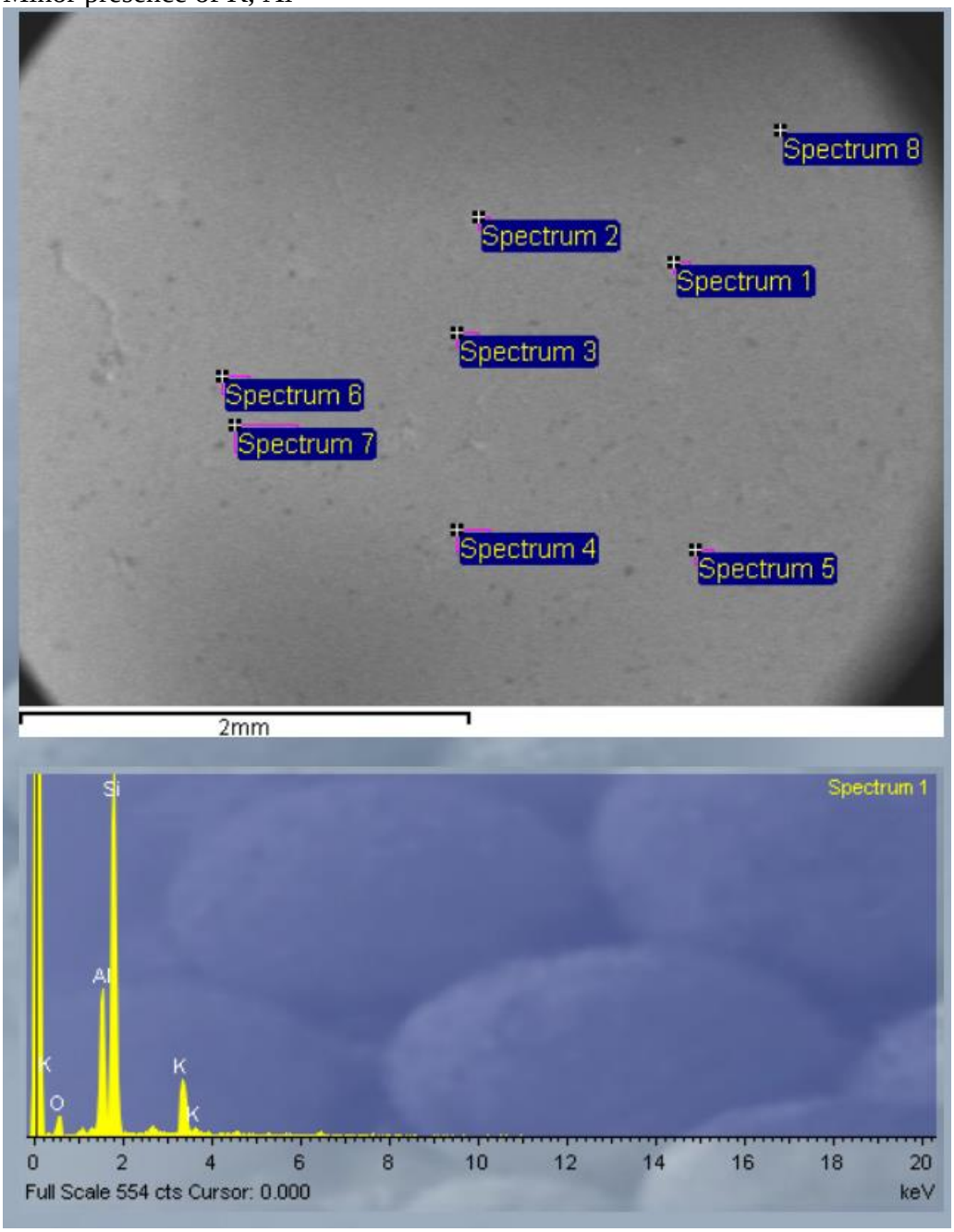

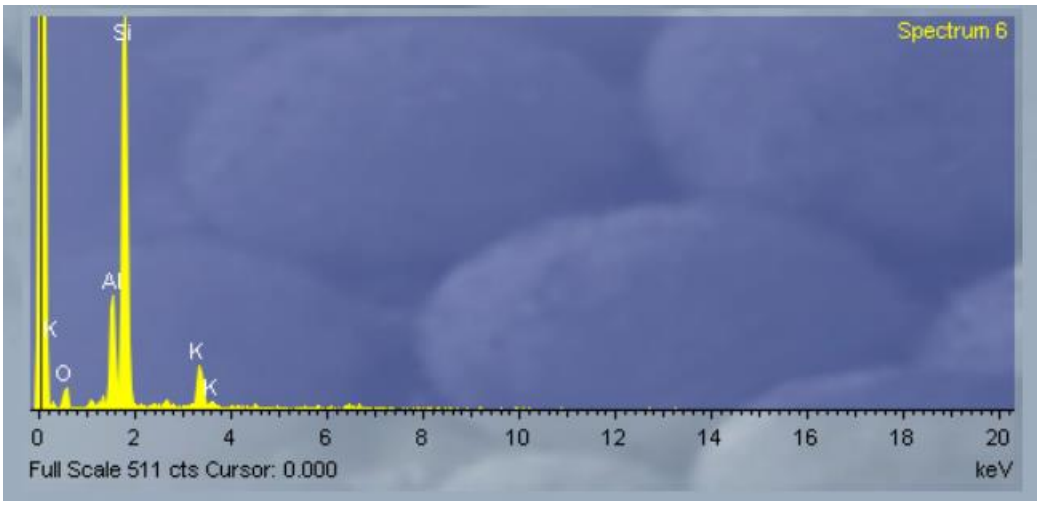
Spectrum 6
Si
Al
K
O
K
K
0 2 4 6 8 10 12 14 16 18 20
Full Scale 511 cts Cursor: 0.000
keV

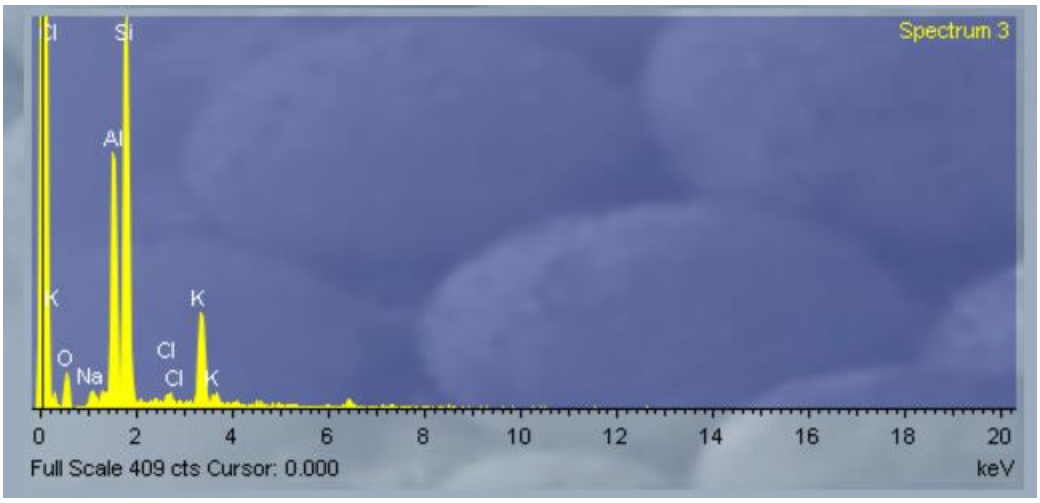
Spectrum 3
Cl
Si
Al
K
K
O
Na
Cl
Cl
K
0 2 4 6 8 10 12 14 16 18 20
Full Scale 409 cts Cursor: 0.000
keV

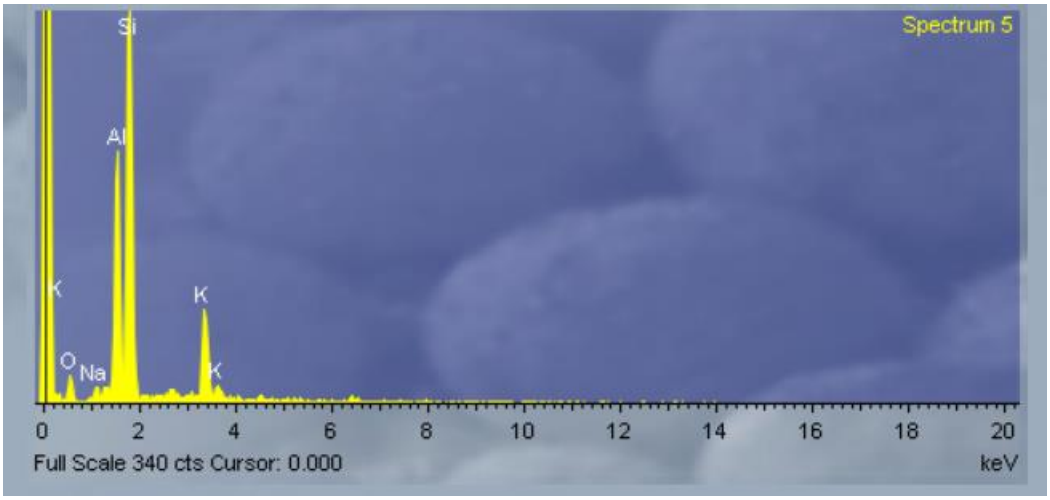
Spectrum 5
Si
Al
K
K
O
Na
K
0 2 4 6 8 10 12 14 16 18 20
Full Scale 340 cts Cursor: 0.000
keV

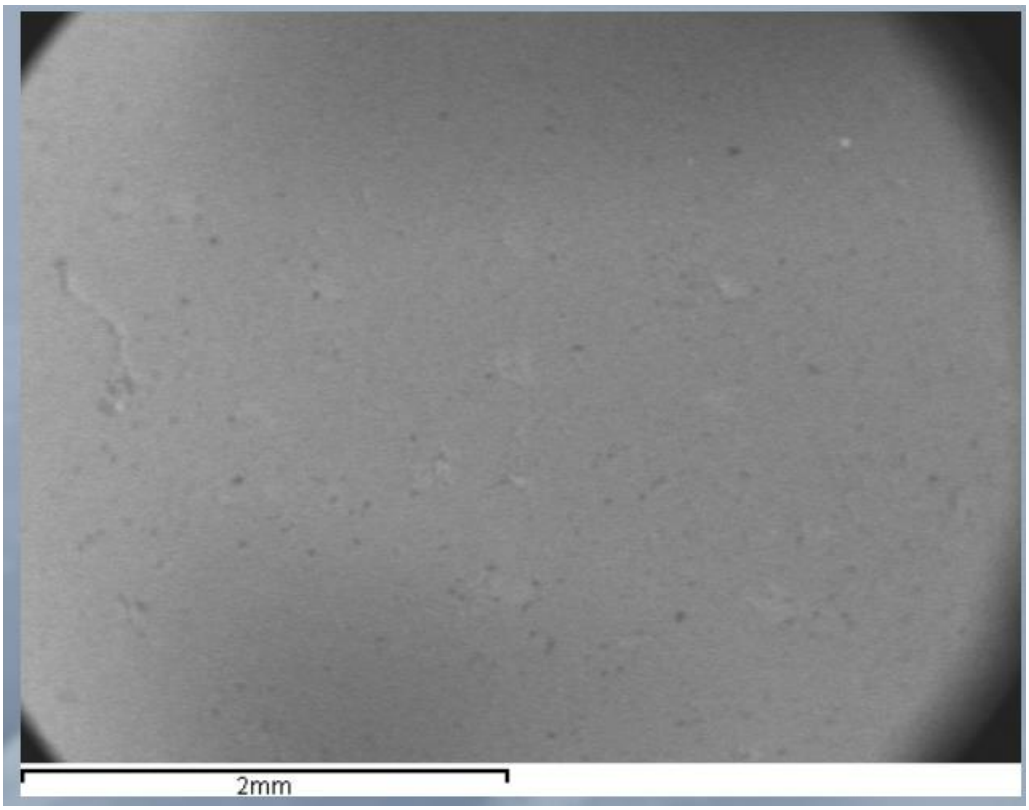
2mm

Core NS1

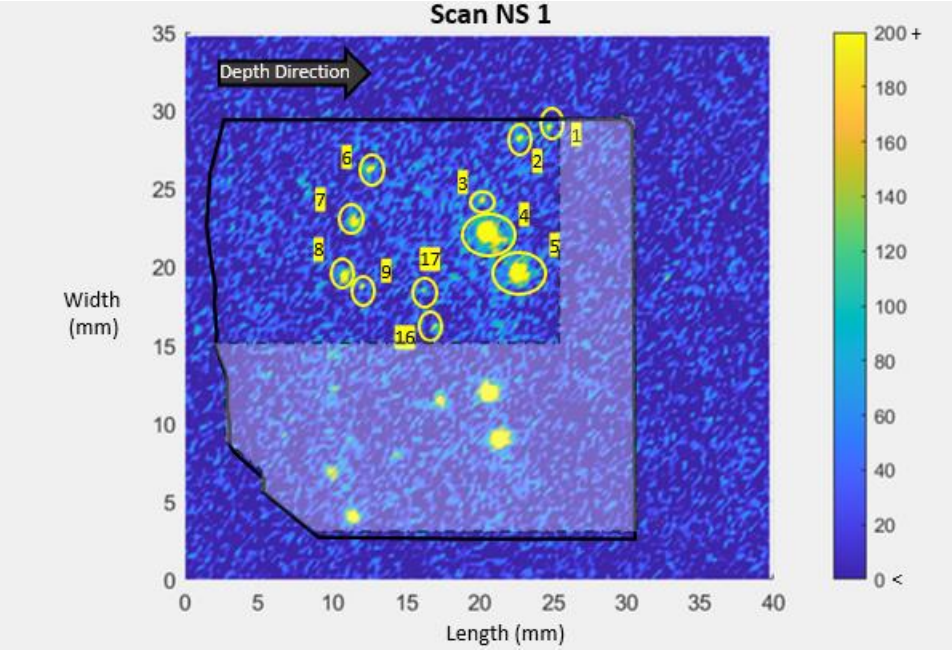

Anomalies presented in this section come from the non-grey region of the OSL scan.

Anomaly 1

Al, K bearing mineral content in region (vague grey area spectrum 1)

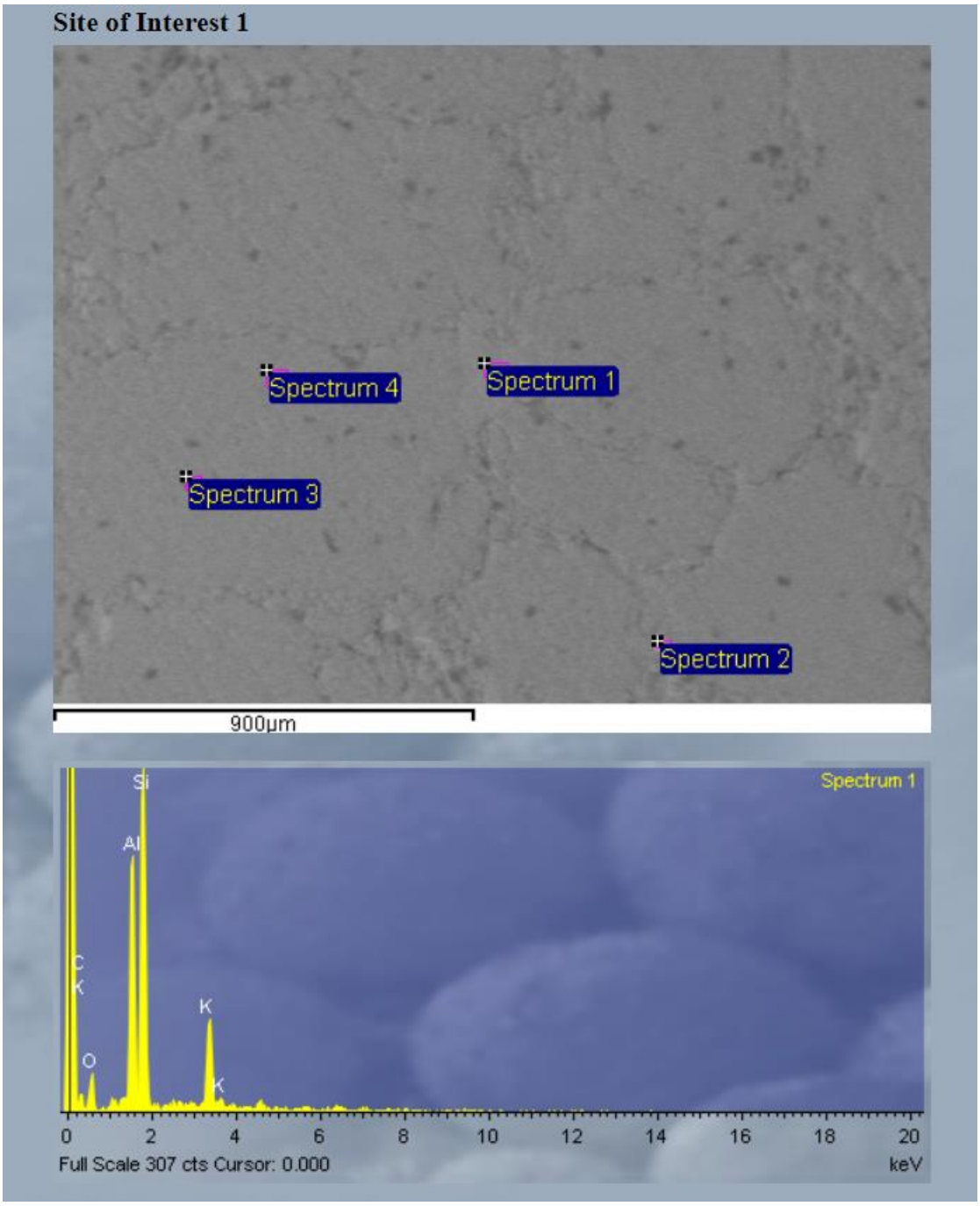

Anomaly 2

Ti mineralogy present in spectrum 1, 5,

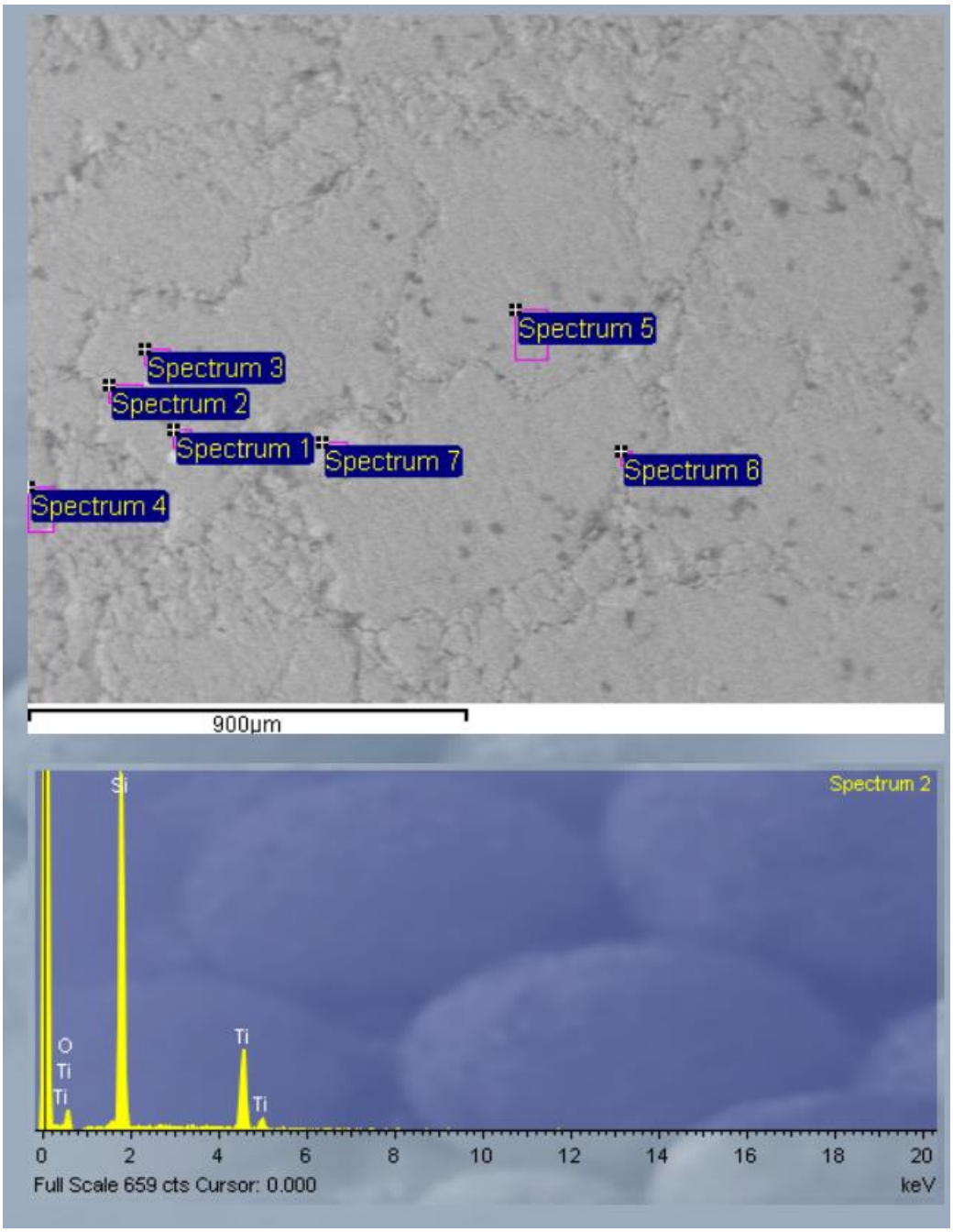

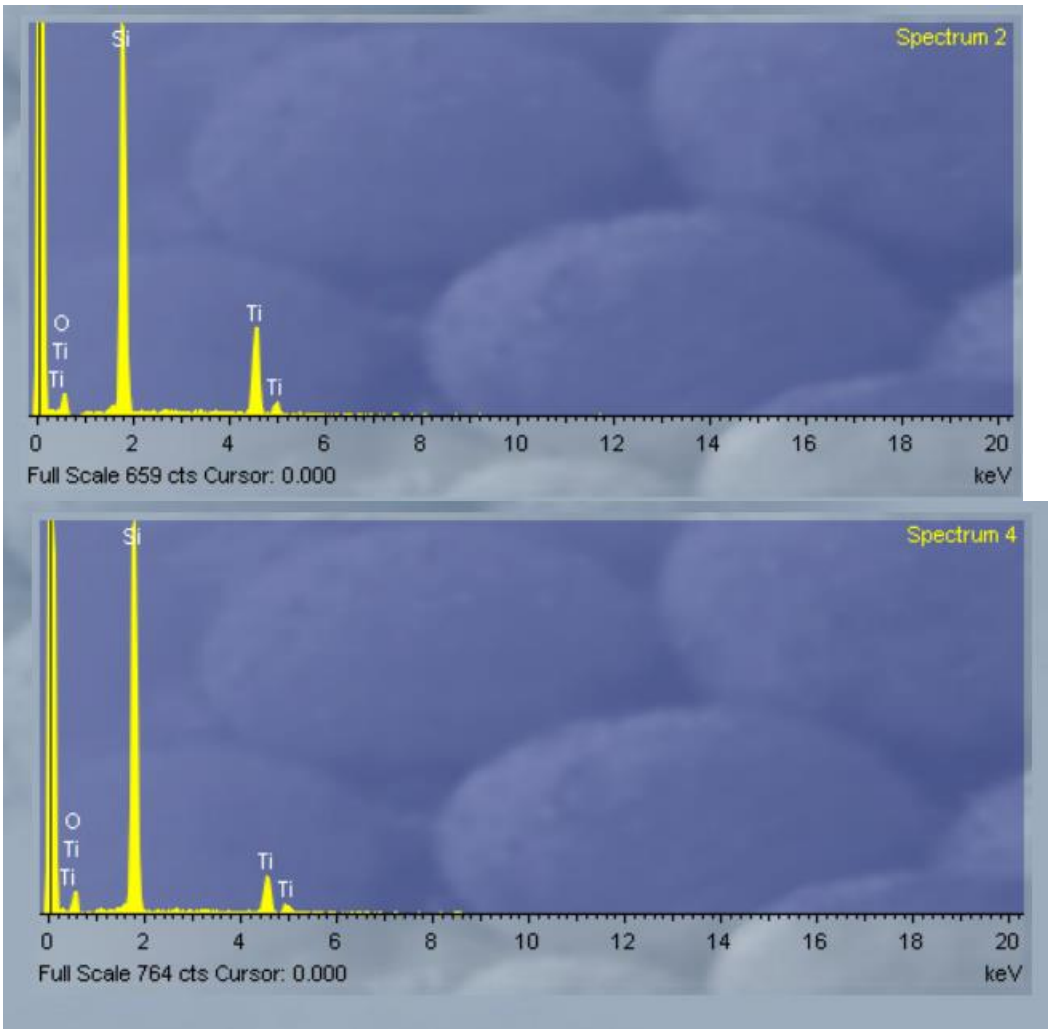
Spectrum 2
Si
O
Ti
Ti
Ti
Ti
0 2 4 6 8 10 12 14 16 18 20
Full Scale 659 cts Cursor: 0.000
keV
Spectrum 4
Si
O
Ti
Ti
Ti
Ti
0 2 4 6 8 10 12 14 16 18 20
Full Scale 764 cts Cursor: 0.000
keV

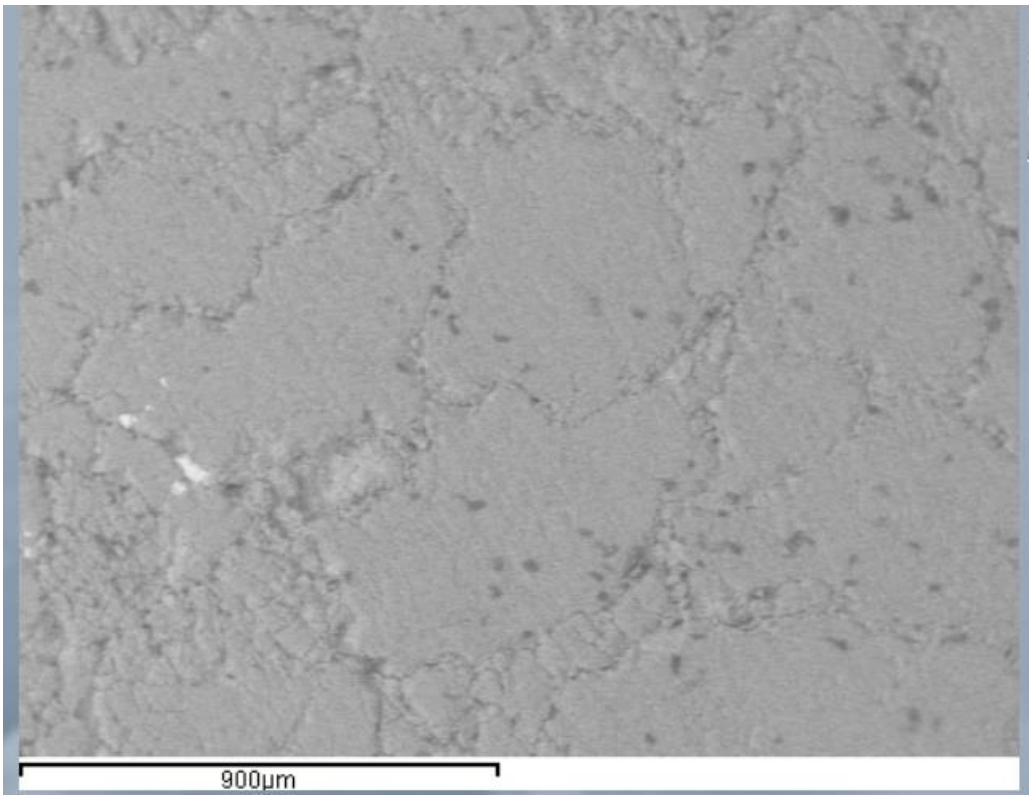
900µm

Anomaly 3

Trace iron oxides – still removed from depth profile given intensity of signal.

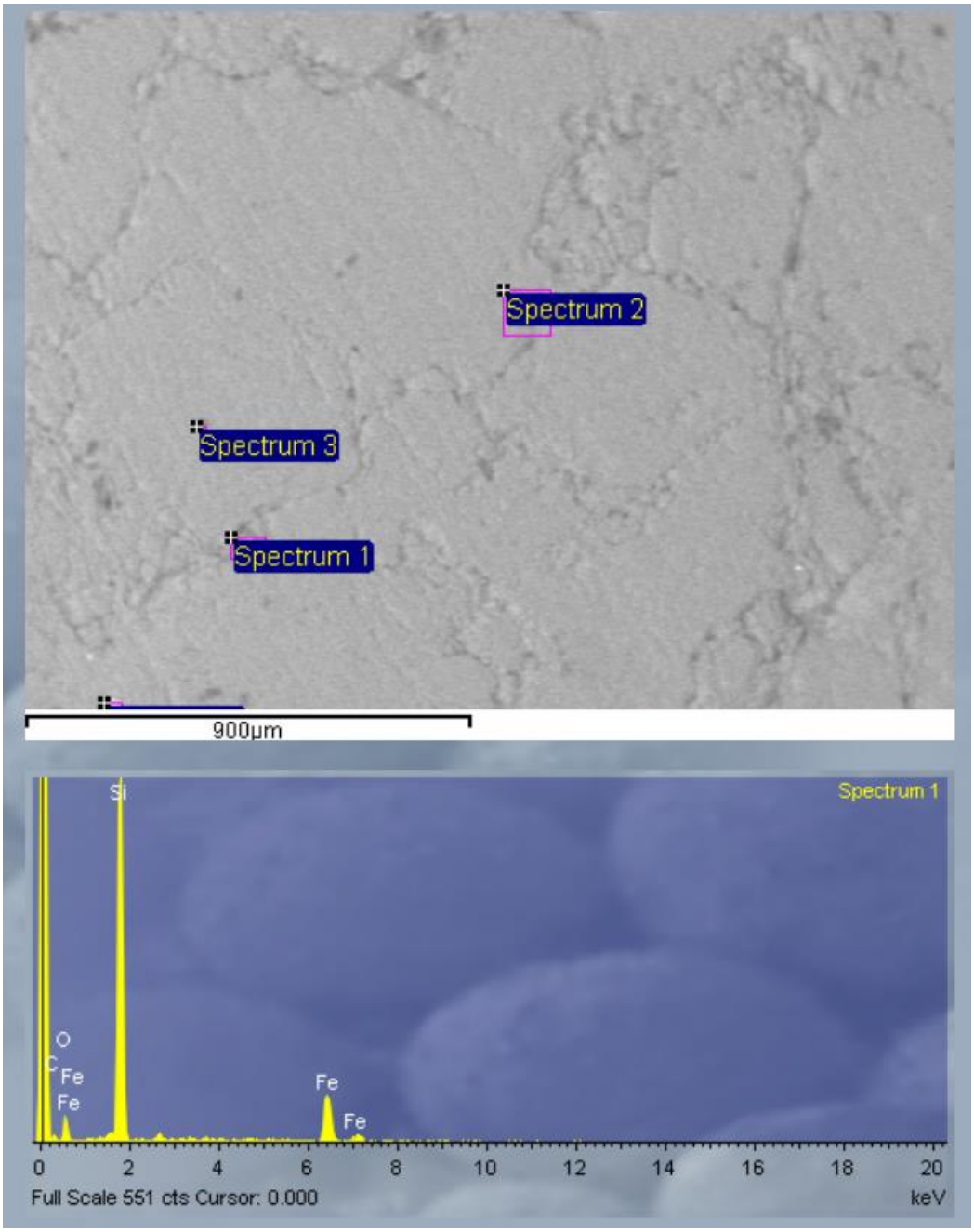

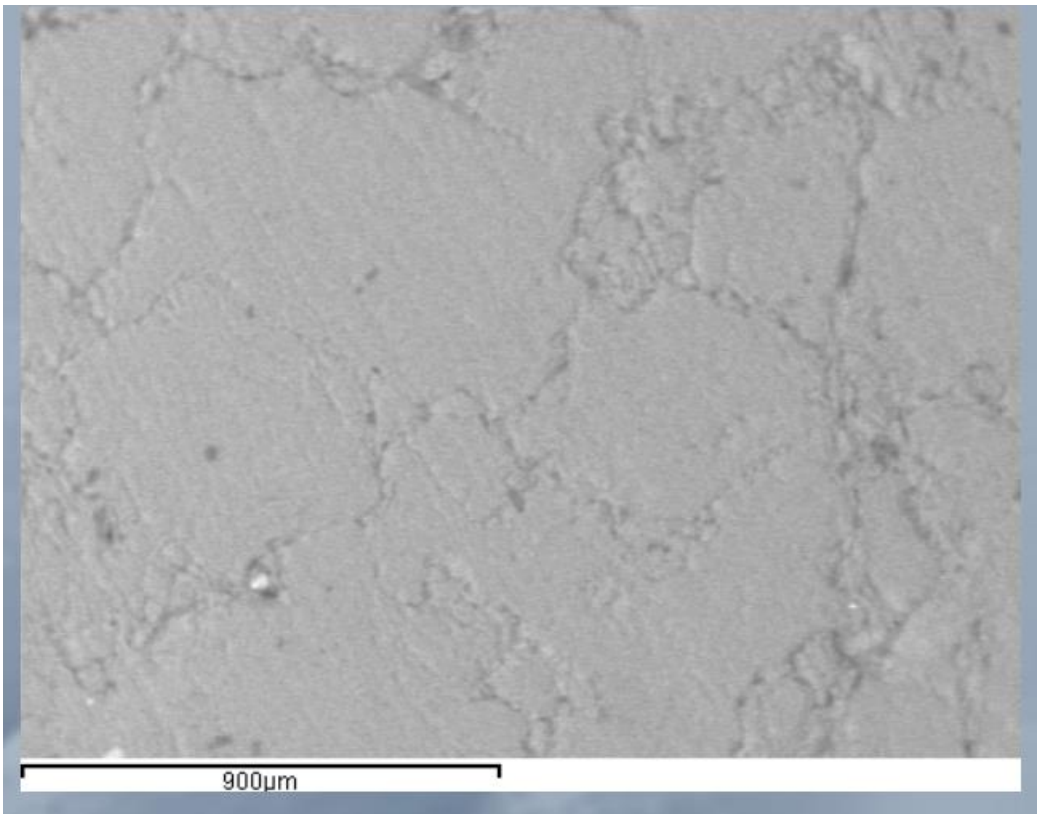
900µm

Anomaly 4

Zircon present in spectrum

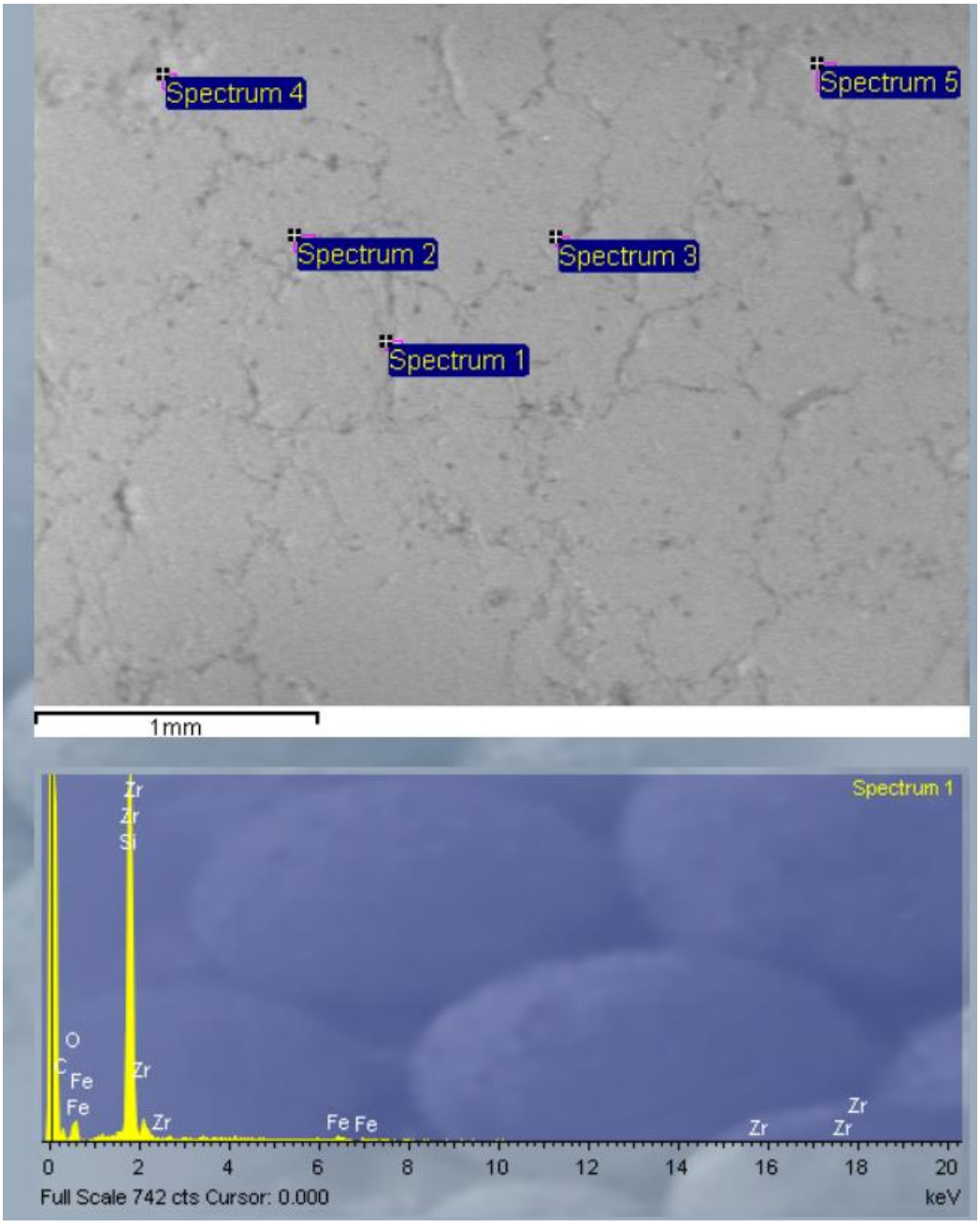

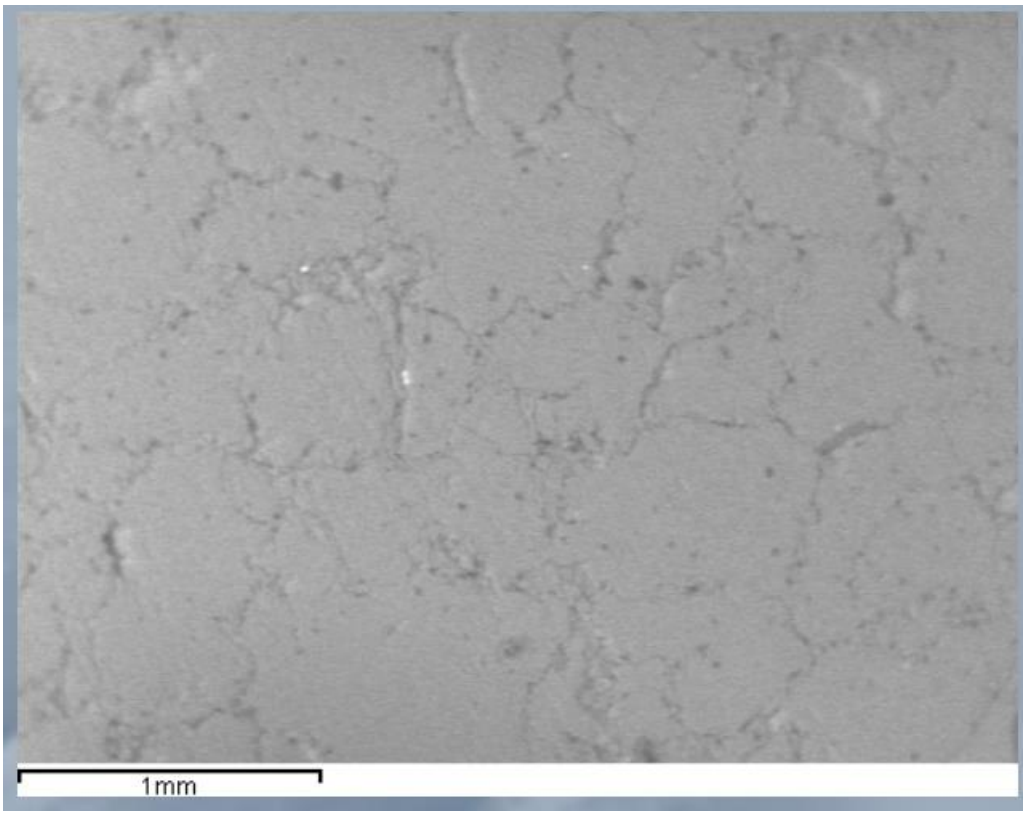
1mm

Anomaly 5

Traces of Ti, Al bearing minerals present in region

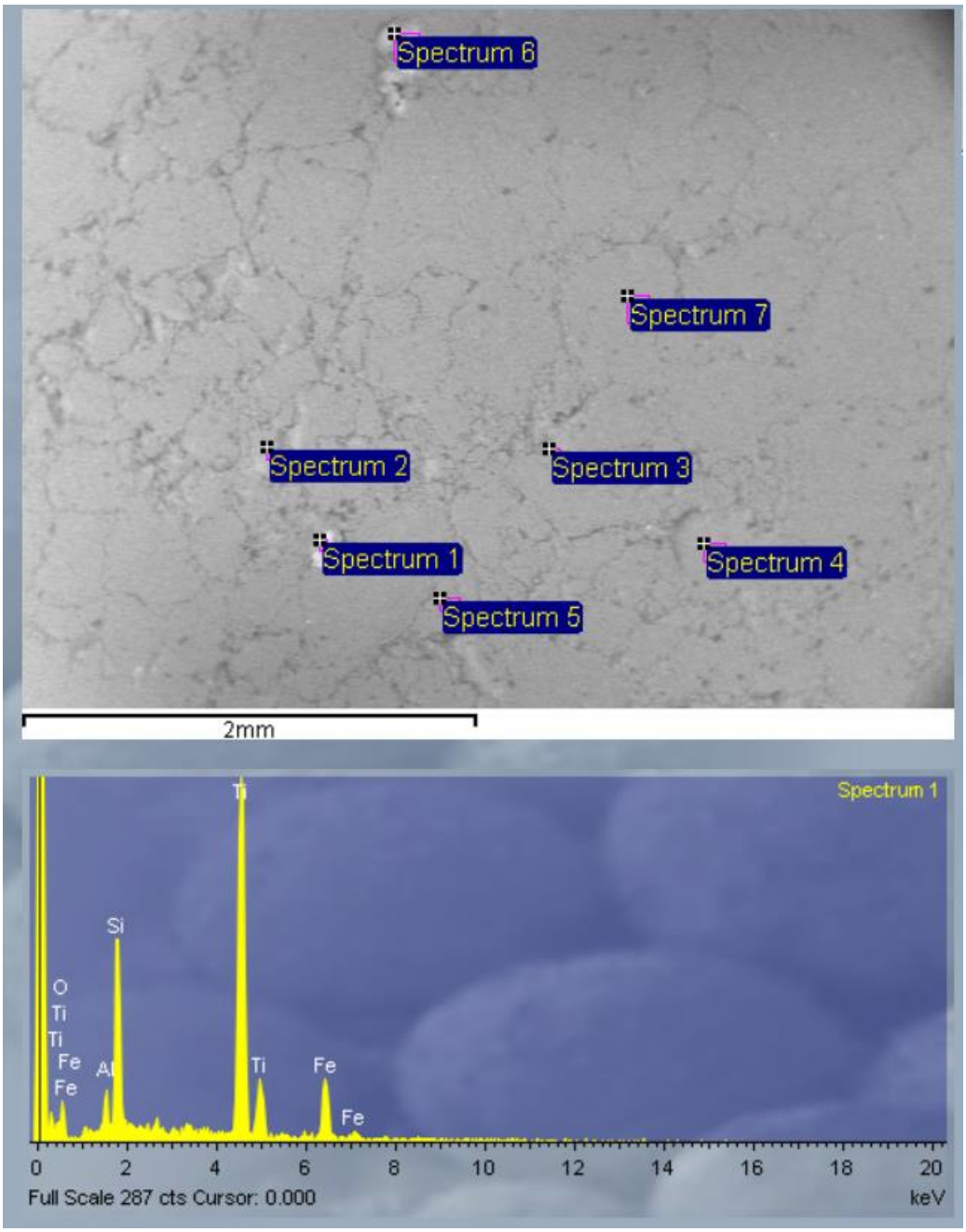

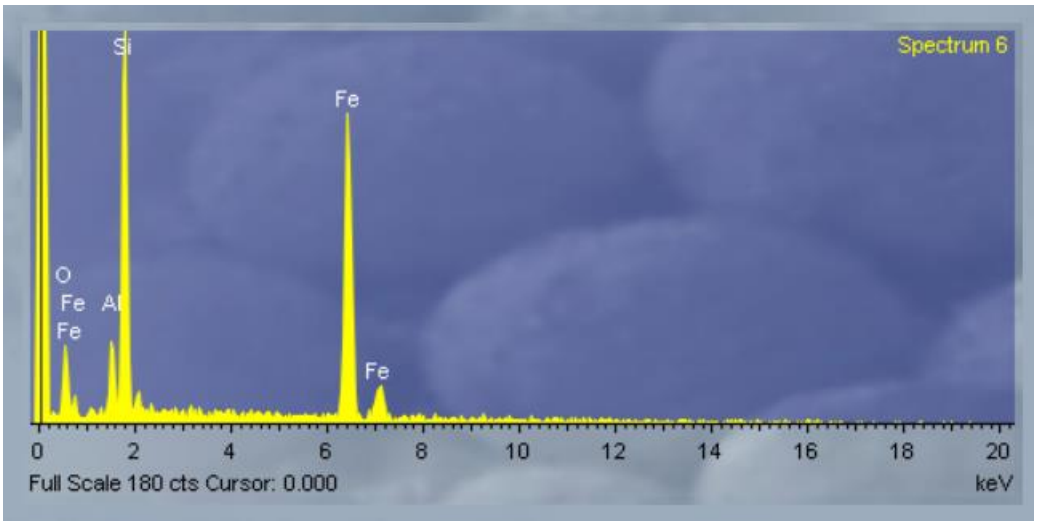
Spectrum 6
Si
Fe
O
Fe
Fe
Al
Fe
0
2
4
6
8
10
12
14
16
18
20
Full Scale 180 cts Cursor: 0.000
keV

Anomaly 6

Trace Ti bearing minerals.

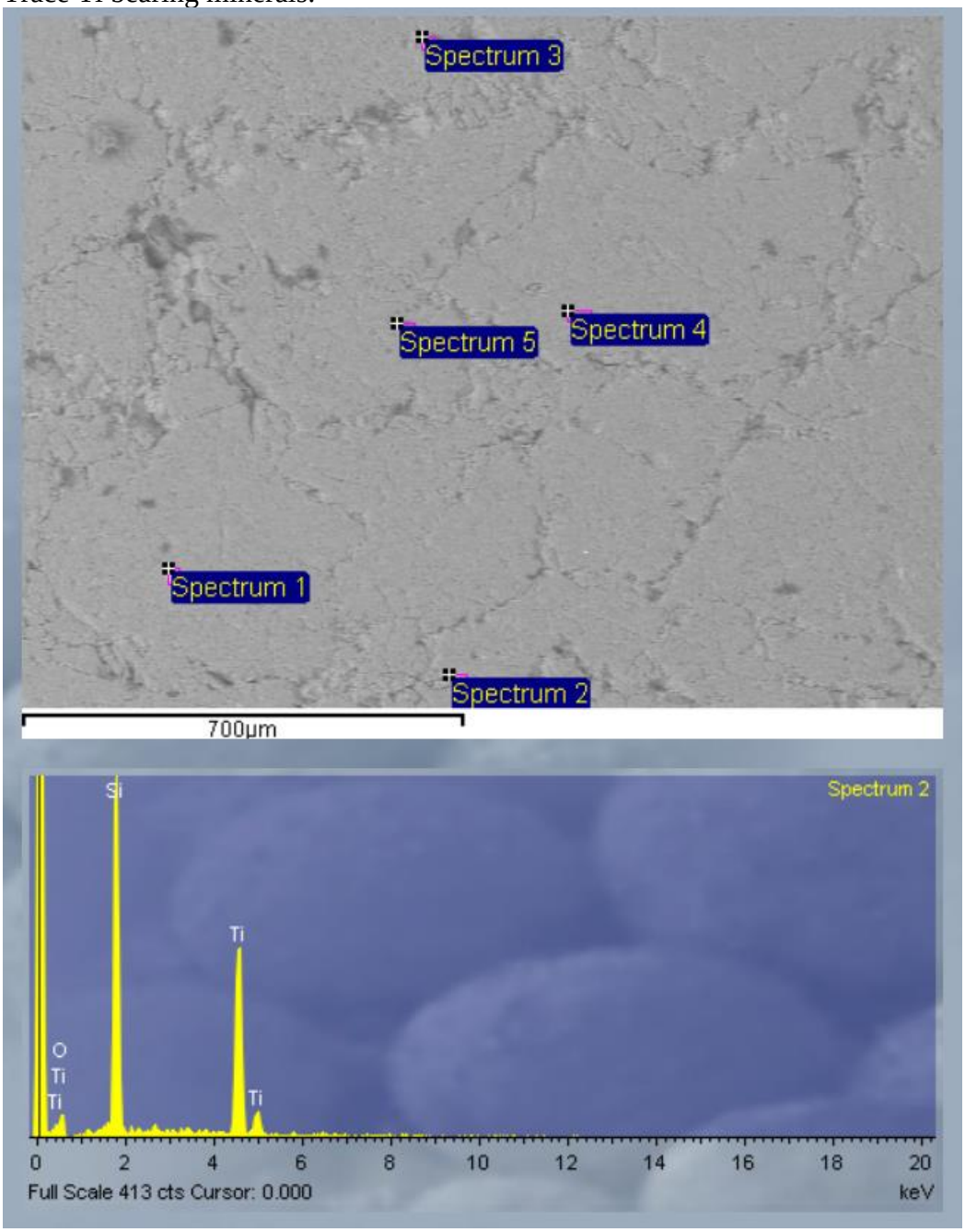

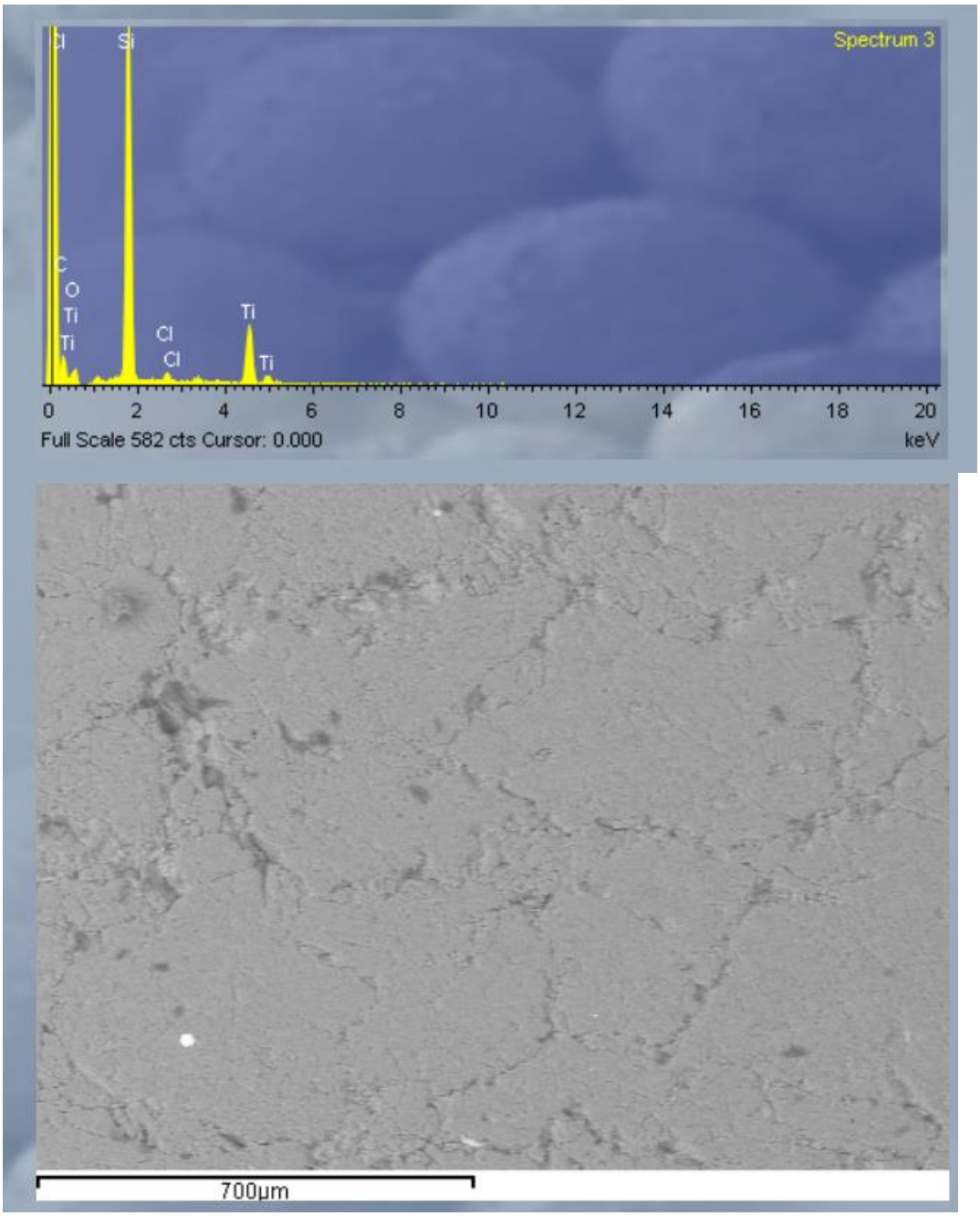
Cl
Si
Spectrum 3
C
O
Ti
Ti
Cl
Cl
Ti
Ti
0
2
4
6
8
10
12
14
16
18
20
Full Scale 582 cts Cursor: 0.000
keV
700µm

Anomaly 7

Ti bearing, Zr bearing minerals on site.

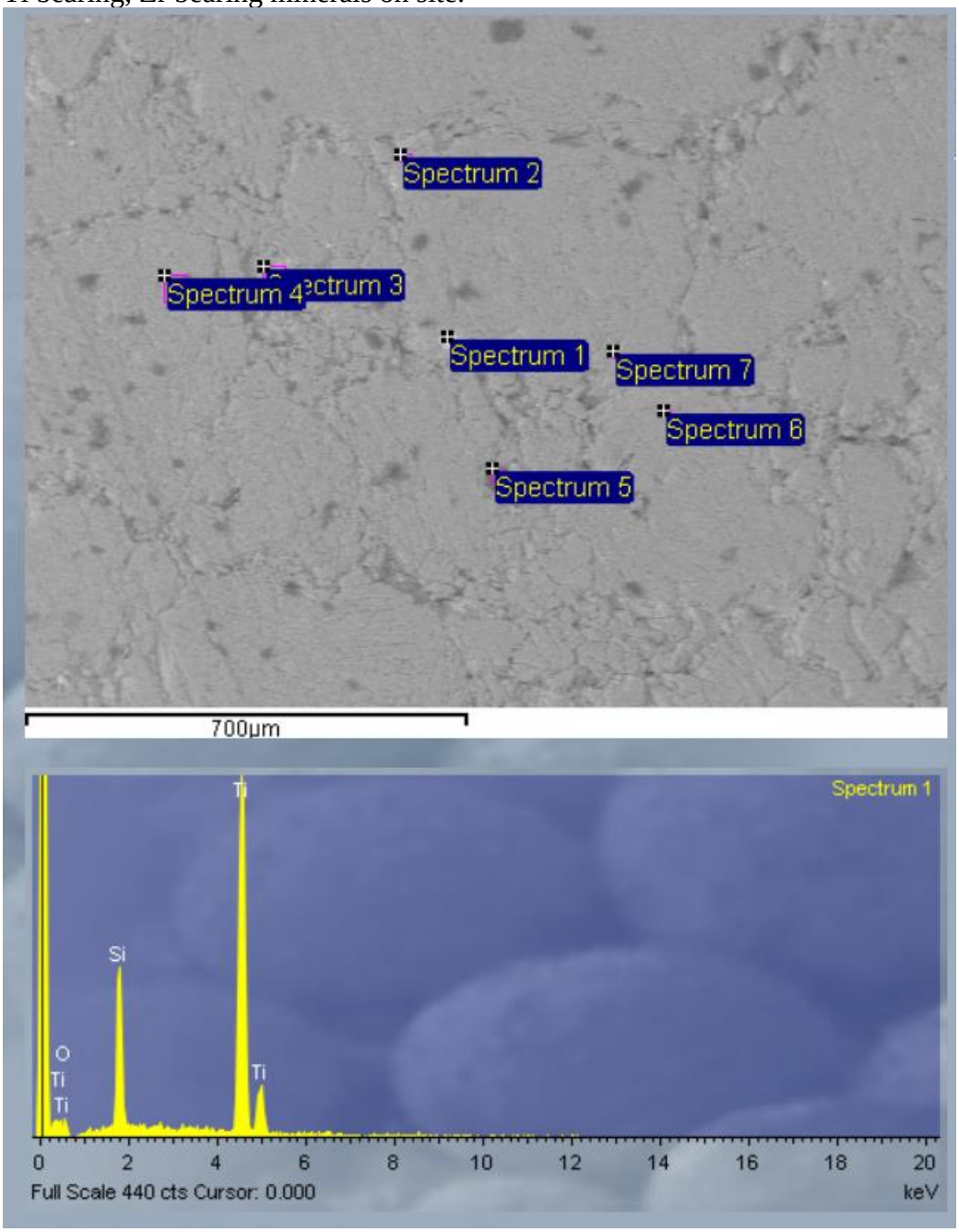

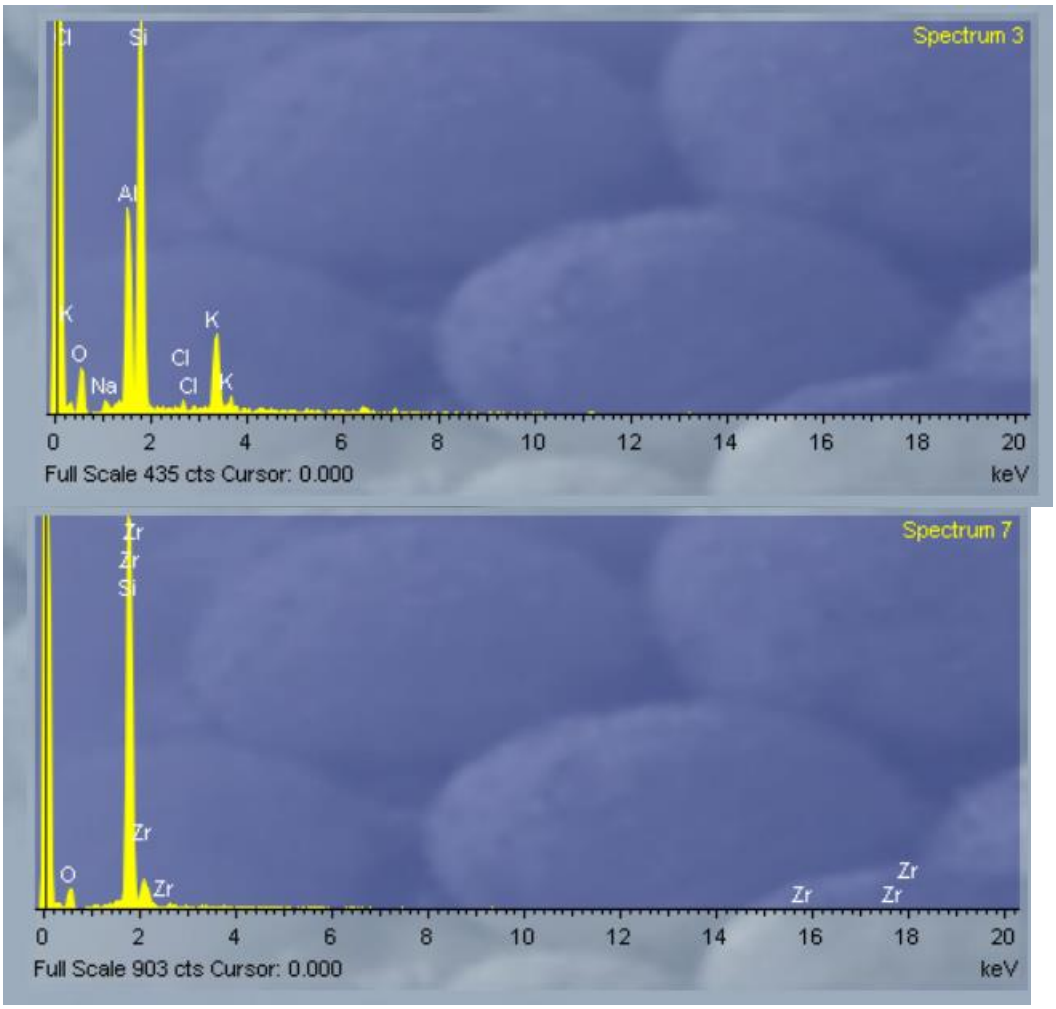
Spectrum 3
Cl
Si
Al
K
O
Na
Cl
Cl
K
K
0 2 4 6 8 10 12 14 16 18 20
Full Scale 435 cts Cursor: 0.000
keV
Spectrum 7
Zr
Zr
Si
Zr
O
Zr
Zr
Zr
Zr
0 2 4 6 8 10 12 14 16 18 20
Full Scale 903 cts Cursor: 0.000
keV

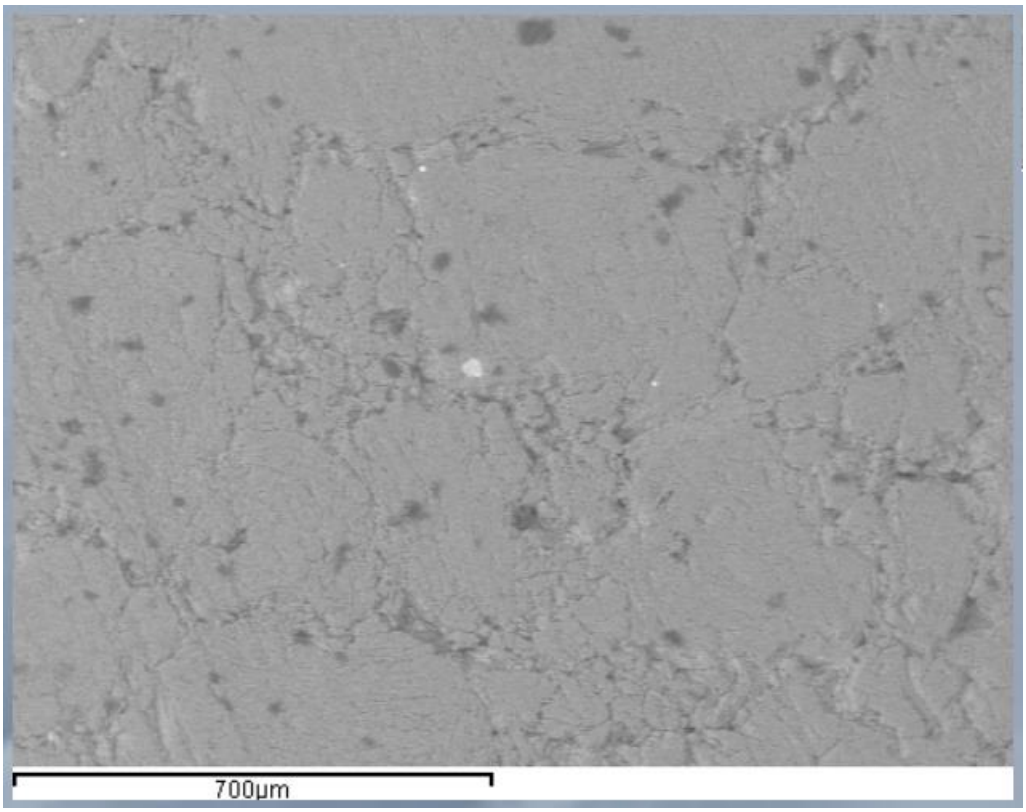
700µm

Anomaly 8

Al, K bearing minerals.

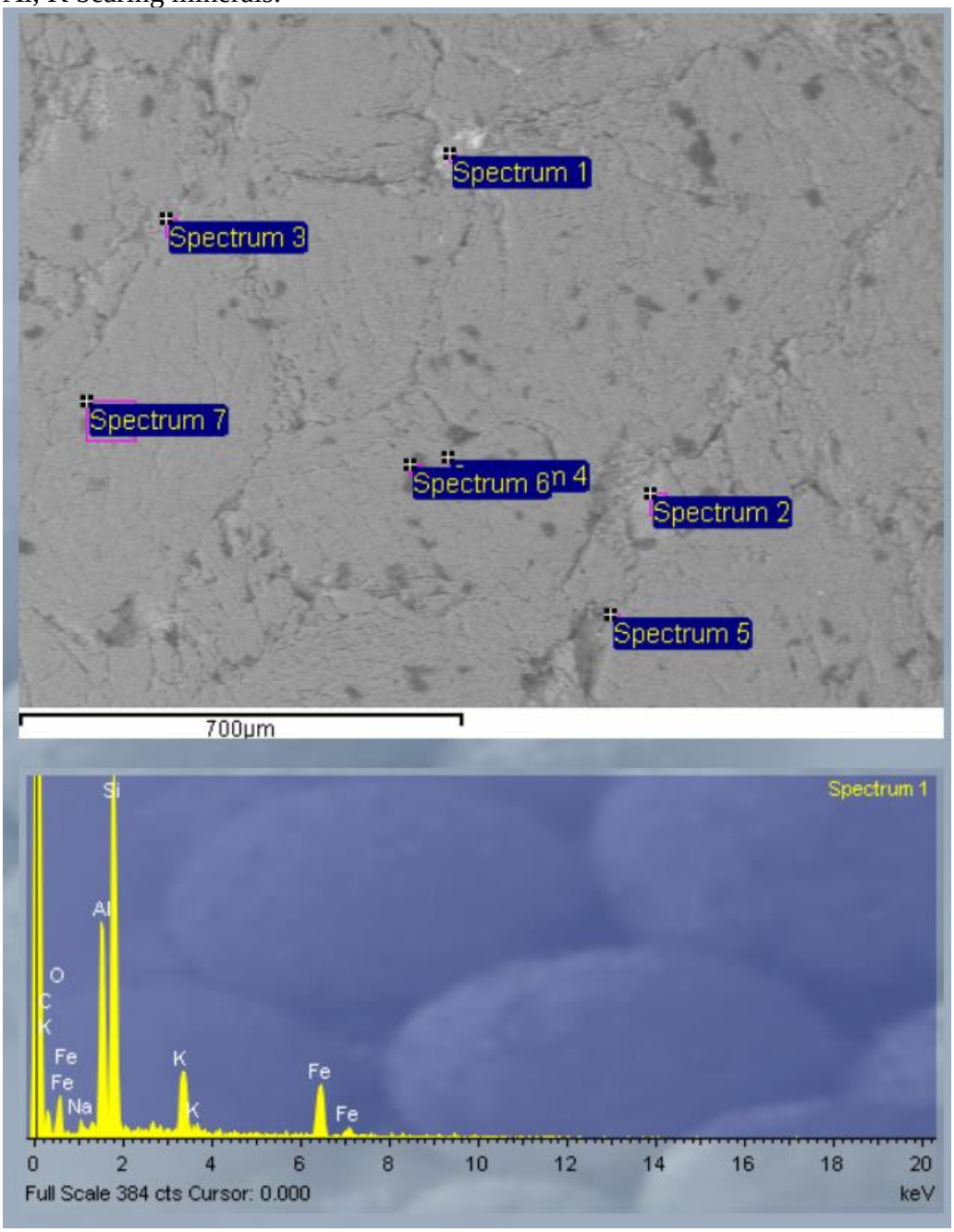

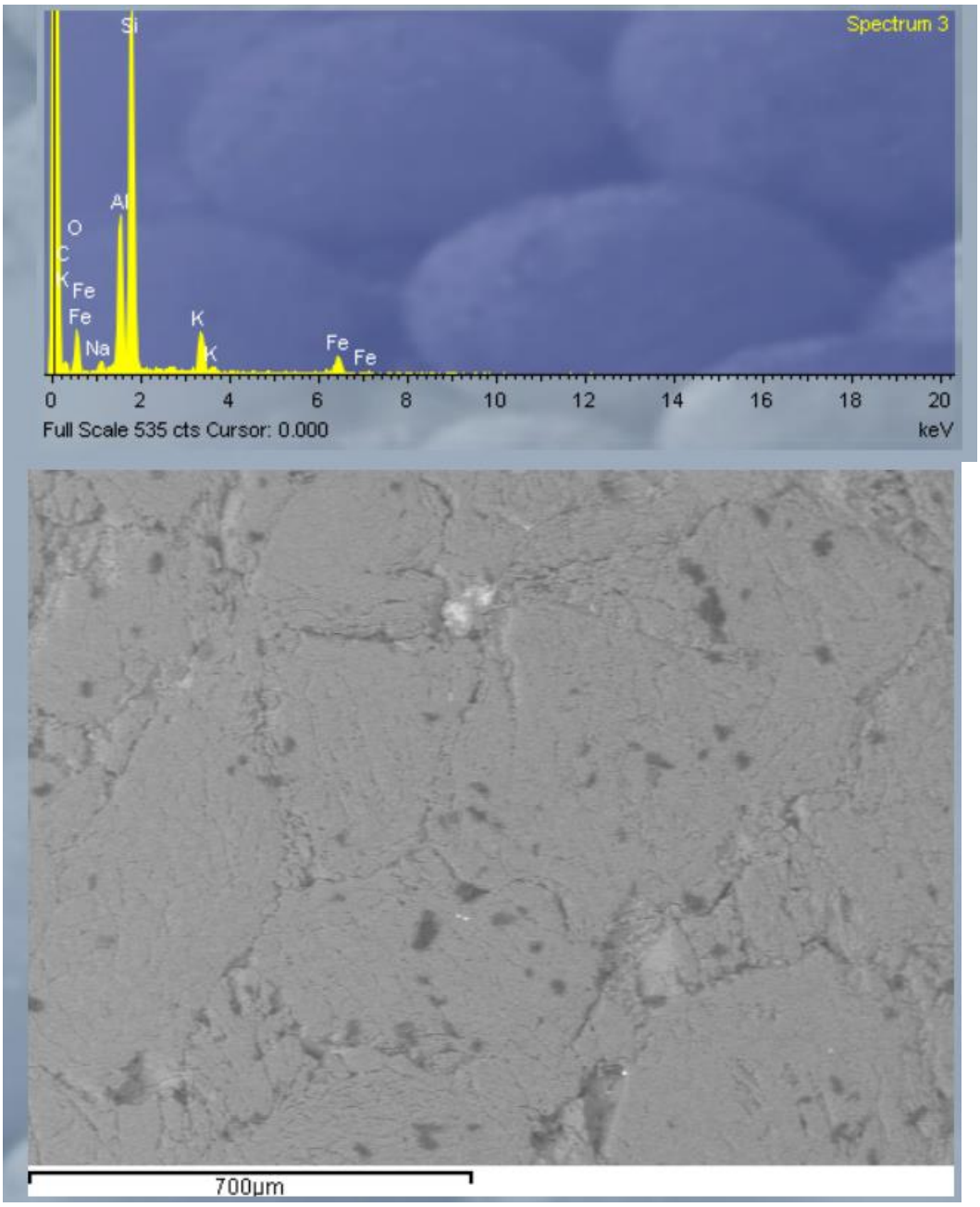

Anomaly 9

Al, K bearing mineral present

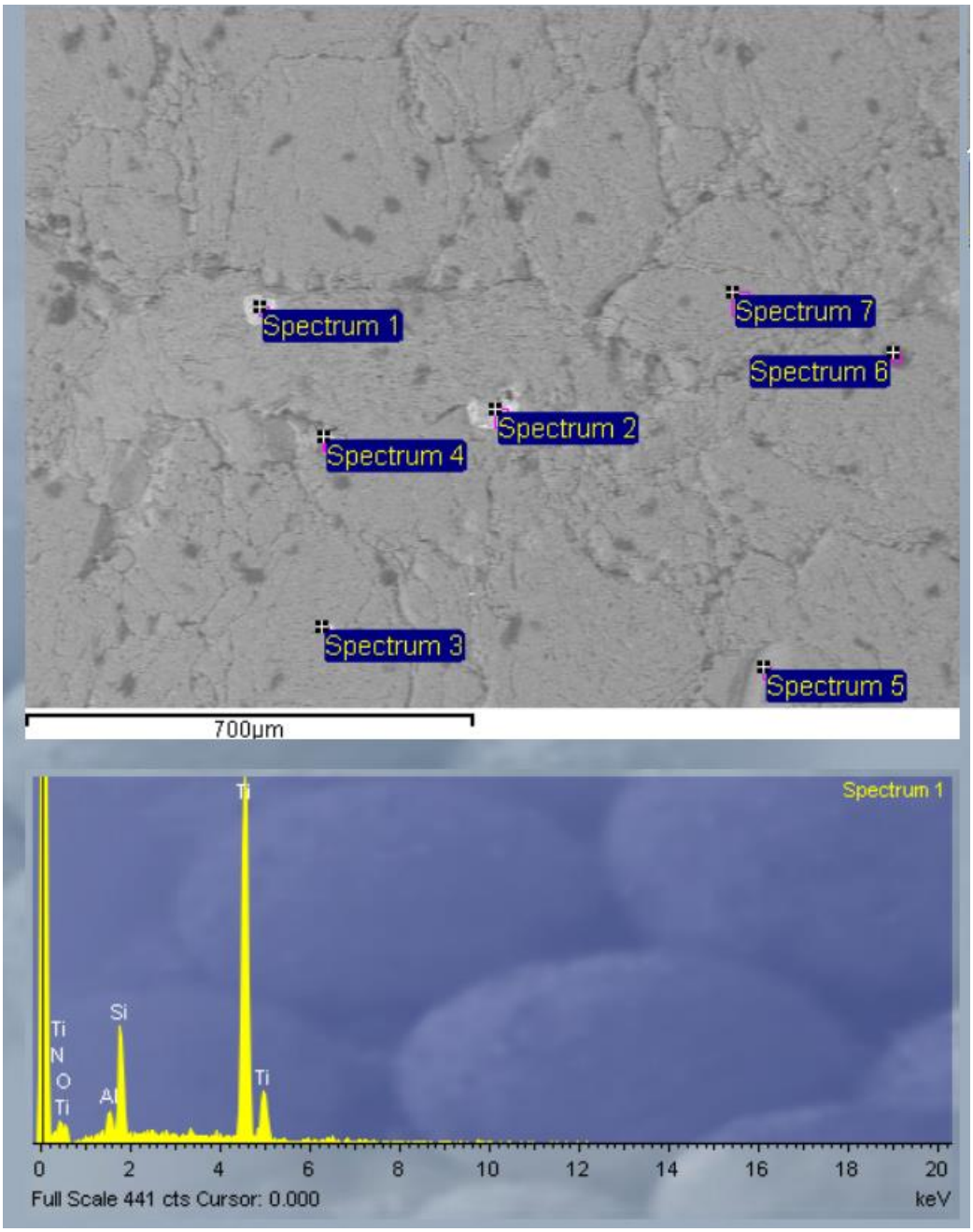
Spectrum 1
Spectrum 7
Spectrum 6
Spectrum 2
Spectrum 4
Spectrum 3
Spectrum 5
700µm
Spectrum 1
Ti
Si
Ti
N
O
Ti
Al
Ti
0
2
4
6
8
10
12
14
16
18
20
Full Scale 441 cts Cursor: 0.000
keV

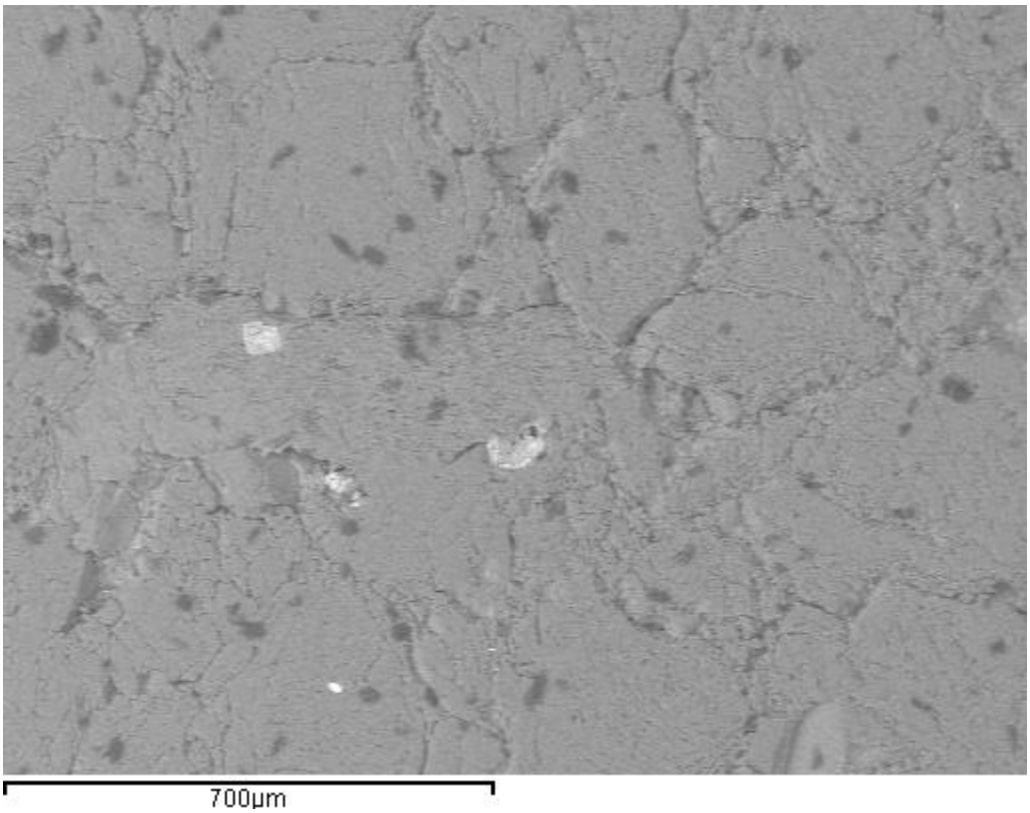
700µm

Anomaly 16

No mineralogy found, besides very trace iron oxides. Still omitted from depth profile.

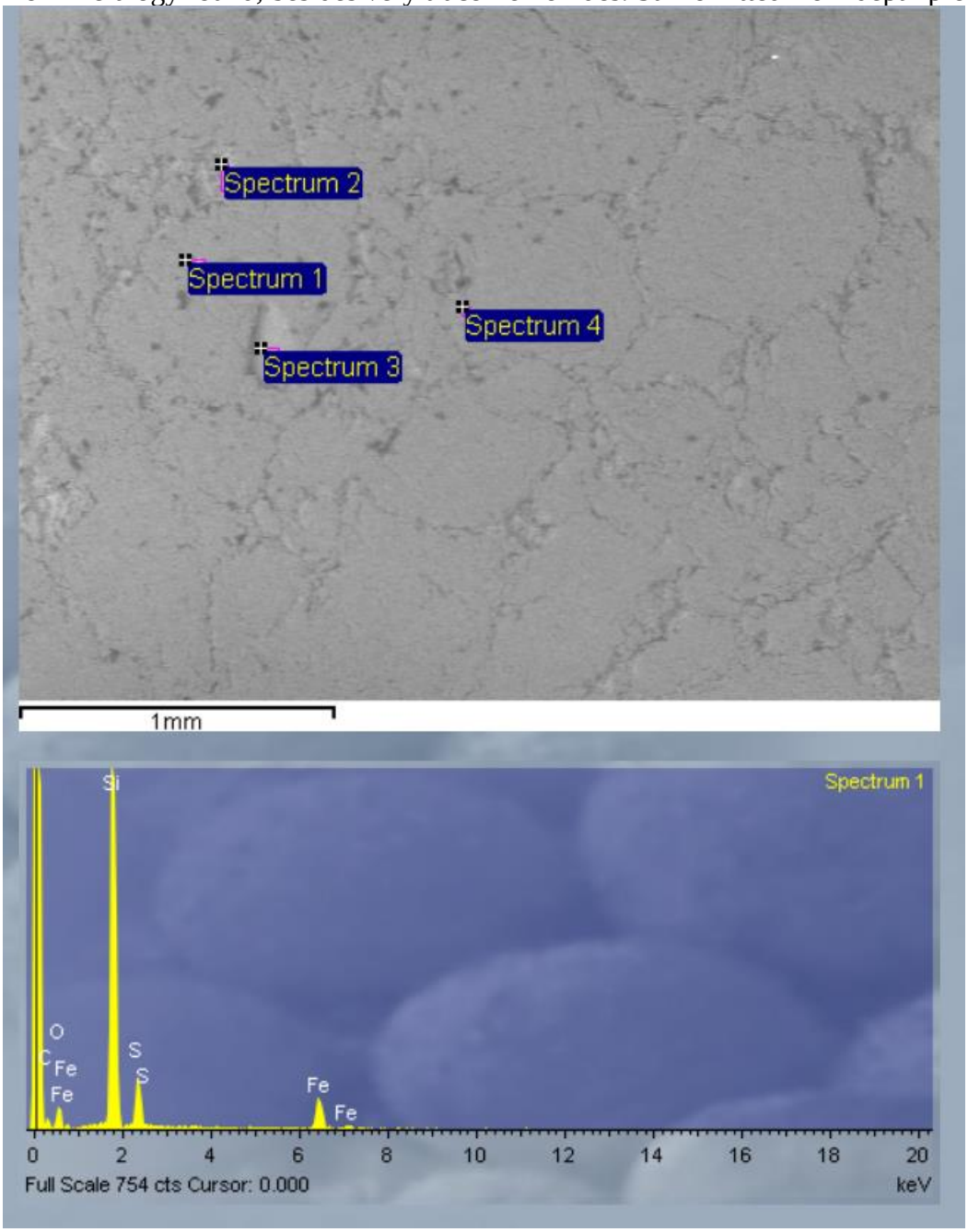

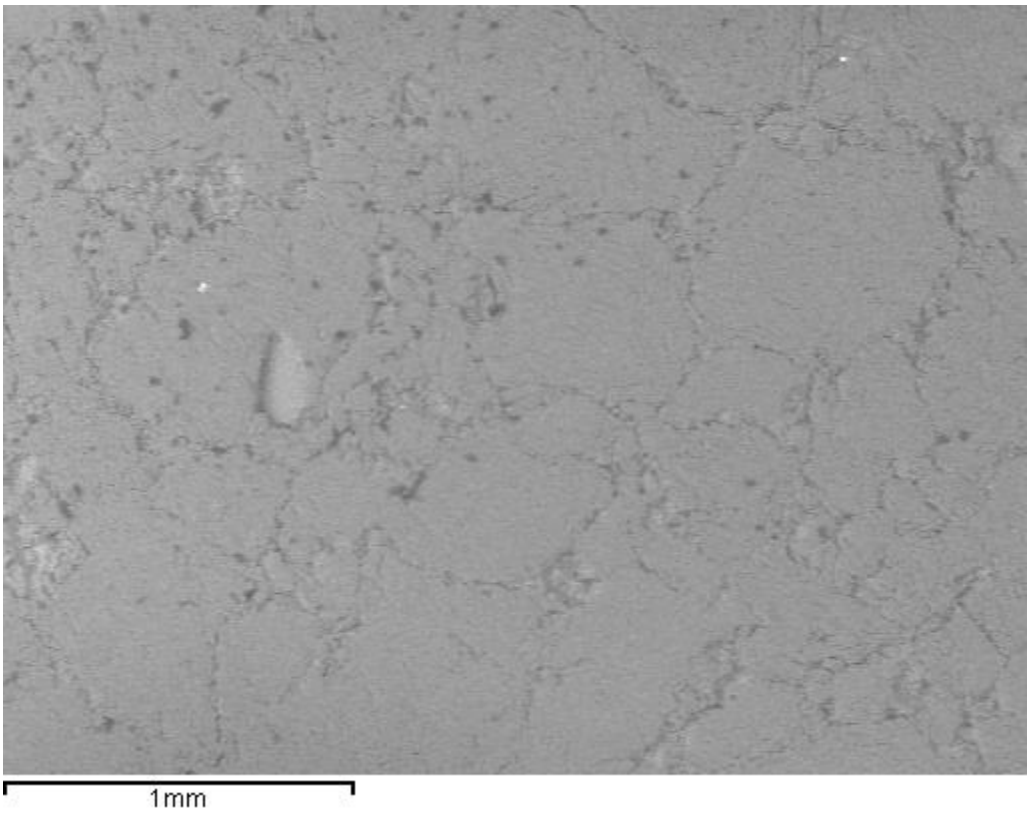
1mm

Anomaly 17

Like with 16, no real trace mineralogy identified apart from Trace Fe, maybe Al in minerals.

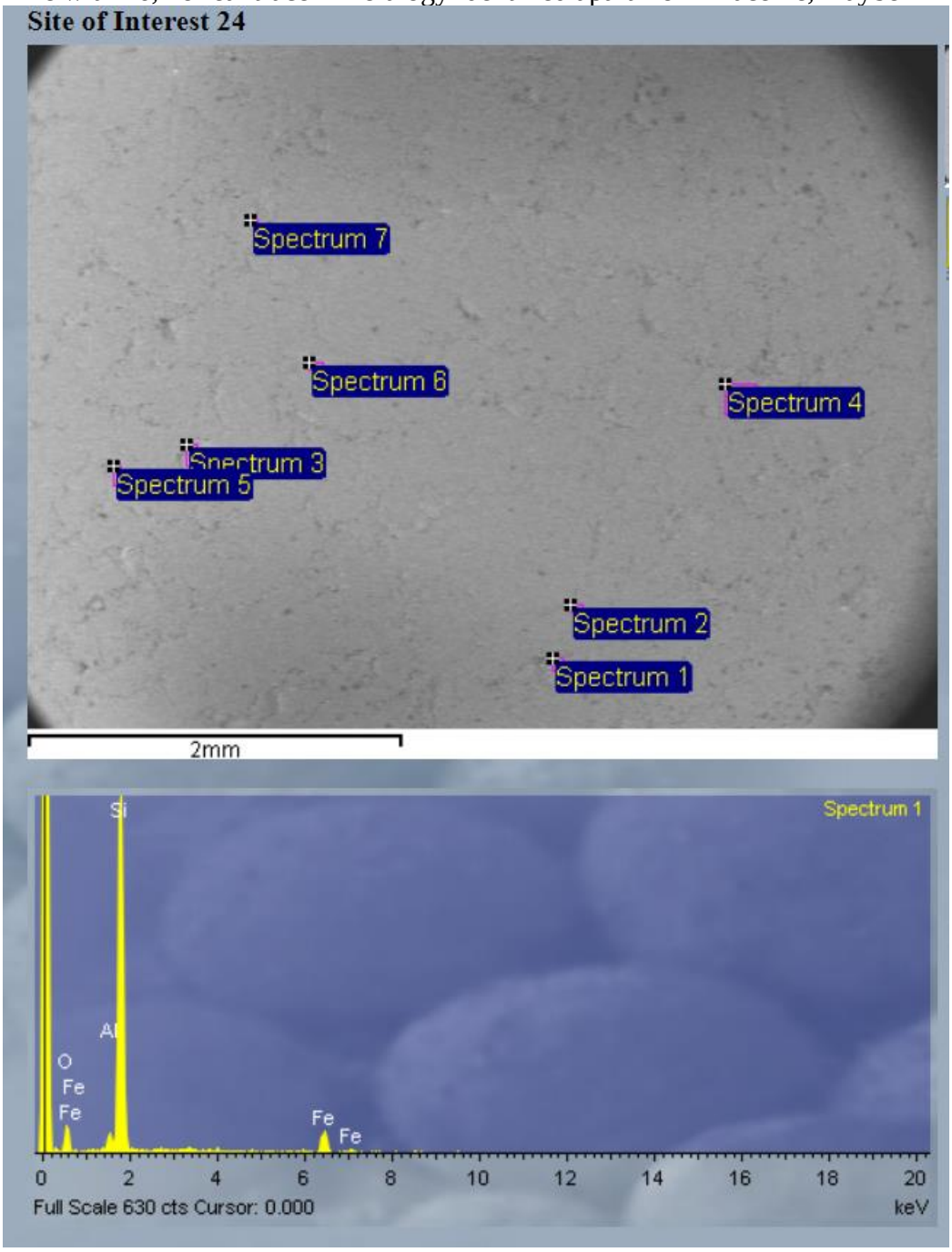

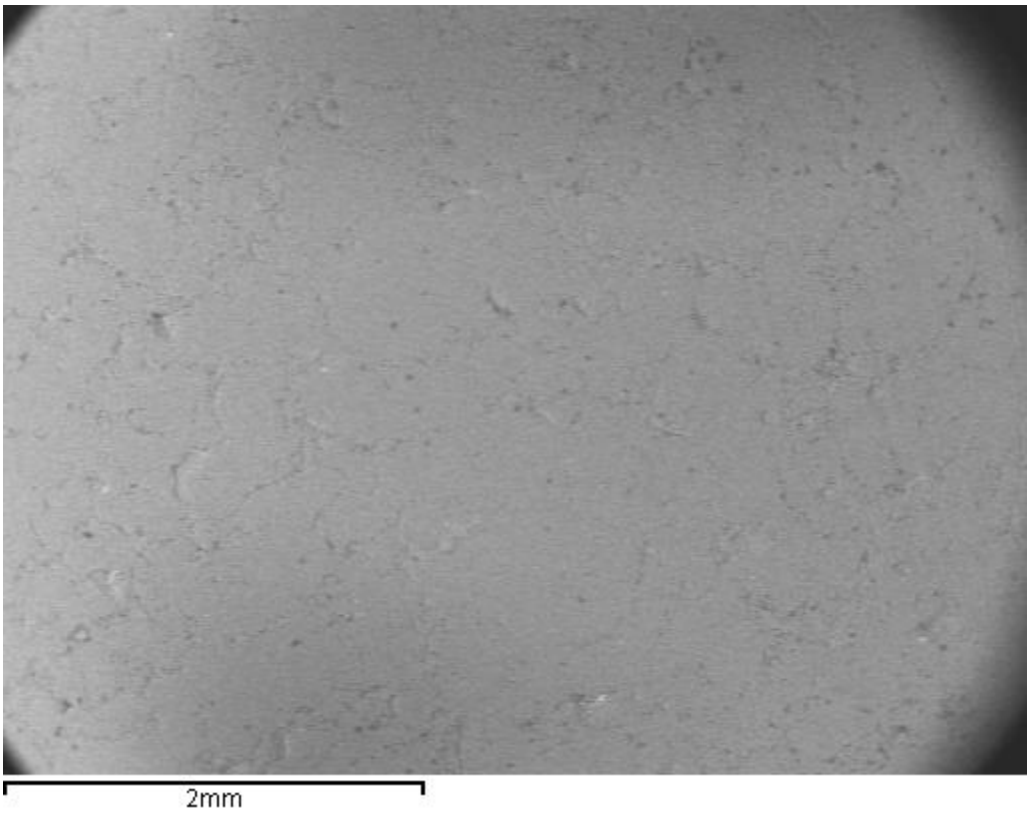
2mm

A4 – Depth Profiles (NS) of Controlled Exposure Experiment

Depth profiles of NS cores NS1, NS2 and NS3. Core NS1 is parameterized (ps = $\overline{\sigma\varphi_0}$; u = μ), however core NS3 is too low in OSL sensitivity to acquire a visible depth profile.

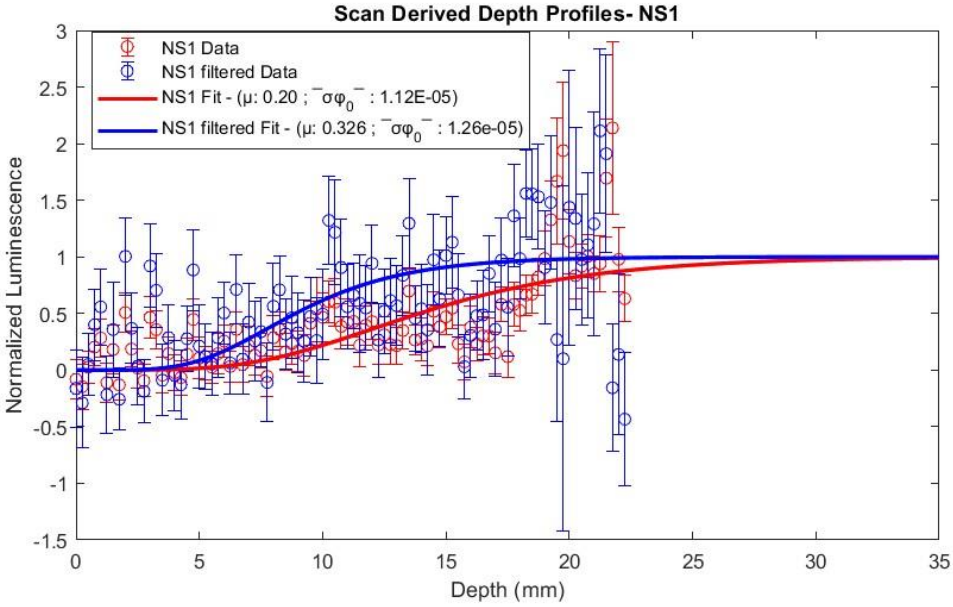

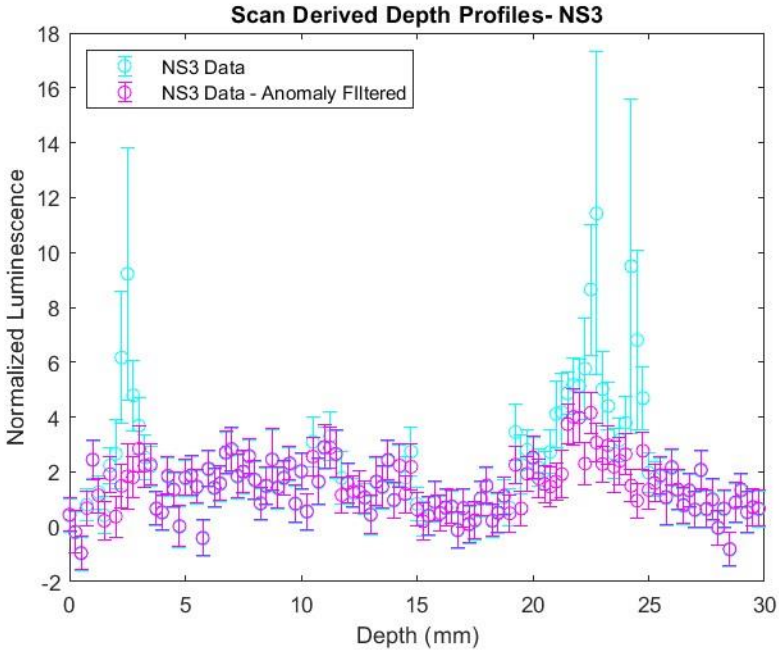

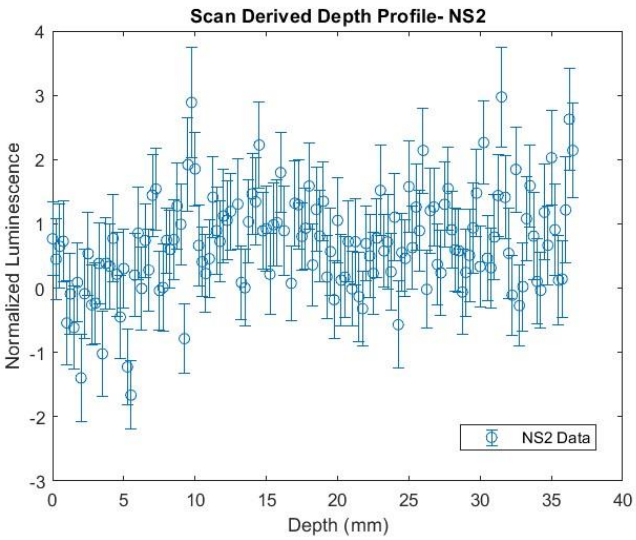
Scan Derived Depth Profile- NS2
Normalized Luminescence
Depth (mm)
NS2 Data
4
3
2
1
0
-1
-2
-3
0
5
10
15
20
25
30
35
40

A5 – Depth Profiles (SS) of Controlled Exposure Experiment

Depth profiles of SS cores 1, 2, and 3, all cores are very low in OSL sensitivity, making it difficult to extrapolate a depth profile. Below is an attempt to parameterize the depth profile of core SS2 ((ps = $\overline{\sigma\varphi_0}$; u = μ)).

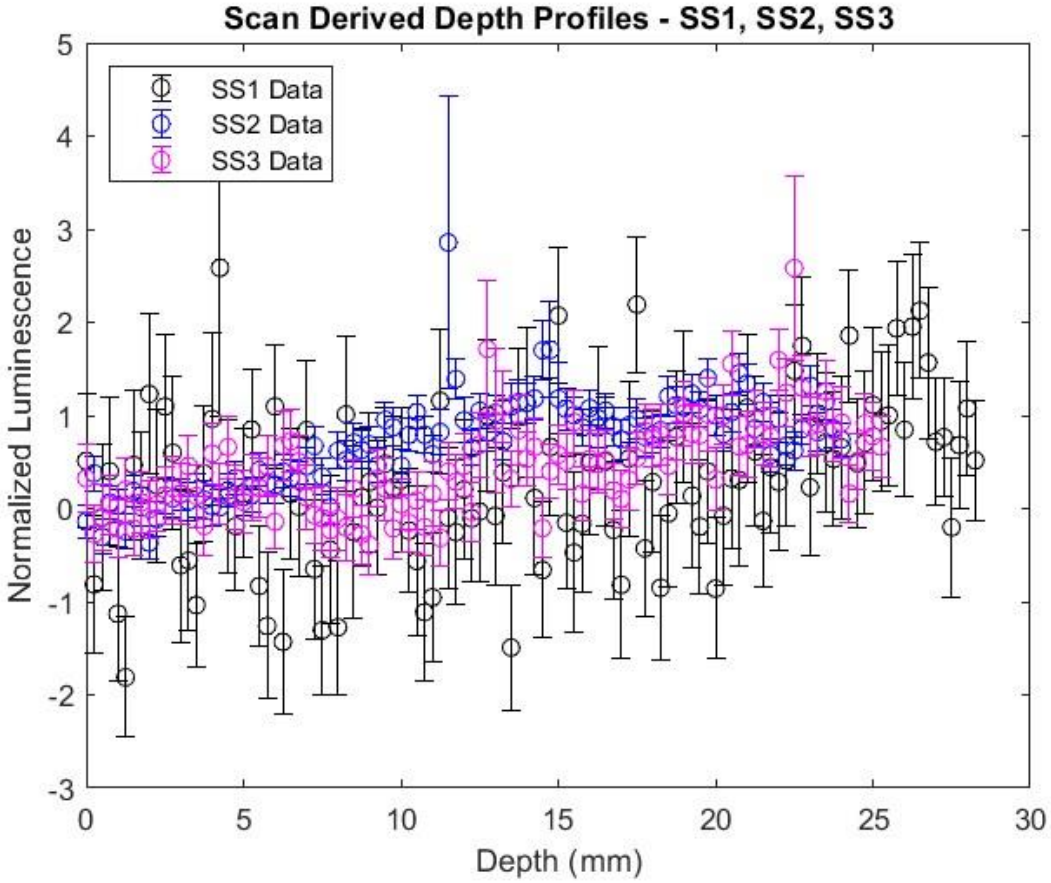

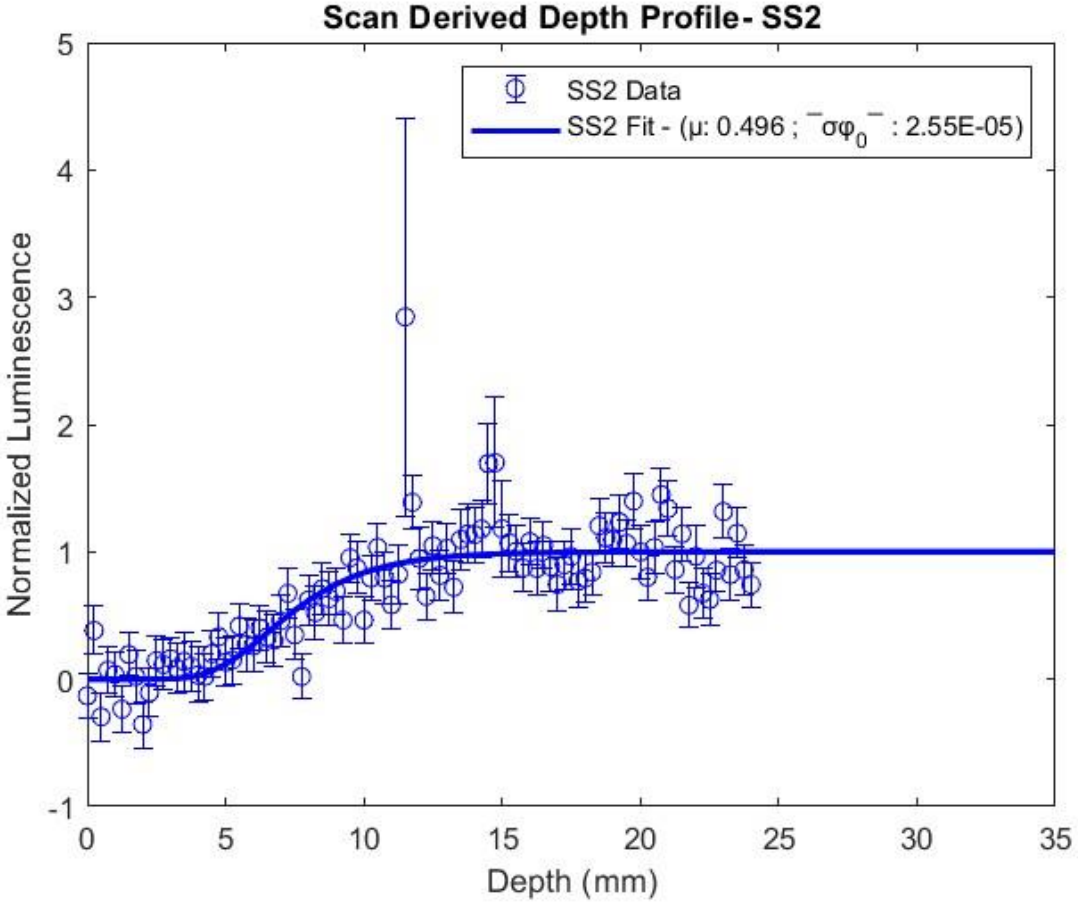
Scan Derived Depth Profile- SS2
SS2 Data
SS2 Fit - (μ: 0.496 ; ¯σφ0¯ : 2.55E-05)
Normalized Luminescence
Depth (mm)
5
4
3
2
1
0
-1
0
5
10
15
20
25
30
35

A6 – Likelihood Plots of Controlled Exposure Cores

Likelihood Plots of NS 1 and SS 2 parameterizations, with parameterization ranges provided (SP = $\overline{\sigma\varphi_0}$; mu = μ). Note that best fit region (yellow) does not correspond to parameter median values.

Result for the calibration
best fit - attenuation = 0.13434
best fit - bleaching rate = 4.7822e-06

Result for the calibration
SP Median = 1.12e-05 s-1
SP 1sigma sup = 0.00014 s-1
SP 1sigma inf = 6.49e-06 s-1
SP 2sigma sup = 0.0115 s-1
SP 2sigma inf = 9.21e-06 s-1
mu Median = 0.2 mm-1
mu 1sigma sup = 0.145 mm-1
mu 1sigma inf = 0.0964 mm-1
mu 2sigma sup = 0.386 mm-1
mu 2sigma inf = 0.0964 mm-1

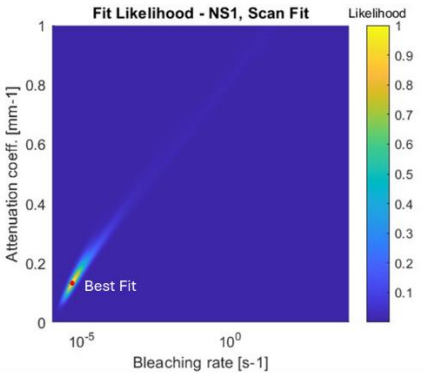

Result for the calibration
best fit - attenuation = 0.1789
best fit - bleaching rate = 4.131e-06

SP Median = 1.26e-05 s-1
SP 1sigma sup = 0.000215 s-1
SP 1sigma inf = 9.67e-06 s-1
SP 2sigma sup = 0.000955 s-1
SP 2sigma inf = 1.12e-05 s-1
mu Median = 0.326 mm-1
mu 1sigma sup = 0.299 mm-1
mu 1sigma inf = 0.15 mm-1
mu 2sigma sup = 0.449 mm-1
mu 2sigma inf = 0.25 mm-1

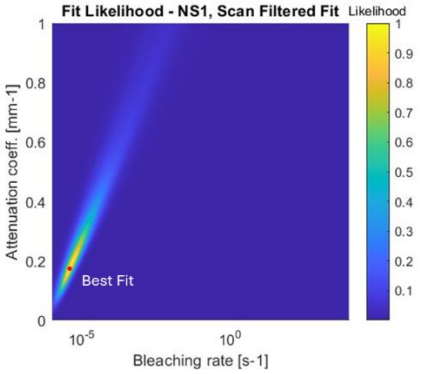

Result for the calibration
best fit - attenuation = 0.38596
best fit - bleaching rate = 1.1988e-05

SP Median = 2.55e-05 s-1
SP 1sigma sup = 6.16e-05 s-1
SP 1sigma inf = 1.8e-05 s-1
SP 2sigma sup = 0.000172 s-1
SP 2sigma inf = 2.05e-05 s-1
mu Median = 0.496 mm-1
mu 1sigma sup = 0.161 mm-1
mu 1sigma inf = 0.121 mm-1
mu 2sigma sup = 0.282 mm-1
mu 2sigma inf = 0.202 mm-1

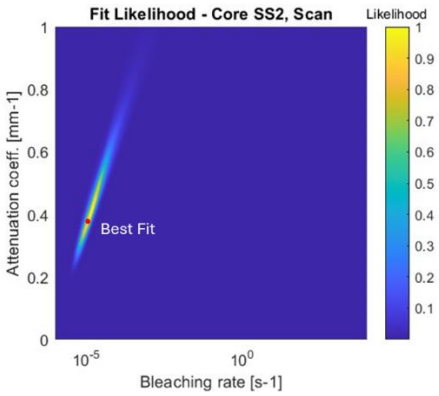

A7 – Parameter likelihoods of combined cores from Surfaces HRQ and P

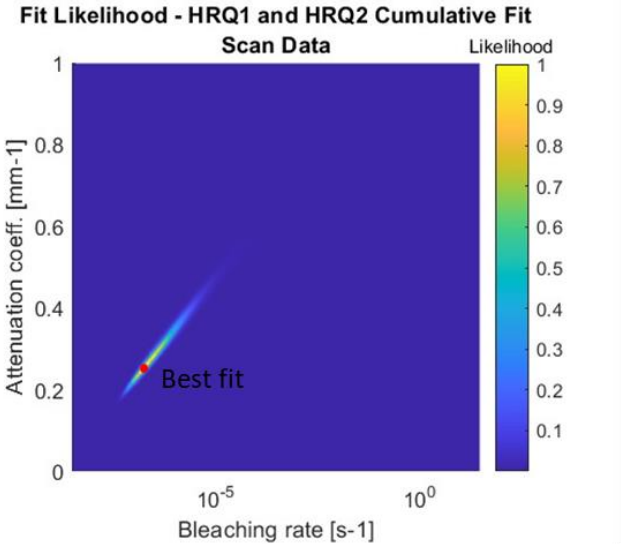

Parameter Median (Best fit, -1σ,+1 σ)

μ = 0.293 mm^{-1} (0.252; .0.037, 0.074)

$\overline{\sigma\varphi_0}$ = 3.28E-07 s^{-1} (1.60E-07; 1.59E-07, 9.02E-07)

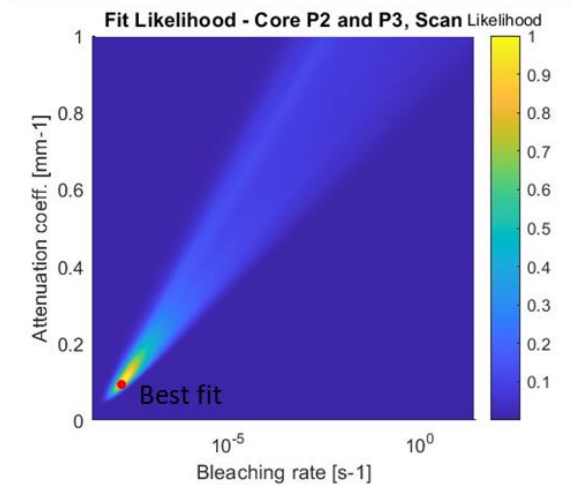

Parameter Median (Best fit, -1σ,+1 σ)

μ = 0.491 mm^{-1} (0.105; .0.337, 0.337)

$\overline{\sigma\varphi_0}$ = 6.27E-06 s^{-1} (1.98E-08; 6.20E-06, 0.0054)

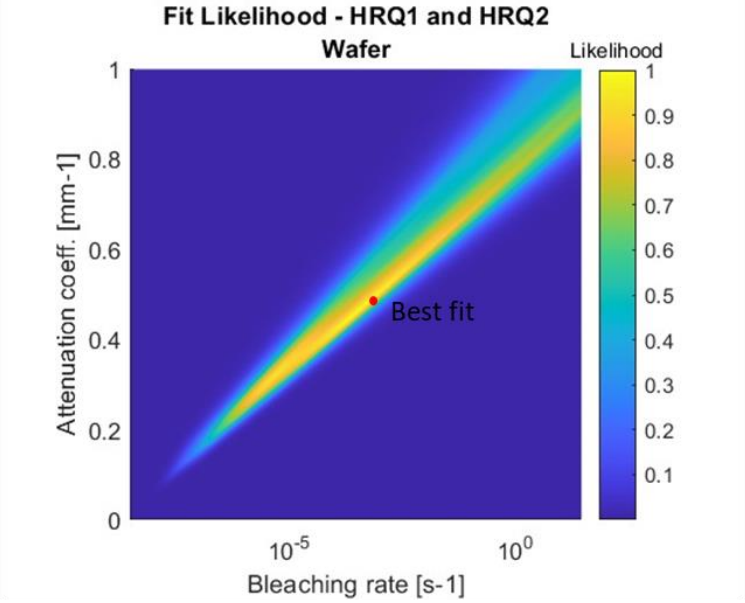

Parameter Median (Best fit, -1σ,+1 σ)

μ = 0.64 (0.486; 0.239, 0.191)

$\overline{\sigma\varphi_0}$ = 6.71E-03 (5.87E-04; 6.68E-03, 1.75)

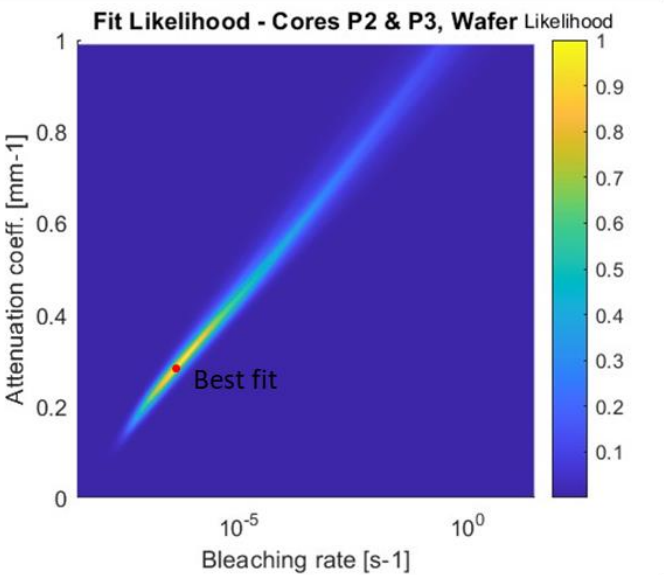

Parameter Median (Best fit, -1σ,+1 σ)

μ = 0.463 (0.306; 0.183, 0.275)

$\overline{\sigma\varphi_0}$ = 2.61E-05 (6.54E-07; 2.57E-05, 5.31E-03)

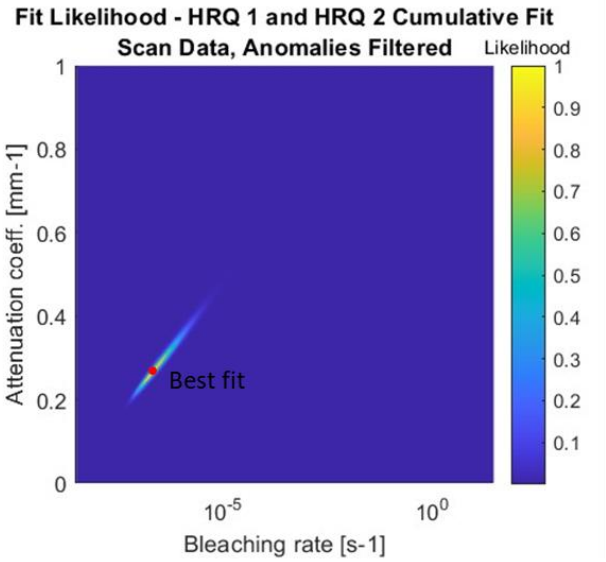

Parameter Median (Best fit, -1σ,+1 σ)

μ = 0.271 mm^{-1} (0.265; .0.037, 0.056)

$\overline{\sigma\varphi_0}$ = 2.13E-07 s^{-1} (1.98-07; 5.95E-08, 5.76E-07)

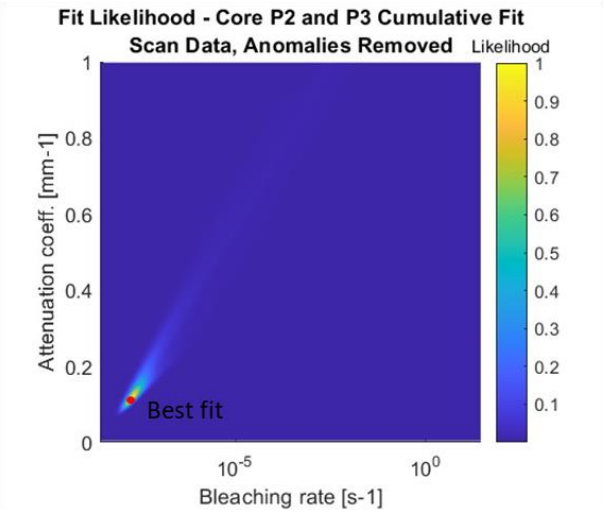

μ = 0.118 mm^{-1} (0.114; 0.046, 0.28)

$\overline{\sigma\varphi_0}$ = 3.11E-08 s^{-1} (1.82E-08; 0, 3.33 E-06).

A7a – Plots of combined core parameter fit values

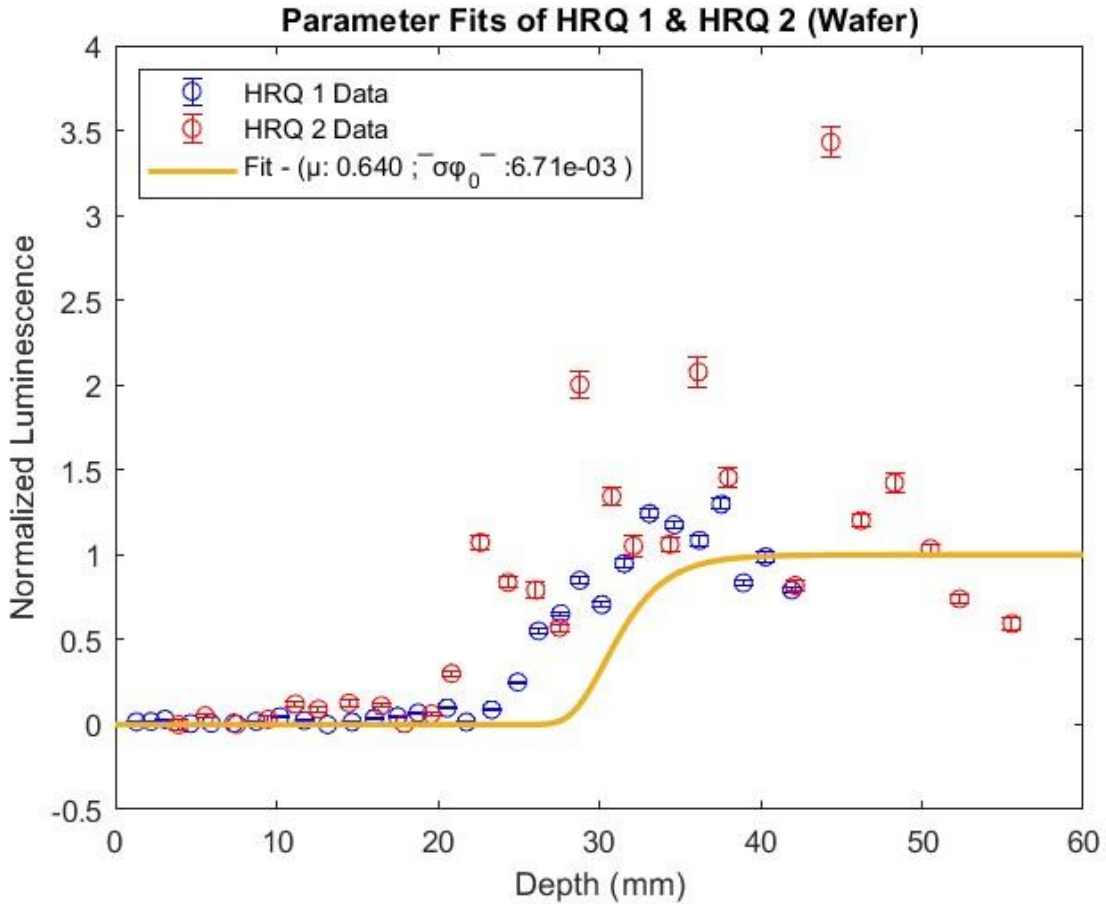

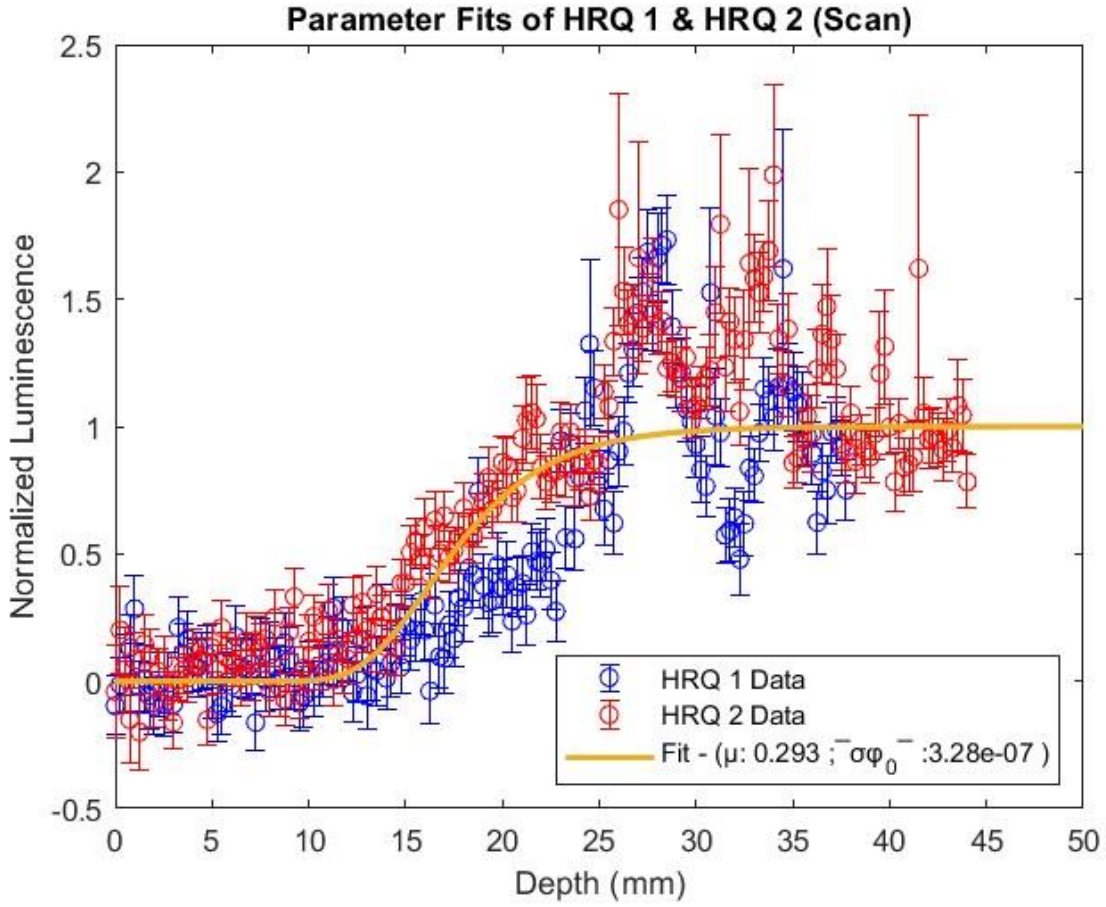
Parameter Fits of HRQ 1 & HRQ 2 (Scan)
Normalized Luminescence
Depth (mm)
HRQ 1 Data
HRQ 2 Data
Fit - (μ: 0.293 ; σφ0 :3.28e-07)
2.5
2
1.5
1
0.5
0
-0.5
0
5
10
15
20
25
30
35
40
45
50

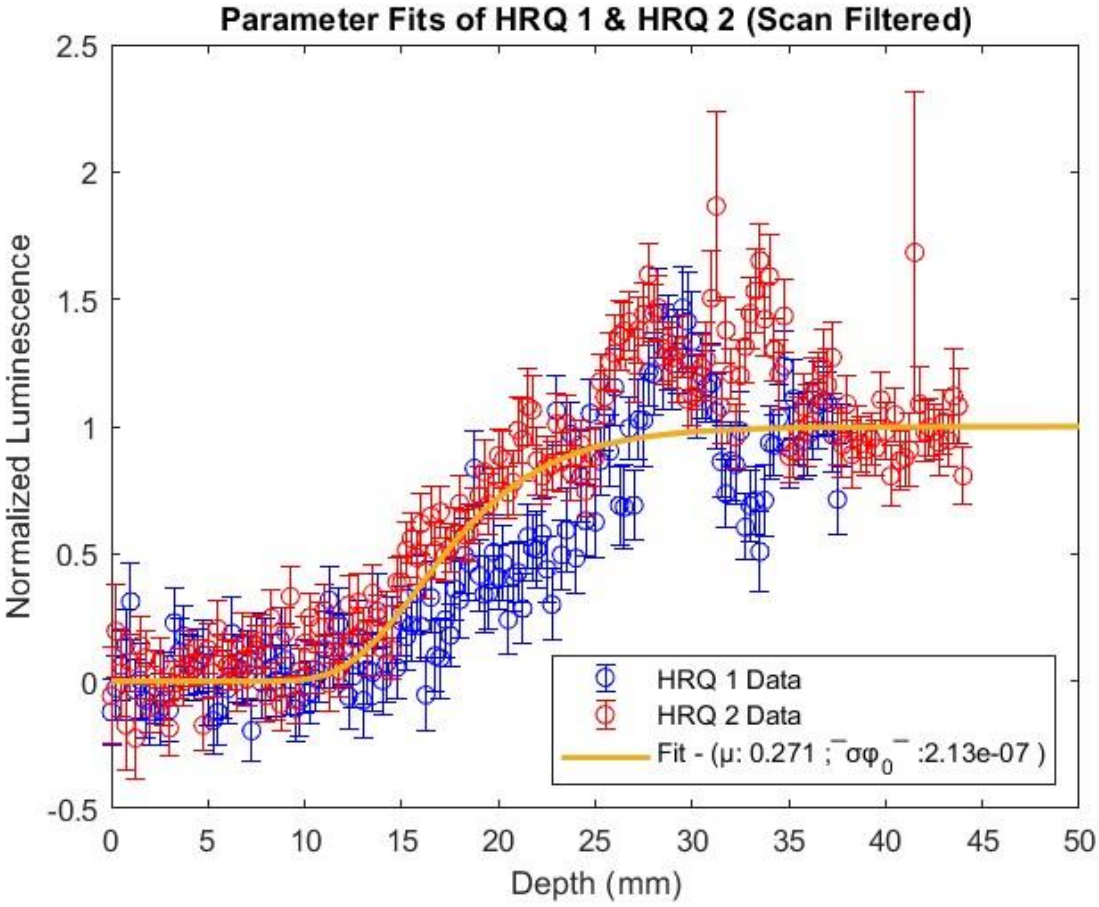
Parameter Fits of HRQ 1 & HRQ 2 (Scan Filtered)
Normalized Luminescence
Depth (mm)
HRQ 1 Data
HRQ 2 Data
Fit - (μ: 0.271 ; σφ0 :2.13e-07)
2.5
2
1.5
1
0.5
0
-0.5
0
5
10
15
20
25
30
35
40
45
50

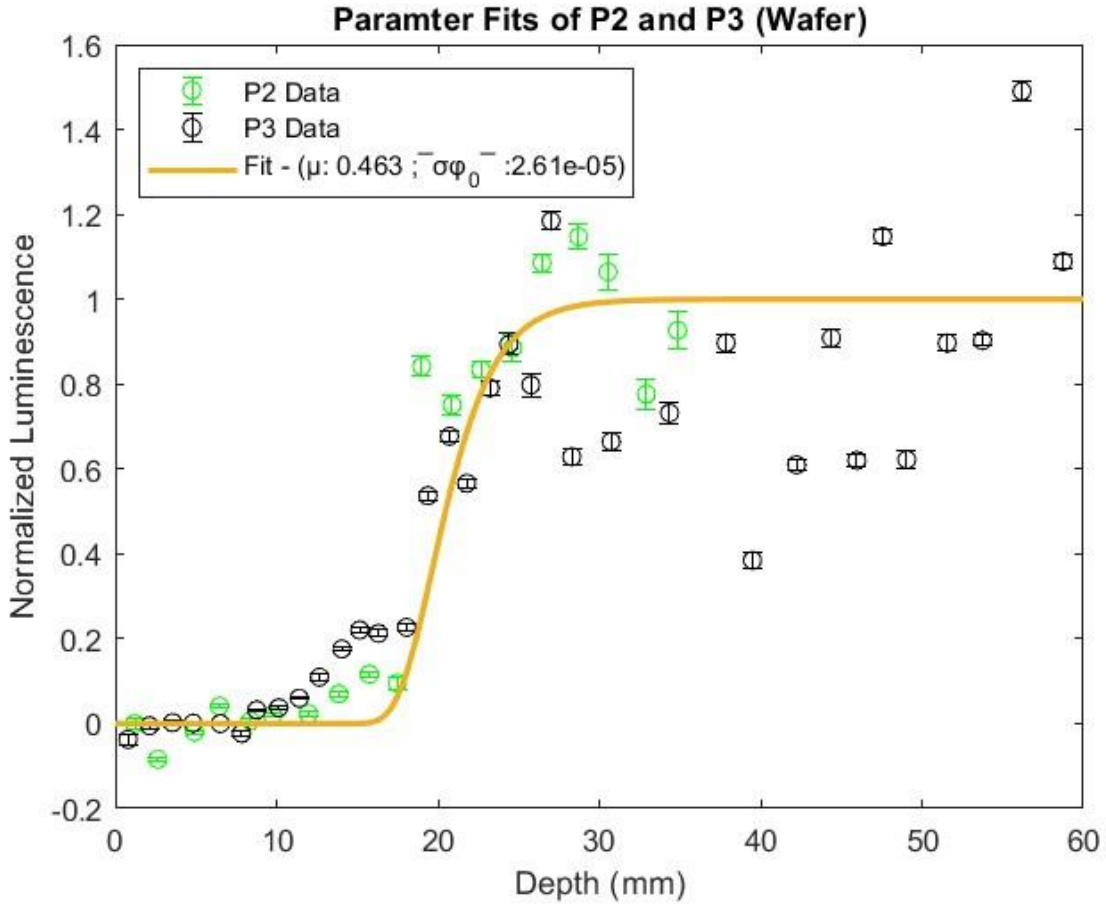
Paramter Fits of P2 and P3 (Wafer)
P2 Data
P3 Data
Fit - (μ: 0.463 ; $\bar{\sigma\varphi_0}$:2.61e-05)
Normalized Luminescence
Depth (mm)
1.6
1.4
1.2
1
0.8
0.6
0.4
0.2
0
-0.2
0
10
20
30
40
50
60

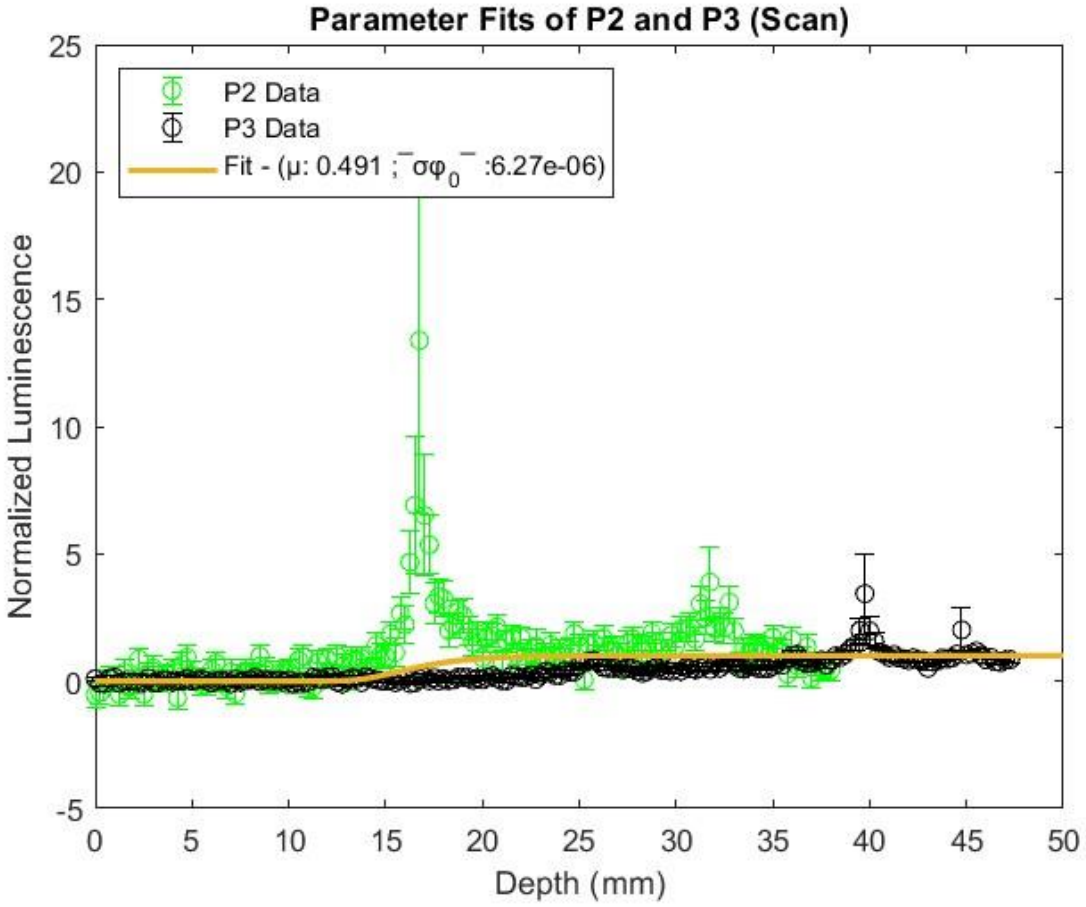
Parameter Fits of P2 and P3 (Scan)
P2 Data
P3 Data
Fit - (μ: 0.491 ; $\bar{\sigma}\varphi_0\bar{}$:6.27e-06)
Normalized Luminescence
Depth (mm)
25
20
15
10
5
0
-5
0
5
10
15
20
25
30
35
40
45
50

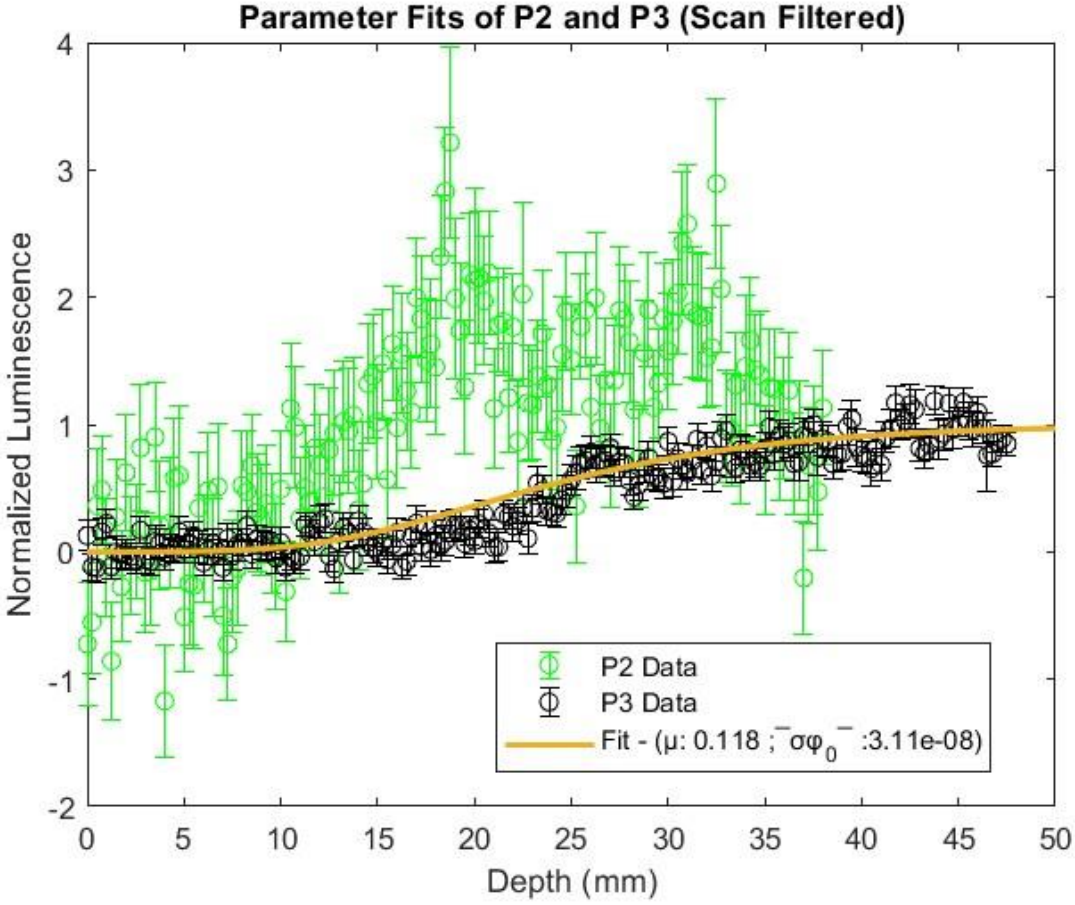
Parameter Fits of P2 and P3 (Scan Filtered)
Normalized Luminescence
Depth (mm)
P2 Data
P3 Data
Fit - (μ: 0.118 ; $\bar{\sigma}\varphi_0$:3.11e-08)
4
3
2
1
0
-1
-2
0
5
10
15
20
25
30
35
40
45
50

A8 – Age Fits Individual cores, Scan data

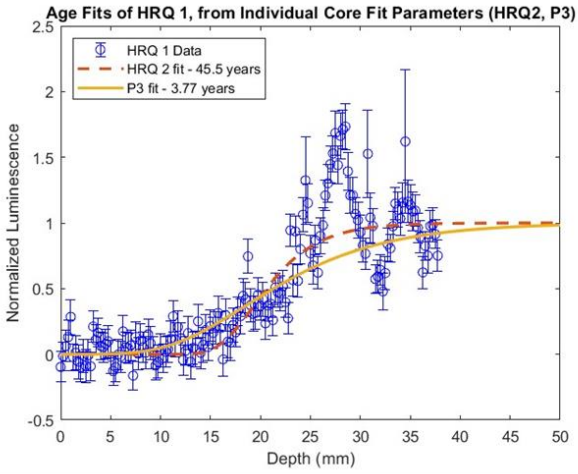

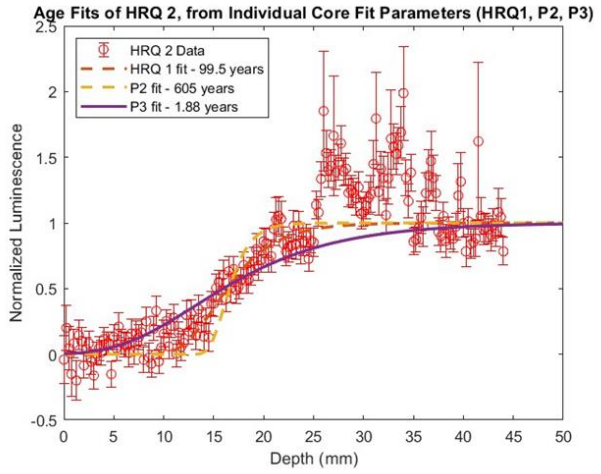

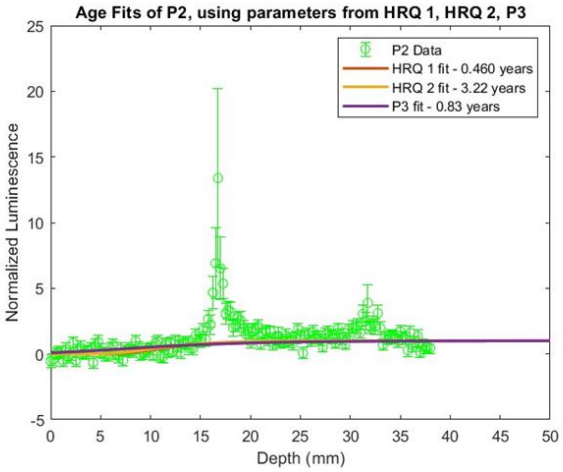

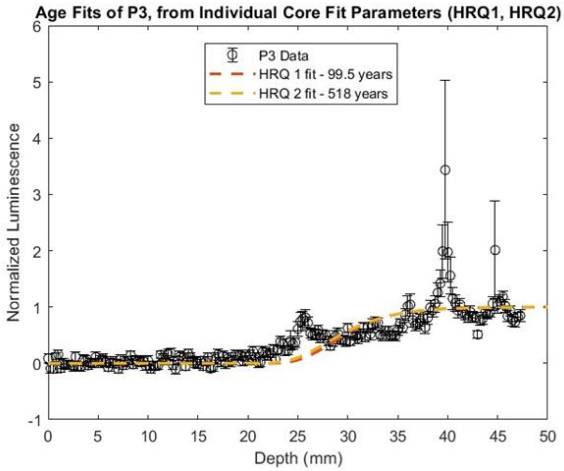

A9 – Age Fits from Individual Cores, Scan Data, Anomalies Removed

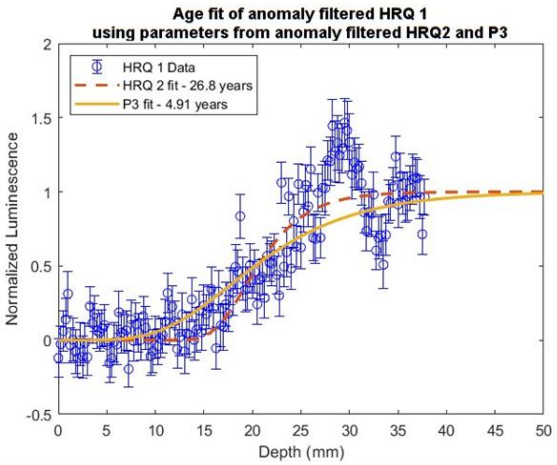

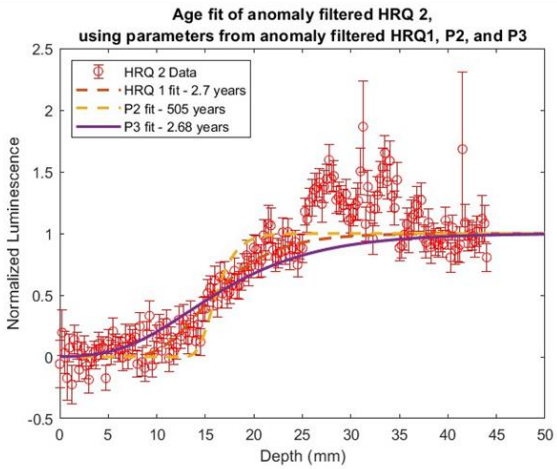

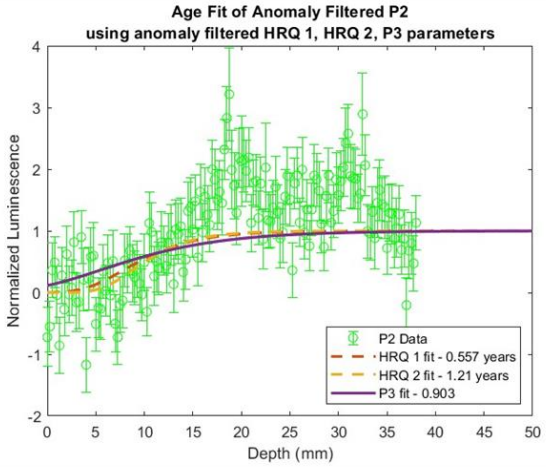

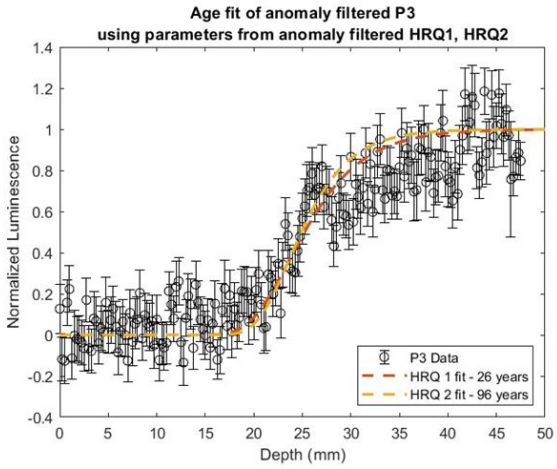

A10 – Age Fits from Individual Cores, Wafer Data

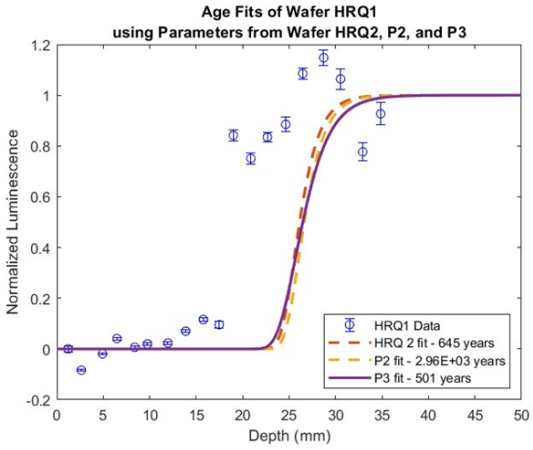

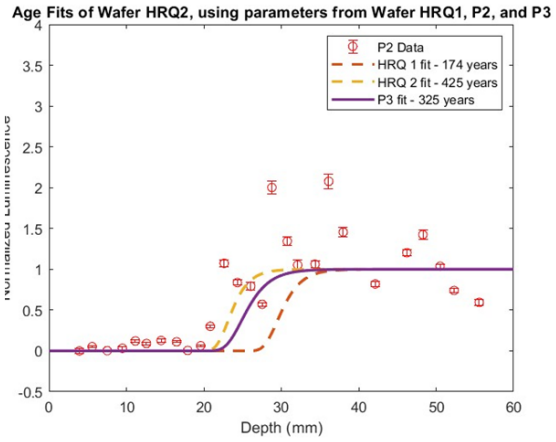

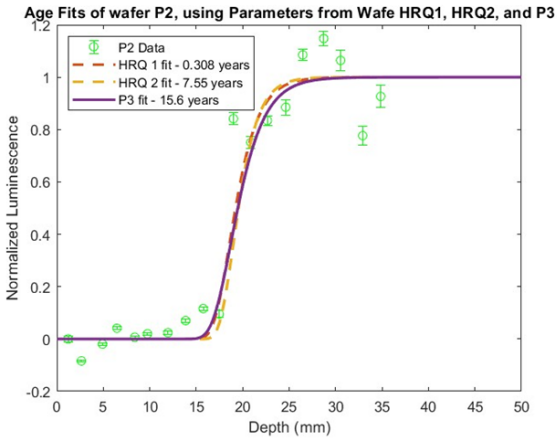

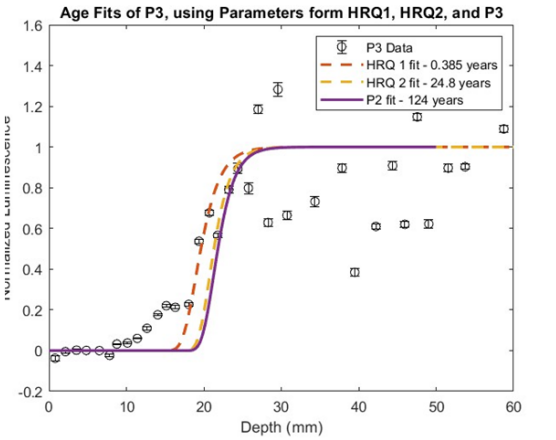

A11 – Age fits of HRQ using P2 and P3 Cumulative Parameters; Scan Data

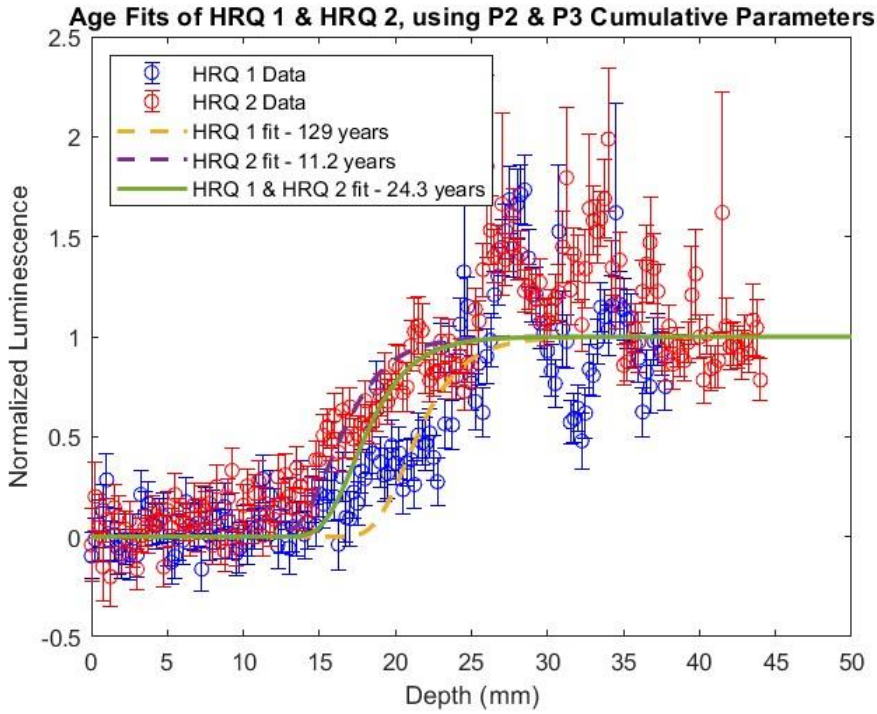

HRQ 1 fit – HRQ 1 data fitted to P2 and P3 parameterization

HRQ 2 fits – HRQ 2 data fitted to P2 and P3 parameterization

HRQ1 and HRQ 2 fit - HRQ1 and HRQ 2 data fitted to P2 and P3 parameterization

A12 – Age fits of P using HRQ1 and HRQ 2 Cumulative Parameters; Scan Data

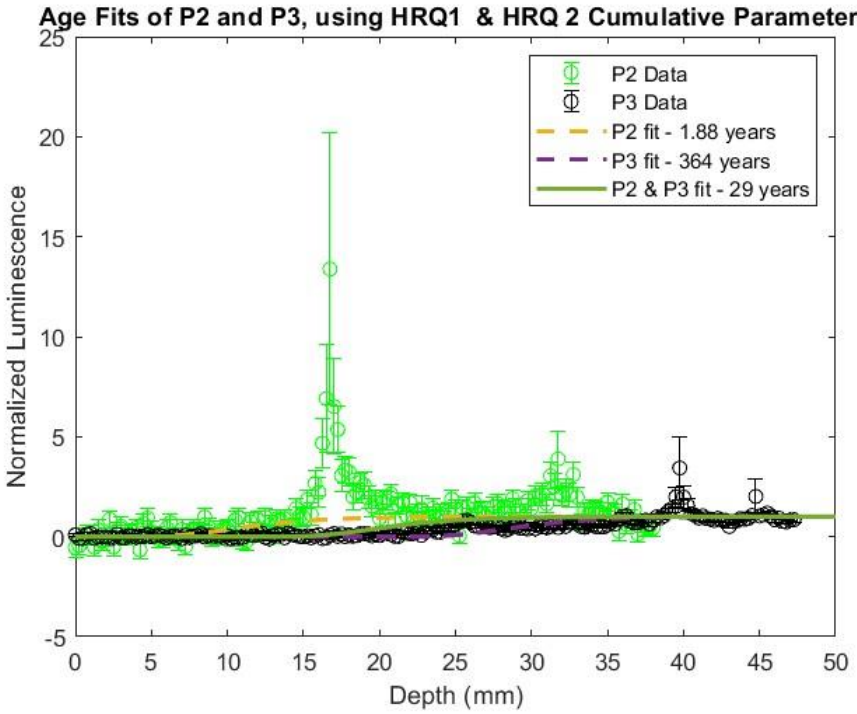

P2 fit – P2 data fitted to HRQ1 and HRQ2 parameterization

P3 fits – P3 data fitted to HRQ1 and HRQ2 parameterization

P2 and P3 fit – P2 and P3 data fitted to HRQ1 and HRQ2 parameterization

A13 – Age fits of HRQ using P2 and P3 Cumulative Parameters; Anomaly Filtered Scan Data

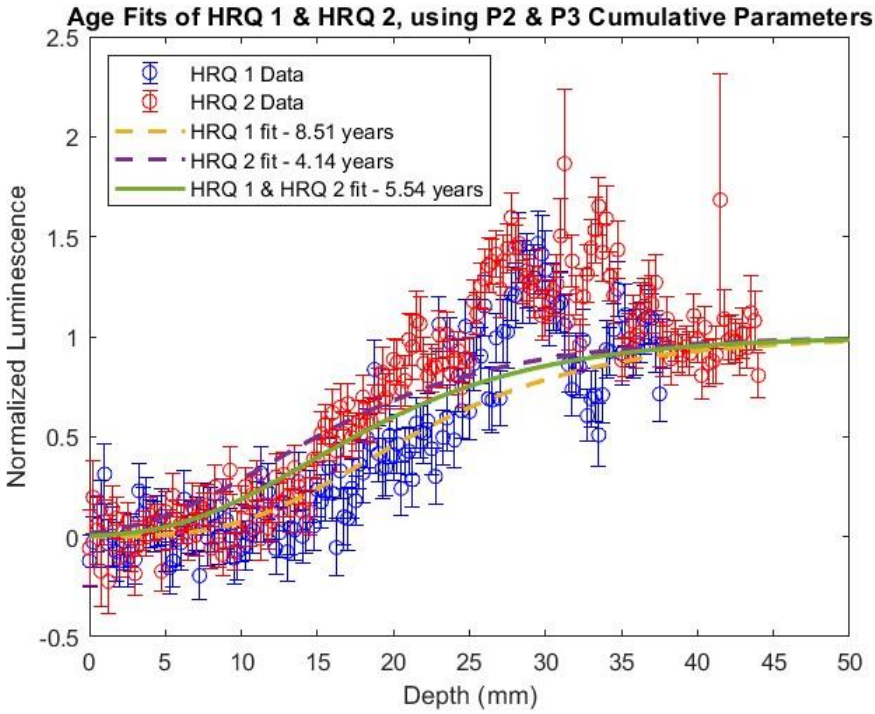

HRQ 1 fit – HRQ 1 data fitted to P2 and P3 parameterization

HRQ 2 fits – HRQ 2 data fitted to P2 and P3 parameterization

HRQ1 and HRQ 2 fit - HRQ1 and HRQ 2 data fitted to P2 and P3 parameterization

A14 – Age fits of P using HRQ1 and HRQ2 Cumulative Parameters, Anomaly Filtered Scan Data

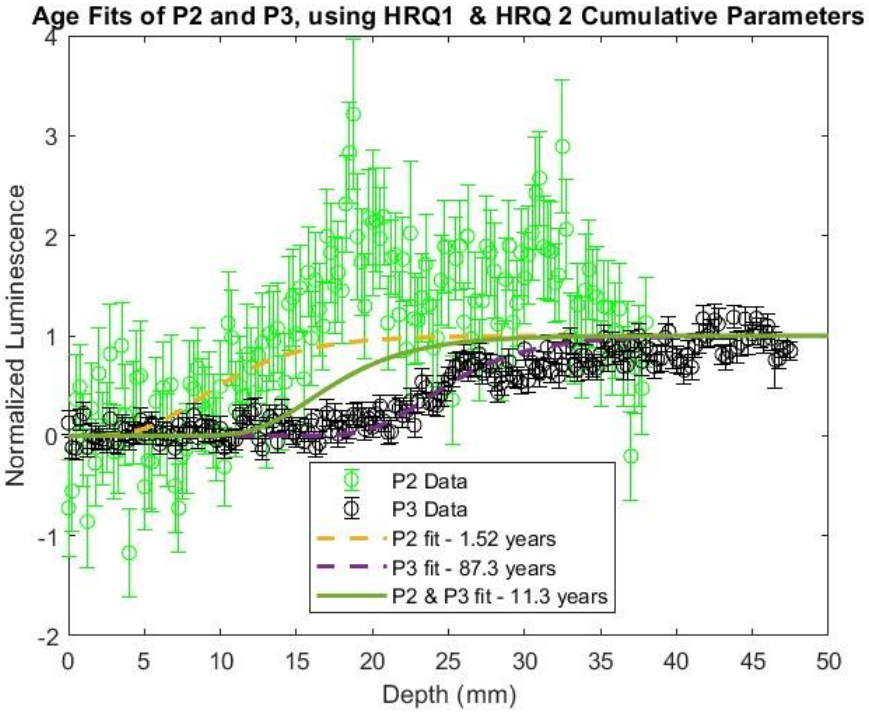

P2 fit – P2 data fitted to HRQ1 and HRQ2 parameterization

P3 fits – P3 data fitted to HRQ1 and HRQ2 parameterization

P2 and P3 fit – P2 and P3 data fitted to HRQ1 and HRQ2 parameterization

A15 – Age fits of HRQ using P2 and P3 Cumulative Parameters, Wafer Data

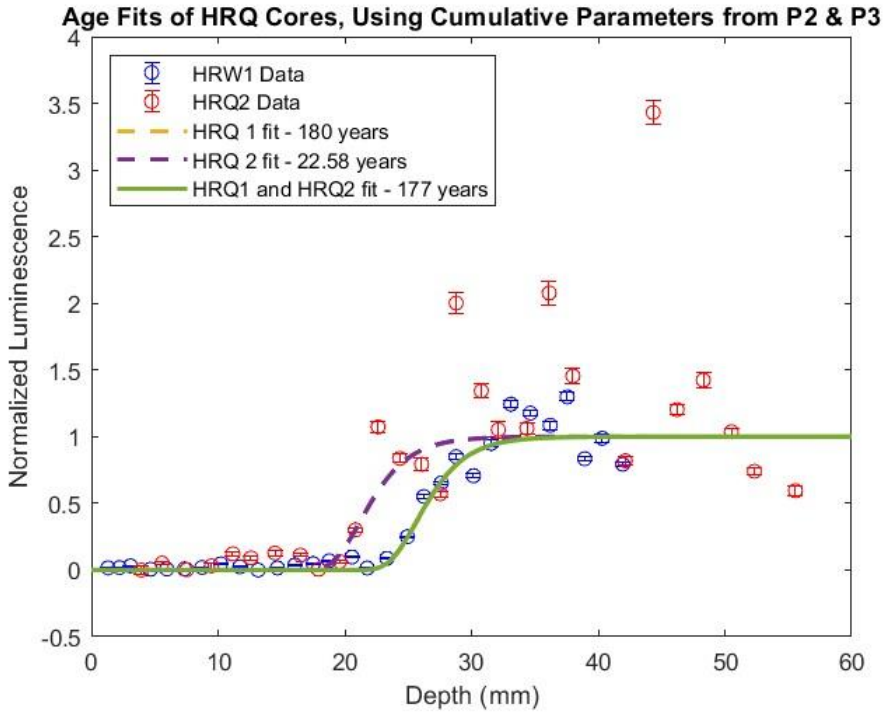

HRQ 1 fit – HRQ 1 data fitted to P2 and P3 parameterization

HRQ 2 fits – HRQ 2 data fitted to P2 and P3 parameterization

HRQ1 and HRQ 2 fit - HRQ1 and HRQ 2 data fitted to P2 and P3 parameterization

A16 – Age fits of P using HRQ1 and HRQ 2 Cumulative Parameters, Wafer Data

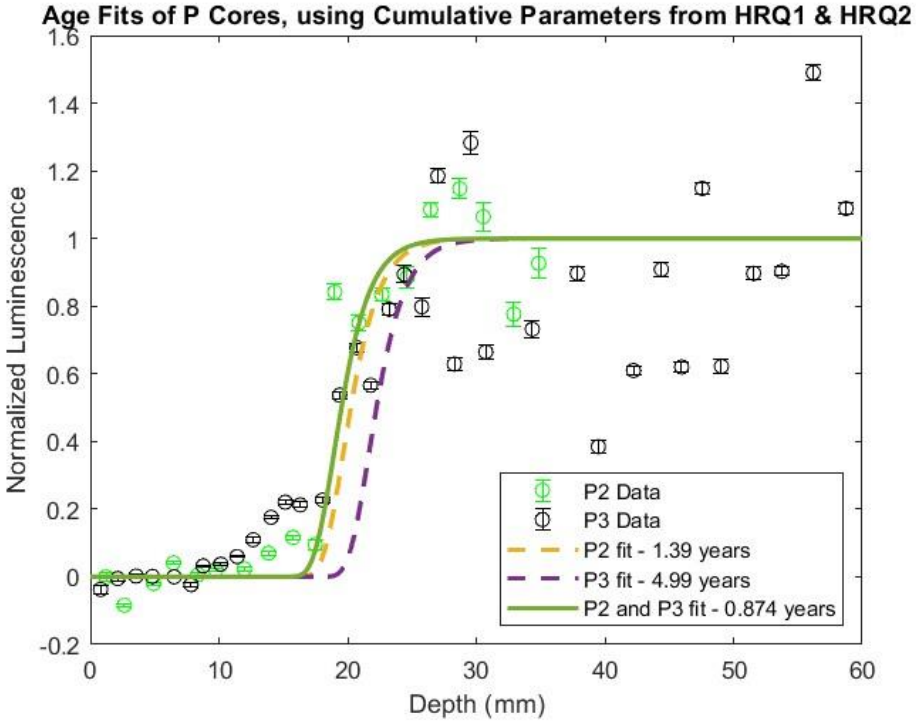

P2 fit – P2 data fitted to HRQ1 and HRQ2 parameterization

P3 fits – P3 data fitted to HRQ1 and HRQ2 parameterization

P2 and P3 fit – P2 and P3 data fitted to HRQ1 and HRQ2 parameterization

A17 – Figures of Light Attenuation Curves for Lane Mountain Samples

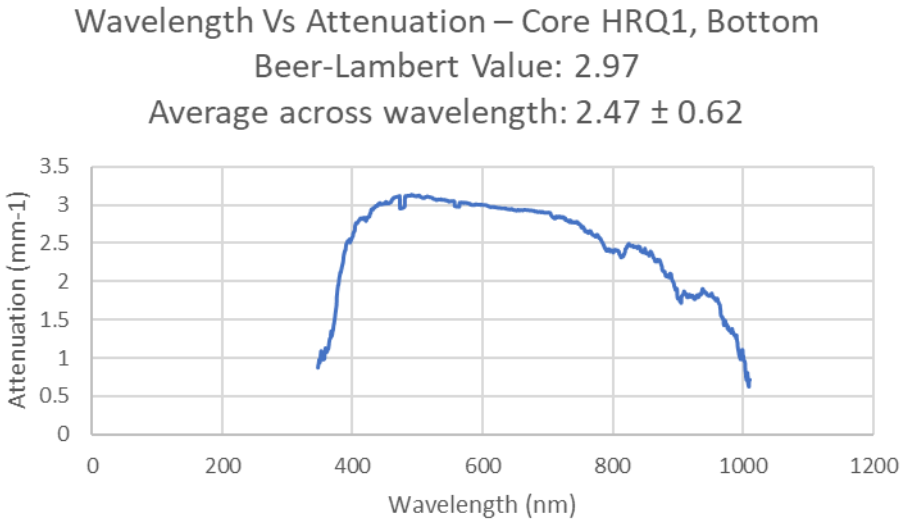

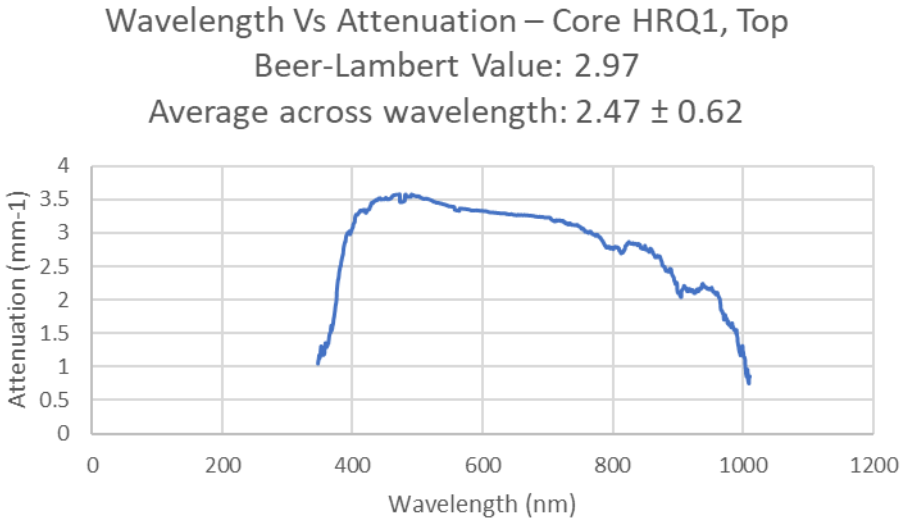

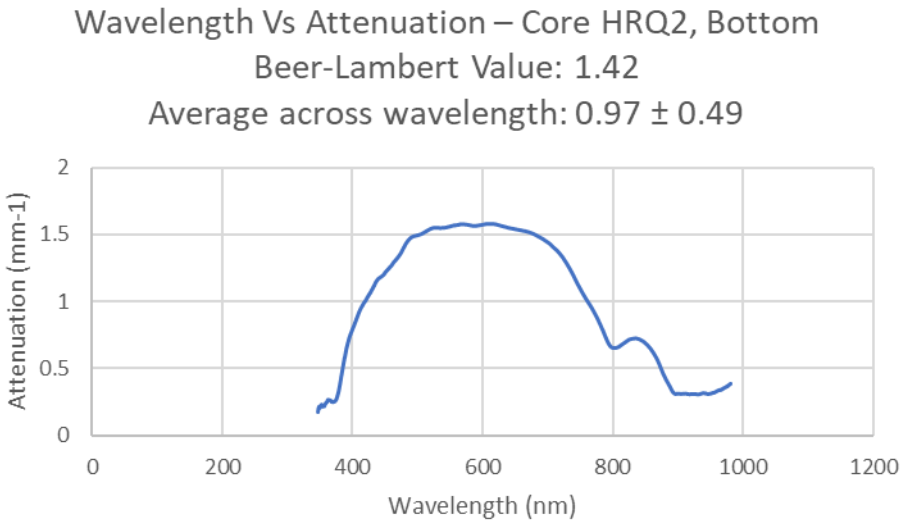
Wavelength Vs Attenuation – Core HRQ2, Bottom
Beer-Lambert Value: 1.42
Average across wavelength: 0.97 ± 0.49
Attenuation (mm-1)
2
1.5
1
0.5
0
0
200
400
600
800
1000
1200
Wavelength (nm)

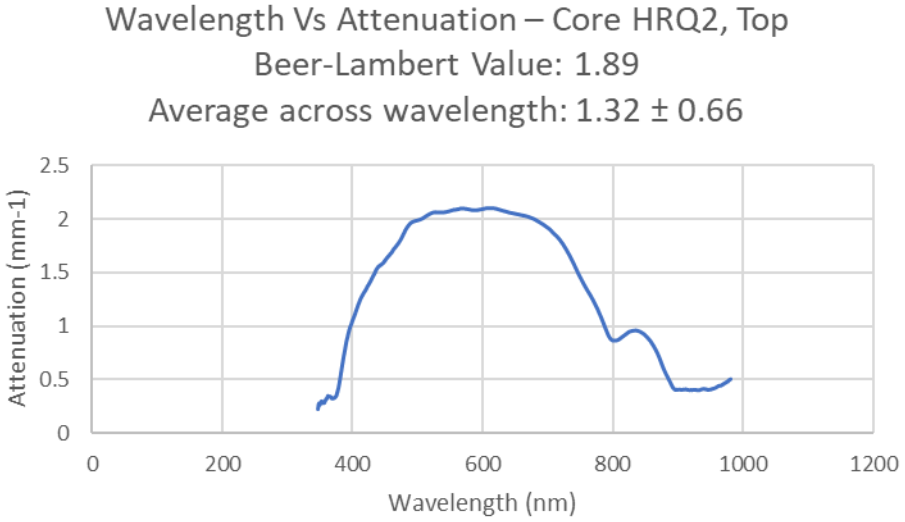
Wavelength Vs Attenuation – Core HRQ2, Top
Beer-Lambert Value: 1.89
Average across wavelength: 1.32 ± 0.66
Attenuation (mm-1)
2.5
2
1.5
1
0.5
0
0
200
400
600
800
1000
1200
Wavelength (nm)

Wavelength Vs Attenuation – Core P2, Bottom
Beer-Lambert Value: 2.47
Average across wavelength: 1.71 ± 0.87

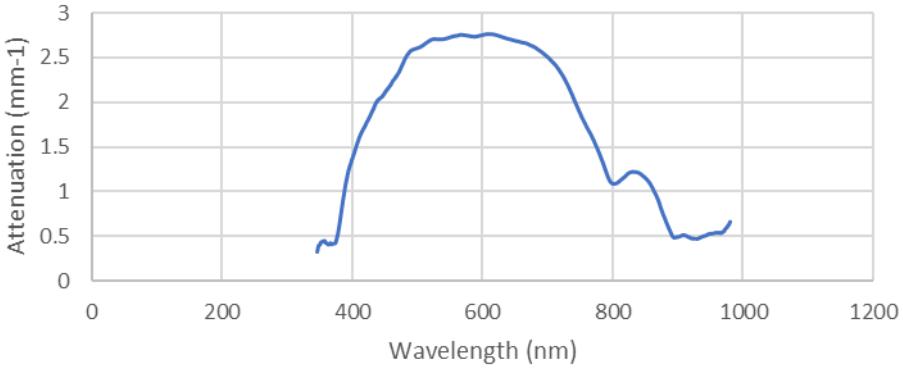

Wavelength Vs Attenuation – Core P2, Top
Beer-Lambert Value: 2.52
Average across wavelength: 1.90 ± 0.72

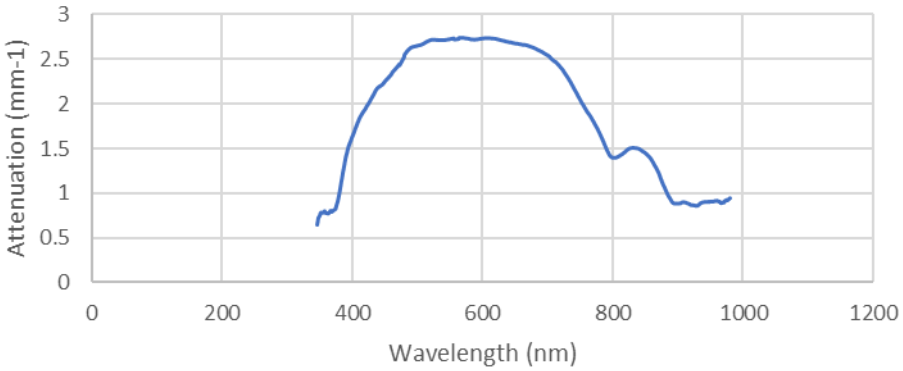

Wavelength Vs Attenuation – Core P3, Bottom
Beer-Lambert Value: 2.16
Average across wavelength: 1.44 ± 0.82

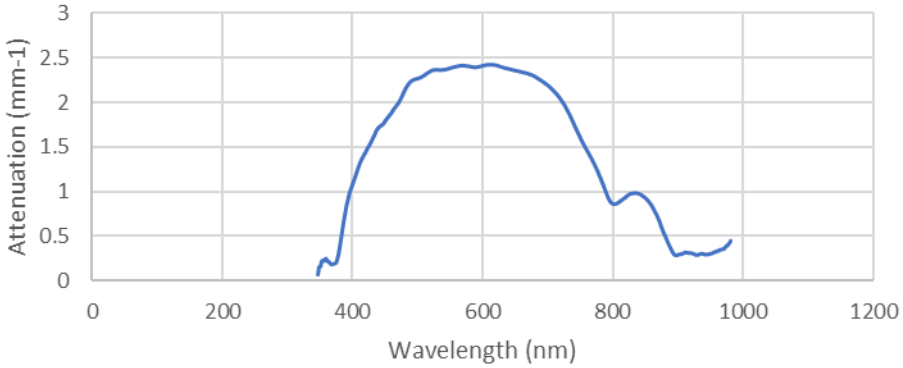

Wavelength Vs Attenuation – Core P3, Top
Beer-Lambert Value: 2.32
Average across wavelength: 1.76 ± 0.63

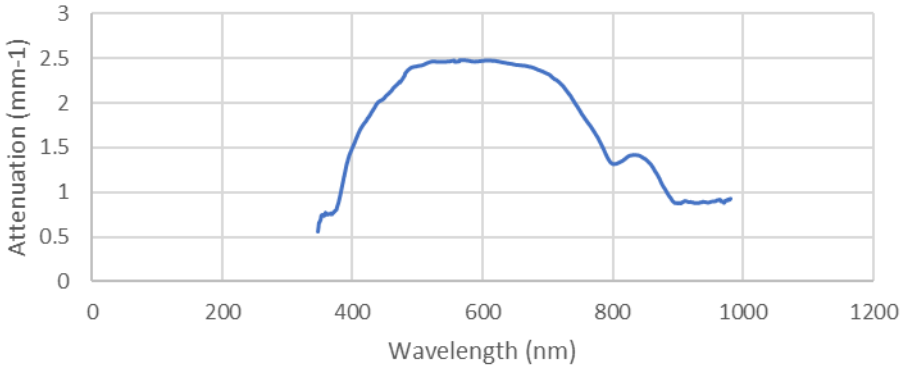

A17a – Setup of light attenuation experiment

Light Attenuation Experiment

1

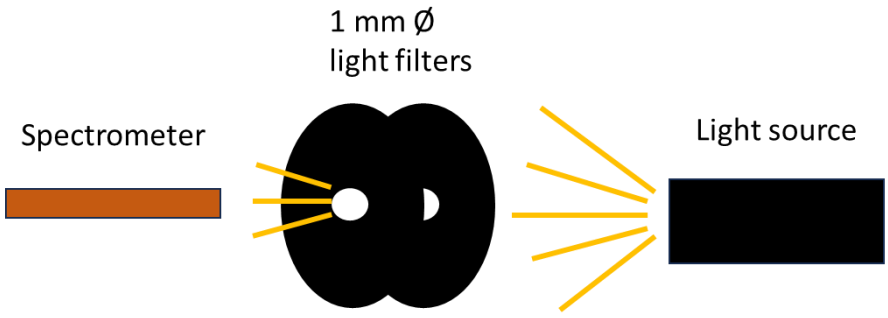

Measuring I_0 - Light from source is filtered through two 1 mm holes, recorded by spectrometer.

2

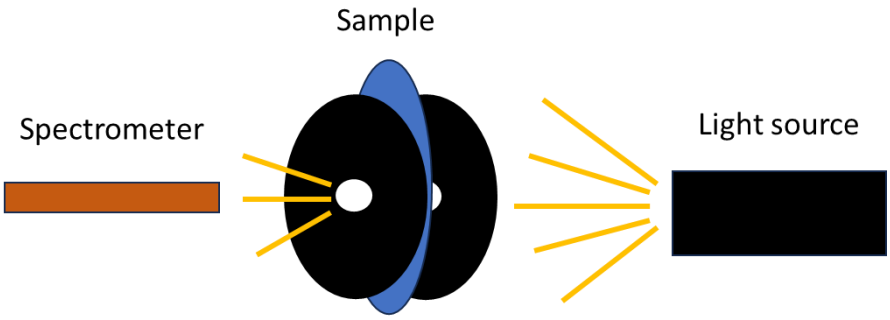

Measuring I - Sample is placed between two 1 mm holes, light filtered from sample is recorded by spectrometer.

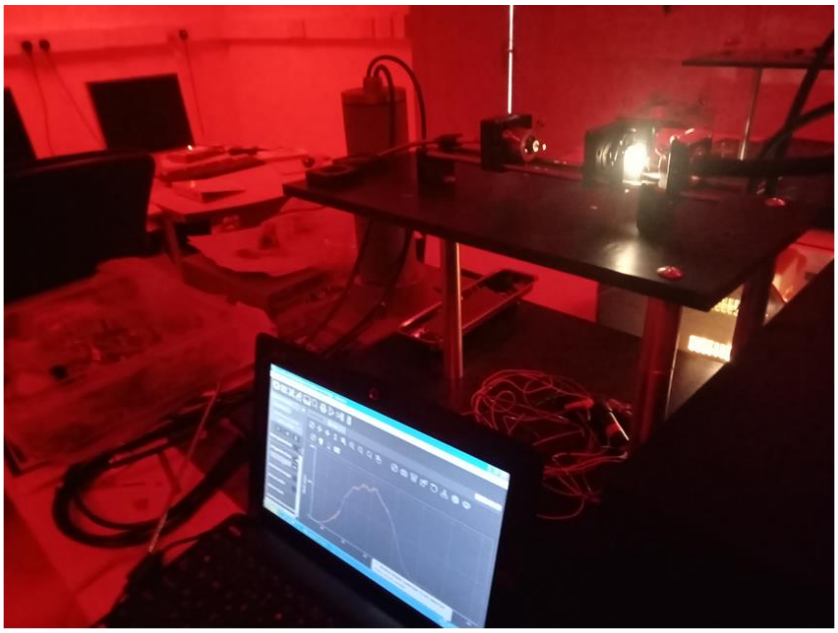

Spectrometer measuring light intensity.

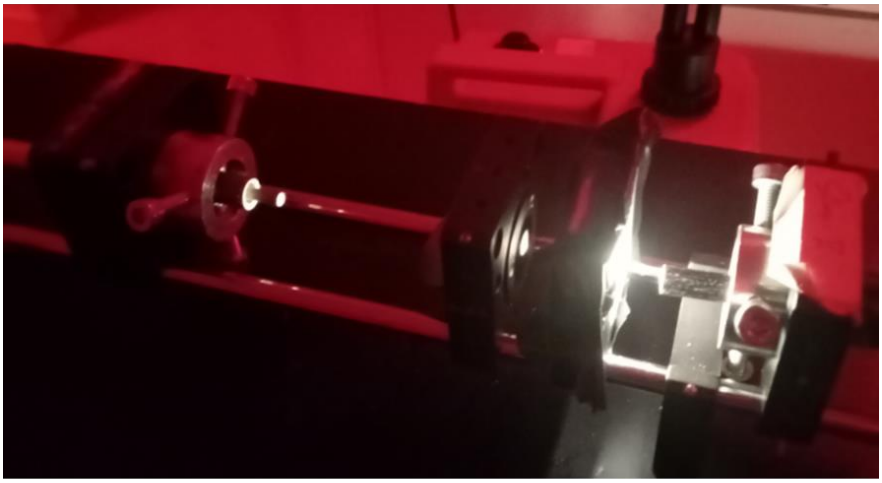

Spectrometer (left) lined up to light source (right). Near the light source are the two 1 mm light filters used to direct incident light onto sample.

A18 – Scan thickness tests

Laser scatter within the sample is an issue we were conscious of, which is why samples were cut approximately 2 mm in thickness.

We agree that the effect on sample thickness may produce optical stimulation variations, however given the sensitivity issues with the instrument, a relationship between OSL scatter stimulation and thickness could not be well established. The images below represent 250 um scan images of the sample quartzite sample with OSL saturation and with varied thicknesses, using a 20 micron beam diameter.

For this inquiry, we compared scans using 150, 250, and 350 micron datasets from three OSL saturated samples of the same rock core at thicknesses of 1.11 mm. The scan images for 250 and 350 um shows minimal effect in the intensity of luminescence nor resolution of scan extent. However, for 150 um there appears to be more of a deficit in measured OSL. Potentially this may be due to the scatter associated with the laser and its associated proximal bleaching beyond the 150 um bounds for each pixel. Still, this trend may be due to unique OSL sample characteristics, it is too difficult to tell.

Ideally, very thin transverse slices near thin section thicknesses would be preferred for reducing the effect of volumetric scatter. However, the limitations of the precision rock saw used for sample cutting limited the minimum dimensions of the transverse core slices to near 2 millimeters before the samples would disintegrate. It is still a point of inquiry to find a way to produce thin samples in a dark room setting for OSL scanning.

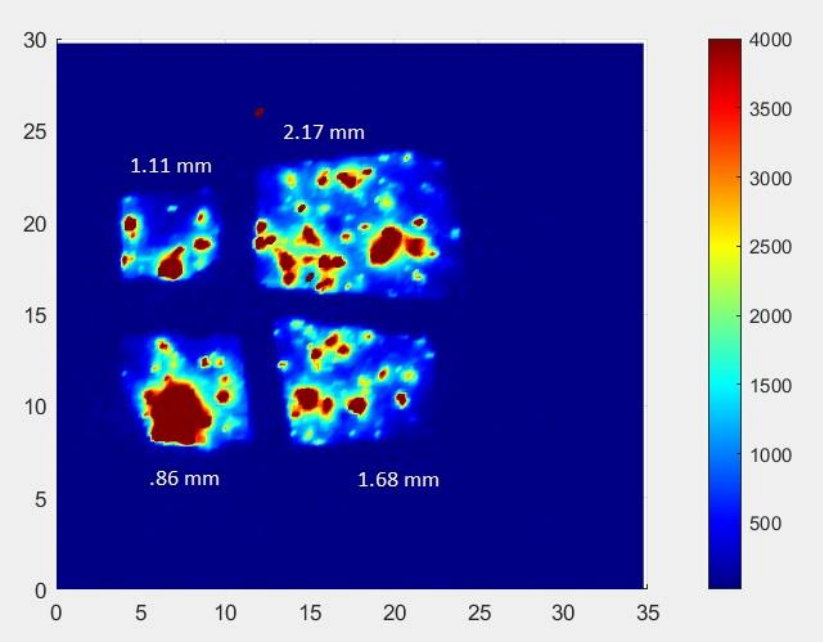
2.17 mm
1.11 mm
.86 mm
1.68 mm
30
25
20
15
10
5
0
0
5
10
15
20
25
30
35
4000
3500
3000
2500
2000
1500
1000
500

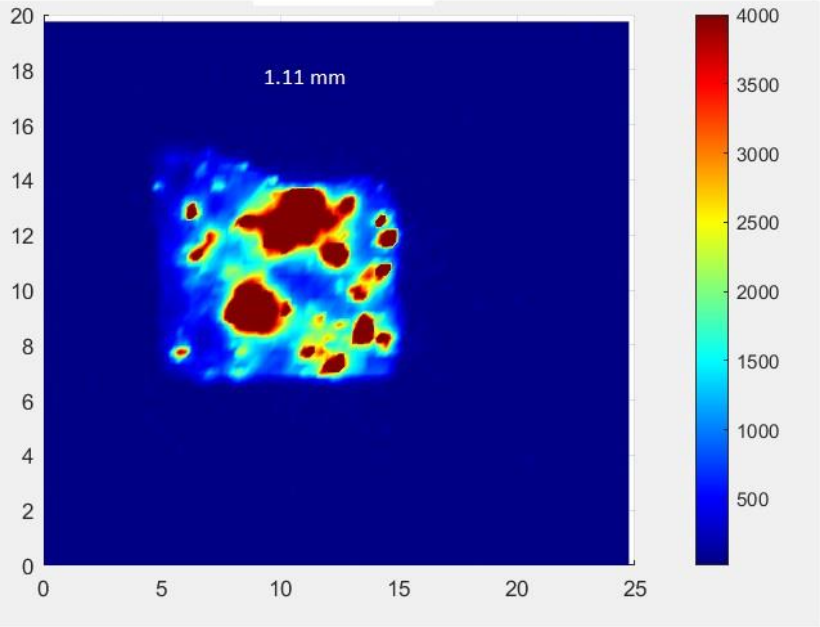
1.11 mm
20
18
16
14
12
10
8
6
4
2
0
0
5
10
15
20
25
4000
3500
3000
2500
2000
1500
1000
500

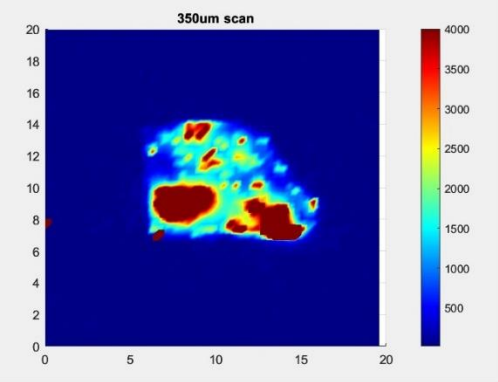
350um scan
0 2 4 6 8 10 12 14 16 18 20
0 5 10 15 20
4000 3500 3000 2500 2000 1500 1000 500

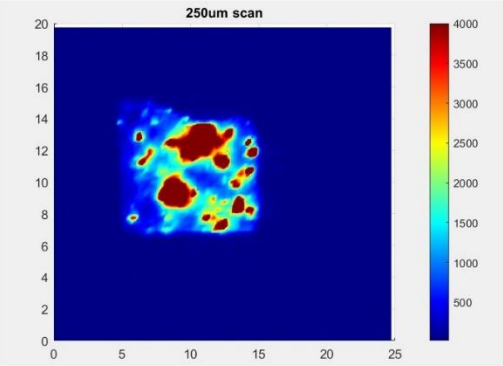
250um scan
0 2 4 6 8 10 12 14 16 18 20
0 5 10 15 20 25
4000 3500 3000 2500 2000 1500 1000 500

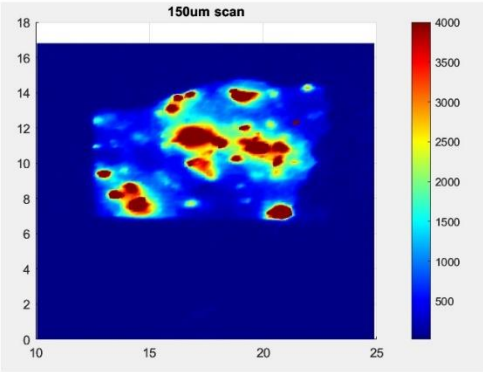
150um scan
0 2 4 6 8 10 12 14 16 18
10 15 20 25
4000 3500 3000 2500 2000 1500 1000 500

4. Exposure Dating the Foothills Erratic Train

Abstract

The Foothills Erratics Train is a depositional feature of quartzite erratics, interpreted to have been deposited along the margins of the Cordilleran and Laurentide ice sheets during their final stage of retreat. Ongoing controversies with the timing of the opening of the ice-free corridor and the deposition of the erratics provide motivation to use optically stimulated luminescence as an alternative chronometer to exposure date the erratic surfaces. The application utilizes controlled exposure experiments, using simulated unidirectional light sources, to extrapolate dating parameters from the erratic surfaces, and measures OSL depth profiles from the erratic samples using spatially resolved OSL laser scanning techniques. Age results offered sub-annual to centennial exposure ages for the erratics, with only one parameter set producing millennial-scale age, offering no insight on the deposition timeline of the erratics. However, the results indicate many possible implications in the evolution of the OSL depth profile over decamillennial time that are not accounted for in the exposure dating model, which includes variations in mineralogy, the limits of using solar simulated light and simplified assumptions of light exposure, the presence of weathering rinds, the fitting approach for parameter extrapolation, and the lack of erosion rate considerations in calculating age. With continued experiments and trials on these subjects, the ability to date millennial-decamillennial exposed surfaces can be more effectively evaluated for applied study.

4.1 Introduction

The Foothills Erratics Train is a sequence of quartzite erratics southwest Alberta, Canada, which are interpreted to have been deposited along the margins of the Cordilleran and Laurentide Ice

Sheets during their latest glacial retreat (Jackson Jr. et al. 1997). The significance of the age of deposition of the erratics allows insight on the timeline of the formation of the ice-free corridor in North America and the associated climate transitions during its development. Further, the opening of the ice-free corridor implicates the timeline of the peopling of the Americas through land migration routes. As such, it is of pertinent study to improve the precision and accuracy of the timeline of the Erratics Train deposition to allow for more thorough interpretations of human migration and glacial histories in the Americas.

Prior to the dating of the Erratic Train, North American ice sheet retreat histories document retreat timelines beginning as early as 13 ka for the southernmost portions of the ice-free corridor using ^{14}C proxy dates; however, general retreat chronologies for the Laurentide and Cordilleran ice sheets span from 18-13 ka (Dyke 2004; Dyke and Prest 1987; Munyikwa et al. 2011; Mukyikwa et al. 2017).

Later, exposure ages were then calculated for the erratic surfaces using geochemical techniques. For instance, ^{36}Cl cosmogenic dates of several erratics from the Train give wide range surface ages within mid-late Wisconsin substages showcasing no retreat direction (10.9 – 53.3 ka), with all measures producing a mean age of 15.91 ka excluding a 53.3 ka outlier date (Jackson Jr. et al. 1997; Jackson Jr. et al. 1999; Jackson et al. 2011). However, more precise geochronometers such as ^{10}Be can be used to attempt refining calculated exposure dates for the erratics. In response, an additional study was performed on the erratic surfaces using ^{10}Be, which supported a mean age of 14.9 ± 0.9 ka for the sampled erratics, but also provides no clear temporal retreat trends (Margold et al. 2019). Still, the improvements in age calculations using ^{10}Be still do not eliminate ongoing controversies on the timeline of the opening of the ice-free corridor, with prevalent inconsistencies in relating paleogenetic, paleoclimatic, and archaeological evidence to

corridor openings (Pedersen et al. 2016; Potter et al. 2018; Froese et al. 2019; Clark et al. 2022; Feathers 2023). For instance, postglacial archaeological sites and vegetation dates within the corridor region supports corridor opening ages near 12.6 ka, thousands of years after purported placement of the erratics (Pedersen 2016). Other luminescence assessments point dates as early as 15 ka for the opening of the ice-free corridor, and ^{14}C proxy dates of approximately 13-21 ka were dated near the Erratic Train placements, offering a wide range of age deposition timeline possibilities (Dyke 2004; Margold et al. 2019). The precision of ^{10}Be dates is also influenced by the effects of snowfall cover on erratic surfaces during their placement, but this metric is not well understood for the expected timeline of deposition, given complexities associated with measuring climatic shifts in the late Pleistocene (Clark et al. 2022). Further, while ^{10}Be is a more precise chronometer for quartz than ^{36}Cl, it is being used to date surfaces at its youngest viable age thresholds, which can face concerns in calculated age precision. Also, the exposure ages from the Margold et al. (2019) study assume that erosion is negligible for the site, which may provide younger than expected ages for deposition if erosion was significant enough to impact ^{10}Be production rates.

The dated range of the ice-free corridor, therefore, is still tenuous. The use of a chronometer more sensitive to millennial timescales, such as with OSL exposure dating, may provide enhanced insight to glacial retreat chronology of the North American ice sheets. Prior methodologies for OSL exposure dating would not be able to date erratic surfaces given the lack of known age proxy rock surfaces onsite. Additionally, limitations in the resolution of OSL depth profiles from millimeter rock slices would possibly limit the precision of age calculations as seen in other examples of luminescence dating applications on boulders or erratics (Luo et al. 2018; Sohbati et al. 2018; Brill et al. 2020). However, the use of controlled exposure experiments and

spatially resolved OSL measurements offer the possibility of dating these surfaces with enough precision to produce viable exposure ages.

In this application, an attempt is made to luminescence exposure date three erratic surfaces of the Foothills Erratics Train, which host no known age proxy surfaces, with the use of controlled exposure experiments and spatially resolved OSL. In addition to providing an alternative chronometer for the Erratics Train, the assessment aims to determine the effectiveness of using OSL as a chronometer for exposure dating millennial-decamillennial exposed surfaces when using controlled exposure experiments and spatially resolved OSL measurements. Further, the work aims to highlight potential temporal impacts to the parameterizations for OSL exposure dating over millennial-decamillennial time, with discussion on how to effectively parameterize rock surfaces. Specific comments on the effectiveness of the use of curve fitting to acquire physical parameters over millennial-decamillennial time, as well as the impacts on surface features and depth profile evolution, will be highlighted in this discussion. With these insights, the potential and improvements needed for OSL exposure dating in late Quaternary contexts will be evaluated.

4.2 Dating Erratics using Controlled Exposure Experiments, Spatially Resolved OSL

4.2.1 Introduction

An attempt to date the exposed quartzite surfaces of the Foothills Erratics Train will be conducted using both OSL laser scanning for depth profile measuring and controlled exposure experiments for parameter extrapolation. Results from the controlled exposure application in this study will provide insight on the experimental conditions and model parameters needed to accurately estimate depth profile development, particularly examining the feasibility of using single rates for photon flux and monochromatic functions for light attenuation and

photoionization cross sections to calculate decamillennial exposure. Further, the impact of the surface characteristics of the sample and the resultant impact of the depth profile will be directly examined.

4.2.1.1 Sampled Sites

Three erratic surfaces were sampled from the Erratics Train, labelled as sites 3, 6, and 8 (Figure 4.1-4.7, Table 4.1). Each of these sites host flat sampling surfaces and are in open field settings, offering near unobstructed light exposure. Solar radiation is equivalent between sites also, roughly at 300 W/m^2 (±30) over the Holocene and late Pleistocene, also making it feasible to attempt roughly simulating constant rate sunlight exposure for decamillennial timescales, as defined in the exposure dating model (Gallée et al. 1992; Sengupta et al. 2018; Sohbati et al. 2012). Erratic 3, 6 and 8, in order from North to South, are approximately 25 kilometers from each other, hosting ^{10}Be ages of 14.7 ka (±1), 8.2 ka (±.5), and 15.1 ka (±1 ka), assuming no erosion rate factor (Table 4.1; Margold et al. 2019). Including a 2 mm/ka erosion rate, sample ages are 15.1 ka (±1 ka) for Erratic 3, 8.3 ka (±0.6 ka) for Erratic 6, and 15.5 ka (±1.1 ka) for Erratic 8 (Table 4.1; Margold et al. 2019).

Table 4.1
^{10}Be ages of the sampled erratic surfaces from the Foothills Erratics Train, published by Margold et al. (2019). Samples in bold, Erratic 3, 6, and 8, are dated using OSL exposure dating in this chapter.

Erratic	^{10}Be age (ka) (no erosion)	^{10}Be age (2mm /ka erosion)
1	17.7 ± 1.2	18.2 ±1.2
3	14.7 ± 1.0	15.1 ± 1.0
6	8.2 ± 0.5	8.3 ± 0.6
8	15.1 ± 1.0	15.5 ± 1.1
13	14.6 ± 1.0	14.9 ± 1.0
14	N/A	N/A

These exposure ages relatively match deposition timelines of glacial retreat from ^{14}C studies in the region, so no indications of supraglacial transport were specified in the interpretation of the age of deposition of the erratics, concluding englacial transport as the likely mechanism to deposition (Margold et al. 2019). However, supraglacial exposure histories were considered in explaining the data scatter of the internal uncertainties presented in the ^{10}Be age results (Margold et al. 2019). Erosion rates may also be greater than the applied 2 mm/ka, and if a higher erosion rate metric was used as a factor for age calculation, calculated ages would be greater than what is presented in the publication. Still, the possibility of supraglacial transport could be observed from luminescence depth profiles sampled from the erratics if ages are calculated within decamillennial time beyond postglacial ^{14}C ages.

To perform the controlled exposure parameterization technique, one core from each erratic was reserved to be dated, while the remainders were used to conduct controlled exposure experiments (Figures 4.8-4.11). Each of the cores set aside for controlled exposures were cut in half into two samples using a diamond sawblade. This cut produced a Top portion, hosting a naturally altered surface, and a Bottom portion, hosting nonweathered, unaltered bedrock (Figure 4.9-4.11).

The two core portions will be used from each erratic to perform separate controlled exposure experiments for model parameter extrapolation. This is performed to assess if weathering rinds or other surface features play a role in altering depth profile forms, and how the presence of such features implicates the use of samples with no surface altered features to parameterize naturally exposed rock surfaces for exposure dating.

Figure 4.1

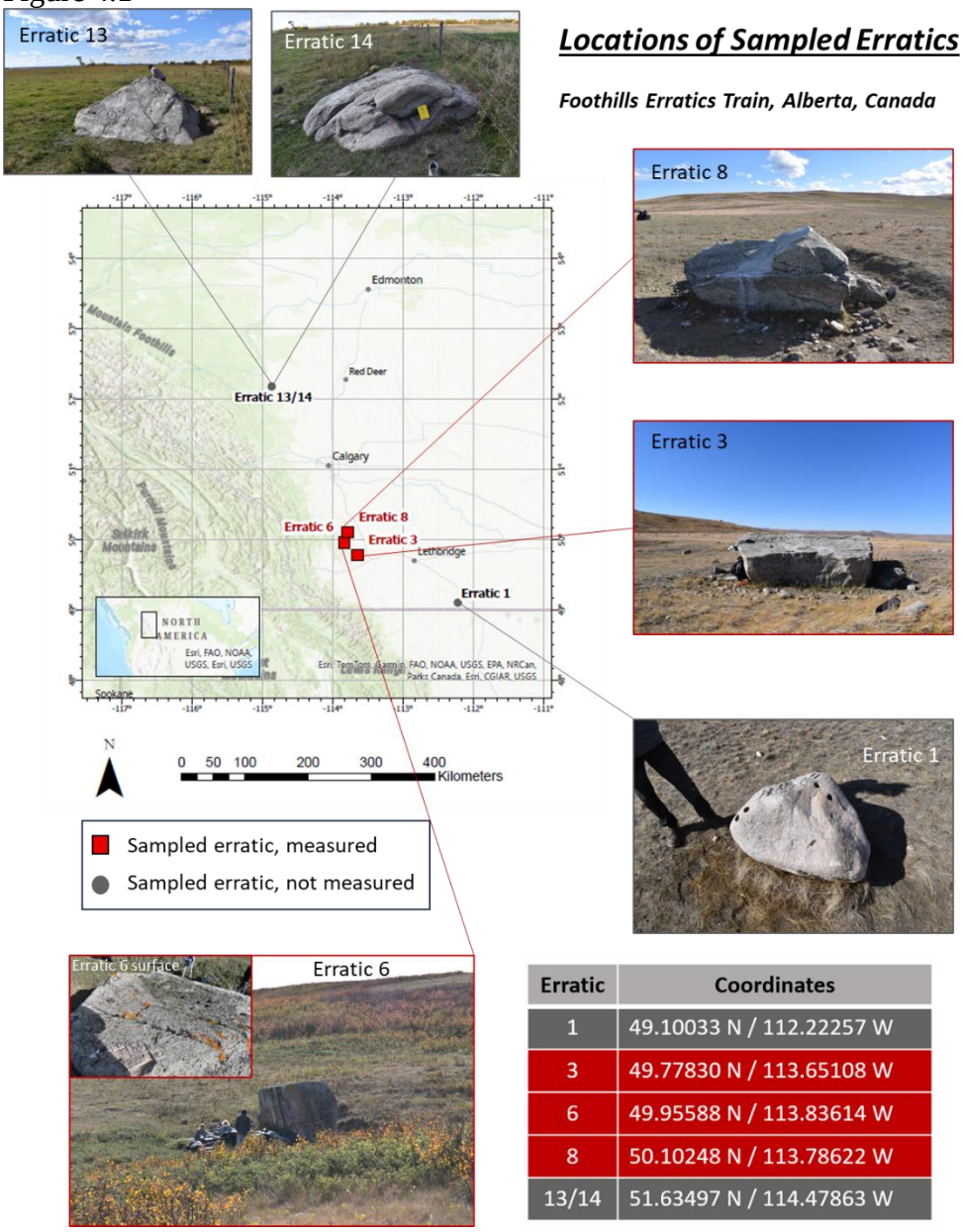

Erratic	Coordinates
1	49.10033 N / 112.22257 W
3	49.77830 N / 113.65108 W
6	49.95588 N / 113.83614 W
8	50.10248 N / 113.78622 W
13/14	51.63497 N / 114.47863 W

Locations of erratics where samples were retrieved during field visits from September 26 – October 1, 2021. Erratics 1, 3, 6, 8, 13, and 14 were sampled, but Erratics 3, 6, and 8 were dated using OSL exposure dating procedures.

4.2.1.2 Sample Descriptions

The Top samples show a variety of different surface alterations. For Top samples 3-5 and 3-6, surfaces are nearly totally covered by a dark brown lichen growth (Figure 4.2, 4.5). Top sample

3-8 shows partial lichen growth on approximately half of the surface, with signs of surface abrasion on the remaining exposed surface. For Top samples, 8-2 and 8-4, no lichen growth is documented, however the surfaces are rough and more friable from physical abrasion, and appear whiter in color than their Bottom surface counterparts (Figures 4.4, 4.5). Top samples 6-1 and 6-4 from Erratic 6 both show near complete lichen coverage on the surface, while sample 6-2 shows no lichen growth (Figures 4.3, 4.5). Conversely, all Bottom core surfaces show unaltered bedrock from the erratic.

Within the Top sample subsurfaces, samples from Erratic 3 show signs of weathering or chemical alteration, with darkened rinds approximately 8 millimeters in thickness for 3-5 Top and 3-6 Top, but roughly 5 millimeters in thickness for 3-8 Top (Figure 4.10). Top samples of Erratic 8 show minor signs of darkened subsurface alteration, with 8-4 Top hosting darkened rock hue within the first two millimeters of depth, but sample 8-2 Top showcasing a darkened rind in the first 7 millimeters of sample (Figure 4.12). Erratic 6 samples 6-1 Top and 6-4 Top host dark rock weathered rinds roughly 2-3 millimeters in thickness, while 6-2 Top shows a slightly darkened hue for the first 5 millimeters of sample depth (Figure 4.11).

Before undergoing controlled light exposures to date the natural exposed cores, the Top and Bottom samples must host saturated levels of OSL, to ensure that past exposure histories are not incorporated in depth profile data for rock parameterization. To ensure complete OSL saturation for the cores used for controlled exposures, all Top samples and Bottom samples, with the exception of 3-6 Bottom, were irradiated to 1000 Gy of ^{60}Co gamma source at the Pacific Northwest National Laboratory's Radiological Exposures and Metrology laboratory. Sample 3-6 Bottom was not artificially irradiated, and achieved trap saturated from natural radiation exposure.

Figure 4.2

Erratic 3- Additional photos, sampled area of surface. Notable features surface weathering present. Sampling holes labelled.

Figure 4.3

Erratic 8 – Additional photos, sampled rea of surface. Sampling areas labelled. Some surface coverage presented, minor erosion features.

Figure 4.4

Erratic 6 – Additional photos, sampled area of surface. Sampling holes labelled. Major surface coverage and weathering features presented in this sample.

4.2.1.3 Controlled Exposure Procedure, Sample Processing for Laser Scanning

Before light exposure, all samples were wrapped in three layers of aluminum foil and an outer layer of black tape, to where only the sample surfaces could be exposed to light.

The assessment opted for unidirectional, single intensity, lab simulated light for controlled exposure. For the Foothills Erratics Train, solar radiation is equivalent between sampled sites, roughly at an annual daylight average of 300 W/m^2 (±30) over the Holocene and late Pleistocene (Gallée et al. 1992; Sengupta et al. 2018). The single rate of photon flux, although simplified, follows the model assumption of constant incident photon flux presented in the exposure dating model (Sohbati et al. 2012). This exposure setting also does not consider other potential natural influences to depth profile evolution over decamillennial time, such as temporal surface coverage or erosion, as none of these are parameterized in the model form.

Thus, Top and Bottom sample sets were thus controlled exposed to unidirectional artificial light using an Applied Photophysics Solar Simulator at this intensity (Applied Photophysics Limited, 1982). Top samples were exposed for 2.7156E+6 seconds, while Bottom samples were exposed for 2E+6 seconds. The longer exposure time for the Top samples was to ensure a viable depth profile could be generated from the samples, given the significant lichen coverage present in the samples (Figures 4.2,4.3,4.4).

After light stimulation, the exterior portions of the samples were trimmed in subdued red light conditions using a water cooled diamond rock saw to make samples no more than 30 millimeters wide, suitable for preparing transverse slices in a precision rock saw. Transverses slices of 1-2 mm thickness were then produced under subdued red light conditions using a Lamplan Cutlam Micro 1.1 precision cutting machine with 400 µm diamond coated brass blades. The transverse slices were then used to measure OSL depth profiles by OSL laser scanning.

4.2.1.3.1 Justification for using simulated light exposures

For the controlled exposure experiments, only unidirectional, single intensity, lab simulated light is used. This decision is in counter to the promising results from the Lane Mountain trials using controlled exposures for rock surface parameterization, which showed that natural sunlight controlled exposed samples produced the most accurate ages, and simulated sunlight exposures produced the least accurate ages (Section 2). However, the results of this study were derived from poor resolution datasets, which resultingly produced parameter and age fits with high uncertainties.

Attempts were made to produce higher resolution depth profiles from the cores using spatially resolved OSL measuring techniques to further validate the results of the wafer study, but unfortunately the OSL acquired from the samples were too low in sensitivity to be used effectively for age extrapolation (Section 3, A4-A5). Given these results, it could not be determined if spatially resolved OSL data would replicate the results of the wafer derived datasets where natural sunlight exposures would produce more precise fits for age calculation.

Figure 4.5

Approximate cut cross section

Top Core Surfaces

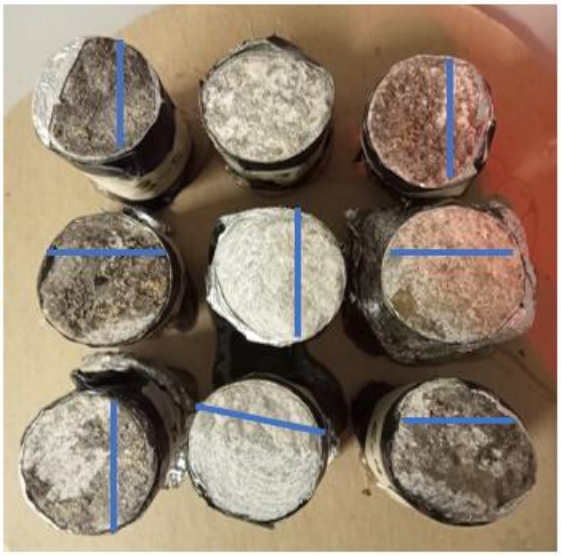

Labels
Top-down perspective:

3-5	8-1 (not used)	6-1
3-6	8-2	6-2
3-8	8-4	6-4

Top surfaces for Erratics 3, 6, and 8. Blue lines indicate estimate surface region where thin sections were produced for the sample.

Figure 4.6

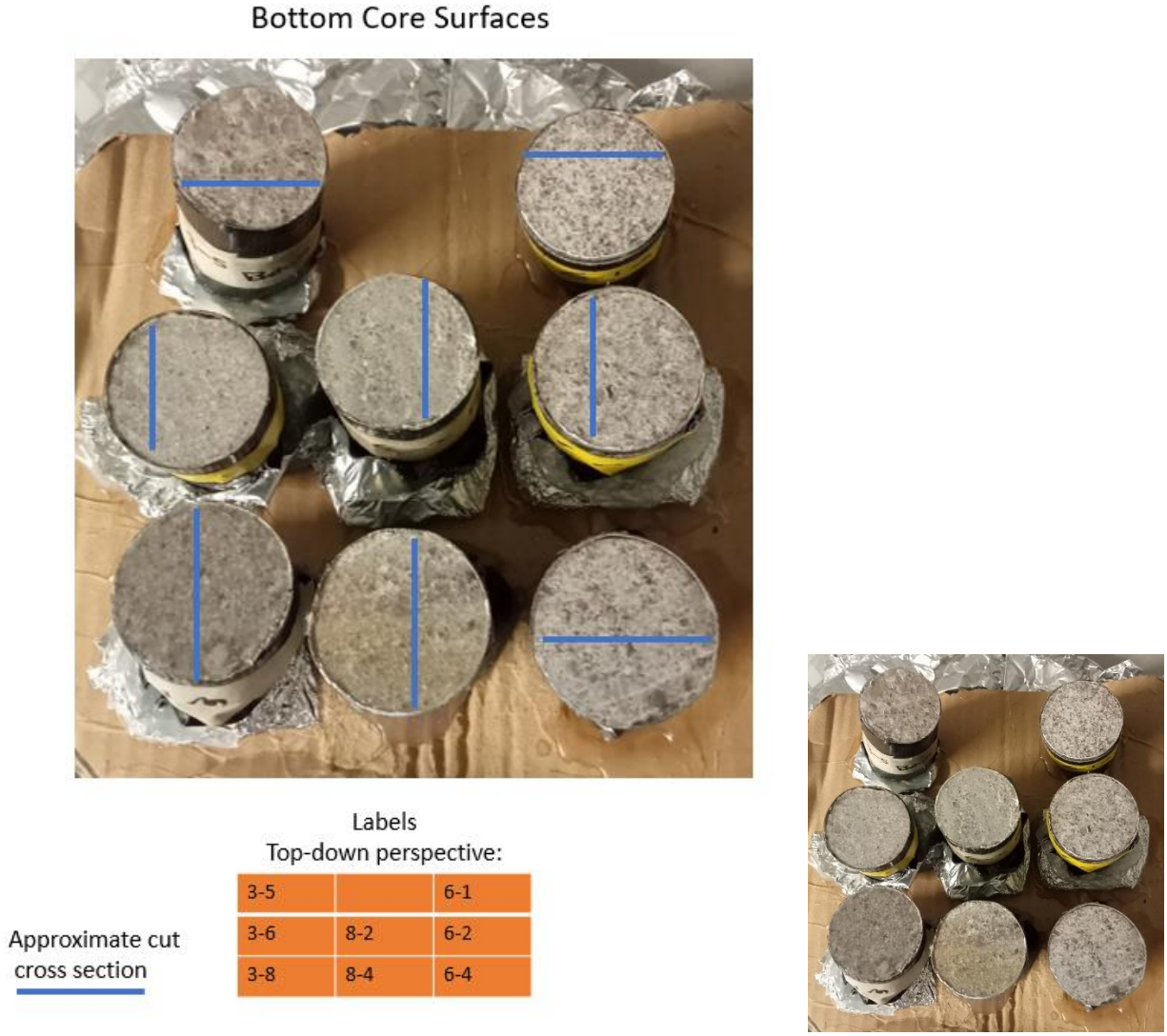

Top surfaces for Erratics 3, 6, and 8. Blue lines indicate estimate surface region where thin sections were produced for the sample.

Figure 4.7

Surfaces of natural exposed cores 3-7, 6-3, and 8-3.

It is still unknown if unidirectional, constant flux sunlight exposures could accurately simulate sunlight exposure for exposure dating applications. Given that the first order model does not consider effects of solar angles or variations in photon flux in quantifying depth profile

evolution, if model conditions are adequate, the use of simulated sunlight should produce viable parameters for age extrapolation when using controlled surface exposure experiments.

Further, when using natural sunlight exposures, it can be difficult to emulate the site's solar irradiation average, as this format of solar stimulation relies on consistent weather conditions that aim to match the average for the sampling site. This was a weighed risk with the Lane Mountain study, where an attempt was made to simulate average irradiance for the site with natural sunlight in the month of August 2021. With longer natural sunlight exposures spanning a year or more, the use of natural sunlight exposures is more likely to capture an average irradiance value for the controlled exposed cores that could match the sampled site characteristics, and less risk is imposed for inaccurate light exposure simulation. Still, the difficulty of emulating these conditions with natural sunlight brought concerns to whether such a procedure could be successfully accomplished in the established timeframe of this thesis work, and a more conservative simulation choice was ultimately decided. The use of this light source at least guarantees that some equivalence in solar radiation was applied to the controlled exposed samples for parameter extrapolation. However, future studies should be conducted to attempt natural sunlight exposures for parameter extrapolation. Further, these natural light surface exposure studies should include short term and long term experiments to determine if either temporal constraint is more effective at simulating surface exposure conditions.

4.2.1.4 OSL Measuring Procedure

OSL scans were performed on the transverse sections using scanning equipment at the Luminescence Research Lab at the Scottish Universities Environmental Research Centre (SUERC), (Sanderson et al. 2001; Bench et al. 2023). The scan configuration for this experiment used an Acculase brand 520 nm, 10 mW laser with a 20-micron diameter beam. The apparatus

holds the laser in a fixed position, which stimulates OSL from the sample which is mounted on a high precision X-Y stage with minimum half step resolutions of 1.6 microns. In these experiments the sample moves in 250 micron increments after every stimulation period. Directly above the X-Y stage is a photomultiplier hosting a 9 mm UG-5 and a 2 mm UG-11 filter, which measures the emitted OSL. The procedure recorded OSL in 0.1 second increments from 1 second of laser stimulation for each X-Y step, following 1 second of 0.1 second incremented background photon measures (Martin et al. 2022, 2023). Beam scattering within the sample subsurface has the potential to cause OSL to stimulate beyond the 20-um beam diameter, which is why 250-micron resolution steps were used to limit the effect of measuring sample area, which could have been stimulated from prior laser steps. This procedure produces the 250-micron resolution OSL maps of each sample, with offers 16 OSL datapoints per square millimeter of sample (Figure 4.8-4.12).

Before laser scanning, each sample was preheated in a laboratory furnace for 90 minutes at 135°C. After the spatially resolved scans were produced, the scan data were converted to spreadsheets, where net OSL values from each measured 250-micron pixel are corrected for background by subtracting the average of the 1 second background measure for the pixel. A depth profile of 250-micron increments is then produced from the scan data by taking the average and standard error of pixels from each 250 microns of depth. The resulting depth profile data are then normalized using 0 to represent the mean OSL of the first millimeter of the depth profile and 1 representing the mean of the deepest 9 millimeters of the depth profile.

4.2.1.5 Fitting Protocol

4.2.1.5.1 Parameterizing $\overline{\sigma\varphi_0}$ and μ

Least absolute error regressions were used on the OSL depth profile data to extrapolate $\overline{\sigma\varphi_0}$ and μ parameter values from the erratic surfaces (Lehman et al. 2019; Bench et al. 2023). The approach calculates $\overline{\sigma\varphi_0}$ and μ from core depth profile data, applying known age of 2.7156E+06 seconds for Top samples, and 2.00E+06 seconds for Bottom samples, using least absolute residuals misfits from 10^6 randomized fit simulations. Random parameter combinations are chosen from ranges of applied parameter values for $\overline{\sigma\varphi_0}$ and μ.

To produce parameter medians from the misfit results, a maximum likelihood estimate protocol is performed where the fitted parameter combinations are randomly resampled to produce a probability density function of parameter likelihoods for the tested parameters. The resultant distribution is then used to derive median parameter and uncertainty values for the fitted core samples.

4.2.1.5.2 Cumulative Core Fits

To acquire parameters for age fitting of Erratics 3, 6, and 8, Top and Bottom core data from each erratic were fit cumulatively to produce standard Erratic parameter sets (Figure 4.16-4.18). The purpose of fitting combined datasets to produce one parameter set is to offer parameter values which consider the variation in OSL depth profile evolution in the sampled surface. Parameter values from the cumulative core fits from Erratic 3 Top, Erratic 3 Bottom, Erratic 6 Top, Erratic 6 Bottom, Erratic 8 Top, and Erratic 8 Bottom were produced for age fitting, using value ranges of 0-1 for μ, and 0-10 for $\log(\overline{\sigma\varphi_0}*t)$, the results of which are converted to $\overline{\sigma\varphi_0}$ after performing fits (Appendix A4).

4.2.1.5.3 Individual core fits

Using this parameter fitting protocol, cores were also fitted individually based on their controlled exposure age, to assess potential variations in depth profile evolution between samples of the same erratic (Figure 4.13-4.15). Differences in sampling locations, as well as varied physical characteristics such as weathering rinds or different mineral compositions, may implicate depth profile shapes and rock surface parameterizations. Such observations are also useful in contextualizing age calculations from the erratics.

All cores from Erratics 3, 6, and 8 were fitted individually. For the individual fitting of cores from Erratics 3 and 8, the range of parameters fitted for μ were between 0-1, except for 3-5 Top and 3-6 Bottom (Appendix A1-A3). For fitting parameter μ, a range of 0-0.5 was used for 3-5 Top, and a range of 0-2 was used for sample 3-6 Bottom. Values between 0 and 10 were fitted using the parameter $\log(\overline{\sigma\varphi_0}*t)$ for all samples (Appendix A1). For erratic 6, only the depth profiles of cores 6-4 Top and 6-2 Top were able to be parameterized, using μ fit values between 0-1 and $\log(\overline{\sigma\varphi_0}*t)$ values of 0-10 for 6-2 Top, and μ values of 0-3 and $\log(\overline{\sigma\varphi_0}*t)$ values of -5 to 5 for 6-4 Top (Appendix A2).

4.2.1.5.4 Parameterizing natural exposed surfaces using ^{10}Be ages

The theoretical conditions of the first order model indicate that regardless of exposure time, parameters $\overline{\sigma\varphi_0}$ and μ remain equivalent for a given sample. However, it is possible there are unaccounted for conditions that may impact $\overline{\sigma\varphi_0}$ and μ parameterizations. Given million second timescales are used to derived parameters to quantify decamillennial exposure, however, it is worth considering if such effects can be observed through the discrepancies of parameter fits

between the two timescale differences. To provide this comparison, parameterizations of $\overline{\sigma\varphi_0}$ and μ were also fitted against the natural exposed depth profiles of the erratic surfaces.

For fitting $\overline{\sigma\varphi_0}$ and μ to the natural exposed surfaces of the erratics samples 3-7, 6-3, and 8-3, exposure ages from ^{10}Be from Margold et al. (2019), considering no erosion, were used as the exposure times fitted to the depth profiles. The same least absolute error regression fit approach was used as with the controlled exposed cores. A known age of 14.7 ka was fitted for sample 3-7, 8.2 ka for sample 6-3, and 15.1 ka for sample 8-3. The range of parameters fitted for μ were between 0-1 for cores 3-7 and 8-3. For 6-3, a range of 0-3 was used to fit μ. Values between 0 and 10 were fitted using the parameter $\log(\overline{\sigma\varphi_0}*t)$ for samples 3-7 and 8-3, and a range of -5 to 5 was used for sample 6-3.

4.2.1.6 Parameterizing age

With the parameters $\overline{\sigma\varphi_0}$ and μ acquired from the Top and Bottom controlled exposed samples, age calculations were then fitted for the natural exposed erratics samples, which include sample 3-7 from Erratic 3, Sample 6-3 from Erratic 6, and sample 8-3 from Erratic 8. Least absolute error regressions were used to calculate exposure ages from 10^6 randomized age simulations, applying the derived parameter values for $\overline{\sigma\varphi_0}$ and μ from controlled exposure experiments for the erratic. Age ranges from 0-10^5 years were initially applied to each erratic to determine the estimated best fit age and uncertainty ranges, then the erratic data were subsequently refitted to smaller age ranges by decreasing the magnitude of the maximum range to produce the most precise statistics for the age distributions. For the fits, the maximum range is two magnitudes greater than the fitted age value. A maximum likelihood estimate protocol is then used where the

fitted ages and associated misfits are randomly resampled to produce a probability density function of age likelihoods. A median age can then be produced from this distribution.

Exposure ages were additionally calculated for the natural exposed surfaces (cores 3-7, 6-3, and 8-3) using parameters $\overline{\sigma\varphi_0}$ and μ acquired from fitting ^{10}Be ages to the natural exposed surface cores. The calculation mimicked a proximal rock dating procedure, where the age of one erratic surface was calculated using the parameters acquired from the two other sampled erratic surfaces. Ages were calculated with a range of 0-10E+5 years for cores 3-7 and 6-3, and a range of 0 - 1E+07 years for sample 8-3.

4.2.1.7 Attempting X-Ray Element Mapping

Following the measurement of OSL from laser scanning instruments, element map images were planned to be produced for select samples to determine the minerals that are contributing to the OSL anomalies present in the OSL scan data.

The element mapping was conducted at the Geosciences Electron Microprobe/SEM Facility at the University of Massachusetts, Amherst. The sample thin sections are first carbon coated for use in the facility's Cameca SX100 electron probe, which then undergo automated EMPA scanning analyses to produce element maps of elements Potassium, Sodium, Magnesium, Silicon, and Aluminum. Examples of the provided maps are found in Appendix A12.

Upon obtaining evidence from the element maps that the source of OSL anomalies is non-quartz, denoted by the significant presence of non-Si elements in the OSL anomaly dimensions, the anomaly data dimensions of each scan would be filtered out of the generated OSL depth profiles. The resultant depth profiles should be less influenced by data scatter caused by the anomalies (Bench et al. 2023). From the Lane Mountain application, fit precision using anomaly filtered

data did modify parameter fit values, but precision was only slightly improved for some samples (Section 3).

Unfortunately, in preparing the thin sections from the samples, the original dimensions of the samples were damaged, and some samples appear to have been etched on the unscanned side of the transverse slice, preventing the ability to accurately align mineralogy and OSL scan dimensions using the mineral maps as intended. Still, the element maps provide insight on the potential sources of OSL variability present in the sample scans and generated depth profiles. While not possible in the scope of this study for the Foothills Erratics Train, the slight improvements in parameter precision using anomaly filtered depth profile data in the Lane Mountain application warrants the application of anomaly filtering in future exposure dating studies to validate its use in refining parameter fit precision and age assessment.

Element maps were produced from cores 3-1 (not used, but from Erratic 3), 3-5, 3-7, 8-3, and 6-3. These maps showcase non-quartz mineral assemblages of roughly 20-35%, which may indicate a portion of OSL recorded in the OSL scans are of non-quartz origin. The associated non-quartz mineralogy of the rocks likely has feldspar components given the prevalence of Al and K in certain regions, but perhaps minor micaceous minerals are also present given the associated percentages of Mg and Al. The significant presence of non-quartz mineralogy likely impacts the OSL depth profile form and contributions to the observed OSL scatter in the samples.

4.2.1.8 Attempting physical parameterizations

A major difficulty in attempting luminescence exposure dating is the acquisition of parameters which accurately portray the physical characteristics of the rock material pertinent to quantifying the temporal evolution of luminescence depth profiles. The characterization of what impacts the

evolution of luminescence depth profiles has been difficult to examine, with few physical experiments that attempt to provide accurate parameterized techniques for exposure dating.

These difficulties have influenced how the first order exposure dating model was developed. With the development of the applied first order model, the simplified characterization of $\overline{\sigma\varphi_0}$ and μ endorsed in the initial applications was made in part due to the forecasted difficulty in quantifying photoionization cross section across the visible spectrum, in addition to the expected laboratory difficulties in quantifying the wavelength- depth impacts of photon flux for every sample, which is why the model also incorporates the attenuation coefficient value to summarize the depth dependence of photon flux (Sohbati et al. 2011).

However, since the model was published, few physical experiments have been made to verify the adequacy of this parameterization format. As such, it should be determined if parameters derived from curve fits are equivalent to parameters derived from physical measurements. Any observed discrepancies may indicate the first order model is not adequate in summarizing luminescence depth profile evolution. The potential for the first order exposure dating model to inaccurately quantify attenuation may implicate age estimates are produced from the Foothills Erratics Train samples.

To assist interpreting age estimates, physical parameterizations of light attenuation are performed on samples from the Foothills Erratics Train, to determine if discrepancies in physical and fitted light attenuation are apparent. To test the viability of physically measuring $\overline{\sigma\varphi_0}$ and comparing the physical value to the fitted value of $\overline{\sigma\varphi_0}$, an attempt using LM-OSL to acquire a photoionization cross section value for a 470 nm wavelength will be applied to Foothills Erratics

sample 3-7. With an average photon flux measure of the 470 nm wavelength for the site, then an estimated $\overline{\sigma\varphi_0}$ value can be produced and compared with fitted $\overline{\sigma\varphi_0}$ values for the Erratic.

4.2.1.8.1 Attenuation - procedure for physical measurements

The experimental setup for measuring light attenuation from the Erratics Train sample involves measuring in differences of incident and transmitted light intensity using the Beer-Lambert Law of Attenuation:

$$I= I_o e^{-\mu x}$$

Where I_0 is incident light intensity, I is the light intensity after transmission through the sample, x is the sample thickness, and μ is the attenuation coefficient for the sample.

The equation can be adjusted to solve for the attenuation coefficient, with the knowledge of the fraction of measured light intensity and thickness of the sample:

$$\mu=-\ln(\frac{I}{I_o})/x$$

The configuration of the light attenuation experiment is presented in Appendix A15a, and is based on physical attenuation experiments from Smillie et al. (2011) and Sanderson et al. (2011), as well as Ou et al. (2018). Samples were measured for light attenuation coefficients using an Ocean Optics USB 200 spectrometer, with a gooseneck microscope illuminator as a light source. The light source is filtered through two 1 mm Ø holes to ensure the light is concentrated to a location that the spectrometer can collect.

The first measure conducted for an attenuation procedure is a measure of the background photon counts, then the photon counts of the light source alone are measured. Given the strong light intensity from the light source, an integration time of 5 ms is used to record the light spectra to

not oversaturate the spectrometer. After these measures, a sample is then placed in between the 1 mm Ø light filter holes, where the resulting change in light intensity is recorded at an integration time of 700 ms.

The fraction of light intensity lost from the sample light attenuation is then able to be calculated from these metrics by first adjusting the integration times of the photon count spectrum to be equivalent. Then, two attenuation calculations are produced. The first attenuation coefficient value is referred to as 'summed attenuation', which measures the fraction of light intensity based on the total sum of photon counts measured for the recorded spectral range (347-980 nm or 347 – 1010 nm). The second measure is the 'attenuation average', or the average light attenuation coefficient measured from each individual spectra component that was measured from the spectrometer (347-980 nm or 347 nm – 1010 nm).

4.2.1.8.2 Photoionization cross section - procedure for physical measurements

Issues with the accurate parameterization of light attenuation also bring up implications on the accuracy of obtaining parameter $\overline{\sigma\varphi_0}$ from curve fitting. Few direct studies on the fitting precision accuracy for parameter $\overline{\sigma\varphi_0}$ have been performed. Gliganic et al.'s (2019) study on characterizing parameters of $\overline{\sigma\varphi_0}$ and μ from a rock site indicated that the depth profiles produce wide ranges of fitted parametrizations for $\overline{\sigma\varphi_0}$, even though rock type and setting was similar for the sampled specimens.

Physically deriving the parameter $\overline{\sigma\varphi_0}$ would entail measuring of the photoionization cross section across incident photon flux spectra, which presents a difficult laboratory challenge (Sohbati et al. 2011). Still, the use of linearly modulated optically stimulated luminescence (LM-OSL) can be performed to estimate photoionization cross section values for rock samples with

the use of an applied light wavelength (Bulur 1996). When paired with a recorded photon flux value for the given wavelength used in LM-OSL, an estimation for $\overline{\sigma\varphi_0}$ for a wavelength can be calculated physically, which can be used to reference the viability of fitted $\overline{\sigma\varphi_0}$ values for the rock core.

For extrapolating the photoionization constant σ from a sample using LM-OSL, an intensity of applied light stimulation is steadily increased to produce OSL vs time plots, which can be deconvolved for σ using the model (Bulur et al. 2000):

$$L_{LM}(t)=n_0\left(\frac{\sigma I_0 t}{t_{max}}\right)e^{-\frac{(\sigma I_o)t^2}{(2t_{max})}}$$

Where n_0 represents the value for OSL sample saturation, t_{max} represents total exposure time, I_o represents maximum stimulation light intensity from the stimulating light (photons/(s*cm^2)) applied to the sample. LM-OSL can be stimulated from samples with the use of Riso TL/OSL readers using LED's, with one of the available LED sources as the stimulation sources on default instruments.

Wafer slices from sample 3-7 were measured for LM-OSL using a 470 nm light source on a Risø DA-15 model TL/OSL reader. The sequence follows an LM-OSL protocol used in Choi et al. (2006) for low OSL intensity rock samples. The protocol runs a 3600 second protocol recording 4 second iterations of OSL, holding a temperature at 125 °C, and increasing LED intensity from 0 to 100% power.

The acquired LM-OSL plots are found in Appendix A16. Using these LM-OSL plots, individual components of the photoionization cross sections can be calculated using decomposition scripts

from the numOSL R script package (Peng et al. 2023). Results of the photoionization values for the samples are provided in Appendix A19.

Correspondingly, the environmental incident photon flux of 470 nm for Erratic 3 was estimated from the average irradiance for the sample location from the National Renewable Energy Laboratory's National Solar Radiation Database (Sengupta et al. 2015; 2018). The average annual global horizontal irradiance (GHI) for the Erratic 3 coordinates was estimated at 150 W/m^2. To determine the fraction of irradiance contributed from 470 nm, the fraction of irradiance contributing to the average solar spectrum was multiplied to the GHI value for Erratic 3 to produce the GHI from 470 nm estimate for the site. This produces a $\varphi_{0(470)}$ value of 4.138 E+18 photons/cm^2 s^{-1}.

The equation for parameter $\overline{\sigma\varphi_0}$ summarizes the relationship of the photoionization cross section and photon flux across the visible solar spectrum as:

$$\overline{\sigma\varphi_0} = \int_{\lambda_i}^{\lambda_f} \sigma(\lambda)\varphi_0(\lambda)\ d\lambda$$

Calculating the 470 nm wavelength variant of $\overline{\sigma\varphi_0}$ (s^{-1}) can be estimated with the product of σ (cm^2) and φ ($cm^{-2}\,s^{-1}$) at 470 nm:

$$\overline{\sigma\varphi_{0(470)}} = \sigma_{470} * \varphi_{0(470)}$$

4.2.1.9 Erosion Rates

The surface conditions of the sampled erratics indicate processes of both gradual and abrupt erosion, including surface fractures, rock splays, and smoothed exposed surface edges (Figures 4.2-4.4, Appendix A22). The environmental setting of the Foothills Erratics train is at the foothills of the Canadian Rockies, a region which host climatic events that would contribute to

significant erosive processes. For instance, the Chinook Winds are a weather event in the foothills of the Canadian Rockies, which regularly impact the erratics with winds as high as 60-120 kilometers per hour (Bullock et al. 1992). Further, the regular precipitation and freezing temperatures in the region can promote erosion from ice wedging, which may explain why certain rock features exhibit splayed forms, such as with Erratic 8 (Appendix A22). Other more gradual effects of erosion are observed in the form of granular weathering in Erratic 6, given the quartzite erratic exhibits coarse grained mineralogy (Appendix A22). More gradual physical weathering in Erratics 3 and 8 due to the higher degree of cementation observed from these erratics (Appendix A22).

The interpretation of ^{10}Be dates From Margold et al. (2019) argue that erosion is negligible for the site, however, supporting the age results which do not account for erosion. Also, the study does not consider snow coverage to be a significant parameter, given the dry continental conditions associated with the region.

Considering that only the first few centimeters of rock sample is measured for dating, is fair to consider if significant processes of erosion could have removed portions or entire sections of the original natural exposed depth profile that would quantify erratic placement. Estimates for rock surface erosion of the erratics can be estimated with the available ^{10}Be data from Margold et al. (2019), using prior assumptions on established ages for glacial retreat, as well as using proxy dates from other chronometers. These results will be used to interpret the evolution of depth profile forms and calculated ages of the erratic surfaces.

4.2.2 Results

4.2.2.1 Individual core parameterizations

The scanned images acquired from cores from Erratic 3 are shown in Figure 10, from Erratic 6 in figure 11, and from Erratic 8 in Figure 4.12. Each sample displays variations of OSL anomalies (2500+ counts), producing scattered peaks of OSL in the extrapolated depth profiles (Figures 4.13-4.18).

The plotted depth profiles of each controlled exposed sample from Erratic 3 are presented in Figure 4.13, Erratic 6 in Figure 4.14, and Erratic 8 in Figure 4.15. The parameter likelihood plots for Erratic 3 are presented in Appendix A1, for Erratic 6 in Appendix A2, and for Erratic 8 in Appendix A3.

For every sample, the OSL anomalies present in the scan data are clearly represented as luminescence values seen in the depth profile. Given their exposure times were ~7E+05 seconds longer, Top samples generally show deeper OSL bleaching than their Bottom counterpart (Figure 4.10-4.12). An exception to this trend is seen in samples from core 3-8, which shows an opposite trend where the Bottom sample has produced a slightly deeper bleaching front than the Top sample (Figure 4.10; 4.13).

The parameterizations of samples from Erratic 3, 6, and 8 are presented in Table 4.2. For Erratic 3, Top sample portions show lower light attenuation values than their Bottom sample counterparts. Fitted median attenuation coefficients from Erratic 3 Top samples are 0.108 mm^{-1} (0.019 -1σ, 0.038 +1σ) for 3-8 Top, 0.463 mm^{-1} (0.186 -1σ, 0.326 +1σ) for sample 3-6 Top, and 0.103 mm^{-1} (0.023 -1σ, 0.023 +1σ) for sample 3-5 Top. Bottom samples from Erratic 3 show attenuation parameter fits of 0.534 mm^{-1} (0.238 -1σ, 0.285 +1σ) for sample 3-8 Bottom, 1.41 mm

$^{-1}$ (0.448 -1σ, 0.448 +1σ) for sample 3-6 Bottom, and 0.388 mm^{-1} (0.196 -1σ, 0.342 -1σ) for sample 3-5 Bottom.

Similarly, for sample 3-5 Top, parameter $\overline{\sigma\varphi_0}$ fits are smaller in value to their Bottom counterpart samples, in this case by a magnitude. The fitted median value of $\overline{\sigma\varphi_0}$ for 3-5 Top was 2.37E-06 s^{-1} (8.08E-07 -1σ, 1.23E-06 +1σ), and for 3-5 Bottom the value was 1.01E-05 s^{-1} (8.13E-06 -1σ, 7.80E-05 +1σ). Core 3-6 follows a similar trend but hosts more inequivalent $\overline{\sigma\varphi_0}$ parameterizations; its Top sample fits a $\overline{\sigma\varphi_0}$ value of 2.25E-04 s^{-1} (2.18E-04 -1σ, 1.76E-02 +1σ), and its Bottom counterpart fits a value of 0.149 s^{-1} (0.147 -1σ, 11.2 +1σ). For core 3-8, this trend is not as apparent, where the fitted median value of $\overline{\sigma\varphi_0}$ for 3-8 Top was 1.22E-06 s^{-1} (2.33E-07 -1σ, 6.45E-07 +1σ), and the fit for 3-8 Bottom produced a value of 8.27E-05 s^{-1} (6.98E-05 -1σ, 8.43E-03 +1σ).

The parameterizations for Erratic 8 produce more equivalent $\overline{\sigma\varphi_0}$ values between Top and Bottom samples. Sample 8-2 Top produces a fitted median value of 1.54E-04 s^{-1} (1.19E-04 -1σ, 5.88E-03 +1σ) and 8-2 Bottom produces a value of 1.15E-04 s^{-1} (9.14E-04 -1σ, 8.25E-04 +1σ). Sample 8-4 Top produces a value of 5.67E-06 s^{-1} (2.81E-06 -1σ, 5.58E-06 +1σ), while 8-4 Bottom produces a value of 2.53E-06 s^{-1} (4.06E-07 -1σ, 1.06E-06 +1σ).

Like with the Top vs Bottom attenuation trends seen in Erratic 3, the fitted attenuation values for sample 8-2 Top (0.429 mm^{-1}; 0.127 -1σ, 0.254 +1σ) is also lower than the attenuation value fitted from 8-2 Bottom (0.610 mm^{-1}; 0.245 -1σ, 0.163 +1σ). However, this trend is not measured from samples of core 8-4, where the Top sample attenuation fit is 0.173 mm^{-1} (0.037 -1σ, 0.037 +1σ), and the Bottom sample attenuation fit is 0.107 mm^{-1} (0.011 -1σ, 0.033 +1σ).

Figure 4.8

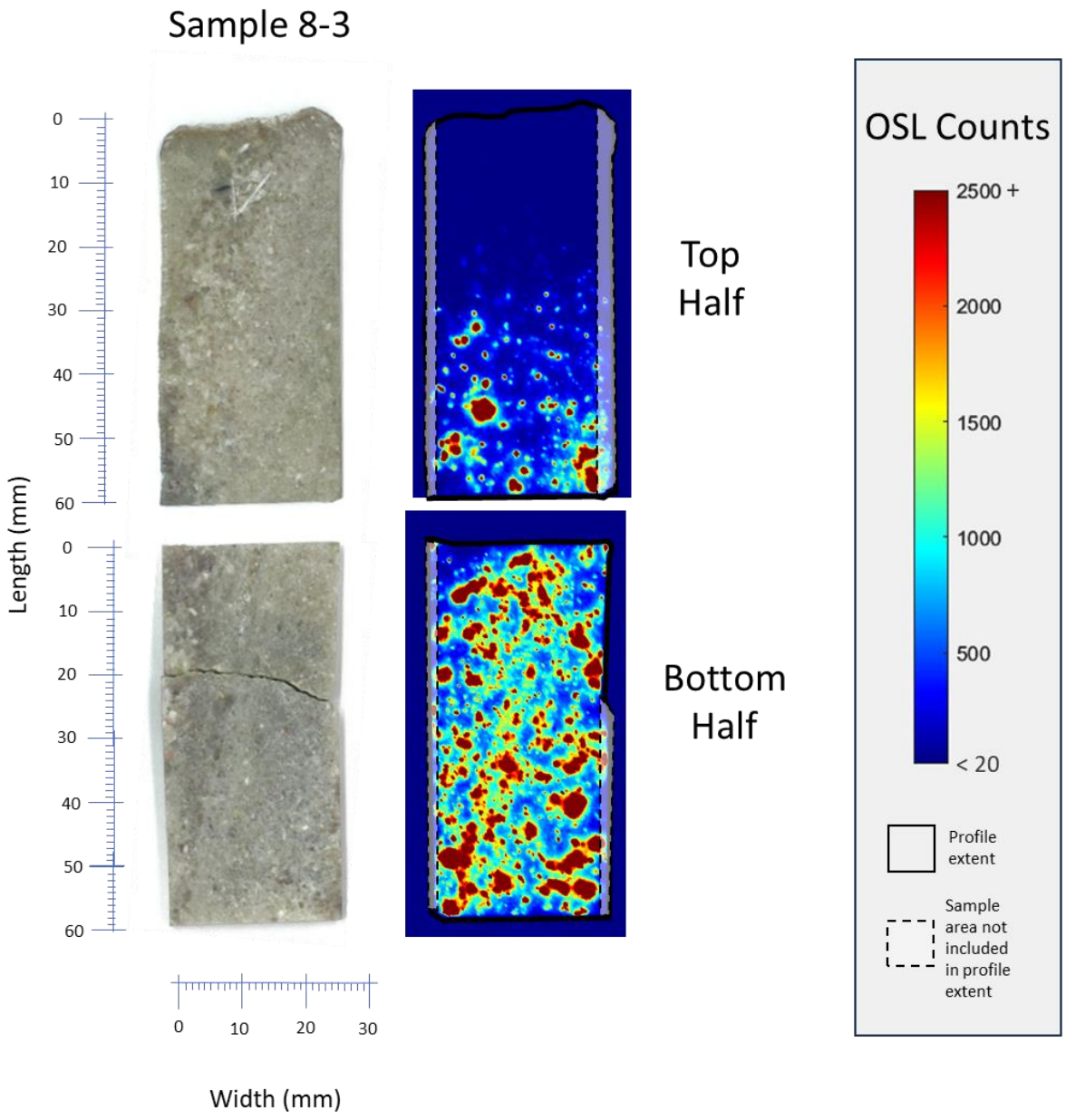

Spatially resolved OSL map of sample 8-3.

Figure 4.9

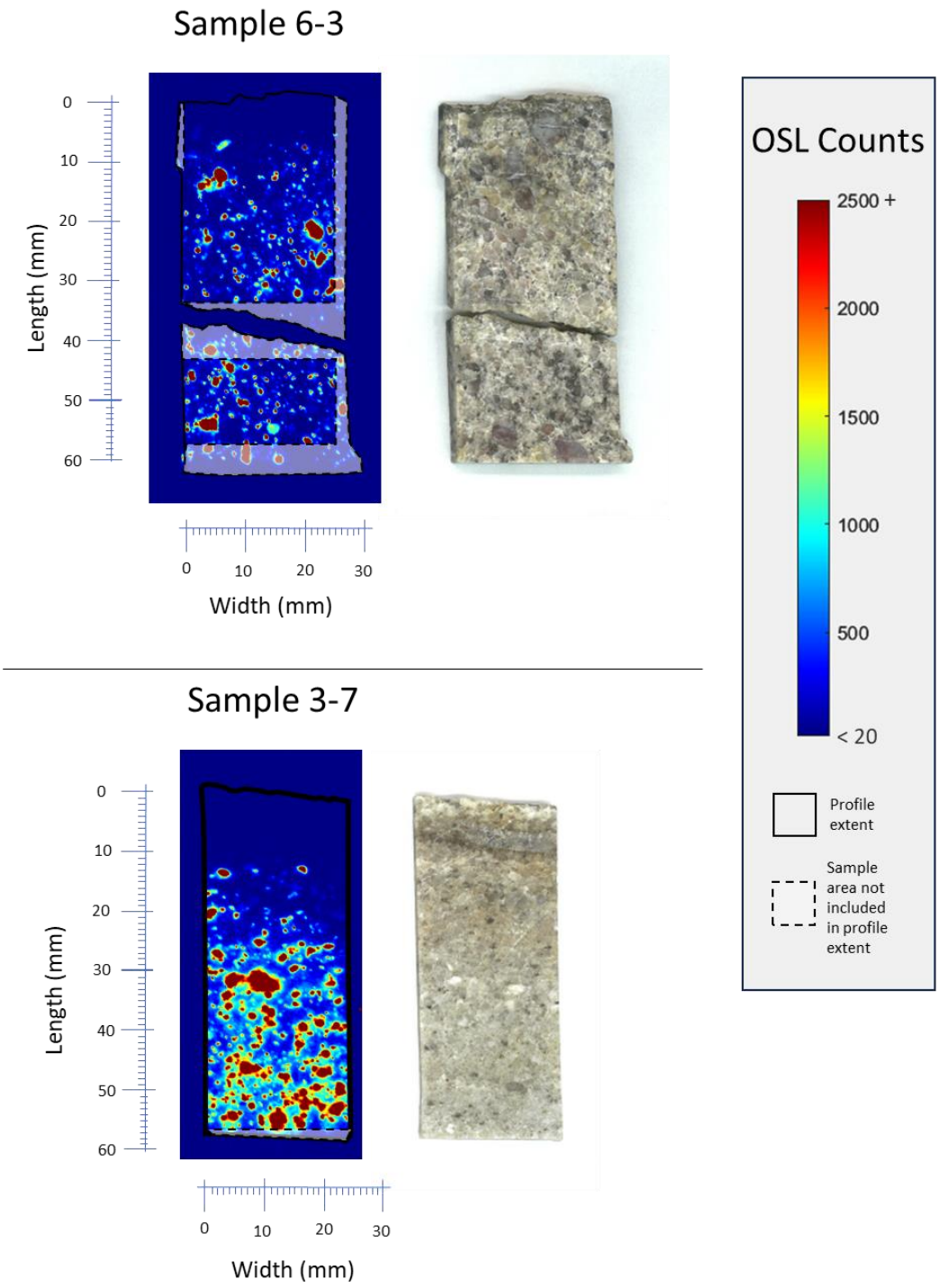

Spatially resolved OSL maps of Natural exposed samples 6-3, and 3-7.

Table 4.2
Parameter fits of individual cores, controlled exposed.

Sample	Parameter Median (Best fit; -1σ infimum, +1σ supremum)

Erratic 3	
3-5 Top	μ = 0.103 mm^{-1} (0.907; 0.023, 0.023) $\overline{\sigma\varphi_0}$ = 2.37E-06 s^{-1} (2.87E-06; 8.08E-07, 1.23e-06)
3-5 Bottom	μ = 0.388 mm^{-1} (0.265; 0.196, 0.342) $\overline{\sigma\varphi_0}$ = 1.01E-05 s^{-1} (3.39E-06; 8.13E-06, 7.80E-05)
3-6 Top	μ = 0.463 mm^{-1} (0.190; 0.186, 0.326) $\overline{\sigma\varphi_0}$ = 2.25E-04 s^{-1} (3.89E-06; 2.18E-04, 1.76E-02)
3-6 Bottom	μ = 1.41 mm^{-1} (1.07; 0.448, 0.448) $\overline{\sigma\varphi_0}$ = 0.149 s^{-1} (7.26E-03; 0.147, 11.2)
3-8 Top	μ = 0.108 mm^{-1} (0.098; 0.019, 0.038) $\overline{\sigma\varphi_0}$ = 1.22E-06 s^{-1} (1.10E-06; 2.33E-07, 6.45E-07)
3-8 Bottom	μ = 0.534 mm^{-1} (0.263; 0.238, 0.285) $\overline{\sigma\varphi_0}$ = 8.27E-05 s^{-1} (5.95E-06; 6.98E-05, 8.43E-03)
Top (cumulative)	μ = 0.130 mm^{-1} (0.119; 0.042, 0.042) $\overline{\sigma\varphi_0}$ = 2.39E-06 s^{-1} (1.99E-06; 1.16E-06, 2.27E-06)
Bottom (cumulative)	μ = 0.509 mm^{-1} (0.334; 0.170, 0.256) $\overline{\sigma\varphi_0}$ = 2.57E-05 s^{-1} (7.19E-06; 2.02E-05, 3.11E-04)
Erratic 6	
6-1 Top	μ = 0.035 mm^{-1} (0.007; 0, 0.345) $\overline{\sigma\varphi_0}$ = 9.91E-07 s^{-1} (4.23E-07; 7.3E-07, 7.72E-04)
6-2 Top	μ = 0.09 mm^{-1} (0.98; 0, 0.045) $\overline{\sigma\varphi_0}$ = 9.28E-07 s^{-1} (8.31E-07; 3.02E-07, 2.28-07)
6-4 Top	μ = 1.58 mm^{-1} (0.678; 0.046, 0.046) $\overline{\sigma\varphi_0}$ = 6.42E-04 s^{-1} (9.10E-06; 6.21E-04, 5.21E-03)
6-1 Bottom	μ = 1.35 mm^{-1} (0.599; 0.599, 0.399) $\overline{\sigma\varphi_0}$ = 1.55E-04 s^{-1} (5.10E-06; 1.45E-04, 9.56E-03)
6-2 Bottom	μ = 0.0871 mm^{-1} (0.077; 0.0299, 0.0299) $\overline{\sigma\varphi_0}$ = 1.71E-06 s^{-1} (1.27E-06; 6.94E-07, 1.17E-06)
6-4 Bottom	μ = 0.076 mm^{-1} (0.052; 0.0499, 0.499) $\overline{\sigma\varphi_0}$ = 9.51E-07 s^{-1} (6.05E-07; 5.06E-07, 3.4E-06)
Top (Cumulative)	μ = 0.177 mm^{-1} (0.101; 0.099, 0.199) $\overline{\sigma\varphi_0}$ = 1.44E-06 s^{-1} (7.96E-07; 6.18E-07, 1.08E-06)
Bottom (Cumulative)	μ = 0.15 mm^{-1} (0.102 ; 0.049, 0.291) $\overline{\sigma\varphi_0}$ = 1.16E-06 s^{-1} (1.03E-06; 3.50E-07, 2.25E-06)
Erratic 8	
8-2 Top	μ = 0.429 mm^{-1} (0.273; 0.127, 0.254) $\overline{\sigma\varphi_0}$ = 1.54E-04 s^{-1} (1.42E-05; 1.19E-04, 5.88E-03)
8-2 Bottom	μ = 0.610 mm^{-1} (0.504; 0.245, 0.163) $\overline{\sigma\varphi_0}$ = 1.15E-04 s^{-1} (4.66E-05; 9.14E-05, 8.25E-04)
8-4 Top	μ = 0.173 mm^{-1} (0.156; 0.037, 0.037) $\overline{\sigma\varphi_0}$ = 5.67E-06 s^{-1} (3.99E-06; 2.81E-06, 5.58E-06)
8-4 Bottom	μ = 0.107 mm^{-1} (0.113; 0.011, 0.033)

	$\overline{\sigma\varphi_0}$ = 2.53E-06 s^{-1} (2.70E-06; 4.06E-07, 1.06E-06)
Top (cumulative)	μ = 0.238 mm^{-1} (0.206; 0.037, 0.037) $\overline{\sigma\varphi_0}$ = 1.19E-05 s^{-1} (6.47E-06; 5.26E-06, 9.43E-06)
Bottom (Cumulative)	μ = 0.25 mm^{-1} (0.223; 0.045, 0.133) $\overline{\sigma\varphi_0}$ = 7.22E-06 s^{-1} (5.60E-06; 3.01E-06, 1.4E-05)

For Erratic 6, most controlled exposed samples produced very shallow bleaching fronts of less than 2-3 millimeters, with abrupt, highly varied OSL saturation plateaus, making it difficult to fit parameters to the depth profiles using the first order exposure dating model (Figure 4.11, 4.14). The controlled exposures were likely not long enough for the samples to produce viable depth profiles for precise parameter extrapolation. The cause for this issue is interpreted to be from the dark composition of the samples, which prevented light from effectively bleaching into the subsurface.

Most fits from Erratic 6 cores offer high uncertainty or unrealistic parameterizations. Core 6-1 Top, for instance, hosts a bleaching front of about 1 millimeter, yet fits a near zero μ parameterization of 0.035 mm^{-1} with a wide range of uncertainty (0 -1σ, 0.345 +1σ). The $\overline{\sigma\varphi_0}$ fit for the sample is 9.91E-07 s^{-1}, also with a wide uncertainty (7.3E-07 -1σ, 7.72e-04 +1σ). Core 6-2 Top features a similar trend of a μ fit of 0.090 mm^{-1} (0 -1σ, .040 +1σ), and a $\overline{\sigma\varphi_0}$ fit of 9.28E-07 s^{-1} (2.28E-07 -1σ, 3.02E-07 +1σ). Core 6-4 Top produced higher parameterization values, with a fit of 1.58 mm^{-1} for μ (0.046 -1σ, 0.046 +1σ) and a fit of 6.42E-04 s^{-1} for $\overline{\sigma\varphi_0}$ (6.21E-04 -1σ, 5.21E-03 +1σ).

Bottom samples also show low attenuation parameterizations, even though bleaching fronts are observed to be abrupt in the sample. Core 6-2 Bottom has a μ fit of 0.0871 mm^{-1} (0.030 -1σ, 0.030 +1σ) and a $\overline{\sigma\varphi_0}$ value of 1.71E-06 s^{-1} (6.94E-7 -1σ, 1.17e-6 +1σ). For 6-4 Bottom, μ was

fitted as 0.076 (0.0499 -1σ, 0.449 +1σ) 9.51E-07 s^{-1} (5.06E-07 -1σ, 3.4E-06 +1σ). Conversely, Core 6-1 Bottom has a more realistic μ fit of 1.35 mm^{-1} (0.599 -1σ, 0.399 +1σ) and a $\overline{\sigma\varphi_0}$ value of 1.55E-04 s^{-1} (1.45E-4 -1σ, 9.56E-03 +1σ).

4.2.2.2 Cumulative core parameterizations

Table 4.2 offers the parameter fit results of cumulative fits of Top and Bottom samples from Erratics 3 and 8, which are used to calculate ages for the Erratics surfaces. For Erratic 3, depth profile data from Top samples 3-5, 3-6, and 3-8 were fitted to produce a μ fitted value of 0.13 mm^{-1} (0.042 -1σ, 0.042 +σ) and a $\overline{\sigma\varphi_0}$ fitted value of 2.39E-06 s^{-1} (1.16E-06 -1σ, 2.27E-06 +1σ). Bottom samples 3-5, 3-6, and 3-8 were fitted to produce a higher μ value of 0.509 mm^{-1} (0.170 -1σ, 0.256 +1σ) and a higher $\overline{\sigma\varphi_0}$ value of 2.57E-05 s^{-1} (2.02E-05 -1σ, 3.11E-04 +1σ).

Fitting Top samples 8-2 and 8-4 from Erratic 8 offers a μ value of 0.238 mm^{-1} (0.037 -1σ, 0.037 +1σ), and a $\overline{\sigma\varphi_0}$ value of 1.19E-05 (5.26E-06 -1σ, 9.43E-06 +1σ). A similar μ value of 0.25 mm^{-1} (0.045 -1σ, 0.133+1σ) was fitted to Bottom samples 8-2 and 8-4, yet the fit produced a lower $\overline{\sigma\varphi_0}$ value of 7.22E-06 s^{-1} (3.01E-06 -1σ, 1.4E-05 +1σ).

For Erratic 6, Top and Bottom samples were also cumulatively fitted, producing similar parameterizations to each other. Fitting combined data from the Top samples of 6-1, 6-2, and 6-4 produced a μ value of 0.177 mm^{-1} (0.099 -1σ, 0.199 +1σ) and a $\overline{\sigma\varphi_0}$ value of 1.44E-06 s^{-1} (6.18e-07 -1σ, 1.08e-06 +1σ). For Bottom samples, a value of 0.15 mm^{-1} (0.049 -1σ, 0.291 +1σ) for μ, and a value of 1.16E-06 s^{-1} (3.5E-07 -1σ, 2.25E-6 +1σ) for $\overline{\sigma\varphi_0}$.

Figure 4.10

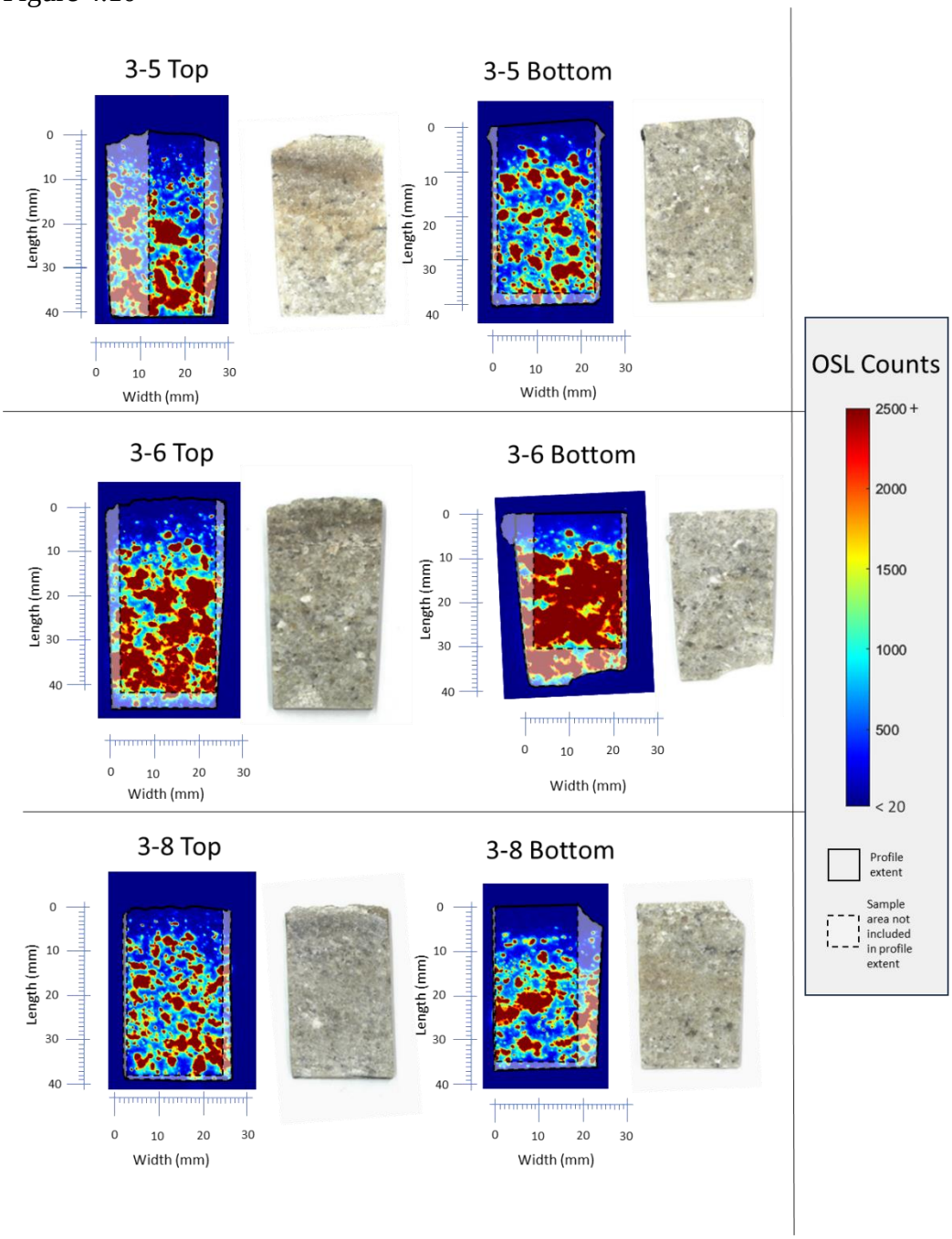

Spatially resolved OSL maps of controlled exposed samples from Erratic 3 (3-5 Top, 3-5 Bottom; 3-6 Top, 3-6 Bottom; 3-8 Top, 3-8 Bottom).

Figure 4.11

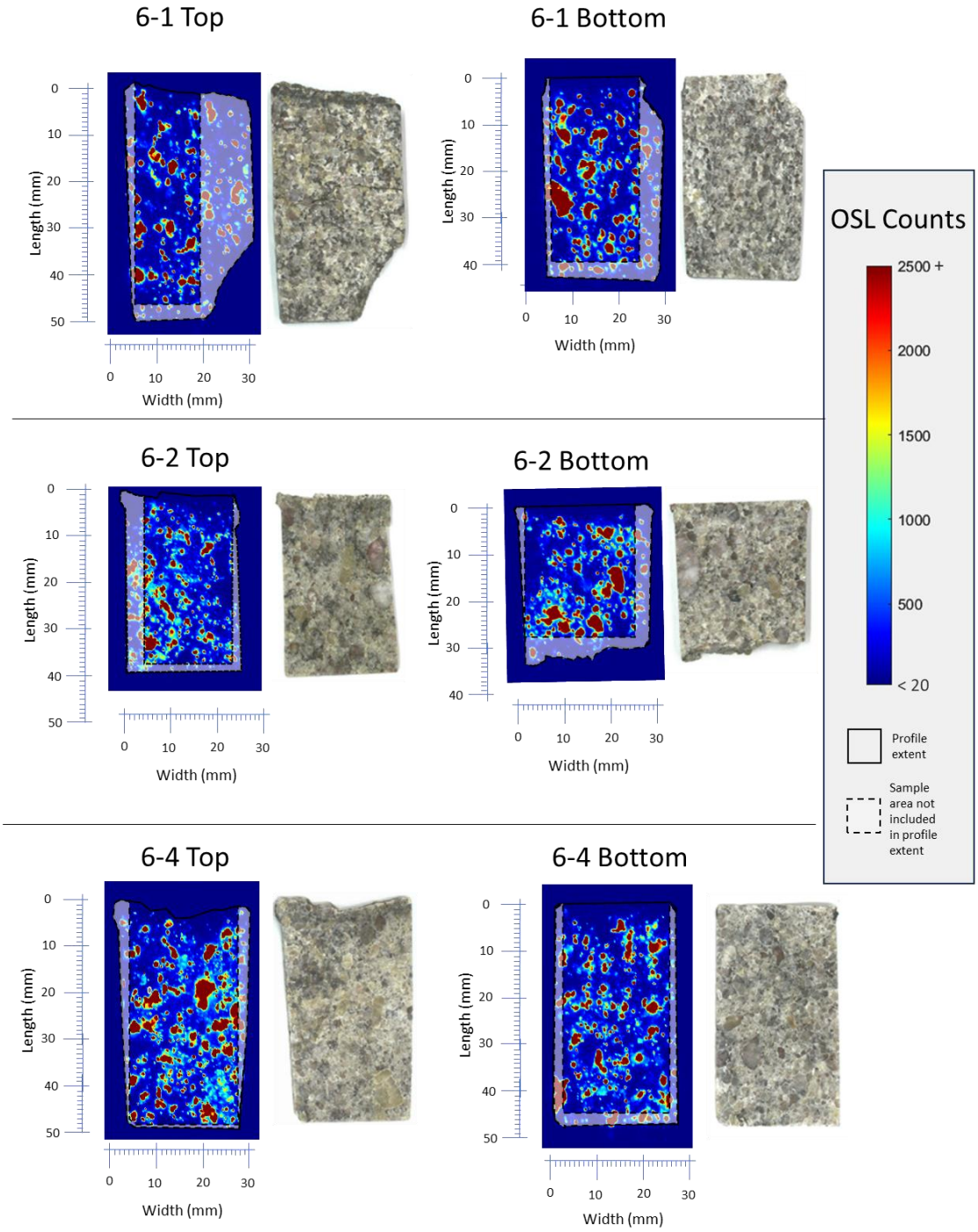

Spatially resolved OSL maps of controlled exposed samples from Erratic 3 (6-1 Top, 6-1 Bottom; 6-2 Top, 6-2 Bottom; 6-4 Top, 6-4 Bottom).

Figure 4.12

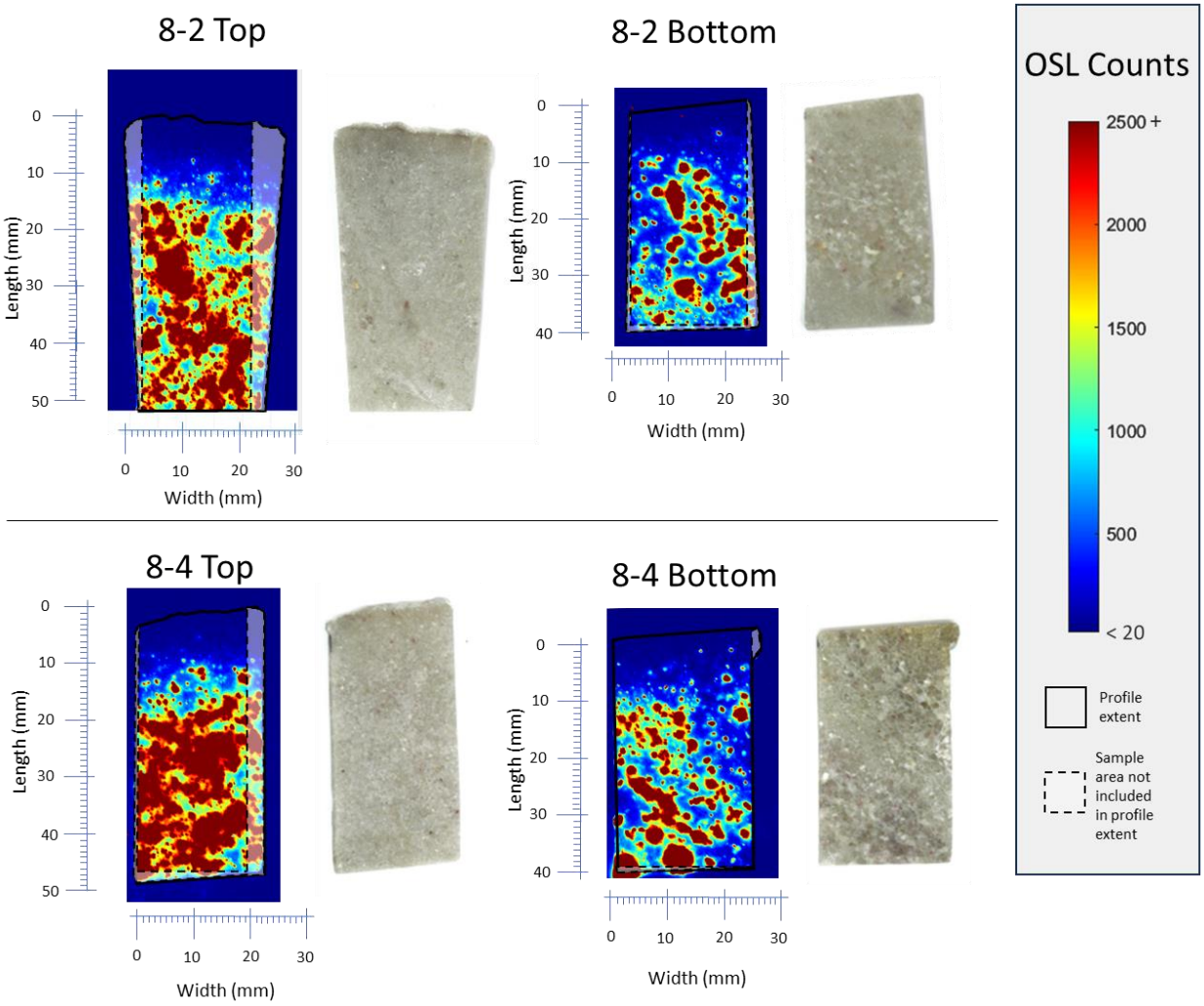

Spatially resolved OSL maps of controlled exposed samples from Erratic 3 (8-2 Top, 8-2 Bottom; 8-4 Top, 8-4 Bottom).

4.2.2.3 Parameter and age calculations using ^{10}Be Data

The parameter results for $\overline{\sigma\varphi_0}$ and μ are presented in Table 4.5, and parameter plots are in Figures 4.19-4.21. Likelihood plots for each Erratic are in Appendix A5. The results show very low $\overline{\sigma\varphi_0}$ values for the cores, with sample 3-7 producing a fitted value of 2.45E-11 s^{-1} (1.01E-11 -1σ, 3.89E-12 +1σ), 6-3 producing a value of 2.14E-10 s^{-1} (5.51E-08 -1σ, 2.01E-10 +1σ), and 8-3 a value of 5.19E-11 s^{-1} (1.48E-11 -1σ, 6.19E-11 +1σ). This counters the fitted values for $\overline{\sigma\varphi_0}$ from controlled exposures, with parameter ranges for Erratic 3 controlled exposed samples within 2.37E-06 – 0.149, for Erratic 6 within 9.91e-07 - 1.55E-04, and for Erratic 8 within 1.15E-04 - 5.67e-06. Fitted values for μ are generally low also, with values of 0.103 mm^{-1} (0.014 -1σ, 0.021 +1σ) for 3-7, 0.281 mm^{-1} (0.496 -1σ, 0.198 +1σ) for 6-3, and 0.084 mm^{-1} (0.014 -1σ, 0.008 +1σ) for 8-3. These values are similar to lower parameter bounds for the controlled exposed cores, which range from 0.103 – 1.41 mm^{-1} for Erratic 3, 0.035 – 1.58 mm^{-1} for Erratic 6, and 0.173 – 0.617 mm^{-1} for Erratic 8. These results show that controlled exposed samples promote much higher values for $\overline{\sigma\varphi_0}$ for the rock than what should be observed for the decamillennial exposed samples. Further, attenuation values appear to have low end fit values, which could be retrievable with controlled exposure results.

4.2.2.4 Natural Exposed Cores, Age Calculations from Cumulative Parameters

Erratics 3, 6, and 8 were age fitted from applying Top and Bottom cumulative parameterizations to the natural exposed sampled depth profiles of each erratic, which for Erratic 3 was sample 3-7, for Erratic 6 was sample 6-3, and for Erratic 8 sample 8-3 (Figure 4.19-4.21). OSL scans for each of these samples are presented in Figures 4.8 and 4.9. Of the observed scans, the depth profiles and sample 8-3 and 6-3 incorporate two sample pieces. For sample 8-3, the sample needed to be cut in half in order to produce longitudinal slices of the core material using the

precision saw. As such, approximately 2 millimeters of depth was cut between the Top and Bottom samples, which is factored into the depth profile form for the sample. Sample 6-3 was brittle, and broke in half during sample preparation.

With the use of parameters for μ and $\overline{\sigma\varphi_0}$ gathered from the cumulative fits of controlled exposed cores, age calculations for the erratic surfaces were performed, listed in Table 4.3. The calculated ages were all at or less than centennial age, lower than the expected millennial-decamillennial exposure times. Age fit distributions are presented in Appendices A9-A11. Given the poor results, in Table 4.4, no ages from cumulative parameter fits were doubled for reference to roughly account for estimated equivalent exposure ages.

For Erratic 8, sample 8-3 was fitted to an age of 31.5 years (13.2 -1σ, 4.4 +1σ) using Top sample parameter fits (μ = 0.238 mm^{-1}; $\overline{\sigma\varphi_0}$ = 1.19E-05 s^{-1}). Using Bottom parameter fits (μ = 0.25 mm^{-1}; $\overline{\sigma\varphi_0}$ = 7.22E-06 s^{-1}), an age of 86.8 years (45.3 -1σ, 22.6 +1σ) is produced for the depth profile. For Erratic 3, sample 3-7 was fitted to an age of 0.349 years (0.069 -1σ, 0.046 +1σ) using Top Parameter fits (μ = 0.130 mm^{-1}; $\overline{\sigma\varphi_0}$ = 2.39E-06 s^{-1}) for the erratic. Bottom parameters from Erratic 3 (μ = 0.509 mm^{-1}; $\overline{\sigma\varphi_0}$ = 2.57E-05 s^{-1}), however, produced an age of 343 years (82.4 -1σ, 82.4 +1σ) for sample 3-7. Erratic sample 6-3 shows the lowest age parameterizations for both Top and Bottom parameters, with Top parameters producing an age of 0.377 years (0.239 -1σ, 0.239 +1σ), and Bottom parameters producing an age of 0.317 years (0.08 -1σ, 0.16 +1σ).

Figure 4.13

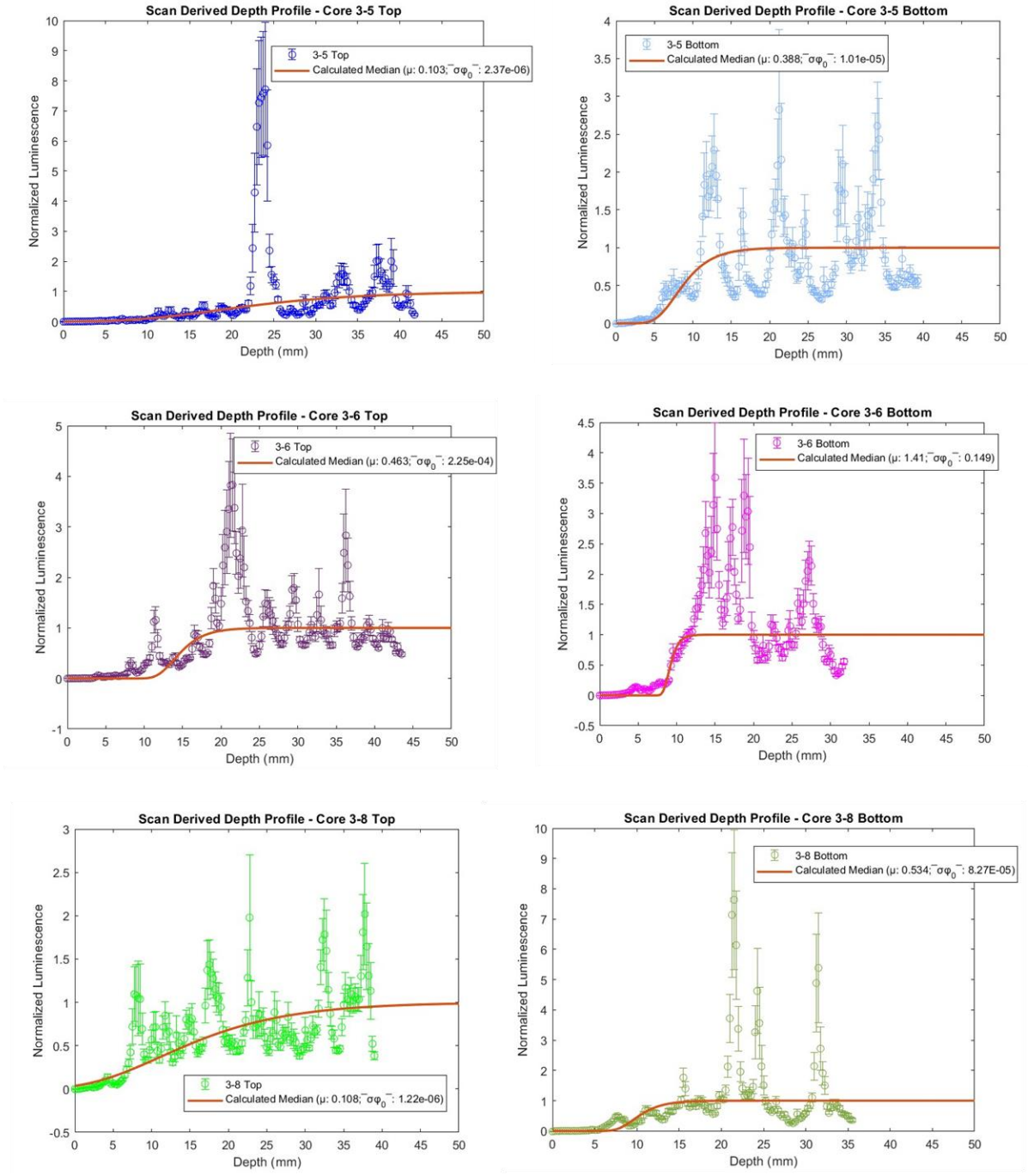

OSL depth profile fits of controlled exposed samples from Erratic 3 (3-5 Top, 3-5 Bottom; 3-6 Top, 3-6 Bottom; 3-8 Top, 3-8 Bottom).

4.13a – axes equivalent depth profiles

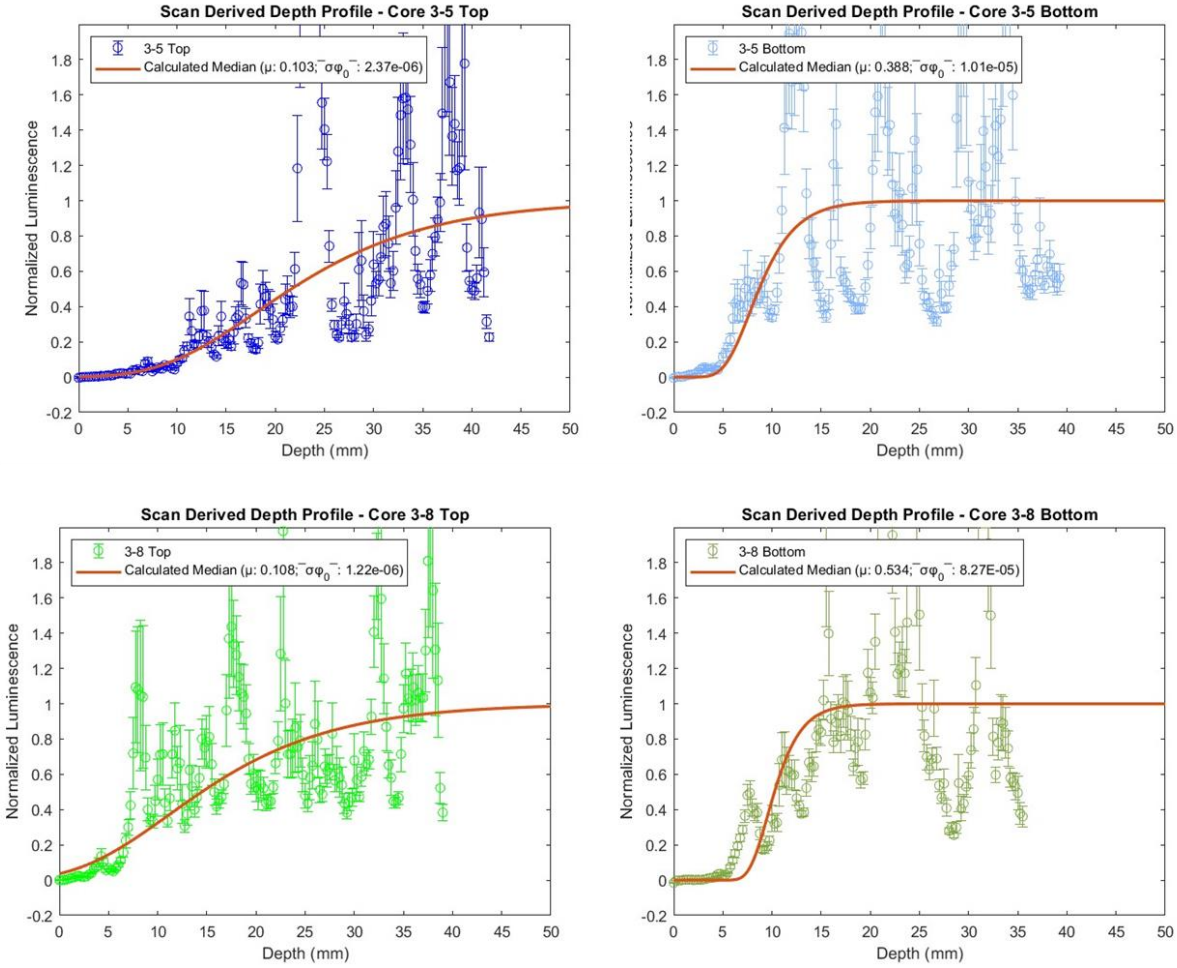

4.13b – first 20 mm

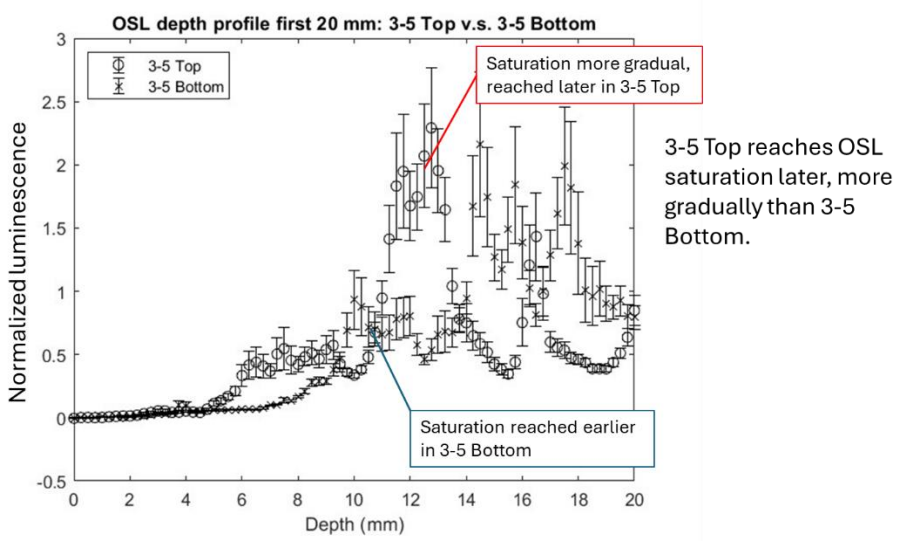

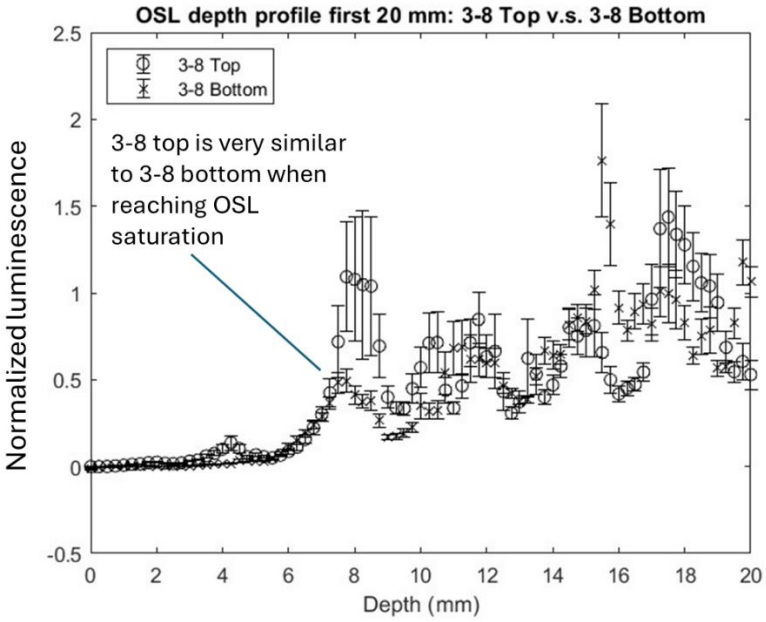

Presented are close-up plots of the first 20 mm of the depth profiles of the cores sampled from the Foothills Erratics Train. We plot these to show potential trends in the gradual evolution of the OSL-depth gradient, and compare depth profile trends to the visual gradient of OSL observed in the scan data. Normalization mitigates observed impacts on the evolution of the depth profile, however trends are still apparent.

Figure 4.14

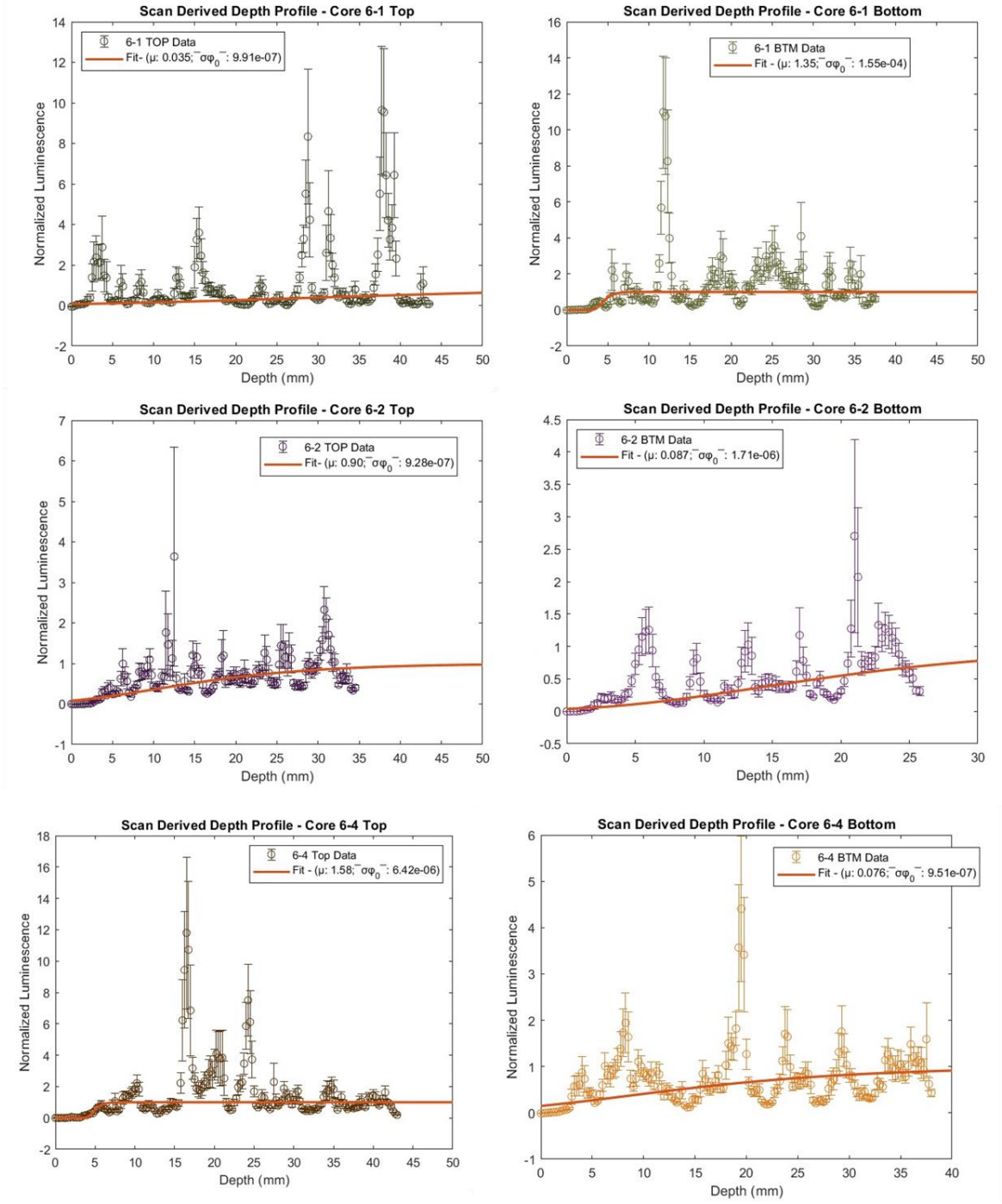

Spatially resolved OSL maps of controlled exposed samples from Erratic 6 (6-1 Top, 6-1 Bottom; 6-2 Top, 6-2 Bottom; 6-4 Top, 6-4 Bottom).

Figure 4.15

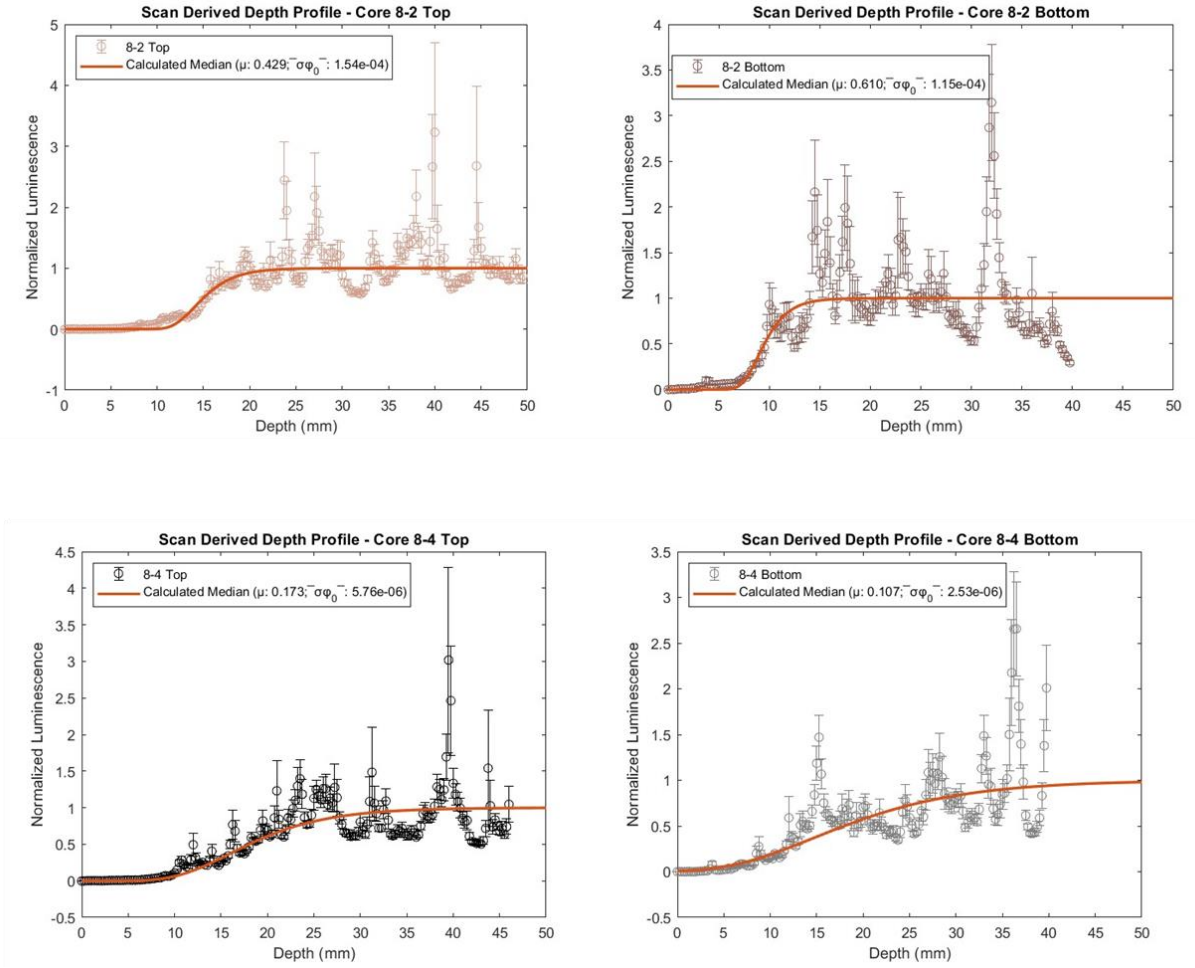

Spatially resolved OSL maps of controlled exposed samples from Erratic 8 (8-2 Top, 8-2 Bottom; 8-4 Top, 8-4 Bottom).

Figure 4.15a – axes equivalent depth profiles

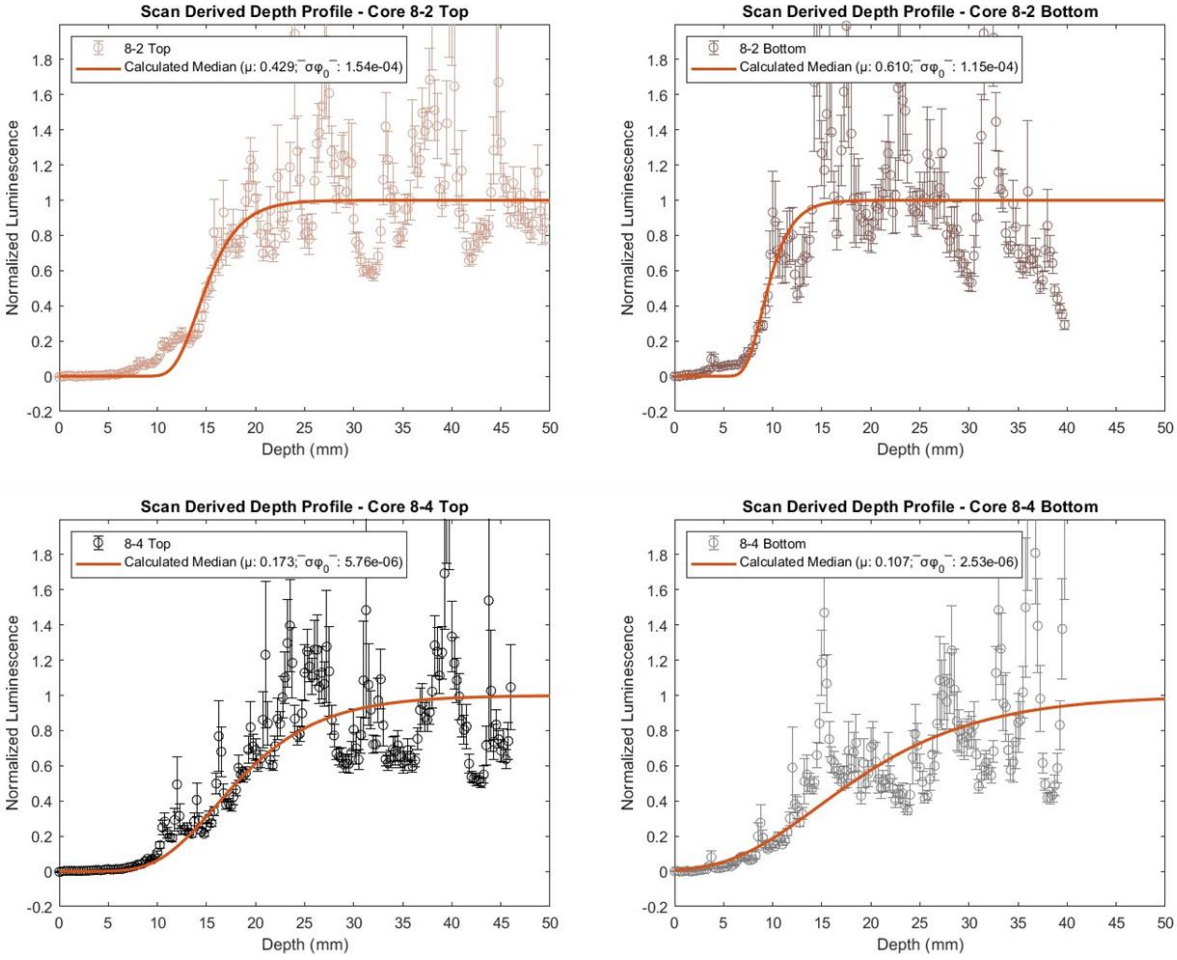

Figure 4.15b

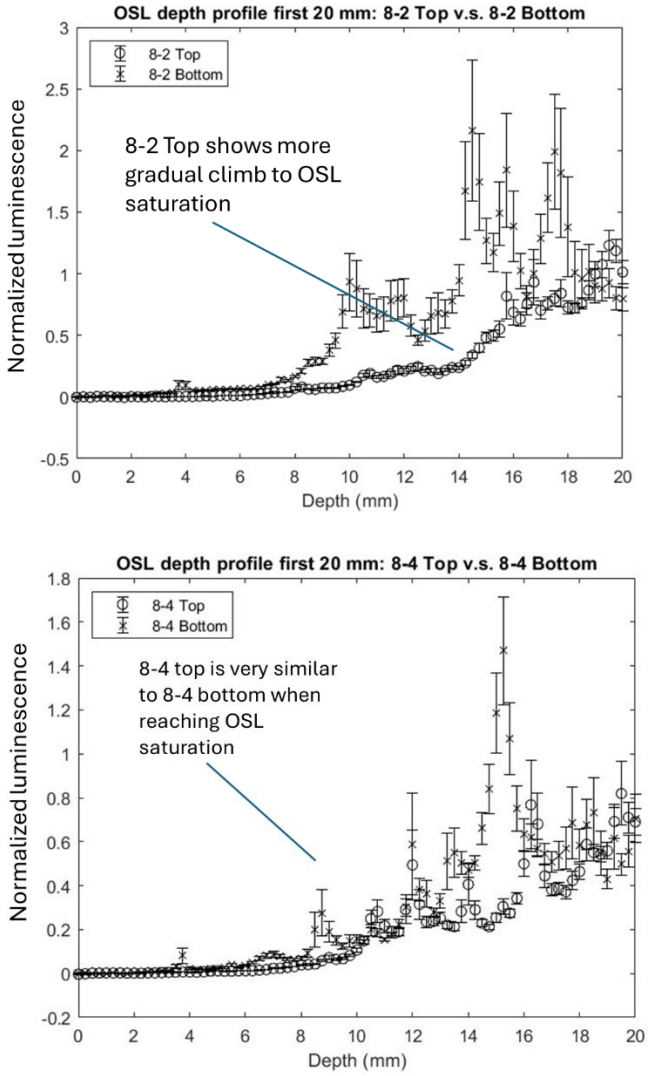

Presented are close-up plots of the first 20 mm of the depth profiles of the cores sampled from the Foothills Erratics Train. We plot these to show potential trends in the gradual evolution of the OSL-depth gradient, and compare depth profile trends to the visual gradient of OSL observed in the scan data. Normalization mitigates observed impacts on the evolution of the depth profile, however trends are still apparent.

Figure 4.16

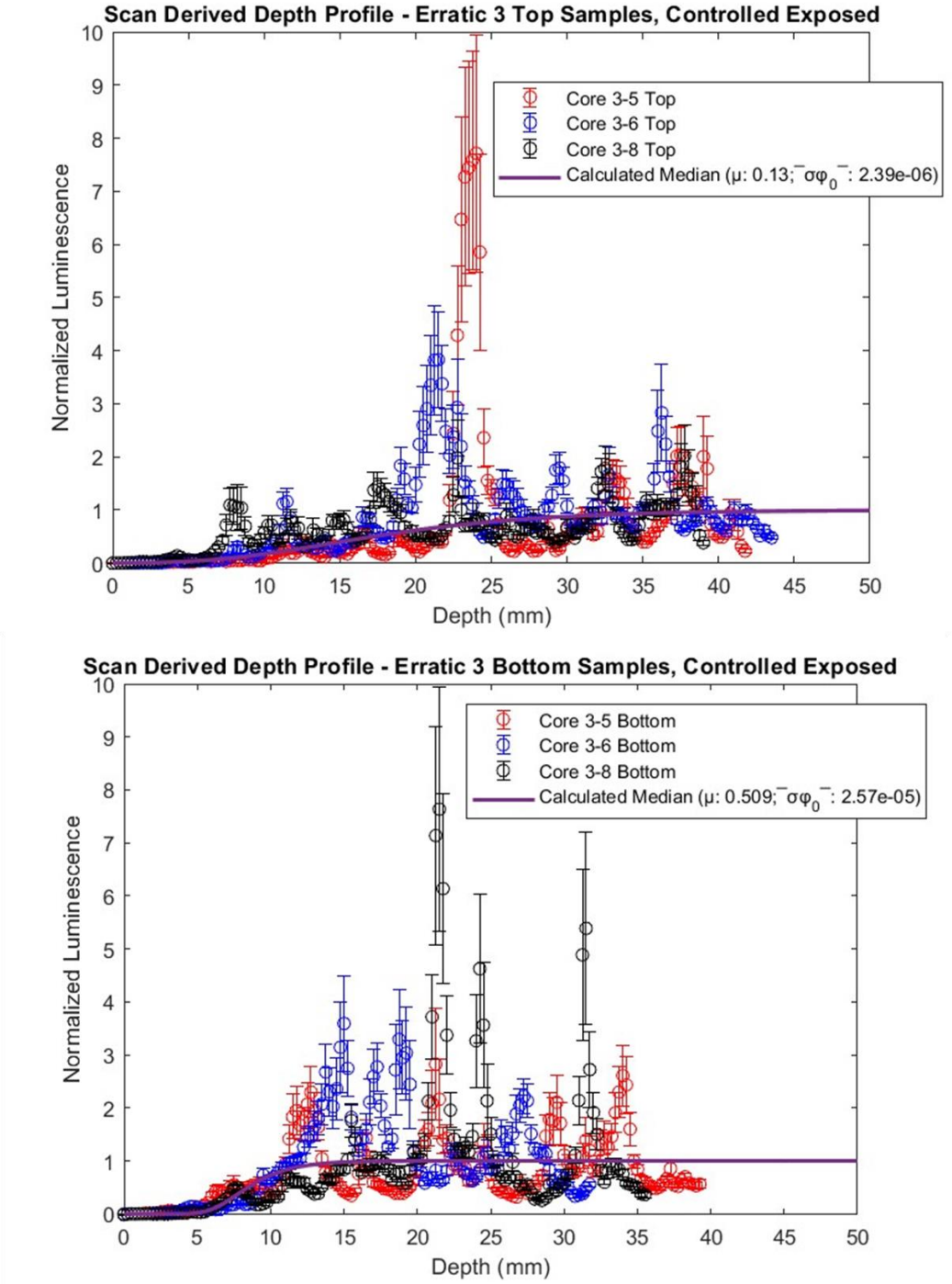

Cumulative parameter fit results of Top and Bottom samples, Erratic 3.

Figure 4.17

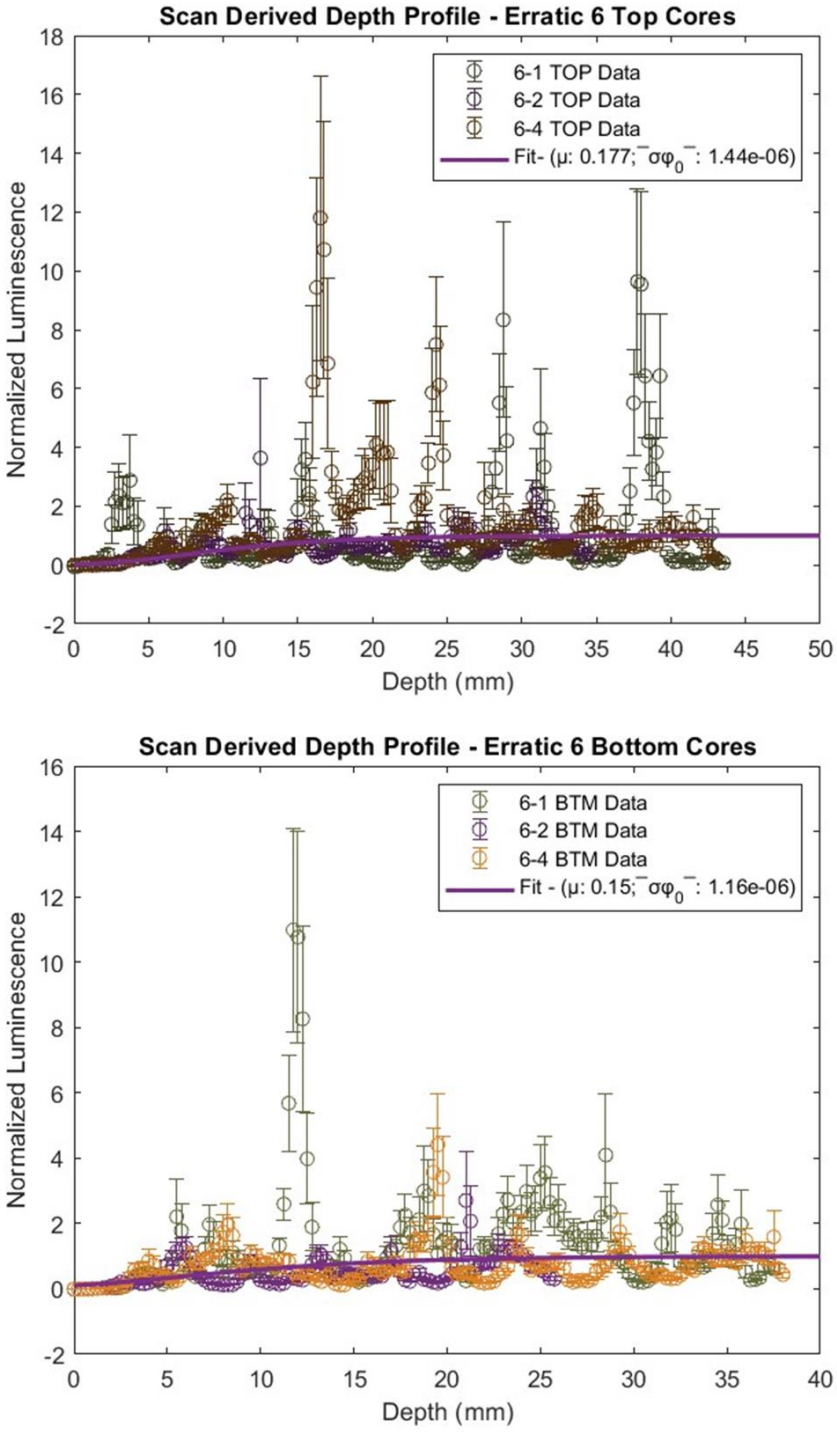

Cumulative parameter fit results of Top and Bottom samples, Erratic 6.

Figure 4.18

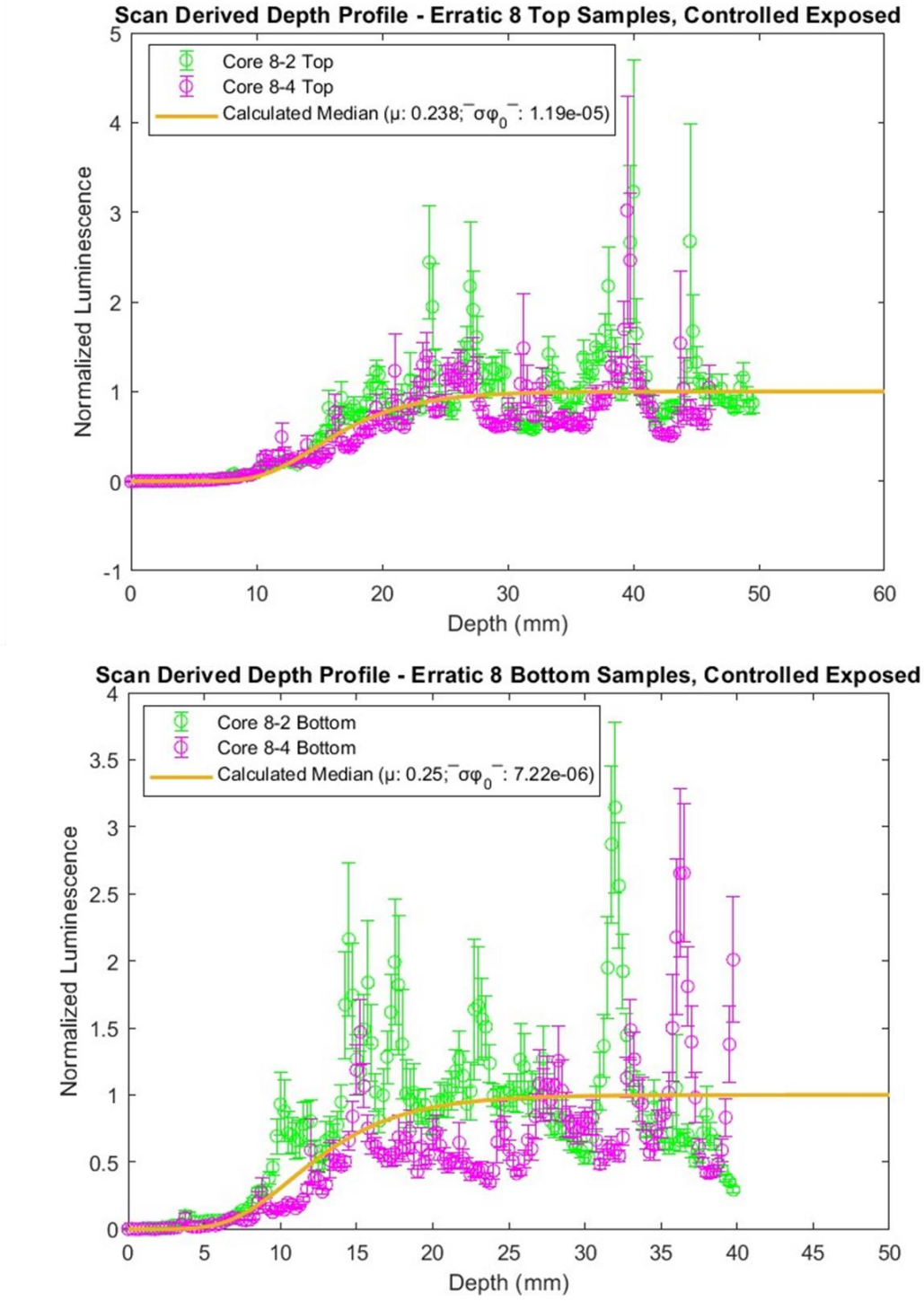

Cumulative parameter fit results of Top and Bottom samples, Erratic 8.

4.2.2.5 Age Calculations from Individual Core Parameters

In response to the low ages produced from cumulative parameterizations, age calculations for each erratic surface from individual core parametrizations were also produced, to determine the possibility whether specific samples may can more closely characterize the natural exposed erratic surface. Age results are presented in Table 4.4. Certain core parameters were not able to fit ages to the depth profile curve, as age distributions were not able to be generated in the fit procedure. Such parameters are designated as 'NaN' in Table 4.4. Age distributions of fits for each core are presented in Appendices A6-A8. For these cores, in Table 4.4, no ages were doubled for reference to roughly account for estimated equivalent exposure ages, apart from core 8-2 Top.

For dating Erratic 3, sample 3-7 was age fitted from the individual parameterizations of each controlled exposed core from Erratic 3. The parameters from 3-5 Top produced an age of 0.164 years (.022 -1σ, .022 +1σ), while 3-5 Bottom produced an age of 36.6 years (9.35 -1σ, 14 +1σ). Only the parameterizations of the Top sample of core 3-6 were able to produce an age for 3-7, which was 9.97 years (2.72 -1σ, 5.45 +1σ). Core 3-8 Top produced an age of 0.342 years (0.046 -1σ, 0.069 +1σ), while core 3-8 Bottom produced an age of 155 years (46.5 -1σ, 93 +1σ).

Dating Erratic 6 was difficult with individual core parameterizations, as most cores did not offer parameters which could viable date Erratic sample 6-3. Only cores 6-1 Top, 6-2 Top, and 6-4 Bottom were able to produce a distribution of ages where a median and uncertainty could be extrapolated (Table 4.2). 6-1 Top producing an age of 0.063 years (0.01 -1σ, 0.013 +1σ), and 6-2 Top producing an age of 0.155 years (0.015 -1σ, 0.045 +1σ) while 6-4 Bottom produced an age of 0.128 years (0.019 -1σ, 0.028 +1σ).

Individual core parameters from Erratic 8 produced a wide range of age metrics like that of Erratic 3. Parameters from core 8-4 Top produced an age of 5.41 years (0.786 -1σ, 1.18 +1σ), while parameters from 8-4 Bottom produced an age of 0.767 years (0.128 -1σ, 0.102 +1σ). 8-2 Top produced the most realistic age for the Erratic surface, producing an age of 4.85E+03 years (1.34E+03 -1σ, 2,24E+03 +1σ), while the parameters for 8-2 Bottom could not produce an age fit for the erratic.

4.2.2.6 Age calculations using ^{10}Be derived proximal parameters

Exposure ages can be calculated for each natural exposed erratic surface using parameters μ and $\overline{\sigma\varphi_0}$ acquired from fitting ^{10}Be ages to erratic surface depth profiles. The age results can be used to evaluate the effectiveness of using proximal rock parameterization techniques to extrapolate millennial-decamillennial ages.

The results of these age calculations are found in Figure 4.22 and are presented in Table 4.3a. For Erratic 3, a median age of 4.84E+03 years (+703/-703) was produced using parameters acquired from sample 8-3, and a median age of 9.26E+04 years (+2.95E+04/-2.21E+04) was produced using parameters from sample 6-3. For Erratic 6, median age of 7.43E+03 years (+1.55E+03/-1.55E+03) was produced using parameters acquired from sample 3-7, and a median age of 2.49E+03 years (+754/-503) was produced using parameters from sample 8-3. For Erratic 8, median age of 4.85E+04 years (+9.61E+03/-6.41E+03) was produced using parameters acquired from sample 3-7, and a median age of 6.61E+06 years (+1.81E+06 /-1.81E+06) was produced using parameters from sample 8-3.

Table 4.3
Age estimations from controlled exposure experiments on natural exposed erratic samples 3-7, 6-3, and 8-3.

Sample	Age (years) using Top parameters Age Median (Best fit; -1σ infimum, +1σ supremum)	Age (years) using Bottom parameters Age Median (Best fit; -1σ infimum, +1σ supremum)
8-3	31.5 (30.3; 13.2, 4.4)	86.8 (78.2; 45.3, 22.6)
3-7	0.349 (0.328; 0.069, 0.032)	343 (300.7; 82.4, 82.4)
6-3	0.377 (0.225; 0.235, 0.235)	0.317 (0.226; 0.17, 0.08)

Table 4.3a
Age estimations from natural exposed erratic samples 3-7, 6-3, and 8-3, using parameters acquired from 10 Be age fits.

Sample	Erratic parameters used: Best Fit Age (Median; +1σ sup, +1σ inf) (years)
3-7	6-3: 9.27E+04 (9.26E+04; 2.95E+04, 2.21E+04) 8-3: 4.79E+03 (4.84E+03; 703, 703)
6-3	3-7: 7.16E+03 (7.43E+03; 1.55E+03, 1.55E+03) 8-3: 2.54E+03 (2.49E+03; 754, 503)
8-3	3-7: 4.82E+04 (4.85E+04; 9.61E+03, 6.41E+03) 6-3: 7.07E+06 (6.61E+06;1.81E+06, 1.81E+06)

Table 4.4
Age calculations from individual core parameterizations on samples 3-7, 6-3, and 8-3.

Erratic 3-7	
Core (Parameters)	Age (years) Age Median (Best fit; -1σ infimum, +1σ supremum)
3-5 Top (μ = 0.103 mm^{-1} ; $\overline{\sigma\varphi_0}$ = 2.37E-06 s^{-1})	0.164 (0.158; 0.022, 0.022)
3-6 Top (μ = 0.463 mm^{-1} ; $\overline{\sigma\varphi_0}$ = 2.25E-04 s^{-1})	9.97 (8.51; 2.72, 5.45)
3-8 Top (μ = 0.108 mm^{-1} ; $\overline{\sigma\varphi_0}$= 1.22E-06 s^{-1})	0.342 (0.342; 0.046, 0.069)
3-5 Bottom (μ = 0.388 mm^{-1} ; $\overline{\sigma\varphi_0}$ = 1.01E-05 s^{-1})	36.6 (31.65; 9.35, 14)
3-6 Bottom (μ = 1.41 mm^{-1} ; $\overline{\sigma\varphi_0}$ = 0.149 s^{-1})	NaN
3-8 Bottom (μ = 0.534 mm^{-1} ; $\overline{\sigma\varphi_0}$= 8.27E-05 s^{-1})	155 (141.36; 46.5, 93)
Erratic 6-3	

Core (Parameters)	Age
6-1 Top (μ = 0.035 mm^{-1} ; $\overline{\sigma\varphi_0}$ = 9.91E-07 s^{-1})	0.063 (0.061; 0.010, 0.013)
6-2 Top (μ = 0.09 mm^{-1} ; $\overline{\sigma\varphi_0}$ = 9.28E-07 s^{-1})	0.155 (0.158; 0.015, 0.045)
6-4 Top (μ = 1.58 mm^{-1} ; $\overline{\sigma\varphi_0}$ = 6.42E-04 s^{-1})	NaN
6-1 Bottom (μ = 1.35 mm^{-1} ; $\overline{\sigma\varphi_0}$ = 1.55E-04 s^{-1})	NaN
6-2 Bottom (μ = 0.087 mm^{-1} ; $\overline{\sigma\varphi_0}$ = 1.71E-06 s^{-1})	NaN
6-4 Bottom (μ = 0.076 mm^{-1} ; $\overline{\sigma\varphi_0}$= 9.51E-07 s^{-1})	0.128 (0.121; 0.019, 0.028)
Erratic 8-3	
Core (Parameters)	Age
8-2 Top (μ = 0.429 mm^{-1} ; $\overline{\sigma\varphi_0}$= 1.54E-04 s^{-1})	4.85E+03 (4.12E+03; 1.34E+03, 2.24E+03) (Equivalent exposure, roughly incorporating nighttime durations: 9.7E+03)
8-4 Top (μ = 0.173 mm^{-1} ; $\overline{\sigma\varphi_0}$= 5.67E-06 s^{-1})	5.41 (5.22; 0.786, 1.18)
8-2 Bottom (μ = 0.610 mm^{-1} ; $\overline{\sigma\varphi_0}$= 1.15E-04 s^{-})	NaN
8-4 Bottom (μ = 0.107 mm^{-1} ; $\overline{\sigma\varphi_0}$ = 2.53E-06 s^{-1})	0.767 (0.722; 0.128, 0.102)

Table 4.5
Natural Exposure Erratics Parameterizations

Sample	10 Be Age (ka)	Parameter Median (Best fit; 1σ sup, 1σ inf)
3-7	14.7	μ = 0.103 mm^{-1} (0.094; 0.014, 0.021) $\overline{\sigma\varphi_0}$ = 2.45E-11 s^{-1} (2.37E-11; 1.01E-11, 3.89E-12)
6-3	8.2	μ = 0.281 mm^{-1} (0.083; 0.496, 0.198) $\overline{\sigma\varphi_0}$ = 2.14E-10 s^{-1} (1.57E-11; 5.51E-08, 2.01E-10)
8-3	15.1	μ = 0.084 mm^{-1} (0.079; 0.014, 0.008) $\overline{\sigma\varphi_0}$ = 5.19E-11 s^{-1} (1.57E-11; 1.48E-11, 6.19E-11)

Figure 4.19

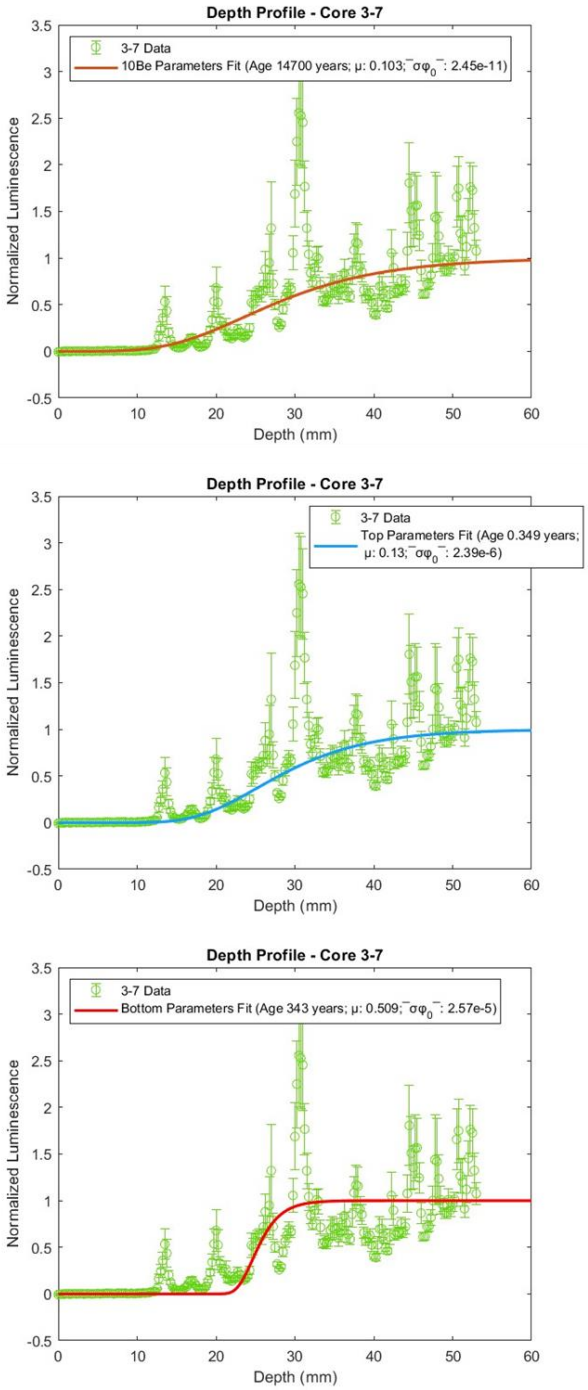

Age fit calculations of ^{10}Be, Top controlled exposed, and Bottom controlled exposed parameters for Erratic 3 (Core 3-7).

Figure 4.20

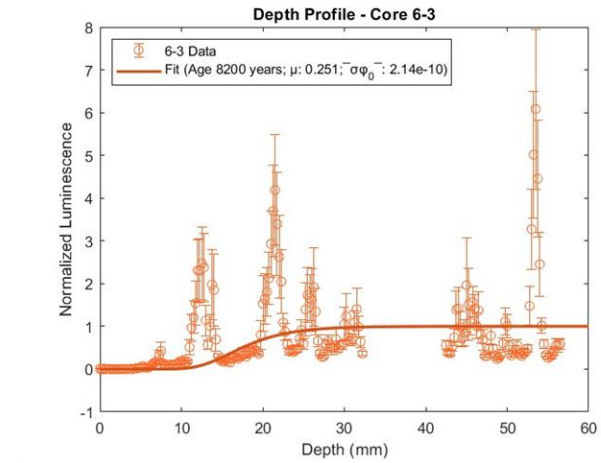

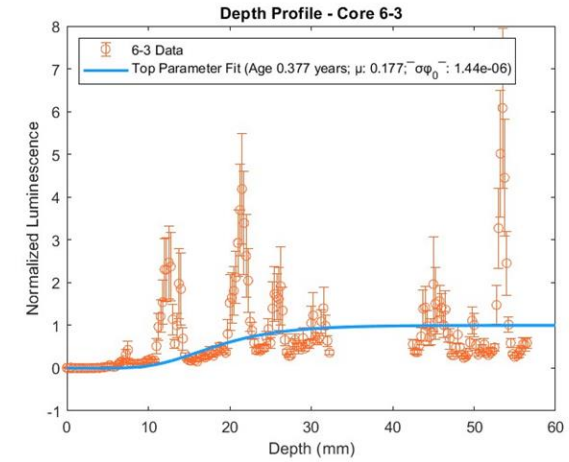

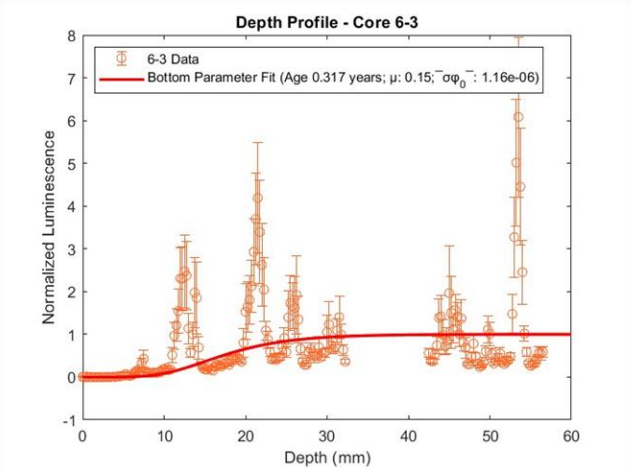

Age fit calculations of ^{10}Be, Top controlled exposed, and Bottom controlled exposed parameters for Erratic 6 (Core 6-3).

Figure 4.21

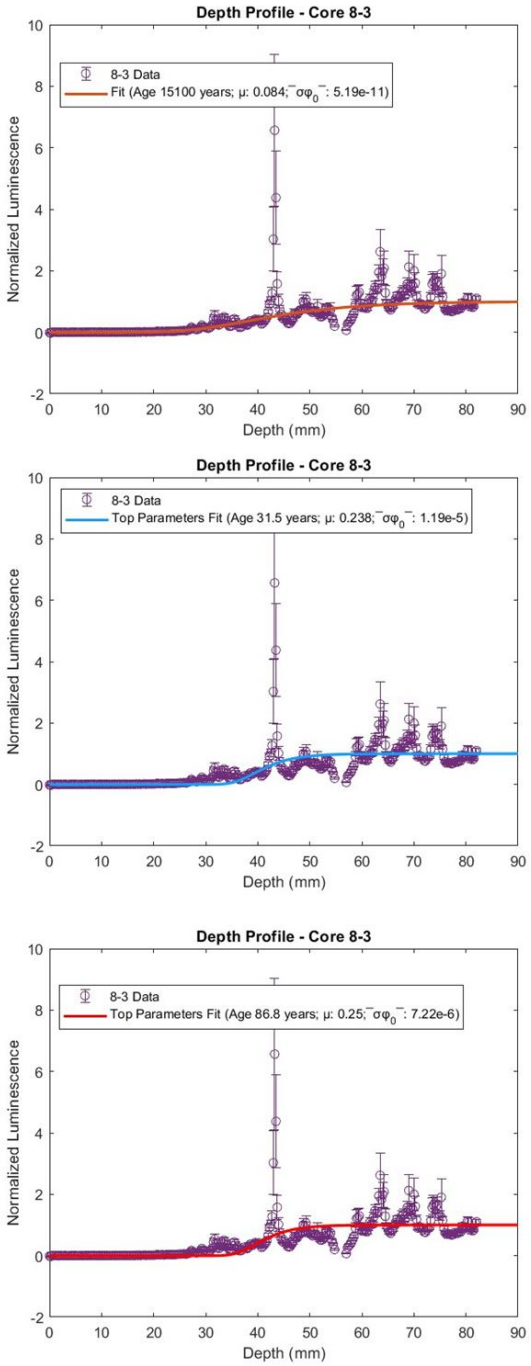

Age fit calculations of ^{10}Be, Top controlled exposed, and Bottom controlled exposed parameters for Erratic 8 (Core 8-3).

4.2.2.7 Physical parameter estimates of light attenuation

Attenuation measures of each OSL scanned sample from the Foothills Erratics Train are presented in Table 4.6 and Appendix A15, showing both the summed attenuation and the average attenuation values against the fitted median values from each core's depth profile. Appendix A17 shows individual attenuation versus spectra plots for the Foothills samples. Average attenuation values were generally slightly lower than summed attenuation values for all cores. All samples show a physically measured light attenuation value that is generally one magnitude greater than the fitted attenuation value, matching what was generally observed in Ou et al.'s (2018) study. For the samples which were large enough to measure individual subcomponent areas of attenuation, there is no clear trend seen in sample depth and attenuation in these measures (Appendix A18).

For larger samples, top, middle, and bottom portions of the transverse slice were measured for attenuation also, to attempt to indicate whether trends in sample depth and attenuation are apparent. For the samples which were large enough to measure individual subcomponent areas of attenuation, there is no clear trend seen between sample depth and attenuation in the Foothills Erratics Train samples (Appendix A18). Still, the nature of the experiment was not precise, and relatively determined top, middle, and bottom sample portion constraints. A more precise assessment of attenuation and sample depth should be performed to determine such corrections more accurately.

A more detailed attempt at measuring light attenuation at depth can be performed using millimeter wafer slices from a core sample, for example. Millimeter wafers were acquired from the edge of Erratic 3-7 to be measured for light attenuation, to observe any attenuation-depth

trends. The measures of each attenuation are presented in Table 4.6, and are plotted with respect to wafer depth in Appendix A18.

Much like what was seen in the transverse core sample measures from the Foothills Erratics Train and Lane Mountain, the wafers from Erratic 3-7 produce measured attenuation values which are generally a magnitude higher than what is observed from fitted attenuation values for Erratic 3. Further, the wafers produced attenuation values that are higher than what is observed in the measured attenuation values of the other core samples from Erratic 3. For the wafer attenuation trends, there is a minor reduction in light attenuation with respect to depth. Summed attenuation presents a regression of -0.1392 mm^{-1} per millimeter of depth, and for averaged attenuation, there is a regression value of -0.1563 mm^{-1} per millimeter of depth (Appendix A18).

4.2.2.8 Physical parameter estimates of photoionization cross section

Photoionization cross section values for slices 3 through 9 from Erratic 3-7 are presented in Appendix A19. Each component promotes a percent contribution of the LM-OSL curve to the associated photoionization cross section value. For estimating a single photoionization cross section value from the percentages, a weighted average using the percentage contributions is calculated for each sample. For the slices from Erratic sample 3-7, photoionization cross section weighted averages range from 7.46E-19 cm^2 to 5.72E-18 cm^2 (Appendix A19). These values represent slow and very slow components of bleaching for quartz dominant rock samples, but are not uncharacteristic values for quartz predominant samples (Choi et al. 2006).

When paired with the estimated photon flux for the Erratic 3 site, values of $\overline{\sigma\varphi_{0(470)}}$ for the slices range from 3.09 – 23.66 s^{-1} (Appendix A19). These results are larger in magnitude to fitted values of $\overline{\sigma\varphi_0}$ for Erratic 3, which range in values between 2.39E-06 - 2.57E-05 s^{-1} from the

controlled exposure experiment parameterizations, and a value of 2.45E-11 s^{-1} when using the ^{10}Be age reference to fit Erratic 3-7.

Table 4.6
Attenuation calculations of Foothills Erratics Train Samples

Slice	Beer-Lambert attenuation calculation (mm^{-1})	Average attenuation across visible light spectrum (mm^{-1})
Erratic 3-7		
Fits from profiles: Attenuation from ^{10}Be: 0.103 mm^{-1} Attenuation of Erratic 3, Top samples: 0.130 mm^{-1} Attenuation of Erratic 3, Bottom samples: 0.509 mm^{-1}		
1	10.91	8.91 ± 1.92
2	4.44	4.23 ± 0.41
3	5.93	5.15 ± 1.16
4	6.05	5.29 ± 1.24
5	7.52	6.64 ± 1.10
6	4.47	3.17 ± 1.49
7	6.61	5.61 ± 1.34
8	7.14	5.51 ± 1.82
9	7.88	6.31 ± 1.85
11	5.75	4.67 ± 1.16
12	4.23	2.78 ± 1.66
13	6.80	6.01 ± 1.24
14	3.92	2.65 ± 1.44
15	4.97	3.54 ± 1.63
16	6.57	5.75 ± 1.23
17	4.87	3.35 ± 1.64

Table 4.6a – Sample 3-7 $\overline{\sigma\varphi_0}$ parameter calculations, 470 nm

Sample	Photoionization cross section average (cm^2)	$\overline{\sigma\varphi_0}$ for 470 nm (s^{-1})	Fitted $\overline{\sigma\varphi_0}$ for Erratic 3
3	7.70E-19	3.19	^{10}Be parameterization 3-7 - $\overline{\sigma\varphi_0}$= 2.45E-11 s^{-1} Top parameters Erratic 3, $\overline{\sigma\varphi_0}$= 2.39E-06 s^{-1} Bottom Parameters Erratic 3: $\overline{\sigma\varphi_0}$ = 2.57E-05 s^{-1}
4	7.46E-19	3.09	
5	2.01E-18	8.31	
6	2.34E-18	9.67	
7	4.52E-18	18.71	
8	5.72E-18	23.66	
9	3.43E-18	14.20	

Figure 4.22

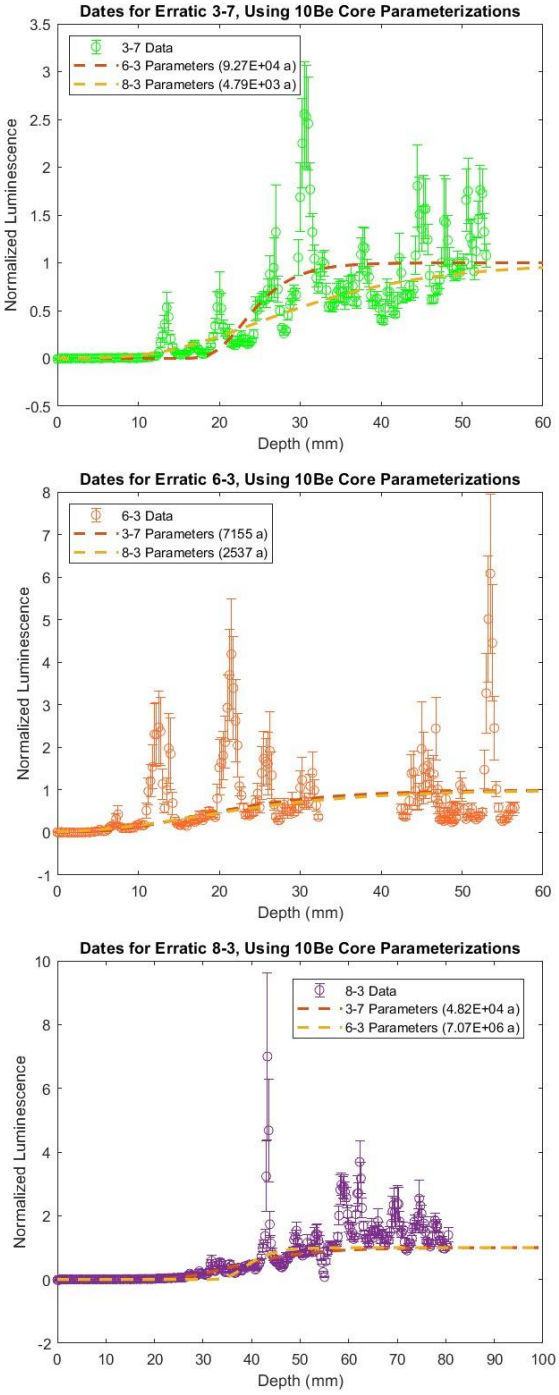

Plots of age best fit calculations using parameters acquired from ^{10}Be age fits from natural exposed erratic samples 3-7, 6-3 and 8-3.

4.2.2.9 Estimating Erosion Rates of Erratic surfaces

Using the CRONUS version 3.0 calculator, estimates of erosion rates can be applied to ^{10}Be data of Erratics 3 and 8 to configure expected exposure age timelines after Erratic deposition (Balco et al. 2008). Margold et al. (2019) provides a list of ^{14}C ages from sediment, Bison, Mammuthus, Equus conversidens, Microtus, Gyttja sediment, and various wood samples near the Erratic Train sampled sites, producing a calibrated ^{14}C age range of 21773 – 13157 years BP for erratic placement (Margold et al. 2019; Appendix A23).

Using this age range, erosion rates can be estimated using ^{10}Be data assuming a time of deposition within the forecasted age range. Thus, erosion rates were applied to ^{10}Be data to acquire ages of approximately 21 ka, 18 ka, and 16 ka, which fall within the ^{14}C time window for the erratic sites. The results of the erosion fits are presented in Table 4.7.

For Erratic 3, an erosion estimate of 6.6 mm/ka provides a deposition age of approximately 16 ka (±1.2 ka), while an erosion rate of 14.5 mm/ka provides an exposure age of 18 ka (±1.49 ka). For Erratic 8, an erosion estimate of 6.8 mm/ka is produced to acquire an exposure age of 16ka, while an erosion rate of 14.6 mm/ka is produced to acquire an age of 18 ka. For an estimated age of 21 ka (± 2.10 ka), an erosion rate for Erratic 3 is 22.5 mm/ka, while for Erratic 8 an erosion metric of 22.7 mm/ka is calculated for the surface assuming an age of 21 ka (± 2.15 ka). External uncertainty is presented for each erratic.

4.2.3 Discussion - Interpreting the Fitted Ages

The results of the Erratics fits, using parameters derived from controlled exposure experiments, produced younger than anticipated exposure ages using parameters derived from controlled exposure experiments, both for individual core parameters and cumulative ‘Top’ and ‘Bottom’

fit parameters. All fit scenarios, except for parameters acquired from the controlled exposed sample 8-2 Top, produced surface exposure ages of less than a millennium for the erratics.

For the ages produced using proximal rock procedures, with depth profile parameters acquired from ^{10}Be ages, the calculated proximal ages were more closely associated with millennial-decamillennial time, better matching the ^{10}Be calculated ages than what controlled exposure ages provided, apart from the date of Erratic 8-3 using parameters from 6-3 (Table 4.3a). The sampled depth profiles are better parameterized for decamillennial time using ^{10}Be ages than what simulated sunlight cores can provide, at least for when using two parameters for summarizing depth profile evolution for proximal age calculations. However, the specific effects contributing to the evolution of luminescence depth profiles, as well as the age variations between cores, are not quantified independently, and the parameter fits are only founded from the ^{10}Be data for the erratics, which faces its own limits in calculated age accuracy. Further, while the calculated ages for the erratic surfaces from proximal rock sampling produce more millennial-decamillennial ages than controlled exposed age calculations, the ages provide poor precision and accuracy against ^{10}Be age results, and do not match the calculated ^{10}Be ages for the Erratics, meaning that specific factors of depth profile evolution may not be accounted for or adequately parameterized in the luminescence exposure dating model. As such, the limitations imposed from proximal rock sampling techniques are still prevalent in the application at the Foothills Erratics Train.

Table 4.7
Calculated surface exposure age estimations assuming erosion rate values, estimated using ^{10}Be data from Margold et al. (2019) and calculated using CRONUS 3.0.3 (Balco et al. 2008). LSDn production rate scaling is utilized to produce ages, with internal and external calculated uncertainty.

Erratic 3	
Age estimation (internal uncertainty external uncertainty)	Applied rate of erosion (cm/yr)
14743 (425 971)	0
16009 (504 1153)	0.00066 (6.6 mm/ka)
18026 (651 1487)	0.00145 (14.5 mm/ka)
20998 (920 2102)	0.00225 (22.5 mm/ka)

Erratic 8	
Age estimation (internal uncertainty external uncertainty)	Applied rate of erosion (cm/yr)
14705 (458 984)	0
16010 (547 1174)	0.00068 (6.8 mm/ka)
18005 (703 1511)	0.00146 (14.6 mm/ka)
21023 (1000 2148)	0.00227 (22.7 mm/ka)

Figure 4.23

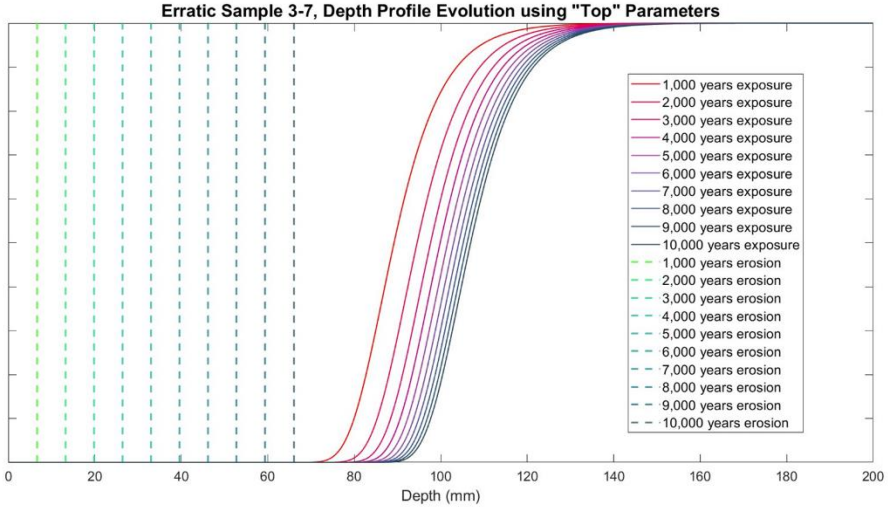

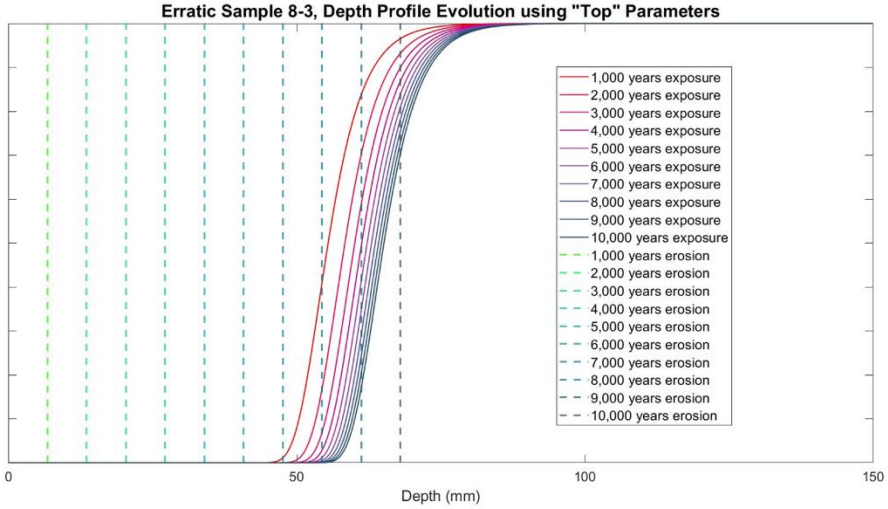

Erosion estimates, in correspondence to exposure age, of the natural exposed erratic surfaces. Dashed lines indicate the extent of erosion from ^{10}Be estimates for an age of 16ka for the rock surface (6.6 mm/ka for sample 3-7, and 6.8 mm/ka for sample 8-3). Solid lines indicate the expected depth profile form, assuming no erosion, of the Erratic surfaces.

The centennial or younger exposure ages from controlled exposure parameterization, which are independent from ^{10}Be data, do not provide insight on the deposition timeline of the erratics.

However, the age results do provide insight on the evolution of the OSL depth profile forms over millennial-decamillennial time. Several distinct impacts, including variations in mineralogy, recorded data scatter, the use of unidirectional simulated sunlight, the variations of surface features in the tested samples, the method of parameterization, and erosion, are not accounted for in the production of the exposure dates when using controlled exposure experiments. The inconsistent results then question the effectiveness of the dating model's ability to produce viable and consistent parameterizations from surfaces hosting varied surface alterations, as discussed in the following sections.

4.2.3.1 Addressing Depth Profile Scatter - Mineralogy

One feature for the wide age discrepancies between samples is that for all depth profiles, wide ranges of OSL data scatter are presented, which implicates fit precision (Figures 4.4-4.5). Several factors contribute to the observed depth profile scatter in this study, including variations in mineralogy between Top and Bottom samples, and potentially the lack of using test dose corrections to mitigate sensitivity variations (Bench et al. 2023).

When measuring OSL, samples of the same origin can host inequivalent variations in mineralogy that offer less reliable OSL dosimetry to that of quartz and can cause scatter to depth profile forms, examples of which may include zircon, rutile, or potassium feldspar for the samples in this study (Ou et al. 2018; Meyer et al. 2013; Polymeris et al. 2019; Bulur et al. 2014; Sanjurjo-Sanchéz et al. 2013).

Identifying the source mineralogy of specific components of spatially resolved OSL can be used to evaluate whether to incorporate or remove such data in depth profiles to improve the precision of depth profile parameterizations, as was seen in Section 3, where anomaly-filtered scan data (Bench et al. 2023). This was attempted on the Erratics samples with the use of X-ray element

mapping. Samples 3-7, 3-5 Top, 3-5 Bottom, 6-3, and 8-3 were mineral mapped, and are presented with further details in Appendix A12. Unfortunately, the resultant mineral scans were not able to be used to identify the mineralogy of OSL anomalies presented in the scans, as the incorrect side of the sample was etched for thin section production. Still, the element maps show non-quartz mineral assemblages of roughly 20-35% for most of the samples, which may indicate significant portions of OSL recorded in the OSL scans are of non-quartz origin. In future dating applications with samples that host varied non-quartz mineralogy, it should be attempted to filter OSL from quartz/only sources to mitigate OSL depth profile scatter and improve parameter precision.

4.2.3.2 Addressing Depth Profile Scatter - Test Dose Corrections, Irradiations

The use of test dose normalization on spatially resolved OSL datasets could also mitigate the variations in OSL sensitivities and improve depth profile data uncertainty and fitting precision, however, such procedures were not conducted for this study due to difficulties in administering doses for all samples (Bench et al. 2023, Sellwood et al. 2022b). Other spatially resolved studies for exposure dating have presented similar difficulties in obtaining regenerative irradiation doses for centimeter scale transverse slices (Sellwood et al. 2022b). Still, a preliminary investigative attempt to observe effects of test dost normalization on depth profile forms was performed on two additional transverse slices from core 3-5 Top and 3-5 Bottom, which were test dose irradiated to 200 Gy using an ELSEC ^{90}Sr irradiator. To irradiate larger areas, than the 1 cm discs for which the system was originally configured samples were irradiated in steps with polygonal offsets on position – to enhance the irradiated areas to the dimensions of the sample. The assessment figures can be found in Appendix A13. The results from the test are inconclusive, and present difficulties in ensuring adequate dose applications across centimeter

scales. Performing additional and more thorough test dose applications on other cores and on other rock compositions can provide further insight to how performing test dose normalization procedures impact depth profile forms for exposure dating. To prevent issues regarding sensitivity variations between samples, future assessments using spatially resolved OSL should consider acquiring the means for test dose irradiations to conduct exposure dating applications (Sellwood et al. 2022a).

Another possible impact on sensitivity may come from using a ^{60}CO gamma source to irradiate samples for controlled surface exposure. All samples were irradiated apart from 3-6 Bottom to account for the possibility that OSL sensitivity variations may differ between irradiated and non-irradiated samples (Murray and Wintle 2000; Roberts et al. 1994). In observing effects of 3-6 samples, the non-^{60}Co irradiated Bottom sample generally hosts more concentrated OSL sensitivity than the Top sample, and fits a higher attenuation coefficient and a bleaching rate value several magnitudes higher than any fitted value from the controlled exposed cores (Figure 4.12; Table 4.2). Still, the associated data scatter of the 3-6 samples hinder any clear interpretations to where irradiation method can be observed to impact depth profile fits and shape. Additional studies which specifically observe effects of depth profile evolution of natural and artificially irradiated surfaces may offer insight on sensitivity impacts when performing controlled exposure experiments.

4.2.3.3 Simulated Sunlight Exposures

The method of controlled exposures using unidirectional, single rate photon flux for 10^6 second timescales for the Foothills samples was able to produce distinct depth profiles several millimeters in depth. Still, this method of controlled exposure could impact the variations and accuracies of parameterization also. Specifically, the simplified exposure dating conditions

followed in simulated controlled exposures, which follow parameter conditions for the exposure dating model of constant, unidirectional photon flux, may be too simple in attempting to simulate accurate depth profile development over millennial-decamillennial time.

This concern was attempted to be assessed with the trials conducted at the Lane Mountain site. The Lane Mountain trial of controlled exposure experiments using wafer data showed that the use of simulated sunlight controlled exposures produced parameter fits with higher values of light attenuation, but equivalent bleaching rate parameters than what was observed with the natural sunlight controlled exposed depth profiles (Section 3). This difference impacted age calculations significantly for the surfaces in using wafer data, producing millennial ages for 11-year exposed surfaces when using simulated sunlight controlled exposure parameters. However, the low resolution of wafers likely contributed to the discrepancies in parameter calculations and age fitting for the samples, preventing a firm interpretation of results, and warranting further investigations using more resolute OSL measuring protocols. Then unfortunately, the spatially resolved OSL scans of the controlled exposed samples were too low in OSL output to produce viable depth profiles for parameter extrapolation.

Although incomplete, this prior experiment as reference tells us the parameters acquired from the Foothills samples may still offer equivalent bleaching rate parameters for conventional exposure dating than if natural exposures were used, but other parameters concerning decamillennial time may not be adequately accounted for in characterizing the depth profile. For instance, the angle of solar illumination is ignored in performing the simulated light exposures, but has been shown it may serve a potential impact to depth profile forms in controlled experiments (Fuhrmann et al. 2022). However, the millimeter wafer data utilized for this angle of illumination experiment still

produces varied depth profile forms and inconsistent trends across different samples, limiting interpretability of the results.

The impacts from temporal variations in solar illumination on depth profile development still have not been assessed using more resolute OSL measuring protocols, and are warranted in understanding why parameterization inconsistencies are apparent in this dating application. What can further assist in interpreting the impacts of solar simulated light exposures on depth profile parameterization also is to consider other effects of depth profile development unaccounted for in the first order model, as well as implications of depth profile development that would concern decamillennial time.

4.2.3.4 Examining Impact of Surface Features

Two sets of samples were produced from each core for controlled exposure experiments, with Top samples hosting surface features and Bottom samples hosting no surface altered features. Controlled exposure experiments were performed from each sample to assess if weathering rinds or other surface features play a role in altering depth profile forms, and how the presence of such features implicates the use of samples with no surface altered features to parameterize naturally exposed rock surfaces for exposure dating.

Past examinations of surface and subsurface alterations and their impact on depth profile evolution have been attempted in prior studies, albeit with the use of wafer derived datasets. A study from Luo et al. (2018) attempted to examine the role of surface varnishes in depth profile development derived from wafers, however resolution issues of the sampled depth profiles prevented clear assessments on surface impacts. The use of millimeter wafer derived depth profile datasets in certain applications has been shown to face limitations in parameter fit precision due to low datapoint resolutions (Bench & Feathers 2022; Elkadi et al. 2021; Brill et. al

2020; Moayed et al. 2022). Meyer et al.'s (2018) study on lithological impacts to depth profile development indicated that surface coverage, mineral opacity, and chemical weathering alterations may increase light attenuation values for samples in localized regions. Still, these observed trends from the depth profiles are limited to only one dimension of slice derived point data, which limits direct spatial considerations of surface alterations or unique subsurface mineralogical components documented in the cores (Meyer et al. 2018; Ou et al., 2018; Fuhrmann et al. 2022; Bench et al. 2023).

The ability to spatially identify specific regions in the sample where the emitted OSL is altering depth profile development, such as from weathering rinds or a subsurface region insulated from light, may refine insights on the role that surface alterations serve in altering depth profile forms.

Thus, enhanced assessments on the effects of surface alterations to depth profiles may be improved with the use of spatially resolved luminescence measuring techniques. In addition to providing more enhanced depth profile resolution, the use of spatially resolved OSL can offer direct spatial investigations on unique compositional features of the sample and its impact on measured OSL, including direct spatial assessments of OSL on areas hosting weathering rinds or of unique mineralogy, which can be applied to assess impacts on depth profile forms (Clark-Balzan & Schwenninger, 2012; Meyer et al 2013; Bench et al. 2023).

As such, an evaluation on surface feature impacts to depth profile evolution is performed from this study, focusing on individual Top and Bottom samples from Erratics 3 and 8, which host the deepest depth profiles out of the three sampled erratics. Erratic 6 produced depth profiles which had difficulty producing clear bleaching fronts, which limits the ability to interpret the effects of subsurface features and depth profile evolution.

Further, we also eliminate the interpretation of sample 3-6 for this section, as the Top sample was irradiated but the Bottom sample was not irradiated before simulated sunlight exposure. The potential differences in sensitivity acquired from the cores may implicate depth profile forms enough to limit interpretations in surface altered influences of depth profile evolution.

4.2.3.4.1 Assessment

Before comparison of the Top and Bottom sample depth profiles from Erratics 3 and 8, it was expected that Top samples would produce depth profiles which would fit higher values light attenuation parameters than their Bottom sample counterparts, due to the presence of weathering rinds and surface lichens found on Top samples. This style of trend was observed in Meyer et al. (2018), which inferred that the presence of chemical weathering in samples may increase light attenuation coefficients for the affected samples.

However, from the OSL spatially resolved data, fitted light attenuation values of Top samples are lower than Bottom samples for all cores apart from core 8-4, which produced a light attenuation value for the Top samples slightly higher (0.173 mm^{-1}) than its Bottom sample counterpart (0.107 m^{-1}) (Table 4.2; Figure 4.15).

In examining the spatially resolved OSL maps for the cores, a more gradual increase of OSL at depth until bedrock saturation is observed visually in Top samples 3-5, 3-8, and 8-2 when compared to their Bottom core counterparts (Figure 4.10, 4.12). For core 3-8, the Top sample OSL scan appears to have not completely bleached in the first few millimeters, potentially the result of significant surface coverage preventing substantial light intensity from attenuating into the sample. When compared to the Bottom sample 3-8, which offers no surficial coverage or rinds of weathering, more efficient OSL bleaching is observed in the first few millimeters of depth (Figure 4.10). For core 8-4, similar OSL bleaching gradients are observed visually,

although 8-4 Top generally produced higher OSL intensities at OSL saturated depths (Figure 4.12).

OSL depth profile data trends are more subtle in Figures 4.13 and 4.15, as the data is subject to scatter, and the normalization and averaging of the scan data into 250 μm datapoints mitigates any variations observed in the scans. Further, the y-axes are varied among core depth profile plots to contain all data points of the depth profile in one plot (Figure 4.13, 4.15). For improved insight, supplementary figures are included which plot depth profile data of the cores along equivalent axes, as well as provide close ups of the first 20 millimeters of each sample's depth profile data (Figure 4.13a – 4.13b, 4.15a-4.15b). Even with the mitigating impacts from data normalization, the OSL data depth trends in cores 3-5 and 8-2 indicate a more gradual increase in OSL for the Top samples, as the saturation plateau is deeper than in the Bottom samples (Figure 4.13b, 4.15b). Samples 3-8 and 8-4 showcase transitions in the saturation plateaus that are too subtle to differentiate.

The prevalence of data scatter in the depth profiles likely implicates the fitted parameter values of light attenuation for all cores, as well as how effective the general shape of the depth profile curve compares against the data. This is indicated more clearly in core 3-8, as the Bottom sample hosts very high anomaly OSL values in its saturation plateau, causing a higher attenuation parameter fit compared to the Top sample, even though the OSL depth gradients for the Top and Bottom samples of this core are very similar (Table 4.2, Figure 4.3).

Still, for the samples experiencing less scatter influence, like in cores 8-2 and 3-5, the depth profiles still consistently produce lower attenuation parameter fits for each Top sample. As such, the lower fitted values for light attenuation of the Top samples may have also been influenced by the presence of surface coverage and subsurface weathering rinds. The more gradual OSL-depth

gradient observed in Top samples may be influenced by the presence of surface features like lichen, in addition to the chemical weathering subsurface features which are darker than the rest of the sample subsurface (Meyer et al. 2018). Once light penetrates through the weathered sample regions, this causes the remaining sample depths to be bleached at a lower light intensity. These reductions will resultingly produce a more gradual trend of OSL intensity at depth than expected, and a lower attenuation coefficient fit, if summarizing light attenuation as a single rate for the core. Bottom core samples, which do not possess weathered regions within their subsurfaces, do not face an initial component of increased light attenuation, and thus light can penetrate into deeper regions of the sample with more intensity. With these properties, light will be able to bleach OSL more effectively at deeper regions of the nonweathered Bottom sample, producing a more intense OSL-depth gradient warranting a higher attenuation parameterization (Figures 4.10, 4.12, 4.13, 4.15). For sample 8-4, Top and Bottom depth profile data are very similar in form, with neither core plotting a more obvious gradient of OSL at depth (Figure 4.15a).

This explanation on how weathering impacts light attenuation may also explain why fitted parameter values of light attenuation between 8-4 Top and 8-4 Bottom are most similar among all sampled cores. In comparing the sample features of the Top and Bottom samples, core 8-4 Top features a weathering rind that is roughly two millimeters deep with minimal surficial coverage, which may not have impacted light attenuation enough to produce dissimilar parameterizations between Top and Bottom samples. The lack of prominent weathering in the Top sample thus would offer more comparable depth profile parameterizations to that of the surface unaltered Bottom sample (Table 4.2).

The implications in these observed trends indicate there may be multicomponent factors for light attenuation in sample cores hosting subsurface and surface alterations, echoing discussions from Meyer et al. (2018). The spatially resolved OSL data more clearly shows the relationship between the trend of OSL and depth and the impact of subsurface weathering than what wafer derived datasets can provide. Further, the observed impact from surface coverage and weathering rinds on light attenuation fits may indicate why shallower than expected first order light attenuation values have been commonly fitted in exposure dating studies (Ou et al. 2018; Selwood et al. 2019; 2022; Bench et al. 2023).

It is less clear to explain the trends for luminescence bleaching rate parameters $\overline{\sigma\varphi_0}$, where Erratic 3 Top sample 3-5 produces a $\overline{\sigma\varphi_0}$ value (2.37E-06 s^{-1}) much lower than its Bottom sample (1.01E-05 s^{-1}), yet samples from 3-8 and all samples from Erratic 8 produces more equivalent $\overline{\sigma\varphi_0}$ values for its Top and Bottom samples. Other unique conditions may influence the observed differences in the fitted bleaching rate coefficients, such as the varied distributions of OSL heterogeneities found among samples (Bench et al. 2023).

Another implication for fitting $\overline{\sigma\varphi_0}$ is the effects of OSL sensitivity in weathered sample regions, where it has been observed that weathered sample components may produce lower OSL counts than nonweathered sample equivalents (Jeong et al. 2007; Jeong et al. 2012). Conversely, a study from Bartz et al. (2022) observes no difference in the effects of IRSL sensitivity in weathered sample regions, indicating that sensitivity effects from weathering may serve unique for the sample. Still, such a weakening of OSL sensitivity would not adequately follow first order assumptions concerning wavelength dependent photoionization cross section estimations (Sohbati et al. 2011). An examination of multicomponent behaviors of photoionization or photon

flux in regions of surface and subsurface alteration should be examined in further experiments to account for such effects to depth profile evolution.

4.2.3.4.2 Concerning Future Applications

In this evaluation, the simplified parameterized design of first order kinetic exposure dating model may serve as too basic a model to adequately consider the recorded depth profile variations between surface altered Top and surface unaltered Bottom samples. While the light exposure conditions in this study are simplified to be unidirectional and in a controlled simulated environment to best follow model assumptions, the spatially resolved OSL shows there may still be unaccounted for compositional characteristics between the similar sourced samples, which are not quantified effectively in the model form. Potential multi-order variations in light attenuation and luminescence bleaching kinetics in samples warrant further investigation (Bench & Feathers 2022; Fuhrmann et al. 2022; Gliganic et al. 2019; Freiesleben et al. 2023). This multi-order approach to parameterization can help incorporate other surface covering features which may impact depth profile evolution, but are not yet parameterized in rock surfaces directly. Effects from snowfall cover, for instance, have not yet been quantified in its influence in depth profile evolution, but likely will impact incident light flux on the rock surface.

Thus, in performing rock surface parameterizations for dating applications, it should be considered that the presence of weathering rinds or surface altered samples may have an impact on the exposure dating parameterization of known age surfaces. In evaluating these results, the use of nonweathered, unaltered rock surfaces may not offer the light attenuating trends consistent with exposed surfaces hosting surface and subsurface alterations. Further investigations should be made in evaluating the accuracy of choosing known age samples with weathering rinds to date samples hosting equivalent weathering rinds.

4.2.3.5 Observations from Physical Parameterizations – Foothills Erratics Train

The discrepancies between measured and fitted light attenuation and luminescence bleaching rate parameters for samples from the Foothills Erratics Train highlight concerns from prior applications that the first order model for exposure dating may not offer accurate physical characterizations of the sample that impact depth profile development. Further, the experiments also show the practicality of physically parameterizing photoionization cross section and light attenuation coefficients for a sample.

In the Foothills Erratics Train attenuation measure, the physical parameterizations of light attenuation were generally a magnitude higher for the tested samples than from fitted values, which shows a potential issue with the dating model's characterization of depth altered photon flux with an attenuation constant (Appendix A15, A17-18). The original purpose of the attenuation constant in the exposure dating model was to simplify the multi-order characterization of photon flux attenuation at depth for a given sample (Sohbati et al. 2011), yet the discrepancies in the fitted attenuation values to the physical attenuation measures indicate that depth profile shape may poorly characterize the true physical properties of light attenuation and impact to the depth profile form. A reassignment of the attenuation coefficient in the model, or an adjusted metric that considers potential additional effects like light angle or photon flux variation, may be needed to validate the use of light attenuation in evaluating depth profile evolution.

The light attenuation experiments conducted in this study, though, were able to record changes in light intensity in multi-wavelength components, in relation to the thickness of the measured sample. A linear relationship observed between these two parameters would indicate viability in using an attenuation coefficient for estimating photon flux attenuation. A direct evaluation on the

sample thickness and change in light intensity for Erratic 3-7 is plotted in the end of Appendix A18, where a linear regression of -5.217x + 1.0839 is produced with an R^2 value of 0.0096, indicating for the provided samples that a poor linear relationship of light attenuation and sample thickness is presented. A similar trend is presented in observing all the Erratics Train transverse slice light ratio values with respect to their thickness, producing a linear regression of -56.944x + 1.8638 with an R^2 value of 0.1119 (Appendix A18). A linear relationship is somewhat presented in these experiments, however with further examples and more precise experimental setups for measuring light attenuation, one can better establish the trend of attenuation photon flux and sample depth. Still, the practicality of the light attenuation experiment warrants further trials in attempting physical parameterizations for depth dependent photon flux in exposure dating applications.

Photoionization cross section values were physically derived from wafer slices of erratic sample 3-7 using LM-OSL protocols, but for only a 470 nm wavelength. The limited results make it difficult to make a direct evaluation of the fitted photoionization cross section values against the physically measured value for sample 3-7. To physically parameterize photoionization cross sections in application, more LM-OSL protocols against varied visible light wavelengths need to be administered on samples to estimate comprehensive cross section values. The measured data, however, at least shows it is possible to produce photoionization cross section values physically from core samples. LED's of varying wavelengths can be implemented in Risø TL/OSL readers to perform LM-OSL protocols with the same procedure as conducted in this experiment to acquire more comprehensive photoionization cross section values. Alternatively, spatially resolved LM-OSL can possibly be developed to where lasers of varied wavelengths can be used to stimulate LM-OSL from samples. Another consideration in the results is that wafer slices were

measured from the erratic sample, meaning other non-quartz minerals likely contributed to the LM-OSL curve to produce the photoionization cross section value. Ideally, LM-OSL curves should be produced from the stimulation of quartz minerals. However, non-filtered depth profiles will also include non-quartz mineral OSL, and the resultant fits for $\overline{\sigma\varphi_0}$ will be influenced by this non-quartz OSL. For the sake of future trial experiments, fitted and physically measured photoionization cross section values should be attempted from mineral filtered depth profile datasets and mineral filtered wafers to determine if measured versus fit results also do not align when measuring only quartz derived OSL.

The discrepancies reported from the physical parameterization applications offer some quantification over the considered multi-order variations in light attenuation and luminescence bleaching from other applications, but do not reach distinctive conclusions (Bench & Feathers 2022; Fuhrmann et al. 2022; Gliganic et al. 2019; Freiesleben et al. 2023). Still, the success of performing these physical parameterizations provides a realistic path for evaluating current and new model forms in future exposure dating experiments. It is therefore advisable when proposing new models, or discussing current models for exposure dating, that such physical experiments are performed to validate interpretations of luminescence depth profile evolution.

4.2.3.6 Impacts from Erosion

Considering that the parameters acquired from the controlled exposed samples produced centennial or lower ages for the decamillennial exposed surfaces, erosion rates are estimated from the erratic surfaces using ^{10}Be data to investigate whether the rate of erosion is high enough to outpace the evolution of the luminescence depth profile, producing younger than expected ages.

4.2.3.6.1 Expected Parameters from the Erratic Surfaces

For fitting $\overline{\sigma\varphi_0}$ and μ to the natural exposed surfaces of the erratics samples 3-7, 6-3, and 8-3, calculated exposure ages from ^{10}Be from Margold et al. (2019), considering no erosion, were used as known exposure ages. The same least absolute error regression fit approach was used as with the controlled exposed cores. A known age of 14.7 ka was fitted for sample 3-7, 8.2 ka for sample 6-3, and 15.1 ka for sample 8-3. The range of parameters fitted for μ were between 0-1 for cores 3-7 and 8-3. For 6-3, a range of 0-3 was used to fit μ. Values between 0 and 10 were fitted using the parameter log($\overline{\sigma\varphi_0}$*t) for samples 3-7 and 8-3, and a range of -5 to 5 was used for sample 6-3.

The parameter results for $\overline{\sigma\varphi_0}$ and μ are presented in Table 4.5, and parameter plots are in Figures 4.18-4.21. Likelihood plots for each Erratic are in Appendix A5. The results show very low $\overline{\sigma\varphi_0}$ values for the cores, with sample 3-7 producing a fitted value of 2.45E-11 s^{-1} (1.01E-11 -1σ, 3.89E-12 +1σ), 6-3 producing a value of 2.14E-10 s^{-1} (5.51E-08 -1σ, 2.01E-10 +1σ), and 8-3 a value of 5.19E-11 s^{-1} (1.48E-11 -1σ, 6.19E-11 +1σ). This counters the fitted values for $\overline{\sigma\varphi_0}$ from controlled exposures, with parameter ranges for Erratic 3 controlled exposed samples within 2.37E-06 – 0.149 s^{-1}, for Erratic 6 within 9.91e-07 - 1.55E-04 s^{-1}, and for Erratic 8 within 1.15E-04 - 5.67e-06 s^{-1}.

Fitted values for μ are generally low also, with values of 0.103 mm^{-1} (0.014 -1σ, 0.021 +1σ) for 3-7, 0.281 mm^{-1} (0.496 -1σ, 0.198 +1σ) for 6-3, and 0.084 mm^{-1} (0.014 -1σ, 0.008 +1σ) for 8-3. These values are similar to lower parameter bounds for the controlled exposed cores, which range from 0.103 – 1.41 mm^{-1} for Erratic 3, 0.035 – 1.58 mm^{-1} for Erratic 6, and 0.173 – 0.617 mm^{-1} for Erratic 8. In all, the results show that controlled exposed samples promote much higher

values for $\overline{\sigma\varphi_0}$ for the rock than what should be observed for the decamillennial exposed samples. Further, attenuation values appear to have low end fit values, which could be retrievable with controlled exposure results.

When comparing the fit results to physically derived $\overline{\sigma\varphi_0}$ and μ for the cores, μ measured values are a magnitude higher for all cores than what is fitted using millennial-decamillennial known ages (Appendix A15a). Further, $\overline{\sigma\varphi_0}$ fit values for core 3-7 are still several magnitudes lower than measured estimates (Appendix A19). As such, the trends between controlled exposed and physically measured parameters are still similar, even when using millennial-decamillennial timescales.

The low $\overline{\sigma\varphi_0}$ values for the parameter fits can tell us is one of two conditions. First is that a fitted faster rate of luminescence bleaching is generated from the controlled exposure experiment cores, which produce younger than expected depth profile ages for the cores. Investigating this issue would require an evaluation of potential parameters which may be neglected in performing a single rate, unidirectional photon flux, as followed from the first order model assumptions. In evaluating these other factors, additional model parameters will possibly be needed to better quantify luminescence bleaching rate evolution, altering the dating model form. Such work, however, warrants separate physical experiments concerning light exposure.

Another condition could be that the bleaching rate constants from the controlled exposure experiments are viable, but the depth profiles measured from the natural exposed samples are shallower than expected for the expected decamillennial timescales. In this case, erosion rate influences, which are not accounted for in the exposure dating model, may be altering the depth profile form to be shallower than expected for the rock surface. As such, it is pertinent to

consider quantifying erosion rate estimates for the measured rock surfaces to begin considering this influence on the calculated ages.

4.3.2.6.2 Quantifying Erosion Impacts

Erosion rate estimates using ^{10}Be for Erratics 3 are 6.6 mm/ka assuming an age of 16 ka (±1.2 ka), and 14.5 mm/ka assuming an age of 18 ka (±1.49 ka). For Erratic 8, an erosion rate is estimated at 6.8 mm/ka assuming an exposure age of 16ka, while an erosion rate of 14.6 mm/ka is produced assuming an age of 18 ka. Erosion rates of over 22 mm/ka are calculated for each erratic when assuming an exposure age of 21 ka. These estimates, if accurate, alter the evolution of the OSL depth profile acquired from the Erratics Train surfaces, which will not offer a complete post-deposition timeline of surface exposure. Once millennial timescales have been reached, the rate of depth profile bleaching slows to where the rate of erosion will eventually remove the original post-deposition depth profile (Figure 4.23). Erratic 3, for instance, when assuming an erosion rate of 6.6 mm/ka, most of the depth profile, assuming no erosion, would be removed after 10 ka of exposure (Figure 4.23). A similar trend is observed for sample 8-3, when assuming an erosion rate of 6.8 mm/ka from ^{10}Be calculated erosion estimates.

These results may explain why most exposure ages acquired from the rock surfaces of the Erratics Train were less than millennial aged. The rate of erosion as presented would remove most of the original depth profile acquired over millennial time once more than a thousand years of surface exposure has occurred for the erratic surface (Figure 4.23). The observed depth profiles likely result from more complex histories of luminescence bleaching, where deeper sample depths will have first experienced a slower rate of bleaching when the associated region was deeper into the rock interior, then a faster rate of luminescence bleaching when sample subsurface erodes beyond several millimeters. As such, the luminescence bleaching constant,

which does not account for erosion, may be too simple to account for these potential variations of luminescence bleaching.

As such, erosion should be a considered factor for evaluating exposure ages beyond millennial timescales for the Erratics Train. The inclusion of an accurate erosion parameter is warranted to improve the ability to date rock surfaces over longer timescales beyond centennial ages.

In recognizing the potential for an erosion rate parameter for estimating exposure age, an applied factor of weathering as a function of depth can be defined as the following (Sanderson et al. 2011):

$$x=x_0-ct$$

where c is a rate of erosion, t is time, and x_0 is the estimated original thickness of the sample which captures the measured depth profile form. This value for depth can be incorporated into the model form as:

$$L(x)=L_0 e^{-\overline{\sigma\varphi_0}\, te^{-\mu(x_0-ct)}}$$

In incorporating this metric for erosion, however, an estimate of the original depth of the complete luminescence profile shape is required, as well as an independent exposure age chronometer. The procedure to acquire these parameters for estimating an erosion rate from the luminescence depth profile has not been developed, and is worthy of continued investigation.

An alternative model for quantifying erosion, separate from the first order exposure model, was proposed in Sohbati et al. (2018), which follows the form:

$$\frac{n(x,\varepsilon)}{N}=M\left(1,1+\frac{F}{\mu\varepsilon},\frac{E(x)}{\mu\varepsilon}\right)$$

Where an erosion rate ε (mm/ka) is estimated from the fraction of filled traps (n) to total traps for the sample (N) equated against the hypergeometric function (M), which incorporates luminescence filling (F) and eviction (E) rates and light attenuation μ. The Luminescence filling rate is a quotient of a characteristic dose Ḋ over the sample's environmental dose rate D_o ($F = \dot{D} / D_o$), while the emptying rate is a function which incorporates the bleaching rate coefficient and attenuation coefficient for the rock material ($E= \overline{\sigma\varphi_0}\ e^{-\mu x}$). The condition in using this model, however, is that the luminescence depth profile needs to be in steady state, to where the depth profile curve remains non-transient in form over time. As such, no active exposure ages can be calculated from such viable depth profiles when calculating erosion using this model. Further, it is difficult to measure when steady state depth profiles have been obtained in rock surfaces. For instance, the article which presents this model for erosion attempts to configure a depth profile as steady state when its inflection point is at a subsurface depth of roughly 50% or greater than the value of the inverse light attenuation coefficient (1/μ) for the fitted sample, which has not been verified as a valid condition (Sohbati et al. 2018). Further applications concerning the model should be made in validating its form for erosion dating applications.

In recognizing the impact of erosion on the evolution of the depth profile form, and the limitations in estimating exposure ages for millennial-decamillennial time, the use of OSL depth profiles may be very suitable to verify erosion rate estimates used in other geochronometers, once the ability to quantify erosion from the depth profiles has been validated. When luminescence depth profile evolutions are more accurately quantified, future studies can utilize ^{10}Be chronometers to establish estimates of erosion for rock surfaces, and use that information to attempt quantifying erosion from luminescence depth profiles, if assuming a steady state form. The use of luminescence for exposure dating millennial aged or older surfaces may host

complications in depth profile evolution which limits accurate applicable use, or would require significant reparameterizations of depth profile forms. As such, if an erosion rate factor cannot be well quantified, luminescence exposure dating applications may be best suited for exposure dates younger than millennial timescales, or in applications where erosion is very negligible for surfaces.

4.3.2.6.3 Environmental Dose Rates

One other consideration which may impact depth profile forms over millennial-decamillennial time, as well as metrics for erosion, is the impact of the environmental dose rates on the rock subsurface. With enough environmental radiation exposure, luminescence depth profiles shapes can restore levels of saturation, removing prior bleaching history in rock surfaces (Freiesleben et al. 2015). As such, it is worth considering potential effects of natural radiation exposure on the impact of luminescence depth profiles over decamillennial time, and whether this impact may produce depth profiles which produce younger than expected exposure ages for rock surfaces.

Estimates of external dose rates within the Erratics samples are presented in Appendix A21, which incorporate U, Th, and K concentration estimates of each erratic using gamma spectroscopy at Scottish Universities Environmental Research Centre, calculated using the guidelines in Cresswell et al. (2018). Using these estimates, dose rates were then calculated from the site using the DRAC dose rate calculator, calculating external dose rates for the subsurface samples (Durcan et al., 2015). Given the composition is not purely quartz for the Erratics, as observed in Appendix A12, the composition of the rock material was assumed polymineral for calculation, and with particle ranges of 100-1000 microns as a rough average. The calculation offers estimates of 4.699 Gy/ka (±0.073) for Erratic 3, 4.134 Gy/ka (±0.121) for Erratic 6, and 3.764 Gy/ka (± 0.72) for Erratic 8, but incorporate no internal dose rate calculations.

More refined dose rate estimates can be made for the rock materials, but indicate there is a dose rate impact of several Grays per thousand years subjected to the erratic subsurfaces. The impact of dose rates on the evolution of the depth profile form are not well established, however investigations at incorporating dose rate values were applied to an altered exposure dating model form in Lehmann et al. (2018):

$$L(x)=\frac{\overline{\sigma\varphi_0}e^{-\mu x}e^{-t\left(\overline{\sigma\varphi_0}e^{-\mu x}+\frac{\dot{D}}{D_o}\right)}+\frac{\dot{D}}{D_o}}{\overline{\sigma\varphi_0}e^{-\mu x}+\frac{\dot{D}}{D_o}}$$

which incorporates a luminescence filling rate (a^{-1}), using characteristic dose $\dot{D}$ over the sample's environmental dose rate D_o. However, no applications or physical measurements using this model have been made since its inception. With the acquisition of more accurate dose rate values from the Erratics Train, as well as the application of regenerative dose protocols to acquire $\dot{D}$, both can be used to evaluate the change in exposure age for the Erratics Train samples with these inclusions. For this study, regenerative doses were not able to be conducted. Still, experiments should be continued which aim to verify if applied dose rates will impact the transience of luminescence depth profiles enough to alter exposure age calculations. With these results, it can be more effectively considered how or whether to incorporate dose rates in future exposure dating or erosion rate models using luminescence depth profiles.

4.2.4 Prospective Studies

The use of controlled exposure experiments for parameter extrapolation, as well as simple model assumptions for luminescence depth profile evolution, limit success in accurately dating the Foothills Erratics Train surfaces. While the simplified parameters $\overline{\sigma\varphi_0}$ and μ mitigate complexities in measuring unique characteristics of light attenuation and luminescence bleaching

from rock surfaces, it may not adequately account for other physical influences of depth profile evolution. Continued study on the evolution of the luminescence depth profile is needed to identify and more adequately quantify parameters which contribute significantly to depth profile evolution. Specifically, more enhanced study is warranted on the impacts from the light source, and the impacts of sample characteristics, including metrics for light attenuation, photoionization cross section, and erosion. In conducting these studies, it is also important to perform physical experiments in validating modified parameters for exposure dating. With these experimental insights, luminescence depth profiles can be better characterized for exposure dating purposes.

One recommended subject of study for light source impacts is to measure impacts from different angles of sunlight illumination and luminescence bleaching, which are not accounted for in the $\overline{\sigma\varphi_0}$ and μ parameters for the first order exposure dating model due to perceived complexities in quantifying effects to depth profile evolution. Still, studies by Fuhrmann et al. (2022) document effects of illumination angles on rock surfaces and impacts to depth profile forms, which promotes the feasibility of quantifying such effects for dating purposes. Continuing studied on quantifying the effects of illumination angles on depth profiles can assist in establishing temporal trends of depth profile development in relation to sample setting. The effects of different atmospheric settings and impacts on luminescence bleaching are also worthy of study. Diffuse illumination, which is common in overcast atmospheric settings, may not exhibit distinct solar angles of illumination. Given the distinction of these atmospheric settings, their characterization in exposure dating models may be beneficial for producing more accurate results. The use of simulated light experiments can be used to begin observing such effects, where the angles of sunlight illumination can be adjusted in a controlled setting to observe direct impacts.

Variations in photon flux are also not considered in the exposure dating model, where a single rate photon flux is used to generalize the photon flux experienced by the sample surface. Photon flux will vary over the course of the day, and is impacted by atmospheric cover. Direct experimental studies on varied light intensities and depth profile evolution have not been explicitly studied, yet may offer data which can determine if such effects warrant a modified parameterization for luminescence bleaching. This parameter may offer the ability to better account for daily or other temporal variations in photon flux in surface exposure. The use of simulated light sources, with simulations of direct and diffuse illuminations through the modification of light intensity and spectra, may serve as a more approachable start to evaluate such effects. In addressing both angle of illumination and photon flux parameters, the use of long term and short term controlled exposure studies using well documented natural sunlight may be useful as well. For instance, comparing annual and seasonal exposure study results, spanning months to years, may be effective in outlining effects to depth profile evolution for parameterized study, to where solar data is recorded alongside exposure studies to quantify effects of depth profile evolution and recorded variations in solar photon flux and light incidence angles.

With respect to sample characteristics, the effect of luminescence bleaching may be from multi-rate components of photoionization cross sections, and should be examined with physical experiments rather than from curve fit approaches. The current approach for quantifying luminescence bleaching is to assume a single rate of bleaching that encompasses all spectral variations of luminescence bleaching and potential photoionization cross section dimensions for the sample. However, depending on the proportions of photoionization cross section components, parameterizing a rock surface using a single photoionization cross section value

may serve to be too inaccurate for certain samples. The use of multi-order photoionization cross section values to characterize a version of $\overline{\sigma\varphi_0}$ may offer a more accurate parameterization format for exposure dating. To begin this measuring technique, it may be easiest to first conduct simulated single wavelength light simulations on samples, to where luminescence depth profiles and photoionization cross section values from single wavelength LM-OSL protocols can be recorded from samples to evaluate the effects of multi-order influences of luminescence bleaching. In observing these effects for specific spectra, a general relationship may be quantifiable and parameterized for exposure dating applications.

It should be recognized that LM-OSL is traditionally measured from quartz grains only, and that LM-OSL measures from core wafer slices will likely produce OSL from non-quartz sources. This effect will alter the LM-OSL curve and associated parameterizations for the photoionization cross section values. As such, when possible, wafer core samples could be disaggregated and mineral separated before being measured for LM-OSL to ensure the LM-OSL curves are derived from the appropriate mineralogy. This is most useful when looking at mineral filtered depth profile data. Still, it may also be warranted to measure LM-OSL from the wafers as a whole, to use for OSL depth profiles which host no mineral filtered data. In this comparison, estimates of photoionization cross section values from fitted and measured procedures can evaluate the dating effectiveness and accuracy of producing photoionization cross section values from mineral mixed specimens.

The attenuation coefficient is also a sample characteristic that should be analyzed with physical measurements in future study, and measured by individual wavelengths also, to determine spectral variations in light attenuation and the potential impact on depth profile development. Rock samples may not have the same light attenuating effects for certain spectra, which may

allow for deeper or shallower luminescence bleaching depending on the nature of sunlight exposure. In this case, a single value for light attenuation independent of spectra may not adequately represent light attenuating properties for the rock. Performing these measurements can offer more clear quantified relationships of luminescence depth profile evolution, and help better configure the role of light attenuation.

Finally, a reliable metric for calculating an erosion rate would be useful for interpreting exposure ages of samples with millennial or greater exposure ages. To physically derive metrics for erosion, an initial focus on rock surfaces which are likely to host a luminescence depth in a steady state form can be used to characterize erosion, as executed in Sohbati et al. (2018). In this circumstance, chromometers such as ^{10}Be can be used to estimate the erosion rate of the rock surface, where the shape of the steady state luminescence depth profile can then potentially be characterized to this constant rate of erosion with a series of physically derived parameters contributing to luminescence depth profile development. If validating this metric is possible for steady state conditions with physical experimental validation, then future considerations can include estimating exposure ages for surfaces with erosion rate factors. Another alternative option for quantifying erosion effects is to perform micro abrasion controlled exposure studies, where rock surfaces are abraded at micron scales over long term controlled exposure periods, which can offer direct data on erosion and luminescence depth profile evolution.

In performing these erosion studies, it can be better determined how impactful erosion serves in altering depth profile forms, and it can assist in determining how to best quantify erosion to adjust exposure age calculations for applied study. Through understanding these properties, it can be evaluated how effective luminescence depth profiles can serve to calculate surface ages that are millennial aged or older, and whether luminescence depth profiles are better suited for

centennial or younger exposure ages, or in locations where surface erosion is minimal or negligible. It can also determine how effective luminescence depth profiles are for calculating erosion to be used for other surface exposure chronometers such as ^{10}Be, to better interpret surface exposure dating results.

In performing these physical experiments for both solar and sample specific parameters, the use of pure composition samples may be needed to begin characterizing these parameters for model development. Very pure quartzite or artificially produced silica products may be most useful for experimental study. Once a physically validated understanding of luminescence depth profile development can be quantified, more complex compositions can be experimented on to determine parameter impacts. The incorporation of mineral filtering can also be used to isolate OSL from quartz, or IRSL from feldspar, which may optimize depth profile measurements and improve assessments on depth profile evolution. Assessments should then also incorporate a diversity of sample compositions, surface coverages, and weathering features to then document possible variations in depth profile evolutions between these physical differences, and potentially provide insight on more effective parameterizations for affected samples.

These experiments have the potential to provide physical data concerning depth profile evolution, which can be used to modify or validate exposure dating model forms with more certainty than what curve fitting results have offered in exposure dating applications. Through these experiments, new insights can be made on the nature of luminescence depth profiles, and can provide the means to improve the accuracy, precision, and applicability of the dating technique.

4.3 Conclusion

Ages were calculated from three erratics of the Foothills Erratics Train using OSL exposure dating, using controlled exposure experiments to extrapolate parameters for light attenuation and luminescence bleaching rates from the rock surface, as no proximal rocks of known age were available for sampling. Spatially resolved OSL was utilized to produce high resolution OSL depth profiles from the sampled cores. The calculated ages of the erratic surfaces using OSL were between sub-annual to centennial ages, with one parameter set producing a millennial age, lower than the expected millennial-decamillennial ages calculated from the surfaces using cosmogenic nuclides. As such, the ages do not provide significant insight on the deposition of the Erratics Train members. Issues concerning depth profile scatter, the absence of test doses, and the use of solar simulated sunlight may have impacted the poor age fit results. Several other unaccounted for parameters are speculated to cause the age discrepancies of the surfaces. First, discrepancies of parameters fitted from weathered and nonweathered surfaces indicate that the presence of weathering rinds may complicate depth profile evolution beyond what is quantified using the first order model, and that multi-order parameterizations for luminescence bleaching and light attenuation may be needed for more accurate age calculations. Second is that the approach for parameterization through fitting depth profiles may provide inaccurate parameters. Physically measured values for light attenuation and luminescence bleaching were not equal to fitted parameter counterparts from the same Erratics Train samples, indicating that the parameters acquired from curve fitting may not reflect the true physical properties of the rock surface. As such, age calculations from fitted samples do not accurately reflect the modelled physical evolution of luminescence bleaching for the samples, and future applications may warrant the use of physical measures of parameters instead of relying on curve fitting for

extrapolation. Third is that processes of erosion are unaccounted for in the exposure age calculation, yet are likely to impact the shape and evolution of the depth profile form over decamillennial time. The estimated erosion rates for the erratic surfaces, if accurate, would cause the removal of most of the original depth profile form after thousands of years of exposure, with the modified depth profiles producing younger than expected ages for the erratic surfaces. As such, future applications concerning longer term exposure ages may need to consider metrics for erosion in evaluating the age calculations of sampled surfaces. Resultingly, applications of exposure dating are most suitable for ages under millennia timelines, to mitigate potential issues with the removal of OSL bleaching over millennial time due to erosion. Still, the results of the Erratics Train provide insightful results in helping configure adequate parameterizations for exposure dating applications using luminescence, and documenting the limits in quantifying exposure ages from luminescence.

4.4 References

Applied Photophysics Limited, 1982. 1 kW Solar Simulator (AM2 Radiation) Instruction Manual.

Balco, G., Stone, J. O., Lifton, N. A., & Dunai, T. J. (2008). A complete and easily accessible means of calculating surface exposure ages or erosion rates from 10Be and 26Al measurements. Quaternary geochronology, 3(3), 174-195.

Bartz, M., Peña, J., Grand, S., & King, G. E. (2022). Potential impacts of chemical weathering on feldspar luminescence dating properties. Geochronology Discussions, 2022, 1-23.

Bench, T., & Feathers, J. (2022). Trialing the application of controlled exposure experiments for optical exposure dating on quartzite quarry surfaces in Washington State. Radiation Measurements, 156, 106805.

Bench, T., Sanderson, D., Feathers, J., & Warfield, E. (2023). Investigating the use of two-dimensional OSL laser scanning instruments and energy-dispersive x-ray spectroscopy for OSL exposure dating. Radiation Measurements, 167, 106999.

Brill, D., May, S. M., Mhammdi, N., King, G., Burow, C., Wolf, D., ... & Brückner, H. (2020). OSL rock surface exposure dating as a novel approach for reconstructing transport histories of coastal boulders over decadal to centennial timescales. EGU General Assembly, EGU2020-18537. doi, 10.

Bullock, M. S., Larney, F. J., McGinn, S. M., & Olson, B. M. (1992, February). Influence of snow on wind erosion processes in the Chinook belt of southern Alberta. In Soils and Crops Workshop.

Bulur, E. (1996). An alternative technique for optically stimulated luminescence (OSL) experiment. Radiation Measurements, 26(5), 701-709.

Bulur, E., Bøtter-Jensen, L., & Murray, A. S. (2000). Optically stimulated luminescence from quartz measured using the linear modulation technique. Radiation Measurements, 32(5-6), 407-411.

Bulur, E. N. V. E. R., Kartal, E., & Saraç, B. E. (2014). Time-resolved OSL of natural zircon: A preliminary study. Radiation measurements, 60, 46-52.

Chapot, M. S., Sohbati, R., Murray, A. S., Pederson, J. L., & Rittenour, T. M. (2012). Constraining the age of rock art by dating a rockfall event using sediment and rock-surface luminescence dating techniques. Quaternary Geochronology, 13, 18-25.

Chen, Xiaoyan & Leng, Jinhua & Zhang, Dongsheng & He, Bobing. (2020). Study of modified potassium feldspar as a novel β-nucleating agent to the crystal morphology and properties of polypropylene. SN Applied Sciences. 2. 10.1007/s42452-020-2485-x.

Choi, J. H., Duller, G. A. T., Wintle, A. G., & Cheong, C. S. (2006). Luminescence characteristics of quartz from the Southern Kenyan Rift Valley: Dose estimation using LM-OSL SAR. Radiation Measurements, 41(7-8), 847-854.

Clark, J., Carlson, A. E., Reyes, A. V., Carlson, E. C., Guillaume, L., Milne, G. A., ... & Rood, D. H. (2022). The age of the opening of the Ice-Free Corridor and implications for the peopling of the Americas. Proceedings of the National Academy of Sciences, 119(14), e2118558119.

Clark-Balzan, L. & Schwenninger, J. L. First steps toward spatially resolved OSL dating with electron multiplying charge-coupled devices (EMCCDs): System design and image analysis. Radiat. Meas. 47, 797–802 (2012).

Cresswell, A. J., Carter, J., & Sanderson, D. C. W. (2018). Dose rate conversion parameters: Assessment of nuclear data. Radiation Measurements, 120, 195-201.

Durcan, J.A., King, G.E., Duller, G.A.T., 2015. DRAC: Dose rate and age calculator for trapped charge dating. Quaternary Geochronology, 28, 54-61.

Dyke, A. S. (2004). An outline of North American deglaciation with emphasis on central and northern Canada. Developments in quaternary sciences, 2, 373-424.

Dyke, A. S., & Prest, V. K. (1987). Late Wisconsinan and Holocene history of the Laurentide ice sheet. Géographie physique et Quaternaire, 41(2), 237-263.
Elkadi, J., King, G. E., Lehmann, B., & Herman, F. (2021). Reducing variability in OSL rock surface dating profiles. Quaternary Geochronology, 64, 101169.

Feathers, J. (2023). The Contributions of Luminescence Dating of Sediments to Understanding the First Settlement of the Americas. PaleoAmerica, 9(2), 81-114.

Freiesleben, T., Sohbati, R., Murray, A., Jain, M., Al Khasawneh, S., Hvidt, S., & Jakobsen, B. (2015). Mathematical model quantifies multiple daylight exposure and burial events for rock surfaces using luminescence dating. Radiation Measurements, 81, 16-22.

Freiesleben, T. H., Thomsen, K. J., & Jain, M. (2023). Novel luminescence kinetic models for rock surface exposure dating. Radiation Measurements, 160, 106877.

Froese, D., Young, J. M., Norris, S. L., & Margold, M. (2019). Availability and viability of the ice-free corridor and Pacific coast routes for the peopling of the Americas. SAA Archaeol. Rec, 19(3).

Fuhrmann, S., Meyer, M. C., Gliganic, L. A., & Obleitner, F. (2022). Testing the effects of aspect and total insolation on luminescence depth profiles for rock surface exposure dating. Radiation Measurements, 153, 106732.

Gallée, H., Van Yperselb, J. P., Fichefet, T., Marsiat, I., Tricot, C., & Berger, A. (1992). Simulation of the last glacial cycle by a coupled, sectorially averaged climate-ice sheet model: 2. Response to insolation and CO2 variations. Journal of Geophysical Research: Atmospheres, 97(D14), 15713-15740.

Gliganic, L. A., Meyer, M. C., Sohbati, R., Jain, M., & Barrett, S. (2019). OSL surface exposure dating of a lithic quarry in Tibet: Laboratory validation and application. Quaternary Geochronology, 49, 199-204.

Han, S., Löhr, S. C., Abbott, A. N., Baldermann, A., Farkaš, J., McMahon, W., ... & Owen, M. (2022). Earth system science applications of next-generation SEM-EDS automated mineral mapping. Frontiers in Earth Science, 10, 2244.

Hashimoto, T., Yokosaka, K., Habuki, H. & Hayashi, Y. Provenance search of dune sands using thermoluminescence colour images (TLCIs) from quartz grains. Int. J. Radiat. Appl. Instrumentation. Part 16, 3–10 (1989).

Jackson Jr, L. E., Phillips, F. M., Shimamura, K., & Little, E. C. (1997). Cosmogenic 36Cl dating of the Foothills erratics train, Alberta, Canada. Geology, 25(3), 195-198.

Jackson, Jr, L. E., Phillips, F. M., & Little, E. C. (1999). Cosmogenic 36Cl dating of the maximum limit of the Laurentide Ice Sheet in southwestern Alberta. Canadian Journal of Earth Sciences, 36(8), 1347-1356.

Jackson, L. E., Andriashek, L. D., & Phillips, F. M. (2011). Limits of successive Middle and Late Pleistocene continental ice sheets, interior plains of southern and central Alberta and adjacent areas. In Developments in Quaternary sciences (Vol. 15, pp. 575-589). Elsevier.

Jeong, G. Y., Cheong, C. S., & Choi, J. H. (2007). The effect of weathering on optically stimulated luminescence dating. Quaternary Geochronology, 2(1-4), 117-122.

Jeong, G. Y., & Choi, J. H. (2012). Variations in quartz OSL components with lithology, weathering and transportation. Quaternary Geochronology, 10, 320-326.

Lehmann, B., Valla, P. G., King, G. E., and Herman, F. (2018). Investigation of OSL surface exposure dating to reconstruct post-LIA glacier fluctuations in the French Alps (Mer de Glace, Mont Blanc massif). Quaternary Geochronology, 44:63–74

Lehmann, B., Herman, F., Valla, P. G., King, G. E., & Biswas, R. H. (2019). Evaluating post-glacial bedrock erosion and surface exposure duration by coupling in situ optically stimulated luminescence and 10 Be dating. Earth Surface Dynamics, 7(3), 633-662.

Luo, M., Chen, J., Liu, J., Qin, J., Owen, L. A., Han, F., ... & Li, Y. (2018). A test of rock surface luminescence dating using glaciofluvial boulders from the Chinese Pamir. Radiation Measurements, 120, 290-297.

Margold, M., Gosse, J. C., Hidy, A. J., Woywitka, R. J., Young, J. M., & Froese, D. (2019). Beryllium-10 dating of the Foothills Erratics Train in Alberta, Canada, indicates detachment of the Laurentide Ice Sheet from the Rocky Mountains at~ 15 ka. Quaternary Research, 92(2), 469-482.

Martin, L. , Sanderson, D. , Paling, S., Cresswell, A. and Murphy, S. (2022) Advancing dosimetry for dating environmental materials: development of an ultra-sensitive beta dosimeter system and potential for beta autoradiography. Radiation Measurements, 154, 106760. (doi: 10.1016/j.radmeas.2022.106760)

Martin, L. , Sanderson, D. , Paling, S., Cresswell, A. and Fitzgerald, S. (2023) Quantitative beta autoradiography of a heterogeneous granulite sample and implications for luminescence dating. Radiation Measurements, 168, 107001. (doi: 10.1016/j.radmeas.2023.107001

Meyer, M. C., Austin, P., & Tropper, P. (2013). Quantitative evaluation of mineral grains using automated SEM–EDS analysis and its application potential in optically stimulated luminescence dating. Radiation measurements, 58, 1-11.

Meyer, M. C., Gliganic, L. A., Jain, M., Sohbati, R., & Schmidmair, D. (2018). Lithological controls on light penetration into rock surfaces–Implications for OSL and IRSL surface exposure dating. Radiation Measurements, 120, 298-304.

Moayed, N. K., Sohbati, R., Murray, A. S., Rades, E. F., Fattahi, M., & Ruiz López, J. F. (2022). Rock surface luminescence dating of prehistoric rock art from central Iberia. Archaeometry.
Mountjoy, E. W. (1958). Jasper Area Alberta, a Source of the Foothills Erratics Train1. Bulletin of Canadian Petroleum Geology, 6(9), 218-226.

Munyikwa, K., Rittenour, T. M., & Feathers, J. K. (2017). Temporal constraints for the Late Wisconsinan deglaciation of western Canada using eolian dune luminescence chronologies from Alberta. Palaeogeography, Palaeoclimatology, Palaeoecology, 470, 147-165.

Munyikwa, K., Feathers, J. K., Rittenour, T. M., & Shrimpton, H. K. (2011). Constraining the Late Wisconsinan retreat of the Laurentide ice sheet from western Canada using luminescence ages from postglacial aeolian dunes. Quaternary Geochronology, 6(3-4), 407-422.

Munyikwa, K., Rittenour, T. M., & Feathers, J. K. (2017). Temporal constraints for the Late Wisconsinan deglaciation of western Canada using eolian dune luminescence chronologies from Alberta. Palaeogeography, Palaeoclimatology, Palaeoecology, 470, 147-165.

Murray, A. S., & Wintle, A. G. (2000). Luminescence dating of quartz using an improved single-aliquot regenerative-dose protocol. Radiation measurements, 32(1), 57-73.

Ou, X. J., Roberts, H. M., Duller, G. A. T., Gunn, M. D., & Perkins, W. T. (2018). Attenuation of light in different rock types and implications for rock surface luminescence dating. Radiation Measurements, 120, 305-311.

Pedersen, M. W., Ruter, A., Schweger, C., Friebe, H., Staff, R. A., Kjeldsen, K. K., ... & Willerslev, E. (2016). Postglacial viability and colonization in North America's ice-free corridor. Nature, 537(7618), 45-49.

Peng J, Li B, Wang C (2023). numOSL: Numeric Routines for Optically Stimulated Luminescence Dating. R package version 2.8, https://CRAN.R-project.org/package=numOSL.

Polymeris, G. S., Tsirliganis, N., Loukou, Z., & Kitis, G. (2006). A comparative study of the anomalous fading effects of TL and OSL signals of Durango apatite. physica status solidi (a), 203(3), 578-590.

Potter, B. A., Baichtal, J. F., Beaudoin, A. B., Fehren-Schmitz, L., Haynes, C. V., Holliday, V. T., ... & Surovell, T. A. (2018). Current evidence allows multiple models for the peopling of the Americas. Science Advances, 4(8), eaat5473.

Roberts, R. G., Spooner, N. A., & Questiaux, D. G. (1994). Palaeodose underestimates caused by extended-duration preheats in the optical dating of quartz. Radiation Measurements, 23(2-3), 647-653.

Sanderson, D.C.W., Carmichael, L., Murphy, S., Whitely, V., Scott, E. and Cresswell, A. (2001) Investigation of Statistical and Imaging Methods for Luminescence Detection of Irradiated Ingredients. Project Report. Food Standards Agency, London, UK. http://eprints.gla.ac.uk/58359/ Deposited on: 31 January 2012

Sanderson, DCW, Smillie M., McCullagh, R., , Feathers, J., Hauser, N. 2011. Surface exposure dating by luminescence : developing and testing models for surface bleaching rates and erosion rates. 13th International Conference on Luminescence and Electron Spin Resonance Dating, Torun, Poland.

Sanjurjo-Sanchéz, J., Alves, C., & Teixeira, D. (2013). Microscopy studies in support of OSL dating of mortars of historical buildings. Microscopy and Microanalysis, 19(S4), 115-116.

Sellwood, E. L., Guralnik, B., Kook, M., Prasad, A. K., Sohbati, R., Hippe, K., ... & Jain, M. (2019). Optical bleaching front in bedrock revealed by spatially-resolved infrared photoluminescence. Scientific reports, 9(1), 1-12.

Sellwood, E. L., Kook, M., & Jain, M. (2022a). A 2D imaging system for mapping luminescence-depth profiles for rock surface dating. Radiation Measurements, 150, 106697.

Sellwood, E. L., Kook, M., & Jain, M. (2022b). Investigating the potential of rock surface burial dating using IRPL and IRSL imaging. Radiation Measurements, 155, 106783.

Sengupta, M., Weekley, A., Habte, A., Lopez, A., & Molling, C. (2015). Validation of the National Solar Radiation Database (NSRDB)(2005-2012) (No. NREL/CP-5D00-64981). National Renewable Energy Lab.(NREL), Golden, CO (United States).

Sengupta, M., Xie, Y., Lopez, A., Habte, A., Maclaurin, G., & Shelby, J. (2018). The national solar radiation data base (NSRDB). Renewable and sustainable energy reviews, 89, 51-60.

Singarayer, J. S., & Bailey, R. M. (2003). Further investigations of the quartz optically stimulated luminescence components using linear modulation. Radiation Measurements, 37(4-5), 451-458.

Smillie, M. 2011. 5th Year Report: Progress Towards Surface Exposure Dating. Scottish Universities Environmental Research Centre. Glasgow, United Kingdon. Unpublished.

Sohbati, R., Murray, A. S., Jain, M., Buylaert, J. P., & Thomsen, K. J. (2011). Investigating the resetting of OSL signals in rock surfaces. Geochronometria, 38, 249-258.

Sohbati, R., Murray, A. S., Chapot, M. S., Jain, M., & Pederson, J. (2012). Optically stimulated luminescence (OSL) as a chronometer for surface exposure dating. Journal of Geophysical Research: Solid Earth, 117(B9).

Sohbati, R., Liu, J., Jain, M., Murray, A., Egholm, D., Paris, R., & Guralnik, B. (2018). Centennial-to millennial-scale hard rock erosion rates deduced from luminescence-depth profiles. Earth and Planetary Science Letters, 493, 218-230.

Timar-Gabor, A., Constantin, D., Buylaert, J. P., Jain, M., Murray, A. S., & Wintle, A. G. (2015). Fundamental investigations of natural and laboratory generated SAR dose response curves for quartz OSL in the high dose range. Radiation Measurements, 81, 150-156.

4.5 Appendix

A1 – Likelihood Plots of Erratic 3 Controlled Exposures, individual Cores

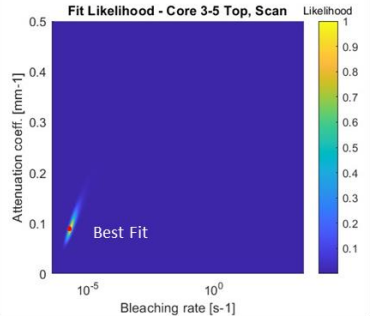

Median (Best Fit; -1σ, +1σ)

μ = 0.103 mm^{-1} (0.907; 0.023, 0.023)

$\overline{\sigma\varphi_0}$ = 2.37E-06 s^{-1} (2.87E-06; 8.08E-07, 1.23e-06)

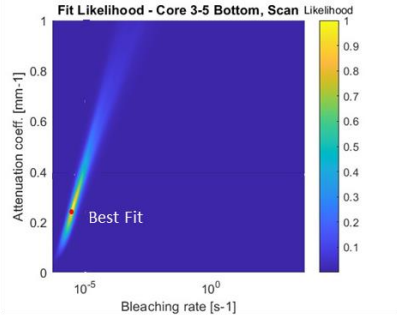

Median (Best Fit; -1σ, +1σ)

μ = 0.388 mm^{-1} (0.265; 0.196, 0.342)

$\overline{\sigma\varphi_0}$ = 1.01E-05 s^{-1} (3.39E-06; 8.13E-06, 7.80E-05)

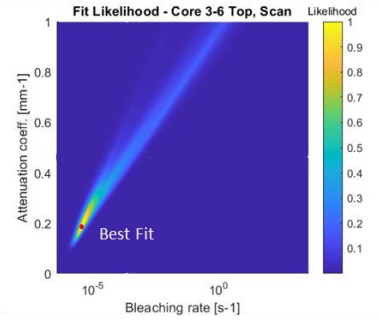

Median (Best Fit; -1σ, +1σ)

μ = 0.463 mm^{-1} (0.190; 0.186, 0.326)

$\overline{\sigma\varphi_0}$ = 2.25E-04 s^{-1} (3.89E-06; 2.18E-04, 1.76E-02)

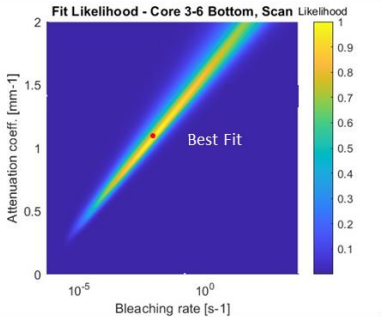

Median (Best Fit; -1σ, +1σ)

μ = 1.41 mm^{-1} (1.07; 0.448, 0.448)

$\overline{\sigma\varphi_0}$ = 0.149 s^{-1} (7.26E-03; 0.147, 11.2)

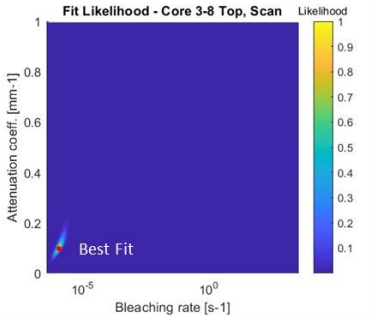

Median (Best Fit; -1σ, +1σ)

μ = 0.108 mm^{-1} (0.098; 0.019, 0.038)

$\overline{\sigma\varphi_0}$ = 1.22E-06 s^{-1} (1.10E-06; 2.33E-07, 6.45E-07)

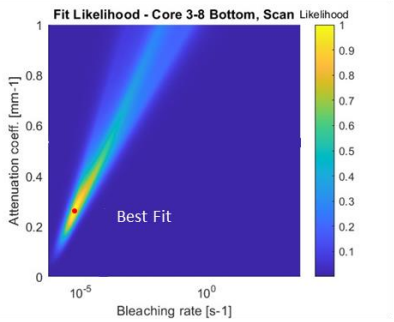

Median (Best Fit; -1σ, +1σ)

μ = 0.534 mm^{-1} (0.263; 0.238, 0.285)

$\overline{\sigma\varphi_0}$ = 8.27E-05 s^{-1} (5.95E-06; 6.98E-05, 8.43E-03)

A2 – Likelihood Plots of Erratic 6 Controlled Exposures, Individual Cores

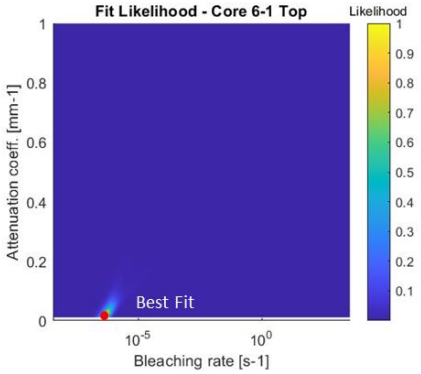

Median	(Best fit, -1σ, +1 σ)
μ = 0.035 mm^{-1}	(0.007; 0, 0.345)
$\overline{\sigma\varphi_0}$ = 9.91E-07 s^{-1}	(4.23E-07; 7.3E-07, 7.72E-04)

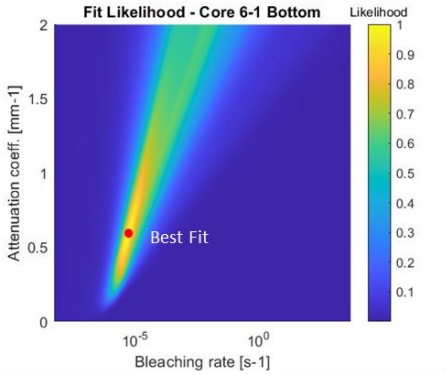

Median	(Best fit, -1σ, +1 σ)
μ = 1.35 mm^{-1}	(0.599; 0.599, 0.399)
$\overline{\sigma\varphi_0}$ = 1.55E-04 s^{-1}	(5.10E-06; 1.45E-04, 9.56E-03)

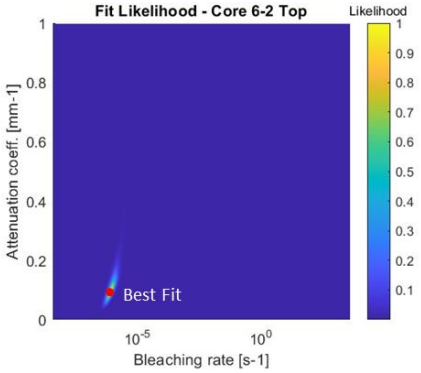

Median	(Best fit, -1σ, +1 σ)
μ = 0.09 mm^{-1}	(0.98; 0, 0.045)
$\overline{\sigma\varphi_0}$ = 9.28E-07 s^{-1}	(8.31E-07; 3.02E-07, 2.28-07)

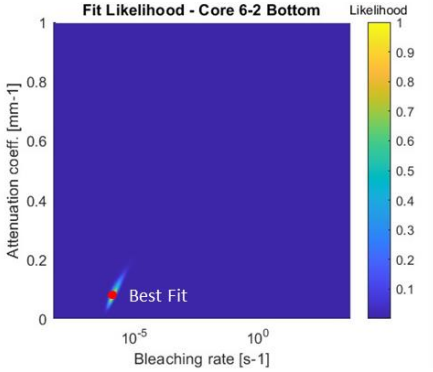

Median	(Best fit, -1σ, +1 σ)
μ = 0.0871 mm^{-1}	(0.077; 0.0299, 0.0299)
$\overline{\sigma\varphi_0}$ = 1.71E-06 s^{-1}	(1.27E-06; 6.94E-07, 1.17E-06)

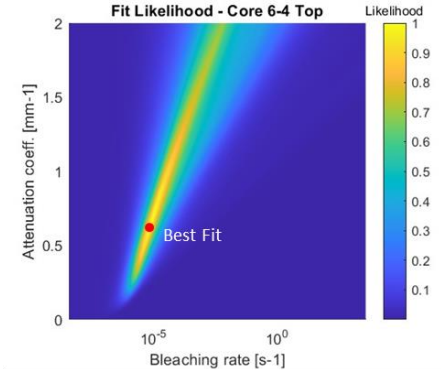

Median	(Best fit, -1σ, +1 σ)
μ = 1.58 mm^{-1}	(0.678; 0.046, 0.046)
$\overline{\sigma\varphi_0}$ = 6.42E-04 s^{-1}	(9.10E-06; 6.21E-04, 5.21E-03)

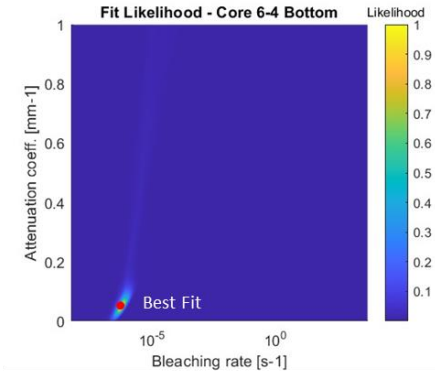

Median	(Best fit, -1σ, +1 σ)
μ = 0.076 mm^{-1}	(0.052; 0.0499, 0.499)
$\overline{\sigma\varphi_0}$ = 9.51E-07 s^{-1}	(6.05E-07; 5.06E-07, 3.4E-06)

A3 – Likelihood Plots of Erratic 8 Controlled Exposures, Individual Cores

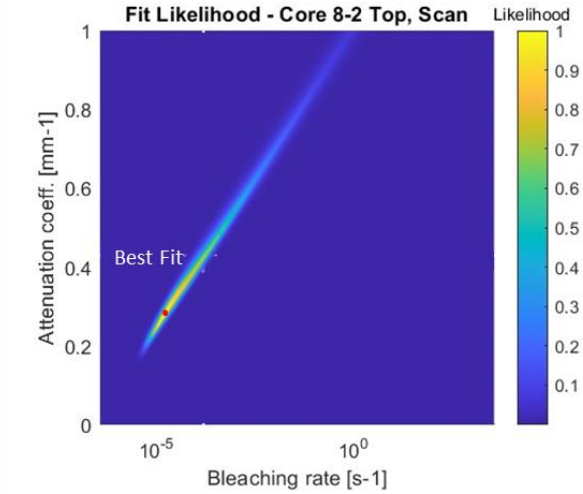

Median (Best fit, -1σ, +1 σ)

μ = 0.429 mm^{-1} (0.273; 0.127, 0.254)

$\overline{\sigma\varphi_0}$ = 1.54E-04 s^{-1} (1.42E-05; 1.19E-04, 5.88E-03)

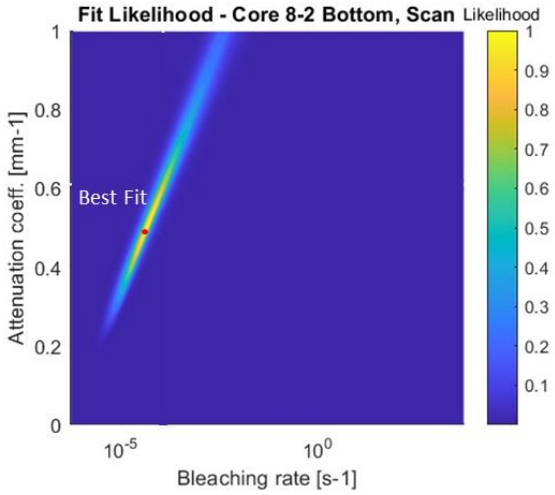

Median (Best fit, -1σ, +1 σ)

μ = 0.610 mm^{-1} (0.504; 0.245, 0.163)

$\overline{\sigma\varphi_0}$ = 1.15E-04 s^{-1} (4.66E-05; 9.14E-05, 8.25E-04)

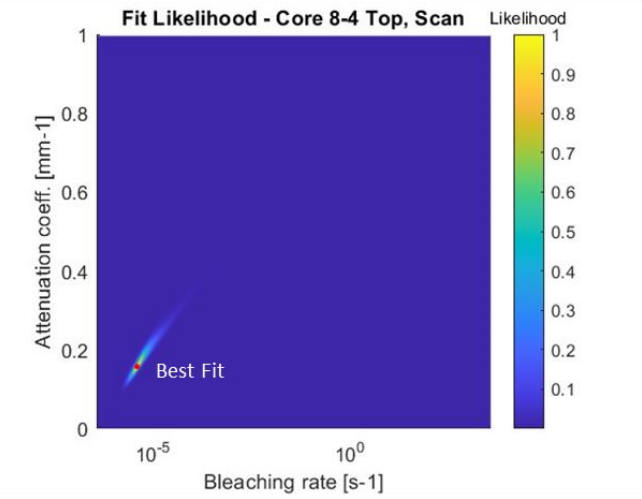

Median (Best fit, -1σ, +1 σ)

μ = 0.173 mm^{-1} (0.156; 0.037, 0.037)

$\overline{\sigma\varphi_0}$ = 5.67E-06 s^{-1} (3.99E-06; 2.81E-06, 5.58E-06)

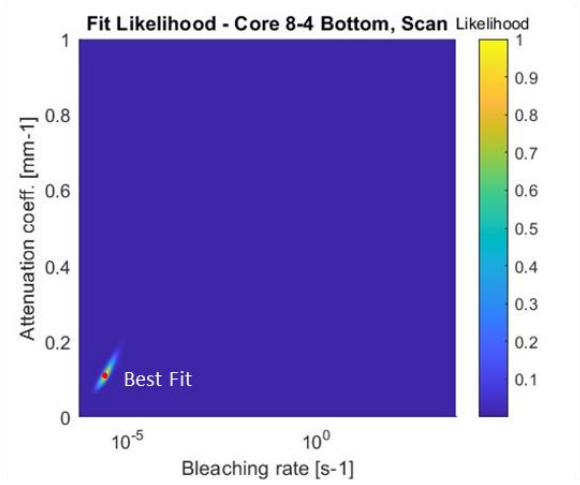

Median (Best fit, -1σ, +1 σ)

μ = 0.107 mm^{-1} (0.113; 0.011, 0.033)

$\overline{\sigma\varphi_0}$ = 2.53E-06 s^{-1} (2.70E-06; 4.06E-07, 1.06E-06)

A4 – Parameter Likelihood Plots of Cumulative Core Fits from Controlled Exposures – Top and Bottom Samples, of Erratics 3, 6, and 8

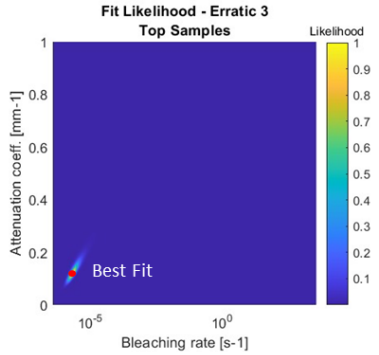

Median	(Best fit, -1σ, +1 σ)
μ = 0.130 mm^{-1}	(0.119; 0.042, 0.042)
$\overline{\sigma\varphi_0}$ = 2.39E-06 s^{-1}	(1.99E-06; 1.16E-06, 2.27E-06)

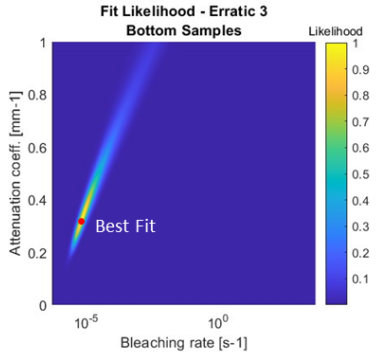

Median	(Best fit, -1σ, +1 σ)
μ = 0.509 mm^{-1}	(0.334; 0.170, 0.256)
$\overline{\sigma\varphi_0}$ = 2.57E-05 s^{-1}	(7.19E-06; 2.02E-05, 3.11E-04)

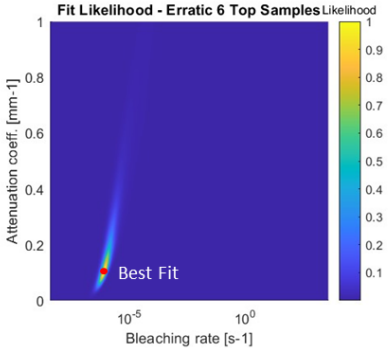

Median	(Best fit, -1σ, +1 σ)
μ = 0.177 mm^{-1}	(0.101; 0.099, 0.199)
$\overline{\sigma\varphi_0}$ = 1.44E-06 s^{-1}	(7.96E-07; 6.18E-07, 1.08E-06)

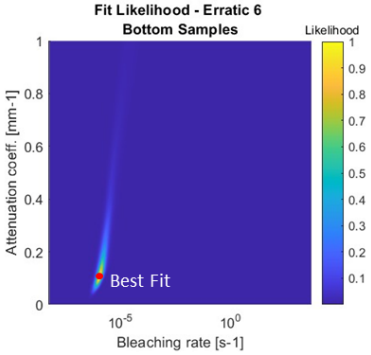

Median	(Best fit, -1σ, +1 σ)
μ = 0.15 mm^{-1}	(0.102 ; 0.049, 0.291)
$\overline{\sigma\varphi_0}$ = 1.16E-06 s^{-1}	(1.03E-06; 3.50E-07, 2.25E-06)

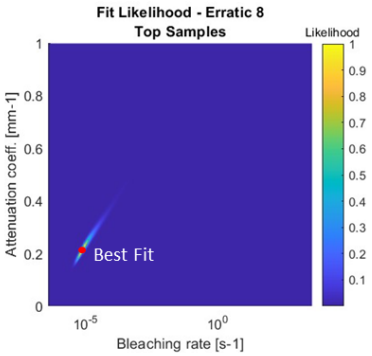

Median	(Best fit, -1σ, +1 σ)
μ = 0.238 mm^{-1}	(0.206; 0.037, 0.037)
$\overline{\sigma\varphi_0}$ = 1.19E-05 s^{-1}	(6.47E-06; 5.26E-06, 9.43E-06)

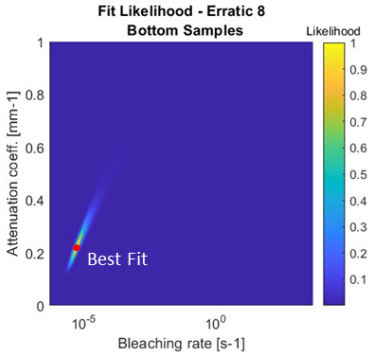

Median	(Best fit, -1σ, +1 σ)
μ = 0.25 mm^{-1}	(0.223; 0.045, 0.133)
$\overline{\sigma\varphi_0}$ = 7.22E-06 s^{-1}	(5.60E-06; 3.01E-06, 1.4E-05)

A5 – Parameter Likelihood Plots of Samples 3-7, 6-3, and 8-3, using ^{10}Be erosionless ages from Margold et al. (2019).

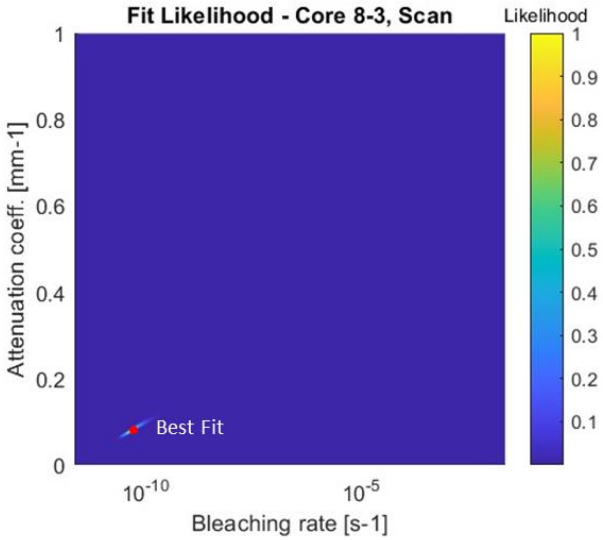

Fitted age: 15.1 ka

Median	(Best fit, -1σ, +1 σ)
μ = 0.084 mm^{-1}	(0.079; 0.014, 0.008)
$\overline{\sigma\varphi_0}$ = 5.19E-11 s^{-1}	(1.57E-11; 1.48E-11, 6.19E-11)

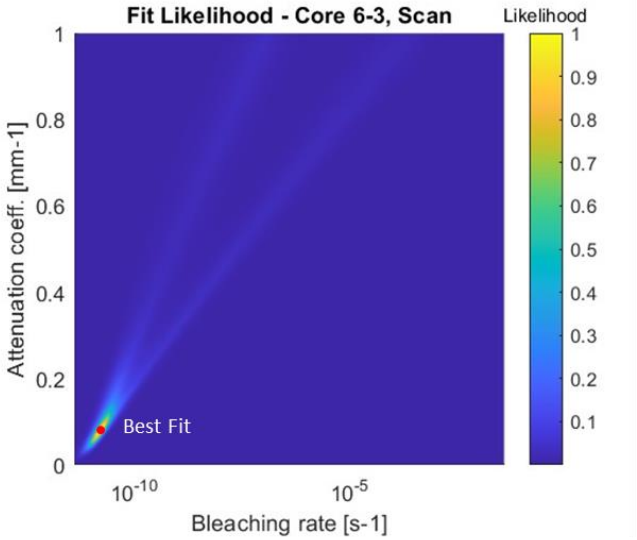

Fitted age: 8.2 ka

Median	(Best fit, -1σ, +1 σ)
μ = 0.281 mm^{-1}	(0.083; 0.496, 0.198)
$\overline{\sigma\varphi_0}$ = 2.14E-10 s^{-1}	(1.57E-11; 5.51E-08, 2.01E-10)

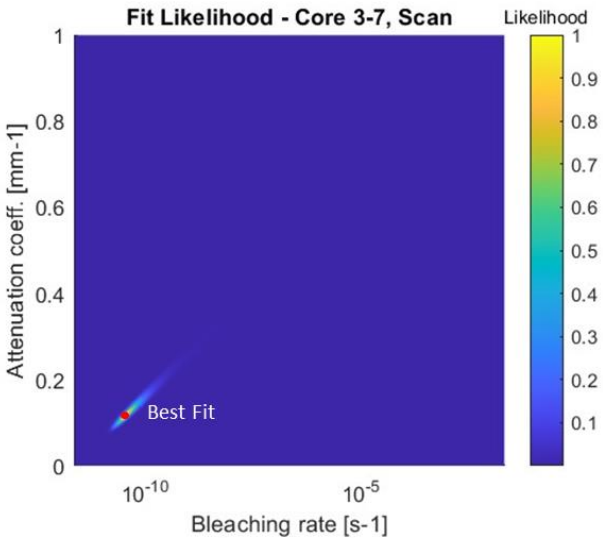

Fitted age: 14.7 ka

Median	(Best fit, -1σ, +1 σ)
μ = 0.103 mm^{-1}	(0.094; 0.014, 0.021)
$\overline{\sigma\varphi_0}$ = 2.45E-11 s^{-1}	(2.37E-11; 1.01E-11, 3.89E-12)

A6 – Age distributions of Erratic 3-7, using controlled exposed parameters of individual cores from Erratic 3. Best fit calculation likelihood plot shown. Median parameterization conducted separately but will follow the plotted distribution similarly.

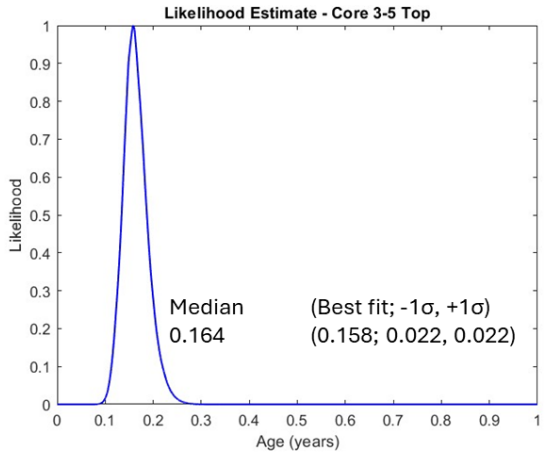

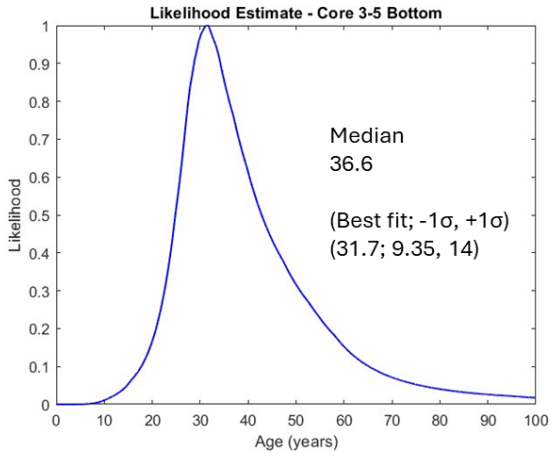

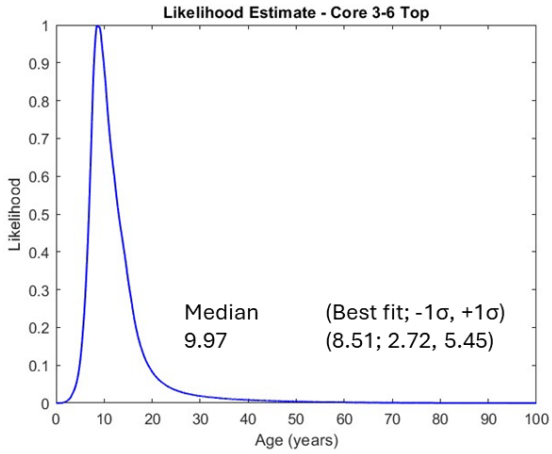

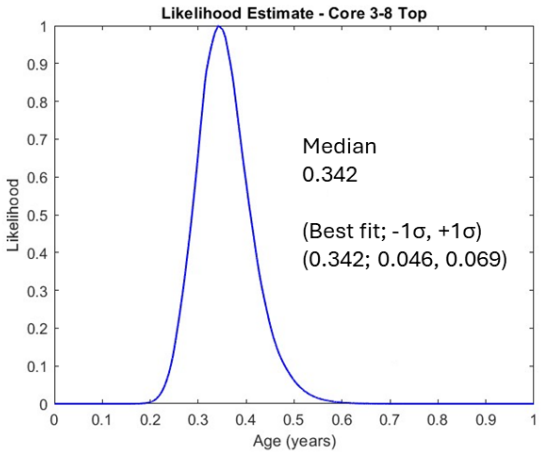

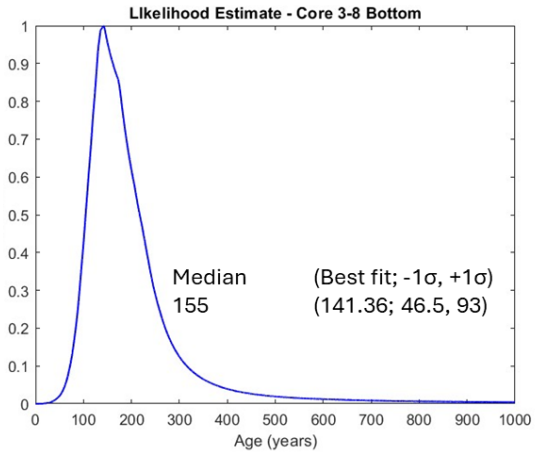

A6a – Depth profile age plots of Erratic 3 (core 3-7) individual core parameters

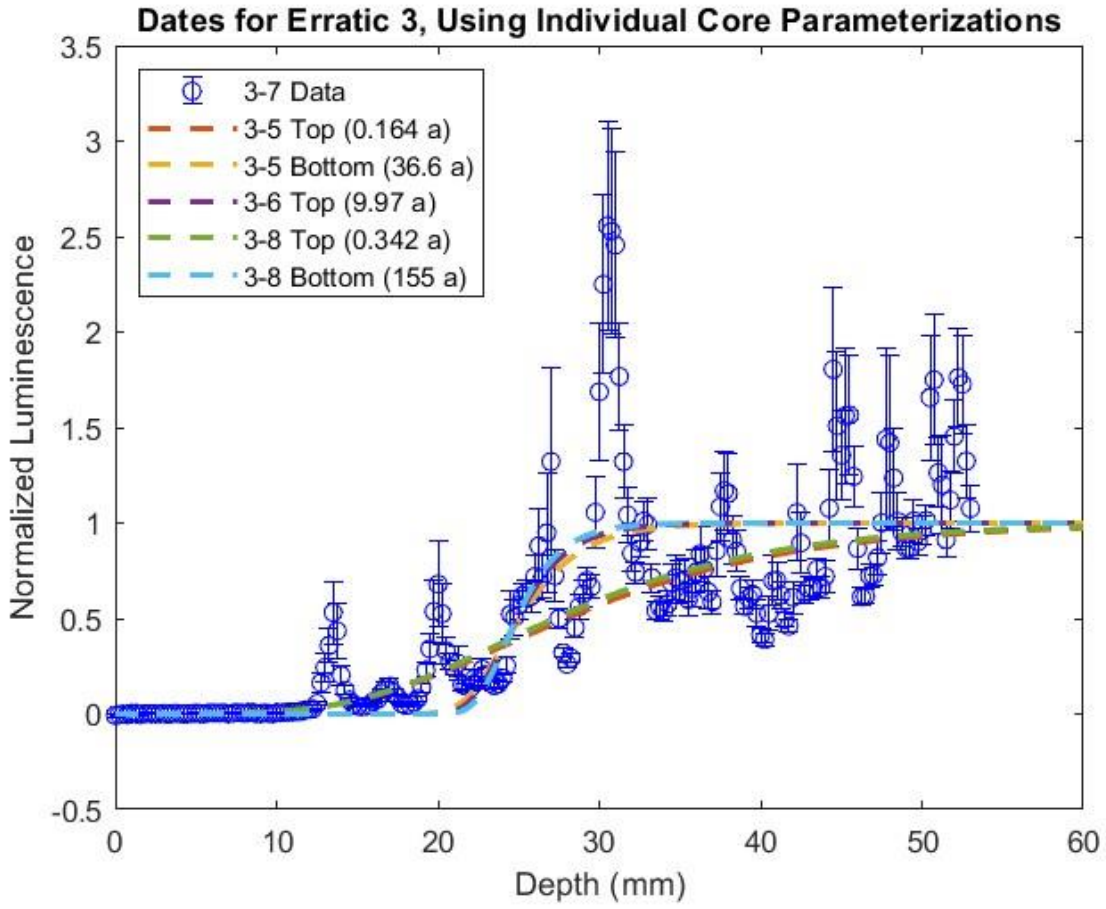

A7 – Age Distribution of Erratic 6-3, using controlled exposed parameters of individual cores from Erratic. Best fit calculation likelihood plot shown. Median parameterization conducted separately but will follow the plotted distribution similarly.

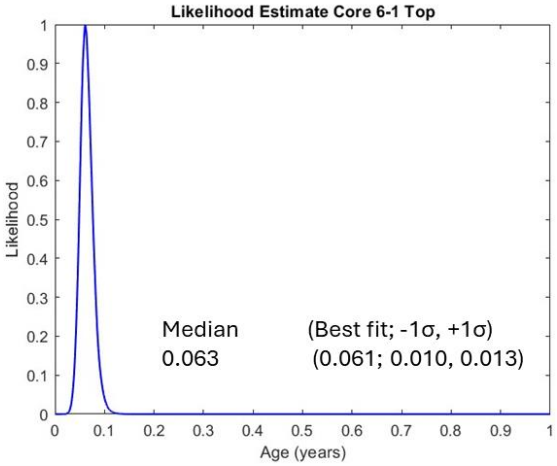

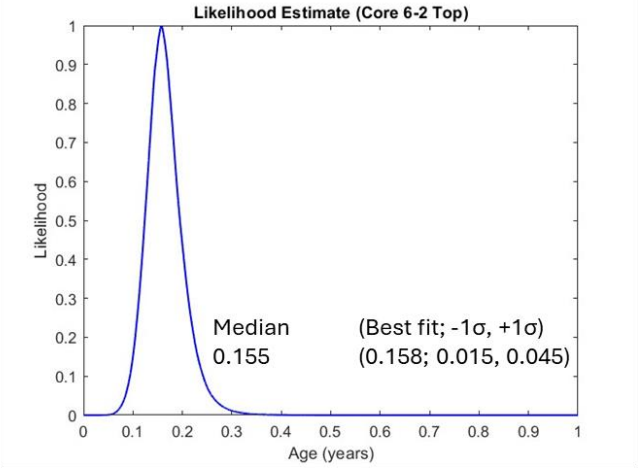

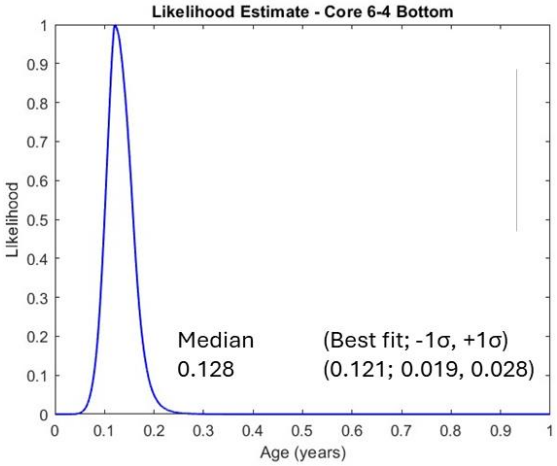

A7a – Depth profile age plots of Erratic 6 (Core 6-3) using individual core parameterizations

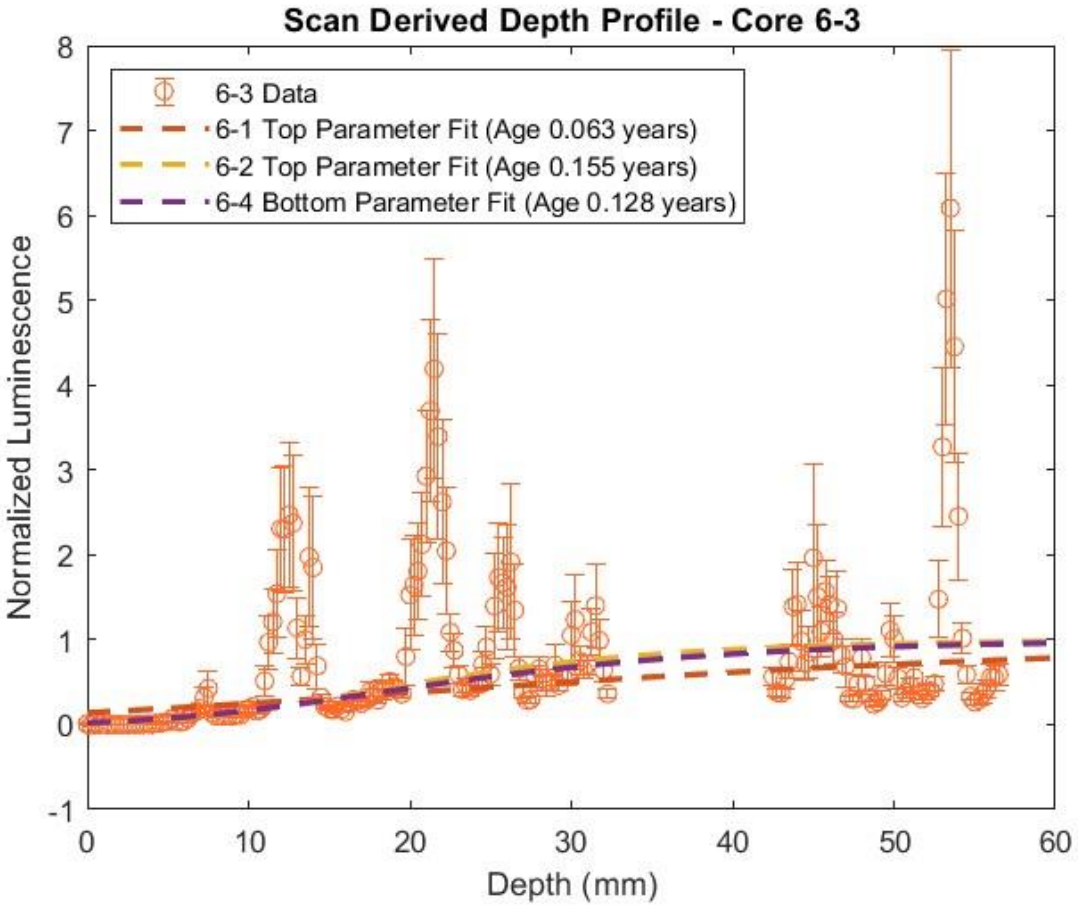

A8 – Age Distributions of Core 8-3, using controlled exposed parameters of individual cores from Erratic 8. Best fit calculation likelihood plot shown. Median parameterization conducted separately but will follow the plotted distribution similarly.

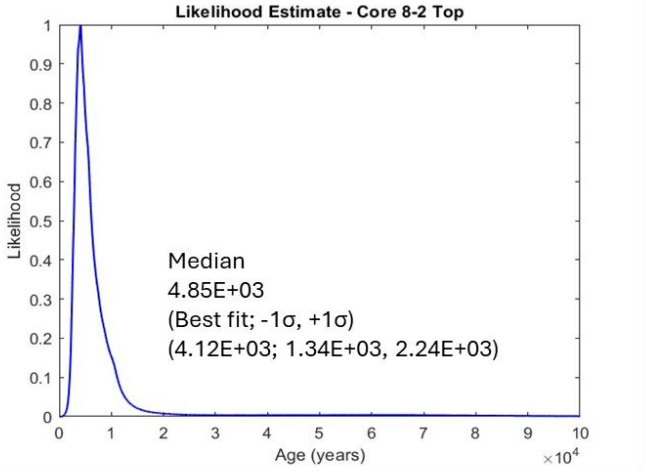

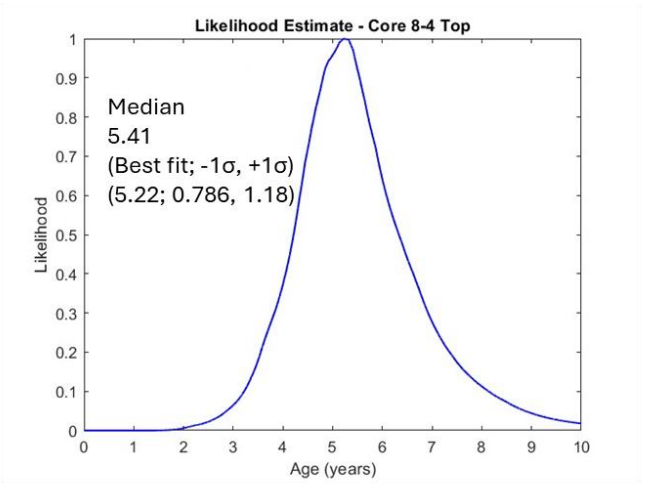

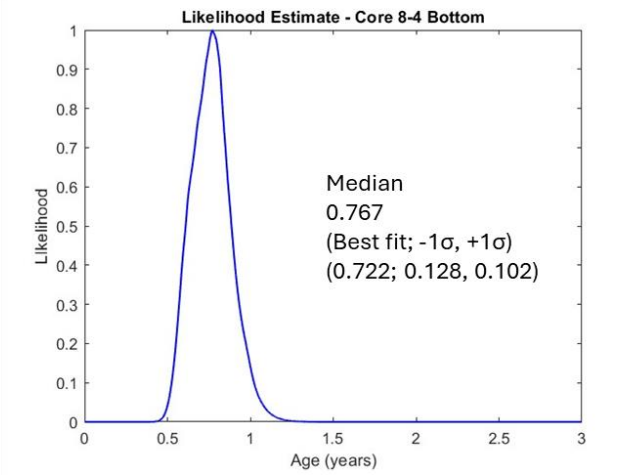

A8a – Depth profile age plots of Erratic 8 (core 8-3), using individual core parameterizations

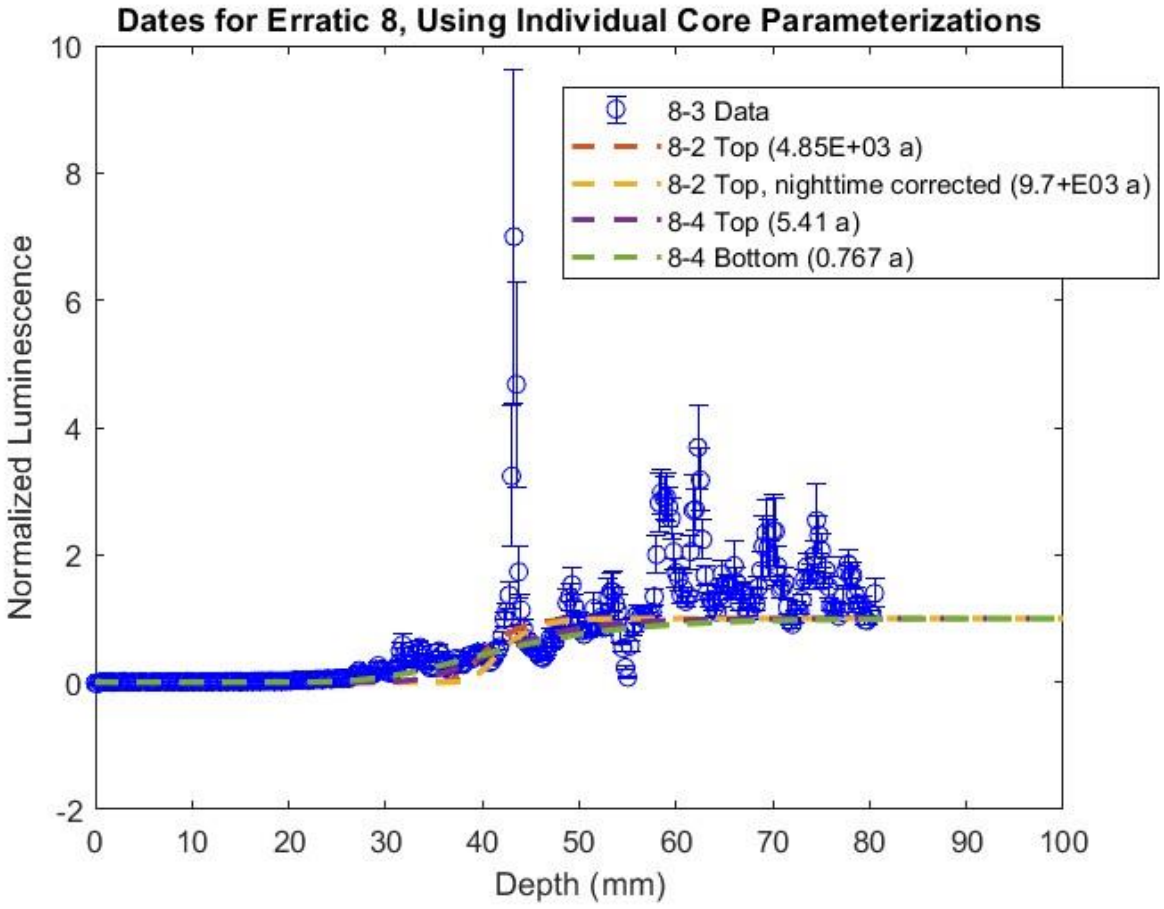

A9 – Age Distributions of Core 3-7, using cumulative controlled exposed core fits from Erratic 3 (Top core parameters, Bottom core parameters). Best fit calculation likelihood plot shown. Median parameterization conducted separately but will follow the plotted distribution similarly.

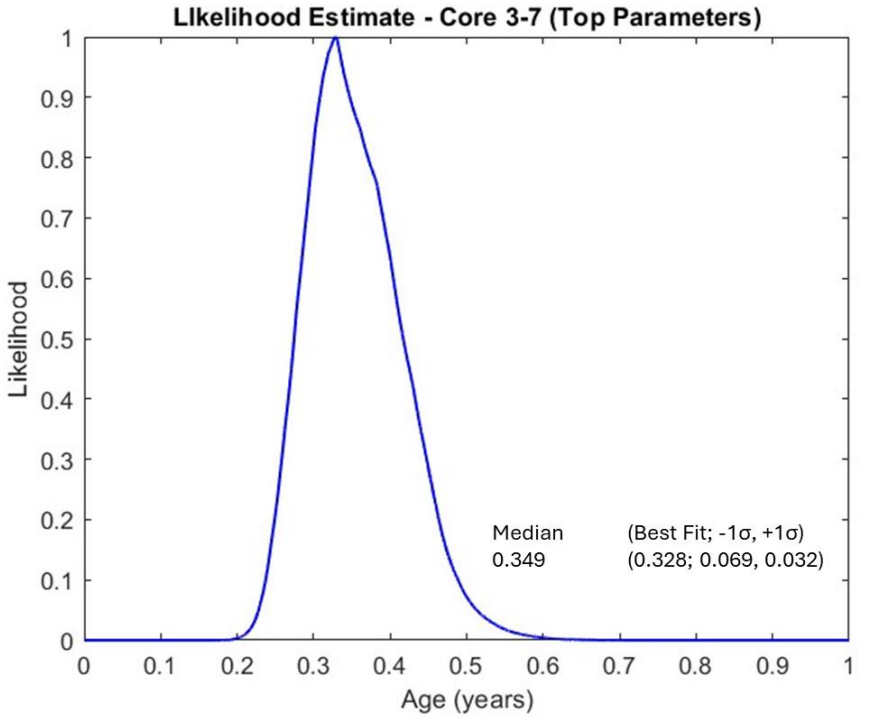

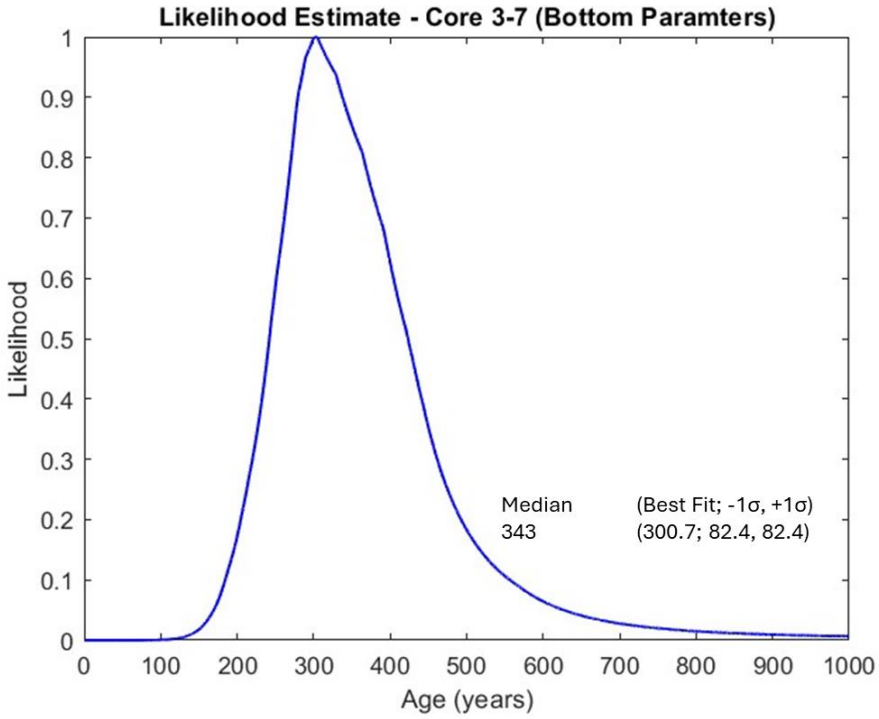

A10 – Age Distributions of Core 6-3, using cumulative controlled exposed core fits from Erratic 6 (Top core parameters, Bottom core parameters). Best fit calculation likelihood plot shown. Median parameterization conducted separately but will follow the plotted distribution similarly.

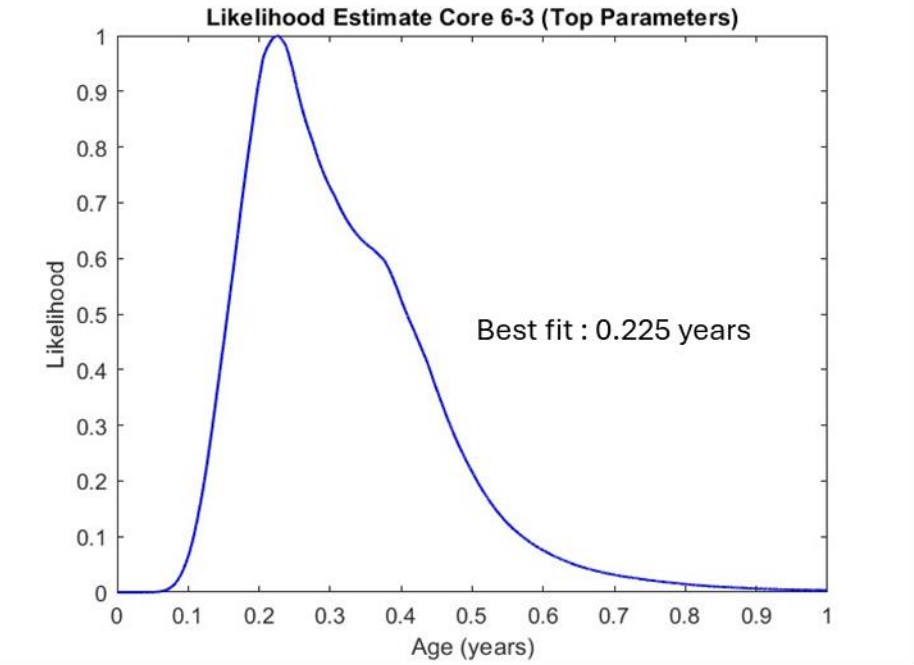

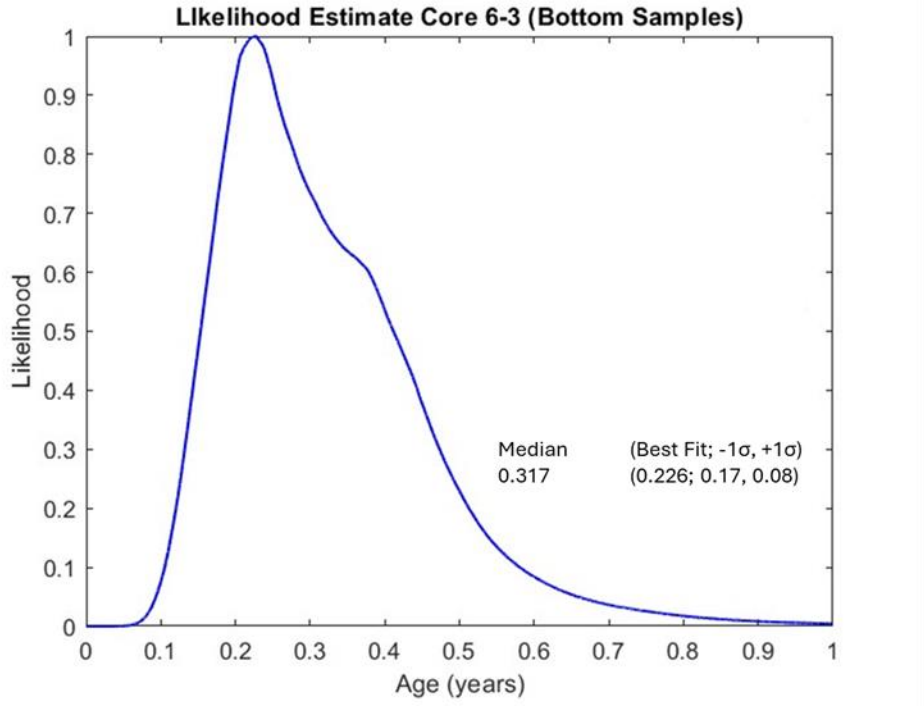

A11 – Age Distributions of Core 8-3, using cumulative controlled exposed core fits from Erratic 8 (Top core parameters, Bottom core parameters). Best fit calculation likelihood plot shown. Median parameterization conducted separately but will follow the plotted distribution similarly.

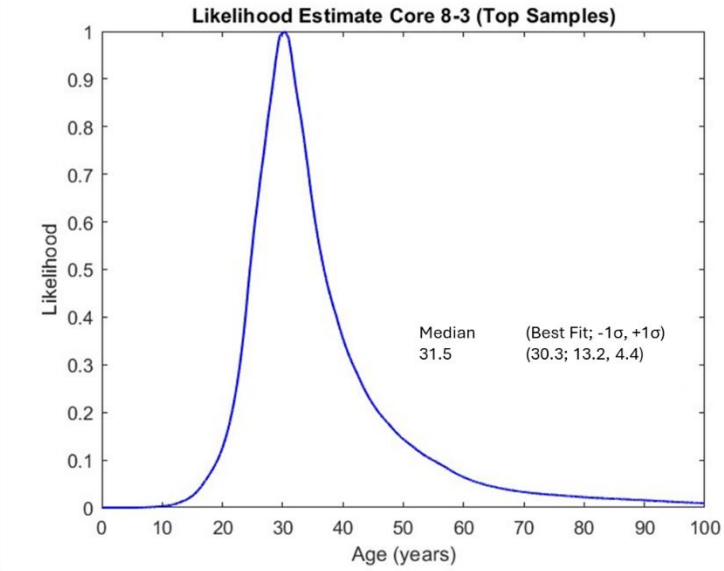

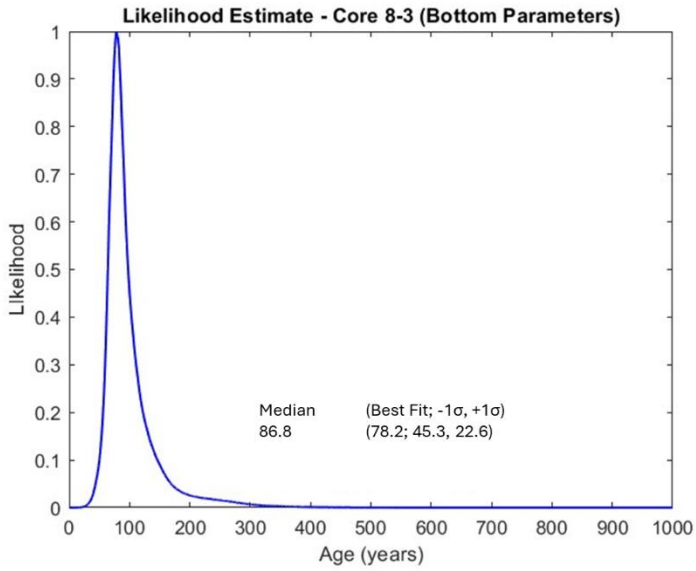

A12 – Mineral Maps

Thin sections 3-5 Top, 3-5 Bottom, 3-7 Top, 3-7 Bottom (not plotted in experiment, but scanned), 6-3, and 8-3 were produced at the University of Massachusetts, Amherst microprobe

facility. The percentage values of non-quartz mineralogy for each thin section were estimated by identifying regions of element maps which express the highest general Si compositions of the sample, denoting areas greater than 80% of measured relative intensity of the scan. Using this technique, sample 3-1 Top is estimated to have a quartz concentration at 66% SiO_2, while sample 3-5 Bottom is estimated to have 76% SiO_2, 3-5 Top at 65% SiO_2, 3-7 Bottom at 75% SiO_2, 3-7 Top at 70% SiO_2, 6-3 at 78% SiO_2, and 8-3 at 85% SiO_2. The remaining minerals in the samples host concentrations of Mg, Al, and lesser intensities of Na and Mg. Uniquely, an Mg bearing cement is often measured in between major mineral components in these samples. With respect to metamorphic texture, each sample displays non-foliated morphology, with the exception of sample 3-7 Top, which displays perhaps minor signs of foliation in the central region of the sample.

The higher presence of non-quartz mineralogy in the samples complicates the use of OSL for exposure dating applications of the Erratics Train, given the OSL dosimetry properties of various non-quartz minerals will generally be less predictable for dating than if mostly quartz was measured (Ou et al. 2018; Meyer et al. 2013; Polymeris et al. 2019; Bulur et al. 2014; Sanjurjo-Sanchéz et al. 2013).

Non-quartz mineral heterogeneity could be isolated and removed from OSL datasets using mineral maps, as discussed in Section 4. However, in preparing the thin sections from the samples, the original dimensions of the samples were damaged, preventing the ability to accurately align mineralogy and OSL scan dimensions using the mineral maps. Still, the maps provide insight on the potential sources of OSL variability present in the sample scans.

Erratics 3, 6, and 8 were purported to be quartzite in Margold et al. (2019). Thin section element maps from the OSL scanned erratics samples, however, present more non-quartz mineralogy (> 10%) than would warrant a quartzite classification (Figure 2). Instead, a more general metamorphic sandstone classification would serve appropriate for the samples.

Erratic 3

Sample 3-1 Top
Total pixel counts: 610132

Si

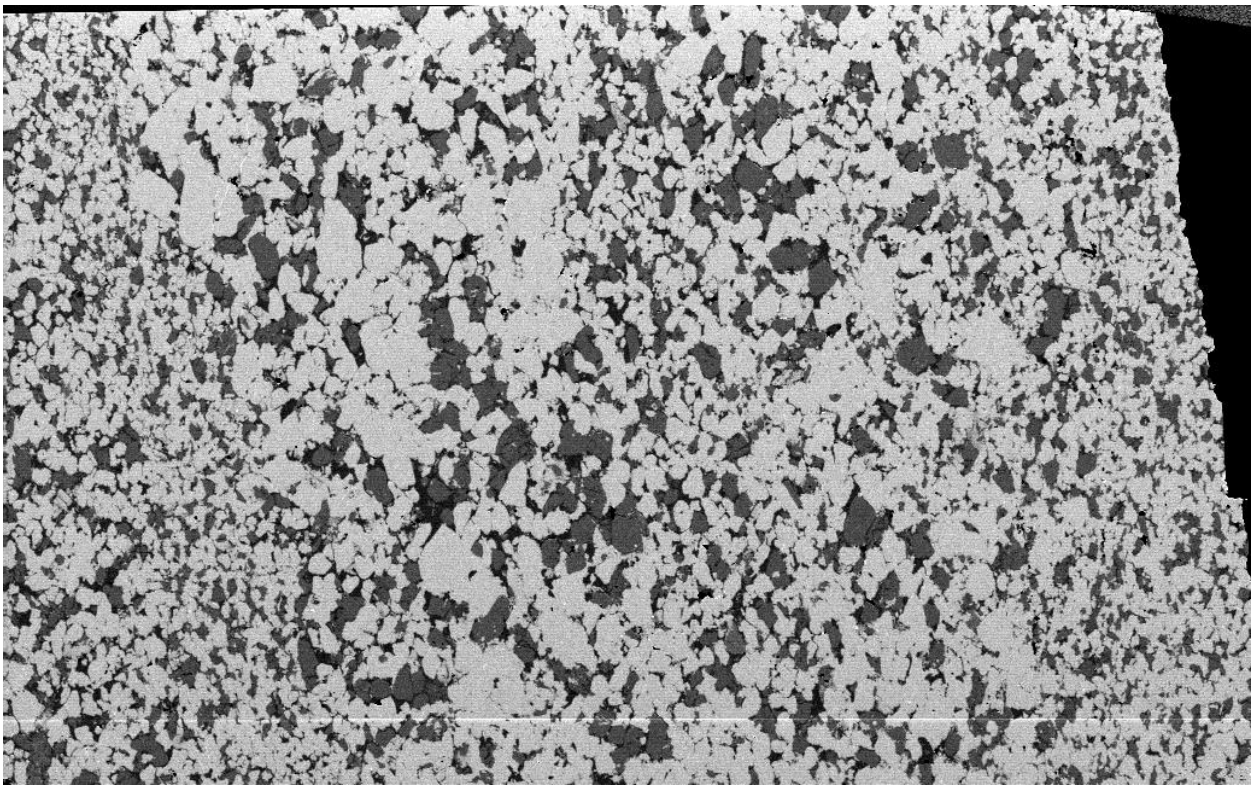

Pixels: 401676 / 610132

Percentage: ~66%

Al

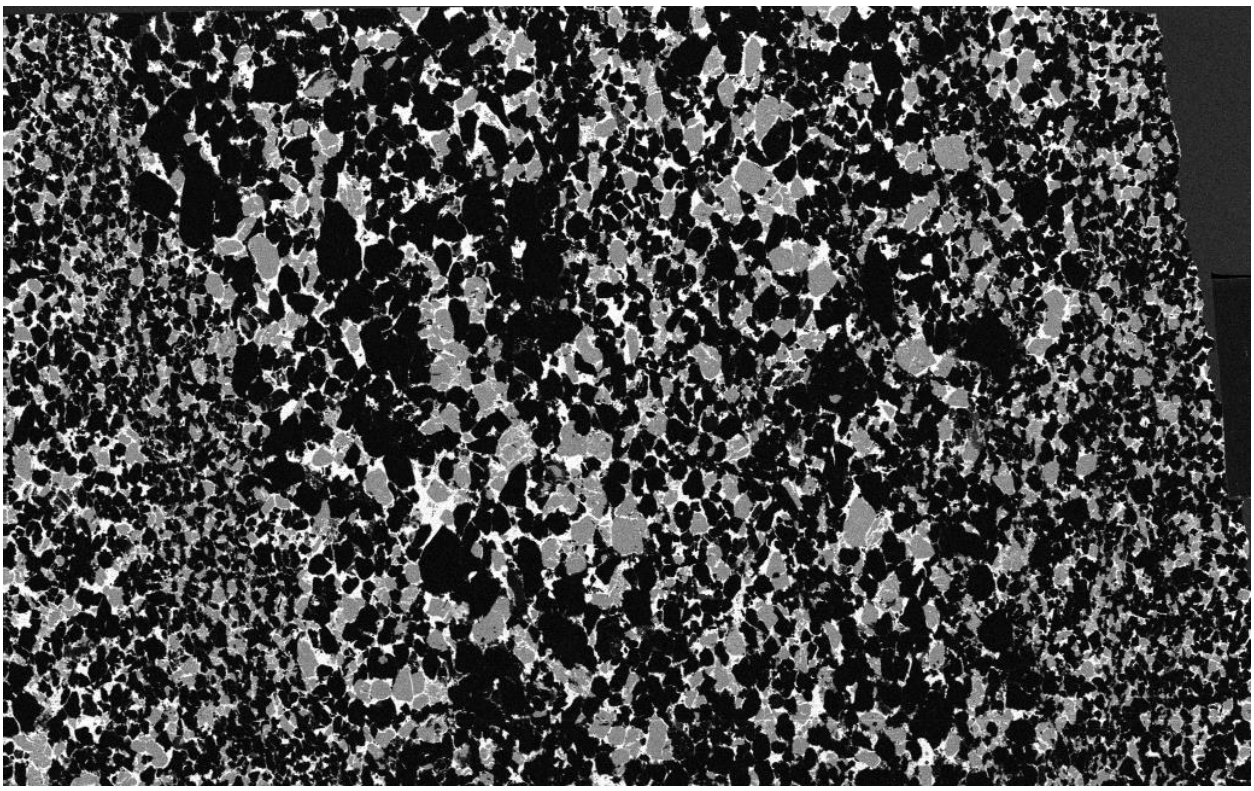

Pixels: 231805

231805/610132 = ~38%

K

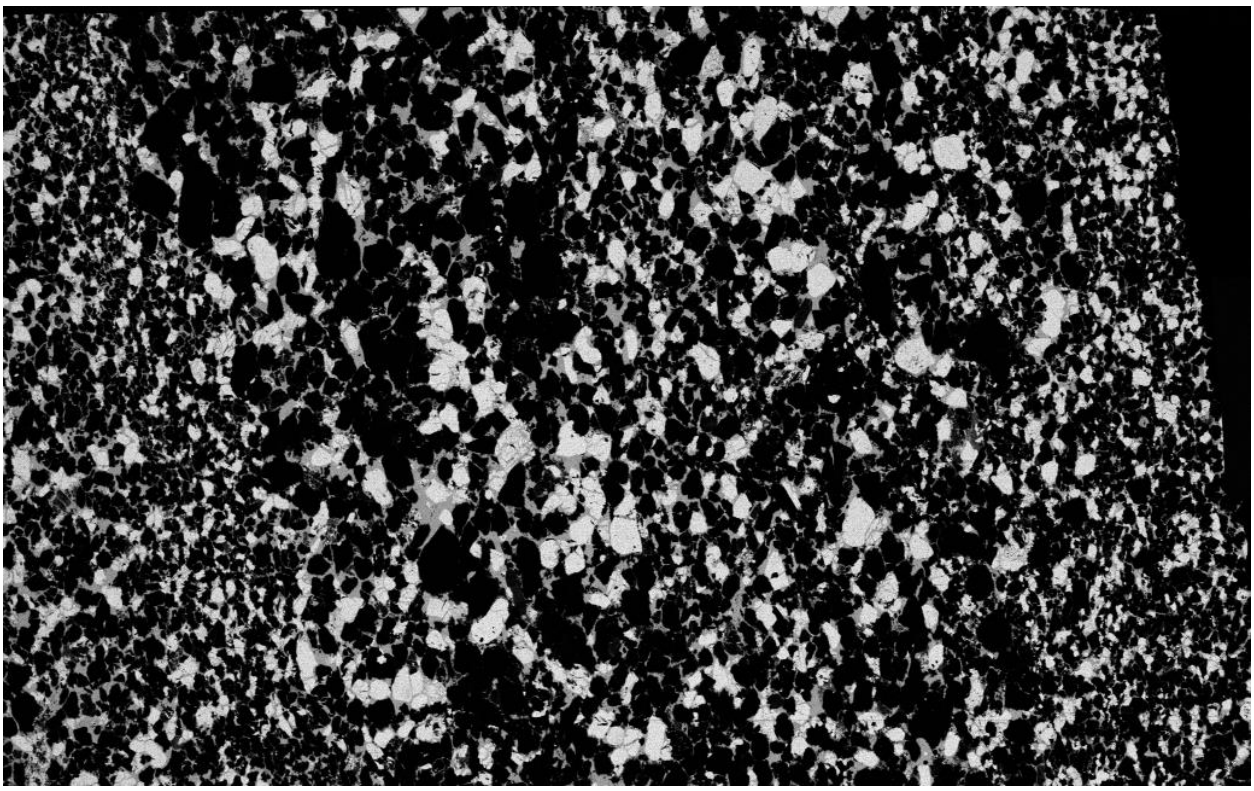

Pixels: 176795

176795/610132 = ~29%

Mg

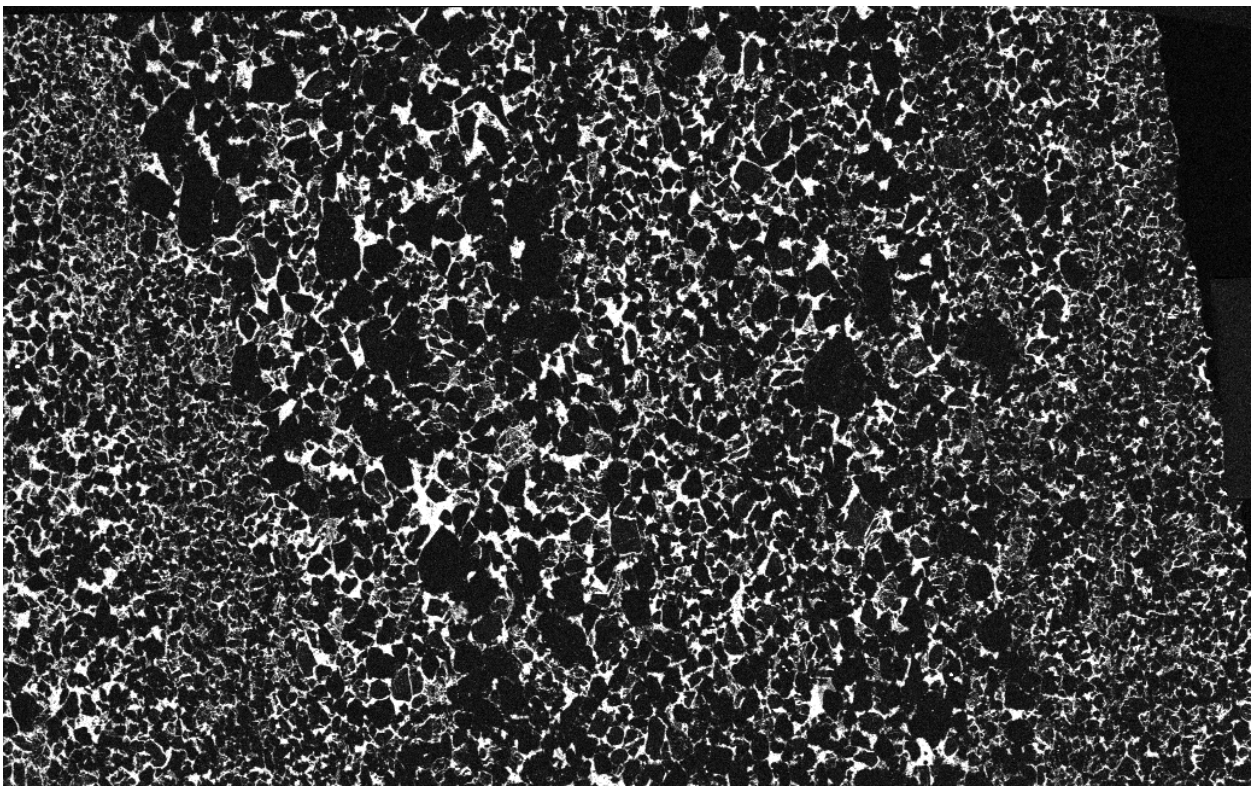

39093

122430/610132 = 20%

Na

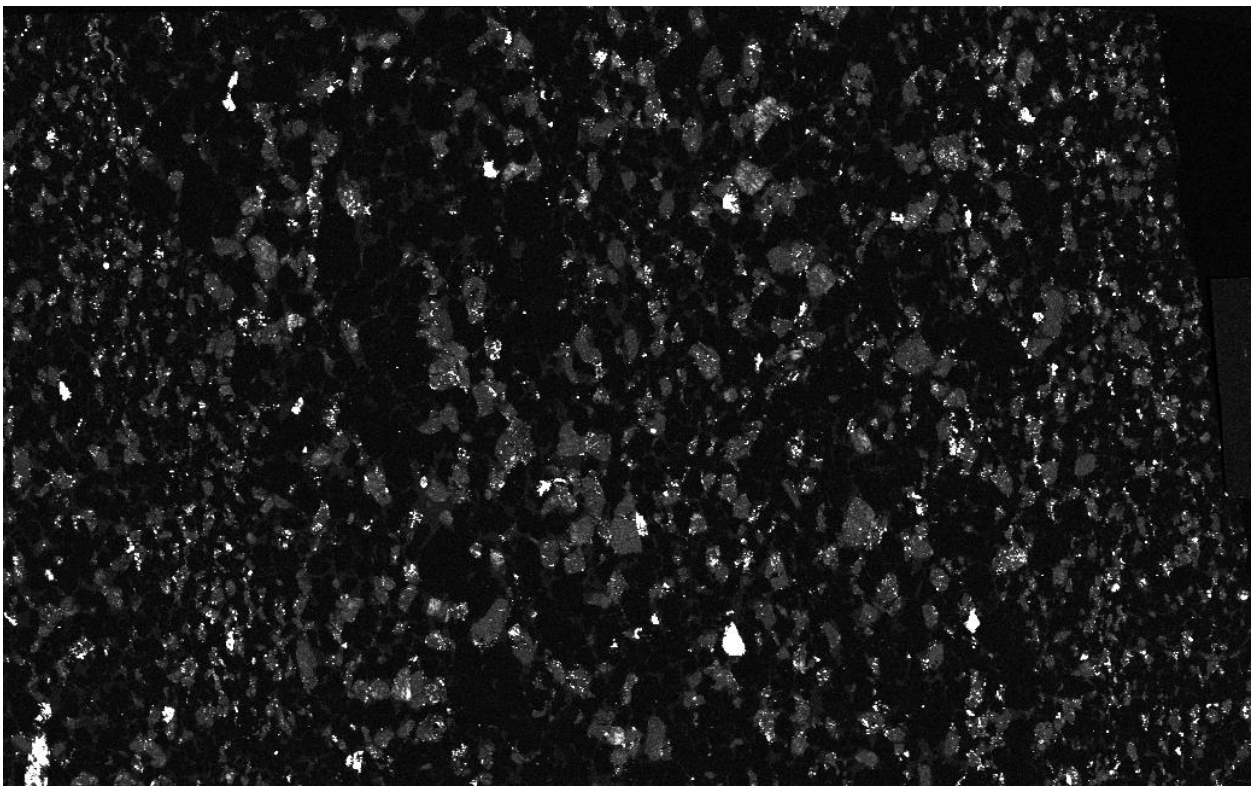

132144/610132 = 22%

Sample 3-5 Bottom

Total counts: 698700

Si

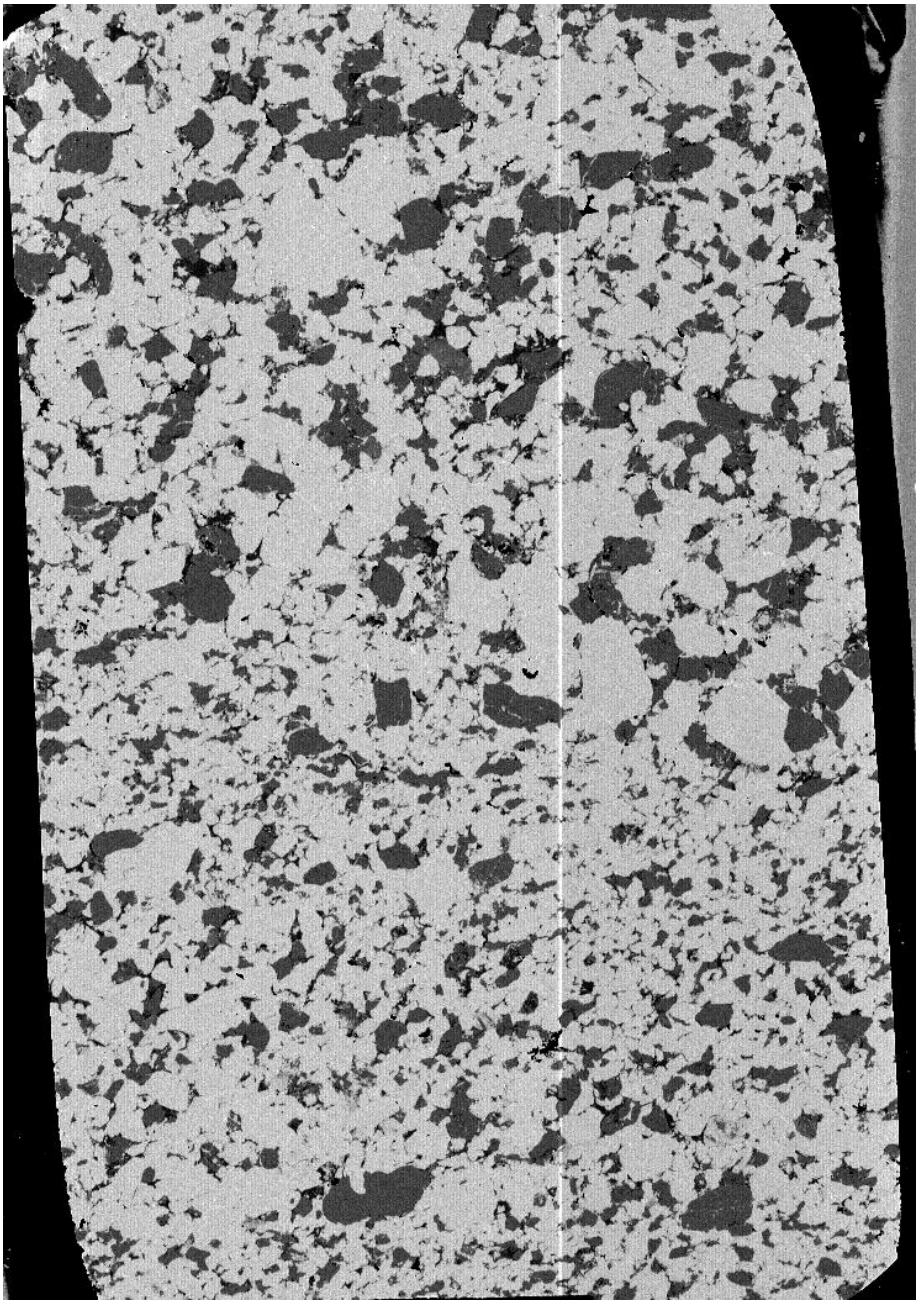

530269

530269/ 698700 = ~76%

Al

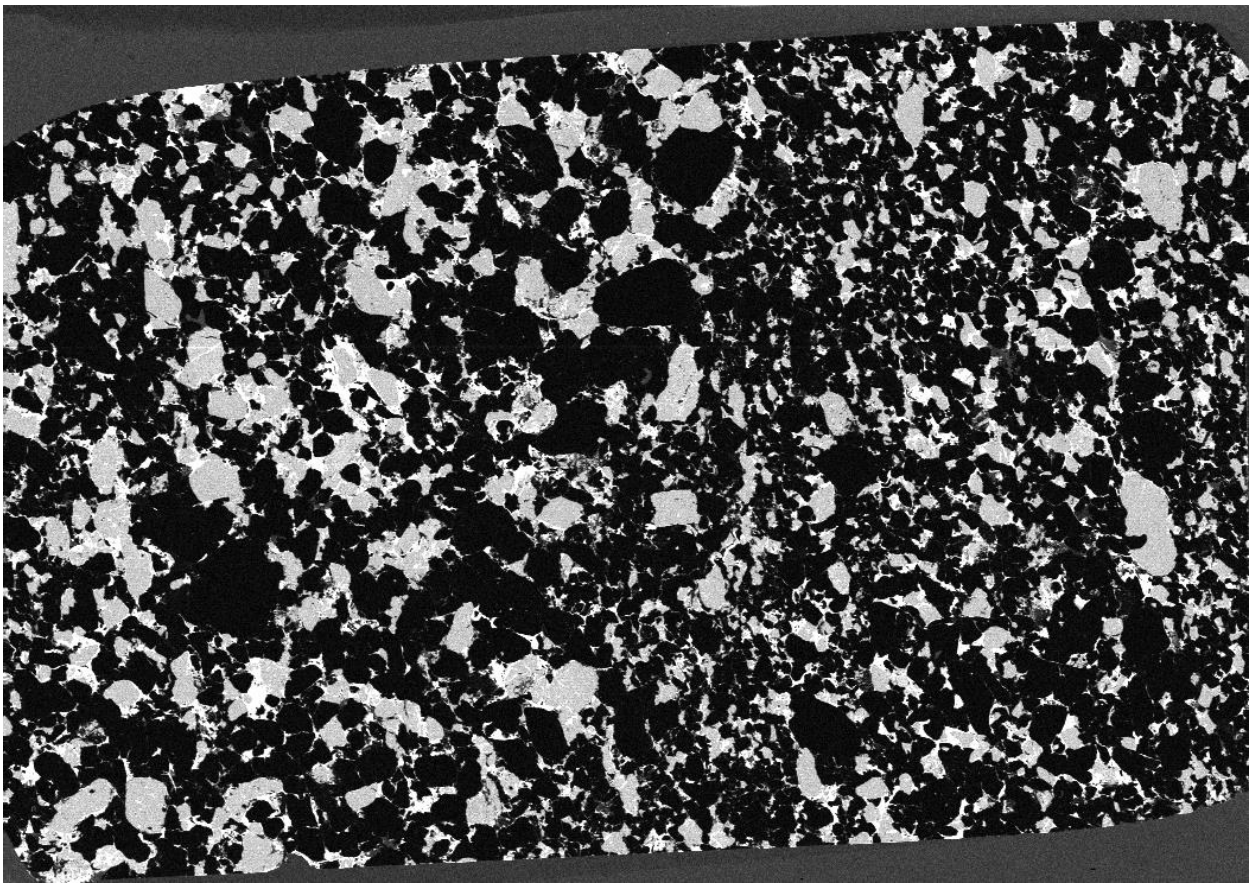

180401

180401/698700 = ~25%

K

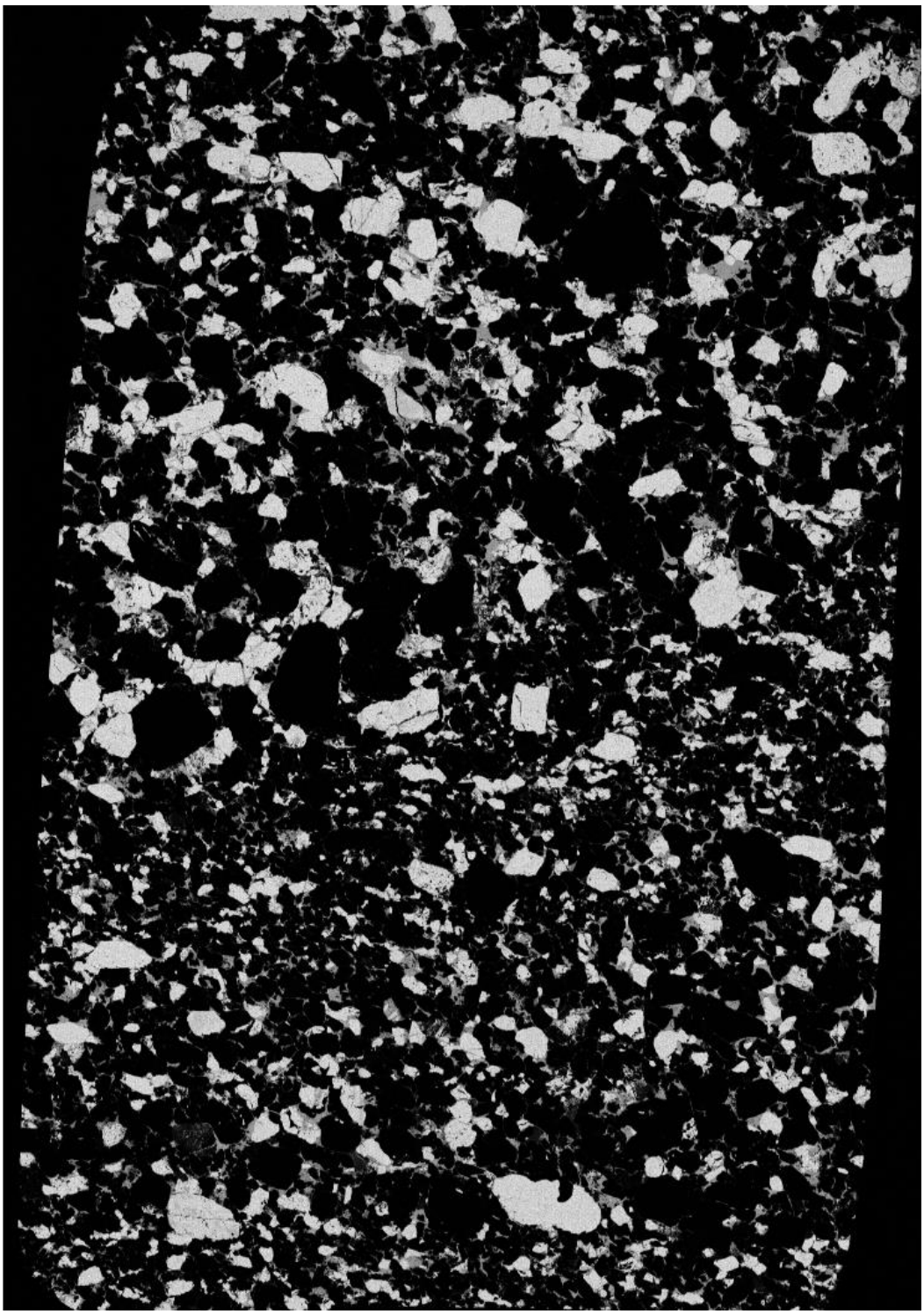

170960

170960/698700 = ~24%

Mg

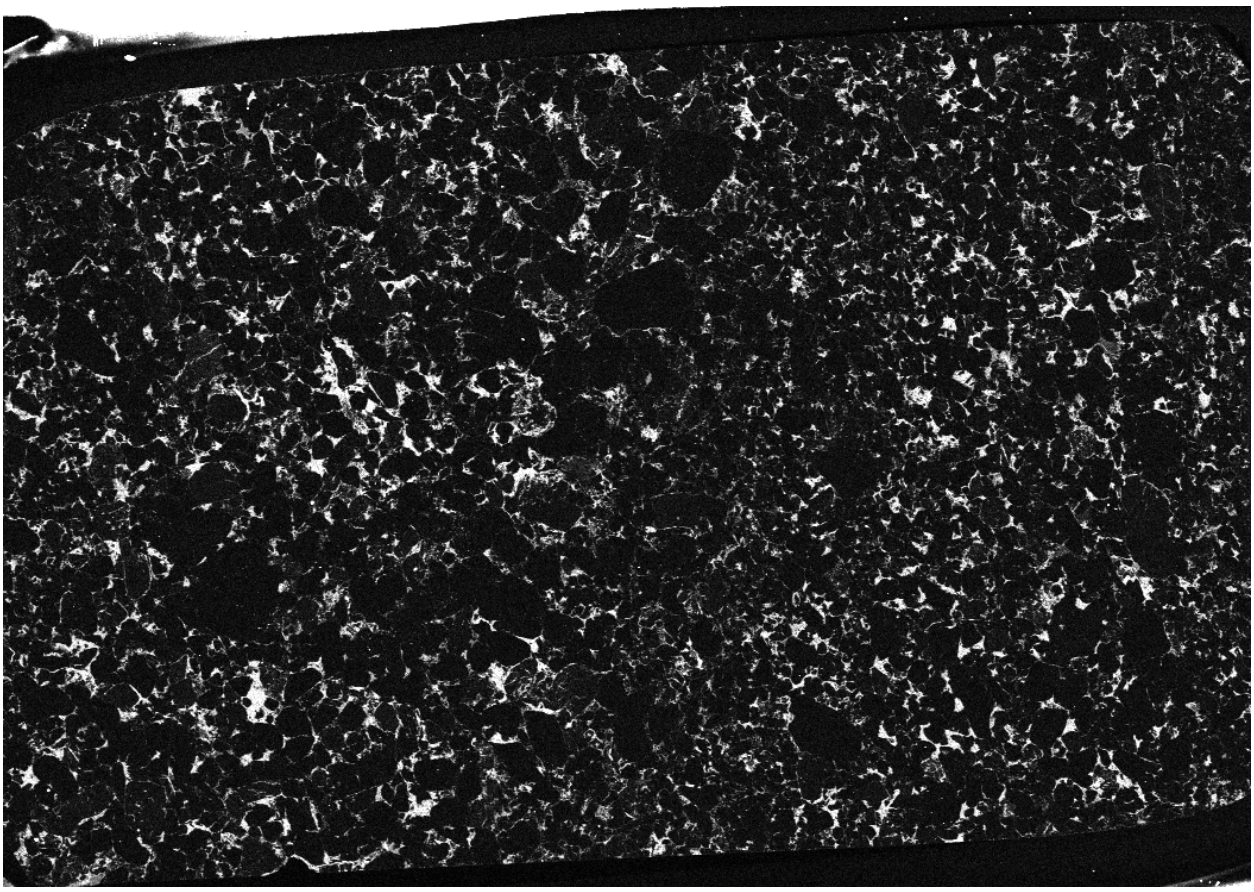

34947/698700 = 5%

Na

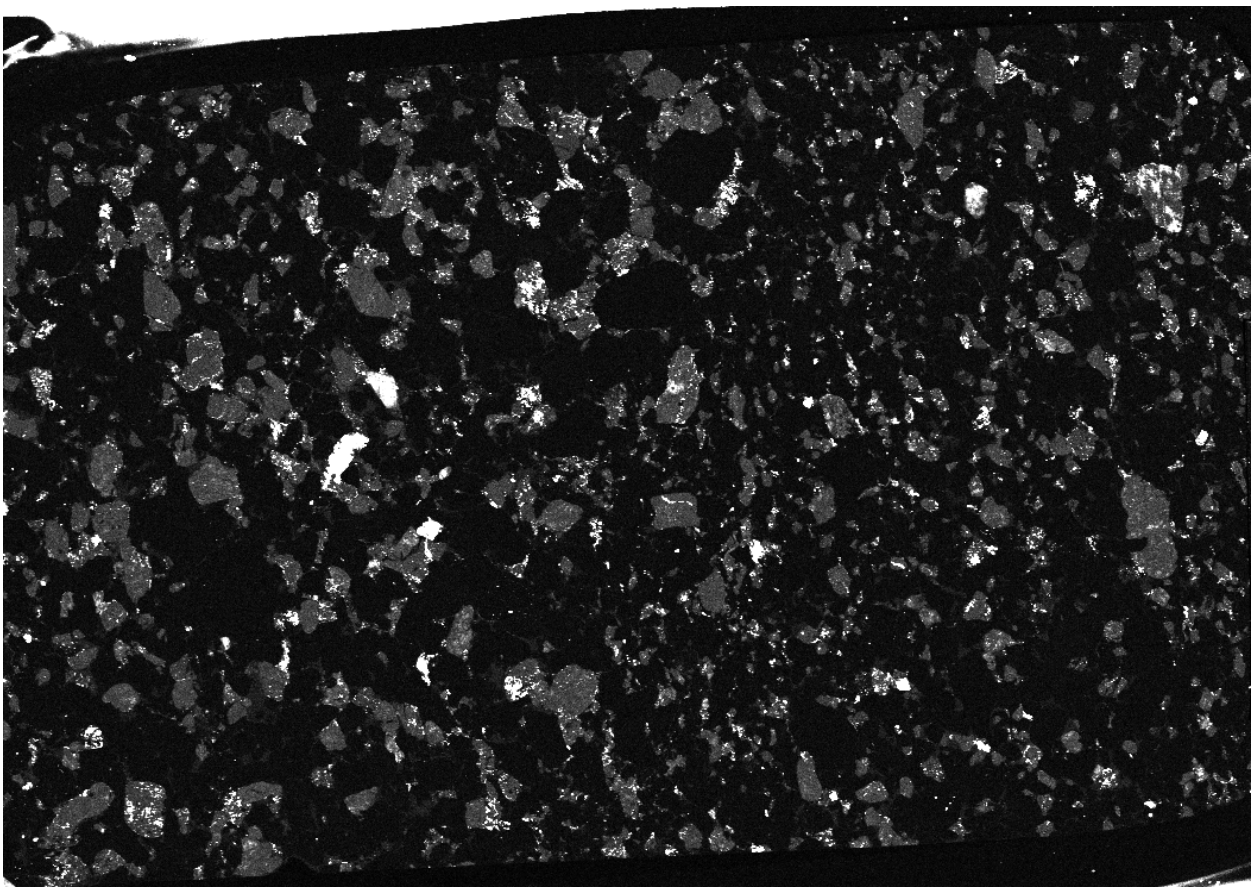

109832/698700 = ~16%

Sample 3-5 Top
295445 pixel count

Si

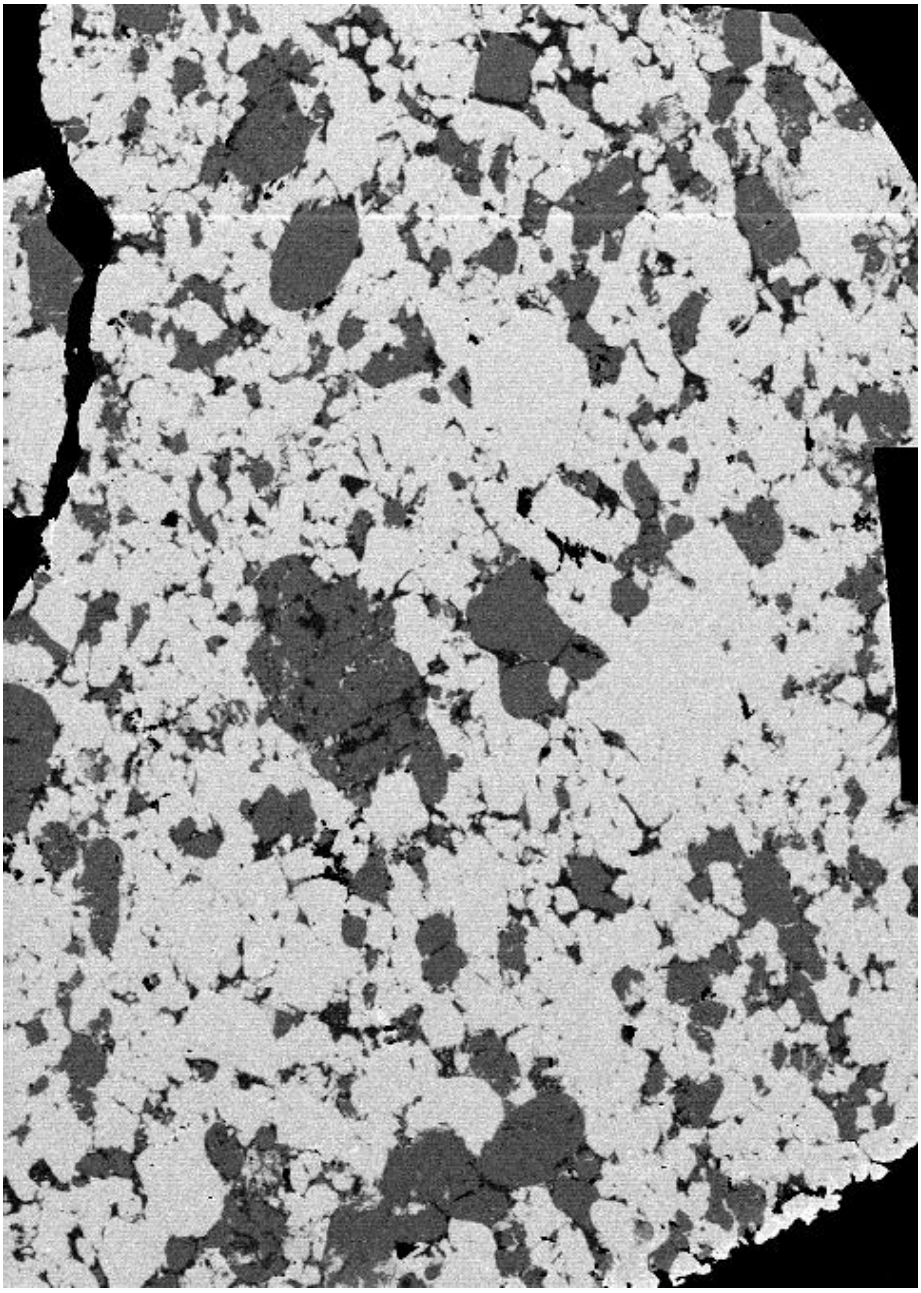

191558/295445 = ~65%

Al

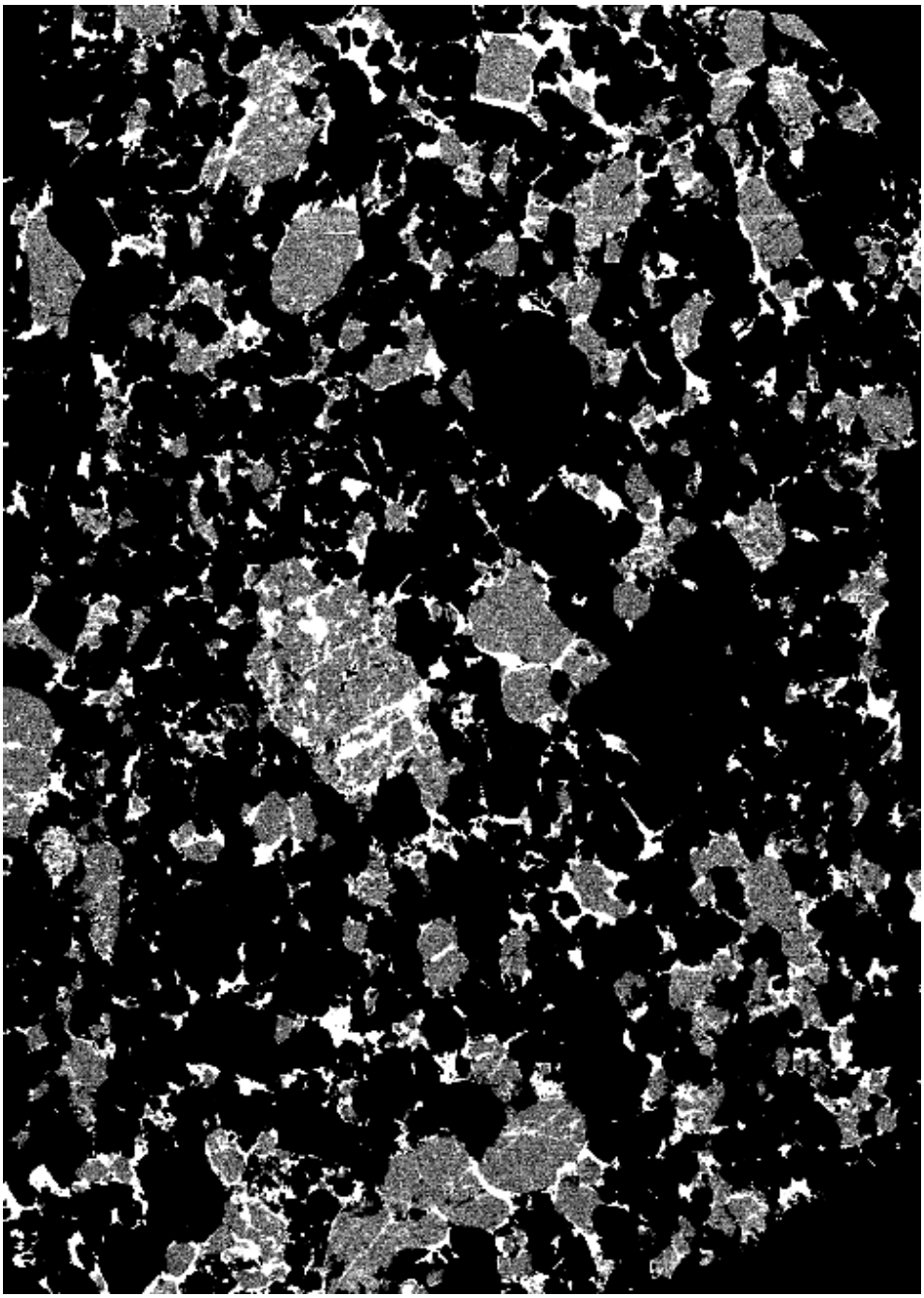

84993/295445 = ~29%

K

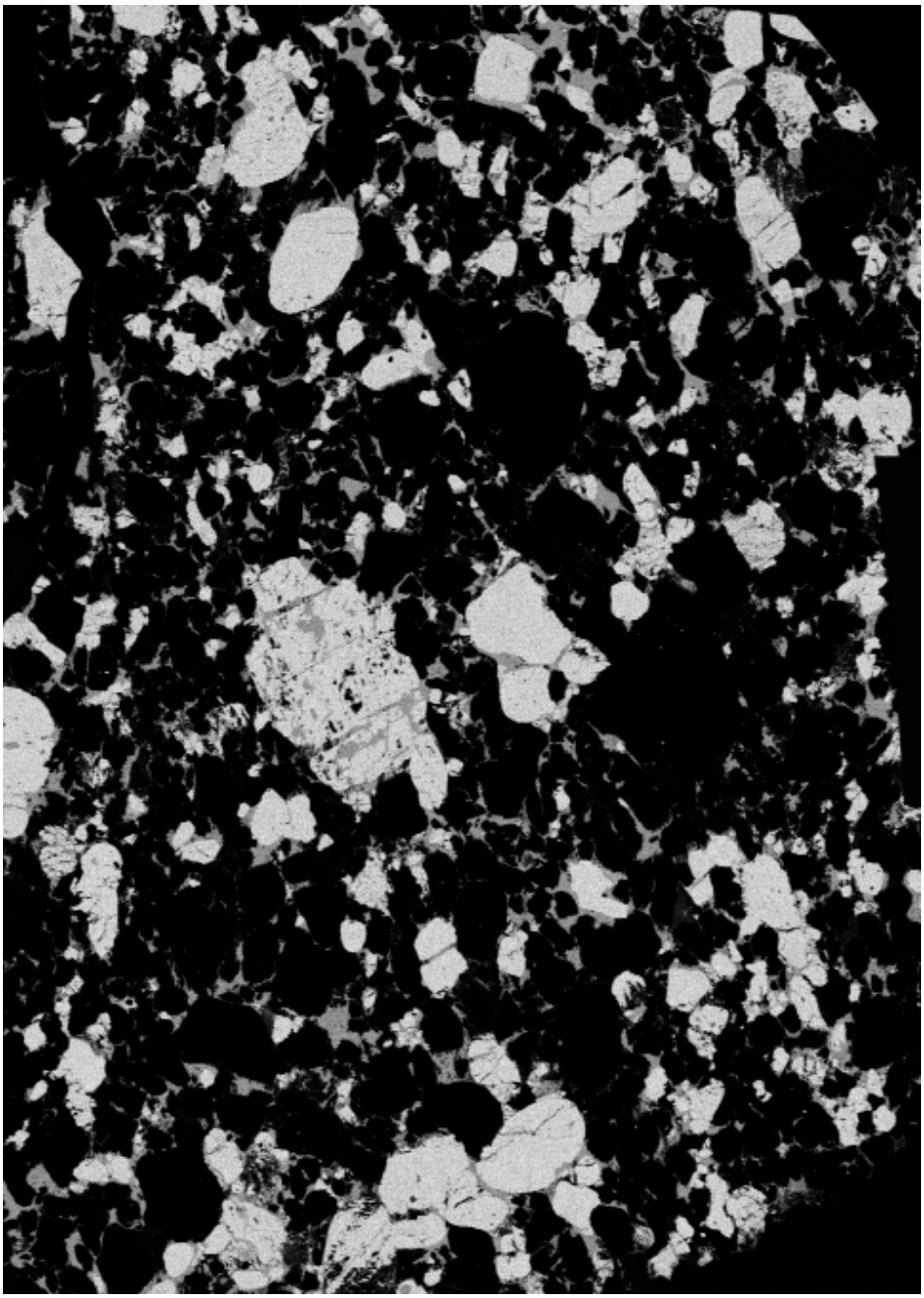

95802/295445 = ~32%

Mg

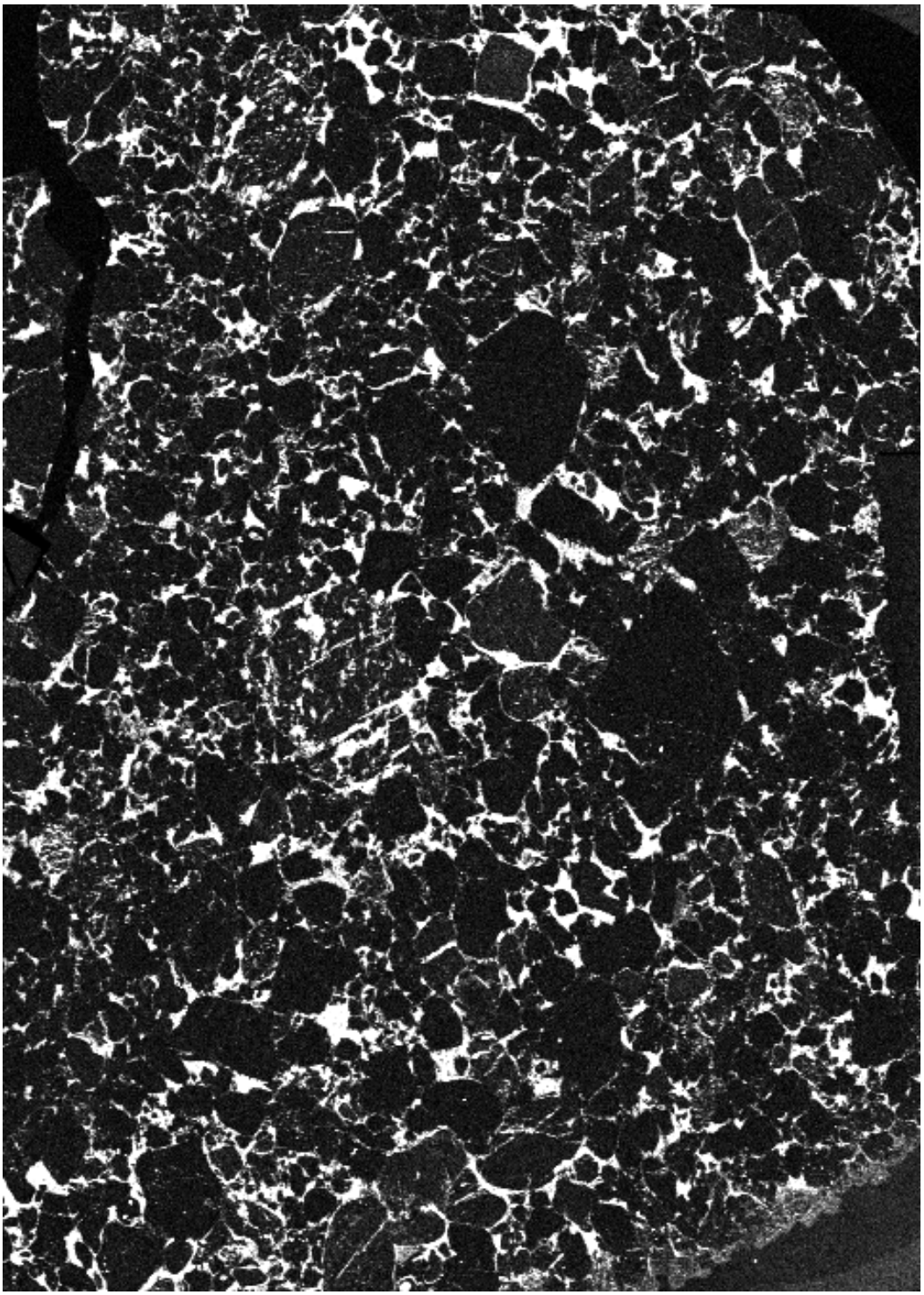

64135 / 295445 = ~22%

Na

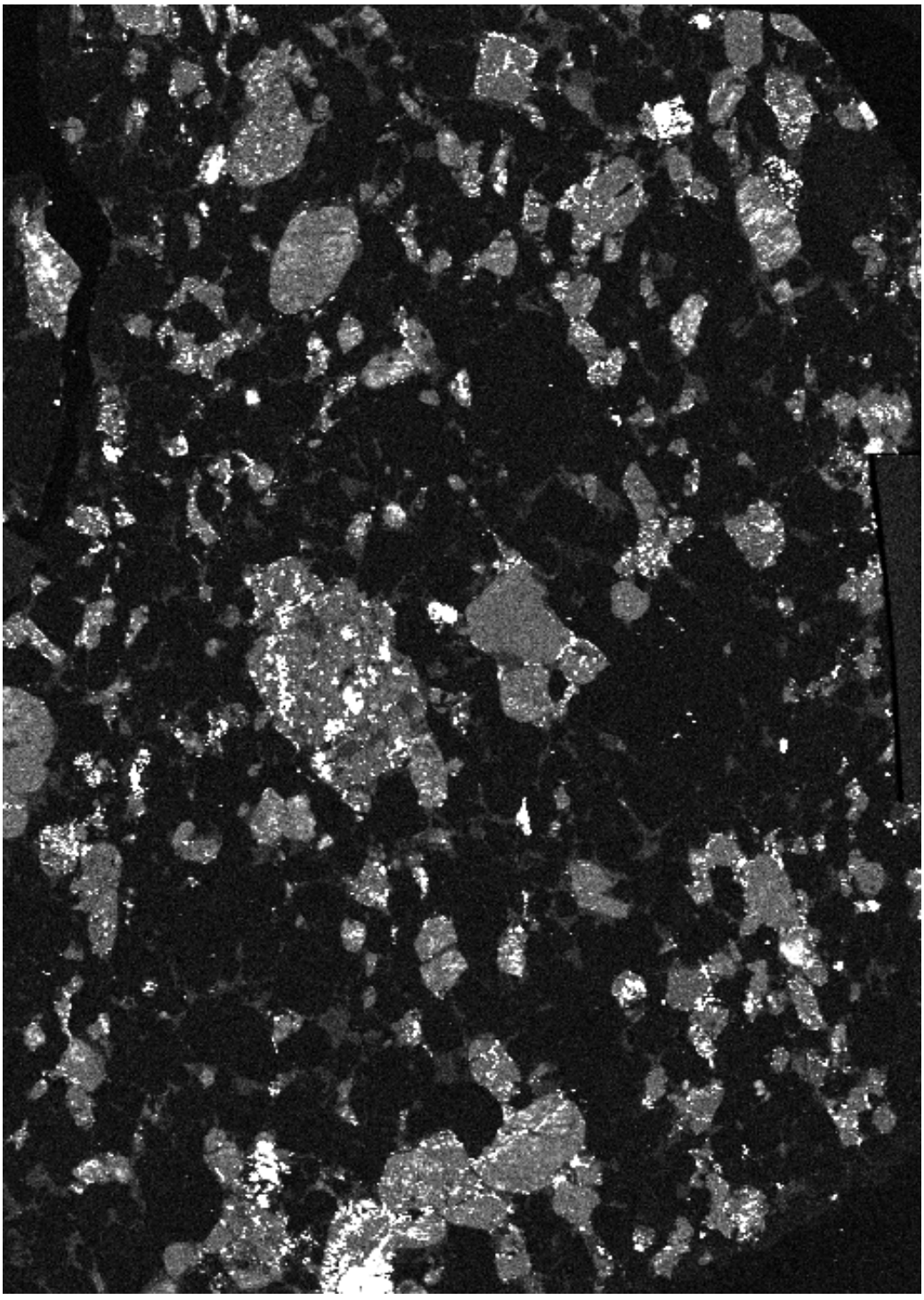

84913 / 295445 = ~29%

Sample 3-7 Bottom
605800 total count

Si

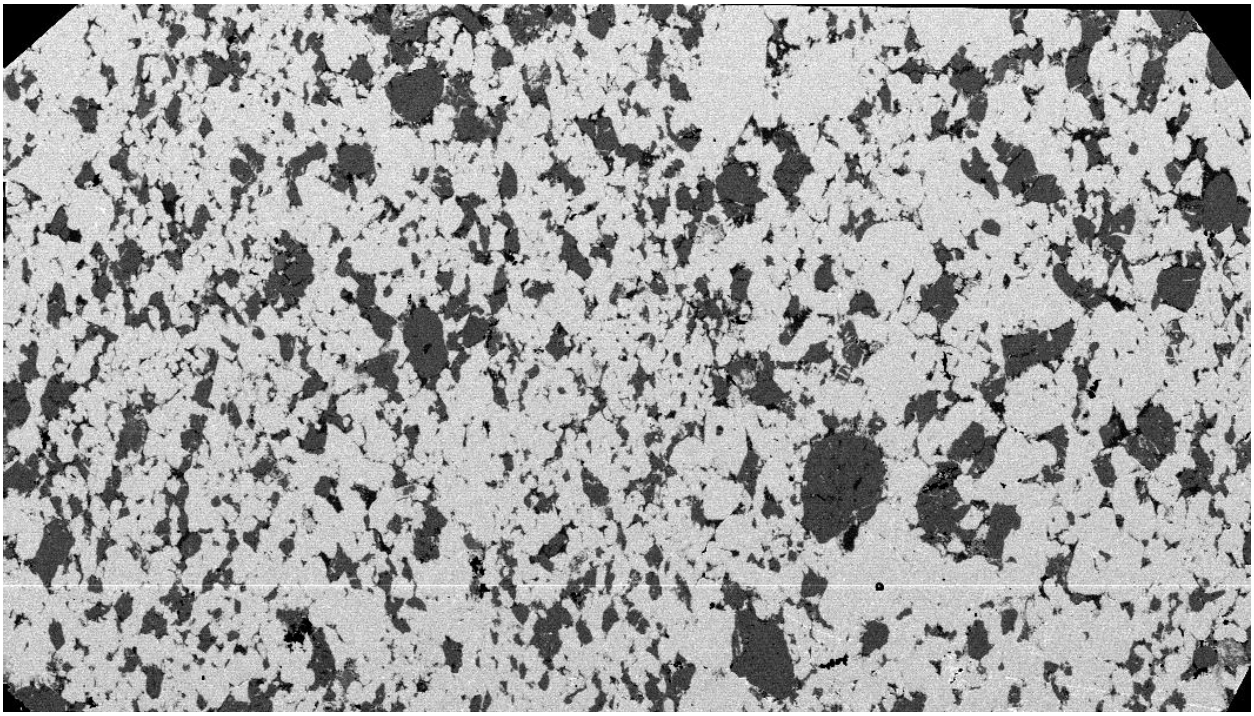

454111/605800 = ~75%

K

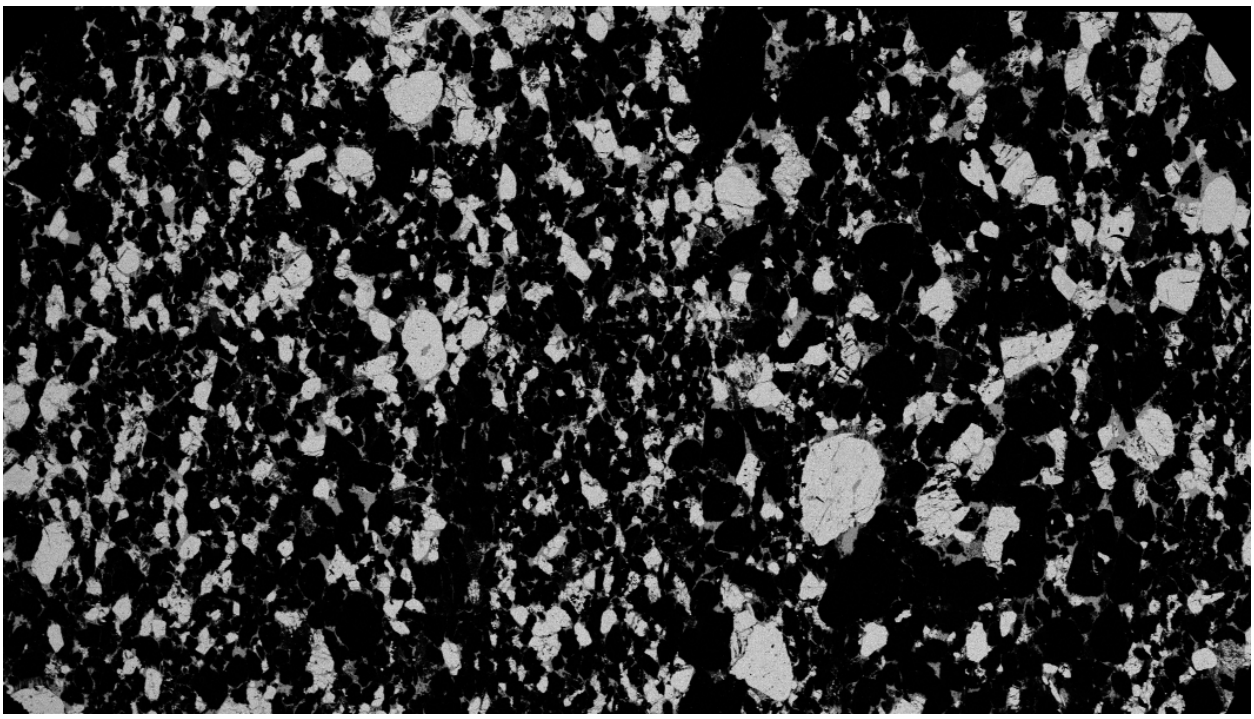

156310/605800 = ~26%

Al

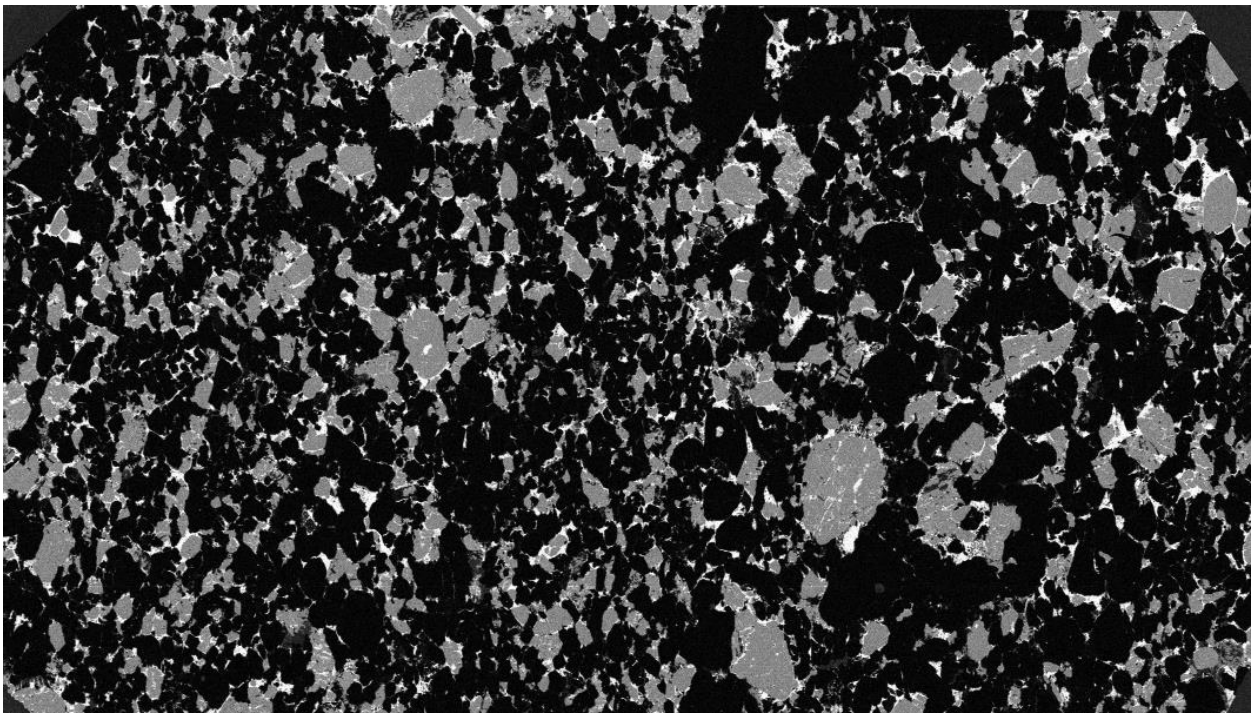

163513 / 605800 = 27%

Mg

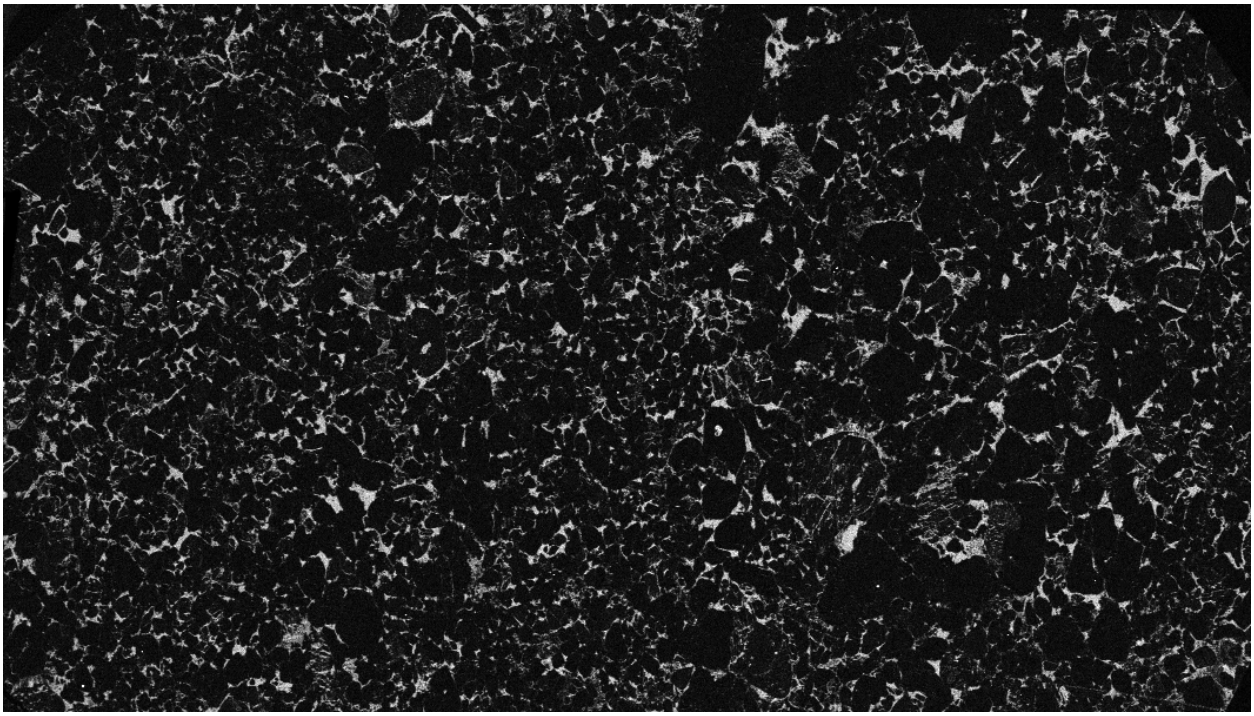

51096 / 605800 = ~8%

Na

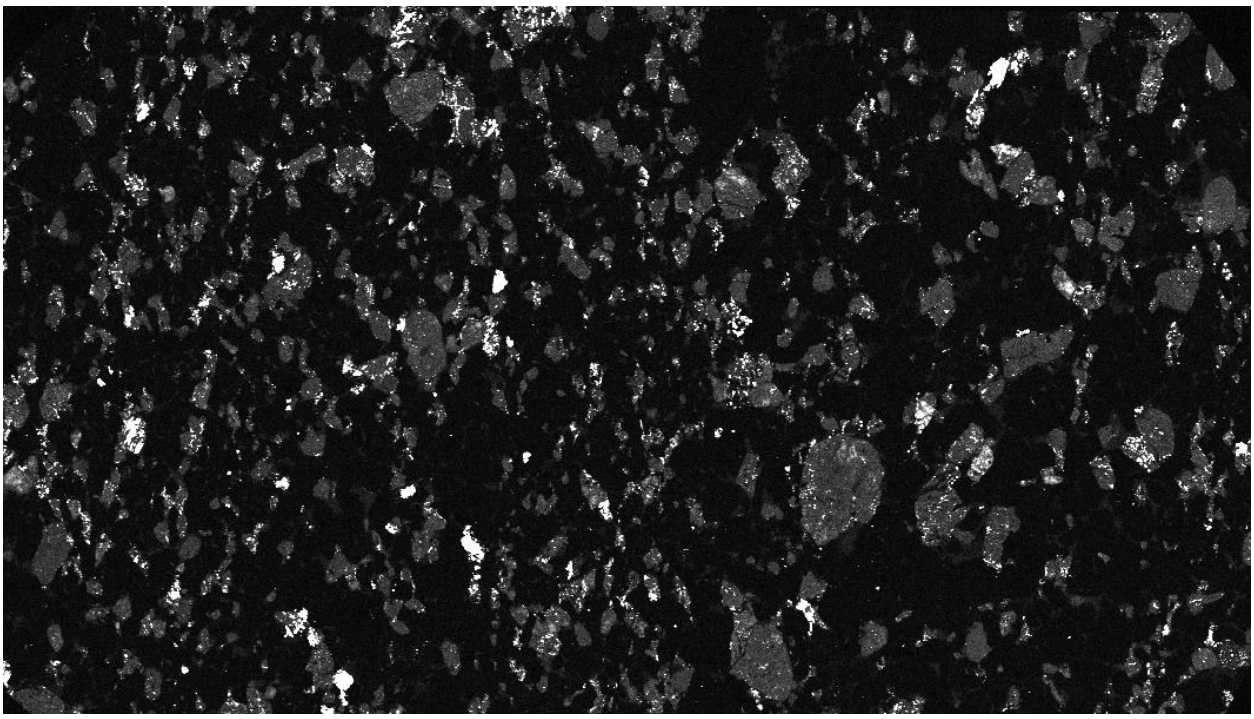

121841 / 605800 = 20%

Sample 3-7 Top
Total count 569449

Si

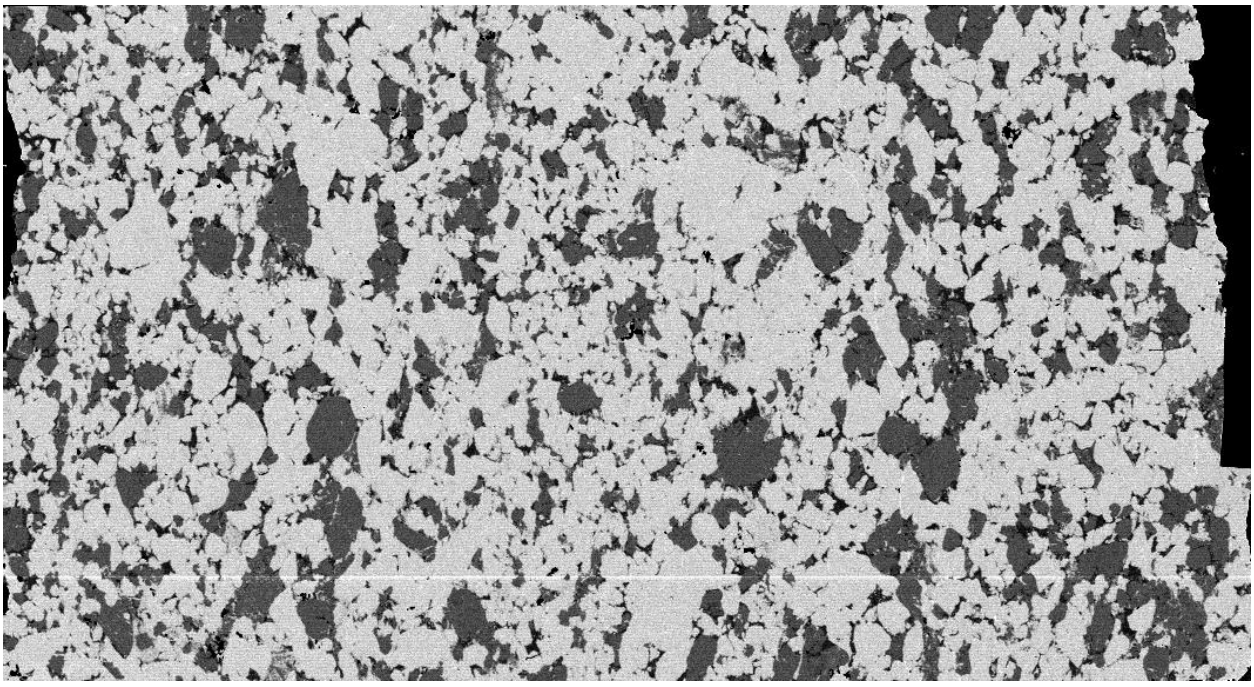

399283 / 569449 = ~70%

Al

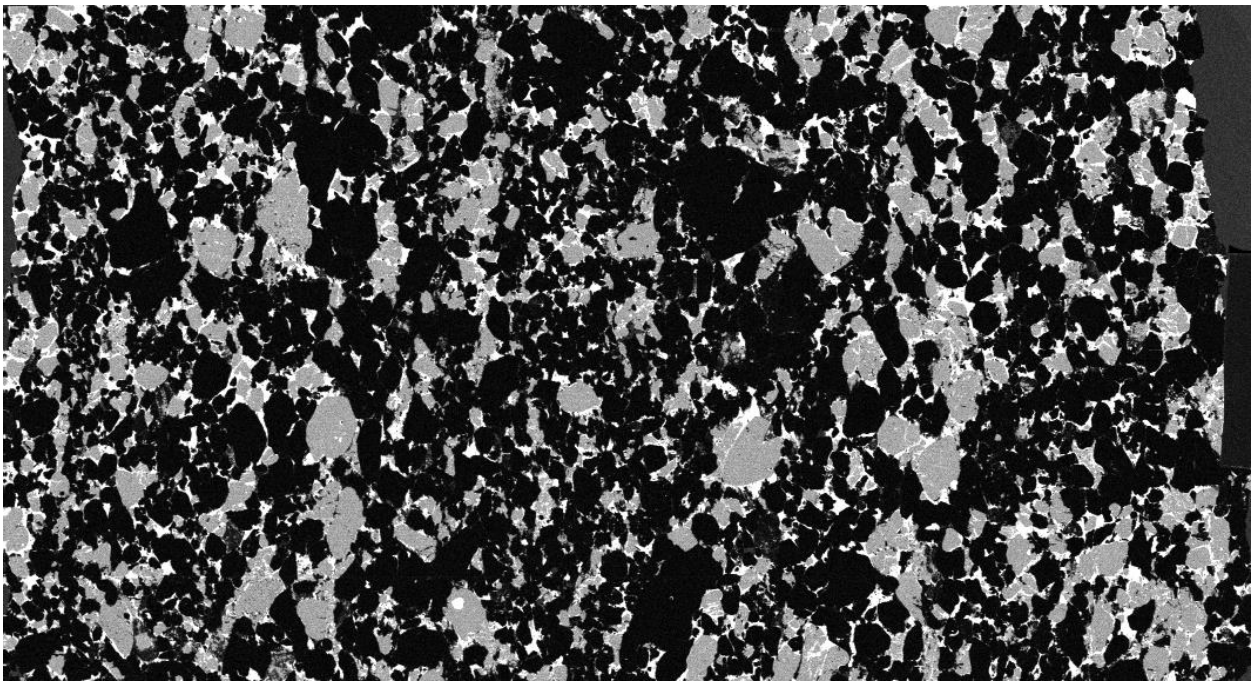

186239 / 569449 = 33%

K

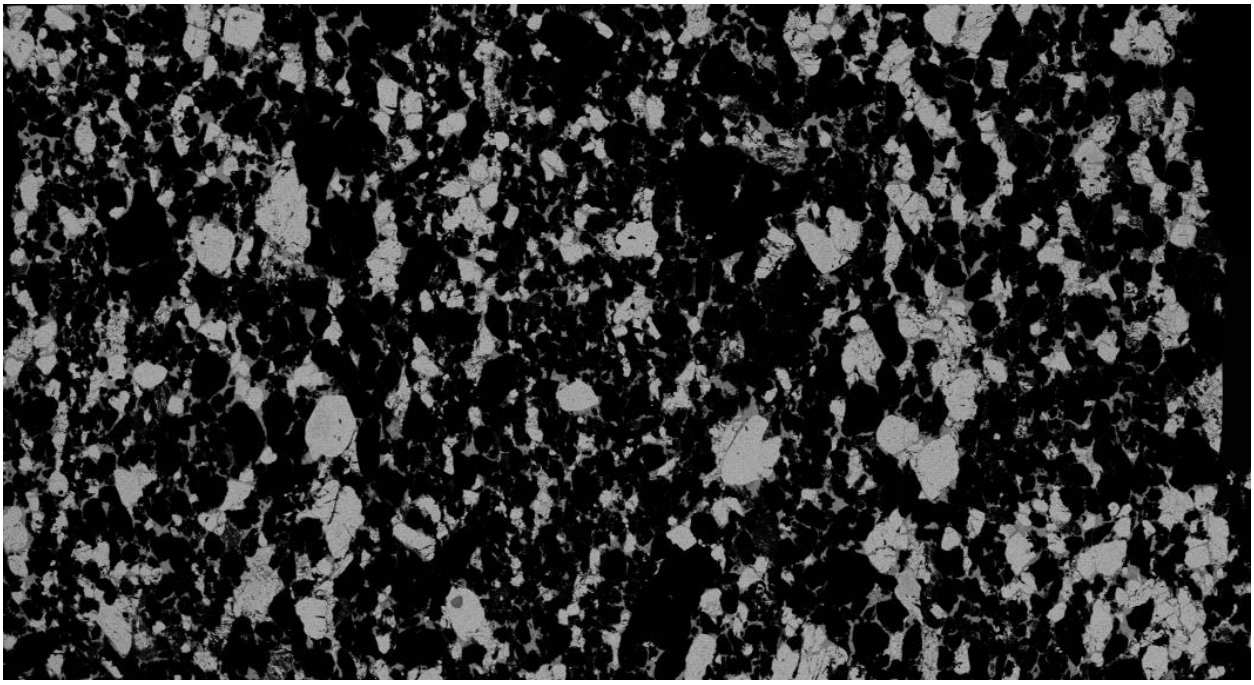

213041 /569449 = 37%

Mg

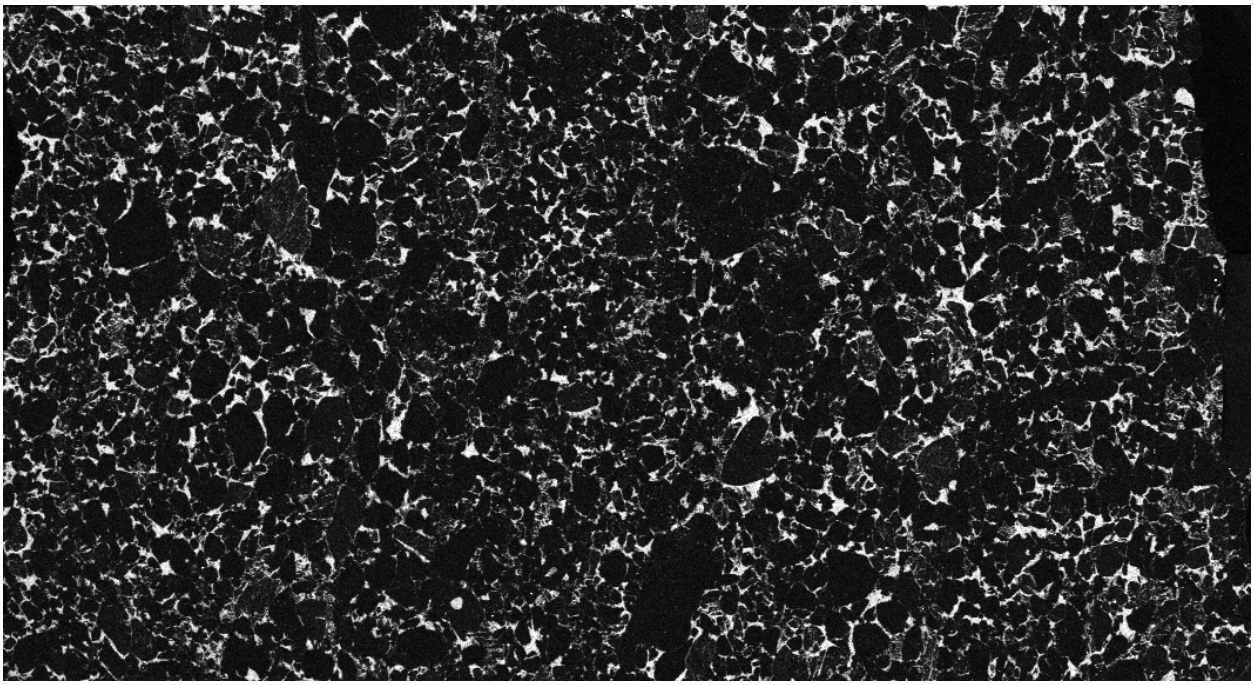

98913 / 569449 = 17%

Na

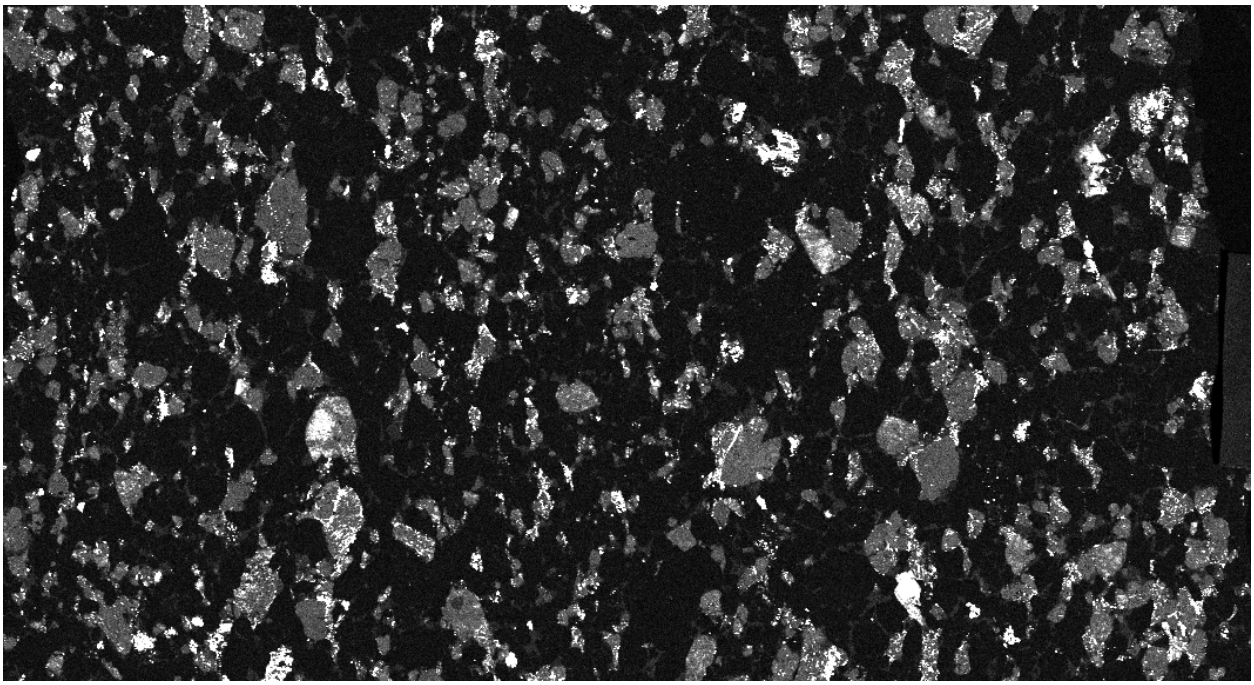

122775 / 569449 = 22%

Erratic 6
Sample 6-3
Total count 589040

Si

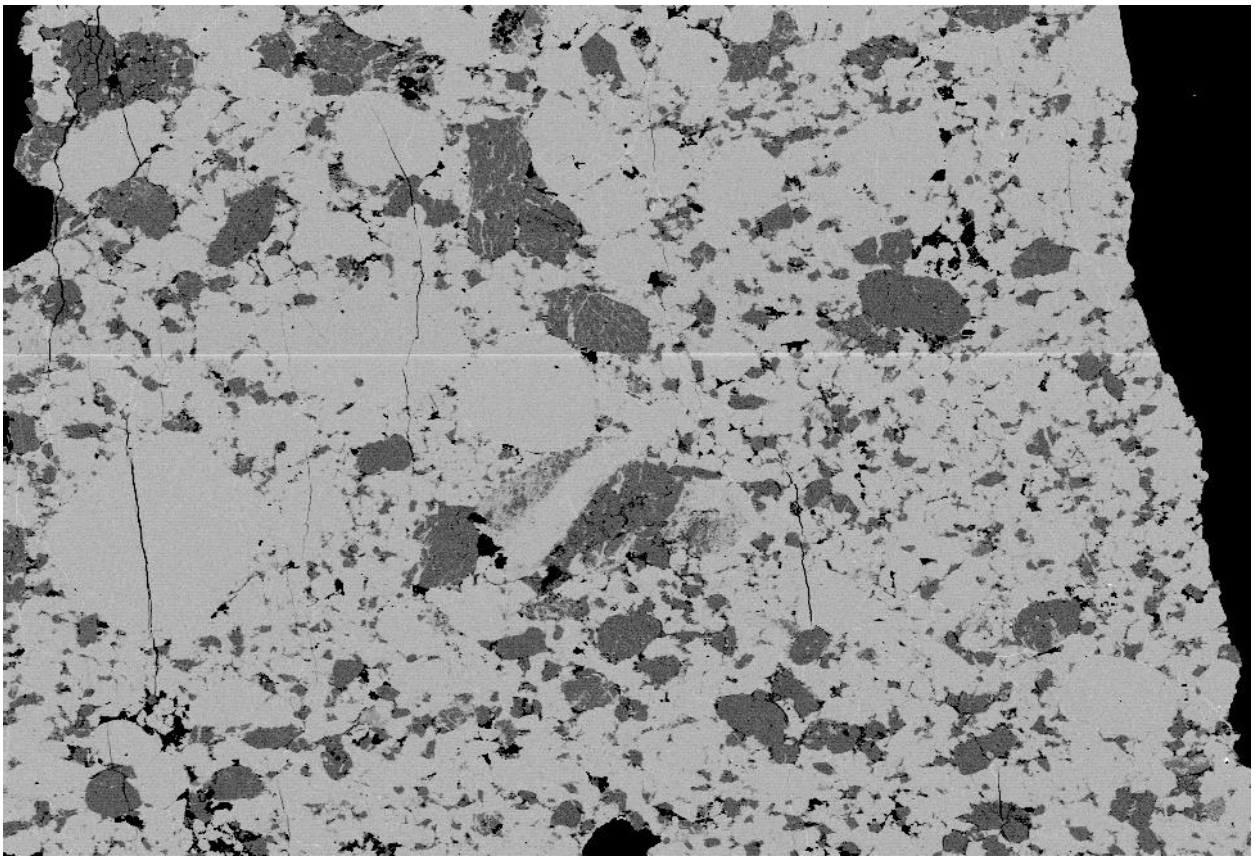

461608 / 589040 = 78%

Al

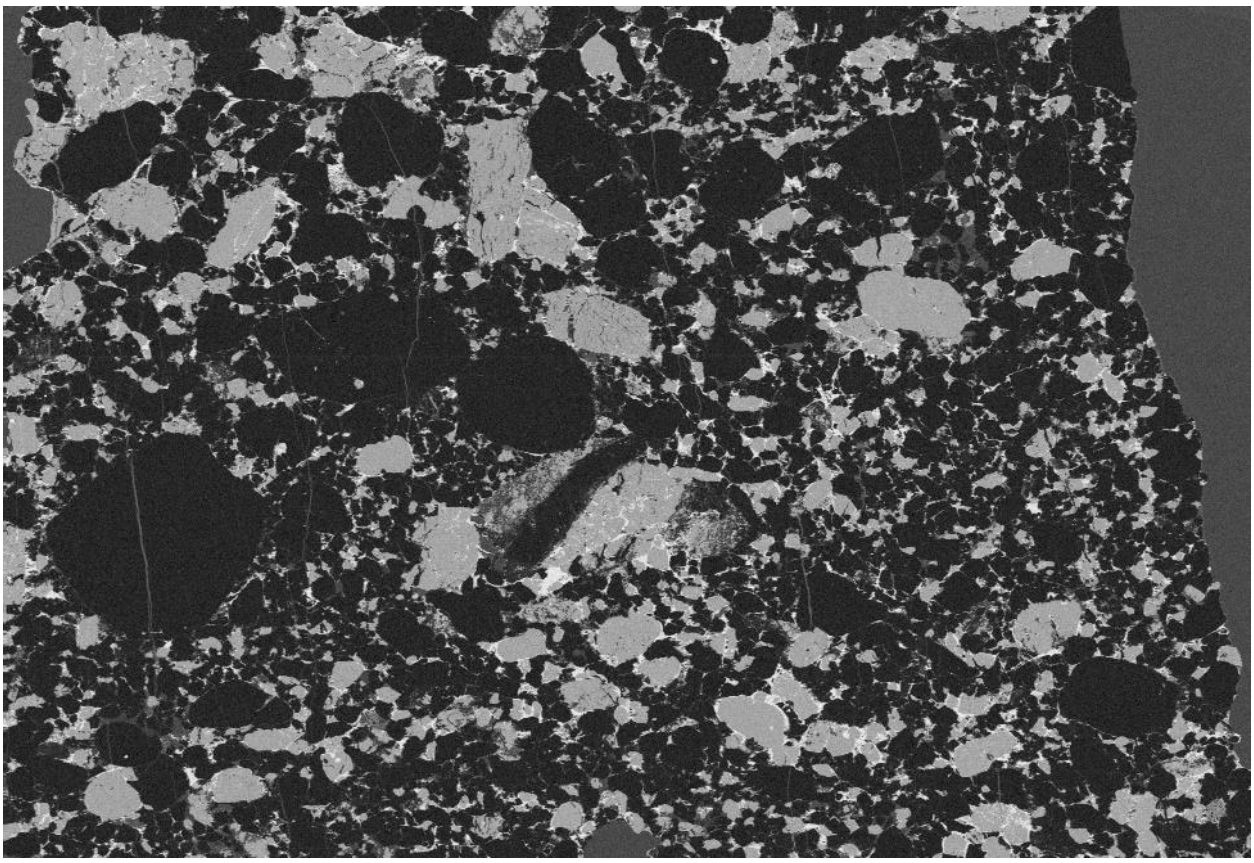

153733 / 589040 = ~27%

K

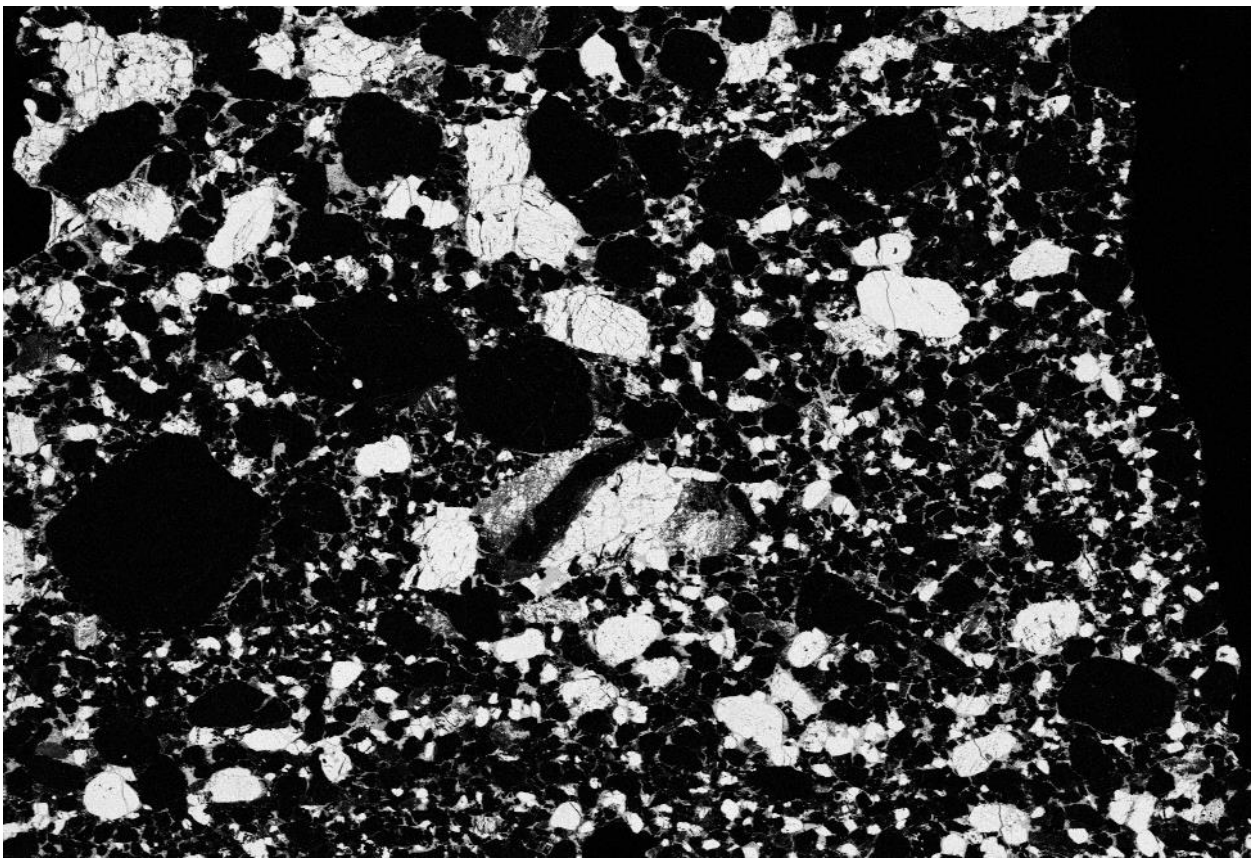

186437 / 589040 = ~32%

Mg

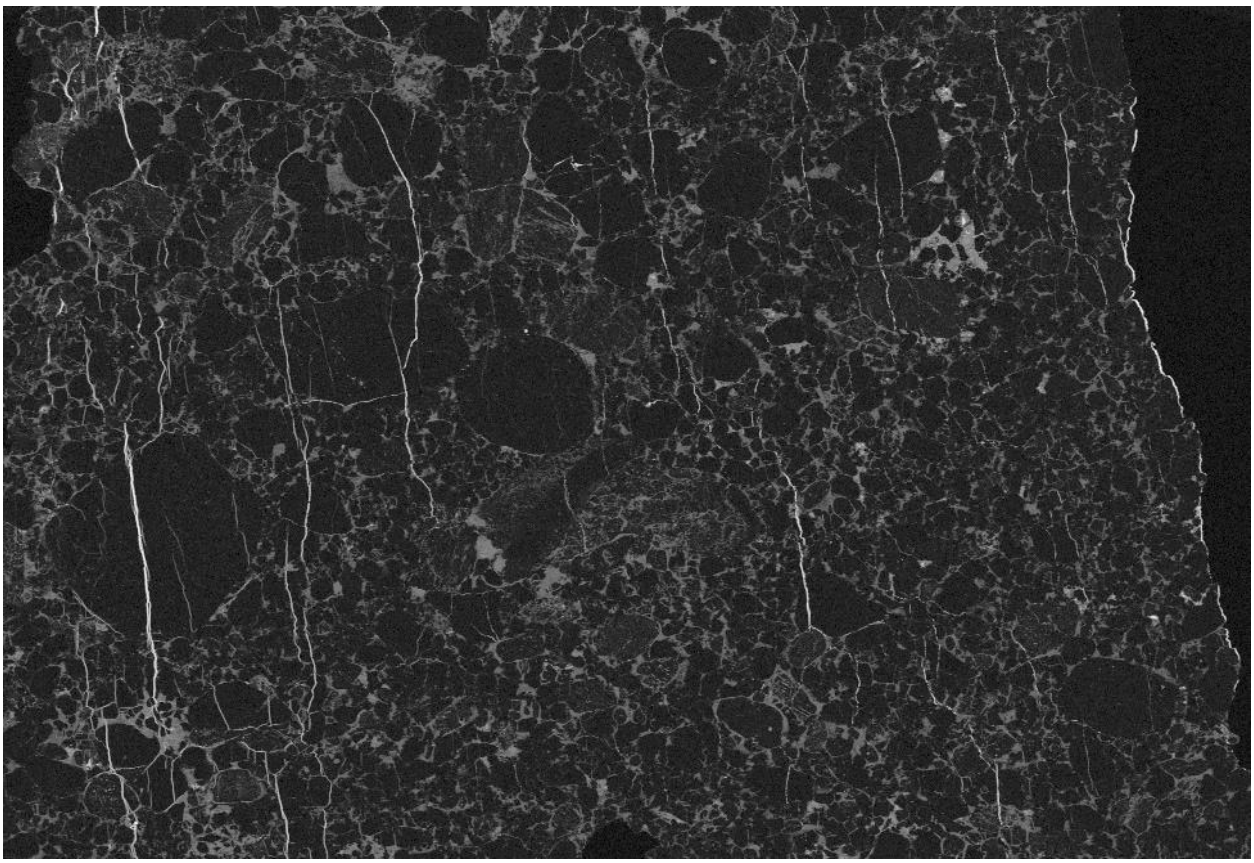

72302 / 589040 = ~12%

Na

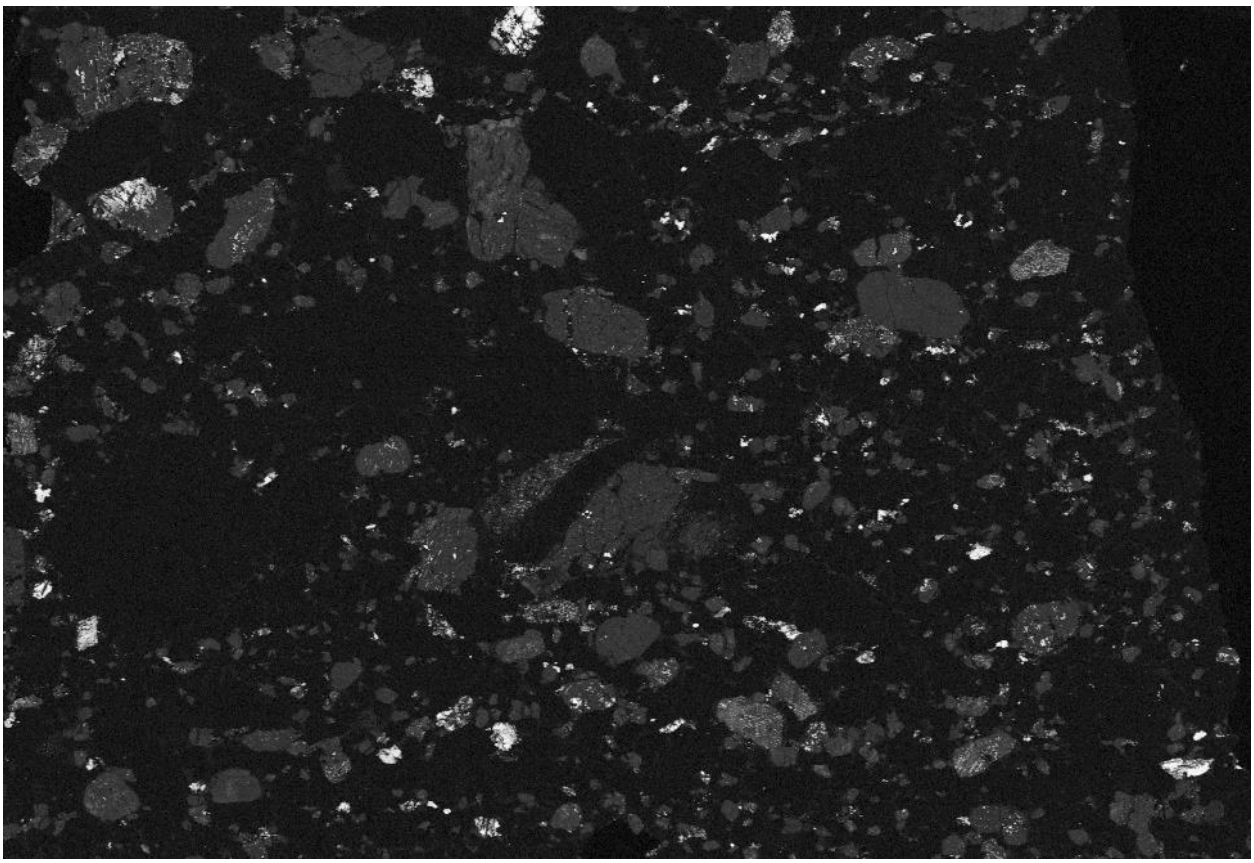

137697 / 589040 = ~23%

Erratic 8
Sample 8-3
Total count 421933

Si

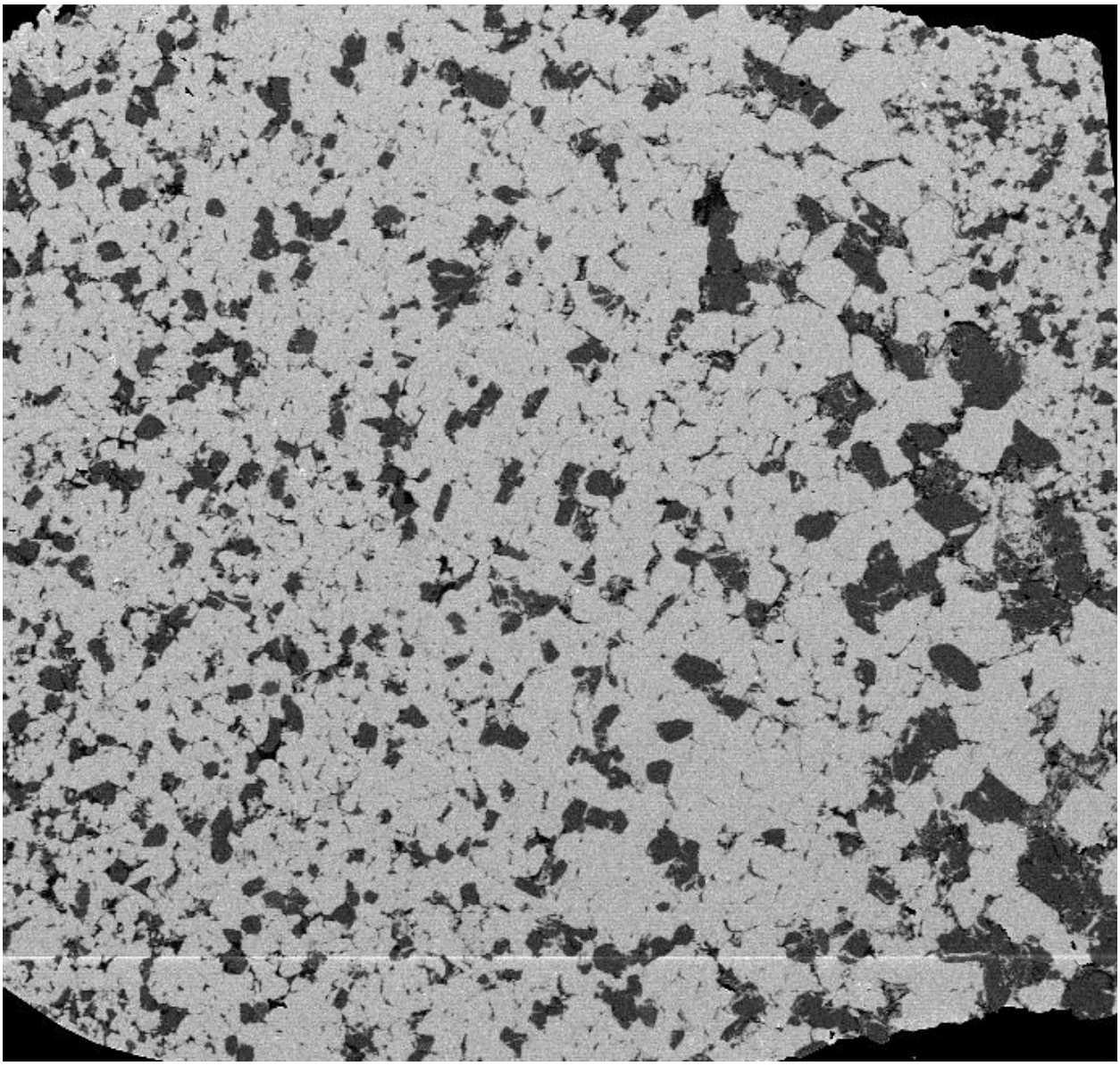

359516 / 421933 = ~85%

Al

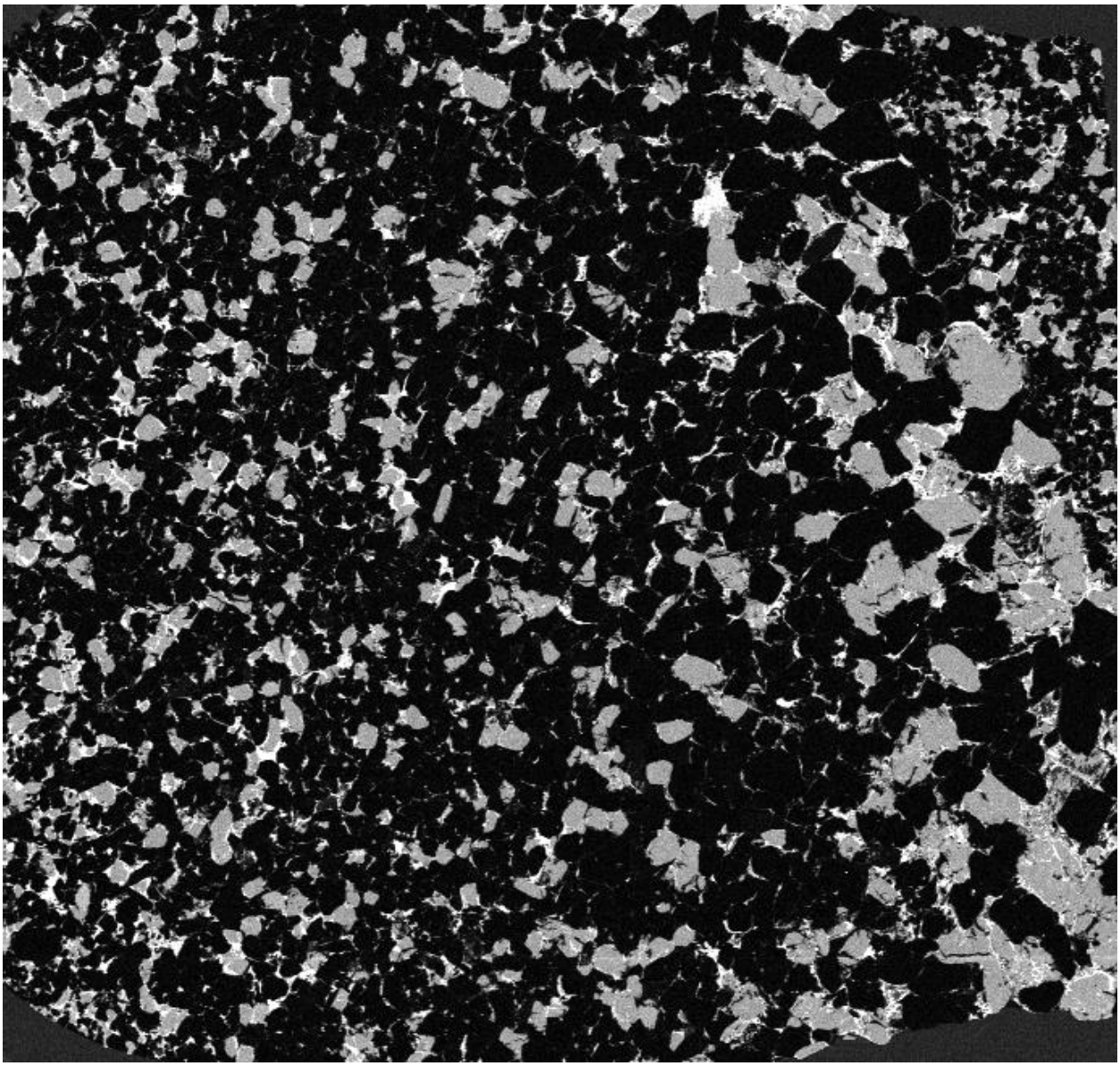

100592 / 421933 = ~24%

K

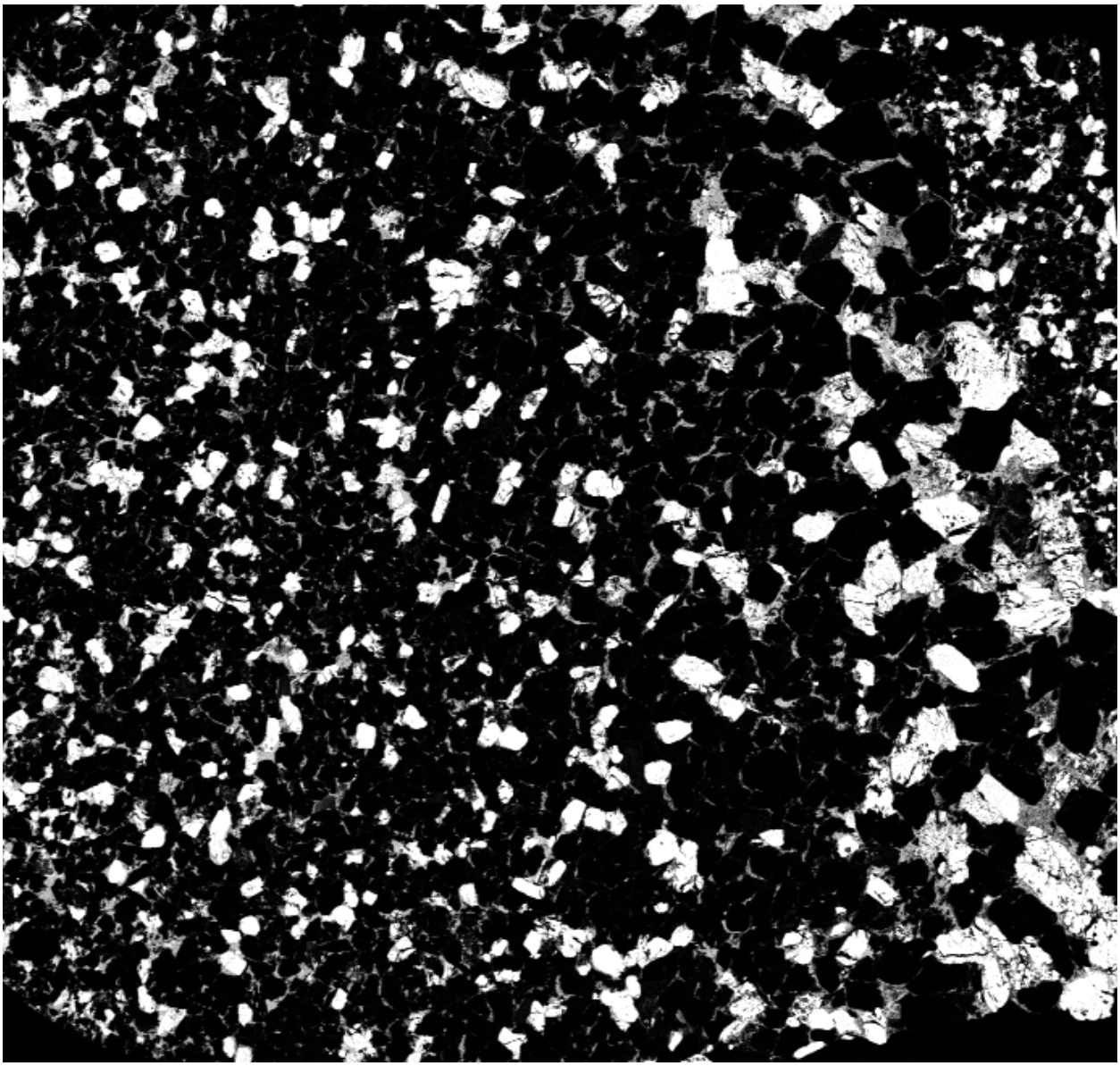

91729 / 421933 = ~22%

Mg

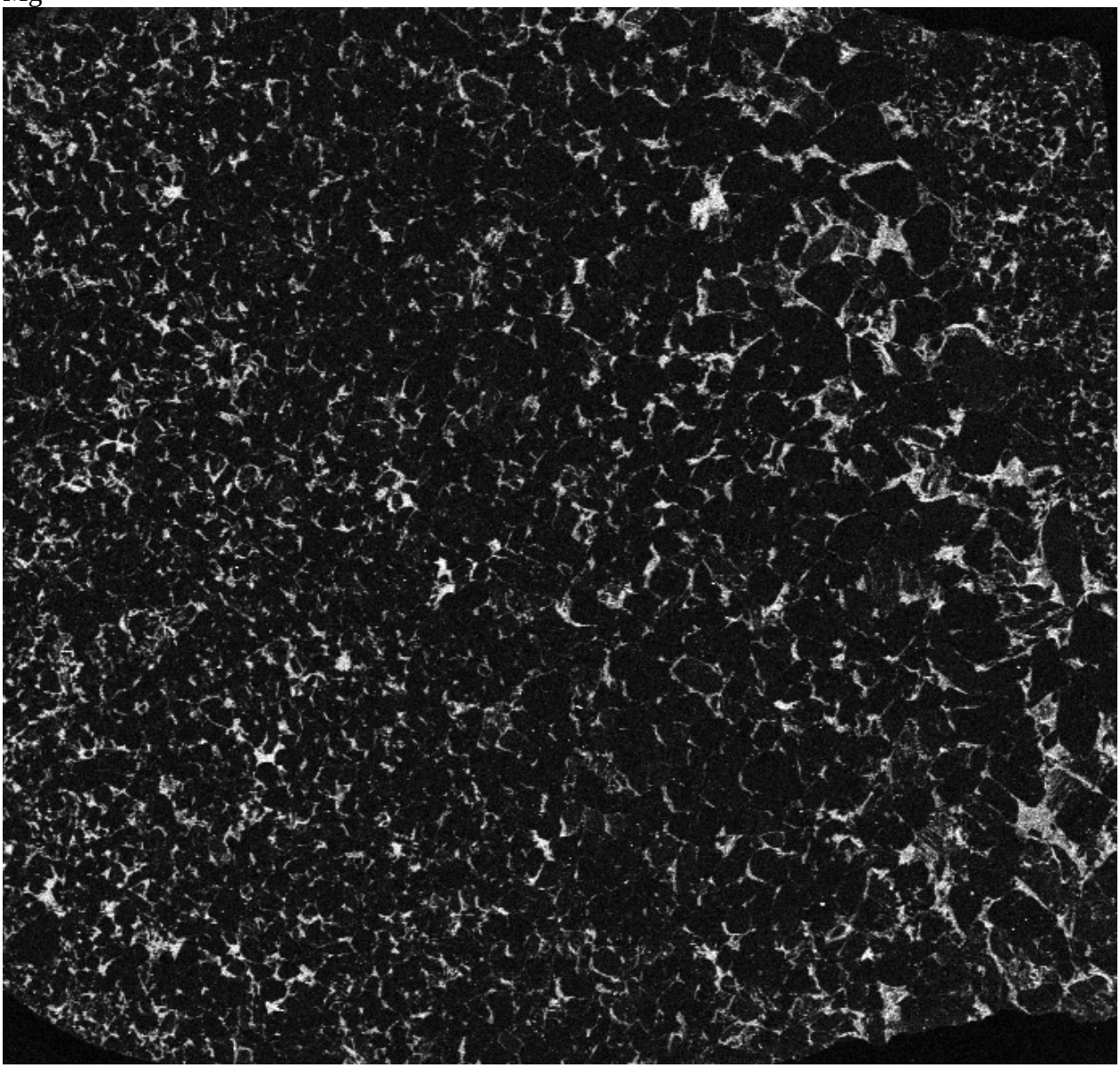

35942 / 421933 = 9%

Na

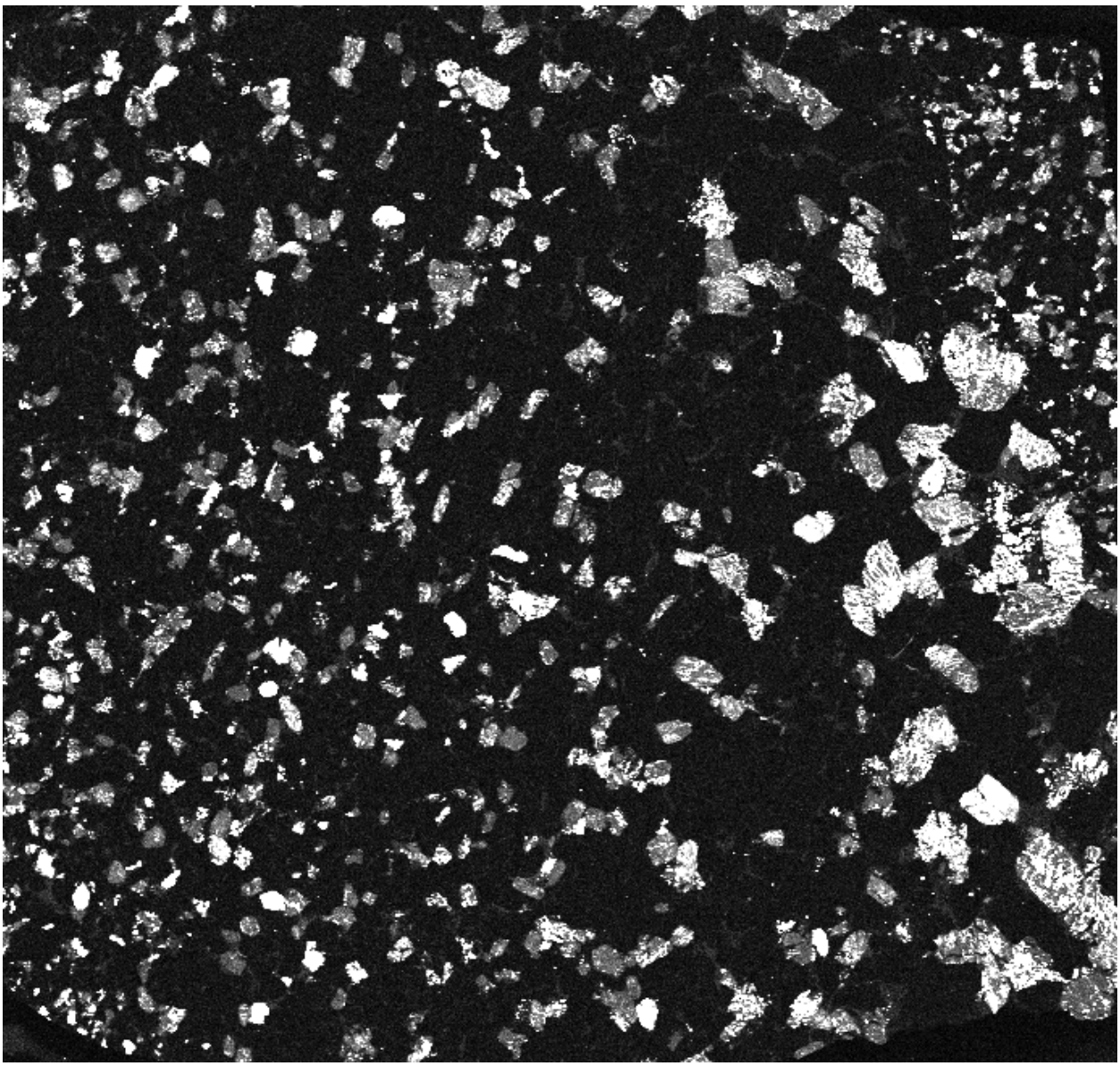

78311 / 421933 = ~19%

A13 – Test Dose correction samples (200 Gy) from separate slice of core 3-5

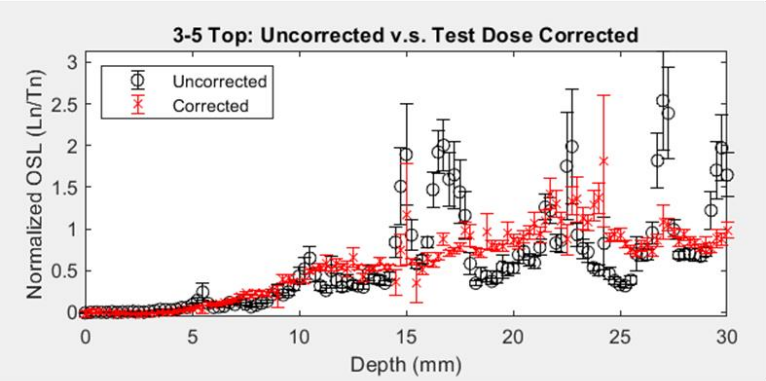

Uncorrected:
$\overline{\sigma\varphi_0}$ Median = 3.51e-06 s-1
μ Median = 0.175 mm-1

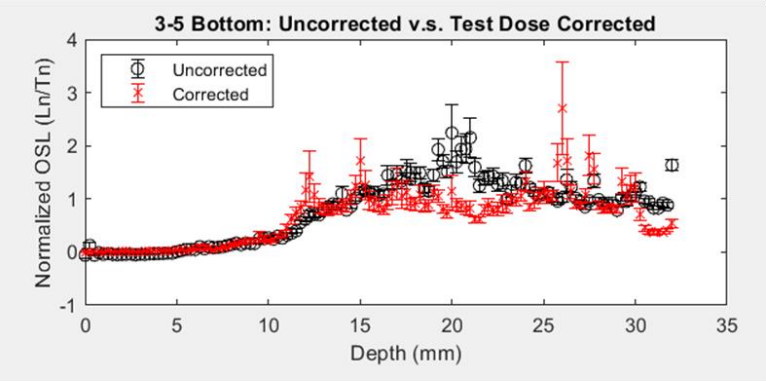

Uncorrected:
$\overline{\sigma\varphi_0}$ Median = 0.00023 s-1
μ Median = 0.644 mm-1

3-5 Top

Uncorrected:

Result for the calibration
SP Median = 3.51e-06 s-1
SP 1sigma sup = 8.41e-06 s-1
SP 1sigma inf = 1.6e-06 s-1
mu Median = 0.175 mm-1
mu 1sigma sup = 0.14 mm-1
mu 1sigma inf = 0.0468 mm-1
>>

Test Dose Corrected:

Result for the calibration
SP Median = 2.9e-06 s-1
SP 1sigma sup = 1.19e-06 s-1
SP 1sigma inf = 5.93e-07 s-1
mu Median = 0.212 mm-1
mu 1sigma sup = 0.0302 mm-1
mu 1sigma inf = 0.0302 mm-1
>>

3-5 Bottom

Uncorrected:

Result for the calibration
SP Median = 0.00023 s-1
SP 1sigma sup = 0.00272 s-1
SP 1sigma inf = 0.0002 s-1
mu Median = 0.644 mm-1
mu 1sigma sup = 0.209 mm-1
mu 1sigma inf = 0.209 mm-1

Test Dose Corrected:

Result for the calibration
SP Median = 0.00087 s-1
SP 1sigma sup = 0.0109 s-1
SP 1sigma inf = 0.000687 s-1
mu Median = 0.687 mm-1
mu 1sigma sup = 0.221 mm-1
mu 1sigma inf = 0.147 mm-1

A14 – Table of Physically Derived Photoionization Cross Section Parameterizations, Erratic sample 3-7

Erratic 3-7 Slices, Photoionization Values

Slice 3

Component	σ	Percent Contribution
Component 1	2.74E-17 cm^2	0.8%
Component 2	2.92E-18 cm^2	7.7%
Component 3	6.31E-19 cm^2	36.9%
Component 4	1.43E-19 cm^2	54.5%

Weighted average:
7.70331E-19 cm^2

Slice 4

Component	σ	Percent Contribution
Component 1	4.10E-18 cm^{-2}	9.6%
Component 2	7.44E-19 cm^{-2}	35.3%
Component 3	1.62E-19 cm^{-2}	55.1%

Weighted average:
7.46132E-19 cm^2

Slice 5

Component	Σ	Percent Contribution
Component 1	8.79E-18 cm^{-2}	6.4%
Component 2	2.46E-18 cm^{-2}	15.4%
Component 3	6.33E-19 cm^{-2}	36.5%
Component 4	1.46E-19 cm^{-2}	41.7%

Weighted average:
2.00734E-18 cm^{-2}

Slice 6

Component	σ	Percent Contribution
Component 1	8.66E-18 cm^{-2}	21%
Component 2	1.22E-18 cm^{-2}	34%
Component 3	2.35E-19 cm^{-2}	45%

Weighted Average:
2.33683E-18 cm^{-2}

Slice 7

Component	σ	Percent Contribution
Component 1	1.23E-17 cm^{-2}	31.3%
Component 2	1.88E-18 cm^{-2}	30%
Component 3	2.87E-19 cm^{-2}	38.8%

Weighted Average:
4.52251E-18 cm^{-2}

Slice 8

Component	σ	Percent Contribution
Component 1	1.33E-17 cm^{-2}	38.5%
Component 2	1.83E-18 cm^{-2}	28.6%
Component 3	2.81E-19 cm^{-2}	33%

Weighted average:
5.71785E-18 cm^{-2}

Slice 9

Component	σ	Percent Contribution
Component 1	1.04E-17 cm^{-2}	27.5%
Component 2	1.47E-18 cm^{-2}	31.5%
Component 3	2.53E-19 cm^{-2}	41%

Weighted average:
3.43355E-18 cm^{-2}

A15 – Table of Physically Derived Light Attenuation Parameters, Foothills Erratics Train

Foothills Erratics Train			
Sample Portion	Beer-Lambert attenuation calculation (mm^{-1})	Average attenuation across visible light spectrum (mm^{-1})	Fitted Attenuation (mm^{-1})
3-5 Top	6.32	5.82 ± 0.94	0.103
3-5 Bottom	4.27	2.99 ±1.45	0.388
3-6 Bottom	2.84	2.28 ± 0.63	1.41
3-7 Top portion	2.46	1.64 ± 0.94	Attenuation from ^{10}Be: 0.103 mm^{-1} Attenuation of Erratic 3, Top samples: 0.130 mm^{-1} Attenuation of Erratic 3, Bottom samples: 0.509 mm^{-1}
3-7 Middle portion	2.48	1.66 ± 0.94	
3-7 Bottom Portion	3.95	3.40 ± 0.74	
3-8 Top, bottom portion	2.10	1.42 ± 0.79	0.108
3-8 Top, top portion	3.64	3.11± 0.72	
3-8 Bottom	4.71	3.54 ± 1.32	0.534
6-2 top, top portion	4.11	2.82 ± 1.49	0.09
6-2 top, bottom portion	4.91	3.80 ± 1.23	
6-3 Top	1.34	0.91 ± 0.49	Attenuation from ^{10}Be 0.281 Attenuation of Erratic 6, Top Samples: 0.177 Attenuation from Erratic 6, Bottom Samples: 0.15
6-4 Bottom	3.79	2.58 ± 1.39	0.076
6-4 Top, top portion	3.71	3.59 ± 0.30	1.58
6-4 top, middle portion	6.42	5.45 ± 1.29	
6-4 top, bottom portion	3.99	2.78 ± 1.40	
8-2 Bottom	4.91	3.45 ± 1.68	0.610

8-2 top, bottom portion	3.27	2.32 ± 1.08	0.429
8-2 top, middle portion	4.51	4.07 ± 0.69	
8-2 top, top portion	3.53	2.54 ± 1.12	
8-3 bottom	2.63	1.74 ± 1.02	Attenuation from ^{10}Be: 0.084 Attenuation of Erratic 8, Top Samples: 0.238 Attenuation of Erratic 8, Bottom Samples: 0.25
8-3 top, bottom portion	3.41	2.38 ± 1.17	
8-3 top, top portion	3.84	2.80 ± 1.19	
8-4 bottom	4.48	3.33 ±1.29	0.107
8-4 top, bottom portion	2.98	2.12 ±0.98	0.173
8-4 top, middle portion	4.27	3.78 ± 0.70	
8-4 top, top portion	2.70	1.80 ± 1.03	

Erratic 3-7 Slices Attenuation from ^{10}Be: 0.103 mm^{-1} Attenuation of Erratic 3, Top samples: 0.130 mm^{-1} Attenuation of Erratic 3, Bottom samples: 0.509 mm^{-1}		
Slice	Beer-Lambert attenuation calculation	Average attenuation across visible light spectrum
1	10.91	8.91 ± 1.92
2	4.44	4.23 ± 0.41
3	5.93	5.15 ± 1.16
4	6.05	5.29 ± 1.24
5	7.52	6.64 ± 1.10
6	4.47	3.17 ± 1.49
7	6.61	5.61 ± 1.34
8	7.14	5.51 ± 1.82
9	7.88	6.31 ± 1.85
11	5.75	4.67 ± 1.16
12	4.23	2.78 ± 1.66
13	6.80	6.01 ± 1.24
14	3.92	2.65 ± 1.44
15	4.97	3.54 ± 1.63
16	6.57	5.75 ± 1.23
17	4.87	3.35 ± 1.64

A15a – Setup of light attenuation experiment

Light Attenuation Experiment

1

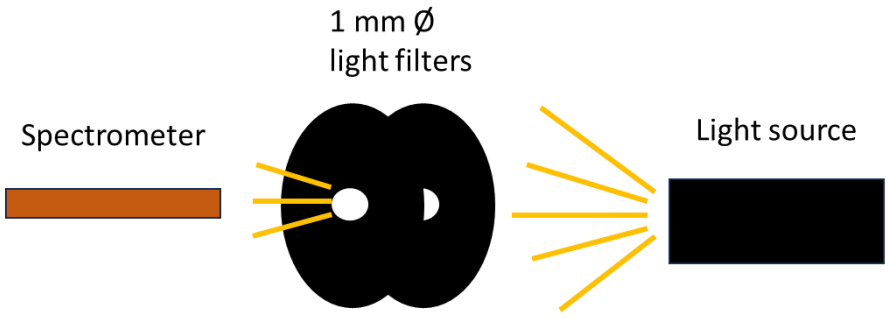

Measuring I_0 - Light from source is filtered through two 1 mm holes, recorded by spectrometer.

2

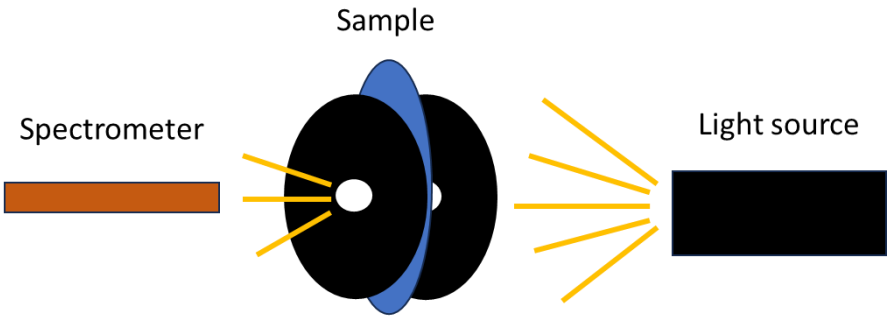

Measuring I - Sample is placed between two 1 mm holes, light filtered from sample is recorded by spectrometer.

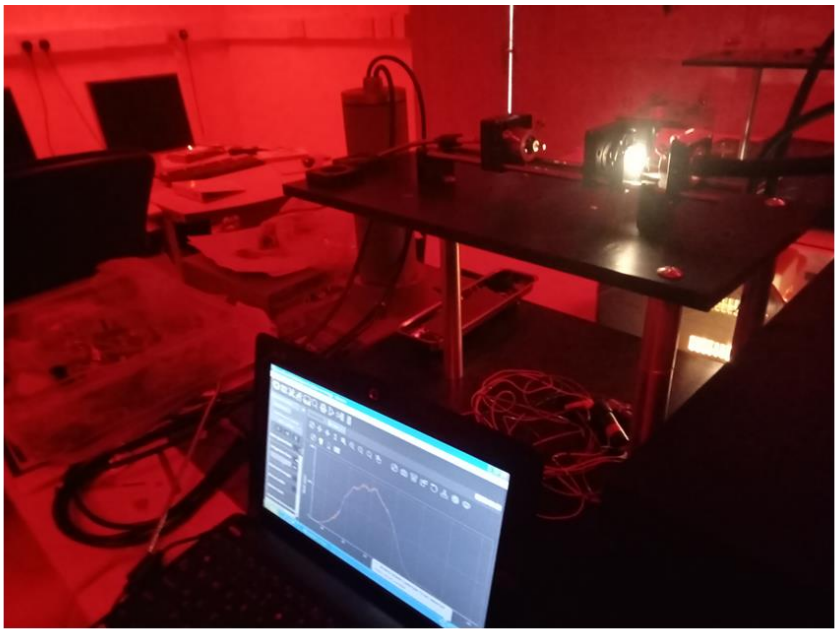

Spectrometer measuring light intensity.

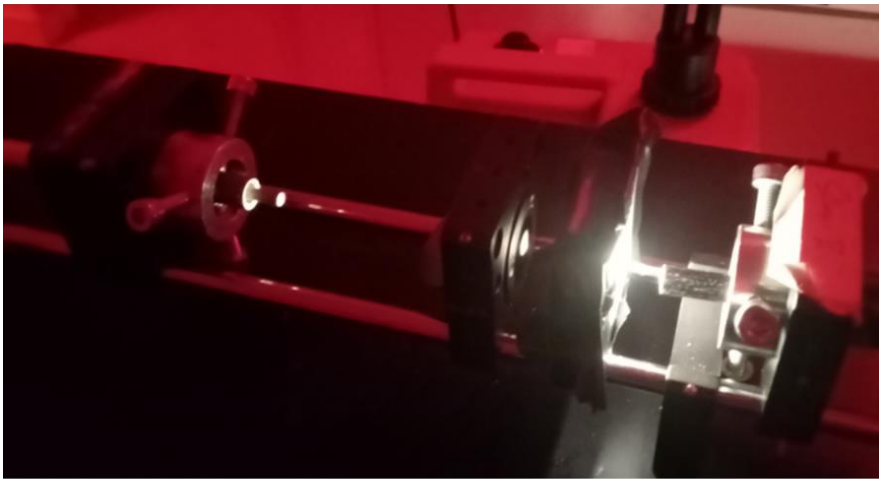

Spectrometer (left) lined up to light source (right). Near the light source are the two 1 mm light filters used to direct incident light onto sample.

A16 – Figures of LM-OSL curves for Erratic 3-7 slices

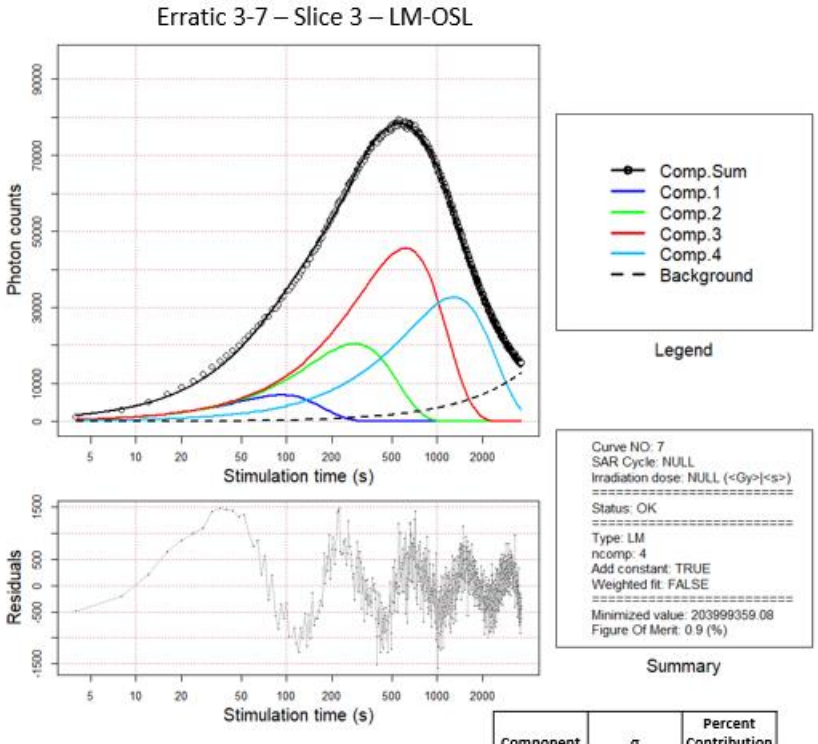

Component	σ	Percent Contribution
Component 1	2.74E-17 cm²	0.8%
Component 2	2.92E-18 cm²	7.7%
Component 3	6.31E-19 cm²	36.9%
Component 4	1.43E-19 cm²	54.5%

Erratic 3-7 – Slice 4 – LM-OSL

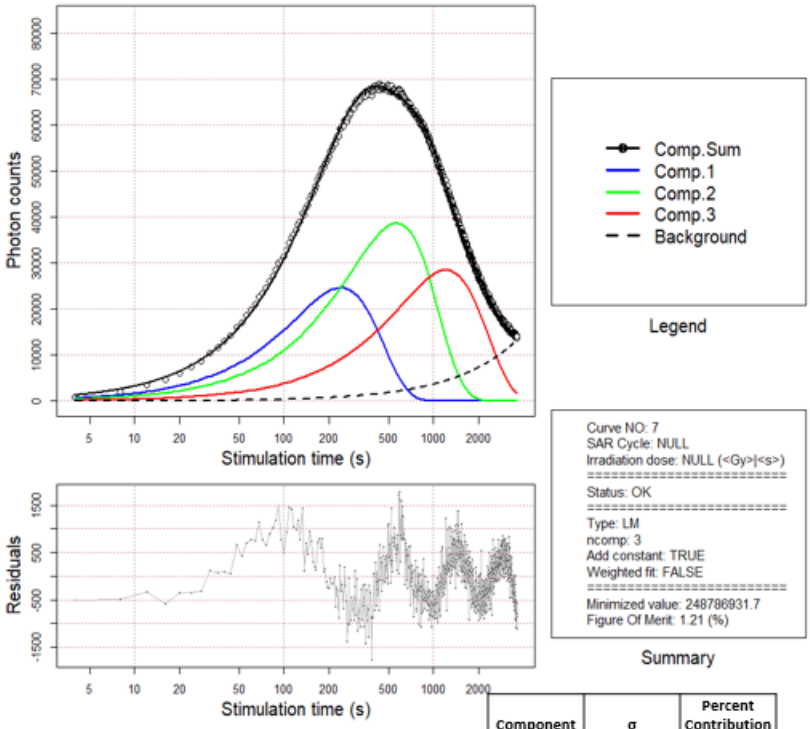

Component	σ	Percent Contribution
Component 1	4.10E-18 cm^{-2}	9.6%
Component 2	7.44E-19 cm^{-2}	35.3%
Component 3	1.62E-19 cm^{-2}	55.1%

Erratic 3-7 – Slice 5 – LM-OSL

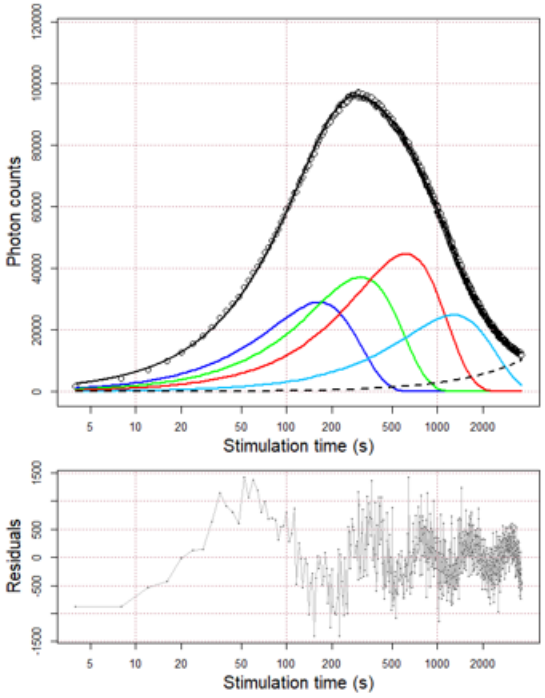

Component	σ	Percent Contribution
Component 1	8.79E-18 cm^{-2}	6.4%
Component 2	2.46E-18 cm^{-2}	15.4%
Component 3	6.33E-19 cm^{-2}	36.5%
Component 4	1.46E-19 cm^{-2}	41.7%

Erratic 3-7 – Slice 6 – LM-OSL

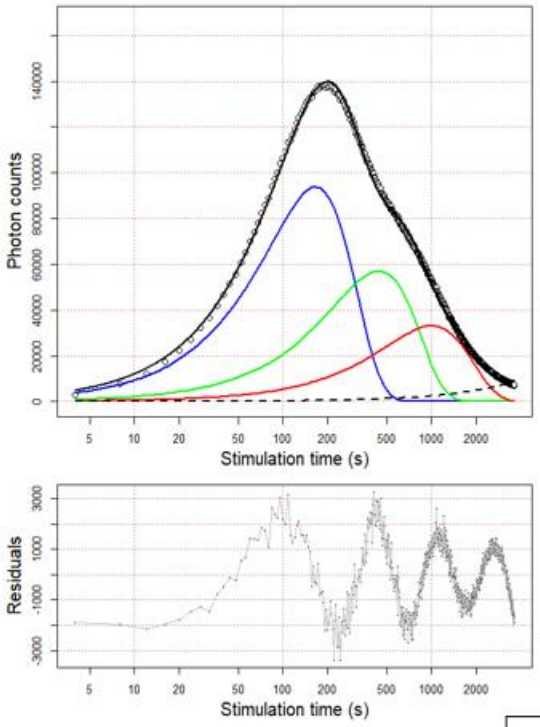

Component	σ	Percent Contribution
Component 1	8.66E-18 cm^{-2}	21%
Component 2	1.22E-18 cm^{-2}	34%
Component 3	2.35E-19 cm^{-2}	45%

Erratic 3-7 – Slice 7 – LM-OSL

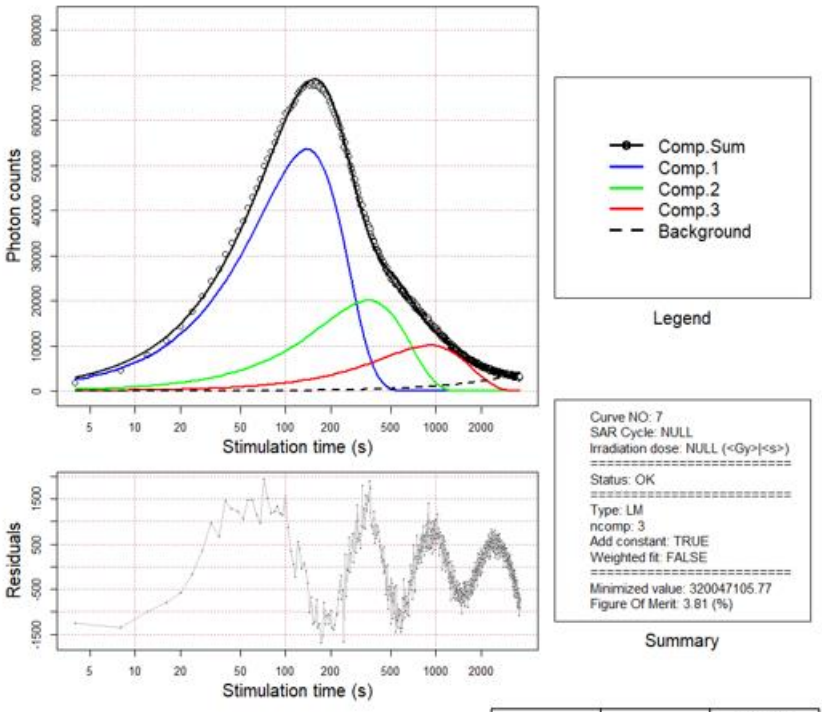

Component	σ	Percent Contribution
Component 1	1.23E-17 cm^{-2}	31.3%
Component 2	1.88E-18 cm^{-2}	30%
Component 3	2.87E-19 cm^{-2}	38.8%

Erratic 3-7 – Slice 8 – LM-OSL

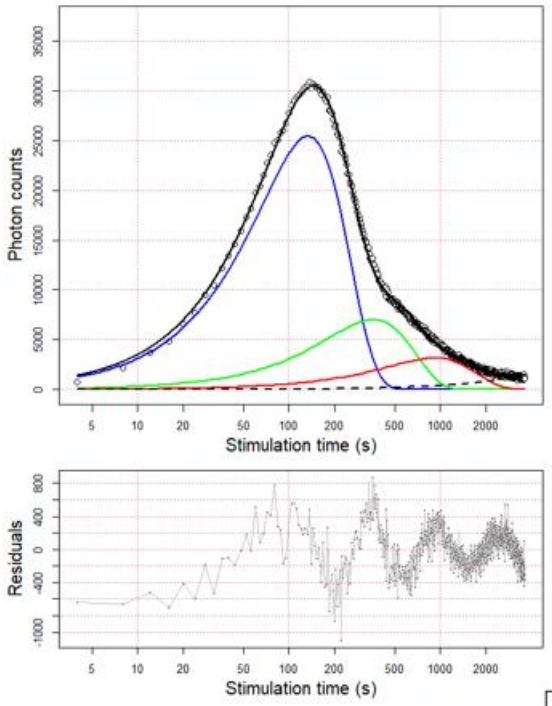

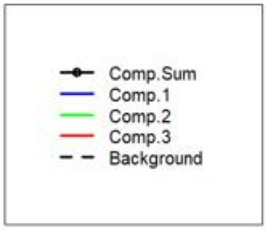

Legend

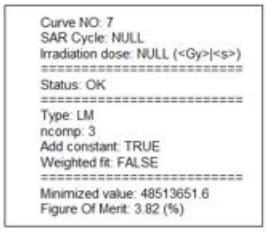

Summary

Component	σ	Percent Contribution
Component 1	1.33E-17 cm^{-2}	38.5%
Component 2	1.83E-18 cm^{-2}	28.6%
Component 3	2.81E-19 cm^{-2}	33%

Erratic 3-7 – Slice 9 – LM-OSL

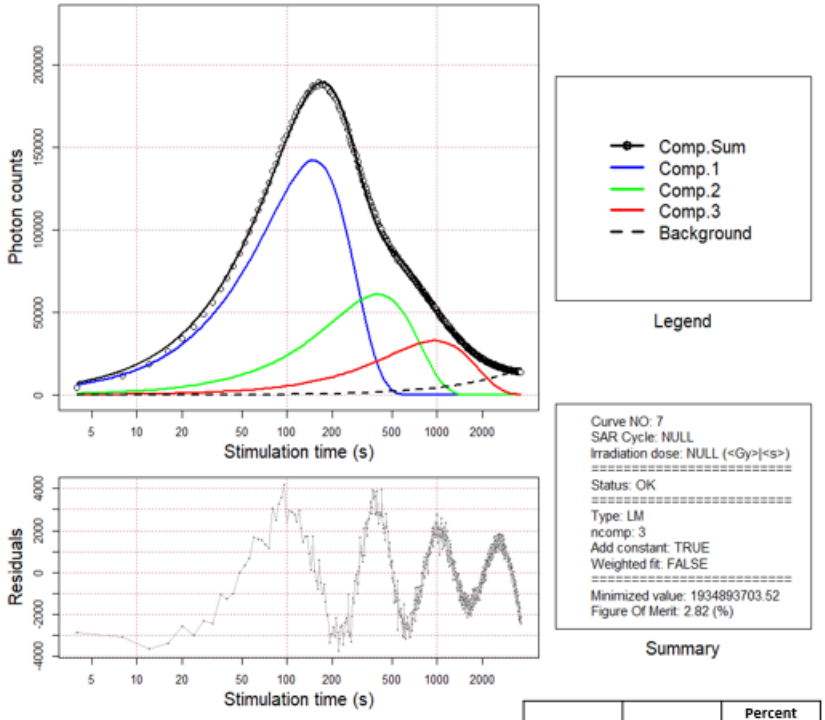

Component	σ	Percent Contribution
Component 1	1.04E-17 cm^{-2}	27.5%
Component 2	1.47E-18 cm^{-2}	31.5%
Component 3	2.53E-19 cm^{-2}	41%

A17 – Light attenuation plots from the Foothills Erratics Train Samples

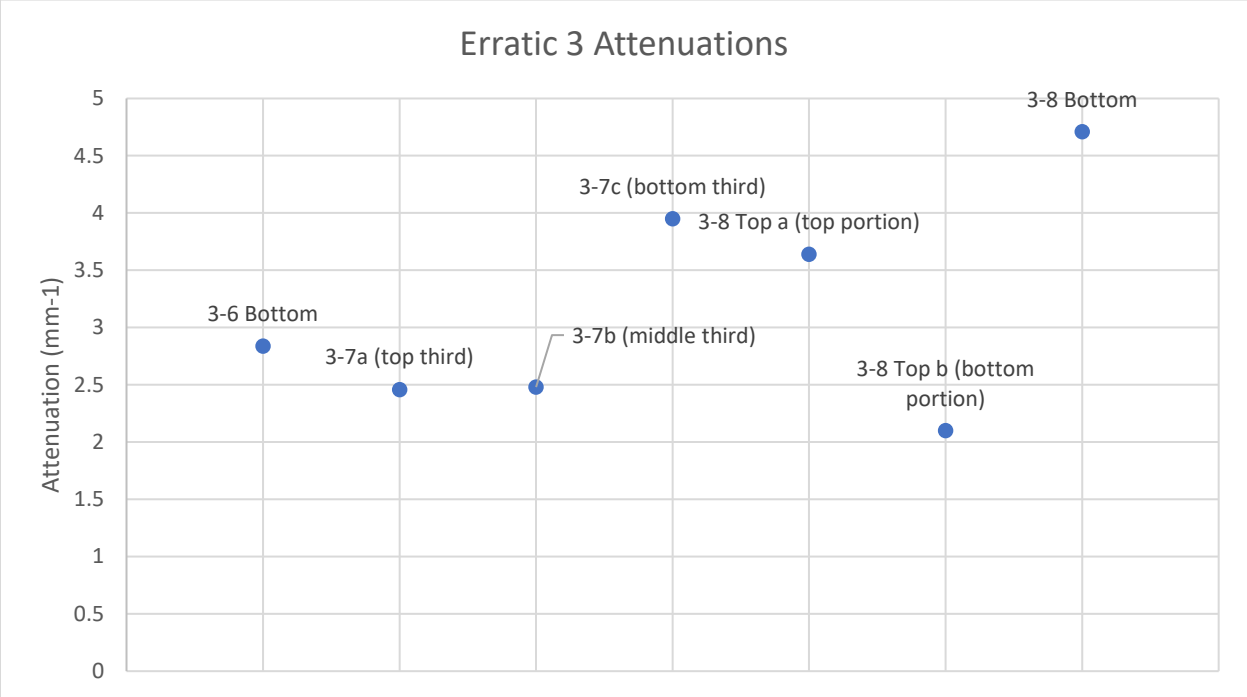

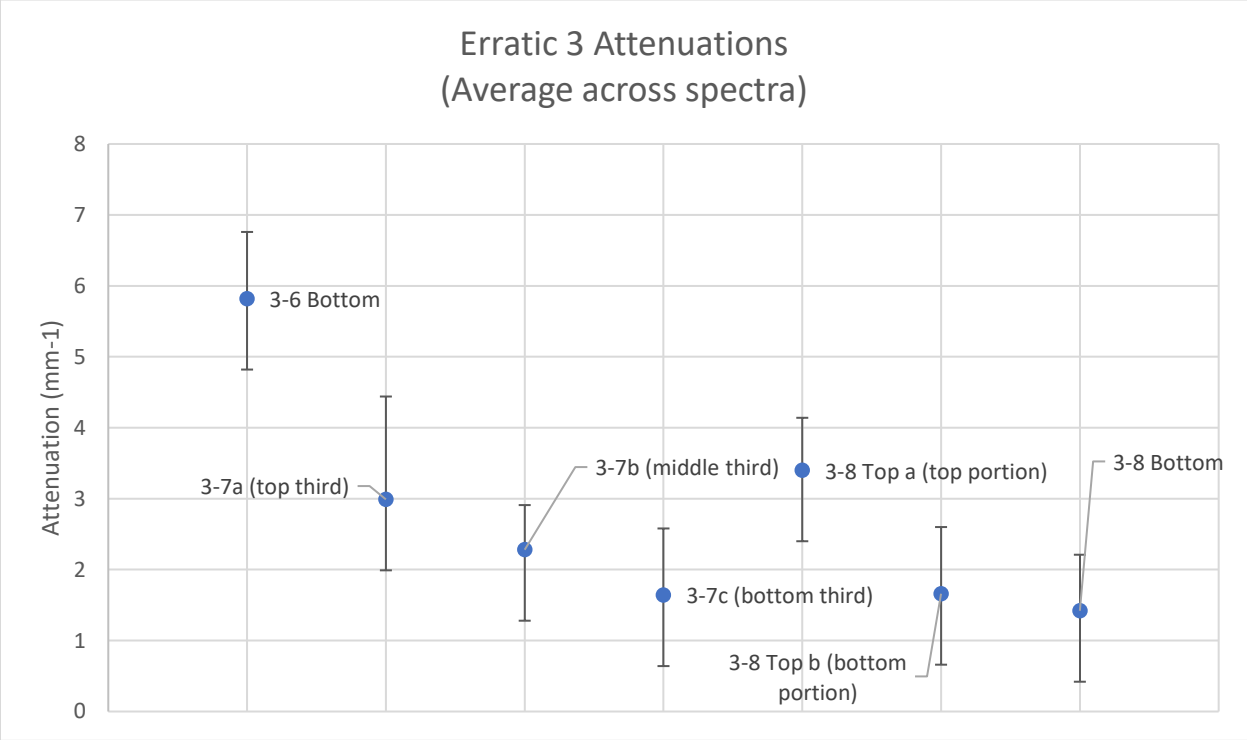

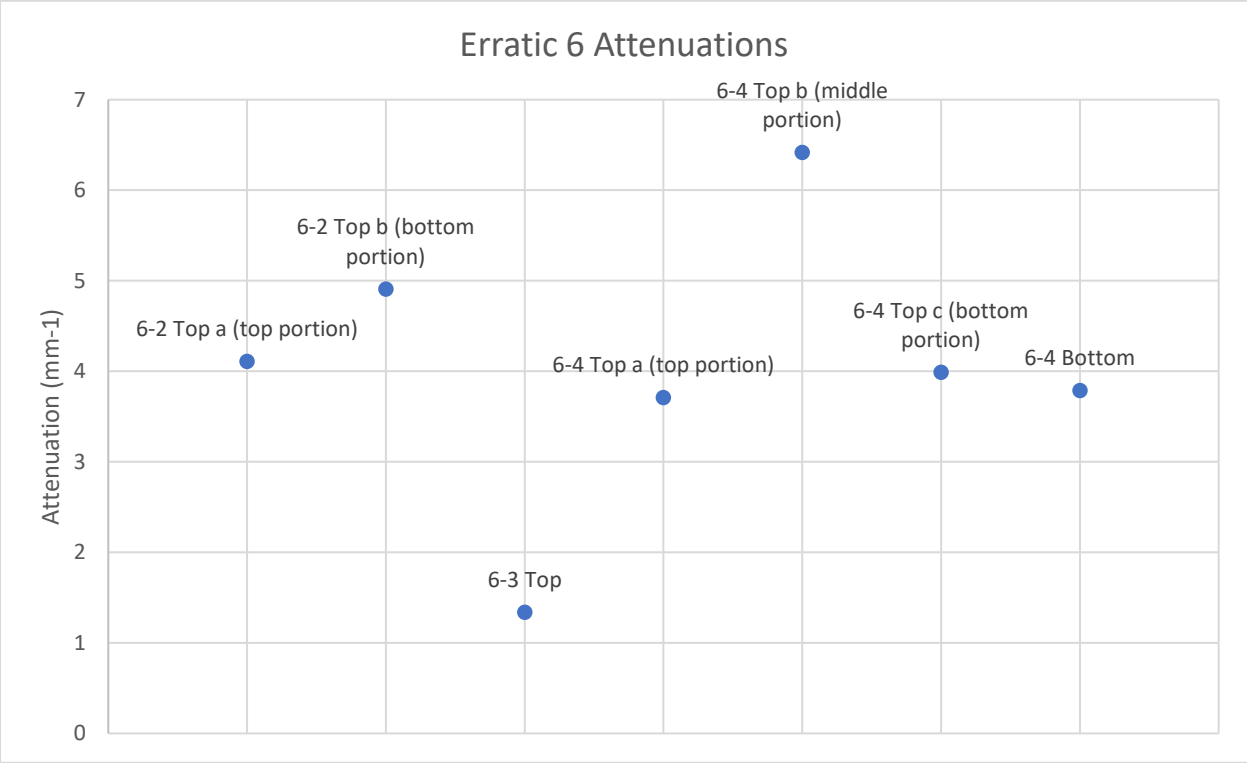
Erratic 6 Attenuations
Attenuation (mm-1)
0
1
2
3
4
5
6
7
6-2 Top a (top portion)
6-2 Top b (bottom portion)
6-3 Top
6-4 Top a (top portion)
6-4 Top b (middle portion)
6-4 Top c (bottom portion)
6-4 Bottom

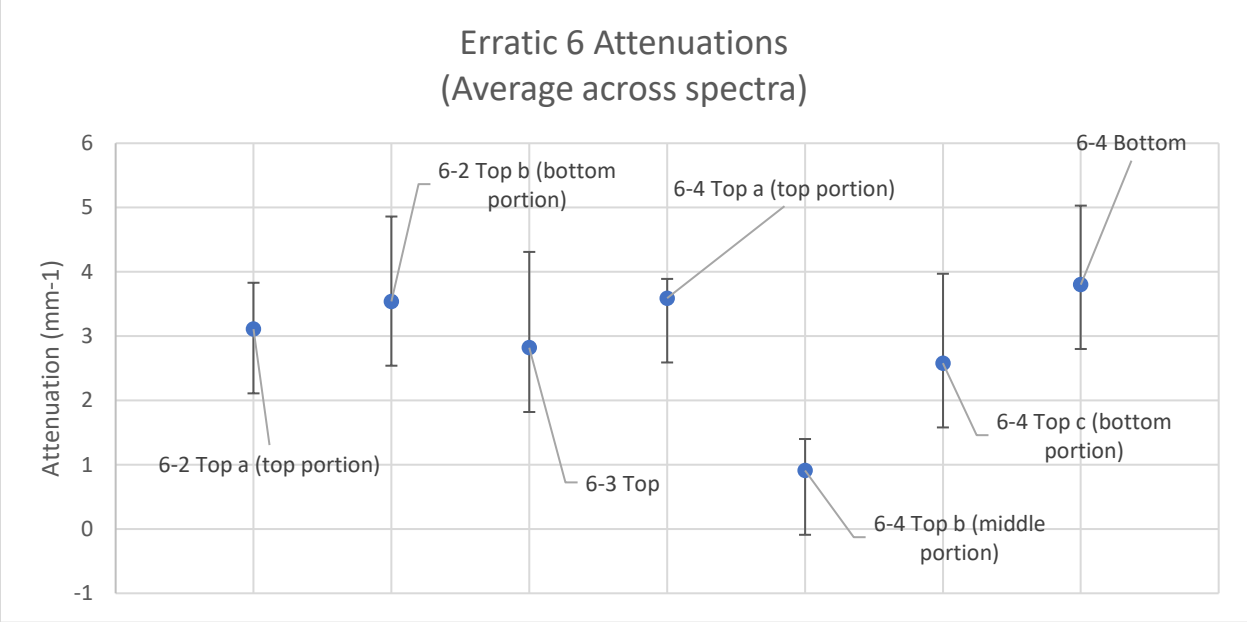
Erratic 6 Attenuations
(Average across spectra)
Attenuation (mm-1)
-1
0
1
2
3
4
5
6
6-2 Top a (top portion)
6-2 Top b (bottom portion)
6-3 Top
6-4 Top a (top portion)
6-4 Top b (middle portion)
6-4 Top c (bottom portion)
6-4 Bottom

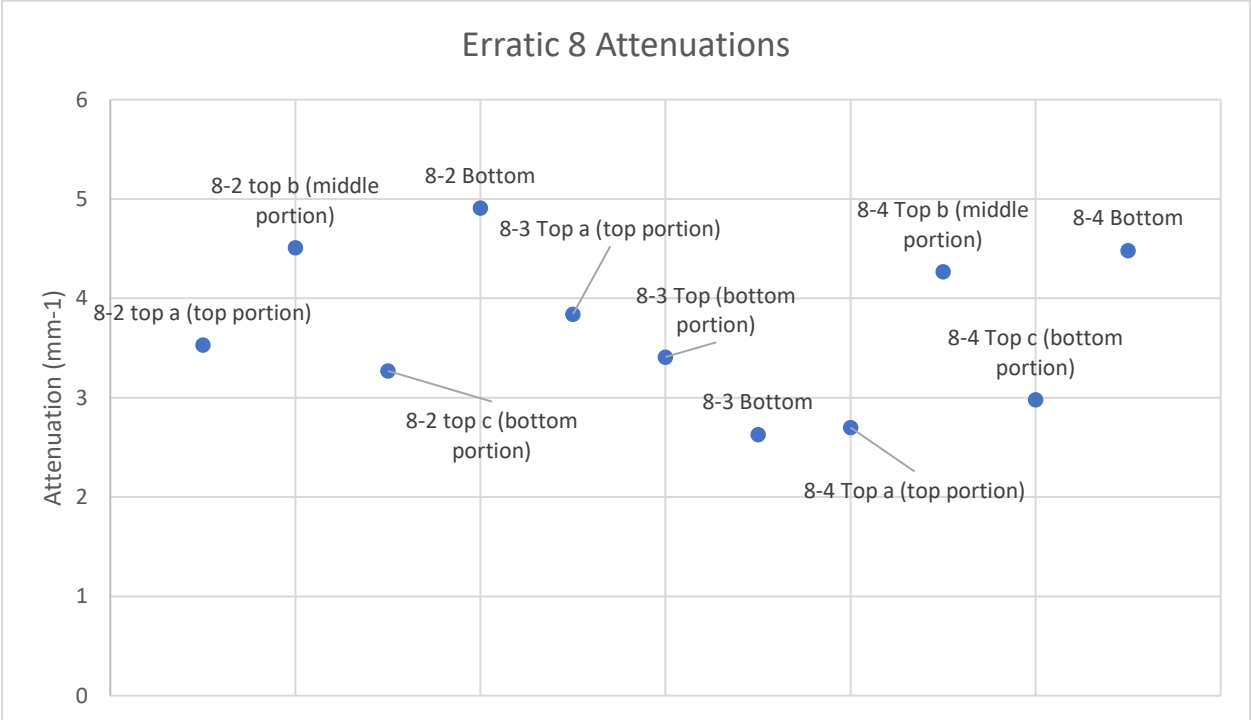
Erratic 8 Attenuations
Attenuation (mm-1)
0
1
2
3
4
5
6
8-2 top b (middle portion)
8-2 Bottom
8-3 Top a (top portion)
8-4 Top b (middle portion)
8-4 Bottom
8-2 top a (top portion)
8-3 Top (bottom portion)
8-4 Top c (bottom portion)
8-2 top c (bottom portion)
8-3 Bottom
8-4 Top a (top portion)

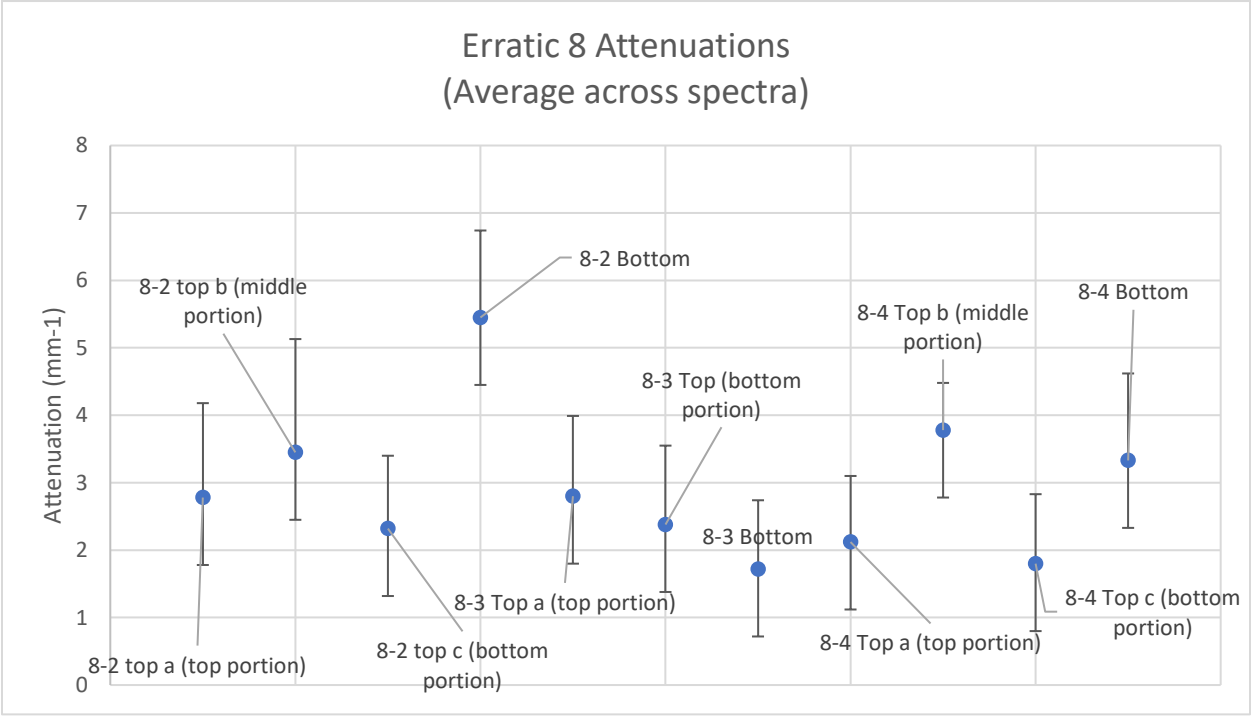
Erratic 8 Attenuations
(Average across spectra)
Attenuation (mm-1)
0
1
2
3
4
5
6
7
8
8-2 top b (middle portion)
8-2 Bottom
8-4 Top b (middle portion)
8-4 Bottom
8-3 Top (bottom portion)
8-3 Bottom
8-2 top a (top portion)
8-3 Top a (top portion)
8-2 top c (bottom portion)
8-4 Top a (top portion)
8-4 Top c (bottom portion)

A17a – Figures of Light Attenuation Curves for Lane Mountain Samples

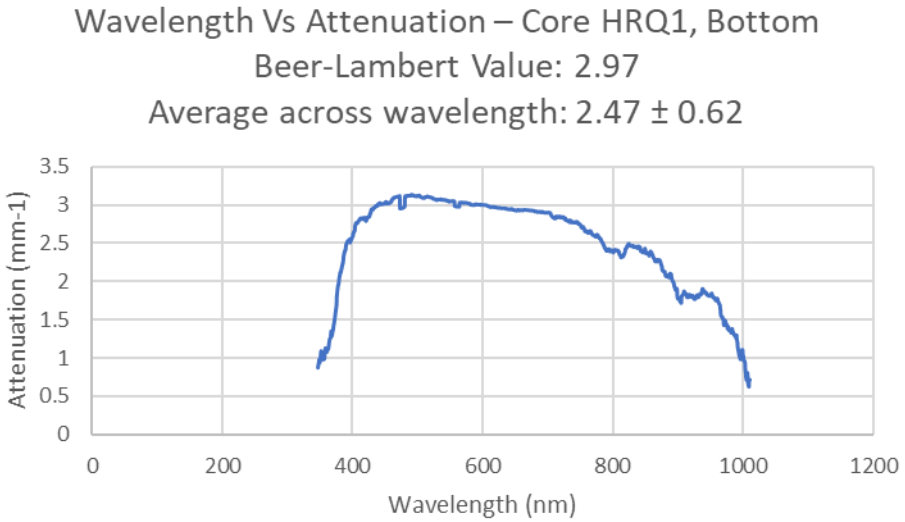

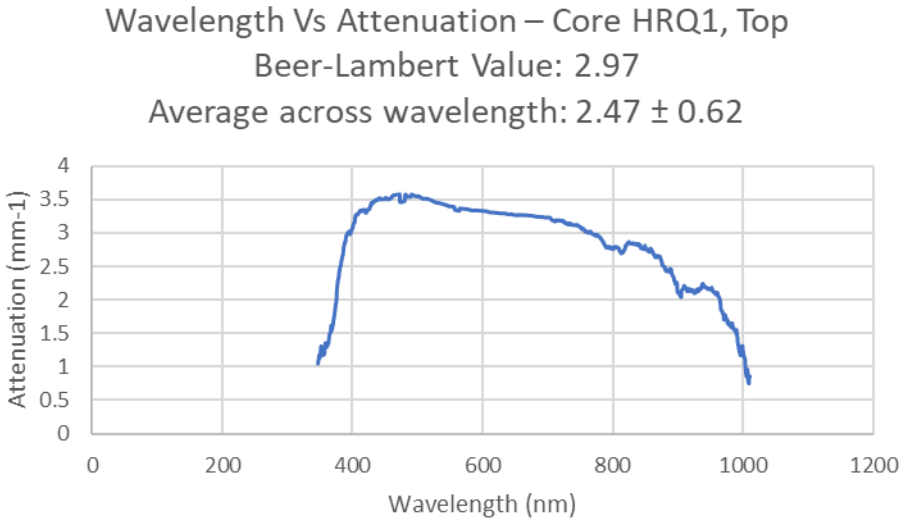

Wavelength Vs Attenuation – Core HRQ2, Bottom
Beer-Lambert Value: 1.42
Average across wavelength: 0.97 ± 0.49

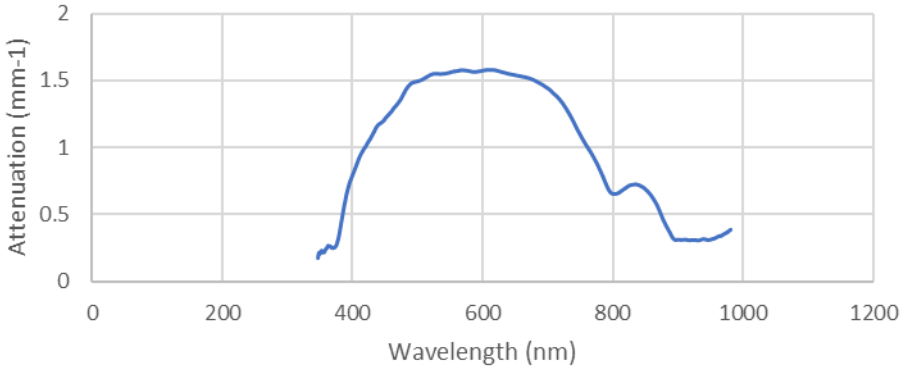

Wavelength Vs Attenuation – Core HRQ2, Top
Beer-Lambert Value: 1.89
Average across wavelength: 1.32 ± 0.66

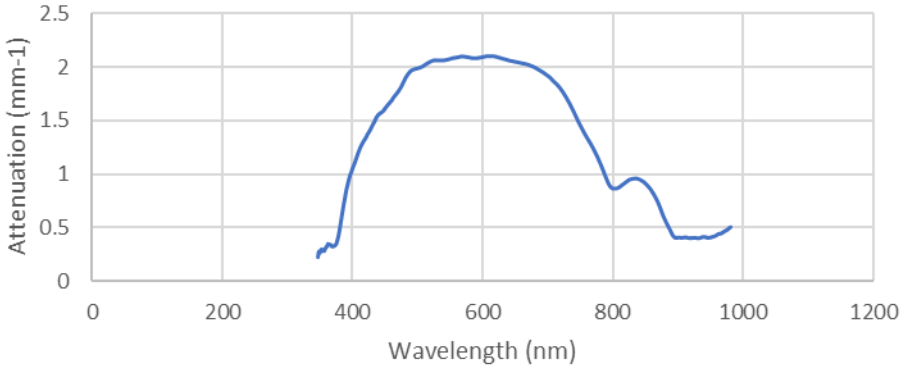

Wavelength Vs Attenuation – Core P2, Bottom
Beer-Lambert Value: 2.47
Average across wavelength: 1.71 ± 0.87

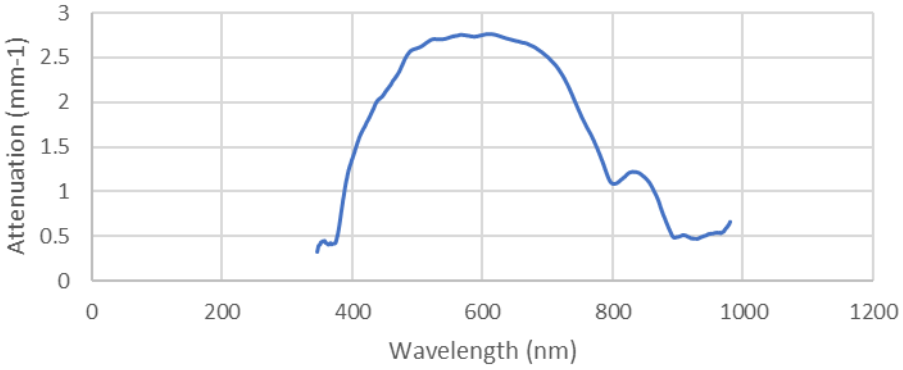

Wavelength Vs Attenuation – Core P2, Top
Beer-Lambert Value: 2.52
Average across wavelength: 1.90 ± 0.72

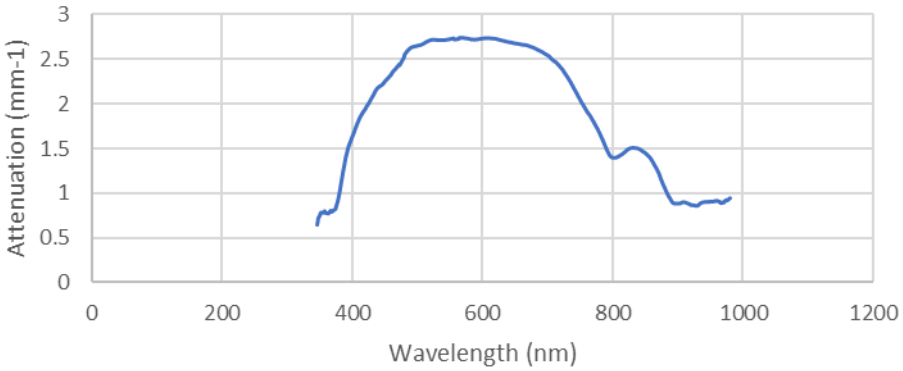

Wavelength Vs Attenuation – Core P3, Bottom
Beer-Lambert Value: 2.16
Average across wavelength: 1.44 ± 0.82

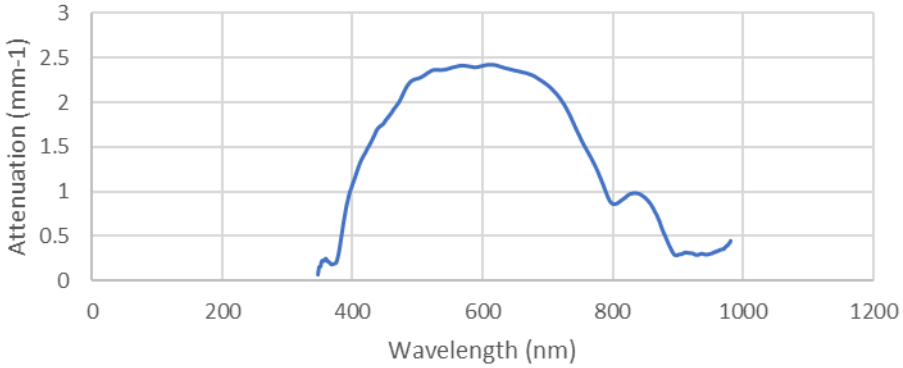

Wavelength Vs Attenuation – Core P3, Top
Beer-Lambert Value: 2.32
Average across wavelength: 1.76 ± 0.63

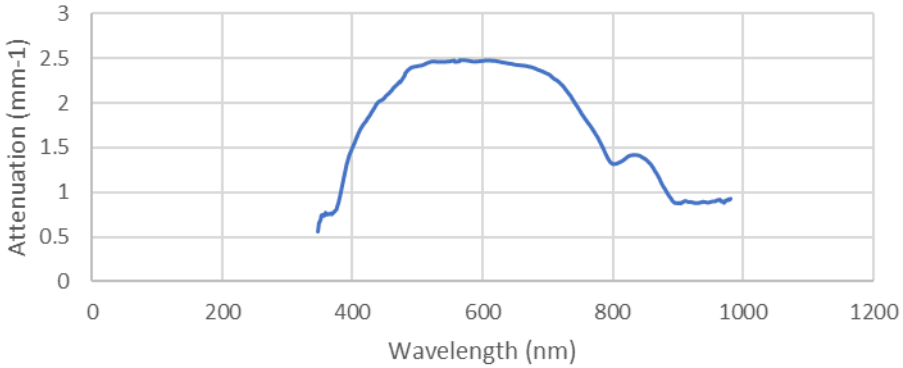

A18 – Figures of Light Attenuation versus Depth, Light attenuation versus spectra, light attenuation versus sample thickness, for Foothills Erratics Train Sample 3-7

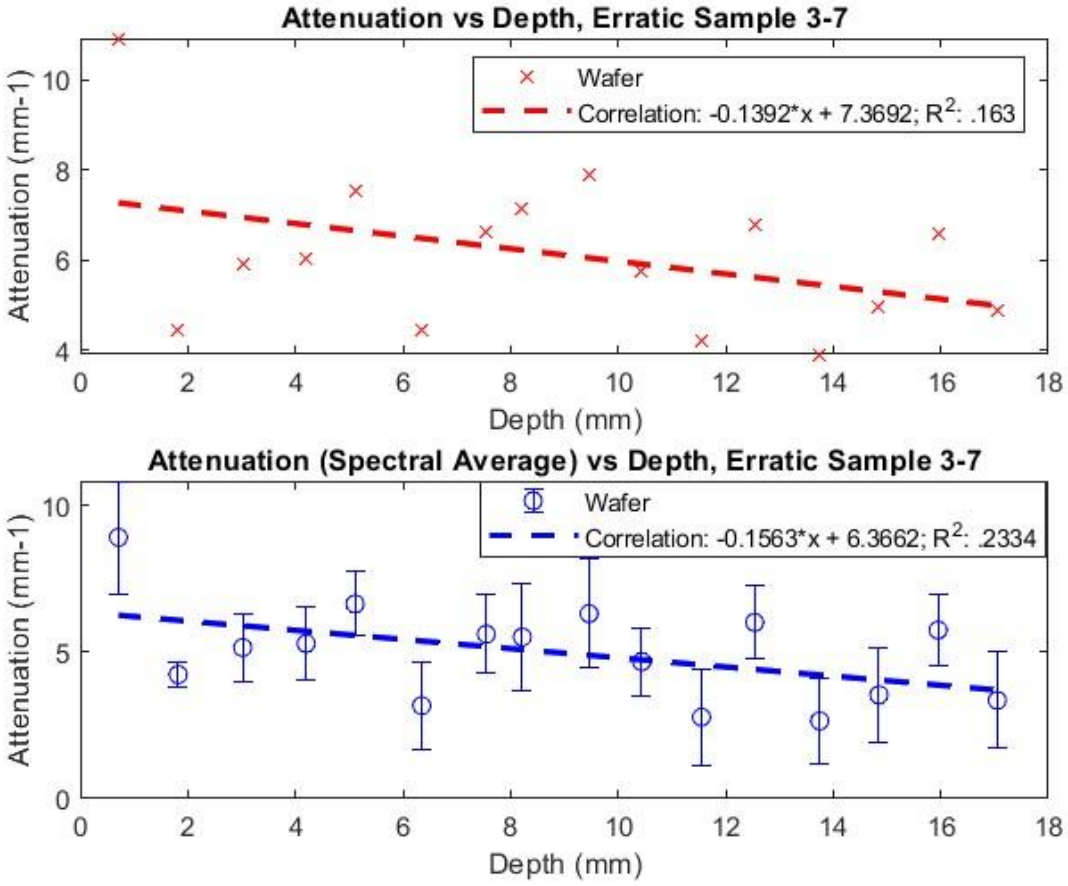

Wavelength Vs Attenuation – Core 3-7, Slice 1
0.71 mm thick
Beer-Lambert Value: 10.19
Average across wavelength: 8.91 ± 1.92

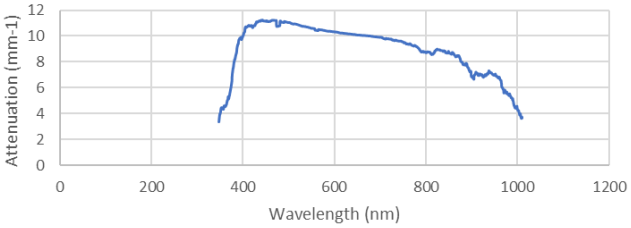

Wavelength vs Attenuation – Core 3-7, Slice 2
(1.11 mm thick)
Beer-Lambert Value: 4.44
Average across wavelength: 4.23 ± 0.41

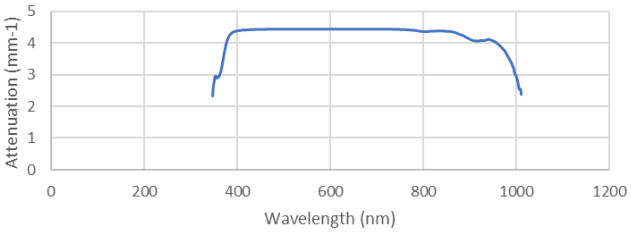

Wavelength vs Attenuation – Core 3-7, Slice 3
(1.20 mm thick)
Beer-Lambert Value: 5.93
Average across wavelength: 5.15 ± 1.16

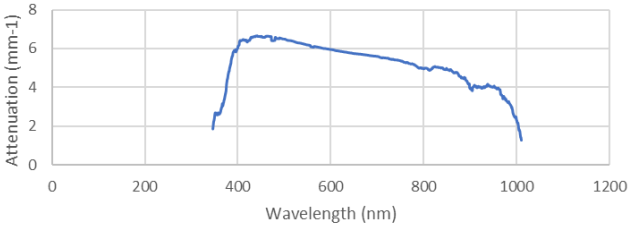

Wavelength Vs Attenuation – Core 3-7, Slice 4
1.18 mm thick
Beer-Lambert Value: 6.05
Average across wavelength: 5.29 ± 1.24

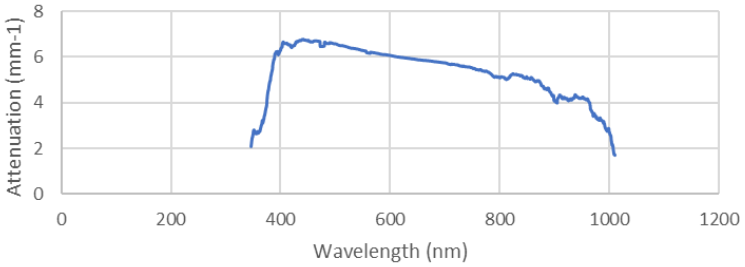

Wavelength Vs Attenuation – Core 3-7, Slice 5
0.91 mm thick
Beer-Lambert Value: 7.52
Average across wavelength: 6.64 ± 1.40

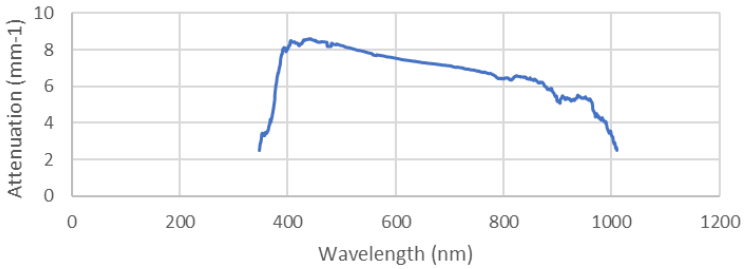

Wavelength Vs Attenuation – Core 3-7, Slice 6
1.24 mm thick
Beer-Lambert Value: 4.47
Average across wavelength: 3.17 ± 1.49

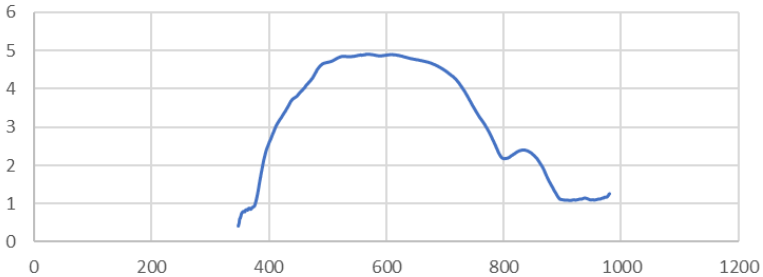

Wavelength Vs Attenuation – Core 3-7, Slice 7
1.20 mm thick
Beer-Lambert Value: 6.61
Average across wavelength: 5.61 ± 1.34

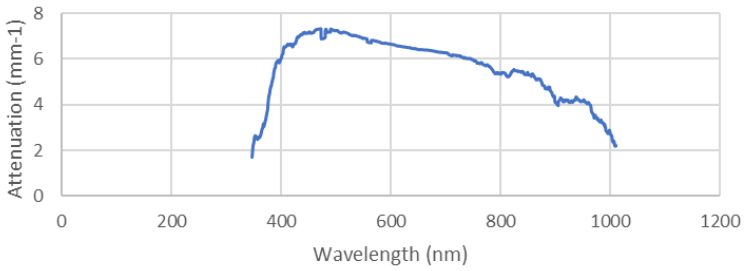

Wavelength Vs Attenuation – Core 3-7, Slice 8
0.67 mm thick
Beer-Lambert Value: 7.14
Average across wavelength: 5.51 ± 1.82

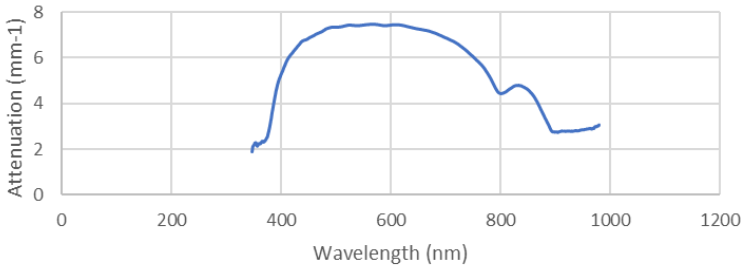

Wavelength Vs Attenuation – Core 3-7, Slice 9
1.24 mm thick
Beer-Lambert Value: 7.88
Average across wavelength: 6.31 ± 1.85

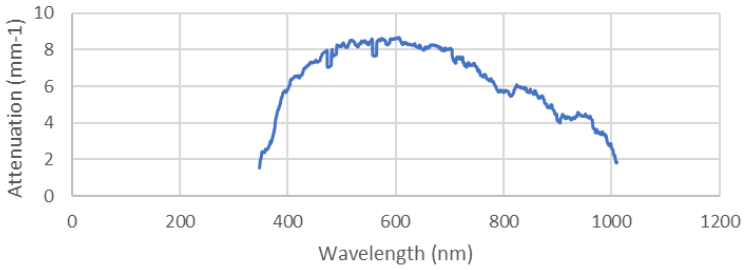

Wavelength Vs Attenuation – Core 3-7, Slice 11
0.98 mm thick
Beer-Lambert Value: 5.75
Average across wavelength: 4.67 ± 1.16

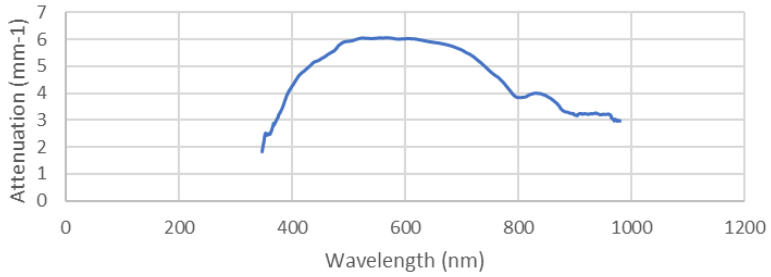

Wavelength Vs Attenuation – Core 3-7, Slice 12
1.11 mm thick
Beer-Lambert Value: 4.23
Average across wavelength: 2.78 ± 1.66

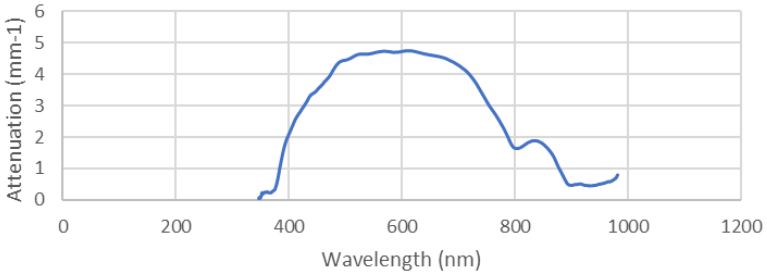

Wavelength Vs Attenuation – Core 3-7, Slice 13
0.99 mm thick
Beer-Lambert Value: 6.80
Average across wavelength: 6.01 ± 1.24

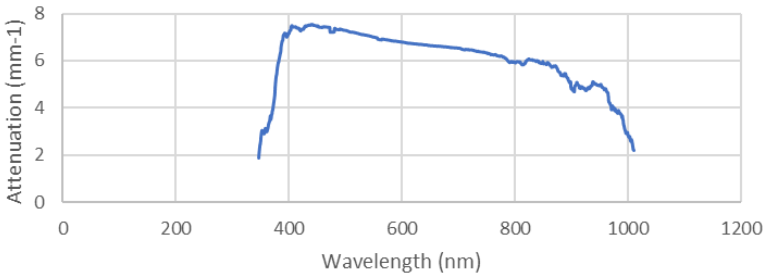

Wavelength Vs Attenuation – Core 3-7, Slice 14
1.21 mm thick
Beer-Lambert Value: 3.92
Average across wavelength: 2.65 ± 1.44

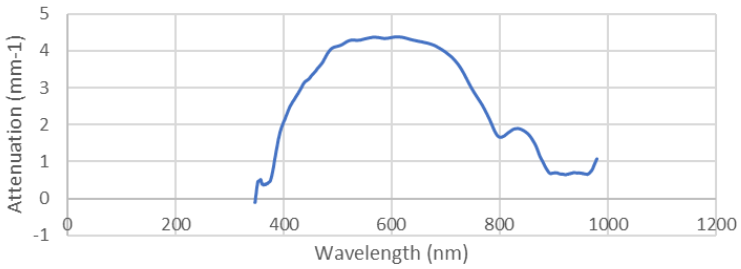

Wavelength Vs Attenuation – Core 3-7, Slice 15
1.1 mm thick
Beer-Lambert Value: 4.97
Average across wavelength: 3.54 ± 1.63

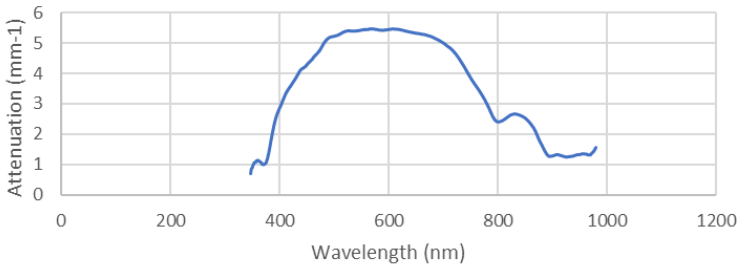

Wavelength Vs Attenuation – Core 3-7, Slice 16
1.1 mm thick
Beer-Lambert Value: 6.57
Average across wavelength: 5.75 ± 1.23

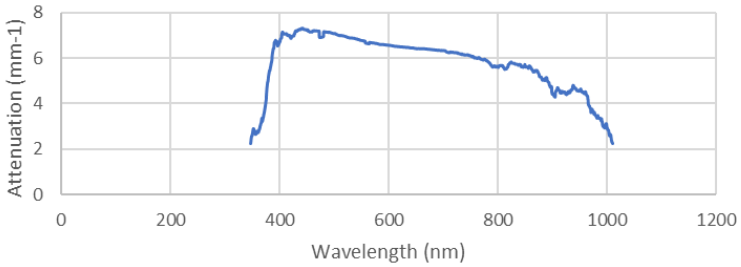

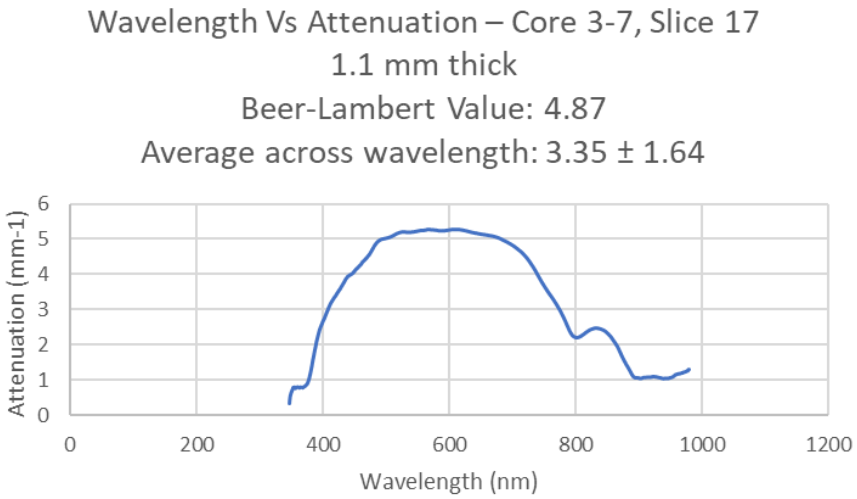
Wavelength Vs Attenuation – Core 3-7, Slice 17
1.1 mm thick
Beer-Lambert Value: 4.87
Average across wavelength: 3.35 ± 1.64
Attenuation (mm-1)
0
1
2
3
4
5
6
0
200
400
600
800
1000
1200
Wavelength (nm)

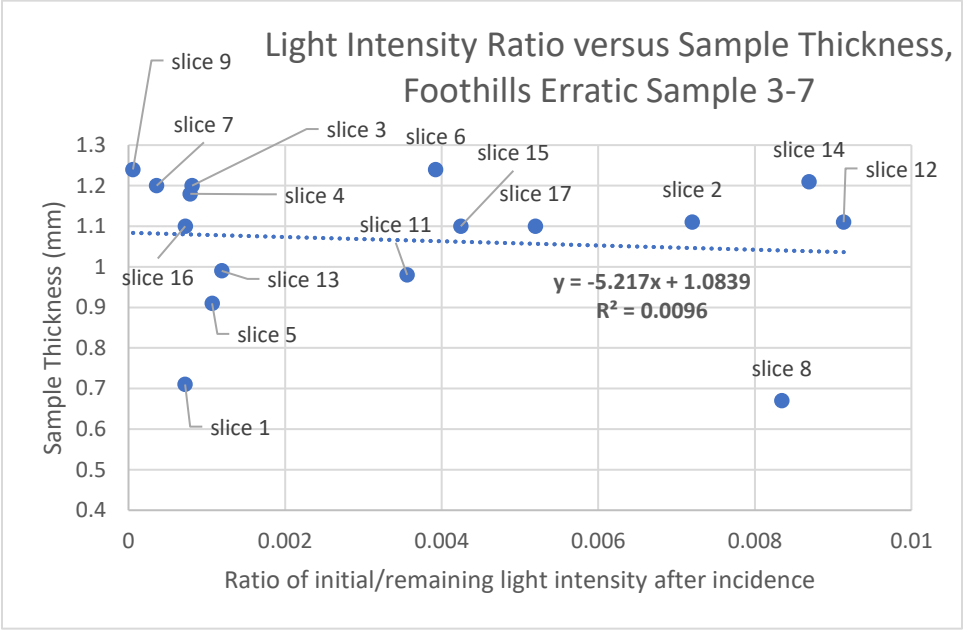
Light Intensity Ratio versus Sample Thickness, Foothills Erratic Sample 3-7
slice 9
slice 7
slice 3
slice 6
slice 15
slice 14
slice 12
slice 4
slice 17
slice 2
slice 11
slice 16
slice 13
slice 5
slice 8
slice 1
y = -5.217x + 1.0839
R² = 0.0096
Sample Thickness (mm)
0.4
0.5
0.6
0.7
0.8
0.9
1
1.1
1.2
1.3
0
0.002
0.004
0.006
0.008
0.01
Ratio of initial/remaining light intensity after incidence

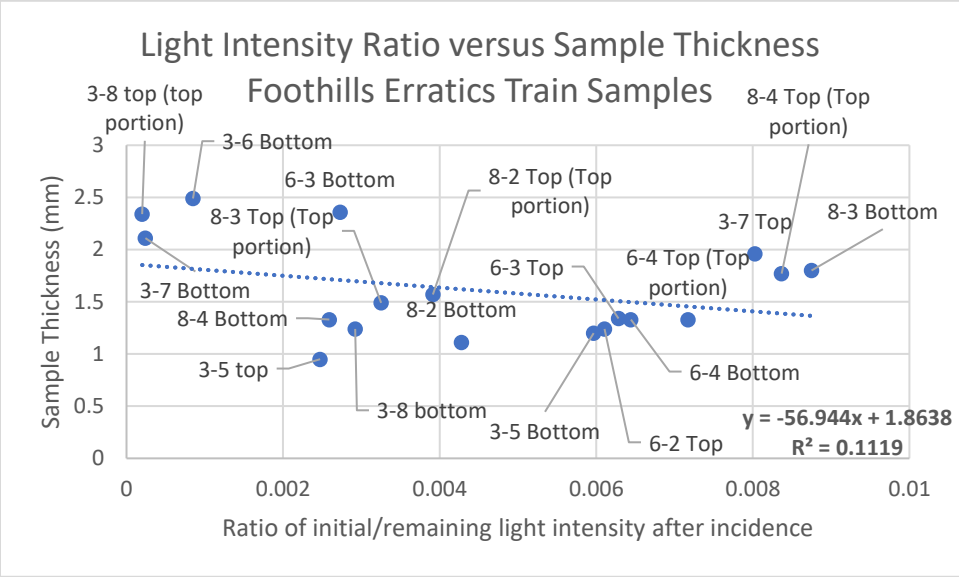
Light Intensity Ratio versus Sample Thickness
Foothills Erratics Train Samples
Sample Thickness (mm)
Ratio of initial/remaining light intensity after incidence
3-8 top (top portion)
3-6 Bottom
6-3 Bottom
8-3 Top (Top portion)
8-2 Top (Top portion)
8-4 Top (Top portion)
3-7 Top
8-3 Bottom
6-4 Top (Top portion)
6-3 Top
3-7 Bottom
8-4 Bottom
8-2 Bottom
3-5 top
3-8 bottom
3-5 Bottom
6-2 Top
6-4 Bottom
y = -56.944x + 1.8638
R² = 0.1119
0
0.5
1
1.5
2
2.5
3
0
0.002
0.004
0.006
0.008
0.01

A19 – Sample 3-7 $\overline{\sigma\varphi_0}$ parameter calculations, 470 nm

Sample	Photoionization cross section average (cm^2)	$\overline{\sigma\varphi_0}$ for 470 nm (s^{-1})	Fitted $\overline{\sigma\varphi_0}$ for Erratic 3
3	7.70E-19	3.19	^{10}Be parameterization 3-7 - $\overline{\sigma\varphi_0}$= 2.45E-11 s^{-1} Top parameters Erratic 3, $\overline{\sigma\varphi_0}$= 2.39E-06 s^{-1} Bottom Parameters Erratic 3: $\overline{\sigma\varphi_0}$= 2.57E-05 s^{-1}
4	7.46E-19	3.09	
5	2.01E-18	8.31	
6	2.34E-18	9.67	
7	4.52E-18	18.71	
8	5.72E-18	23.66	
9	3.43E-18	14.20	

A20 – Images of Erratic 3-7 Slices for LM-OSL and Attenuation Measures

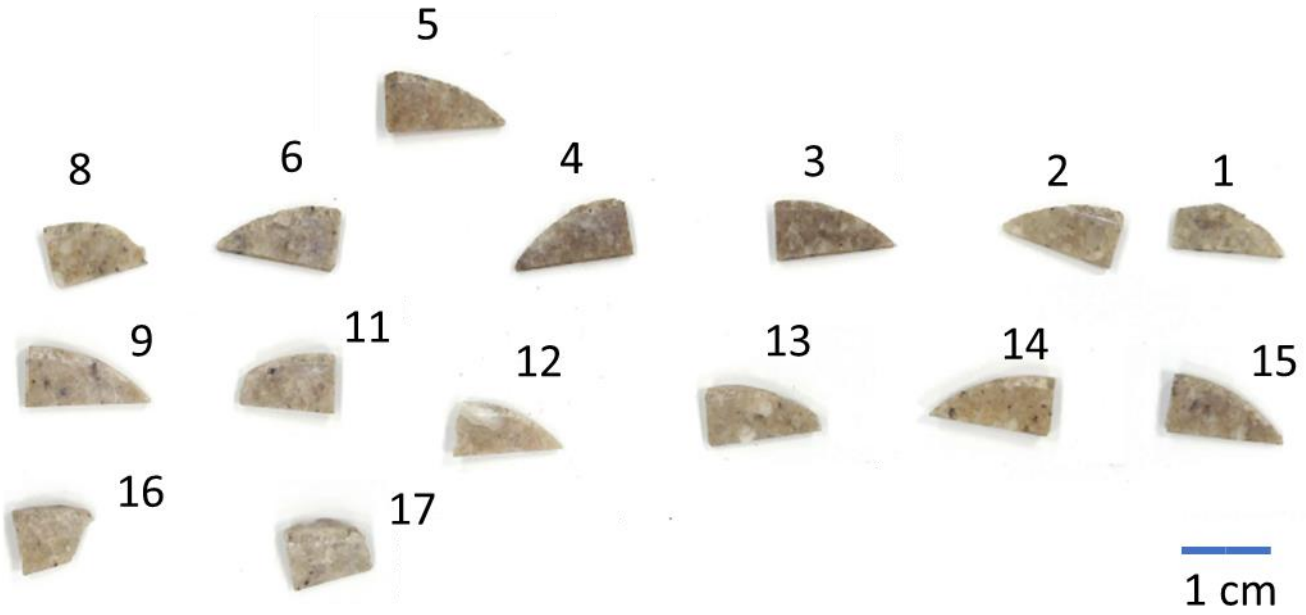

A21 – Dose Rate Calculations of Erratics 3, 6, and 8

Measured concentrations (Cresswell et al. 2018)

Sample	% K		ppm eU		ppm eTh	
TB 3-2	4.118	0.051	1.757	0.081	6.402	0.198
TB 6-2	2.814	0.153	1.796	0.098	14.329	0.396
TB 8-7	3.185	0.172	1.400	0.083	5.665	0.236

DRAC -inputs (Durcan et al. 2015)

DRAC-FT3	Polymineral	PM	Guerinetal2011			1.757	0.081	6.402	0.198	4.118	
0.051	0	0	Y	X	X	X	X	X	X	X	X
N	X	X	X	X	X	X	X	X	Y	100	1000
Bell1980		Mejdahl1979	0	0	Bell1979		0.086	0.0038	0	0	
0.1	0.05	2.7	0.1	49.77830		-113.65108		1120	X	X	X
X											
DRAC-FT6	Polymineral	PM	Guerinetal2011			1.796	0.098	14.329	0.396	2.814	
0.153	0	0	Y	X	X	X	X	X	X	X	X
N	X	X	X	X	X	X	X	X	Y	100	1000
Bell1980		Mejdahl1979	0	0	Bell1979		0.086	0.0038	0	0	
0.1	0.05	2.7	0.1	49.95588		-113.83614		1209	X	X	X
X											
DRAC-FT8	Polymineral	PM	Guerinetal2011			1.400	0.0083	5.665	0.236	3.185	
0.172	0	0	Y	X	X	X	X	X	X	X	X
N	X	X	X	X	X	X	X	X	Y	100	1000
Bell1980		Mejdahl1979	0	0	Bell1979		0.086	0.0038	0	0	
0.1	0.05	2.7	0.1	50.10248		-113.78622		1132	X	X	X
X											

DRAC outputs

Sample	α	αerr	β	βerr	γ	γerr	Cosmicdoserate (Gy.ka-1)	errCosmicdoserate (Gy.ka-1)
Erratic 3	0.105	0.061	3.009	0.012	1.274	0.022	0.498	0.05
Erratic 6	0.175	0.11	2.316	0.008	1.327	0.038	0.498	0.05
Erratic 8	0.089	0.052	2.345	0.009	1.018	0.039	0.498	0.05

Sample	Environmental Dose Rate (Gy.ka-1)	errEnvironmental Dose Rate (Gy.ka-1)
Erratic 3	4.699	0.073
Erratic 6	4.134	0.121
Erratic 8	3.764	0.072

A22 – Moss coverage of Erratics, Splay of Erratic 8

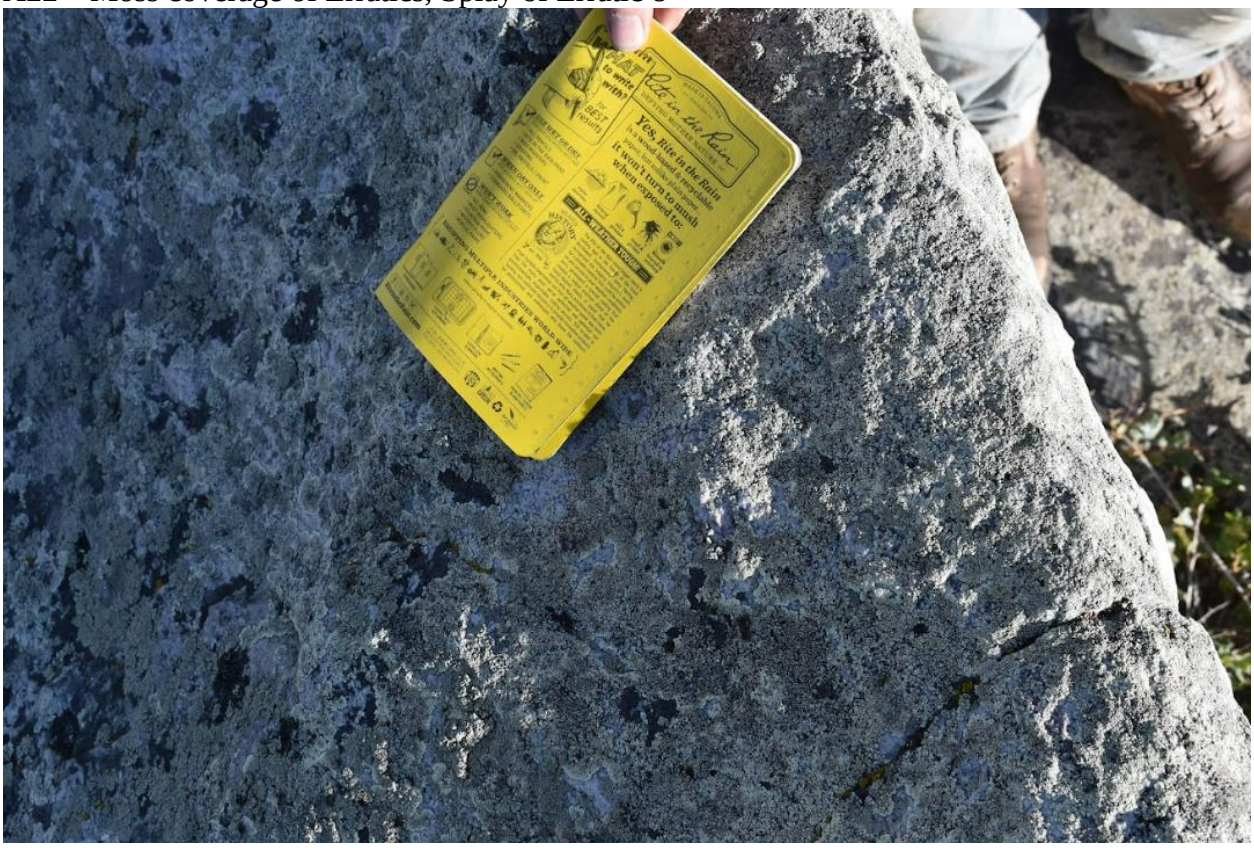

Erratic 8 moss coverage, along edge of erratic. Granular weathering also observed.

Erratic 8 surface – lichens/moss present on surface.

Moss/lichen coverage, Erratic 3 surface.

Erratic 6 moss and lichen coverage near surface.

Granular, blocky weathering observed in Erratic 6 surface.

Erratic 8 appears split into two portions at some point after its deposition along the Erratic Train. Half of the original erratic has splayed, in front, while behind the splayed portion is the remainder of the erratic in its original orientation.

A23 – ^{14}C age calculations from Margold et al. (2019), CRONUS Inputs

Sample	Location		Elevation	Dated	Radiocarbon	Calibrated		
laboratory no.	Latitude (°N)	Longitude (°W)	(m asl)	material	(^{14}C yr BP)	(cal yr BP)	Locality	Reference
TO-2742	56.167	120.733	~ 600	Wood	13,970 ± 170	17,464–16,417	Ft. St John	Catto et al., 1996
AA-46352	56.28083	121.22750	~500	*Microtus*	12,567 ± 49	15,150–14,565	Bear Flat fan	Hebda et al., 2008
SFU-223	55.575	119.425	871	*Populus* wood	11,700 ± 260	14,223–13,030	Boone Lake	White et al., 1979, 1985; Bobrowski and Rutter, 1992
WAT-408	55.575	119.425	871	Gyttja	12,650 ± 320	15,991–13,946	Boone Lake	White et al., 1979
AECV-430C	52.75	117.66667	~1780	Lake sediments	12,350 ± 440	15,901–13,416	Lorraine Lake	Bobrowsky and Rutter, 1992
AECV-1203C	53.5	113.75	~710	*Bison*	11,620 ± 170	13,780–13,108	Clover Bar Pit	Burns, 1996
AECV-1117C	53.1	113.85	~815	Lake sediments[b]	11,570 ± 290	14,093–12,809	Wizard Lake	Beaudoin (unpublished), cited in Dyke et al., 2003
AECV-411C	54.517	110.5	550	Lake sediments	11,830 ± 330	14,896–13,063	Moore Lake	Hickman and Schweger, 1996
GSC-648	53.238	105.725	442	Lake sediments	11,560 ± 640	15,656–12,079	Prince Albert	Mott, 1973
S-246	50.83333	108.11667	~650	*Mammuthus*[c]	12,000 ± 200	14,645–13,432	Kyle	McCallum and Wittenberg, 1968
AECV-1053C	51.05	115.13333	~1500	Charcoal	11,680 ± 250	14,142–13,051	Bow Corridor	Newton (1991); Dyke et al., 2003
TO-5190	50.39583	114.46667	~1500	Wood in lake sediments[d]	15,670 ± 960	21,773–16,872	Cartwright L	Beierle and Smith, 1998
GSC-2275	50.15833	114.95555	1355	Wood	12,200 ± 160	14,897–13,731	Elkford	Harrison, 1976
OxA-14273	50.083	112	~780	*Equus conversidens*	11,620 ± 150	13,754–13,157	Gertzen site, Vauxhall	Burns, 2010

[a] The ages were calibrated using Oxcal 4.3 (Bronk Ramsey, 2009) with IntCal13 calibration curve (Reimer et al., 2013).
[b] Comments in Dyke et al. (2003): Possible hard-water error.
[c] Comments in Dyke et al. (2003): Questioned by Clayton et al. (1980) but not problematic for deglaciation; bone dates generally too young rather than too old.
[d] Comments in Dyke et al. (2003): Collector regards date as anomalously old for enclosing sediment; however, not improbable for this location (kettle lake).

Erratic 3 CRONUS 3.0 inputs (no erosion, 16 ka, 18 ka, 21 ka)

```
FT3 49.77830 -113.65108 1120 std 2.5 2.65 1 0.000 2015;
    FT3 Be-10 quartz 162270 4660 07KNSTD;
FT3-16 49.77830 -113.65108 1120 std 2.5 2.65 1 0.00066 2015;
    FT3-16 Be-10 quartz 162270 4660 07KNSTD;
FT3-18 49.77830 -113.65108 1120 std 2.5 2.65 1 0.00145 2015;
    FT3-18 Be-10 quartz 162270 4660 07KNSTD;
FT3-21 49.77830 -113.65108 1120 std 2.5 2.65 1 0.00225 2015;
    FT3-21 Be-10 quartz 162270 4660 07KNSTD;
```

Erratic 3 CRONUS 3.0 inputs (no erosion, 16 ka, 18 ka, 21 ka)

```
FT8 50.10248 -113.78622 1132 std 2 2.65 1 0.000 2015;
    FT8 Be-10 quartz 165040 5120 07KNSTD;
FT8-16 50.10248 -113.78622 1132 std 2 2.65 1 0.00068 2015;
    FT8-16 Be-10 quartz 165040 5120 07KNSTD;
FT8-18 50.10248 -113.78622 1132 std 2 2.65 1 0.00146 2015;
    FT8-18 Be-10 quartz 165040 5120 07KNSTD;
```

FT8-21 50.10248 -113.78622 1132 std 2 2.65 1 0.00227 2015;

FT8-21 Be-10 quartz 165040 5120 07KNSTD;

5. Conclusions

Optically stimulated luminescence exposure dating opens new horizons for late Quaternary dating applications, offering the ability to date $<10^2$-10^4 year exposed rock surfaces. The framework of the dating technique, in using the first order model, calculates an exposure age from the shape of OSL versus depth trends measured from rock surface cores, which are correlated to parameters for subsurface light attenuation and a simplified luminescence bleaching rate. The exposure dating technique is still fairly novel, and faces sampling limitations and data resolution issues. For application, it is required that separate, proximal known age rock surfaces are available to parameterize the attenuation and OSL bleaching rate properties for a rock surface of an unknown age, yet such surfaces are commonly absent at sampling sites. Even with successful surface calibrations, however, the millimeter data resolution of depth profiles, offered from wafer slice OSL measuring techniques, prevents precise age calculations, limiting the dating technique's viability.

To improve sampling and measuring limitations for the technique, and to assist in evaluating the viability of the first order model for dating, two alternative measuring and sampling protocols were trialed on 11 year and millennial-decamillennial exposed rock surfaces. This includes the use of lab-controlled surface exposed samples for rock surface parameter calibration, to eliminate the need for known age rock sources on site for dating, as well as the use of spatially resolved OSL laser scanning for depth profile measurements to attempt producing more resolute OSL depth profiles for dating applications. Complementing the spatially resolved OSL measures are assessments on identifying and filtering non-quartz mineralogy in regions recording high OSL counts regions, and determining if such filtering procedures can refine parameter precision and data resolution.

The first round of trial applications focuses on performing controlled exposure experiments for parameter sampling on 11-year exposed surfaces from Lane Mountain Quarry, Washington State. Wafer data was acquired from the sampled cores, where both natural light and simulated light controlled exposures were performed on samples acquired from the rock surface to be dated, to compare the depth profile evolutions and parameters against proximal rock samples acquired from the site. For the controlled exposure trial, the use of wafer data produced low precision uncertainties for rock surface parameterization, with ranges magnitudes greater than the fitted median results. The results, in response, are evaluated conservatively, with calls for more resolute measuring techniques to verify the observed trends. Individual core parameterizations across all samples displayed variability, indicating inconsistent sample characteristics regardless of sampling source. The calculated age results found that parameter values from natural sunlight controlled exposures produced annal to decadal surface ages, in similar magnitude to the annal to centennial ages produced from proximal rock parameters. Parameters acquired from simulated sunlight controlled exposed cores produced age ranges from centennial to decamillennial age for the 11-year exposed rock. With more resolute measuring techniques, the promising results of the controlled exposure technique can be verified.

The results of wafer derived controlled exposures justified a second trial at Lane Mountain with the use of spatially resolved OSL laser scanning measurements, to see if the measuring technique can improve the resolution of depth profiles and precision of parameterizations for exposure dating. Through this second part of the trial, spatially resolved OSL was retrieved from each 11-year exposed core, and the parameters from these data were compared with the parameter results from the wafer derived depth profiles. From this assessment, it was found that individual datum error in depth profiles were higher with spatially resolved OSL data, however the precision of

parameter fits improved when using spatially resolved OSL depth profile data. The measuring techniques were also conducted on the controlled exposed cores, however the samples were too low in OSL sensitivity to produce viable depth profiles for parameter and age extrapolation. As such, age calculations were performed on the 11 year exposed samples using the spatially resolved OSL with proximal rock fitting techniques, where results produced inconsistencies in ages between known age surfaces of rocks P and HRQ, but with improved calculated precision. Combined core age fits using scan data produced more accurate age results than from individual core fits generally, but with comparable precision to that of individual core fits. Still, inconsistencies in age fitting, even in using spatially resolved data, are likely to be produced when using proximal rock surfaces for exposure dating parameterization. The results, albeit from a limited sample size, indicate there is potential in combining data from multiple cores of the same surface to produce generalized parameter values for the surface that improve the accuracy of age calculations.

The spatially resolved data also recorded regions of high OSL which contributed to high scatter of the depth profile form in some samples. In response, the mineralogy in zones where high OSL measurements were identified using SEM-EDS imaging to determine if the source of OSL scatter in the depth profile data is derived from non-quartz minerals. In the case that regions hosted non-quartz mineralogy, a modified dataset was produced which incorporated OSL that did not include the high OSL non-quartz regions. These anomaly filtered depth profiles produced generally smoother depth profile trends, with anomaly affected data having their OSL error bounds reduced. However, parameter fits remained mostly similar to that of the nonfiltered scan fits, with precision improving only slightly for some of the depth profiles. Proximal age calculations were also performed using the scan filtered datasets, where fit precisions were

generally comparable with a slight improvement to fit results using nonfiltered scan depth profiles.

The positive precision results in using spatially resolved OSL, coupled with the promising controlled exposure trial at Lane Mountain, motivate an application to date the millennial-decamillennial exposed surfaces the Foothills Erratics Train, Canada. The application uses controlled exposure experiments under simulated light to determine if such a technique can adequately parameterize rock surfaces, or if other parameters such as angles of illumination and variations in photon flux need to be considered for more effective controlled exposures. Further, the application provides insight on dating longer term exposures, with the spatially resolved data offering insights on the impacts of surface coverage and weathering rinds to depth profile development, as well as other unaccounted for parameters including erosion.

Age results of the Erratics Train samples produced sub-annual to centennial ages, in counter to the expected millennial-decamillennial surface ages presented from ^{10}Be data for the erratics. The scatter in data and the constant flux, unidirectional simulated light sources for controlled exposures produced parameters with poor precision for dating applications, yet other unaccounted for parameters are speculated to possibly contribute to age discrepancies. For instance, there were observed discrepancies of attenuation parameters fitted from weathered and nonweathered surfaces, which may indicate that weathering rinds have an impact on depth profile evolution that is not accounted for in the dating model. In response, multi-order parameterizations for luminescence bleaching and light attenuation may be needed for more accurate age calculations. Further, the approach in acquiring parameters for dating involves fitting depth profiles, which may provide inaccurate parameters against the true physical conditions of light exposure and the sample's properties. It was observed that physically

measured values for light attenuation and luminescence bleaching performed in this study were not equal to fitted parameter counterparts from the same Erratics Train samples. As such, future applications should use physical measures of parameters instead of relying on curve fitting for extrapolation. Third is that erosion rates, which are likely to impact depth profile evolution, are unaddressed in the calculated ages. Depth profiles from the natural exposed erratic surfaces were much shallower than expected, which may be the result of erosion eliminating the original depth profile history of the rock surface. If erosion rates from ^{10}Be data were realistic, it is likely that most of the original depth profile form after 10ka of exposure would be removed from the surface, producing shallower than expected depth profiles and younger than expected ages. Future applications concerning longer term exposure ages should consider metrics for erosion in evaluating the age calculations of sampled surfaces.

The results of the Erratics Train did not provide the expected ages for the site and provide little in the interpretation of the Erratics Train deposition, but do provide insightful results in how depth profiles are generated in samples over millennial-decamillennial timescales. Continued trials and experiments in parameterizing rock surfaces for OSL exposure dating that also concern surface coverage, erosion, and variations in light flux and illumination angles can improve the understanding of the limits and applicable scope of the dating technique for geological surface dating applications.

The trials at Lane Mountain and the Foothills Erratics Train show that OSL exposure dating benefits from using spatially resolved OSL for parameter extrapolation. The use of this higher resolution data offers improved insight on the limits of the dating technique than what millimeter wafer datasets offer, and documents the complex reality of depth profile evolution for both decadal and millennial-decamillennial exposure settings. Parameter fit precision was also

improved when utilized and compared against wafer datasets. Further, the use of spatially resolved data also offered the ability to identify areas of OSL anomalies, allowing for mineralogy to be identified which could contribute to OSL scatter in depth profile data.

Generally, there is still promise in using controlled exposures for parameter extrapolations if solar conditions can be replicable with controlled exposures. The results in using controlled exposure experiments at both sites show that single rate assumptions of luminescence bleaching may be too simple for defining depth profile evolution in rock samples for some applications, given that unidirectional light and constant applied photon fluxes were not able to adequately emulate natural sunlight exposure for the applied samples. Further, the use of natural light controlled exposures did show promising use in the Lane Mountain study, indicating that surface exposures which account for natural sunlight variations may be more effective for parameterization. In recognizing these implications, more specific, multi-order parameters concerning luminescence bleaching with respect to light flux, illumination angle, and variations in photoionization cross sections may be needed to parameterize depth profiles more accurately for exposure dating purposes. However, the impact of erosion also likely needs to be considered when dating rock surfaces over millennial age, to where controlled exposures as conducted would not be able to account for these impacts. Physical or controlled applied experiments on examining erosion and the impact on the depth profile form are warranted to evaluate how to best quantify this parameter for exposure dating study beyond millennial ages. Further, these experiments can be used to determine methods for quantifying erosion rates for rock surfaces exceeding millennial age, or when applicable, to be used in tandem with other longer term exposure dating chronometers.

In using spatially resolved OSL, continued trials of controlled exposure experiments can offer more precise characterizations of light exposure properties that implicate the shape of the OSL depth profile. Further, a motivation to physically measure parameters such as light attenuation and photoionization cross sections from rock surfaces can help validate current and novel model forms for exposure dating applications, and provide more quantitative insight on how depth profiles evolve over time. Specific physical experiments on angles of illumination, variations in photon flux, light attenuation, and photoionization cross section values can provide more insight on developing appropriate models for luminescence exposure dating.

The use of spatially resolved OSL and controlled exposure experiments can improve the effectiveness of continued research in establishing adequate parameterizations for exposure dating. Further, the number of studies with OSL exposure dating can be expanded with these techniques, offering new insights on the nature of OSL depth profile evolution. Continued research with these tools will provide the means to substantiate OSL exposure dating as an established geochronometer.